



**HAL**  
open science

# Metal-oxide-semiconductor capacitor for diamond transistor : simulation, fabrication and electrical analysis

Aurélien Maréchal

► **To cite this version:**

Aurélien Maréchal. Metal-oxide-semiconductor capacitor for diamond transistor : simulation, fabrication and electrical analysis. Micro and nanotechnologies/Microelectronics. Université Grenoble Alpes, 2015. English. NNT : 2015GREAT094 . tel-01250367

**HAL Id: tel-01250367**

**<https://theses.hal.science/tel-01250367>**

Submitted on 4 Jan 2016

**HAL** is a multi-disciplinary open access archive for the deposit and dissemination of scientific research documents, whether they are published or not. The documents may come from teaching and research institutions in France or abroad, or from public or private research centers.

L'archive ouverte pluridisciplinaire **HAL**, est destinée au dépôt et à la diffusion de documents scientifiques de niveau recherche, publiés ou non, émanant des établissements d'enseignement et de recherche français ou étrangers, des laboratoires publics ou privés.

## THÈSE

Pour obtenir le grade de

### **DOCTEUR DE L'UNIVERSITÉ GRENOBLE ALPES**

Spécialité : **Nano Electronique Nano Technologies (NENT)**

Arrêté ministériel : 7 août 2006

Présentée par

**Aurélien MARÉCHAL**

Thèse dirigée par **Etienne GHEERAERT** et  
co-dirigée par **Nicolas ROUGER** et  
co-encadrée par **Julien PERNOT**

préparée au sein du **Institut Néel / Grenoble Electrical  
Engineering Lab (G2ELab)**  
dans **Electronique, Electrotechnique, Automatique et  
Traitement du signal (EEATS)**

## **Metal-Oxide-Semiconductor capacitor for diamond transistor: simulation, fabrication and electrical analysis**

Thèse soutenue publiquement le **27 Novembre 2015**,  
devant le jury composé de :

**M. Philippe BERGONZO**

Directeur de recherche, CEA (France), Rapporteur

**M. Etienne GHEERAERT**

Professeur, Université Joseph Fourier (France), Directeur de thèse

**M. Philippe GODIGNON**

Professeur, Centro Nacional de Microelectrónica (Espagne), Membre

**M. Julien PERNOT**

Maître de conférences, Université Joseph Fourier (France), co-encadrant

**M. Dominique PLANSON**

Professeur, INSA Lyon (France), Rapporteur

**M. Nicolas ROUGER**

Chargé de recherches (HDR), G2Elab (France), co-directeur de thèse

**Mme Tanya TRAJKOVIC**

CEO, Cambridge Microelectronics Ltd. (United Kingdom), Membre

**M. Christophe VALLÉE**

Professeur, Université Joseph Fourier (France), Président

**M. Satoshi YAMASAKI**

Professor, University of Tsukuba and AIST (Japon), invité





# Contents

<b>List of Figures</b>	<b>vii</b>
<b>List of Tables</b>	<b>xvii</b>
<b>Introduction</b>	<b>1</b>
<b>1 Diamond: the future of power electronics</b>	<b>5</b>
1.1 Context of Power Electronics . . . . .	6
1.2 Wide band gap materials . . . . .	7
1.3 Diamond: the ultimate semiconductor . . . . .	11
1.4 State of the art of diamond devices . . . . .	20
1.5 On the need for reliable simulation tools . . . . .	26
1.6 Conclusion . . . . .	27
<b>2 Diamond electrical properties and ideal MOS concepts</b>	<b>29</b>
2.1 Introduction . . . . .	30
2.2 Diamond properties: Numerical models . . . . .	31
2.2.1 Temperature dependent band gap and intrinsic carrier concentration	31
2.2.2 Incomplete ionization of dopants . . . . .	34
2.2.3 Empirical mobility model . . . . .	40
2.2.4 Shockley-Read-Hall and Auger recombination models . . . . .	41
2.2.5 Summary . . . . .	42
2.3 Ideal MOS capacitor theory . . . . .	43
2.3.1 Metal-Oxide-Semiconductor principle of operation . . . . .	44
2.3.2 Identification of MOS working regimes through the $Q\Psi$ graph . . . . .	47
2.3.3 MOS capacitance-voltage characteristics . . . . .	50
2.3.3.1 Ideal MOS $C(V)$ characteristics . . . . .	50
2.3.4 Summary . . . . .	55
2.4 Conclusions . . . . .	55
<b>3 Diamond device simulations</b>	<b>57</b>
3.1 Introduction . . . . .	58
3.2 Mathematical models . . . . .	59
3.3 Modelling of a diamond p-n junction . . . . .	60
3.3.1 p-n junction characteristics . . . . .	61
3.3.2 Carrier density profiles . . . . .	62
3.3.2.1 Low injection regime . . . . .	64
3.3.2.2 High injection regime . . . . .	65

3.3.2.3	SRH lifetimes and Auger recombination parameters influence	66
3.3.2.4	Reverse characteristic and breakdown voltage	70
3.3.2.5	Hopping mobility model	72
3.3.3	Summary	76
3.4	Modelling of a diamond metal-oxide-semiconductor field effect transistor	77
3.4.1	Historical framework of the MOSFET <sup>1</sup>	77
3.4.2	MOSFET working principle	78
3.4.3	Design of a planar inversion MOSFET	82
3.4.3.1	Design using TCAD Silvaco	83
3.4.3.2	Electrical simulations	84
3.4.3.3	Blocking characteristics	89
3.4.4	Summary	93
3.5	Conclusions	96
<b>4</b>	<b>Diamond MOS capacitors fabrication and characterization</b>	<b>99</b>
4.1	Introduction	101
4.2	A brief history of diamond metal-oxide-semiconductor capacitors	102
4.3	Fabrication of diamond MOS capacitors	105
4.3.1	Diamond homoepitaxial growth by MPCVD	105
4.3.1.1	Home-made NIRIM type reactor	105
4.3.1.2	Heavily boron doped layer	106
4.3.1.3	Lightly boron doped layer	107
4.3.1.4	Summary	110
4.3.2	Pseudo vertical diamond MOS capacitor fabrication	111
4.3.2.1	Ohmic contacts fabrication	111
4.3.2.2	MOS gate fabrication	112
4.3.3	Summary	114
4.4	Band alignment investigation of Al <sub>2</sub> O <sub>3</sub> /O-terminated diamond heterostructure	115
4.4.1	Xray photoelectron spectroscopy analysis	115
4.4.2	Energy band diagram	118
4.4.3	Summary	120
4.5	Electrical characterization of diamond MOSCAPs	121
4.5.1	Al <sub>2</sub> O <sub>3</sub> /O-terminated diamond MOSCAPs electronic properties	121
4.5.1.1	Experimental setup	121
4.5.1.2	Impedance model	122
4.5.1.3	Capacitance and conductance analysis of interface states	127
4.5.1.4	Summary	135
4.5.2	Al <sub>2</sub> O <sub>3</sub> /O-terminated diamond MOSCAPs leakage currents analysis	136
4.5.2.1	Temperature dependent trap assisted tunneling	136
4.5.2.2	Results and discussion	140
4.5.3	Summary	142
4.6	Experimental realization of a n-type channel MOSFET	143
4.6.1	Sample structure	143
4.6.2	Experimental setup and electrical characterizations	145

<sup>1</sup>this section is based on the extremely detailed review of C. T. Sah [Sah 1988].

---

4.6.2.1	Experimental setup . . . . .	145
4.6.2.2	Electrical characterizations . . . . .	145
4.6.3	Summary . . . . .	154
4.7	Conclusions . . . . .	154
<b>General conclusion and outlook</b>		<b>157</b>
<b>Résumé de thèse en français</b>		<b>161</b>
<b>Publications</b>		<b>199</b>
<b>Curriculum Vitae</b>		<b>255</b>



# List of Figures

1.1	Example of a smart grid. The efficient transmission and generation of electricity from the source of production to the end point of consumption is ensured by the use of low loss devices which in the near future will be made of WBG semiconductors. . . . .	6
1.2	Roadmap for future power devices [Ohashi 2012]. Si has still an important role to play and constant effort is made to increase the device performances. GaN and SiC power devices will coexist and improve toward high blocking voltage applications. Diamond is predicted to cover high blocking voltage applications (10 kV range). . . . .	8
1.3	Principle of the drift layer design for a non-punch-through device. Here, a p-n junction is represented, however the drift layer resistance does not take into account the carrier injection, i.e. the resistivity modulation is not considered [Rouger 2015]. $-x_{pmax}$ represent the maximum expansion of the space charge region in the p-type region. . . . .	13
1.4	Illustration of the advantage of WBG semiconductors over Si in terms of the $R_{onS}$ vs. $BV$ trade off [Rouger 2015]. WBG semiconductors show smaller contact areas as well as thinner drift region (represented by the double side arrow). . . . .	15
1.5	Scaling of Fig.1.4 considering a blocking voltage of 1 kV [Rouger 2015]. Among WBG semiconductors, diamond is unbeatable in terms of size. . . . .	15
1.6	Specific on-resistance as a function of the breakdown voltage for Si, SiC and diamond in the case of vertical unipolar device [Umezawa 2012]. . . . .	16
1.7	Illustration of the different contributions to the total resistance in a planar n-channel MOSFET. The total resistance is composed of the contact resistance, the $n^+$ -type resistance, the channel resistance and the drift layer resistance. . . . .	17
1.8	Power losses as a function of the semiconductor area, for a unipolar device with specifications 1200 V/10 A – 35 kHz – $\alpha = 0.5$ . The total losses $P_{tot}$ is the sum of the conduction losses $P_{cond}$ ( $\propto 1/A$ ) and the commutation losses $P_{com}$ ( $\propto A$ ) [Kolar 2012, Rouger 2015]. . . . .	20
1.9	Example of semiconductor area optimization in the case of a vertical unipolar power device with 1200 V/10 A – 35 kHz – $\alpha = 0.5$ . A comparison is made between Si, SiC, GaN and diamond. a) A reduction in the $R_{onS}$ results in a reduced semiconductor area and an improvement of the power losses in the power device. b) Even though an increase of the switching frequency ( $f_{WBG} = 100 \times f_{Si}$ ) does not result in a significant reduction of the power losses, the semiconductor area is reduced [Rouger 2015]. . . . .	21

1.10	Energy band configuration of the Al <sub>2</sub> O <sub>3</sub> /H-diamond heterojunction as determined by X-ray photoelectron spectroscopy [Liu 2012]. The resulting alignment is of type II. . . . .	23
1.11	Type I band diagram configuration of the Al <sub>2</sub> O <sub>3</sub> /O-diamond heterojunction deduced from the electron affinity method. . . . .	24
1.12	a) Al/Al <sub>2</sub> O <sub>3</sub> /O-diamond MOS schematic view and corresponding SEM image and b) cross section showing the stack [Chicot 2013b]. . . . .	24
1.13	a) C(V) characteristic of the Al/Al <sub>2</sub> O <sub>3</sub> /O-diamond MOSCAP for various frequencies. b) 1/C <sup>2</sup> (V) plot showing constant slope for deep depletion regime [Chicot 2013a]. Measurements were performed at 300 K. The 20 nm thin Al <sub>2</sub> O <sub>3</sub> layer was deposited at 100 °C by ALD. The gate contact diameter is 200 μm. . . . .	25
1.14	a) Hysteresis behavior of the C(V) characteristic at 100 kHz when biasing the structure from accumulation to deep depletion and from deep depletion to accumulation. b) Current-voltage I(V) characteristic of the device showing leakage currents [Chicot 2013a]. The 20 nm thin Al <sub>2</sub> O <sub>3</sub> layer was deposited at 100 °C by ALD. . . . .	25
2.1	Temperature dependence of diamond band gap energy. Open circles represent the data taken from [Clark 1964] and the solid line is obtained by using Eq.2.1 with the parameters from Tab.2.1 . . . . .	32
2.2	Temperature dependence of the intrinsic carrier concentration in diamond, 4H-SiC, GaN and Si taking into account the temperature dependence of the band gap energy. At 300 K the intrinsic concentrations are 2×10 <sup>-27</sup> cm <sup>-3</sup> , 3×10 <sup>-8</sup> cm <sup>-3</sup> and 3×10 <sup>-10</sup> cm <sup>-3</sup> for diamond, 4H-SiC and GaN respectively, whereas in the case of Si $n_i = 1 \times 10^{10}$ cm <sup>-3</sup> . . . . .	35
2.3	Activation energy of dopants as a function of the impurity concentration in diamond. The experimental boron activation energies are taken from the literature [Okano 1989, Fujimori 1990, Visser 1992, Windheim 1993, Borst 1995, Deguchi 1996, Lagrange 1999, Klein 2007, Gajewski 2009, Volpe 2009] and the solid curve is drawn after Pearson and Bardeen law [Pearson 1949]. Phosphorus activation energies are taken from the literature [Koizumi 1997, Kato 2005, Kato 2007, Pinault 2007, Kato 2008, Pinault-Thaury 2011, Stenger 2013]. Its value is assumed to be constant over the entire doping range. . . . .	37
2.4	Carrier concentration as a function of 1000/T for n-type diamond, p-type diamond, n-type 4H-SiC and n-type GaN. The compensation was set to 10%. The energy band gap temperature dependence was taken into account both for diamond (see Eq.2.1) and 4H-SiC, $E_g^{4H-SiC}(eV) = 3.265 - 3.3 \times 10^{-2} T^2 / (10^5 + T)$ , $E_g^{GaN}(eV) = 3.47 - 7.7 \times 10^{-4} T^2 / (600 + T)$ . . . . .	38
2.5	Schematic diagram illustrating the dopant ionization energies for Si, 4H-SiC, GaN and Diamond, for both n-type (donors) and p-type (acceptors) dopants. Also indicated are the ionization ratios in each case. . . . .	39
2.6	Theoretical a) hole and b) electron mobility calculated at 300 K and 500 K using the empirical model from [Volpe 2009, Pernot 2008]. . . . .	41
2.7	Shockley-Read-Hall (SRH) and Auger recombination process. $E_t$ is the trap energy where the electron-hole pair recombines. Auger recombination involves three particles, an electron and a hole which recombine and give off the energy to a third particle, an electron in the present exemple. . . . .	41

2.8	a) Metal-oxide-semiconductor capacitor (MOSCAP) and b) the corresponding energy band diagram in flat band condition with a gate voltage bias $V = 0V$ for a p-type semiconductor. The origin of the axis is taken at the oxide/semiconductor interface. . . . .	44
2.9	Structure and energy band diagram of a p-type MOSCAP in a) accumulation regime for $V < 0$ , b) depletion regime for small positive bias voltage $V > 0$ and c) inversion regime for high positive bias voltage, with $q > 0$ the elementary charge. . . . .	45
2.10	Energy band diagram at the p-type semiconductor surface. . . . .	48
2.11	Total charge per unit area $Q_{SC}^A$ in the semiconductor as a function of the surface potential $\Psi_s$ for a p-type semiconductor in the case of an ideal MOSCAP. . . . .	49
2.12	Graphical solution of the semiconductor charge per unit area as a function of the gate voltage for an ideal MOS structure. For a given gate bias voltage $V_G$ , the surface potential $\Psi_s$ is given by the abscissa at the intersection between the curve of Eq.2.11 (blue curve) with the straight line of Eq.2.37 (dashed red line). . . . .	50
2.13	Simple equivalent circuit of the MOS capacitor with the bias independent oxide capacitor $C_{ox}$ and bias dependent semiconductor capacitance $C_s$ . . . . .	51
2.14	Behavior of the equilibrium MOS differential capacitance. . . . .	52
2.15	Theoretical $C(V)$ characteristic of an ideal MOSCAP. . . . .	52
2.16	a) Charge per unit area $Q_{SC}^A$ as a function of the surface potential $\Psi_S$ in the diamond MOSCAP calculated from Eq.2.36. b) Corresponding capacitance vs. voltage ideal characteristic, with $N_A = 2 \times 10^{17} \text{ cm}^{-3}$ , $V_{FB} = -2.5$ , $A = 9 \times 10^{-4} \text{ cm}^2$ and $\epsilon_{ox} = 9$ . . . . .	55
3.1	Simplified p-n junction structure for the 1D equation resolution. . . . .	61
3.2	(a) Electric field calculated across the junction at different forward bias voltages. (b) Ionized dopants concentration as a function of the position at different forward bias voltages. The transition between the space charge region and the neutral regions is correctly modeled. (c) Band structure corresponding to the junction at zero bias and $T = 300 \text{ K}$ , where CB and VB corresponds to the conduction band minimum and valence band maximum respectively. . . . .	63
3.3	(a) Hole and electron concentrations for different low forward bias conditions. (b) Band diagram of the simulated p-n junction at $300 \text{ K}$ for $V_{bias} = 4 \text{ V}$ , showing constant $q-FL$ , $E_{Fp}$ and $E_{Fn}$ respectively. . . . .	64
3.4	(a) Hole and electron concentrations for different high forward bias conditions. In the $n^+$ -type region, the hole concentration is higher than the electron concentration. (b) Band diagram of the simulated p-n junction at $300 \text{ K}$ for $V_{bias} = 7 \text{ V}$ , showing band bending in the structure. . . . .	66
3.5	Simulated $J(V)$ characteristics at different temperatures without using SRH nor Auger models. The experimental $J(V)$ characteristic (open circles), measured at room temperature and reported in [Koizumi 2013], was used to validate the models and parameter values. The numerical precision limit is approximately $10^{-11} \text{ A.cm}^{-2}$ and the high injection threshold is $4.7 \text{ V}$ . . . . .	67

3.6	Effect of the SRH lifetimes ( $\tau = \tau_p = \tau_n$ ) on the carrier concentrations in the (a) low ( $V_{bias} = 1$ V) and (b) high ( $V_{bias} = 7$ V) injection regime. The simulations were done at 300 K and for a constant value of $\Gamma_p = \Gamma_n = 10^{-30}$ cm <sup>6</sup> .s <sup>-1</sup> . . . . .	68
3.7	Effect of the Auger recombination parameter ( $\Gamma = \Gamma_p = \Gamma_n$ ) on the carrier concentrations in the (a) low ( $V_{bias} = 1$ V) and (b) high ( $V_{bias} = 7$ V) injection regime. The temperature was set to 300 K and the SRH lifetimes were $\tau_p = \tau_n = 10^{-9}$ s. . . . .	68
3.8	(a) Influence of the SRH lifetimes ( $\tau = \tau_p = \tau_n$ , $\Gamma = 10^{-30}$ cm <sup>6</sup> .s <sup>-1</sup> ) on the simulated J(V) characteristics. (b) Simulated J(V) characteristics for different Auger parameter values ( $\Gamma = \Gamma_p = \Gamma_n$ , $\tau = 10^{-9}$ s), $T = 300$ K. . . . .	69
3.9	Fit of the experimental J(V) characteristic reported in [Koizumi 2013], at 300 K with a contact resistance $R_{contact} = 10$ $\Omega$ .cm <sup>2</sup> and $\tau = \tau_p^{SRH} = \tau_n^{SRH} = 2 \times 10^{-10}$ s. This value is calculated according to the diffusion length of holes reported by Kato et al. [Kato 2013] using $L_h = \sqrt{D\tau}$ , where D is the diffusion coefficient, $D = k_B T \mu / q$ . The ideality factor $n$ of the experimental I(V) is 3.5. . . . .	70
3.10	Theoretical reverse J(V) breakdown characteristic of the simulated diamond p-n junction. The simulation end condition was chosen by setting a compliance current of $1 \times 10^{-2}$ A.cm <sup>-2</sup> . The insert represents the electric field as a function of the depth at breakdown. The maximum electric field is 7.7 MV.cm <sup>-1</sup> . . . . .	73
3.11	Resistivity calculated from a uniform 1D n-type diamond layer taking into account the combined effect of band and hopping mechanisms (solid line) compared to the band conduction mechanism (dashed line). . . . .	75
3.12	Calculated resistivity as a function of $1000/T$ for $N_D = 8 \times 10^{19}$ cm <sup>-3</sup> at different compensation values. The open circles represent the experimental data reported in [Oyama 2009]. . . . .	75
3.13	Schematic structure of an n-type channel MOSFET. $L$ , $W$ and $t_{ox}$ represent the gate length, the gate width and the oxide thickness respectively. . . . .	78
3.14	Threshold voltage calculated at 300 K from Eq.3.19, showing the p-type doping level $N_A$ and oxide thickness $t_{ox}$ influence. . . . .	80
3.15	Local inversion charge as a function of the surface potential [Vincent 2008]. The current is proportional to the area $A_{Q\Psi}$ delimited by the two vertical lines $2\Psi_b$ and $2\Psi_b + V_{DS}$ , the square root of depletion and the oxide capacitance straight line. . . . .	81
3.16	a) $I_{DS}$ vs. $V_{DS}$ characteristic of the simulated diamond MOSFET with $N_A = 10^{15}$ cm <sup>-3</sup> , $t_{ox} = 20$ nm and $T = 300$ K. The curve is characterized by the linear increase of $I_{DS}$ (linear regime), followed by the saturation when $V_{DS} = V_{DSAT} = V_{GS} - V_{th}$ . b) Corresponding $I_{DS}$ vs. $V_{GS}$ characteristic (transconductance) with $V_{DS} = 1$ V. . . . .	83
3.17	Structure of the simulated planar MOSFET. The Source and Back gate contact are short circuited and grounded. . . . .	84
3.18	a) Transconductance characteristic $I_{DS}$ vs. $V_{GS}$ for $V_{DS} = 1$ V, $N_A = 10^{15}$ cm <sup>-3</sup> , $t_{ox} = 20$ nm, simulated for temperatures ranging from 300 K to 600 K. b) Corresponding threshold voltage as a function of temperature. . . . .	86
3.19	Electron concentration as a function of the depth to the oxide/diamond interface extracted at various temperatures. The simulation was performed with $N_A = 10^{15}$ cm <sup>-3</sup> , $t_{ox} = 20$ nm, $V_{DS} = 2$ V and $V_{GS} = 10$ V. . . . .	86

3.20 a) $dI_{DS}/dV_{GS}$ vs. $V_{GS}$ for $V_{DS} = 1$ V, $N_A = 10^{15}$ cm <sup>-3</sup> , $t_{ox} = 20$ nm, simulated for temperatures ranging from 300 K to 600 K. b) Corresponding $d^2I_{DS}/dV_{GS}^2$ vs. $V_{GS}$ . The threshold voltage is extracted from the maximum value of the $d^2I_{DS}/dV_{GS}^2$ plot. The negative values of the $d^2I_{DS}/dV_{GS}^2$ plot are omitted. . . . .	87
3.21 a) $I_{DS}$ vs. $V_{GS}$ characteristic for $V_{DS} = 1$ V, $T = 300$ K, $t_{ox} = 20$ nm, simulated for gate oxide thicknesses ranging from 20 nm to 200 nm. b) Corresponding threshold voltage as a function of the oxide thickness. The simulation was performed for a doping level of $10^{15}$ cm <sup>-3</sup> at a temperature of 300 K. . . . .	87
3.22 a) $I_{DS}$ vs. $V_{GS}$ characteristic for $V_{DS} = 1$ V, $T = 300$ K, $t_{ox} = 20$ nm, simulated for p-type doping concentrations ranging from $10^{15}$ cm <sup>-3</sup> to $10^{18}$ cm <sup>-3</sup> . b) Corresponding threshold voltage as a function of the p-type doping concentration. The simulation was performed for a gate oxide thickness of 20 nm at a temperature of 300 K. . . . .	88
3.23 2D simulated diamond MOSFET structure showing the potential distribution (color plot) and the current distribution (current flowlines) for a doping level of a) $10^{15}$ cm <sup>-3</sup> and b) $10^{18}$ cm <sup>-3</sup> , a gate oxide thickness of 20 nm and at 300 K. . . . .	89
3.24 a) Electron concentration as a function of the depth to the oxide/diamond interface for p-type doping level ranging from $10^{15}$ cm <sup>-3</sup> to $10^{18}$ cm <sup>-3</sup> for $V_{DS} = 2$ V, $V_{GS} = 10$ V, $t_{ox} = 20$ nm and $T = 300$ K. b) Corresponding band diagram of the MOS contact in the strong inversion regime for $N_A = 10^{15}$ cm <sup>-3</sup> and c) $N_A = 10^{18}$ cm <sup>-3</sup> . . . . .	90
3.25 a) $I_{DS}$ vs. $V_{DS}$ characteristic of the simulated diamond MOSFET with $V_{GS} = 0$ V and $T = 300$ K. In this $V_{DS}$ range, due to the very low intrinsic carrier concentration, the leakage currents are extremely small. b) Electric field at the oxide surface near the gate contact, with $V_{DS} = 2, 10, 50$ and $200$ V. . . . .	91
3.26 Electric field distribution in the simulated 2D diamond MOSFET for an oxide thickness of 200 nm, a p-type doping level of $10^{15}$ cm <sup>-3</sup> and a temperature of 300 K at a) $V_{DS} = 50$ V and b) $V_{DS} = 200$ V . . . . .	92
3.27 Potential and leakage currents flow lines distributions in the 2D diamond MOSFET structure, $V_{DS}$ ranging from 10 V to 300 V. . . . .	94
3.28 $I_{DS}$ vs. $V_{DS}$ characteristic of the simulated diamond MOSFET with $V_{GS} = 0$ V and $T = 300$ K. When $V_{DS}$ reaches a value close to 290 V, $I_{DS}$ increases, inducing the turn-on of the transistor. . . . .	95
3.29 Potential diamond MOSFET structures envisioned for next generation power device applications. . . . .	96
3.30 Specific on-resistance as a function of the breakdown voltage. The Si limit is calculated through Baliga's law as $R_{on}S = 8.37 \times 10^{-9} \cdot BV^{2.5}$ [Baliga 2012]. . . . .	97
4.1 Schematic cross section (left) of the fabricated diamond MOSCAP and the corresponding actual device (right). . . . .	101

4.2	a) Capacitance vs. bias voltage and b) $1/C^2$ vs. bias voltage for the (001) substrate taken from [Geis 1991]. The measurement temperature was 250 °C and the ac signal frequency 10 kHz. The inset of a) shows the energy band diagram of the structure biased into depletion and the one in b) is a schematic of the diamond MOSCAP. . . . .	103
4.3	a) Schematic view of the home-made NIRIM type MPCVD reactor. b) Picture of the growth chamber [Fiori 2012]. . . . .	106
4.4	Boron incorporation as a function of the [B]/[C] ratio in the gas mixture for various $[CH_4]/[H_2]$ ratios, taken from [Fiori 2012] . . . . .	107
4.5	Typical surface morphology of the heavily boron doped diamond layer with mean roughness $Sa = 0.22$ nm and Root Mean Square (RMS) $Sq = 0.27$ nm. . . . .	107
4.6	Secondary Ion Mass Spectroscopy profile of the sample prepared for the doping concentration calibration. . . . .	109
4.7	Typical surface morphology of the p-type boron doped layer with $Sa = 0.46$ nm and $Sq = 0.82$ nm on the $127 \times 95 \mu m^2$ area. . . . .	110
4.8	Schematic describing the ohmic contacts fabrication process. . . . .	112
4.9	I(V) characteristic of the ohmic contact deposited on heavily boron doped diamond. The contact resistance is of the order of 25 $\Omega$ . The value is extracted from the slope of the I(V) characteristic measured between the two ohmic contacts. . . . .	113
4.10	Schematic describing the MOS contact fabrication steps. . . . .	114
4.11	Schematic cross section of the samples prepared for the XPS analysis. . . . .	116
4.12	C 1s spectrum of the 2 nm thick $Al_2O_3$ layer deposited on O-diamond. The relevant component is the C-Al binding energy which is $284.08 \pm 0.2$ eV. . . . .	117
4.13	C 1s spectrum of the O-diamond sample. The different peaks are attributed to $sp^3$ (C-C), $CH_x$ , ether (C-O-C) and carbonyl (C=O) group respectively. . . . .	118
4.14	Al $2p_{3/2}$ spectrum of the 20 nm thick $Al_2O_3$ sample. The binding energy between the aluminum atom and the oxygen atom is measured as $74.35$ eV $\pm 0.2$ . . . . .	118
4.15	Valence band spectra for the O-diamond and the $Al_2O_3$ (20 nm). The valence band maxima are respectively $2.07 \pm 0.2$ eV and $3.20 \pm 0.2$ eV. . . . .	119
4.16	a) Al $2p$ core level and the valence band of the dielectric layer. b) When the 2 nm thin $Al_2O_3$ is brought in contact with the O-diamond surface, the valence band discontinuity $\Delta E_V$ develops. c) C 1s core level together with the valence band of the O-diamond. . . . .	119
4.17	Schematic energy band diagram of the $Al_2O_3$ /O-diamond with Ti in contact with the oxide layer, deduced from XPS measurement. The valence band offset is $1.34 \pm 0.2$ eV and the conduction band offset is $0.56 \pm 0.2$ eV. The oxide band gap value is taken from [Kim 2006]. . . . .	120
4.18	Picture of the probe station used for I(V) and C(V) characterization of the samples. The sample characterization is made under vacuum ( $<10^{-3}$ Torr) and in the dark to avoid any effects due to optical excitation. The temperature is controlled with a Linkam cooling system from liquid nitrogen temperature to 600 °C. . . . .	122

4.19	Equivalent models used to extract the capacitance from the impedance measurement, respectively a) the three elements equivalent circuit, b) the series $C_s R_s$ equivalent circuit and c) the parallel $C_p R_p$ equivalent circuit. . . . .	123
4.20	a) Schematic cross section showing the MIMCAP characterization procedure (left) and picture of the $\text{Al}_2\text{O}_3/\text{O}$ -diamond MOSCAP (right) showing the MIM, MOS and ohmic contacts respectively. b) $C(V)$ characteristic of the MIMCAP measured at 300 K with small signal parameters $f = 1$ kHz and $V_{ac} = 50$ mV. c) $C(f)$ curve showing no clear frequency dependence of the capacitance over the range 100 Hz to 2 MHz. d) $J(V)$ characteristic of the MIMCAP. These measurements were performed on a circular contact with diameter of 100 $\mu\text{m}$ . . . . .	124
4.21	a) $C(V)$ curve measured for frequencies ranging from 1 kHz to 1 MHz at 300 K. b) $1/C^2$ plot used to extract the flat band voltage and the doping concentration. c) Imaginary part $-X(\omega)$ as a function of the real part $R(\omega)$ of the complex impedance, high and low referring to the high and low frequency conditions. The fit corresponds either to the three d) or to the five e) element equivalent circuit. . . . .	125
4.22	a) Equivalent circuit with interface traps. b) At low frequency $R_{it}$ is set to zero whereas c) at high frequency $C_{it}$ tends to infinity such that the $R_{it}C_{it}$ branch of a) is ignored. . . . .	128
4.23	Normalized high frequency experimental $C(V)$ curve (1 MHz) compared to the calculated ideal one with $N_A = 2.3 \times 10^{17} \text{ cm}^{-3}$ , $N_D = 10^{16} \text{ cm}^{-3}$ and $V_{FB} = -7.1$ V. The insert is a zoom in where $\Delta V$ is indicated. . . . .	130
4.24	Interface states density as function of the energy, distributed inside the diamond band gap, extracted using Terman's method [Schroder 2006]. . . . .	131
4.25	Energy band diagram of the MOSCAP biased into accumulation in the presence of interface traps density $D_{it}$ . Electron-occupied interface traps are represented by the small horizontal heavy lines whereas the unoccupied ones are represented by the light lines. . . . .	132
4.26	Equivalent parallel conductance $G_p/\omega$ as a function of $\omega$ measured under bias voltage of -8 V and at a temperature of 300 K. . . . .	133
4.27	Equivalent circuits for conductance measurements. . . . .	134
4.28	$\ln [1/\nu_{th}\tau_{it}N_v]$ as a function of temperature (reciprocal axis). The slope of the linear fit is proportional to the trap capture cross section and found to be $3 \times 10^{-18} \text{ cm}^2$ . . . . .	136
4.29	$J(V)$ characteristics of a circular MOSCAP with diameter of 150 $\mu\text{m}$ measured at various temperatures. A specific feature is the absence of leakage currents in the depletion regime. . . . .	137
4.30	Energy band diagram of the $\text{Al}_2\text{O}_3/\text{O}$ -diamond MOSCAP established using nextnano. The band offsets are adjusted from the XPS measurements [Maréchal 2015]. The trap energy level is depicted and equals 0.7 eV. The top electrode work function is 4.3 eV and corresponds to Ti. A bias voltage of -8 V is applied to the top electrode. . . . .	139
4.31	a) Experimental $J(V)$ characteristics measured at various temperatures for a circular contact with diameter of 150 $\mu\text{m}$ . b) Calculated $J(V)$ characteristics at various temperatures using the TAT model described by Eq.4.21. As evidenced the temperature dependence is stronger for the theoretical $J(V)$ than for the experimental one. . . . .	141

4.32 a) Optical microscope view of the MOSFET sample and b), c) and d) shows a close up on the three different geometries referred to as A, B and C respectively. e) Schematic 3D view. The MOSFET is composed of 4 terminals, the Source $S$ , the Drain $D$ , the Gate $G$ and the Back gate $B$ . The channel length $L$ and width $W$ are also indicated. . . . .	144
4.33 Experimental setup for the MOSFET characterization. 4 independent probes allow to control the bias voltage of the 4 contacts. . . . .	145
4.34 a) $C(V)$ properties of device BI1_3_101 measured as a function of the frequency at a temperature of 300 K. In this frequency range, the $C(V)$ did not show frequency dependence. b) Hysteresis measured on device BI1_3_101. The dc bias sweep rate was set to $250 \text{ mV.s}^{-1}$ and the ac signal amplitude was 50 mV. . . . .	146
4.35 a) $1/C^2$ plot of device BI1_3_101 for frequencies ranging from 50 Hz to 1 MHz. b) Comparison between the experimental and ideal $1/C^2$ plot at 1 MHz with doping concentration of $8 \times 10^{13} \text{ cm}^{-3}$ and flat band voltage of -2.2 V. . . . .	147
4.36 Doping profile ( $N_A - N_D$ ) as a function of depletion layer width $W$ extracted from the measured $C(V)$ at 1 MHz and 300 K. . . . .	148
4.37 Comparison between the experimental 1 MHz $C(V)$ curve (empty dots) and the corresponding ideal characteristic (solid line) for $T = 300 \text{ K}$ . The corresponding oxide relative dielectric constant of 4 was set as well as a doping level of $8 \times 10^{13} \text{ cm}^{-3}$ to fit the accumulation capacitance and the deep depletion capacitance respectively. The flat band voltage was adjusted to -2.2 V. . . . .	149
4.38 Principle of the MOSFET characterization. A bias voltage is applied between the source and drain contacts $V_{DS}$ , while the source and back gate contacts are short-circuited. The gate bias $V_{GS}$ is controlled independently. . . . .	150
4.39 Gate leakage currents characteristics of the top gate contact of MOSFET BI1_3_101 measured when biasing the gate from 0 V to 10 V during a drain voltage bias from 0 V to 16 V. . . . .	150
4.40 a) Drain current as a function of the drain bias for device BI1_3_101 measured at 573 K. b) Drain current as a function of the gate voltage measured at 573 K and at constant drain bias of 12 V. . . . .	151
4.41 Gate leakage currents characteristics of the top gate contact measured when biasing the gate from 0 V to 10 V during a drain voltage bias from 0 V to 15 V for sample AI3_1_50. . . . .	151
4.42 $C(V)$ characteristic of device AI3_1_50 measured at a) 500 Hz and b) 1 kHz. Both measurements were performed at 573 K. . . . .	152
4.43 a) Drain current as a function of the drain bias for device AI3_1_50 measured at 573 K. b) Drain current as a function of the gate voltage measured at 573 K and at constant drain bias of 12 V. . . . .	152
4.44 $C(V)$ properties measured at 573 K and 1 kHz ( $V_{ac} = 50 \text{ mV}$ ) for device a) BIV4_5_200 ( $L = 5 \mu\text{m}$ $W = 200 \mu\text{m}$ ), b) BI1_3_101 ( $L = 3 \mu\text{m}$ $W = 101 \mu\text{m}$ ) and c) AI3_1_50 ( $L = 1 \mu\text{m}$ $W = 50 \mu\text{m}$ ). . . . .	153
4.45 Illustration de l'avantage de WBGSc Si en termes de compromis <i>Rons</i> vs <i>BV</i> [Rouger 2015]. Les WBGSc montrent les plus petites régions de contact ainsi que mince zone de dérive (représenté par la double flèche). . . . .	166

4.46	Mise à l'échelle de Fig.1.4 en considérant une tension de blocage de 1 kV [Rouger 2015]. Parmi les WBGSc, le diamant est imbattable en termes de taille. . . . .	166
4.47	Exemple de l'optimisation de la zone de semi-conducteur dans le cas d'un dispositif de puissance unipolaire verticale avec 1200 V/10 A – 35 kHz – $\alpha = 0.5$ . Une comparaison est faite entre Si, SiC, GaN et le diamant. a) Une réduction dans les $R_{on}S$ sur les résultats dans une zone de semi-conducteurs réduit et une amélioration des pertes de puissance dans le dispositif d'alimentation. b) Même si une augmentation de la fréquence de commutation ( $f_{WBG} = 100 \times f_{Si}$ ) ne conduit pas à une réduction significative des pertes de puissance, la zone de semi-conducteurs est réduite [Rouger 2015]. . . . .	168
4.48	a) Al/Al <sub>2</sub> O <sub>3</sub> /O-diamond MOS schematic view and corresponding SEM image and b) cross section showing the stack [Chicot 2013b]. . . . .	169
4.49	a) C(V) characteristic of the Al/Al <sub>2</sub> O <sub>3</sub> /O-diamond MOSCAP for various frequencies. b) 1/C <sup>2</sup> (V) plot showing constant slope for deep depletion regime [Chicot 2013a]. Measurements were performed at 300 K. The 20 nm thin Al <sub>2</sub> O <sub>3</sub> layer was deposited at 100 °C by ALD. The gate contact diameter is 200 $\mu$ m. . . . .	169
4.50	a) Hysteresis behavior of the C(V) characteristic at 100 kHz when biasing the structure from accumulation to deep depletion and from deep depletion to accumulation. b) Current-voltage I(V) characteristic of the device showing leakage currents [Chicot 2013a]. The 20 nm thin Al <sub>2</sub> O <sub>3</sub> layer was deposited at 100 °C by ALD. . . . .	170
4.51	a) Charge per unit area $Q_{SC}^A$ as a function of the surface potential $\Psi_S$ in the diamond MOSCAP calculated from Eq.2.36. b) Corresponding capacitance vs. voltage ideal characteristic, with $N_A = 2 \times 10^{17} \text{ cm}^{-3}$ , $V_{FB} = -2.5$ , $A = 9 \times 10^{-4} \text{ cm}^2$ and $\epsilon_{ox} = 9$ . . . . .	171
4.52	Fit of the experimental J(V) characteristic reported in [Koizumi 2013], at 300 K with a contact resistance $R_{contact} = 10 \Omega \cdot \text{cm}^2$ and $\tau = \tau_p^{SRH} = \tau_n^{SRH} = 2 \times 10^{-10} \text{ s}$ . This value is calculated according to the diffusion length of holes reported by Kato et al. [Kato 2013] using $L_h = \sqrt{D\tau}$ , where D is the diffusion coefficient, $D = k_B T \mu / q$ . The ideality factor $n$ of the experimental I(V) is 3.5. . . . .	174
4.53	Structure of the simulated planar MOSFET. The Source and Back gate contact are short circuited and grounded. . . . .	176
4.54	a) Transconductance characteristic $I_{DS}$ vs. $V_{GS}$ for $V_{DS} = 1 \text{ V}$ , $N_A = 10^{15} \text{ cm}^{-3}$ , $t_{ox} = 20 \text{ nm}$ , simulated for temperatures ranging from 300 K to 600 K. b) Corresponding threshold voltage as a function of temperature. . . . .	176
4.55	a) $I_{DS}$ vs. $V_{DS}$ characteristic of the simulated diamond MOSFET with $V_{GS} = 0 \text{ V}$ and $T = 300 \text{ K}$ . In this $V_{DS}$ range, due to the very low intrinsic carrier concentration, the leakage currents are extremely small. b) Electric field at the oxide surface near the gate contact, with $V_{DS} = 2, 10, 50$ and $200 \text{ V}$ . . . . .	177
4.56	Electric field distribution in the simulated 2D diamond MOSFET for an oxide thickness of 200 nm, a p-type doping level of $10^{15} \text{ cm}^{-3}$ and a temperature of 300 K at a) $V_{DS} = 50 \text{ V}$ and b) $V_{DS} = 200 \text{ V}$ . . . . .	179
4.57	Potential and leakage currents flow lines distributions in the 2D diamond MOSFET structure, $V_{DS}$ ranging from 10 V to 300 V. . . . .	180

4.58	Potential diamond MOSFET structures envisioned for next generation power device applications. . . . .	181
4.59	Specific on-resistance as a function of the breakdown voltage. The Si limit is calculated through Baliga's law as $R_{on}S = 8.37 \times 10^{-9} \cdot BV^{2.5}$ [Baliga 2012]. . . . .	182
4.60	Schematic cross section (left) of the fabricated diamond MOSCAP and the corresponding actual device (right). . . . .	183
4.61	a) Schematic view of the home-made NIRIM type MPCVD reactor. b) Picture of the growth chamber [Fiori 2012]. . . . .	184
4.62	Schematic describing the ohmic contacts fabrication process. . . . .	185
4.63	Schematic describing the MOS contact fabrication steps. . . . .	186
4.64	Schematic cross section of the samples prepared for the XPS analysis. . . . .	187
4.65	Schematic energy band diagram of the $Al_2O_3/O$ -diamond with Ti in contact with the oxide layer, deduced from XPS measurement. The valence band offset is $1.34 \pm 0.2$ eV and the conduction band offset is $0.56 \pm 0.2$ eV. The oxide band gap value is taken from [Kim 2006]. . . . .	188
4.66	Normalized high frequency experimental $C(V)$ curve (1 MHz) compared to the calculated ideal one with $N_A = 2.3 \times 10^{17} \text{ cm}^{-3}$ , $N_D = 10^{16} \text{ cm}^{-3}$ and $V_{FB} = -7.1$ V. The insert is a zoom in where $\Delta V$ is indicated. . . . .	190
4.67	Interface states density as function of the energy, distributed inside the diamond band gap, extracted using Terman's method [Schroder 2006]. . . . .	191
4.68	a) Experimental $J(V)$ characteristics measured at various temperatures for a circular contact with diameter of $150 \mu\text{m}$ . b) Calculated $J(V)$ characteristics at various temperatures using the TAT model described by Eq.4.21. As evidenced the temperature dependence is stronger for the theoretical $J(V)$ than for the experimental one. . . . .	192
4.69	a) Optical microscope view of the MOSFET sample and b), c) and d) shows a close up on the three different geometries referred to as A, B and C respectively. e) Schematic 3D view. The MOSFET is composed of 4 terminals, the Source $S$ , the Drain $D$ , the Gate $G$ and the Back gate $B$ . The channel length $L$ and width $W$ are also indicated. . . . .	193

# List of Tables

1.1	Physical properties of Silicon (Si) and Silicon Carbide (SiC), Gallium Nitride (GaN) and diamond used in power electronics and the related figures of merit (FOM) (Johnson, Keyes and Baliga). $i$ and $d$ denote respectively indirect and direct band gap. The values are given at room temperature. The FOM were calculated at 300 K for electrons except for diamond for which holes were considered. . . . .	9
1.2	$N_{drift}$ , $W_{drift}$ and $R_{on}S$ calculated for a breakdown voltage $BV = 1$ kV [Rouger 2015] for Silicon (Si) and Silicon Carbide (SiC), Gallium Nitride (GaN) and diamond used in power electronics. . . . .	14
2.1	Parameters used to describe the band gap temperature dependence obtained by fitting the data reported in [Clark 1964] with Eq.2.1. $E_g(300K)$ represents the diamond band gap at 300 K. . . . .	32
2.2	Electrons and holes effective masses after [Willatzen 1994], [Gheeraert 2001] and [Naka 2013] respectively, in unit of $m_0$ . . . . .	34
2.3	Empirical mobility model parameters implemented in Silvaco finite element based software after [Volpe 2009, Pernot 2008]. . . . .	40
3.1	Impact ionization coefficients for electron and hole after [Hiraiwa 2013]. . . . .	72
4.1	Growth sequences with plasma type, gas flow, gas composition and duration of each step used to calibrate the boron doped diamond layer using oxygen in the gas phase. . . . .	108
4.2	Boron concentration and growth rate of the NiD and doped diamond layers extracted from the SIMS profile. . . . .	109
4.3	C 1s, Al $2p_{3/2}$ and O 1s binding energies (eV) of the core level spectra for the O-terminated diamond, the 20 nm $Al_2O_3$ and 2 nm $Al_2O_3$ samples. The valence band maxima (VBM) were recorded for the O-terminated diamond and the 20 nm thick $Al_2O_3$ . . . . .	117
4.4	Les propriétés physiques du silicium (Si), du carbure de silicium (SiC), du nitrure de gallium (GaN) et du diamant utilisés dans l'électronique de puissance et les figures de mérite respectives (FOM) (Johnson, Keyes et Baliga). $i$ et $d$ désignent respectivement bande interdite directe et indirecte. Les valeurs sont données à température ambiante et les FOM ont été calculés à 300 K pour les électrons à l'exception du diamant pour lequel les trous ont été considérés. . . . .	165

---

4.5 C 1s, Al  $2p_{3/2}$  and O 1s binding energies (eV) of the core level spectra for the O-terminated diamond, the 20 nm  $\text{Al}_2\text{O}_3$  and 2 nm  $\text{Al}_2\text{O}_3$  samples. The valence band maxima (VBM) were recorded for the O-terminated diamond and the 20 nm thick  $\text{Al}_2\text{O}_3$  . . . . . 187

# Introduction

Electrical energy consumption and demand has been continuously increasing in both advanced and developing countries. Recently fossil fuels have seen their prices drastically decreased, from nearly 100\$ per barrel in mid 2014 to below 50\$ per barrel in the beginning of the year 2015 [IEA 2015]. At a global scale this decrease acts as an economic stimulus. However, the combustion of fossil fuels for energy purposes represents a large amount of green house gas emissions (about two thirds of all anthropogenic green house gas emissions), which, due to their long lifetime resulting in the cumulative built up in the atmosphere is responsible for the observed global warming and their role in the climate change is now well established. As the world population is continuously increasing (for instance the global population is increasing by 1.18 % per year, representing 83 millions people per year [Eeckhout 2015]) so is the electricity demand. Thus, in aiming to limit green house gas emission and more specifically to keep the global warming below the critical threshold of 2 °C, governments have signed an international environmental treaty (the United Nations Framework Convention on Climate Change) on long term objectives toward deep cuts in global green house gas emissions [IEA 2015]. In order to fulfill its pledge, EU must reduce its green house gas emission by at least 40% below the 1990 levels by 2030. The progresses toward this goal are assessed at the yearly United Nations Climate Change Conferences, this year held in Paris <sup>2</sup>.

Thus, sustainable growth in both advanced and developing countries relies on the reduction of green house gas emissions. This reduction is possible by developing the field of green electronics [Ohashi 2012], i.e. cleaner and more efficient technologies are mandatory to achieve carbon emissions reduction. In this manner, two approaches can be envisioned [Baliga 2012]. On one hand, electricity production should rely on more and

---

<sup>2</sup><http://www.cop21.gouv.fr>

more renewable energy sources, such as solar power, wind power, tidal power or hydropower which uses power electronics to convert the generated ac power to well suited power that could be used by consumers. Power semiconductor based devices are key components to sustain high voltage and current, high temperature and high power density during such conversion. The second approach consists in achieving low losses and high efficiency systems for the management and the transfer of power from the point of production to the point of consumption.

At the heart of the system is the power semiconductor, which is at present mainly based on Silicon. In fact, as compared to other materials, it has a performances/cost ratio which leads to a commercial figure of merit unbeatable at present [Udrea 2015]. However, even if specific architectures, such as super junction transistors [Antoniu 2010] are developed, Si based power devices are reaching the material limits. Thus, power devices based on WBG semiconductors such as SiC, GaN or Diamond are emerging. The superior physical properties of WBG semiconductors makes them suitable for high power switching applications. SiC devices as well as GaN based devices are already under commercialization. Diamond, still, is at the research and development stage and is intensively studied by several groups around the world (France, Japan, USA, Russia, Spain, UK...).

Over two decades of technological progresses in growth quality, doping control and device processing have led to the emergence of new potentialities for power electronic applications. As diamond represents the ultimate semiconductor owing to its superior physical properties, efforts have been conducted to develop various electronic devices, such as Schottky diodes, field effect transistors, bipolar transistor, p-i-n junctions...

As a prerequisite to the development of new generation diamond power devices, on one side, is the development of simulation tools able to anticipate the device electrical properties as well as its architecture in order to take full advantage of the material physical properties. On the other hand, experimental study of the gate contact, the second building block of the transistor, is fundamental in order to develop high performance devices. In this regard, one can consider several open questions: (i) Are the simulation tools able to take into account the specificities of diamond to model electrical devices? (ii) Is the aluminum oxide suitable to develop a MOSFET gate contact? (iii) If so, is the oxide/diamond interface of good enough quality? (iv) Is the fabrication of a diamond MOSFET

a technological issue? In order to address these questions, this manuscript is organized as follows:

Chapter 1: In this first chapter, the main stakes for power electronics will be presented. For low-carbon emission technologies, Wide BandGap (WBG) semiconductors such as SiC, GaN and diamond will play a fundamental role in future applications. Emphasize on the diamond physical properties will help to understand why this material is the ultimate WBG semiconductor. State of the art diamond devices will be presented focusing on field effect transistors. A complementary topic for the development of new generation diamond power device is the anticipation of device electrical properties and architecture through finite element base simulation software. Thus, the need for reliable simulation tools will be presented.

Chapter 2: The main models implemented in the simulation tools will be presented and emphasize on the diamond electrical properties will be given. For the simulation of diamond metal-oxide-semiconductor field effect transistor (MOSFET), the study of two building blocks is required: the p-n junction and the gate contact. The later ideal properties will be presented while the former will serve as a basis for the calibration of the physical parameters implemented in the finite element based software.

Chapter 3: This chapter will present the main results concerning the diamond device simulations. In a first part, results on the p-n junction simulation will be presented. In particular, generation-recombination models influence on the simulated p-n junction electrical properties will be discussed. Finally, the simulation of the electrical properties of a diamond metal-oxide-semiconductor field effect transistor (MOSFET) will be shown.

Chapter 4: In this final chapter, focus will be made on diamond metal-oxide-semiconductor capacitor (MOSCAP) fabrication and characterization. Specifically, the interfacial band configuration of the Al<sub>2</sub>O<sub>3</sub>/oxygen-terminated diamond (O-diamond) has been investigated using X-ray photoelectron spectroscopy. The results helped to establish the band diagram of the Al<sub>2</sub>O<sub>3</sub>/O-diamond heterostructure. Then, the electrical properties of the diamond MOSCAP will be shown. In particular, investigation of the interface states density revealed the pinning of the Fermi level at the interface between the Al<sub>2</sub>O<sub>3</sub> and the O-diamond. Moreover, the leakage currents through the Al<sub>2</sub>O<sub>3</sub> layer will be discussed in terms of temperature dependent trap assisted tunneling of holes from the diamond layer to the top gate contact. Finally, the electrical characterization of the first O-diamond

---

MOSFET, performed at the National Institute for Advanced Industrial Science and Technology (AIST) in Japan, will be presented. Even if this first attempt was unsuccessful, it is promising for the development of diamond MOSFET since the demonstration of the actual realization of the device is clearly established.

A general conclusion will then follow and the outlook of the present work will be discussed.

# Chapter 1

## Diamond: the future of power electronics

### Contents

---

<b>1.1</b>	<b>Context of Power Electronics</b>	<b>6</b>
<b>1.2</b>	<b>Wide band gap materials</b>	<b>7</b>
<b>1.3</b>	<b>Diamond: the ultimate semiconductor</b>	<b>11</b>
<b>1.4</b>	<b>State of the art of diamond devices</b>	<b>20</b>
<b>1.5</b>	<b>On the need for reliable simulation tools</b>	<b>26</b>
<b>1.6</b>	<b>Conclusion</b>	<b>27</b>

---

## 1.1 Context of Power Electronics

In the context of fast increase in the energy consumption with the need to reduce greenhouse gas emissions, greener technologies are required. For competitive low-carbon renewable energy and smart grid applications, the impact of Power Electronics (PE) is striking. In the smart grid of Fig.1.1 [3M], consisting of a network of modernized systems which ensures the efficient distribution of electricity from the source to the end point of consumption, Wide BandGap (WBG) semiconductors will play a fundamental role towards greener and more efficient technologies.

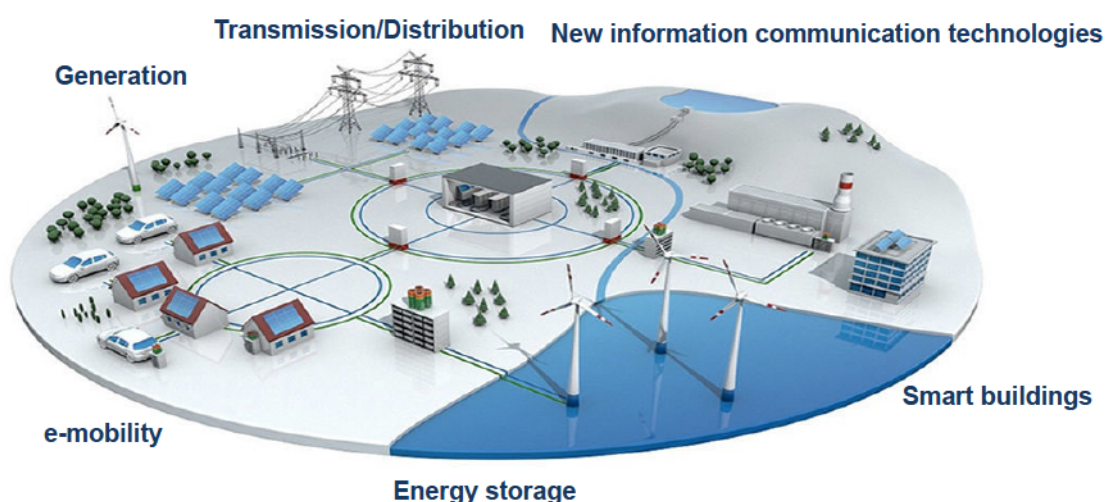


*Figure 1.1:* Example of a smart grid. The efficient transmission and generation of electricity from the source of production to the end point of consumption is ensured by the use of low loss devices which in the near future will be made of WBG semiconductors.

Currently, approximately 30% of all electric power generated utilizes PE somewhere between the point of generation and its end use [Department for Business 2011]. PE is used for more efficient renewable energy production and distribution including in highly-efficient electricity distribution over long distances via High Voltage Direct Current power lines (HVDC) as well as in the better control of loads and sources in switching power supplies and variable-speed drives for motors that drive fans, pumps, and compressors. By 2030, it is expected that as much as 80% of all electric power will use PE somewhere between generation and consumption [Tolbert 2005]. Even with state-of-the-art electric equipment, the transformation of the electrical energy occurs with significant losses<sup>1</sup>

<sup>1</sup>partly due to the semiconductor power devices

(for example 5% in France from the source to the point of use<sup>2</sup>), because available semiconductors (mainly Silicon) are not ideal for high power applications. In future smart grids involving delocalized renewable energy sources, these energy losses become even more important, since PE are needed throughout the grid to monitor and control the ever-changing supply and demand of low-carbon electricity transiting through the grid. This is even more critical in the case of offshore wind farms where an efficient energy transportation technology, such as HVDC, is required.

The key to the efficient transmission and conversion of low-carbon electrical energy is the improvement of PE devices, which must be durable and reliable in high power high temperature environments to eliminate the need for auxiliary systems. "Green electronics" [Ohashi 2012], i.e. highly efficient electronic devices are crucially important for our future energy system as they will increase the efficiency of electricity production and distribution with very disruptive gains expected at the system level. First estimation gives a factor of 4 improvement, i.e. 75% reduction in losses, representing about 10 MW energy saving on a 300 MW HVDC converter. They will also provide more flexibility, facilitating the introduction of variable and distributed sources of renewable energies into the grid.

Diamond is one of the most promising material for future power electronic applications. It is a WBG semiconductor having exceptional physical properties which are compared to SiC and GaN in the next section.

## 1.2 Wide band gap materials

Roadmaps for future WBG semiconductor electronics envision the emergence of SiC and GaN power devices for high voltage applications and energy saving, specifically for high switching speed and low loss characteristics [Okumura 2015]. Diamond is the youngest technology among the WBG semiconductors. Nevertheless, it is seen as the next generation material for very high power applications owing to its outstanding physical properties, and is predicted to have applications where high blocking capabilities are required. Fig.1.2 illustrates the roadmap for future advanced power devices [Ohashi 2012]. Si

<sup>2</sup><http://data.worldbank.org/indicator/EG.ELC.LOSS.ZS>

devices remain the cheapest material and have a commercial figure of merit which is unbeatable at present [Udrea 2015]. Moreover, the development of new architectures such as Si Super Junction MOSFET (Metal-Oxide-Semiconductor Field Effect Transistor) allows to reach on-resistances ten times lower than the predicted Si limit [Kagata 2013]. According to this roadmap, it is expected that Si IGBT (Insulated Gate Bipolar Transistor) will be replaced by SiC MOSFET in the voltage range of more than 1 kV and SiC IGBT has potential to reach applications in the 10 kV range. GaN power devices will replace Si in applications such as power integrated circuit area. Diamond has potential applications in the high to very high voltage (> 10 kV) range.

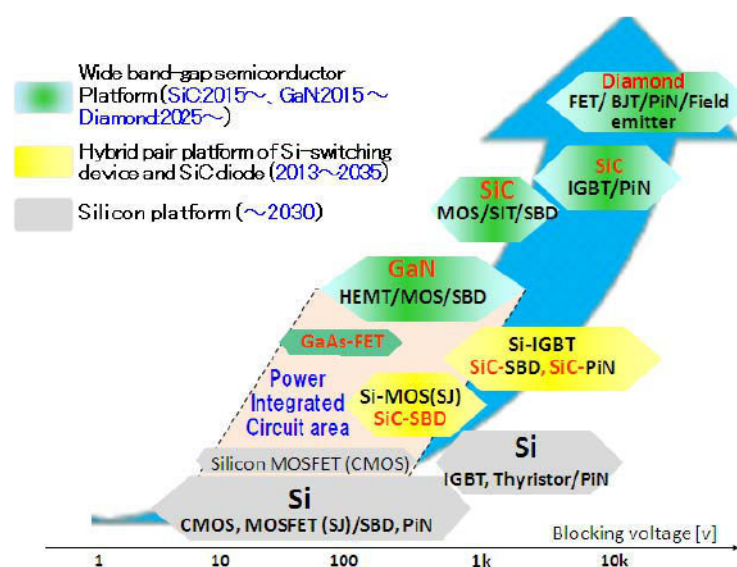


Figure 1.2: Roadmap for future power devices [Ohashi 2012]. Si has still an important role to play and constant effort is made to increase the device performances. GaN and SiC power devices will coexist and improve toward high blocking voltage applications. Diamond is predicted to cover high blocking voltage applications (10 kV range).

The fundamental building block of PE is the semiconductor. Silicon is by far the most advanced semiconductor material and has been developed for more than 50 years. However, it has difficulties in meeting the demand for some high-power applications due to limitations in its intrinsic properties as shown on Tab.1.1.

In particular, the narrow bandgap of Si limits the operating temperature to 150 °C and important thermal management is required to limit the junction temperature below this limit [Tolbert 2005]. Even though specific architectures have been developed, such as

Superjunction Transistors overcoming the Si limit [Antoniou 2010], WBG semiconductors have superior electrical properties as compared to Si. Among WBG semiconductors, Silicon Carbide is the most advanced power semiconductor technology. One of the main reason being the availability of large substrates, even if the device cost still remains expensive as compared to Si devices. However, the performances of SiC devices enables the fabrication of cheaper, smaller and more efficient power systems [Dimitrijevic 2015]. An example of commercial achievement is the integration of a SiC power module in one of the six cars of the Tokyo Metro Ginza line in 2013 with DC voltage rating of 600 V<sup>3</sup>. Compared to the previous Si power modules, this system achieves a reduction of power losses by 30 %.

Gallium Nitride devices are also commercially available in the form of High Electron Mobility Transistors (HEMT) mainly for fast and efficient switching applications with voltage rating of 650 V<sup>4</sup>.

At present, there are still no commercial diamond electronic devices available, but research is progressing very fast to improve substrate quality, size and device performances. During the last decade, significant progresses were made on Schottky devices and RF transistors. These latter devices, working without an inversion layer, use a hole accumulation layer below the hydrogen-terminated surface as conduction channel, controlled

<sup>3</sup><http://www.mitsubishielectric.com/news/2013/0326-a.html>

<sup>4</sup><http://www.gansystems.com/trans-temp.php>.

Property	[unit]	Si	4H-SiC	GaN	Diamond
Band gap	$E_G$ [eV]	1.1 <i>i</i>	3.23 <i>i</i>	3.45 <i>d</i>	5.45 <i>i</i>
Dielectric constant	$\epsilon_r$	11.8	9.8	9	5.7
Critical Field	$E_{crit}$ [MV/cm]	0.3	3	2	10
Thermal conductivity	$\lambda$ [W/cm.K]	1.5	5	1.5	22
Sat. drift velocity e <sup>-</sup>	$v_s$ [ $10^7$ cm/s]	1.0	2.0	2.2	2.7
Sat. drift velocity h <sup>+</sup>	$v_s$ [ $10^7$ cm/s]	1.0			1.1
Electrons mobility	$\mu_e$ [cm <sup>2</sup> /V.s]	1500	1000	1250	1000
Holes mobility	$\mu_h$ [cm <sup>2</sup> /V.s]	480	100	200	2000
Johnson's FOM	$JFM$ [ $10^{23}$ $\Omega.W/s^2$ ]	2	911	490	3064
Keyes' FOM	$KFM$ [ $10^7$ W/K.s]	9	49	16	215
Baliga's FOM	$BFM$ [Si=1]	1	554	188	23017

*Table 1.1:* Physical properties of Silicon (Si) and Silicon Carbide (SiC), Gallium Nitride (GaN) and diamond used in power electronics and the related figures of merit (FOM) (Johnson, Keyes and Baliga). *i* and *d* denote respectively indirect and direct band gap. The values are given at room temperature. The FOM were calculated at 300 K for electrons except for diamond for which holes were considered.

by a top gate. A FET with 850 mA/mm<sup>5</sup> saturation current and 22 GHz of transition frequency for RF applications has been reported [Kawarada 2012]. More details will be given later, but we can mention power device such as the Schottky rectifier, devices with up to 10 kV breakdown voltage [Butler 2003, Volpe 2010, Umezawa 2013, Traoré 2014], as well as Schottky-pn diodes with high current density of 4 kA.mm<sup>-2</sup> and low specific resistance of 0.4 mΩ.cm<sup>2</sup> [Makino 2009]. These rectifiers have a very high rectification ratio, typically 10<sup>10</sup>, and can operate up to 400 °C with very good electrical characteristics. However, little effort has been dedicated to the design of high-voltage specific building blocks such as field plates and guard rings, so that significant improvements in device characteristics are expected with the implementation of these techniques.

In order to have a better insight of the performances of WBG semiconductors their physical properties are summarized in Tab.1.1. In particular, SiC, GaN and Diamond have larger critical field and thermal conductivity than Si. Diamond is "outrageously" better than its competitors. Specifically, its breakdown field is more than 30 times larger than that of Si and 3 times larger than that of SiC, making it suitable for high blocking voltage operations. Its thermal conductivity of 22 W/cm.K makes it a candidate for high temperature applications. Its superior hole mobility makes it suitable for high frequency operation devices and high current applications. Usually, the comparison between WBG semiconductors is made through the calculation of the Figure Of Merit (FOM), either Johnson's FOM, Keyes's FOM or Baliga's FOM depending on the targeted applications. They are described as follows:

**Johnson's figure of merit (*JFM*)** represents the ability of a material for high frequency and high power transistor applications [Johnson 1965]. This FOM is both applicable to FET and with caution to bipolar transistor.

$$JFM = \left( \frac{E_{crit} \cdot v_s}{2\pi} \right)^2 \quad (1.1)$$

**Keyes' figure of merit (*KFM*)** displays the thermal limitation to the switching behavior at high frequency [Keyes 1972].

$$KFM = \lambda \left( \frac{c \cdot v_s}{2\pi \cdot \epsilon_r} \right)^{1/2} \quad (1.2)$$

---

<sup>5</sup>a value greater than the 90mA/mm of SiC planar MOSFET [Noborio 2009] and greater than the 300 mA/mm of AlGaN channel HEMT [Nanjo 2013].

where  $c$  is the light velocity.

**Baliga's figure of merit (BFM)** defines a material efficiency to minimize conduction losses in power applications [Baliga 1982, Baliga 1989].

$$BFM = \epsilon_r \cdot \mu \cdot E_{crit}^3 \quad (1.3)$$

According to the expected FOM presented in Tab.1.1 diamond is by far the most appropriate material for high temperature, high frequency and high power density applications.

### 1.3 Diamond: the ultimate semiconductor

The early days of power electronics were based on the use of Si. However, ever increasing requirements for higher efficiencies and resiliency to harsh environment (such as blocking voltage of 2 kV and above and working temperature of 400 °C [Iacopi 2015]) have led the community to consider WBG semiconductors as replacement to Si. In many applications, the low critical field of Si ( $E_{crit} = 2-3 \times 10^5$  V.cm<sup>-1</sup> depending on the doping level and the breakdown voltage  $BV$  [Baliga 2012]) is the main limiting factor [Dimitrijevic 2015]. Considering a diode or a transistor in the planar structure, the highest breakdown voltage is just over 2900 V, assuming a doping level of  $N_D \approx 10^{14}$  cm<sup>-3</sup><sup>6</sup>. The critical field relates to the strength of the atomic bonds of the material ( $E_g = 1.12$  eV for Si). Thus, the wider the bandgap, the stronger the atomic bonds and as a result the higher the critical electric field. This means that by using WBG semiconductors such as SiC, GaN or diamond, the breakdown voltage can be noticeably increased. For example, in the ideal case, a doping level of  $10^{15}$  cm<sup>-3</sup> [Traoré 2015] for diamond ( $E_{crit} = 10$  MV.cm<sup>-1</sup>,  $\epsilon_{sc} = 5.7$ ), would result in a breakdown voltage of  $BV \approx 150000$  V according to Eq.1.8 which will be discussed later. However, Si devices such as thyristors and IGBTs show remarkable performances. For instance, ABB Semiconductors Ltd. reported the realization of thyristors with voltage rating of 6.7 kV, 7.2 kV and 8.5 kV [Vobecky 2014]. In this case, particular attentions are paid on the carrier lifetime, silicon resistivity and thickness and on the silicon area. Here, the power device covers the entire area of a six inch silicon wafer. As discussed in the following, the use of WBG semiconductors might result in the reduction of the device size as well as in the improvement of the  $R_{on}S$  vs.

<sup>6</sup>The lowest doping level achievable is close to  $10^{13}$  cm<sup>-3</sup>.

$BV$  figure of merit as compared to Si. The use of WBG power devices will however bring new challenges in terms of packaging (high temperature, high electric field, higher switching frequencies), thermal management (high power loss densities) and dedicated gate drivers.

Diamond is considered as the ultimate semiconductor as regards to the calculated FOM (see Tab.1.1). In theory, diamond should be suitable for high frequency, high temperature and high power density applications. Moreover its integration to power module should considerably reduce the size of the power system together with the cooling system. More specifically, the design of a power semiconductor is determined by the drift layer thickness [Rouger 2015]. The thickness of the drift layer  $W_{drift}$  and its doping level  $N_{drift}$  are given by the specifications (required breakdown voltage  $BV$ ) as well as by the physical properties of the semiconductor, such as its relative dielectric constant and its dielectric strength. Thus, in the most simplified approach where the critical electric field  $E_{crit}$  is introduced<sup>7</sup> and for a non-punch-through (NPT) design as illustrated in Fig.1.3, the following relationships are established. First, the breakdown voltage  $BV$  is the integral of the electric field, such that:

$$BV = \int_{-x_{pmax}}^{W_{drift}} E(x)dx \quad (1.4)$$

The space charge region mainly extending in the lowest doped region allows to neglect  $-x_{pmax}$  in Eq.1.4. Thus, integrating this last equation leads to:

$$BV = \frac{W_{drift} \cdot E_{crit}}{2} \quad (1.5)$$

This is simply the area under the electric field curve depicted in Fig.1.3. Then, the drift layer thickness is expressed as a function of the breakdown voltage  $BV$  and the critical electric field  $E_{crit}$  as:

---

<sup>7</sup> $E_{crit}$  is the largest electric field which can be applied to a semiconductor before the avalanche breakdown occurs. This value is a function of the doping level, the electric field profile and the temperature.

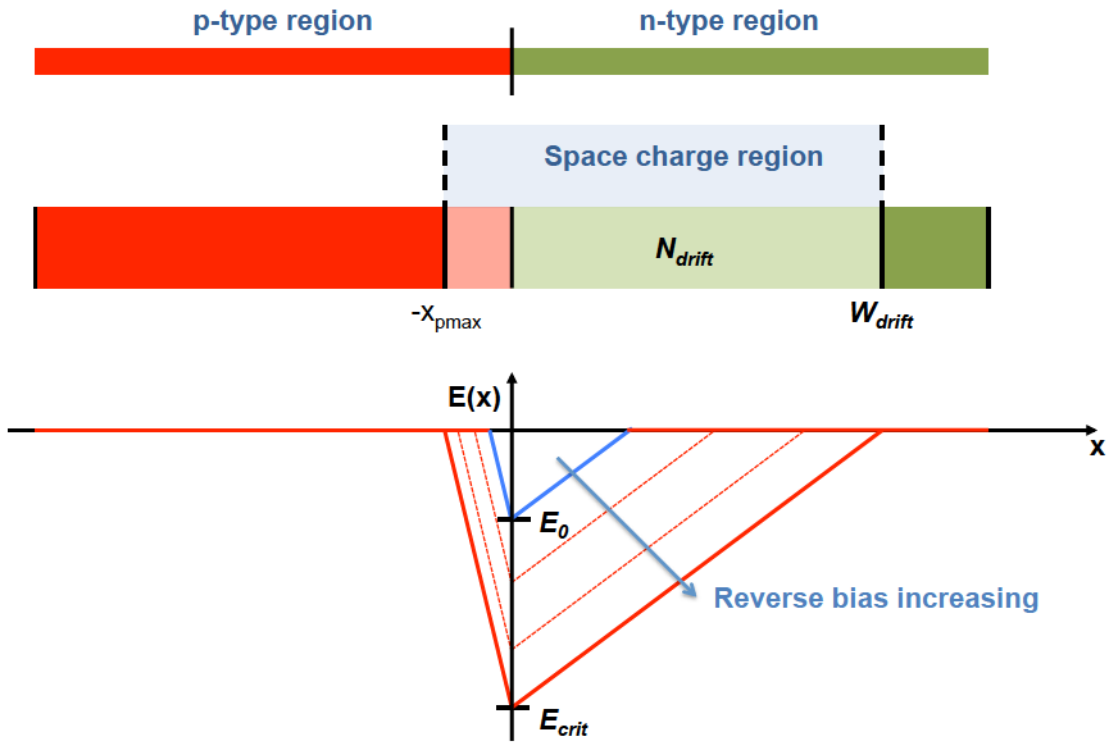


Figure 1.3: Principle of the drift layer design for a non-punch-through device. Here, a p-n junction is represented, however the drift layer resistance does not take into account the carrier injection, i.e. the resistivity modulation is not considered [Rouger 2015].  $-x_{pmax}$  represent the maximum expansion of the space charge region in the p-type region.

$$W_{drift} = E_{crit} \cdot \frac{\epsilon_{sc}\epsilon_0}{qN_{drift}} = \frac{2 \cdot BV}{E_{crit}} \quad (1.6)$$

Solving the one-dimensional Poisson's equation in the space charge region allows to establish the following equation:

$$E_{crit} = \frac{qN_{drift} \cdot W_{drift}}{\epsilon_{sc}\epsilon_0} \quad (1.7)$$

Putting Eq.1.6 together with Eq.1.7, finally leads to the expression of the drift layer doping level  $N_{drift}$  as a function of  $BV$  and  $E_{crit}$  such that:

$$N_{drift} = E_{crit}^2 \cdot \frac{\varepsilon_{sc}\varepsilon_0}{2q \cdot BV} \quad (1.8)$$

where  $q$  is the elementary charge,  $\varepsilon_{sc}$  is the semiconductor relative dielectric constant and  $\varepsilon_0$  is the vacuum permittivity.

Finally, for a unipolar device without resistivity modulation in on-state (for instance Schottky diode, HEMT or MOSFET), assuming the full ionization of dopants<sup>8</sup>, the specific on-resistance  $R_{on}S$ , with  $S$  the semiconductor area, is expressed as:

$$\begin{aligned} R_{on}S &= \frac{W_{drift}}{q\mu N_{drift}} \\ &= \frac{4 \cdot BV^2}{\mu\varepsilon_{sc}\varepsilon_0 \cdot E_{crit}^3} \end{aligned} \quad (1.9)$$

where  $\mu$  is the carrier mobility in the drift layer. One can notice that the denominator in Eq.1.9 represents Baliga's FOM. Thus, it appears that the higher the  $E_{crit}$  of the semiconductor, the higher the doping level (see Eq.1.8). At the same time, the thickness of the drift layer is reduced (see Eq.1.6). Moreover, for a given blocking voltage, the on-resistance will be strongly decreased by replacing Si by a WBG semiconductor due to the presence of the critical field at the denominator of Eq.1.9.

Property	[unit]	Si	4H-SiC	GaN	Diamond
$N_{drift}$ (1 kV)	[cm <sup>-3</sup> ]	$1.3 \times 10^{14}$	$2.5 \times 10^{16}$	$3.7 \times 10^{16}$	$1.6 \times 10^{17}$
$W_{drift}$ (1 kV)	[ $\mu$ m]	100	6.7	4	2
$R_{on}S$ (1 kV)	[m $\Omega$ .cm <sup>2</sup> ]	333	0.19	0.03	0.004

Table 1.2:  $N_{drift}$ ,  $W_{drift}$  and  $R_{on}S$  calculated for a breakdown voltage  $BV = 1$  kV [Rouger 2015] for Silicon (Si) and Silicon Carbide (SiC), Gallium Nitride (GaN) and diamond used in power electronics.

Applying this extremely simplified model to the semiconductors of Tab.1.2, the benefit in using WBG semiconductors over Si is striking.  $N_{drift}$ ,  $W_{drift}$  and  $R_{on}S$  are calculated for a breakdown voltage of 1 kV. It appears clearly that the doping level is increased and that both the drift layer thickness and the specific on-resistance are considerably decreased in the case of SiC, GaN and diamond. The superiority of WBG semiconductors

<sup>8</sup>This is true for high temperature operation.

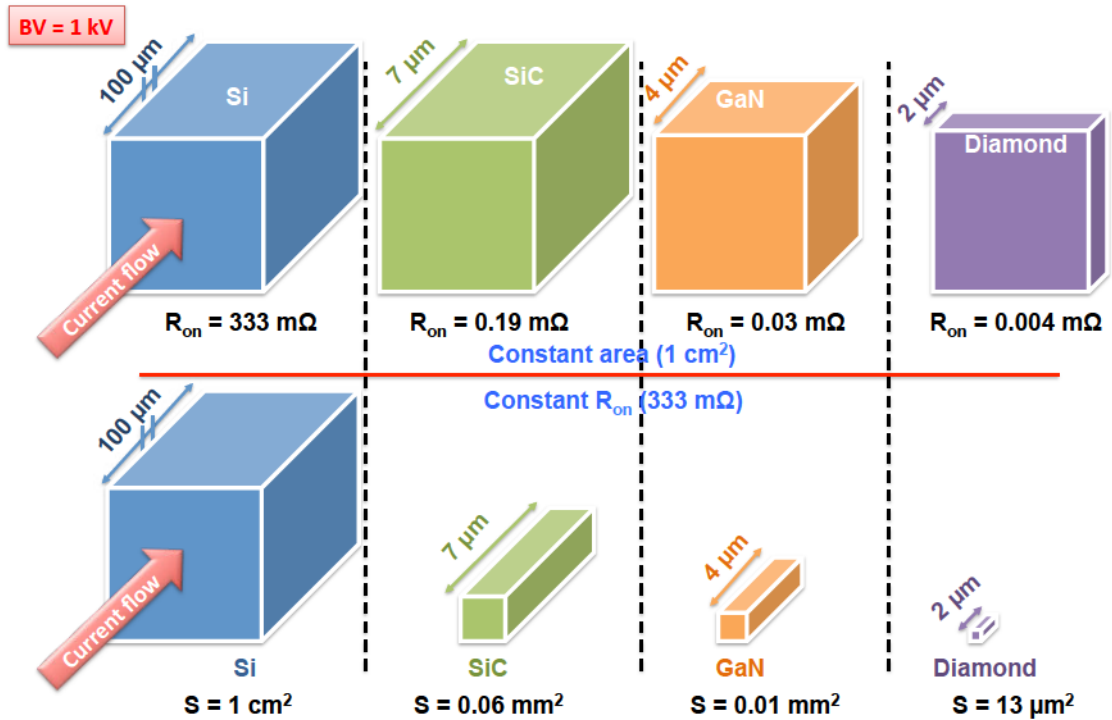


Figure 1.4: Illustration of the advantage of WBG semiconductors over Si in terms of the  $R_{on}S$  vs.  $BV$  trade off [Rouger 2015]. WBG semiconductors show smaller contact areas as well as thinner drift region (represented by the double side arrow).

over Si is further illustrated in Fig.1.4, where the semiconductors are compared for either same contact area or same on-resistance. As a consequence, the on-state losses as well as the dynamic losses could be minimized by the use of WBG semiconductors. Fig.1.5 shows the scaling of Fig.1.4 considering a blocking voltage of 1 kV [Rouger 2015]. Among WBG semiconductors, diamond is unbeatable in terms of size.

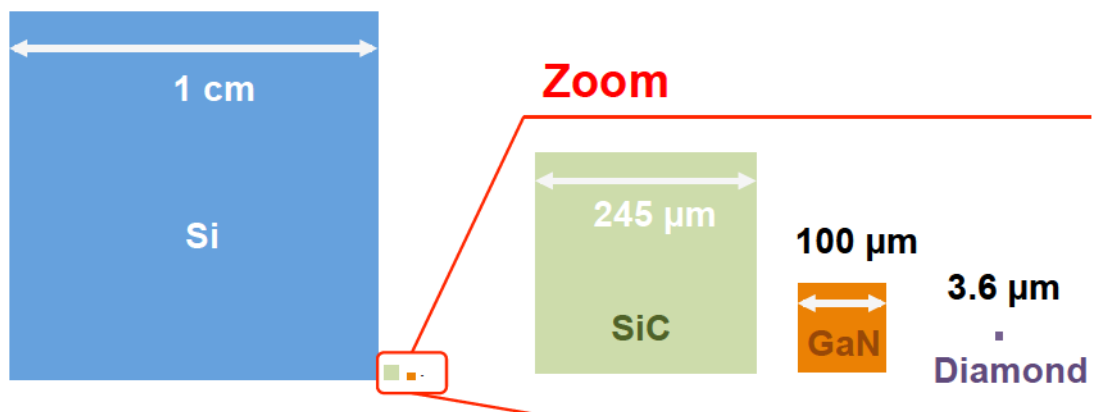


Figure 1.5: Scaling of Fig.1.4 considering a blocking voltage of 1 kV [Rouger 2015]. Among WBG semiconductors, diamond is unbeatable in terms of size.

The above described approach is based on several hypothesis, such as the complete ionization of dopants, the constant mobility of carriers and the negligibly small contact resistance, as well as a design of the drift region with NPT and no bipolar carrier injection to modulate the drift region resistivity. Thus, a more realistic approach consists in taking into account the incomplete ionization of dopants as well as the temperature dependence of the mobility as given by Umezawa et al. [Umezawa 2012], as illustrated in Fig.1.6.

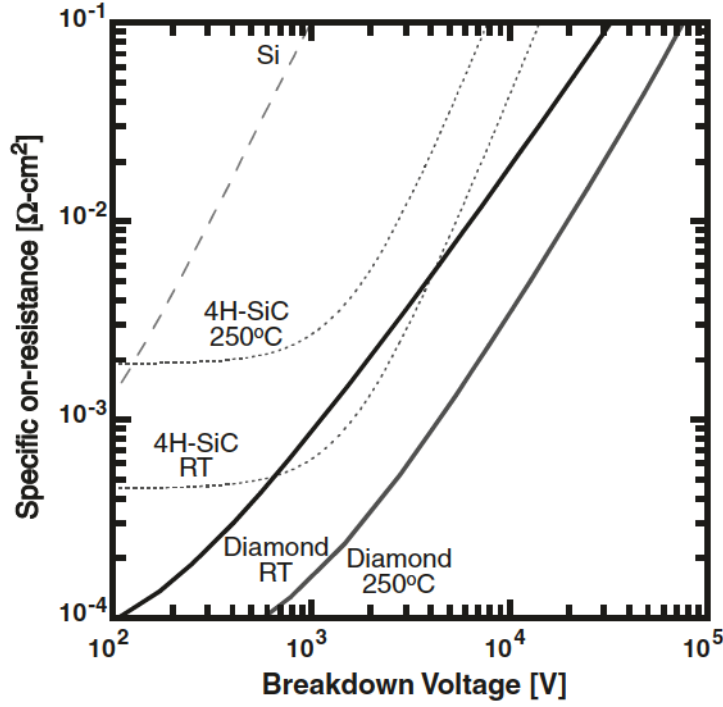


Figure 1.6: Specific on-resistance as a function of the breakdown voltage for Si, SiC and diamond in the case of vertical unipolar device [Umezawa 2012].

In this study, the specific on-resistance  $R_{on}S$  and the breakdown voltage  $BV$  of a pseudo-vertical Schottky diode made out of a stacked  $p^-/p^+$  junction can be expressed by the use of the following relationships, in the case of unipolar devices and in the punch-through configuration [He 2002]:

$$R_{on}S = \frac{W_{PT}}{\rho\mu q} + R_{p^+} + r_c \quad (1.10)$$

$$BV = E_{crit} \times W_{PT} - \frac{qN_A W_{PT}^2}{2\varepsilon_{sc}\varepsilon_0} \quad (1.11)$$

with  $W_{PT}$  is the drift layer thickness in the punch-through design,  $p$  is the hole concentration,  $\mu$  is the hole mobility,  $q$  the elementary charge,  $R_{p^+}$  is the  $p^+$ -type layer resistance,  $r_c$  is the contact resistance and  $N_A$  is the doping level.

As the blocking voltage is increased the specific on-resistance is also increased. Due to its low critical field, Si shows a high  $R_{on}S$  even for blocking voltages below 1 kV. For the same  $BV$ , SiC shows a  $R_{on}S$  about 167 times better than Si at room temperature. For room temperature applications, diamond has no advantages over SiC for  $BV$  below 10 kV due to the incomplete ionization of dopants. As the temperature is increased to 250 °C, the specific on-resistance of SiC is degraded by a factor of  $\sim 3$  while diamond sees its  $R_{on}S$  improved by a factor of  $\sim 2$  when maintaining a breakdown voltage of 1 kV. This behavior comes from the improved ionization ratio at high temperature due to the high activation energy of the boron acceptors in diamond ( $E_a = 0.38$  eV). It has to be noticed that this approach might not be valid due to the fact that the critical electric field  $E_{crit}$  is not accurate. In fact approaches based on the ionization integral calculation for a given electric field profile must be calculated as proposed in [Raynaud 2010, Hiraiwa 2015]. In any case, diamond has a better trade-off characteristic over the entire  $BV$  range and is expected to surpass SiC devices in high temperature applications. Thus, low loss diamond power devices should be available with smaller active area and possibly good performance/cost ratio.

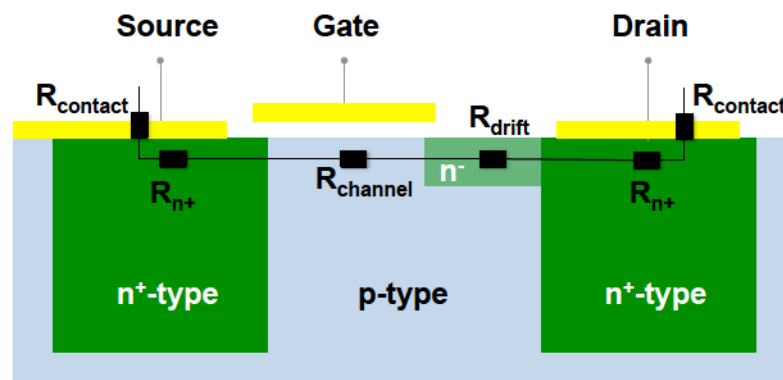


*Figure 1.7:* Illustration of the different contributions to the total resistance in a planar n-channel MOSFET. The total resistance is composed of the contact resistance, the  $n^+$ -type resistance, the channel resistance and the drift layer resistance.

In the planar MOSFET represented in Fig.1.7, the current flow between the source and the drain is induced by creating an inversion layer channel at the surface of the p-type region. The blocking voltage is governed by the  $n^-$ -type layer width, and is referred as

the drift layer. The total resistance in the planar inversion mode MOSFET is determined by the resistance of the component in the current path, such that:

$$R_{total} = 2 \times R_{contact} + 2 \times R_{n^+} + R_{channel} + R_{drift} \quad (1.12)$$

where  $R_{contact}$  is the contact resistance on the  $n^+$ -type layer,  $R_{n^+}$  is the resistance of the  $n^+$ -type layer,  $R_{channel}$  is the channel resistance and  $R_{drift}$  is the drift layer resistance. This last component is the main contribution to the  $R_{on}$  term discussed above. Thus, for diamond several phenomena can modify the results presented in Fig.1.4, such as [Rouger 2015]:

- The critical electric field  $E_{crit}$  introduced in Tab.1.1 is not valid. The ionization integral must be calculated for a given electric field profile, according to reliable impact ionization coefficients [Hiraiwa 2015].
- As already mentioned, the dopant are not fully ionized in WBG semiconductors (especially in diamond), resulting from the large ionization energies. Thus, the room temperature specific on-resistance  $R_{on}S$  is greater than the one predicted by Eq.1.9.
- The doping level strongly influences the mobility in a device. The conduction mechanism, such as hopping conduction in  $n^+$ -type and  $p^+$ -type diamond [Oyama 2009, Hosoda 2013] can be exploited to improve the device properties.
- The punch through factor used to calculate the optimum drift layer properties in the punch through design must be calculated, depending on the device type (unipolar or bipolar), taking into account the carrier lifetime in the case of bipolar device.
- As it is the case for low voltage Si devices ( $< 100$  V), the on-resistance is not only due to the drift layer resistance. The contact resistance, the channel resistance and the  $n^+$ -type layer resistance might have a non-negligible contribution to the total resistance of the device.

To emphasize on this last item, one must consider the planar MOSFET of Fig.1.7. Usually, the total resistance  $R_{total}$  of a Si high voltage power device can be approximated to  $R_{drift}$ , since the other terms can be neglected. In the case of an inversion mode diamond MOSFET, it is not straightforward that the other contributions can be neglected. Specifically, the contact resistance on a  $n^+$ -type diamond layer might not be negligible as compared to the drift layer resistance. Also, the channel resistance  $R_{channel}$  must be considered, specifically in terms of minority carrier mobility in the inversion layer. If the inversion layer mobility is low, as it is the case for SiC MOSFET structures (only  $15 \text{ cm}^2 \cdot \text{V}^{-1} \cdot \text{s}^{-1}$  [Howell 2008]), the channel resistance can become dominant.

Finally, a comparison in terms of losses in a vertical unipolar power device can be made. The total losses are mainly composed of conduction losses (on-state losses) and switching losses. Fig.1.8 represents the total losses  $P_{tot}$ , which is the sum of the conduction losses  $P_{cond}$  and the switching losses  $P_{com}$ , as a function of the device area [Rouger 2015]. Specifically, the curve is calculated for a 1200 V/10 A device with a working frequency of 35 kHz and a duty cycle of  $\alpha = 0.5$ . As represented, the conduction losses are proportional to the inverse area  $A^{-1}$  of the device whereas the switching losses depend linearly on the area  $A$  [Kolar 2012]. The former term is mainly due to the specific on-resistance  $R_{on}S$  of the device. The later contribution, which is simplified here, is related to the charge per unit area or to the capacitance per unit area and strongly depends on how fast these charges are commuted either at the input or at the output of the device.

Fig.1.8 allows to identify the optimum working point, which is given by the intersection of the  $P_{cond}$  with the  $P_{com}$  curves. Here, the optimum is chosen for an area of  $1 \text{ cm}^2$  and a device with 99 % yield and a resulting total semiconductor losses representing 1% of the total power converter input power at the rated nominal power. Thus, depending on the desired design, the consequence of the use of WBG semiconductors is a reduction of the losses together with the device area as compared to Si, as exhibited in Fig.1.9.a).

Even with this simple approach and a more realistic specific on-resistance  $R_{on}S^9$  (see Fig.1.9.a)) the advantage of WBG semiconductors over Si is striking. Also, a simplified model for the calculation of the switching losses was used and Fig.1.9.b) gives an insight of the advantage of using diamond for increasing the switching frequency of a power converter. However, together with the reduction of the semiconductor area, the loss

<sup>9</sup>Here, even if the  $R_{on}S$  is degraded by a factor 100 or 500, for SiC, GaN and diamond respectively, as compared to the calculated ideal value, one can see the advantage of WBG semiconductors over Si.

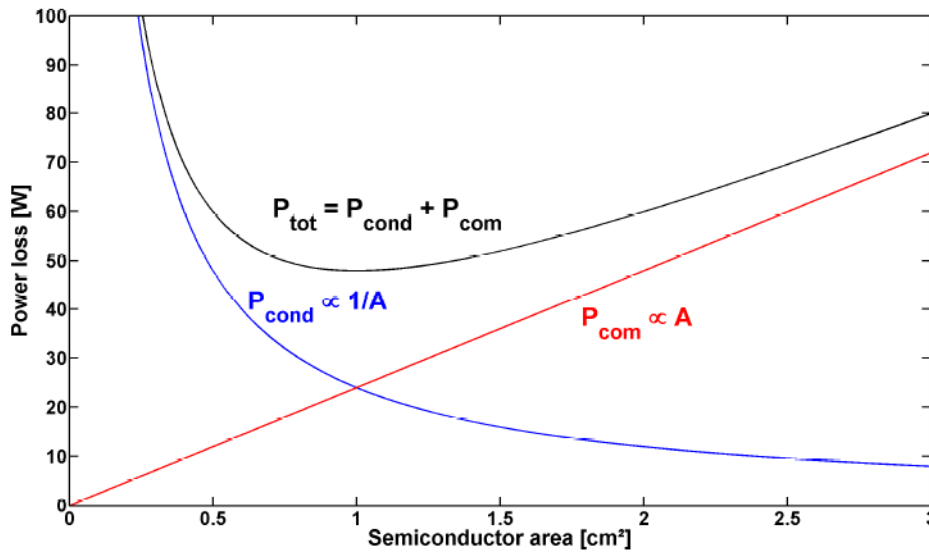


Figure 1.8: Power losses as a function of the semiconductor area, for a unipolar device with specifications 1200 V/10 A – 35 kHz –  $\alpha = 0.5$ . The total losses  $P_{tot}$  is the sum of the conduction losses  $P_{cond}$  ( $\propto 1/A$ ) and the commutation losses  $P_{com}$  ( $\propto A$ ) [Kolar 2012, Rouger 2015].

density and the current density will increase. Thus, particular attention must be paid when designing WBG power devices.

As discussed above, there is a number of exciting challenges to tackle for developing next generation diamond power devices. Several architectures were thus envisioned for developing high performance diamond based devices as discussed in the next section.

## 1.4 State of the art of diamond devices

Constant effort in improving and developing diamond device processing led to the emergence of a number of devices such as Schottky diodes, p-n diodes or p-i-n diodes. Here, focus is made on field effect devices.

Several authors reported the operation of diamond metal-semiconductor field effect transistor (MESFET) using hydrogen-terminated diamond (H-diamond) to control the 2D hole gas at the diamond surface [Kawarada 1994, Ueda 2006, Ueda 2010, Russell 2012]. These devices were aimed to target high frequency applications, but thermal stability under high temperature conditions was not reached. Recently, Umezawa et al.

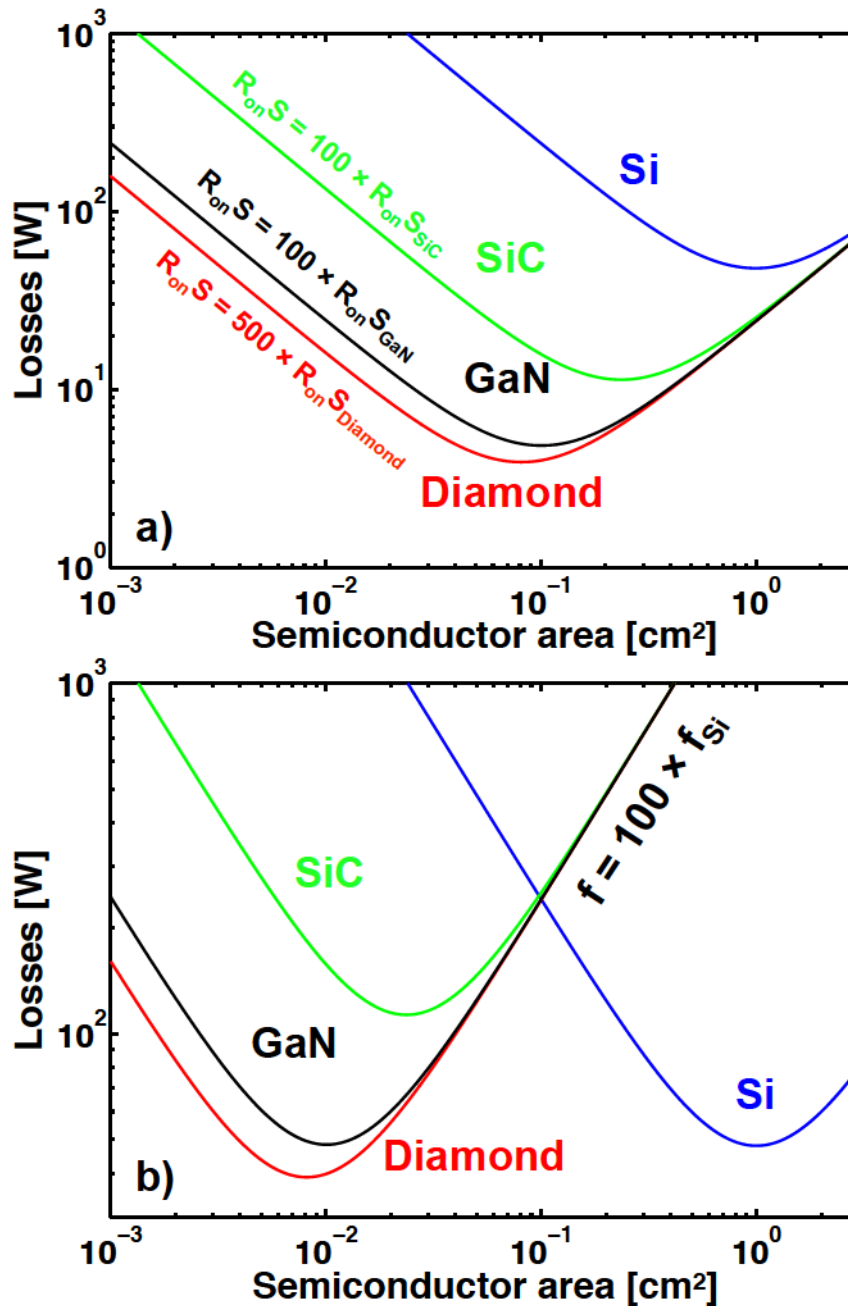


*Figure 1.9:* Example of semiconductor area optimization in the case of a vertical unipolar power device with 1200 V/10 A – 35 kHz –  $\alpha = 0.5$ . A comparison is made between Si, SiC, GaN and diamond. a) A reduction in the  $R_{on}S$  results in a reduced semiconductor area and an improvement of the power losses in the power device. b) Even though an increase of the switching frequency ( $f_{WBG} = 100 \times f_{Si}$ ) does not result in a significant reduction of the power losses, the semiconductor area is reduced [Rouger 2015].

[Umezawa 2014] reported the stable operation of diamond MESFET fabricated on oxygen-terminated diamond. The device exhibited clear FET operation up to 300 °C. However, the high source and drain resistances together with the high specific on-resistance of 1.4 k $\Omega$ .cm limited the device operation, i.e. the current density in on-state. Moreover the normally-on behavior might not be suitable for practical applications since normally-off operation are usually preferred. Normally-off devices could be fabricated by using thin p-type diamond layer, resulting in fully depleted layer.

The JFET architecture that allows to obtain either normally-on or normally-off device operation, was reported by Iwasaki et al. [Iwasaki 2012, Iwasaki 2013] and Hatano et al. [Hatano 2015]. The n<sup>+</sup>-type side gates enable the depletion of the p-type channel resulting in the drain current modulation by the gate voltage. The normally-on and normally-off behaviors are controlled by the channel width. This unique architecture led to very low on-resistance of the order of 52 m $\Omega$ .cm<sup>2</sup> and high current density  $\sim$ 1300 A.cm<sup>-2</sup> measured at 400 °C [Iwasaki 2013]. Also, high blocking capability of more than 600 V at elevated temperature was reported [Iwasaki 2014]. These devices showed drain current of  $I_{DS} = 1.2$  mA.mm<sup>-1</sup> under gate bias of  $V_{GS} = -2$  V and at 200 °C comparable to the performances reported for MESFET [Umezawa 2014]. These devices are promising for applications at high voltage and high temperature and designated for applications to harsh environment.

In 2012, Kato et al. [Kato 2012] reported the current amplification at room temperature in diamond bipolar junction transistor (BJT) on (111) oriented substrate with a maximum amplification of  $\beta = 11.5$  at  $V_{CE} = -10$  V. The same group also demonstrated the operation of diamond BJT on (001) substrate which allowed the determination of the hole diffusion length in the n-type base layer of  $4.2 \times 10^{-5}$  cm [Kato 2013]. Even though there are still room for improving the current amplification of such devices these contributions are major steps towards high power switching applications.

The thermal stability issues of diamond MESFET mentioned above have been circumvented very recently by the atomic layer deposition of Al<sub>2</sub>O<sub>3</sub> at elevated temperature (up to 450 °C) to stabilize the hydrogen-terminated layer [Hiraiwa 2012]. The resulting structure is a normally-on depletion mode metal-oxide-semiconductor field effect transistor (MOSFET) based on the control of the 2D hole gas in the hydrogen-terminated layer. Thus, high cut-off frequency (50 GHz), high temperature operation (400 °C) and

high breakdown voltage (600 V) have been achieved demonstrating the full potential of diamond for power electronic applications [Kawarada 2012, Kawarada 2014]. Also, drain current densities of more than  $1 \text{ A}\cdot\text{mm}^{-1}$  were demonstrated [Kawarada 2012]. These outstanding performances come from the particular band alignment of the  $\text{Al}_2\text{O}_3/\text{H}$ -diamond heterostructure, which is of type II as illustrated in Fig.1.10 [Liu 2012]. Such a configuration allows the confinement of holes in the 2D layer formed by the elevated barrier height at the  $\text{Al}_2\text{O}_3/\text{H}$ -diamond interface. This high barrier height prevents from leakage currents during device operation under accumulation conditions. In aiming to achieve a high density of accumulated holes several high- $\kappa$  dielectric layers have been deposited on H-diamond as reported in [Liu 2013b, Liu 2013a, Liu 2014a, Liu 2014b]. Normally-on and normally-off operation could be realized depending on device processing [Koide 2015].

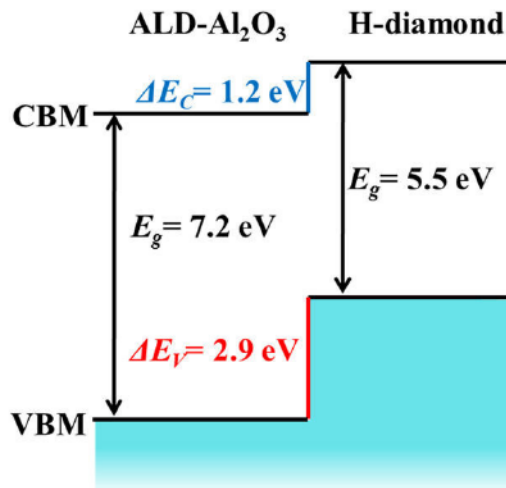


Figure 1.10: Energy band configuration of the  $\text{Al}_2\text{O}_3/\text{H}$ -diamond heterojunction as determined by X-ray photoelectron spectroscopy [Liu 2012]. The resulting alignment is of type II.

The MOSFET structure described above is a depletion mode MOSFET which off-state being obtained by depleting the 2D hole gas underneath the gate electrode. Another approach consists in using the inversion mode MOSFET, which is based on the control of the band bending at the oxide/semiconductor interface, allowing to reach theoretically both accumulation and inversion regime. The device can be realized in the normally-off configuration if the work function difference between the gate metal and semiconducting diamond is chosen appropriately. Thus, the band alignment between the dielectric and the diamond must have a barrier for both electrons and holes in order to limit the leakage current in the different operating regimes. This is possible by using oxygen-terminated diamond (O-diamond), and if a rigid model using electron affinities is used

the band diagram of Fig.1.11 is obtained demonstrating the presence of barrier for holes and electrons.

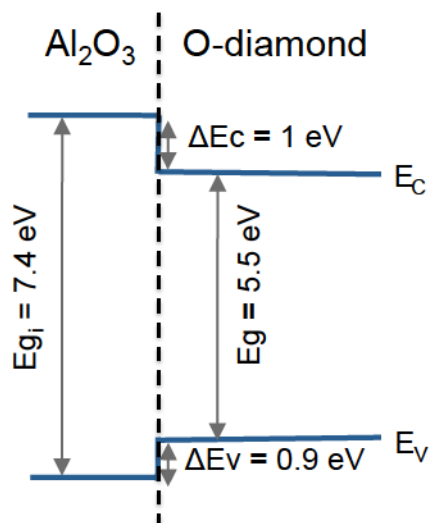


Figure 1.11: Type I band diagram configuration of the  $\text{Al}_2\text{O}_3/\text{O-diamond}$  hetero-junction deduced from the electron affinity method.

Moreover, the properties of the gate contact, the metal-oxide-semiconductor capacitor (MOSCAP) specifically the interface states density at the interface between the diamond and the dielectric layer and the presence of oxide charges in the dielectric layer strongly impact the electrical behavior of the devices.

In order to briefly summarize the current knowledge on  $\text{Al}_2\text{O}_3/\text{O-diamond}$  MOSCAP, results from G. Chicot PhD dissertation are presented [Chicot 2013a]. Fig.1.12 shows the planar MOSCAP structure. The ohmic contact is made of Ti/Pt/Au and the MOS stack is Al/ $\text{Al}_2\text{O}_3$  deposited on oxygen terminated boron doped diamond. The 20 nm thin  $\text{Al}_2\text{O}_3$  layer was deposited by atomic layer deposition (ALD). Details on the fabrication process can be found in [Chicot 2013b].

As shown in Fig.1.13, the diamond MOS structure can be operated under depletion and deep depletion regime (evidenced by the  $1/C^2(V)$  graph of Fig.1.13.b)) for increasing

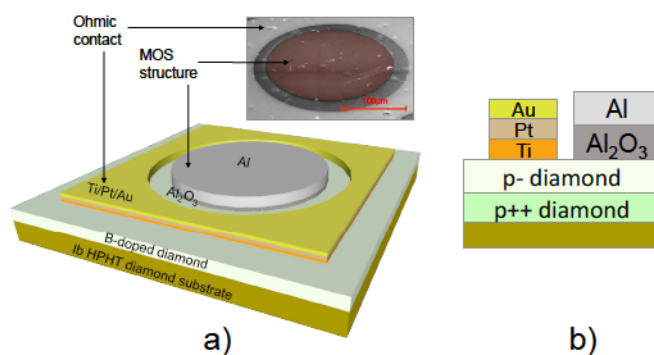


Figure 1.12: a) Al/ $\text{Al}_2\text{O}_3/\text{O-diamond}$  MOS schematic view and corresponding SEM image and b) cross section showing the stack [Chicot 2013b].

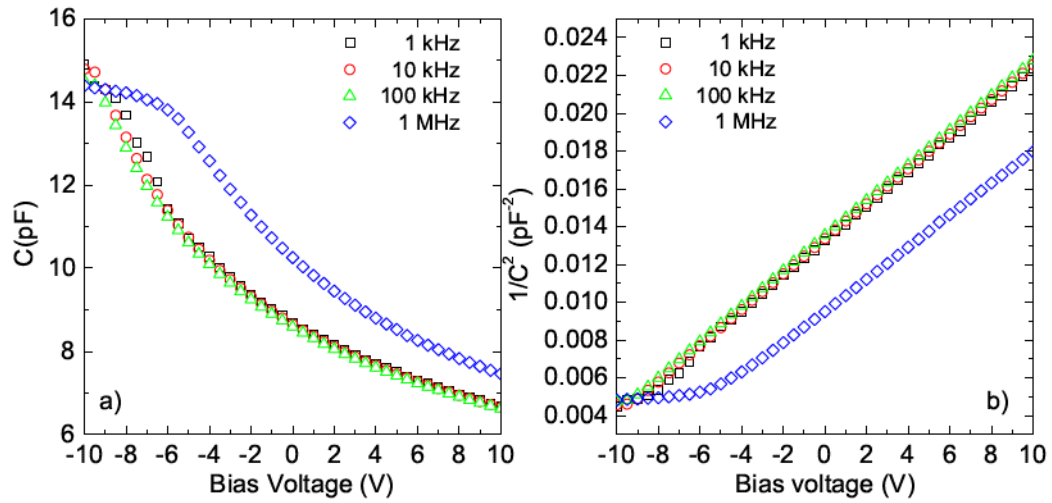


Figure 1.13: a)  $C(V)$  characteristic of the Al/Al<sub>2</sub>O<sub>3</sub>/O-diamond MOSCAP for various frequencies. b)  $1/C^2(V)$  plot showing constant slope for deep depletion regime [Chicot 2013a]. Measurements were performed at 300 K. The 20 nm thin Al<sub>2</sub>O<sub>3</sub> layer was deposited at 100 °C by ALD. The gate contact diameter is 200  $\mu$ m.

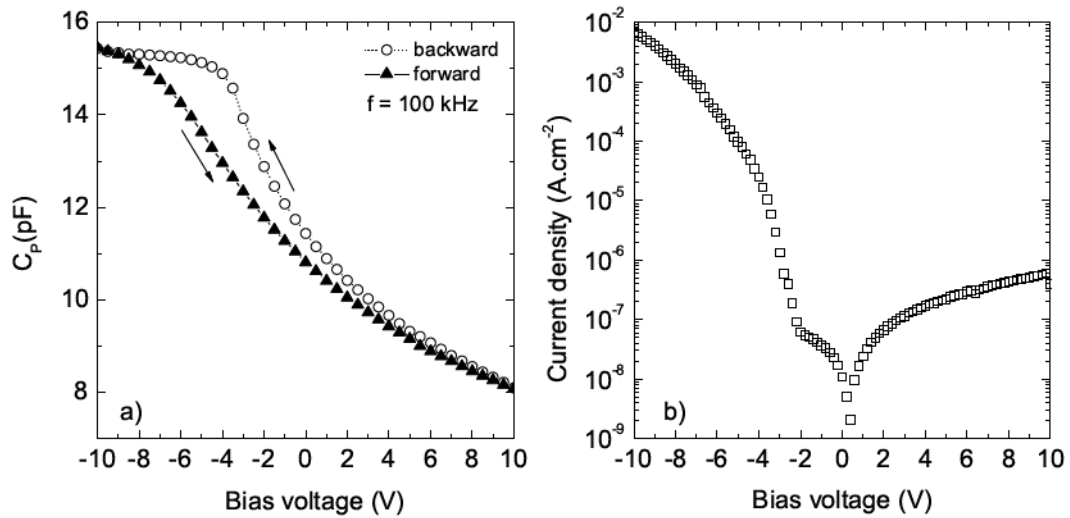


Figure 1.14: a) Hysteresis behavior of the  $C(V)$  characteristic at 100 kHz when biasing the structure from accumulation to deep depletion and from deep depletion to accumulation. b) Current-voltage  $I(V)$  characteristic of the device showing leakage currents [Chicot 2013a]. The 20 nm thin Al<sub>2</sub>O<sub>3</sub> layer was deposited at 100 °C by ALD.

gate bias voltages. Moreover, the accumulation capacitance does not depend on the ac signal frequency, but the stretch out of the  $C(V)$  characteristic is pronounced and varies from 1 kHz to 1000 kHz. At the same time, the expected accumulation capacitance was not reached. Specifically, the measured accumulation capacitance was 10 times smaller than the expected value. The origin of this discrepancy had not been identified, but

will be investigated in the present work using impedance spectroscopy characterization methods. Hysteresis behavior was observed on this device, as exhibited in Fig.1.14.a). This behavior occurs when mobile charges are present in the oxide layer. Thus, the I(V) properties of the device might be influenced by the presence of mobile ions. The current density versus gate bias voltage is plotted in Fig.1.14.b). In the accumulation regime, the current can be as high as  $10^{-2}$  A.cm<sup>-2</sup> at -10 V, whereas, when deep depletion takes place, the current is of the order of  $7.10^{-7}$  A.cm<sup>-2</sup> at 10 V. These currents could be explained by the low theoretical values expected for the electrons and holes barrier heights at the Al<sub>2</sub>O<sub>3</sub>/O-diamond interface [Chicot 2013b].

Thus, in order to have a better understanding of the Al<sub>2</sub>O<sub>3</sub>/O-diamond MOSCAP, a detailed analysis was performed during this thesis on the Al<sub>2</sub>O<sub>3</sub>/O-diamond heterojunction characterizing both the interfacial band configuration and the electrical properties of diamond MOSCAP.

Also, a first attempt in fabricating and characterizing a diamond MOSFET has been realized during a four month stay at the National Institute for Advanced Industrial Science and Technology (AIST) in Tsukuba, Japan. The device did not show ideal electrical behavior and its design could not be anticipated by numerical simulations. This is a consequence of the lack of simulation tools available for diamond device simulation. Thus, in order to predict the electrical behavior of future devices taking into account the specific properties of diamond, the development of simulation tools is highly needed. This is the aim of the second part of the present work.

## 1.5 On the need for reliable simulation tools

The need for anticipating the performances and architecture of future diamond devices is strongly motivated by the great number of experimental devices, which have been reported during the last decade. Simulation tools taking into account the specific properties of diamond must be developed. Efforts were initiated by several contributions mainly focusing on diamond Schottky diode simulations [Rashid 2006, Rashid 2008, Brezeanu 2008, Ding 2010]. Since diamond is a novel material for device simulations, the materials parameters have been specified to accurately reproduce the experiments. The

most important issues addressed were the incomplete ionization of dopants, the temperature and doping concentration dependent mobility model and impact ionization coefficient to model breakdown behaviors. Thus diamond Schottky diodes electrical characteristics were reproduced with relatively good correlations. On the other hand, Thion et al. proposed the design of field plate termination on diamond Schottky diode [Thion 2011]. This contribution demonstrates the possibility to develop simulation tools for the purpose of design optimization of future diamond power devices. However, up to date models such as the mobility models of Volpe et. al and Pernot et. al [Volpe 2009, Pernot 2010], the impact ionization coefficients of Hiraiwa et. al [Hiraiwa 2013, Hiraiwa 2015] or hopping mobility models [Hosoda 2013] are strongly required to perform reliable simulations.

Also, there is a lack of report on the simulation of diamond bipolar devices. This could be attributed to the lack of parameters regarding recombination-generation models for example. Thus, in order to predict the behavior of future diamond MOSFET the simulation of a diamond p-n junction was performed during this thesis. The next step has been to model the MOSFET characterized in Japan. The results will be presented in chapter 3.

## 1.6 Conclusion

Wide band gap semiconductors such as SiC and GaN are the next generation materials for near future applications in power electronics. In a long term approach, Diamond, according to its outstanding properties is envisioned for high power, high temperature and high blocking voltage applications. Diamond is expected to be the key semiconductor to develop greener technologies. However, there are significant challenges to consider, including material science, substrate cost and size, device processing and packaging and the development of simulation tools to anticipate the architecture of future devices. Still, diamond research field is progressing very fast and the results are very promising.

Aiming to address some of the above mentioned challenges, the objectives of this thesis are:

- to develop a simulation tool that takes into account the specific properties of diamond, in particular the hopping conduction mechanism, the partial ionization of dopants. . . ,

- to design a MOSFET based on the simulation model developed,
- to fabricate a MOSCAP according to the above mentioned design,
- to describe accurately the electric properties of the MOSCAP in order to pave the way toward the inversion regime MOSFET.

## Chapter 2

# Diamond electrical properties and ideal MOS concepts

### Contents

---

<b>2.1</b>	<b>Introduction</b>	<b>31</b>
<b>2.2</b>	<b>Diamond properties: Numerical models</b>	<b>32</b>
2.2.1	Temperature dependent band gap and intrinsic carrier concentration	32
2.2.2	Incomplete ionization of dopants	35
2.2.3	Empirical mobility model	41
2.2.4	Shockley-Read-Hall and Auger recombination models	42
2.2.5	Summary	43
<b>2.3</b>	<b>Ideal MOS capacitor theory</b>	<b>44</b>
2.3.1	Metal-Oxide-Semiconductor principle of operation	45
2.3.2	Identification of MOS working regimes through the $Q\Psi$ graph	48
2.3.3	MOS capacitance-voltage characteristics	51
2.3.4	Summary	56
<b>2.4</b>	<b>Conclusions</b>	<b>56</b>

---

## 2.1 Introduction

The development of next generation diamond metal-oxide-semiconductor field effect transistor (MOSFET) must fulfill several requirements in order to reach the material limits. Among them, being able to anticipate the architecture and electrical properties of the devices will stimulate the development and study of new diamond based power devices. In this perspective, some studies report the implementation of the unique physical properties of diamond into finite element based software, to reproduce the behavior of Schottky barrier diode (SBD) [Rashid 2006, Rashid 2008, Ding 2010]. In particular, the incomplete ionization of dopants, the dependence on doping and temperature of the carrier transport were implemented. With the approach of predicting diamond devices electrical properties, Thion et al. [Thion 2011] studied the effect of field plate terminations of p-type diamond SBD. Thus, it is straightforward to envision the advantage of such an approach: the influence of a high number of parameters (field plate thickness, material, active layer doping concentration and thickness) can be studied prior to the actual device realization. Then, the best material combination can be chosen for processing the most suitable device, while targeting specific performances. However, up to now, this approach only considered p-type diamond, the main reason coming from the fact that the carrier lifetimes and generation-recombination (G-R) models are unknown for n-type diamond and thus for diamond bipolar devices. In this work, the diamond physical parameters were implemented into a finite element based software (TCAD Silvaco) in order to reproduce the electrical properties of a p-n junction, in the view of validating the implemented diamond models. The long term target of our approach is to model the properties of future diamond MOSFET to extract trends and design guidelines. Together with the study of p-n junctions by use of TCAD tools, one needs to consider the other building block of the device, the metal-oxide-semiconductor capacitor (MOSCAP). Its experimental realization was studied in previous work of Chicot et al. [Chicot 2013b], where the electrical properties of MOSCAPs fabricated on oxygen-terminated boron doped diamond (O-diamond) using atomic layer deposition of  $\text{Al}_2\text{O}_3$  at 100 °C were investigated. Thus, this chapter is motivated by the need for modelling the behavior of diamond bipolar devices together with the experimental development of the MOSFET gate contact.

In the first part of this chapter, the specific diamond properties implemented into TCAD Silvaco will be given. In particular, the temperature dependent band gap and intrinsic

carrier concentration will be discussed. Particular attention will be paid on the high activation energies of dopants in diamond leading to the incomplete ionization of dopants. Finally, the temperature and doping concentration dependent mobility model will be given and the G-R models will be presented. In the second part, the properties of the ideal MOSCAP will be described and the identification of its working regimes will be made by using the  $Q\Psi$  graph concept developed by Vincent [Vincent 2008]. Finally, the properties of the Al/Al<sub>2</sub>O<sub>3</sub>/O-diamond MOSCAP will be presented, introducing the present work contribution on Al<sub>2</sub>O<sub>3</sub>/O-diamond interfacial and electrical properties investigation.

## 2.2 Diamond properties: Numerical models

In order to take into account the specific properties of diamond, the temperature dependence of the band gap as well as the intrinsic carrier concentration will be highlighted. Then, the incomplete ionization of dopants, the carrier mobility models and the generation-recombination (G-R) processes will be exposed. The influence of the temperature together with the influence of the G-R processes on the simulated p-n junction current densities will be shown.

### 2.2.1 Temperature dependent band gap and intrinsic carrier concentration

The electronic properties of a semiconductor material are determined by its band gap as well as the structure of its conduction and valence band in its vicinity. Diamond has an indirect band gap located between the maximum of the valence band at the  $\Gamma$ -point and the conduction band minimum located along the symmetry line between the  $\Gamma$ -point and the  $X$ -point in the Brillouin zone [Chelikowsky 1984, Monserrat 2014]. The dependence of the diamond band gap with temperature can be modeled by using the semi-empirical Varshni equation [Varshni 1967] as follows [SILVACO 2010]:

$$E_g(T) = E_g(300K) + \alpha \frac{300^2}{\beta + 300} - \alpha \frac{T^2}{\beta + T} \quad (2.1)$$

By fitting the experimental data reported in [Clark 1964] with Eq.2.1, the  $\alpha$  and  $\beta$  parameters are extracted as shown in Tab.2.1.

Symbol	$E_g(300K)$	$\alpha$	$\beta$
Unit	eV	eV.K <sup>-1</sup>	K
	5.46	1.01007	$3.95198 \times 10^6$

*Table 2.1:* Parameters used to describe the band gap temperature dependence obtained by fitting the data reported in [Clark 1964] with Eq.2.1.  $E_g(300K)$  represents the diamond band gap at 300 K.

Fig.2.1 shows the data taken from [Clark 1964] (open circles) together with the simulated temperature dependent band gap energy (solid line). The procedure was to implement the model into the finite element software and extract for each temperature the band gap energy value.

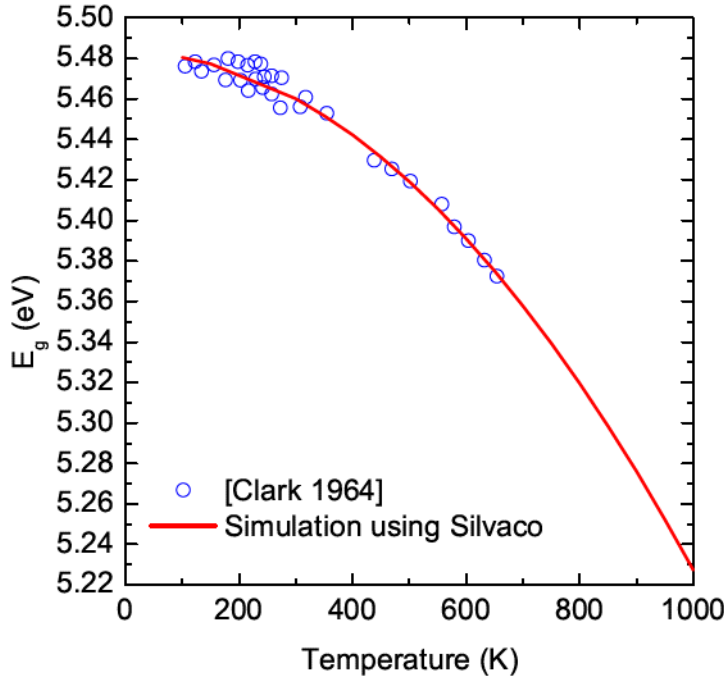


*Figure 2.1:* Temperature dependence of diamond band gap energy. Open circles represent the data taken from [Clark 1964] and the solid line is obtained by using Eq.2.1 with the parameters from Tab.2.1

In the parabolic approximation framework, the effective density of state of the conduction band is given by:

$$N_C = \frac{2 (2\pi m_e^* k_B T)^{3/2}}{h^3} \cdot M_c \quad (2.2)$$

with  $k_B$  Boltzmann's constant,  $T$  the temperature,  $h$  Planck's constant and  $M_c = 6$  the number of equivalent conduction band minima located along  $\Gamma$ -X. The electron density-of-state effective mass is calculated from the experimental values of [Gheeraert 2000]:

$$m_e^* = (m_{\perp}^2 m_{\parallel})^{1/3} \quad (2.3)$$

where  $m_{\perp}$  and  $m_{\parallel}$  are the transverse and longitudinal effective masses respectively.

In addition, the density of state in the valence band is given by:

$$N_v = \frac{2(2\pi m_h^* k_B T)^{3/2}}{h^3} \quad (2.4)$$

The hole density-of-state effective mass  $m_h^*$  is calculated by assuming the three valence bands to be parabolic. Considering (100) and (110) crystallographic orientation, the heavy hole (hh) and light hole (lh) effective masses are calculated as follows [Pernot 2010]:

$$m_{hh}^* = \left[ (m_{hh}^{*110})^2 m_{hh}^{*100} \right]^{1/3} \quad (2.5)$$

$$m_{lh}^* = \left[ (m_{lh}^{*110})^2 m_{lh}^{*100} \right]^{1/3} \quad (2.6)$$

$$(2.7)$$

Finally, the total density-of-state effective mass for holes is computed as<sup>1</sup>:

$$m_h^* = \left( m_{hh}^{*3/2} + m_{lh}^{*3/2} + m_{so}^{*3/2} \right)^{2/3} \quad (2.8)$$

with  $m_{so}^*$  the spin-orbit hole effective mass. Tab.2.2 summarizes the electron and hole effective masses taken from [Willatzen 1994, Gheeraert 2001, Naka 2013].

Recent work from Naka et al. [Naka 2013] on the measurement of the effective mass using cyclotron resonance of optically excited carriers in ultra pure diamond are in good agreement with the data taken from [Gheeraert 2000] and [Willatzen 1994].

<sup>1</sup>The spin-orbit splitting is assumed to be negligible.

Ref.	Electrons		Holes				
	$m_{\perp}$	$m_{\parallel}$	$m_{hh}^{*110}$	$m_{hh}^{*100}$	$m_{lh}^{*110}$	$m_{lh}^{*100}$	$m_{so}^*$
[Willatzen 1994]	0.341	1.5	0.690	0.427	0.276	0.366	0.394
[Gheeraert 2001]	0.306	1.81	-	-	-	-	-
[Naka 2013]	0.280	1.56	0.70	0.54	0.255	0.288	0.375

Table 2.2: Electrons and holes effective masses after [Willatzen 1994], [Gheeraert 2001] and [Naka 2013] respectively, in unit of  $m_0$ .

Due to the wide band gap of diamond, the intrinsic carrier concentration  $n_i$  is extremely small as compared to other semiconductor materials. Using Eq.2.2 and Eq.2.4,  $n_i$  can be calculated as follows:

$$n_i = \sqrt{N_c N_v} \exp\left(\frac{-E_g}{2k_B T}\right) \quad (2.9)$$

Fig.2.2 shows the temperature dependence of the intrinsic carrier concentration for diamond, 4H-SiC, GaN and Si. At 300 K,  $n_i$  is about 19 orders of magnitude smaller in diamond than in 4H-SiC. At low temperature, it can be interpreted as being the probability of exciting an electron from the top of the valence band to the bottom of the conduction band. At elevated temperature,  $n_i$  is still low as compared to the main WBG semiconductors. Since,  $n_i$  is involved in the generation-recombination processes (see section 2.2.4), it is also a key parameter for device simulation.

At elevated temperature, WBG materials will have superior electrical properties as compared to Si. On the other hand, diamond suffers from high activation energies of dopants which will be compared to the above mentioned semiconductors in the next section.

## 2.2.2 Incomplete ionization of dopants

The temperature dependence of the free carrier concentration is described by the charge balance equation. In order to preserve the electrical neutrality [Sze 2007], the total number of positive charges (donor atoms and holes) must be equal to the total density of negative charges (acceptor atoms and electrons) in the material. The total density of donors  $N_D$  is given as:

$$N_D = N_D^0 + N_D^+ \quad (2.10)$$

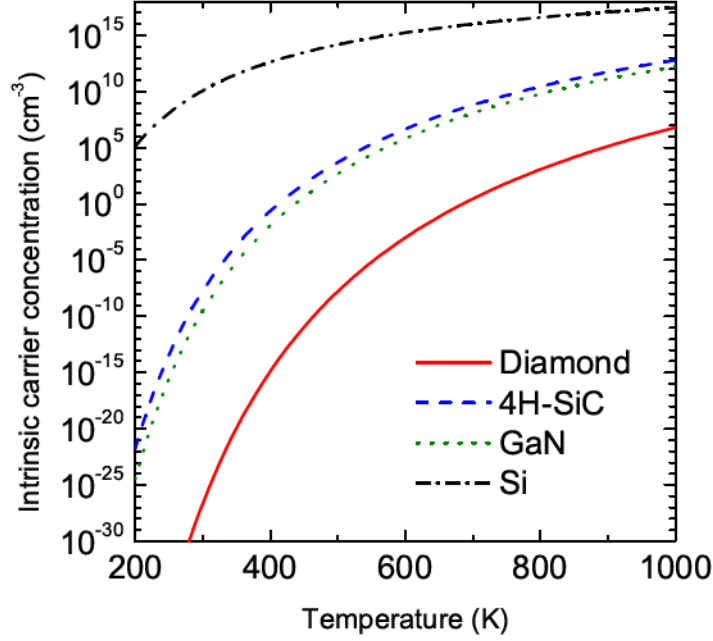


Figure 2.2: Temperature dependence of the intrinsic carrier concentration in diamond, 4H-SiC, GaN and Si taking into account the temperature dependence of the band gap energy. At 300 K the intrinsic concentrations are  $2 \times 10^{-27} \text{ cm}^{-3}$ ,  $3 \times 10^{-8} \text{ cm}^{-3}$  and  $3 \times 10^{-10} \text{ cm}^{-3}$  for diamond, 4H-SiC and GaN respectively, whereas in the case of Si  $n_i = 1 \times 10^{10} \text{ cm}^{-3}$ .

where  $N_D^0$  is the density of neutral donors and  $N_D^+$  is the density of ionized donors. Similarly, for acceptors, the total number  $N_A$  is given by:

$$N_A = N_A^0 + N_A^- \quad (2.11)$$

with  $N_A^0$  is the density of neutral acceptors and  $N_A^-$  is the density of ionized acceptors. Thus, the neutrality equation reads:

$$p + N_D^+ = n + N_A^- \quad (2.12)$$

$p$  being the hole concentration in the valence bands and  $n$  the electron concentration in the conduction bands. In the case of a p-type material  $p \gg n_i \gg n$ , and assuming  $N_D^+ = N_D$ , the neutrality equation can be written as follows:

$$p + N_D = N_A^- \quad (2.13)$$

Considering the occupation probability of  $N_A$  levels with energy  $E_A$ , the neutral acceptor concentration is:

$$N_A^0 = \int_{E_V}^{E_C} N_A \delta(E - E_A) f_F(E) dE = N_A f_F(E_A) \quad (2.14)$$

with  $f_F(E_A)$  the Fermi-Dirac distribution function for localized states, such as:

$$f_F(E_A) = \frac{1}{1 + g_A \cdot \exp\left(\frac{E_A - E_F}{k_B T}\right)} \quad (2.15)$$

where  $g_A = 4$  is the degeneracy factor for holes [Look 1989, Sze 2007]. Rewriting Eq.2.11 gives:

$$N_A^- = N_A (1 - f_F(E_A)) \quad (2.16)$$

Thus, the ionized acceptor concentration  $N_A^-$  is replaced in Eq.2.12:

$$p + N_D = \frac{N_A}{1 + \frac{p}{\phi_a}} \quad (2.17)$$

$$\phi_a = g_h \cdot N_V \exp\left(-\frac{E_a}{k_B T}\right) \quad (2.18)$$

where  $E_a = E_A - E_V$  is the acceptor thermal activation energy and  $g_h = 1/g_A$ . By solving Eq.2.17, the free hole concentration is:

$$p = \frac{1}{2} (\phi_a + N_D) \left( \sqrt{1 + \frac{4\phi_a(N_A - N_D)}{(\phi_a + N_D)^2}} - 1 \right) \quad (2.19)$$

Similarly, the free electron concentration, in an n-type material, is given by:

$$n + N_a = \frac{N_d}{1 + \frac{n}{\phi_d}} \quad (2.20)$$

$$\phi_d = g_e \cdot N_c \exp\left(-\frac{E_d}{kT}\right) \quad (2.21)$$

$$n = \frac{1}{2} (\phi_d + N_A) \left( \sqrt{1 + \frac{4\phi_d(N_D - N_A)}{(\phi_d + N_A)^2}} - 1 \right) \quad (2.22)$$

with  $g_e = 2$  the degeneracy factor for electrons [Look 1989, Sze 2007] and  $E_d = E_C - E_D$  the donor thermal activation energy.

The free carrier concentrations are strongly influenced by the dopants activation energy. In particular, the main dopants in diamond, respectively boron, phosphorus and nitrogen exhibit activation energies of 0.38 eV, 0.57 eV and 1.7 eV respectively. Fig.2.3

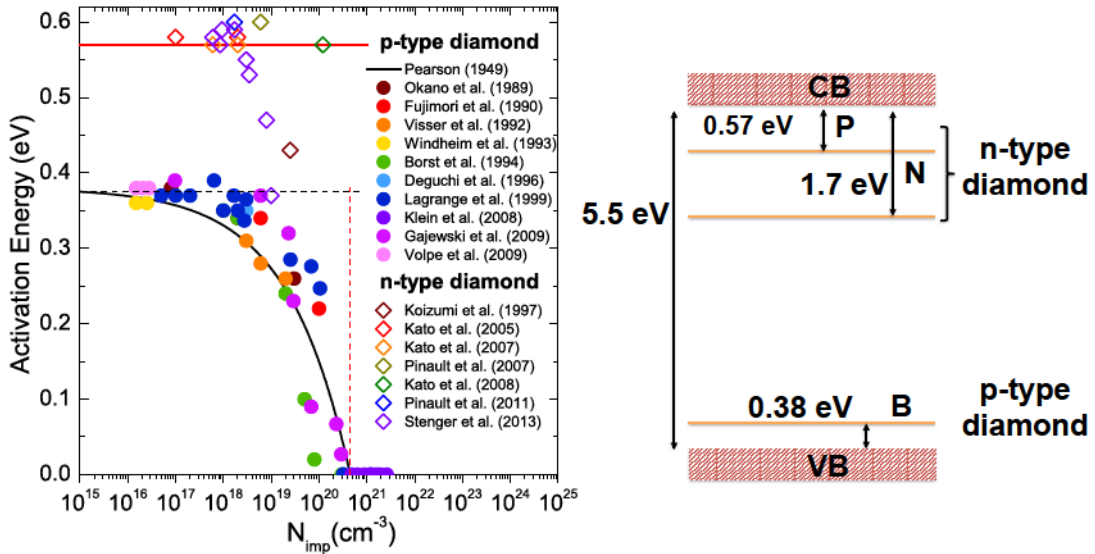


*Figure 2.3:* Activation energy of dopants as a function of the impurity concentration in diamond. The experimental boron activation energies are taken from the literature [Okano 1989, Fujimori 1990, Visser 1992, Windheim 1993, Borst 1995, Deguchi 1996, Lagrange 1999, Klein 2007, Gajewski 2009, Volpe 2009] and the solid curve is drawn after Pearson and Bardeen law [Pearson 1949]. Phosphorus activation energies are taken from the literature [Koizumi 1997, Kato 2005, Kato 2007, Pinault 2007, Kato 2008, Pinault-Thaury 2011, Stenger 2013]. Its value is assumed to be constant over the entire doping range.

represents the activation energy for boron and phosphorus as a function of the impurity concentration. As it can be seen, the boron activation energy is decreasing when increasing the impurity concentration (boron concentration). The physics leading to the reduction of the ionization energy is quite complex, thus an empirical law has been used, following Pearson and Bardeen model [Pearson 1949]. Parameters have been adjusted for boron acceptor in order to get 0.38 eV ionization energy at low dopant concentration [Lagrange 1998] and zero at the insulator-metal transition of  $4.5 \times 10^{20} \text{ cm}^{-3}$  [Klein 2007]:

$$E_a(\text{eV}) = 0.38 - 4.7877 \times 10^{-8} \times N_A^{\frac{1}{3}} \quad (2.23)$$

where  $E_a(eV)$  is the thermal activation energy of the boron acceptor in eV and  $N_A$  is the boron concentration in  $\text{cm}^{-3}$ . In the case of phosphorus donor, a constant value of  $E_d = 0.57$  eV for the activation energy has been assumed [Koizumi 2000, Gheeraert 2000] since reports indicate no measurable reduction up to  $10^{19} \text{ cm}^{-3}$ , and hopping conduction above. However, a recent report [Stenger 2013] indicates a decrease of the activation energy of phosphorus in the presence of high concentration of compensating impurities. In the present work, we only considered low compensated n-type diamond, thus the ionization energy of phosphorus was assumed to be  $E_d = 0.57$  eV.

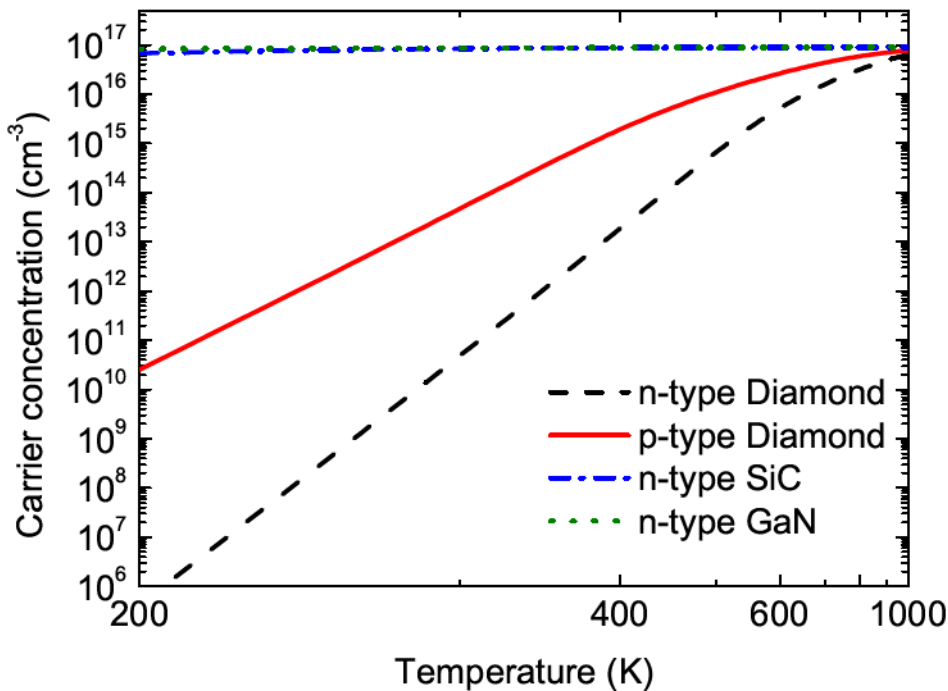


Figure 2.4: Carrier concentration as a function of  $1000/T$  for n-type diamond, p-type diamond, n-type 4H-SiC and n-type GaN. The compensation was set to 10%. The energy band gap temperature dependence was taken into account both for diamond (see Eq.2.1) and 4H-SiC,  $E_g^{4H-SiC}(eV) = 3.265 - 3.3 \times 10^{-2} T^2 / (10^5 + T)$ ,  $E_g^{GaN}(eV) = 3.47 - 7.7 \times 10^{-4} T^2 / (600 + T)$ .

Fig.2.4 shows the free carrier concentration as a function of  $1000/T$  for p-type diamond, n-type diamond, n-type 4H-SiC and n-type GaN. In contrast with 4H-SiC or GaN, diamond exhibits a very low ionization ratio ( $p/(N_A - N_D)$ ) of 3% at room temperature for a doping concentration of  $1 \times 10^{17} \text{ cm}^{-3}$  (obviously lower values will be achieved when taking into account the compensation, here a value of  $10^{16} \text{ cm}^{-3}$  was adopted for both n-type and p-type semiconductors).

Recent results on the measurement of excitonic recombinations in arsenic implanted diamond concluded that arsenic was successfully incorporated in substitutional site [Barjon 2014]. By performing cathodoluminescence measurements in the ultra-violet range on arsenic implanted CVD diamond samples, the authors were able to extract an arsenic ionization energy of 0.41 eV. This value is interesting, as the dopant energy level is closer to the conduction band energy than in the case of phosphorus. However, further electrical measurements must be done to confirm the n-type conductivity. In particular, in order to achieve high reliability of arsenic incorporation, the doping level could be controlled during the CVD growth process. Moreover, Hall measurements must be performed to confirm the electrical activity of arsenic as a donor.

These large activation energies of dopants in diamond (see Fig.2.5), lead to incomplete dopant ionization at room temperature. This is the main reason why regular devices such as junction field effect transistor (FET) have elevated series resistance at room temperature, and specific architectures have been developed such as delta-doped FET [El-Hajj 2008, Chicot 2012] or hydrogen-terminated FET [Kawarada 2012, Liu 2014c]. It is also of great importance for device simulation since the carrier densities at room temperature will be extremely low, leading to numerical convergence problems.

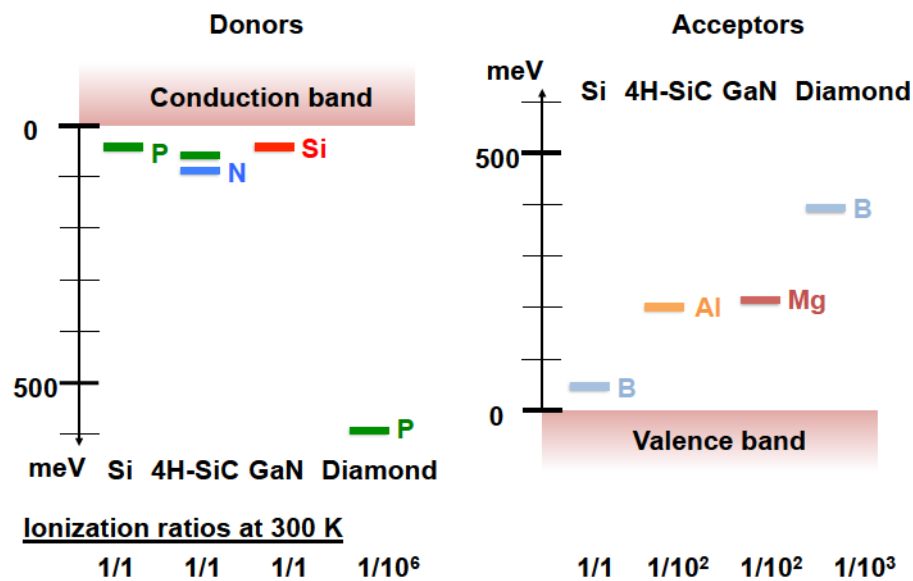


Figure 2.5: Schematic diagram illustrating the dopant ionization energies for Si, 4H-SiC, GaN and Diamond, for both n-type (donors) and p-type (acceptors) dopants. Also indicated are the ionization ratios in each case.

### 2.2.3 Empirical mobility model

A key parameter concerning diamond electronic device performances is the electron and hole mobility. The empirical model used to fit the experimental Hall effect measurements reported in [Volpe 2009, Pernot 2008] (see Eq. 2.24 to 2.26) has been implemented into Silvaco finite element based software via a built-in C language interpreter, in order to take into account the doping and temperature dependence of the mobility. This method has been adopted, instead of the proposed Masetti model [Masetti 1983], in order to implement in a second time the hopping mechanism, presented in section 3.3.2.5. The parameter values are summarized in Table 2.3.

$$\mu(T, N_{imp}) = \mu(300, N_{imp}) \times \left( \frac{T}{300} \right)^{-\beta(N_{imp})} \quad (2.24)$$

$$\beta(N_{imp}) = \beta_{min} + \frac{\beta_{max} - \beta_{min}}{1 + \left( \frac{N_{imp}}{N_{\beta}} \right)^{\gamma_{\beta}}} \quad (2.25)$$

$$\mu(300, N_{imp}) = \mu_{min} + \frac{\mu_{max} - \mu_{min}}{1 + \left( \frac{N_{imp}}{N_{\mu}} \right)^{\gamma_{\mu}}} \quad (2.26)$$

Symbol	$\beta_{min}$	$\beta_{max}$	$N_{\beta}$	$\gamma_{\beta}$	$\mu_{min}$	$\mu_{max}$	$N_{\mu}$	$\gamma_{\mu}$
Unit			$\text{cm}^{-3}$		$\text{cm}^2 \cdot \text{V}^{-1} \cdot \text{s}^{-1}$	$\text{cm}^2 \cdot \text{V}^{-1} \cdot \text{s}^{-1}$	$\text{cm}^{-3}$	
Hole	0	3.11	$4.1 \times 10^{18}$	0.617	0	2016	$3.25 \times 10^{17}$	0.73
Electron	0	2.17	$3.75 \times 10^{17}$	0.585	0	1030	$9.9 \times 10^{16}$	0.564

Table 2.3: Empirical mobility model parameters implemented in Silvaco finite element based software after [Volpe 2009, Pernot 2008].

where  $N_{imp} = (N_A + N_D)$  represents the total number of dopants. This empirical mobility model shows good agreement with the experiments over a wide range of doping concentration, from  $N_A \leq 10^{14} \text{ cm}^{-3}$ , where the mobility is equal to  $2016 \text{ cm}^2 \cdot \text{V}^{-1} \cdot \text{s}^{-1}$ , to  $N_A = 10^{21} \text{ cm}^{-3}$  where the mobility falls down to unity in the case of boron doped diamond. Concerning the phosphorus donor, the mobility is maximum ( $\mu_{max} = 1030 \text{ cm}^2 \cdot \text{V}^{-1} \cdot \text{s}^{-1}$ ) for  $N_D = 10^{14} \text{ cm}^{-3}$ , and close to unity when  $N_D = 10^{20} \text{ cm}^{-3}$ . Fig.2.6 shows the mobility calculated within the model described above, calculated at 300 K and 500 K.

Thus, the temperature and doping dependence of the mobility is taken into account. As the carrier dynamics does not only depend on the concentration and mobility, one needs to consider the generation-recombination models described in the next section.

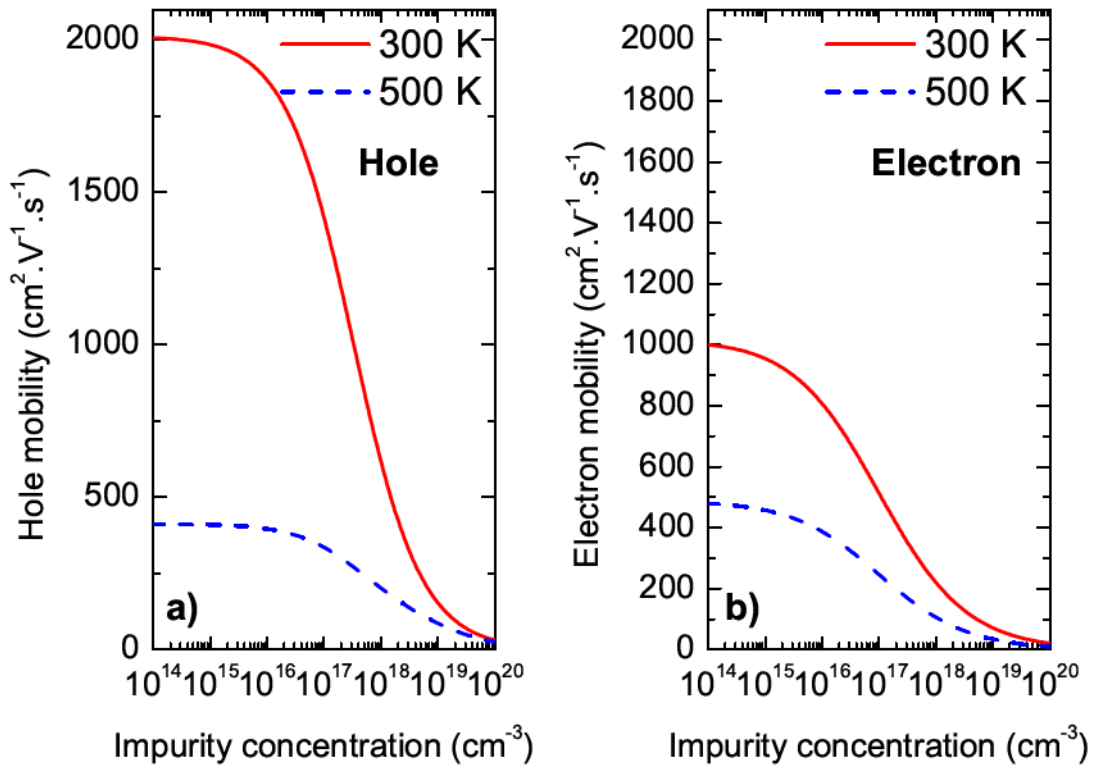


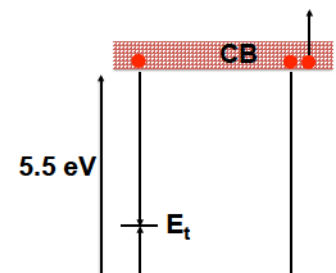
Figure 2.6: Theoretical a) hole and b) electron mobility calculated at 300 K and 500 K using the empirical model from [Volpe 2009, Pernot 2008].

#### 2.2.4 Shockley-Read-Hall and Auger recombination models

The carrier dynamics and distribution in a p-n junction is strongly influenced by recombination processes. In bipolar devices, an electron-hole pair has different ways to recombine. A first way is to recombine through a trap which energy lies in the forbidden gap [Shockley 1952]. This process is described by Shockley-Read-Hall (SRH) statistics and depends on the injected carrier lifetimes. Eq. 2.27 describes the recombination rate of this process,  $R_{srh}$  in cm<sup>-3</sup>.s<sup>-1</sup> as follows:

$$(G - R)_{srh} = \frac{pn - n_i^2}{\tau_p [n + n_i \exp(\frac{E_t}{kT})] + \tau_n [p + n_i \exp(-\frac{E_t}{kT})]} \quad (2.27)$$

with  $\tau_{p(n)}$  being the hole (electron) lifetime,  $E_t$  the energy difference between the trap energy and the intrinsic Fermi level energy. During the simulations, the value of  $E_t = 0$  eV



has been set and corresponds to the most efficient recombination center, located near the middle of the forbidden band gap.

The second recombination process considered was the Auger recombination process occurring at high doping concentration. This process occurs through a non-radiative recombination process in which an electron-hole pair recombines and gives its energy to a third particle. The Auger recombination rate is proportional to the product of the concentrations of the respective reaction partners as described by the following equation:

$$(G - R)_{Auger} = \Gamma_p n (pn - n_i^2) + \Gamma_n p (np - n_i^2) \quad (2.28)$$

with  $\Gamma_{p(n)}$  being the hole (electron) recombination coefficient in  $\text{cm}^6 \cdot \text{s}^{-1}$ . Fig. 2.7 illustrates these two G-R processes. These coefficients have been studied for silicon based devices and do not show temperature dependence [Dziewior 1977].

SRH and Auger G-R models have been widely studied for silicon based devices. However, a major difficulty for diamond based simulation tools relies in the fact that these coefficients remain unknown for diamond and that they are dependent on the fabrication process. Even though, their influences on the carrier densities and on the simulated  $J(V)$  characteristics have been studied in the view of reproducing experimental electrical characteristics, which will be discussed in section 3.3.

### 2.2.5 Summary

In this first part, the main diamond electrical properties implemented in the finite element based software were presented. Specifically, the temperature dependent band gap, the incomplete ionization of dopants, the temperature and doping dependent mobility and the generation-recombination models have been presented. Most of the difficulties encountered in diamond simulations rely on the facts that i) the intrinsic carrier concentration is extremely small in diamond and that ii) the G-R parameters are unknown.

Thus, particular attentions must be paid in order to avoid convergence problems and studying the influence of the G-R parameters is required for reliable diamond device simulations. These models were used to simulate a diamond p-n junction aiming to reproduce experimental data [Makino 2008, Koizumi 2013]. The results will be presented in chapter 3. On the other hand, the simulation of the diamond MOSFET (see section 3.4), based on the experiment performed at AIST (see section 4.6), considered the same parameters as for the p-n junction but only considered ideal MOS gate contact. The description of the working principle of the ideal MOSCAP is performed in the next part of this chapter.

### 2.3 Ideal MOS capacitor theory

Being one of the building blocks of the metal-oxide-semiconductor field effect transistor (MOSFET), it is of fundamental importance to investigate the properties of the metal-oxide-semiconductor capacitor (MOSCAP). As a matter of fact, the MOS structure allows the control of the band bending at the dielectric/semiconductor interface, which permits the control of carrier accumulation, depletion and deep depletion or inversion in the semiconductor. However, in order to operate the MOSCAP in the different working regimes, namely accumulation, depletion and deep depletion or inversion, the interface between dielectric and semiconductor must be of high enough quality. This means that the interface states density must be lowered, otherwise the band bending in the semiconductor at the interface with the dielectric cannot be controlled by the applied gate voltage. In the case of diamond MOSCAP, this is possible by achieving an appropriate surface treatment combined with a high quality diamond surface and the atomic layer deposition of  $\text{Al}_2\text{O}_3$  as the dielectric layer (Néel patented, December 2011) [Chicot 2013a, Chicot 2013b]. In order to give an accurate picture of the state of the art on the Al/ $\text{Al}_2\text{O}_3$ /O-diamond MOSCAP, the MOSCAP working principle will be described. Then, by using the  $Q\Psi$  concept [Vincent 2008], the electrical properties will be presented and will finally lead to the establishment of the MOSCAP capacitance versus voltage  $C(V)$  characteristic.

### 2.3.1 Metal-Oxide-Semiconductor principle of operation

The MOSCAP is formed by sandwiching a thin dielectric layer between a metal electrode (the gate) and a semiconductor connected to a metal electrode (the ohmic contact). The structure is schematically represented in Fig.2.8 in the case of a p-type semiconductor.

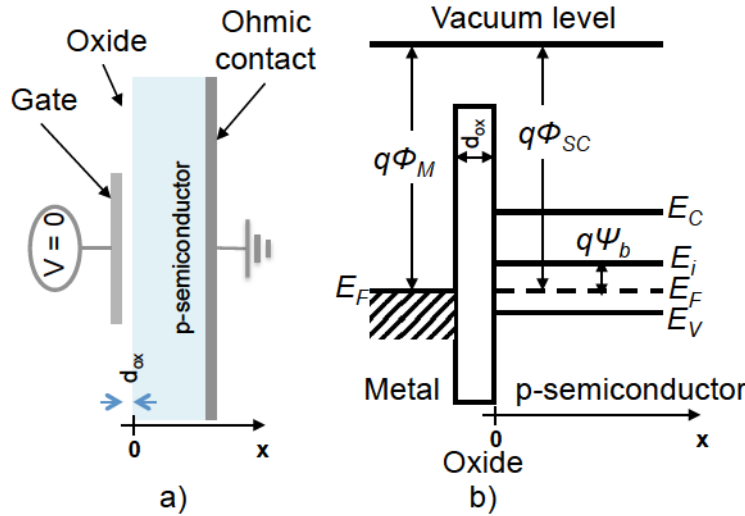


Figure 2.8: a) Metal-oxide-semiconductor capacitor (MOSCAP) and b) the corresponding energy band diagram in flat band condition with a gate voltage bias  $V = 0V$  for a p-type semiconductor. The origin of the axis is taken at the oxide/semiconductor interface.

Fig.2.8.b) shows the energy band diagram of the MOS structure. The position of the Fermi level in the metal and in the semiconductor is drawn as well as the metal and semiconductor work functions,  $q\Phi_M$  and  $q\Phi_{SC}$  respectively. In the present case, these two quantities are equal, leading to the following approximation concerning the flat band voltage  $V_{FB}$ :

$$V_{FB} = \Phi_M - \Phi_{SC} = 0 \quad (2.29)$$

Further hypothesis are required in order to simplify the study of the MOS capacitor [Sze 2007]:

- The oxide is considered to be perfect, which means that there is no carrier transport through the insulating layer. Moreover, the electron and hole barriers are large enough to prevent injection into the dielectric layer.

- There are no fixed nor mobile charges in the oxide. The only existing charges under any biasing conditions are located in the close vicinity of the oxide inside the semiconductor and equal but opposite in sign to the ones accumulated at the gate electrode.
- The doping concentration is constant inside the semiconductor and is p-type, i.e. holes are the majority carriers. Moreover, the dopants are fully ionized.
- As shown in Eq.2.29, the metal work function  $\Phi_M$  is equal to the semiconductor work function  $\Phi_{SC}$  such that the flat band voltage is equal to zero.

The described structure is based on the traditional silicon dioxide/p-type silicon ( $\text{SiO}_2/\text{p-Si}$ ) interface [Nicollian 1982]. One of the most important characteristic of this structure, is the presence of large energy barriers between the gate electrode,  $\text{SiO}_2$  and Si. This comes from the fact that the Si band gap is only 1.12 eV as compared to the 9 eV of the  $\text{SiO}_2$  band gap. Thus, 3.1 eV would be required to take an electron from the gate electrode Fermi level (here Aluminum,  $\Phi_m = 4.08$  eV) to the conduction band of the

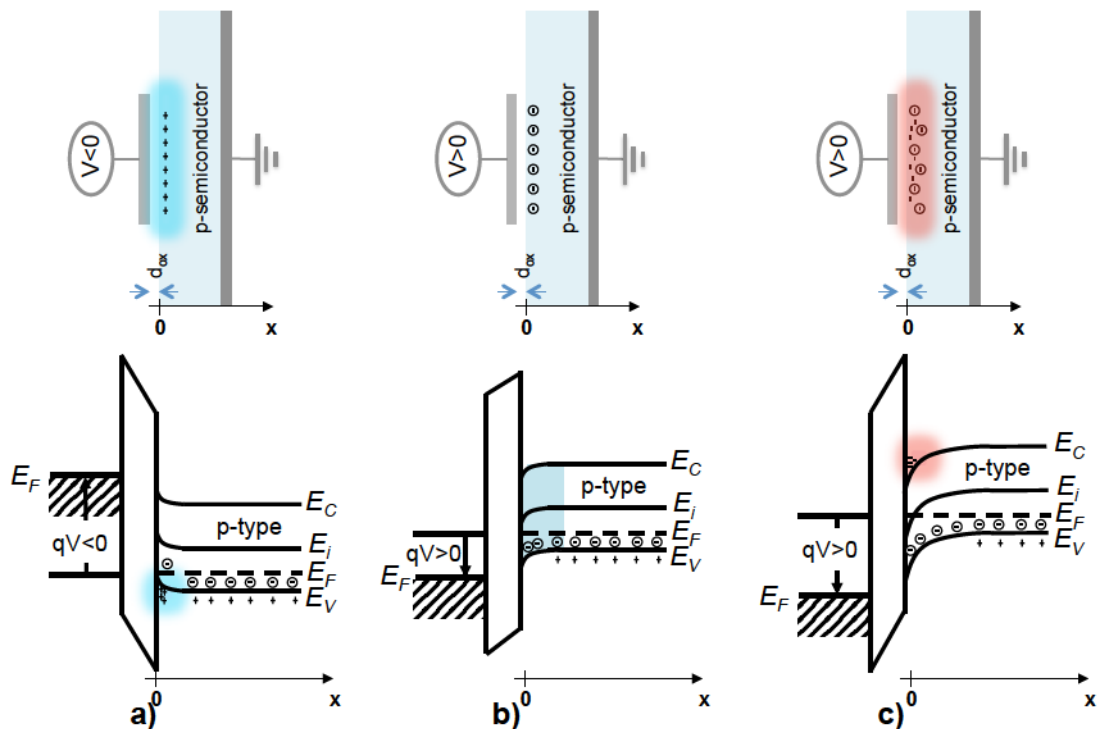


Figure 2.9: Structure and energy band diagram of a p-type MOSCAP in a) accumulation regime for  $V < 0$ , b) depletion regime for small positive bias voltage  $V > 0$  and c) inversion regime for high positive bias voltage, with  $q > 0$  the elementary charge.

SiO<sub>2</sub> and 4.7 eV would be needed to get a hole from the Si valence band to the SiO<sub>2</sub> valence band (with  $\chi_{SiO_2} = 0.9$  eV and  $\chi_{Si} = 4.05$  eV). These two energy barriers prevent from any carrier injection into the oxide, neither from the gate electrode nor from the Si, if the aforementioned hypotheses are respected. The semiconductor surface charge layer can be influenced by the application of a gate bias voltage. Basically, three regimes can be identified depending on the bias voltage conditions as shown in Fig.2.9. First, for negative bias voltage applied to the gate electrode ( $V < 0$  and  $V < V_{FB}$ ), negative charges at the gate attract holes at the semiconductor surface to create an *accumulation layer*. This is a consequence of the upward band bending in the semiconductor at the oxide/semiconductor interface, which brings the semiconductor valence band closer to the Fermi level (see Fig.2.9.a)). Then, when a small positive bias voltage is applied ( $V > 0$  and  $V > V_{FB}$ ), the downward band bending tends to deplete the accumulated majority carriers from the oxide/semiconductor interface. This results in the formation of a space charge region, characteristic of the *depletion regime*. Thus, the positive charges accumulated at the gate electrode are balanced by negative acceptor ions inside the depletion layer (see Fig.2.9.b)). Finally, when increasing the positive gate bias, the intrinsic Fermi level  $E_i$  crosses the Fermi level  $E_F$  near the oxide/semiconductor interface. The band bending is strong enough to confine minority carriers, here electrons, in great number such that the electron concentration could become greater than the hole concentration at the interface, on a thin inversion layer, which thickness is related to the Debye length,  $x_{inv} = \sqrt{2}L_D$ , with  $L_D = \sqrt{\varepsilon_s k_B T / (q^2 N_A)}$ . It is a consequence of thermal equilibrium: as holes are repelled from the interface, the electron density must increase to keep the  $p \times n$  product constant. This regime is called the *inversion regime* (see Fig.2.9.c)). The gate voltage at which the inversion regime occurs is called the threshold voltage  $V_t$  and given by:

$$V_t = 2\Psi_B + \frac{\sqrt{2\varepsilon_s q N_A 2\Psi_B}}{C_{ox}} \quad (2.30)$$

with  $\varepsilon_s$  the semiconductor dielectric constant,  $q$  the elementary charge,  $N_A$  the doping level,  $C_{ox}$  the oxide capacitance and  $\Psi_B$  the potential difference between the Fermi level  $E_F$  and the intrinsic Fermi level  $E_i$  defined as:

$$\Psi_B = E_F - E_i = \frac{k_B T}{q} \ln \left( \frac{N_A}{n_i} \right) \quad (2.31)$$

$k_B$  being Boltzmann's constant,  $T$  the temperature and  $n_i$  the intrinsic carrier concentration. In the case of incomplete ionization of dopants,  $\Psi_B$  must be modified as follows:

$$\Psi_B = \frac{k_B T}{q} \ln \left( \frac{p}{n_i} \right) \quad (2.32)$$

where  $p$  is the free hole concentration calculated using Eq.2.19. As an example, in the case of diamond when using the complete ionization approximation instead of the incomplete ionization of dopants would lead to an overestimation of 7.3 % at 300 K, for an acceptor concentration of  $2 \times 10^{17} \text{ cm}^{-3}$  and compensation of  $1 \times 10^{16} \text{ cm}^{-3}$ .

### 2.3.2 Identification of MOS working regimes through the $Q\Psi$ graph

The MOS capacitor physical and electrical characteristics depend on various parameters, such as the semiconductor doping level and thickness, the oxide thickness and permittivity as well as the temperature. In order to give a simple description of the impact of these parameters on the MOS capacitor behavior, G. Vincent proposed a simple approach based on the use of the  $Q\Psi$  graph, which describes the charge per unit area  $Q_{SC}^A$  as a function of the semiconductor surface potential  $\Psi_s$  [Vincent 2008]. Fig.2.10 shows in more details the energy band diagram at the surface of a p-type semiconductor in contact with an oxide layer. The potential  $\Psi_p(x)$  is defined with respect to the bulk intrinsic Fermi level at a distance  $x$  from the oxide/semiconductor interface and defined by Eq.2.33 as [Sze 2007]:

$$\Psi_p(x) = \frac{E_i(x) - E_i(\infty)}{q} \quad (2.33)$$

The surface potential  $\Psi_s$  is the potential at the semiconductor surface where  $x = 0$ , i.e.  $\Psi_p(0) = \Psi_s$ . The potential  $\Psi_p(x)$  is related to the electron and hole concentration by the Poisson equation:

$$\frac{d^2 \Psi_p(x)}{dx^2} = - \frac{\rho(x)}{\epsilon_s} \quad (2.34)$$

where  $\rho(x)$  is the total space charge density defined by:

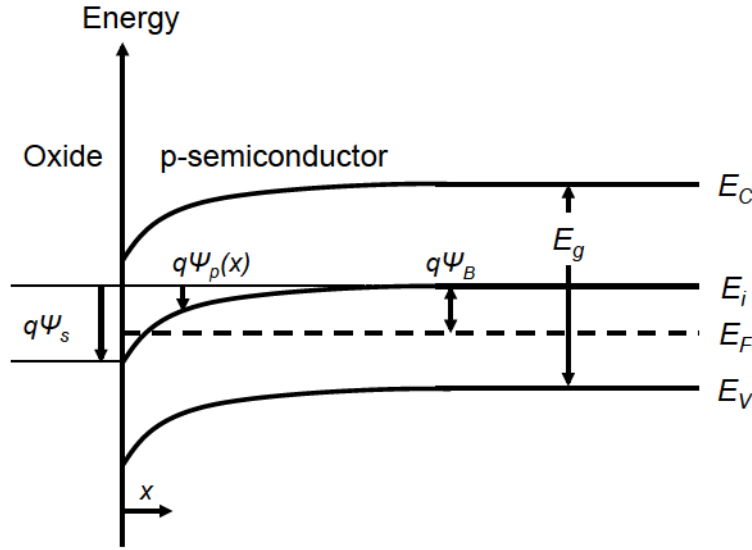


Figure 2.10: Energy band diagram at the p-type semiconductor surface.

$$\rho(x) = q(N_D^+ - N_A^- + p_p - n_p) \quad (2.35)$$

with  $N_D^+$  and  $N_A^-$  being the ionized donor and acceptor densities respectively. The electric field is obtained by integrating Eq.2.34 from the surface to the bulk. Then, using Gauss's law, it is possible to write the total charge per unit area  $Q_{SC}^A$  as a function of the surface potential  $\Psi_s$  [Sze 2007, Vincent 2008]:

$$Q_{SC}^A = -\text{sign}(\Psi_s) \times \left[ 2\varepsilon_s q N_A \left( \frac{k_B T}{q} (e^{-q\Psi_s/k_B T} - 1) + \Psi_s + \frac{k_B T}{q} e^{q(\Psi_s - 2\Psi_B)/k_B T} \right) \right]^{1/2} \quad (2.36)$$

with  $\text{sign}(\Psi_s) = 1$  when  $\Psi_s > 0$  and  $\text{sign}(\Psi_s) = -1$  when  $\Psi_s < 0$ . Fig.2.11 shows the total charge per unit area  $Q_{SC}^A$  plotted as a function of the surface potential  $\Psi_s$ .

From the  $Q\Psi$  graph, the identification of the MOSCAP working regime is obvious:

- When  $\Psi_s < 0$ , the structure is in accumulation, holes are accumulated at the oxide/semiconductor interface. Thus  $e^{q(\Psi_s - 2\Psi_B)/2k_B T} \ll e^{-q\Psi_s/2k_B T}$  leading to  $Q_{SC}^A \approx + \left[ 2\varepsilon_s q N_A \left( \frac{k_B T}{q} (e^{-q\Psi_s/k_B T} - 1) \right) \right]^{1/2}$ .
- In the depletion regime,  $0 < \Psi_s < 2\Psi_B$ ,  $e^{q(\Psi_s - 2\Psi_B)/2k_B T} \ll \sqrt{\Psi_s}$  and  $e^{-q\Psi_s/2k_B T} \ll \sqrt{\Psi_s}$ ,  $Q_{SC}^A \approx -\sqrt{2\varepsilon_s q N_A} \cdot \sqrt{\Psi_s}$ .

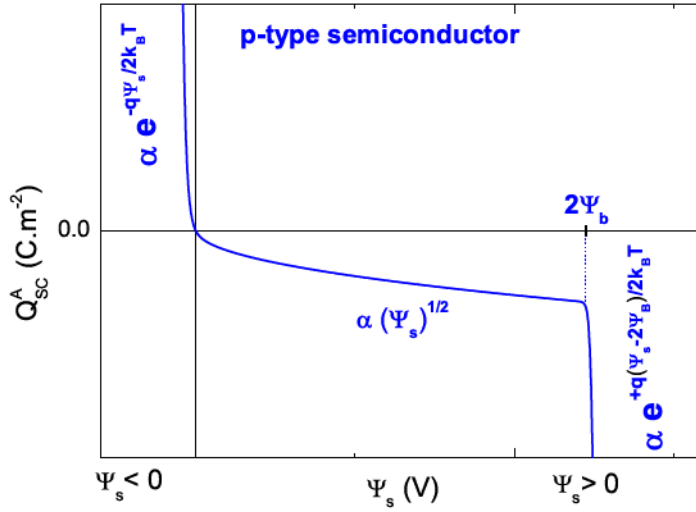


Figure 2.11: Total charge per unit area  $Q_{SC}^A$  in the semiconductor as a function of the surface potential  $\Psi_s$  for a p-type semiconductor in the case of an ideal MOSCAP.

- When the surface potential becomes greater than  $2\Psi_B$ , the MOSCAP is in inversion regime, which is characterized by  $e^{-q\Psi_s/2k_B T} \ll e^{q(\Psi_s - 2\Psi_B)/2k_B T}$  and  $\sqrt{\Psi_s} \ll e^{q(\Psi_s - 2\Psi_B)/2k_B T}$  and the total charge per unit area writes as

$$Q_{SC}^A \approx - \left[ 2\varepsilon_s q N_A \left( \frac{k_B T}{q} e^{q(\Psi_s - 2\Psi_B)/k_B T} \right) \right]^{1/2}.$$

The relationship between the total charge per unit area as a function of the surface potential is now established and the MOS operating regimes are easily identified depending on the value of the surface potential. However, the surface potential can not be directly adjusted. The only adjustable quantity is the gate bias voltage. These two quantities, namely the surface potential  $\Psi_s$  and the gate voltage  $V_G$  can be linked through Gauss's theorem. From this analysis, it can be shown that the electric field in the oxide is constant and given by  $E = -Q_{SC}^A/\varepsilon_{ox}$ . Then,  $Q_{SC}^A$  can be linked to  $V_G$  using the following equation:

$$Q_{SC}^A = \frac{\varepsilon_{ox}}{d_{ox}} (\Psi_s - V_G) \quad (2.37)$$

with  $\varepsilon_{ox}$  the oxide relative dielectric constant and  $d_{ox}$  the oxide thickness. The MOS working regime is thus given by the  $x$ -position at the intersection of the curve of Eq.2.11 with the straight dashed line of Eq.2.37 as represented in Fig.2.12.

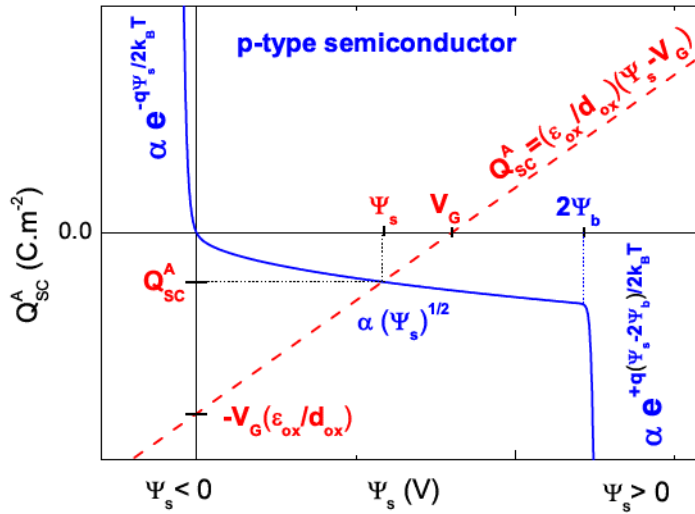


Figure 2.12: Graphical solution of the semiconductor charge per unit area as a function of the gate voltage for an ideal MOS structure. For a given gate bias voltage  $V_G$ , the surface potential  $\Psi_s$  is given by the abscissa at the intersection between the curve of Eq.2.11 (blue curve) with the straight line of Eq.2.37 (dashed red line).

### 2.3.3 MOS capacitance-voltage characteristics

In practice, the measurement of the dynamic capacitance as a function of the gate bias  $C(V_G)$ , is performed by superimposing an alternating voltage (ac voltage) to the constant gate bias voltage. The amplitude of the small ac voltage must be chosen such that  $V_{ac} \approx 2k_B T$  [Nicollian 1982]. Fig.2.13 shows the principle of the capacitance measurement together with the MOS capacitor structure with no interface traps, oxide charges and flat band voltage difference equals to zero. The oxide capacitance  $C_{ox}$  is bias independent whereas the semiconductor capacitance  $C_s$  is bias dependent.

#### 2.3.3.1 Ideal MOS C(V) characteristics

Having established the relationship between the semiconductor total charge per unit area as a function of the surface potential, the different MOS operating regimes are easily identified. However, in practical cases,  $Q_{SC}^A$  is not directly accessible. It can be accessed by measuring the capacitance response as a function of the applied gate bias voltage. In fact, the dynamic capacitance is linked to  $Q_{SC}^A$  by the following equation:

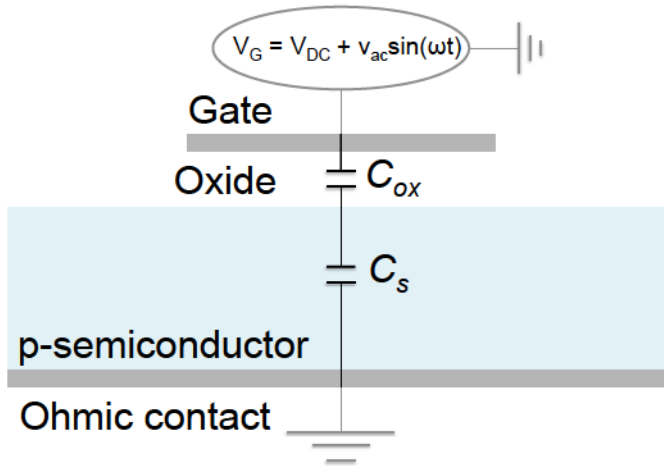


Figure 2.13: Simple equivalent circuit of the MOS capacitor with the bias independent oxide capacitor  $C_{ox}$  and bias dependent semiconductor capacitance  $C_s$ .

$$C^A = -\frac{\partial Q_{SC}^A}{\partial V_G} \quad (2.38)$$

where  $C^A$  stands for the capacitance per unit area. From the graph of Fig.2.11, the value of the capacitance in the different regimes can be evaluated qualitatively. In the accumulation and inversion regimes, the capacitance maximum is reached whereas the minimum capacitance is obtained in the depletion regime. Fig.2.14 illustrate this point. The red sinusoids indicate that when an ac voltage is applied to the gate electrode, a small variation of  $Q_{SC}^A$  is induced. Thus, it becomes obvious that in the accumulation and inversion regime the capacitance is maximum because the charge variation is maximum. Moreover, in the depletion regime the same ac voltage amplitude leads to a very small variation of  $Q_{SC}^A$ . The capacitance value is then minimum at the end of the depletion regime.

The link between the  $Q\Psi$  graph and the applied gate bias voltage enables to reconstruct the  $C(V)$  characteristic of the MOS capacitor. As shown in Fig.2.15, when the MOSCAP is negatively biased, the capacitance saturates to the oxide capacitance given by:

$$C_{ox} = \frac{\epsilon_{ox} S}{d_{ox}} \quad (2.39)$$

where  $\epsilon_{ox}$  is the oxide relative dielectric constant,  $S$  is the gate electrode area and  $d_{ox}$  is the oxide thickness. The oxide capacitance is bias independent, thus the accumulation capacitance is nearly flat. When increasing the bias voltage towards positive values, a space charge region develops in the semiconductor underneath the gate electrode. The

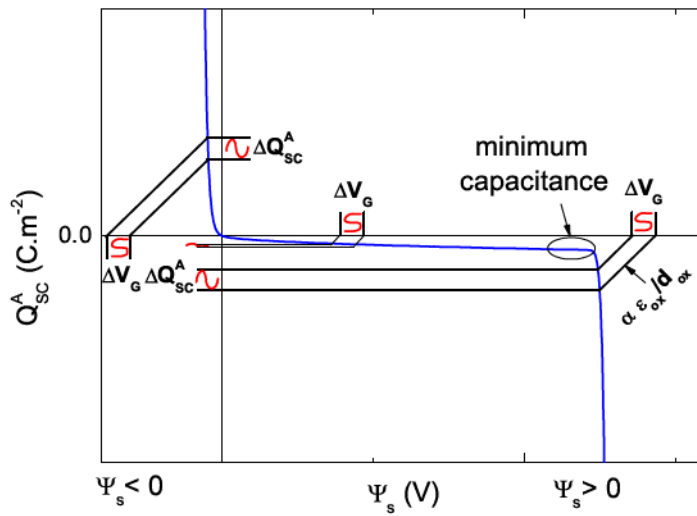


Figure 2.14: Behavior of the equilibrium MOS differential capacitance.

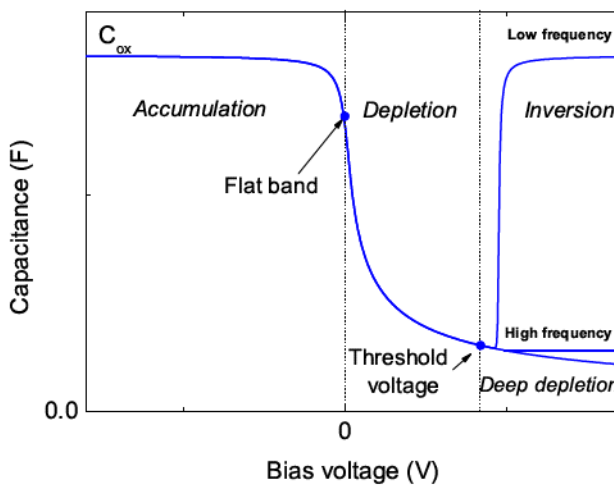


Figure 2.15: Theoretical C(V) characteristic of an ideal MOSCAP.

bias dependent semiconductor capacitance  $C_s(V)$  increases and the total capacitance decreases as follows:

$$C(V) = \left( \frac{1}{C_{ox}} + \frac{1}{C_s(V)} \right)^{-1} \tag{2.40}$$

which corresponds to the equivalent series capacitance circuit as indicated in Fig.2.13. For a larger applied bias, three cases can be distinguished: low frequency inversion, high frequency inversion and high frequency deep depletion.

### Low frequency inversion

When the small ac signal frequency is low enough, both majority and minority carriers can follow the change in ac band bending. Thus equilibrium is maintained. By increasing the gate bias voltage larger than the threshold voltage  $V_t$ , the generation of minority carriers, either from thermal or optical generation, here electrons, overcomes the majority carriers concentration. Then, the capacitance increases and saturates at the oxide capacitance value  $C_{ox}$ . This is explained by the fact that the electron inversion layer screens the depletion layer charge from further increase of the applied electric field.

### High frequency inversion

If the small ac signal frequency becomes too high, minority carriers can not follow the change in ac band bending. In fact, thermal and optical charge generation are slow processes. Thus, charge exchange within the inversion layer maintains the capacitance nearly flat in the high frequency inversion regime.

### High frequency deep depletion

When high measurement frequency is coupled with a rapidly sweeping gate bias voltage, minority carriers are not generated and the depletion layer, space charge region, continues to extend in the semiconductor layer. The capacitance decreases as  $\sqrt{V_G}$ . This regime is also used to extract both the doping level of the semiconductor and the flat band of the MOSCAP, in the case of a perfect oxide/semiconductor interface in the presence of  $V_{FB} \neq 0$ . The gate bias voltage can be written as:

$$V_G = V_{FB} - \frac{Q_{sc}^A}{C_{ox}} + \Psi_s \quad (2.41)$$

where the surface potential  $\Psi_s$  can be expressed as:

$$\Psi_s = \frac{-q(N_A - N_D)\varepsilon_{sc}\varepsilon_0}{2C_D^2} \quad (2.42)$$

with  $C_D$  the depletion layer capacitance. Thus, using Eq.2.40, and after some algebraic manipulations, the capacitance can be expressed as [Muret 2014]:

$$\frac{1}{C_t^2} - \frac{1}{C_{ox}^2} = \frac{2}{q(N_A - N_D)\epsilon_{sc}\epsilon_0} (V_G - V_{FB}) \quad (2.43)$$

where  $C_t$  is the total measured capacitance and  $C_{ox}$  is the oxide capacitance measured in the accumulation regime. Thus, the doping level ( $N_A - N_D$ ) is given by the slope  $\partial(1/C_t^2 - 1/C_{ox}^2)/\partial V_G$  of the linear fit of the  $(1/C_t^2 - 1/C_{ox}^2)$  plot and the flat band voltage value  $V_{FB}$  is read at the  $y$ -intercept.

In the above analysis, the distinction between high and low frequency is directly linked to the time constant for the inversion layer to be established, i.e. to the minority carrier generation rate [Engström 2014]. For instance, in silicon low frequencies are generally lower than 100 Hz [Mathieu 2004].

### 2.3.4 Summary

In this part, the ideal MOSCAP working principle and fundamental equations were presented and its electrical properties were established through the use of the  $Q\Psi$  graph concept. In particular, as represented in Fig.2.16, the charge per unit area in the semiconductor vs. surface potential  $Q_{SC}^A(\Psi_S)$  and the capacitance vs. voltage  $C(V)$  is easily reconstructed. This figure gives an idea of the order of magnitude of  $\Psi_b$  and of the expected accumulation capacitance, which corresponds to the oxide capacitance calculated for an area of  $A = 1.77 \times 10^{-4} \text{ cm}^2$  and an relative dielectric constant of  $\epsilon_{ox} = 9$ .

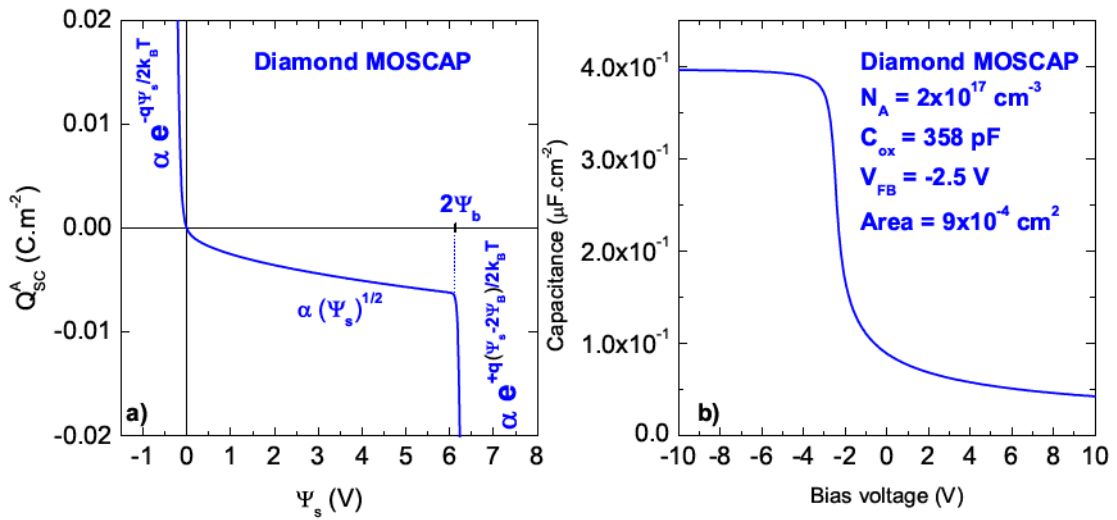


Figure 2.16: a) Charge per unit area  $Q_{SC}^A$  as a function of the surface potential  $\Psi_S$  in the diamond MOSCAP calculated from Eq.2.36. b) Corresponding capacitance vs. voltage ideal characteristic, with  $N_A = 2 \times 10^{17} \text{ cm}^{-3}$ ,  $V_{FB} = -2.5$ ,  $A = 9 \times 10^{-4} \text{ cm}^2$  and  $\epsilon_{ox} = 9$ .

## 2.4 Conclusions

The anticipation of the architecture and electrical properties of diamond based electronic devices, in particular MOSFET, requires the development of finite element based simulation tools which take into account the unique physical properties of diamond. Thus, the first part of this chapter presented the main parameters implemented into TCAD Silvaco. In chapter 3, the implemented models will be discussed through the simulation of a p-n junction. The influence of temperature on the main parameters will be shown

and discussed. Furthermore, the simulation of a diamond MOSFET, based on the implemented parameters values used during the p-n junction simulations, was performed. In this study, the gate contact was considered as ideal, i.e. the oxide is perfect in terms of insulating behavior and free of fixed charges.

However, the electrical properties of a MOSFET are influenced by the quality of its gate electrode. Thus, the second part of this chapter described the properties of the ideal MOSCAP, the most critical part of the MOSFET. Real MOSCAP, still, can show discrepancies related to the presence of interface states at the oxide/semiconductor interface as it is the case for our  $\text{Al}_2\text{O}_3/\text{O}$ -diamond MOSCAP. In order to investigate the  $\text{Al}_2\text{O}_3/\text{O}$ -diamond structure, chapter 4 will be dedicated to the study of the new  $\text{Al}_2\text{O}_3/\text{O}$ -diamond MOSCAP architecture allowing atomic layer deposition at 250 °C. The heterostructure band alignment and electrical properties of the fabricated diamond MOSCAP will be shown and discussed in terms of MOSFET fabrication. Moreover, during a four months stay at the National Institute for Advanced Industrial Science and Technology, the electrical characterization of a diamond MOSFET has been performed and the results will be presented in section 4.6.

# Chapter 3

## Diamond device simulations

### Contents

---

<b>3.1</b>	<b>Introduction</b>	<b>60</b>
<b>3.2</b>	<b>Mathematical models</b>	<b>61</b>
<b>3.3</b>	<b>Modelling of a diamond p-n junction</b>	<b>62</b>
3.3.1	p-n junction characteristics	63
3.3.2	Carrier density profiles	64
3.3.3	Summary	78
<b>3.4</b>	<b>Modelling of a diamond metal-oxide-semiconductor field effect transistor</b>	<b>79</b>
3.4.1	Historical framework of the MOSFET <sup>1</sup>	79
3.4.2	MOSFET working principle	80
3.4.3	Design of a planar inversion MOSFET	84
3.4.4	Summary	95
<b>3.5</b>	<b>Conclusions</b>	<b>98</b>

---

<sup>1</sup>this section is based on the extremely detailed review of C. T. Sah [Sah 1988].

### 3.1 Introduction

In the view of optimizing the architecture and predicting the electrical characteristics of future diamond power devices, implementation of the physical parameters and models of diamond into TCAD finite element based softwares is required.

In this context, Rashid et al. [Rashid 2008] have modeled a 1D diamond Schottky metal-intrinsic-p+ (m-i-p<sup>+</sup>) diode and studied the forward and reverse J(V) characteristics of the structure. The authors presented the implemented models and pointed out the lack of data inherent to diamond material as well as the difficulties encountered to simulate intrinsic diamond layer since the intrinsic carrier concentration is of the order of  $10^{-27}$  cm<sup>-3</sup> at 300 K. They found good correlations between simulated and experimental Schottky diode J(V) characteristics. The architecture of such a unipolar device has also been studied by Thion et al. [Thion 2011]. The authors studied the effect of a field plate on the electric field distribution in the structure showing the importance of numerical simulation for optimizing the device architecture. Nawawi et al. [Nawawi 2011] modeled the static and transient characteristics of a diamond Schottky diode in order to demonstrate the potential of diamond unipolar devices for power electronic applications. However, a more systematic approach for modeling either unipolar or bipolar diamond devices is needed. Since diamond technology is still very young, there is a lack of parameter values in the numerical tools. In the perspective of accurately modeling diamond MOSFETs, it is of fundamental importance to implement the physical parameter values of diamond (impact ionization coefficients, carrier lifetimes) and mobility models into the device simulators, over a wide range of temperature. Thus, studying the building blocks of diamond MOSFET, here the p-n junction, is needed.

In this chapter, the physical parameter values of diamond have been implemented into Silvaco TCAD finite element based software [SILVACO 2010]. The implemented models have then been applied to a diamond p-n junction, data taken from Makino et al. [Makino 2008] and Koizumi et al. [Koizumi 2013]. These references were used to compare the implemented parameter values and models. In a first part, the numerical models will be described. Then, the simulated diamond p-n junction characteristics will be presented. The influence of temperature, Shockley-Read-Hall lifetimes and Auger recombination parameters on the carrier densities and on the J(V) characteristics will be

shown. Moreover, the electrical properties of a simple planar structure MOSFET will be presented and discussed. We will conclude on the perspectives and the main difficulties due to the lack of parameter values and models implemented in the numerical simulation tools.

## 3.2 Mathematical models

In a semiconductor, free carriers displacement induces a current. This current can be caused either by an applied electric field (carrier drift) or by a difference in carrier concentration between two regions (carrier diffusion). These two phenomena are taken into account by solving Poisson's equation together with the carrier continuity equations and drift-diffusion transport equations [SILVACO 2010, Sze 2007]. Poisson's equation associates the electrostatic potential ( $V$ ) to the space charge density ( $\rho$ ) in the semiconductor, and is related to the properties of the p-n junction depletion layer (to be discussed later):

$$\Delta V = -\frac{\rho}{\varepsilon_{sc}} \quad (3.1)$$

where  $\Delta$  is the Laplace operator,  $\varepsilon_{sc}$  is the semiconductor dielectric constant. The electric field is obtained from the gradient  $\nabla$  of the electrostatic potential as:

$$\vec{E} = -\vec{\nabla}V \quad (3.2)$$

The carrier continuity equations are described as follows:

$$\frac{\partial n}{\partial t} = \frac{1}{q} \vec{\nabla} \cdot \vec{J}_n + G_n - R_n \quad (3.3)$$

$$\frac{\partial p}{\partial t} = -\frac{1}{q} \vec{\nabla} \cdot \vec{J}_p + G_p - R_p \quad (3.4)$$

with  $n$  and  $p$  the electron and hole concentrations,  $\vec{J}_n$  and  $\vec{J}_p$  the electron and hole current densities,  $G_n$  and  $G_p$  the electron and hole generation rates and  $R_n$  and  $R_p$  the electron and hole recombination rates. The last set of equations required to describe the

evolution of the electron and hole densities resulting from the transport processes, generation processes and recombination processes are the drift-diffusion transport equations described by Eq.3.5 and Eq.3.6 in the case of Boltzmann statistics:

$$\vec{J}_n = qn\mu_n\vec{E}_n + k_B T\mu_n\vec{\nabla}n \quad (3.5)$$

$$\vec{J}_p = qp\mu_p\vec{E}_p - k_B T\mu_p\vec{\nabla}p \quad (3.6)$$

with  $\mu_n$  and  $\mu_p$  being the electron and hole mobilities,  $n$  and  $p$  the electron and hole concentrations,  $\vec{E}_n$  and  $\vec{E}_p$  the effective electric fields as:

$$\vec{E}_n = -\vec{\nabla}\left(V + \frac{k_B T}{q}\ln(n_i)\right) \quad (3.7)$$

$$\vec{E}_p = -\vec{\nabla}\left(V - \frac{k_B T}{q}\ln(n_i)\right) \quad (3.8)$$

All these equations can be solved analytically by knowing the boundary conditions using Boltzmann approximation and when uniform doping profiles are considered. However, when Fermi-Dirac statistics are considered, one needs to use a numerical tool to solve the equations. Furthermore, if recombination-generation processes are taken into account, or for 2D and 3D structures and nonuniform doping profiles are studied, numerical tools begin to be mandatory. The following section presents the p-n junction characteristics studied to check the validity of the parameter values and models implemented into Silvaco software. Newton's finite element method is used for solving the equations at each finite element of the simulation domain representing the structure.

### 3.3 Modelling of a diamond p-n junction

Due to the large dopant ionization energies, the characteristics of the diamond p-n junctions are expected to be different from classical silicon p-n junctions, mainly due to the deep-dopant effect [Koide 2004]. In order to validate the properties of the diamond p-n junction simulated by Silvaco finite element based software, we studied the electrostatic

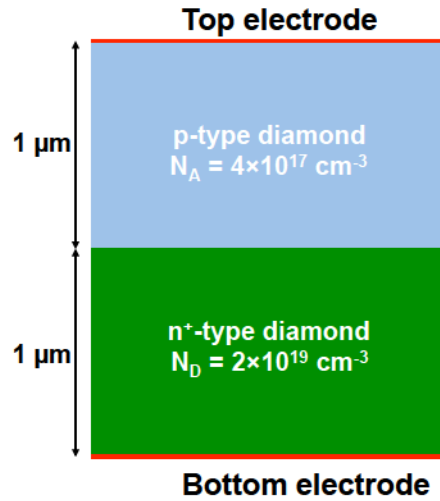


*Figure 3.1:* Simplified p-n junction structure for the 1D equation resolution.

features of the structure as well as the carrier concentrations. The simulation of the mobility neglected the effect of the electric field in the structure as well as the hopping mobility. The effect of the first one would be a decrease of the mobility in the regions of high electric field leading to a decrease of the current density. On the contrary, the hopping mechanism would decrease the resistivity, hence increasing the current density in the p-n junction.

### 3.3.1 p-n junction characteristics

The simulated p-n junction was inspired by the work of Koizumi et al. [Koizumi 2013, Koizumi 2002] and Makino et al. [Makino 2008, Makino 2006]. For simplicity, we considered a 1D equation resolution to check the validity of the different parameter values and models implemented in the numerical simulation tool. The structure of the simulated diode consists in a p-type diamond layer with boron concentration  $N_A = 4 \times 10^{17} \text{ cm}^{-3}$  and thickness of  $1 \mu\text{m}$  defined on top of the n<sup>+</sup>-type diamond layer with phosphorus concentration  $N_D = 2 \times 10^{19} \text{ cm}^{-3}$  and thickness of  $1 \mu\text{m}$ . This structure has been chosen to be vertical in opposition to the pseudo-vertical structure presented in [Koizumi 2013] for simplicity (see Fig.3.1).

The temperature has been set to 300 K. Ohmic boundary conditions were applied by sandwiching the junction between two metallic electrodes covering the entire surface. The compensation ratios are  $c_n = 10\%$  [Pernot 2008] and  $c_p = 1.25\%$  in the n<sup>+</sup>-type and p-type layer respectively. The models presented in section 2.2 were applied to the p-n junction. A particular attention was paid when defining the mesh of the structure to

prevent numerical convergence problems. Fig.3.2.(a) shows the simulated electric field as a function of the position centered at the p-n junction, for different biasing conditions. The maximum electric field value at the p-n junction is linked to the built-in potential according to Eq. 3.9.

$$|E_m| = \sqrt{\frac{2qN_aN_d(\Psi_{bi} - V)}{\epsilon_S(N_a + N_d)}} \quad (3.9)$$

where  $\Psi_{bi} = E_g - E_a - E_d$  is the built-in potential,  $q = 1.602 \times 10^{-19}$  C the elementary charge,  $V$  is the applied voltage and  $\epsilon_{sc} = 5.7\epsilon_0$ . By applying a forward bias voltage to the junction, the width of the space charge region is reduced leading to a decrease in the electric field intensity. The slope of the electric field versus depth in the p-type region, near the metallurgical junction, gives the doping concentration in the space charge region according to  $dE/dx = -qN_A/\epsilon_{sc}$ . The ionized dopants concentration is shown in Fig.3.2.(b). In the space charge region, which mainly extends in the lowest doped region, the dopants are fully ionized. Moving away from the junction, the ionized dopants concentration reaches the compensation concentration. Fig.3.2.(c) shows the band alignment at zero bias voltage and 300 K. The built in potential of  $\Psi_{bi} = 4.7$  eV is reproduced in agreement with experimental data. These first electrostatic simulations clearly demonstrate that the specificities of diamond devices are correctly implemented, and more precisely the incomplete ionization is verified.

### 3.3.2 Carrier density profiles

For calculating the current densities in the p-n junction, it is necessary to solve the drift-diffusion transport equations. They depend on the carrier densities in the device which are affected by the applied voltage as well as the recombination-generation processes. Depending on the bias condition, the structure can be either in the low or high injection regime. The following carrier densities result from the simulation of the diamond p-n junction without activating neither SRH nor Auger models to limit the effects of these recombination models. Their influences will be studied in section 3.3.2.3.

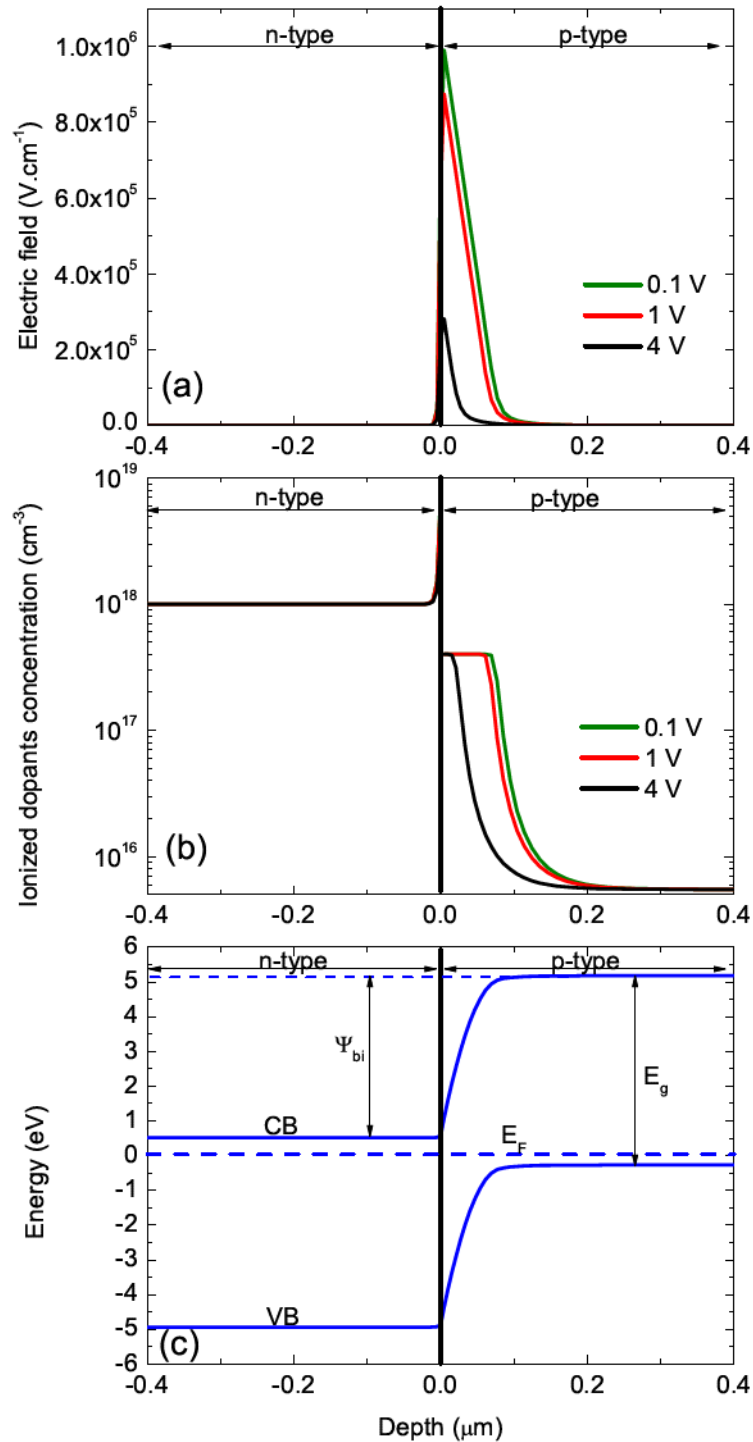


Figure 3.2: (a) Electric field calculated across the junction at different forward bias voltages. (b) Ionized dopants concentration as a function of the position at different forward bias voltages. The transition between the space charge region and the neutral regions is correctly modeled. (c) Band structure corresponding to the junction at zero bias and  $T = 300 \text{ K}$ , where CB and VB corresponds to the conduction band minimum and valence band maximum respectively.

### 3.3.2.1 Low injection regime

In the low injection regime, the hole concentration in the  $n^+$ -type region (minority carriers), is several orders of magnitude below the electron concentration (majority carriers). The hole concentration in the  $n^+$ -type region is enhanced by increasing the applied forward voltage. The effect of the applied forward voltage on the carrier concentrations is presented in Fig.3.3.(a).

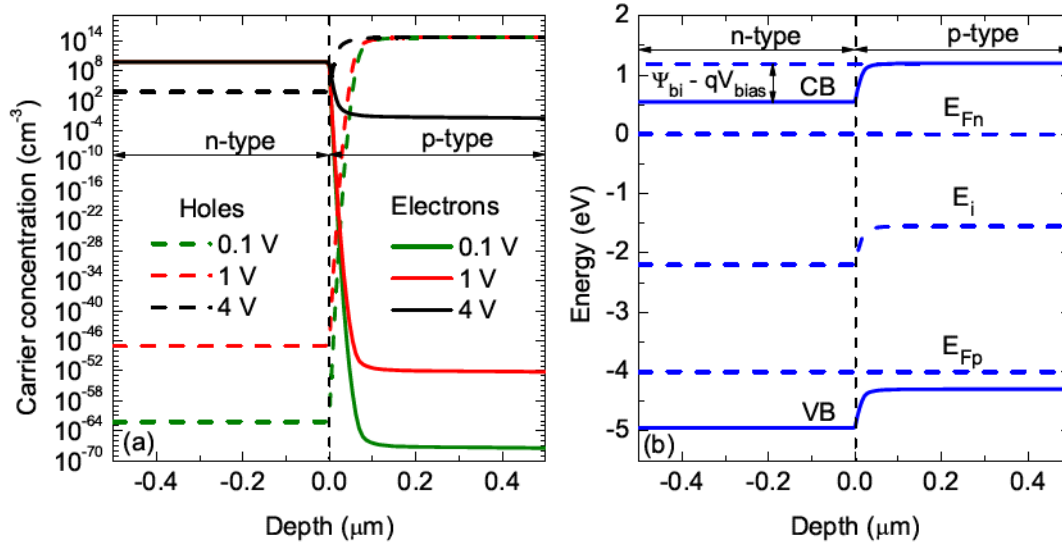


Figure 3.3: (a) Hole and electron concentrations for different low forward bias conditions. (b) Band diagram of the simulated p-n junction at 300 K for  $V_{bias} = 4$  V, showing constant  $q$ - $FL$ ,  $E_{Fp}$  and  $E_{Fn}$  respectively.

The calculated carrier concentrations are extremely low, of the order of  $10^{-63}$  cm<sup>-3</sup> at  $V_{bias} = 0.1$  V, but even with such low concentrations, the results are still consistent. The hole and electron concentrations are related to the quasi-Fermi level ( $q$ - $FL$ ) position relative to the intrinsic Fermi level ( $E_i \approx E_g/2$ ), as shown by Eq. 3.10 [Sze 2007].

$$p = n_i \exp\left(\frac{E_i - E_{Fp}}{kT}\right), n = n_i \exp\left(\frac{E_{Fn} - E_i}{kT}\right) \quad (3.10)$$

where  $n_i$  is the intrinsic carrier concentration,  $E_{Fp}$  and  $E_{Fn}$  are the  $q$ - $FL$  for holes and electrons respectively.

When the difference in energy between the  $q$ - $FL$  for holes and the intrinsic Fermi level is constant, the hole concentration remains constant in the structure. The same holds for

the  $q$ - $FL$  for electrons. This is illustrated by Fig. 3.3.(b), which represents the simulated band diagram of the p-n junction for  $V_{bias} = 4$  V.

The extremely low carrier concentrations result in extremely low diffusion currents in the low injection regime, and reach the numerical precision limit which is one of the main limitation of diamond device simulations. However, this is not a problem since, at low bias the leakage current is mainly governed by the carrier generation within the space charge region rather than diffusion. The leakage current due to carrier diffusion (saturation current) would indeed represent a negligible part of the measured reverse current [Sze 2007]. As it will be shown hereinafter, a more detailed model of generation is required for a precise model of leakage currents.

### 3.3.2.2 High injection regime

The high injection regime appears at higher bias voltage, which threshold is given by  $\Psi_{bi} = 4.7$  eV, deduced from Fig.3.2.(c), at room temperature. Consequently, the hole concentration in the  $n^+$ -type region becomes larger than the electron concentration. Fig.3.4.(a) shows the hole and electron concentrations in the structure. It can be seen that the hole and electron concentrations are no more constant in the neutral regions. This is due to the fact that the injected charges induce the bending of the conduction and valence bands as it is shown on the band diagram presented in Fig.3.4.(b). This bending causes a potential drop at the origin of the series resistance of the p-n junction and the resistivity modulation.

Fig.3.5 shows the simulated  $J(V)$  characteristics of the diode reported in [Koizumi 2013] at three different temperatures. The experimental data are plotted as a comparison. For bias voltage lower than the built-in potential, the simulated current level is of the order of  $10^{-10}$ - $10^{-11}$  A.cm<sup>-2</sup>, and strongly limits the simulations because it reaches the numerical precision limit of approximately  $10^{-11}$  A.cm<sup>-2</sup>.

The comparison between the experimental and simulated  $J(V)$  characteristics shows that the simulated low injection regime current densities do not correspond to the measured one. This is possibly due to parallel leakage conduction paths which are not taken into account during the simulations, and it is also a consequence of material impurities and defects which affects carrier generation. In the high injection regime there is a difference

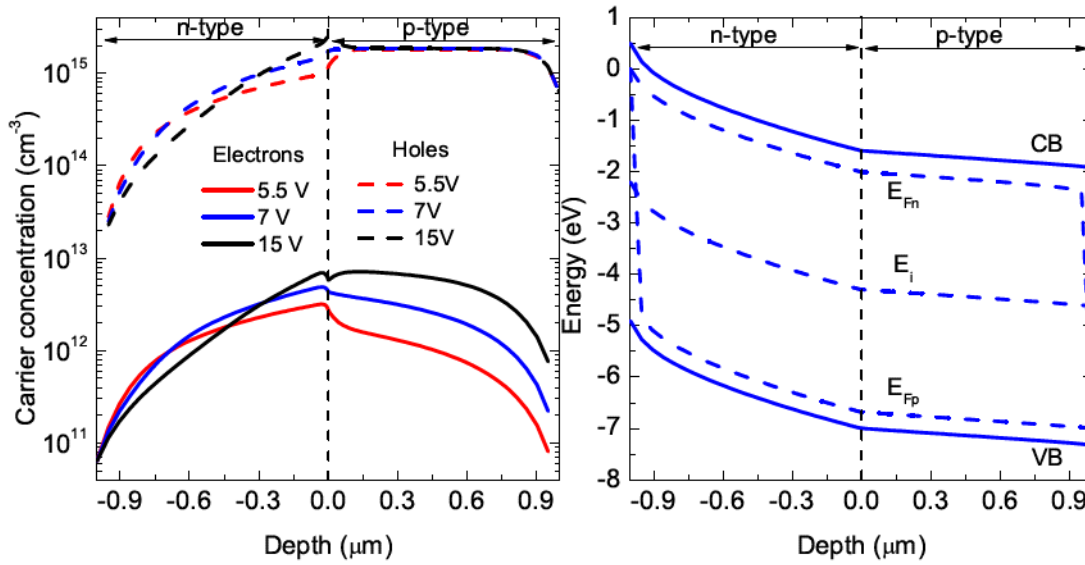


Figure 3.4: (a) Hole and electron concentrations for different high forward bias conditions. In the n<sup>+</sup>-type region, the hole concentration is higher than the electron concentration. (b) Band diagram of the simulated p-n junction at 300 K for  $V_{bias} = 7$  V, showing band bending in the structure.

between experimental and simulated current densities which can be adjusted either by adding a contact/access resistance to the electrodes or by tuning the carrier lifetimes of the recombination models. Moreover, the experimental ideality factor of 3.5 is not reproduced. In order to better fit the experimental J(V) characteristics, we investigated on the effects of SRH and Auger recombination models. The results are presented and discussed in the next section.

### 3.3.2.3 SRH lifetimes and Auger recombination parameters influence

To study the influence of SRH lifetime values on the simulated p-n junction characteristics, we chose the value of  $E_t = 0$  eV which maximizes the SRH recombination rate of Eq.2.27. Fig.3.6 presents the carrier concentrations in the low ( $V_{bias} = 1$  V) and high ( $V_{bias} = 7$  V) injection regime for three SRH lifetimes,  $\tau_p = \tau_n = 10^{-9}$  s,  $10^{-10}$  s and  $10^{-11}$  s with the constant Auger coefficients  $\Gamma_p = \Gamma_n = 10^{-30}$  cm<sup>6</sup>.s<sup>-1</sup>. It can be noticed that, by increasing the carrier lifetimes up to  $10^{-9}$  s, the carrier concentrations are closer to the concentrations calculated when the SRH and Auger recombination models are not implemented.

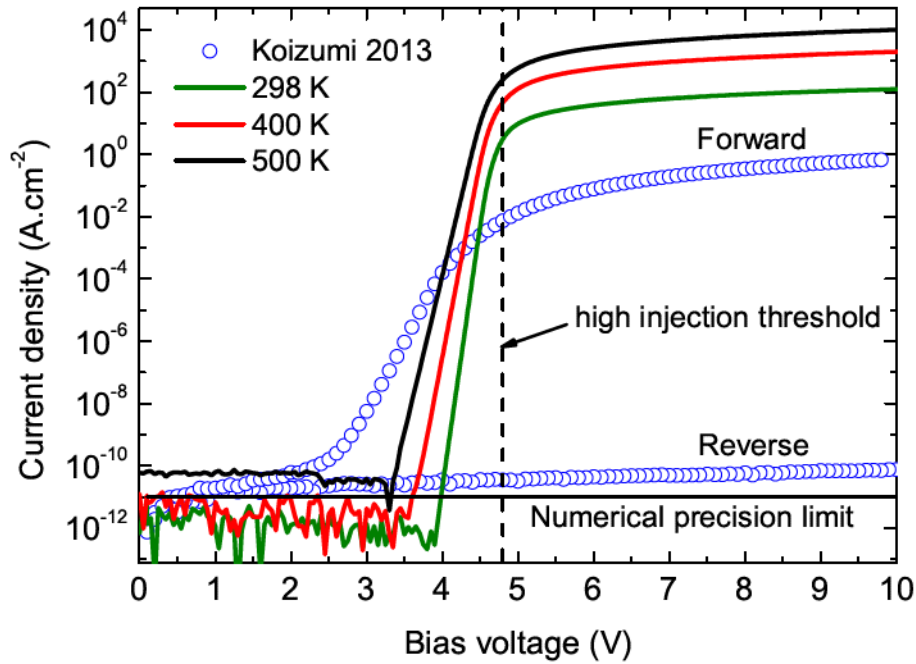


Figure 3.5: Simulated  $J(V)$  characteristics at different temperatures without using SRH nor Auger models. The experimental  $J(V)$  characteristic (open circles), measured at room temperature and reported in [Koizumi 2013], was used to validate the models and parameter values. The numerical precision limit is approximately  $10^{-11}$   $\text{A}\cdot\text{cm}^{-2}$  and the high injection threshold is 4.7 V.

The influence of the Auger recombination parameter on the carrier concentrations is shown in Fig.3.7. For this study, the value of the SRH carrier lifetimes was  $\tau_p = \tau_n = 10^{-9}$  s. When decreasing the Auger recombination parameter down to  $10^{-30}$   $\text{cm}^6\cdot\text{s}^{-1}$ , the carrier concentrations are close to the calculated one without recombination models. The simulations reveal that most of the influence appears in the high injection regime.

The influence of the Auger recombination-generation parameters on the  $J(V)$  characteristics is presented in Fig.3.8. Related to the carrier concentrations, the main influence of the parameter values appears in the high injection regime. In the low injection regime, the minority carrier concentrations are too low to have a significant influence on the current densities.

The study of the influence of the SRH lifetimes and the Auger recombination parameter values show a significant influence on the current densities. For instance, going from  $\tau$

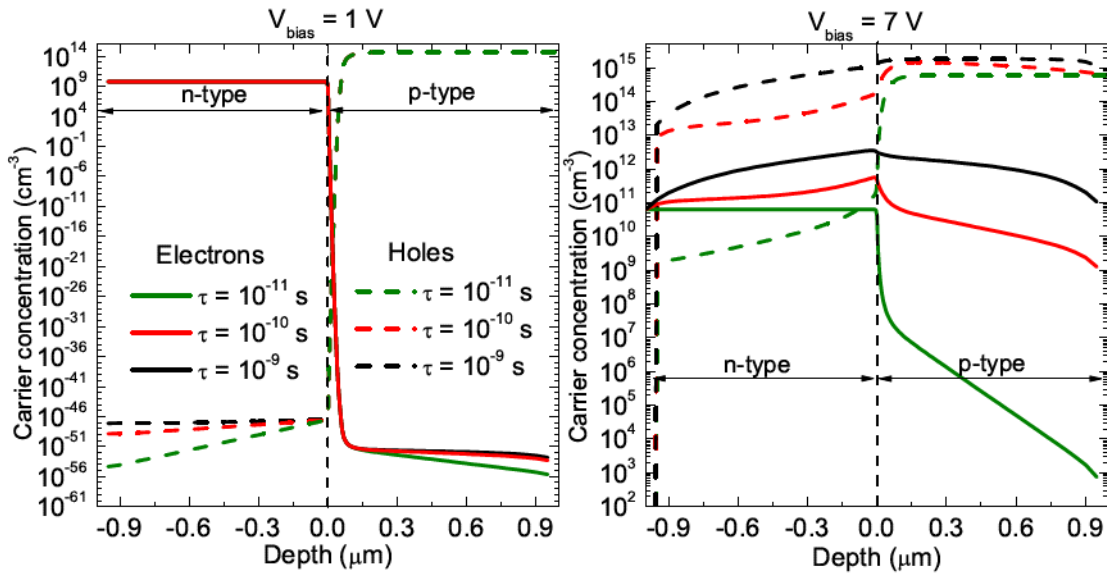


Figure 3.6: Effect of the SRH lifetimes ( $\tau = \tau_p = \tau_n$ ) on the carrier concentrations in the (a) low ( $V_{bias} = 1$  V) and (b) high ( $V_{bias} = 7$  V) injection regime. The simulations were done at 300 K and for a constant value of  $\Gamma_p = \Gamma_n = 10^{-30}$  cm<sup>6</sup>·s<sup>-1</sup>.

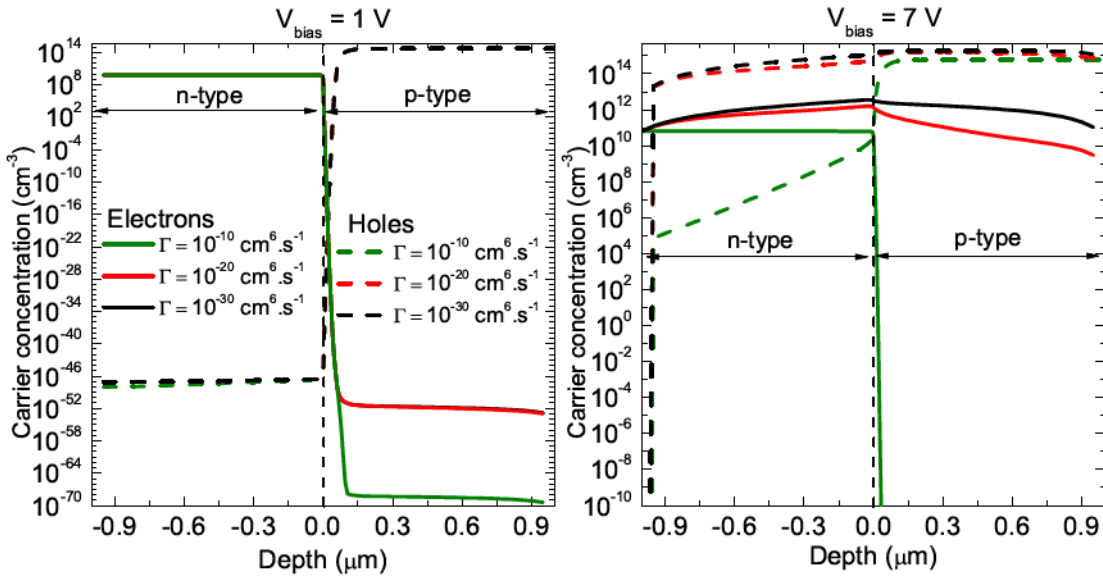


Figure 3.7: Effect of the Auger recombination parameter ( $\Gamma = \Gamma_p = \Gamma_n$ ) on the carrier concentrations in the (a) low ( $V_{bias} = 1$  V) and (b) high ( $V_{bias} = 7$  V) injection regime. The temperature was set to 300 K and the SRH lifetimes were  $\tau_p = \tau_n = 10^{-9}$  s.

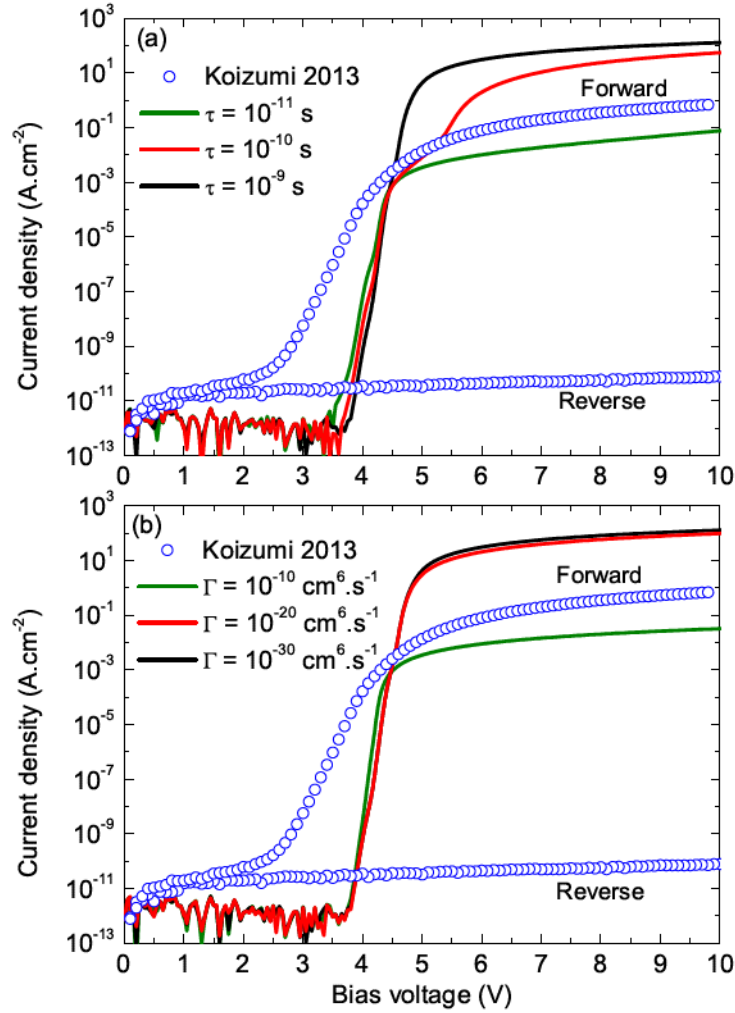


Figure 3.8: (a) Influence of the SRH lifetimes ( $\tau = \tau_p = \tau_n$ ,  $\Gamma = 10^{-30}$  cm<sup>6</sup>.s<sup>-1</sup>) on the simulated J(V) characteristics. (b) Simulated J(V) characteristics for different Auger parameter values ( $\Gamma = \Gamma_p = \Gamma_n$ ,  $\tau = 10^{-9}$  s), T = 300 K.

=  $10^{-11}$  s to  $\tau = 10^{-10}$  s leads to an increase of a factor 728 in the current density at 10 V.

Even though the recombination models have an influence on the current densities, the different parameter values did not lead to a better fit of the experimental J(V) characteristic in the low injection regime (see Fig.3.9). However, in the high injection regime the contact resistance can be tuned to fit the experimental J(V) as shown in Fig.3.9. A combination of generation-recombination models and series/contact resistance must be added, with a particular attention on carrier generation at low forward bias and reverse bias.

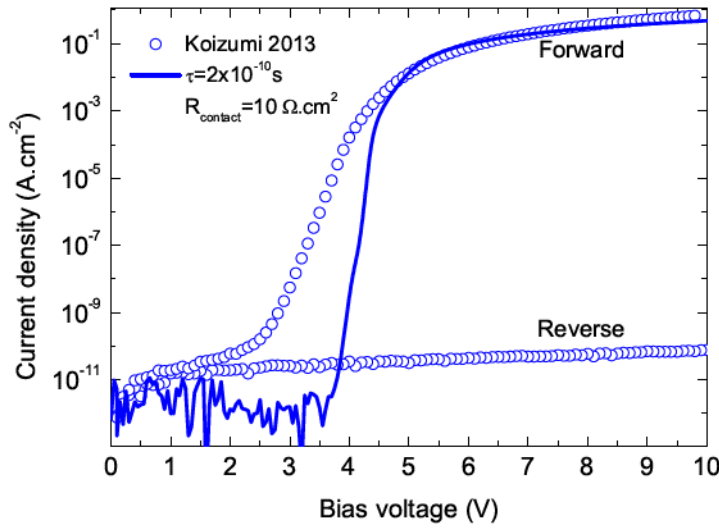


Figure 3.9: Fit of the experimental  $J(V)$  characteristic reported in [Koizumi 2013], at 300 K with a contact resistance  $R_{contact} = 10 \Omega.cm^2$  and  $\tau = \tau_p^{SRH} = \tau_n^{SRH} = 2 \times 10^{-10} s$ . This value is calculated according to the diffusion length of holes reported by Kato et al. [Kato 2013] using  $L_h = \sqrt{D\tau}$ , where  $D$  is the diffusion coefficient,  $D = k_B T \mu / q$ . The ideality factor  $n$  of the experimental  $I(V)$  is 3.5.

### 3.3.2.4 Reverse characteristic and breakdown voltage

As shown in section 3.3, the carrier concentrations are extremely low. As a consequence, when the applied forward voltage is lower than the built-in potential, the current density in the p-n junction is too low to be accurately calculated, as it reaches the numerical precision limit. Impurities and defects must also be introduced and modeled in order to correctly represent the specificities of novel diamond devices. These are ones of the main limitations for diamond device simulation, since the intrinsic carrier density is extremely low as well as the free carrier concentrations. Furthermore, prediction of the electrical device characteristics needs the implementation of avalanche impact ionization parameter values as well as hopping conductivity models into the simulation tools.

To predict the breakdown voltage of the simulated devices, one needs to know the avalanche impact ionization coefficients for holes and electrons,  $\alpha_p$  and  $\alpha_n$  respectively shown in Eq.3.11 and 3.12 [Raynaud 2010, Hiraiwa 2013, Hiraiwa 2015].

$$\alpha_p = a_p \exp\left(-\frac{b_p}{|E|}\right) \quad (3.11)$$

$$\alpha_n = a_n \exp\left(-\frac{b_n}{|E|}\right) \quad (3.12)$$

where  $|E|$  is the absolute value of the electric field in the structure,  $a_p$  ( $a_n$ ) and  $b_p$  ( $b_n$ ) are constants for holes (electrons), or electric field and temperature dependent depending on the implemented impact ionization model. The avalanche impact ionization coefficients are used to calculate the multiplication coefficients for electrons and holes ( $M_n$ ,  $M_p$ ) playing a role in the calculation of the total current density [Sze 2007]. Usually, the breakdown conditions are determined by calculating the ionization integral, such that the integral becomes unity. Specifically, the following equation highlights the relationship between the impact ionization coefficients and the multiplication factor for holes  $M_p$ :

$$1 - \frac{1}{M_p} = \int_0^{W_m} \alpha_p \exp\left\{-\int_0^x (\alpha_p - \alpha_n) dx'\right\} dx \quad (3.13)$$

with the avalanche breakdown voltage defined as the voltage where  $M_p$  becomes infinite, such that:

$$\int_0^{W_m} \alpha_p \exp\left\{-\int_0^x (\alpha_p - \alpha_n) dx'\right\} dx = 1 \quad (3.14)$$

where the avalanche is initialized by holes and the integral runs over the depletion layer thickness,  $W_m$  standing for the maximum value of the depletion layer thickness.

At the present time, there are no experimental reports concerning the impact ionization coefficient values. However, theoretical values extrapolated from silicon and silicon carbide are reported in [Rashid 2008, Raynaud 2010, Ding 2010]. For instance, the values of  $a_{p,n} = 1.935 \times 10^8 \text{ cm}^{-1}$  and  $b_{p,n} = 7.749 \times 10^6 \text{ V.cm}^{-1}$  implemented in the models reported in [Ding 2010] led to breakdown field of  $E_{max} = 1.23 \text{ MV.cm}^{-1}$  for a doping level  $N_A = 1.23 \times 10^{17} \text{ cm}^{-3}$ . The same parameter values used for estimating the breakdown field of the Schottky diode reported in [Volpe 2010], led to a decrease of a factor 10 of the simulated breakdown field as compared to the measured  $E_{max} = 7.7 \text{ MV.cm}^{-1}$  for

	<i>a</i>	<i>b</i>
units	$\text{cm}^{-1}$	$\text{V}\cdot\text{cm}^{-1}$
electron	$1.46 \times 10^5$	$2.4 \times 10^7$
hole	$0.61 \times 10^5$	$1.39 \times 10^7$

*Table 3.1:* Impact ionization coefficients for electron and hole after [Hiraiwa 2013].

a boron concentration of  $N_A = (1.4\text{-}2.8) \times 10^{16} \text{ cm}^{-3}$ . Furthermore, this value is much lower than the predicted  $10 \text{ MV}\cdot\text{cm}^{-1}$  breakdown field. Due to this low breakdown field value, the author of [Ding 2010] used another simulation method which consisted to stop the simulations when the electric field in the Schottky diode reached  $5.6 \text{ MV}\cdot\text{cm}^{-1}$ , a method open to criticism but justified by the lack of impact ionization data available for diamond.

Recently, Hiraiwa and Kawarada [Hiraiwa 2013, Hiraiwa 2015] theoretically reproduced the breakdown voltage as a function of the doping concentration of diamond diodes by empirical estimation of the ionization coefficients. These coefficients were implemented in the simulation tool and are shown in Tab.3.1.

A particular attention was paid for simulating the reverse breakdown characteristic because of the extremely low calculated diffusion currents. Thus, an arbitrary value to the leakage diffusion current was defined before modeling the reverse breakdown characteristic by using the impact ionization model. Fig.3.10 presents the theoretical reverse characteristic of the simulated diamond p-n junction diode. It predicts a breakdown voltage of approximately 225 V. The insert shows the theoretical electric field as a function of the depth at breakdown, the maximum field being  $7.7 \text{ MV}\cdot\text{cm}^{-1}$ .

Ongoing work on the implementation of trap assisted tunneling [Garino 2012] and band to band tunneling in order to model the low injection current and the reverse current of the bipolar devices will eventually lead to a better estimation of the current density in the low injection regime.

### 3.3.2.5 Hopping mobility model

For doping levels of the order of  $10^{18} - 10^{19} \text{ cm}^{-3}$ , below the metal-insulator transition, the conductivity is dominated by carriers hopping from neutral to ionized impurities at room temperature. In the case of boron-doped diamond, the conductivity is governed

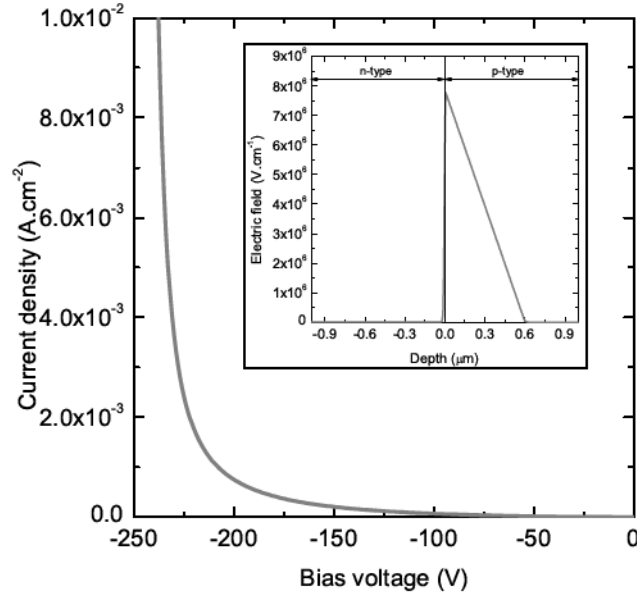


*Figure 3.10:* Theoretical reverse  $J(V)$  breakdown characteristic of the simulated diamond p-n junction. The simulation end condition was chosen by setting a compliance current of  $1 \times 10^{-2} \text{ A.cm}^{-2}$ . The insert represents the electric field as a function of the depth at breakdown. The maximum electric field is  $7.7 \text{ MV.cm}^{-1}$ .

by a combination of band conduction and variable range hopping (VRH) mechanism [Klein 2007, Sato 2000]. Here, the discussion is focused on hopping mechanism occurring in  $n^+$ -type diamond. Unlike silicon, at room temperature, this conduction mechanism plays an important role in diamond. The nearest neighbor hopping (NNH) experimentally observed in  $n^+$ -type diamond leads to a decrease of the resistivity, and hence improves the performance of the device as shown in [Oyama 2009]. In order to take this mechanism into account during the simulations, the NNH formula has been implemented into Silvaco via a built-in C language interpreter. The equivalent mobility ( $\mu_{eq}$ ) is calculated as follows:

$$\sigma_n = q(n_B \mu_B + n_{Hop} \mu_{Hop}) \quad (3.15)$$

$$\sigma_n = q n_B \mu_{eq} \quad (3.16)$$

$$\mu_{eq} = \mu_B + \frac{n_{Hop}}{n_B} \mu_{Hop} \quad (3.17)$$

$$\mu_{Hop} = \frac{1}{6} \frac{q R_{Hop}^2}{kT} \nu_{ph} \exp\left(-2\alpha R_{Hop} - \frac{q W_{Hop}}{kT}\right) \quad (3.18)$$

where the term  $\mu_B$  represents the band conduction mobility, described in section 2.2.3,

and the term  $\mu_{Hop}$  represents the nearest neighbor hopping mobility [Massarani 1978].  $n_B$  is the electron concentration in the conduction band calculated from Eq.2.22 and  $n_{Hop}$  is the hopping carrier concentration given by  $n_{Hop} = N_D - n_B$ , which represents the non-ionized carrier concentration. Since the thermal ionization energy of the phosphorus donor is large in diamond, the density of neutral donor  $n_{Hop}$  is assumed to be  $N_D$ . In this approach, we assumed that all the non-ionized impurities participate to the hopping mechanism. According to [Hosoda 2013],  $\alpha^{-1} = 1.8$  nm is the localization length of the wave function [Shklovskii 1984, Mott 1987],  $W_{Hop}$  is the thermal activation energy for the hopping process,  $R_{Hop} \approx N_D^{-1/3}$  is the mean distance between impurities and  $\nu_{ph} = 2 \times 10^{11}$  s<sup>-1</sup> is related to the phonon frequency [Hosoda 2013].

In order to validate the approach and the possibility of hopping mobility implementation, a uniform 1D n-type diamond layer with a top and a bottom ohmic electrode was simulated in Silvaco using the equivalent mobility formula (see Eq.3.17) implemented via the C language interpreter. The procedure was to apply a small voltage bias between the two electrodes, then from the J(V) characteristics we extracted the total resistance ( $dV/dI$ ) to finally get the resistivity of the n-type diamond layer. Results are presented in Fig.3.11, which shows the resistivity as a function of the doping concentration. The decrease in resistivity due to hopping conductivity mechanism appears clearly at 200 K for a doping level of  $N_D = 2 \times 10^{18}$  cm<sup>-3</sup>, and at 300 K for a doping level of  $N_D = 10^{19}$  cm<sup>-3</sup>. At higher temperature, the effect of hopping mechanism tends to vanish due to the increasing ionization rate of the n-type diamond, as it can be seen for the 500 K and 600 K resistivity curves.

The reliability of the hopping mobility formula implementation is confirmed by Fig.3.12, which presents the simulated resistivity as a function of 1000/T for different compensation values and a doping concentration of  $N_D = 8 \times 10^{19}$  cm<sup>-3</sup>. The compensation was taken as a fitting parameter, in order to reproduce the experimental data reported by Oyama et al. in [Oyama 2009] (blue open circles). It appears that the compensation affects the high temperature region of the curve, which corresponds to the band conduction mechanism. However, from 50 K to 200 K, when taking into account the different compensation values, the resistivity can not be calculated consequently to the extremely low carrier concentrations. The hopping resistivity is not affected by the compensation values as the author in [Werner 1997] reported for boron doped diamond.

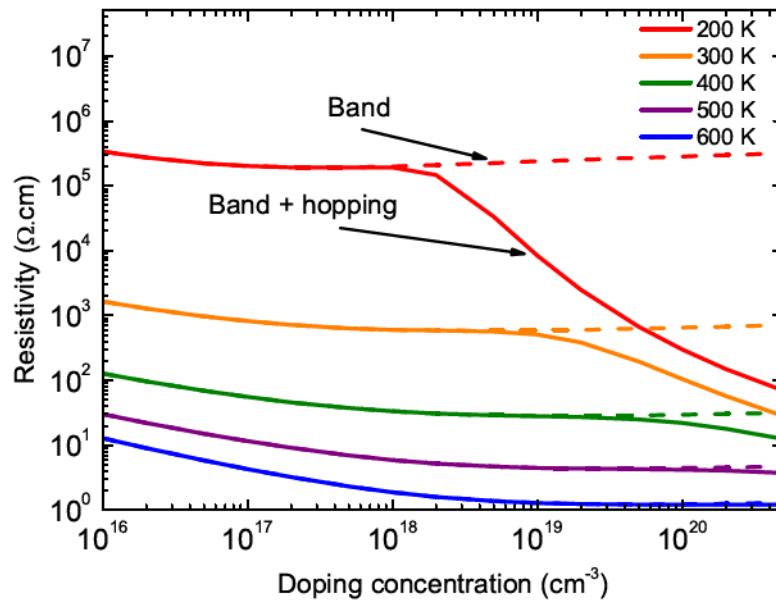


Figure 3.11: Resistivity calculated from a uniform 1D n-type diamond layer taking into account the combined effect of band and hopping mechanisms (solid line) compared to the band conduction mechanism (dashed line).

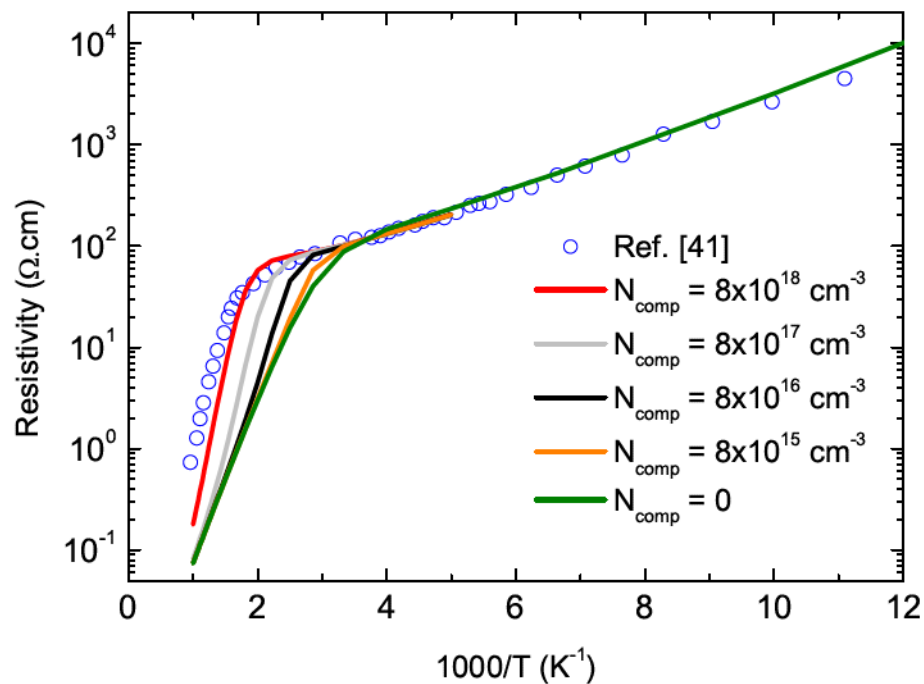


Figure 3.12: Calculated resistivity as a function of  $1000/T$  for  $N_D = 8 \times 10^{19} \text{ cm}^{-3}$  at different compensation values. The open circles represent the experimental data reported in [Oyama 2009].

This model successfully takes into account the hopping conduction mechanism and reproduces the experimental resistivity reported in [Oyama 2009]. Furthermore, it will be used to predict the effect of hopping conduction on the device electrical characteristics, without falsely contributing to other phenomena.

### 3.3.3 Summary

Electric and electronic properties of diamond p-n junction were simulated for the first time using Silvaco finite element based software. Due to an effect of large activation energy in the large band gap system, carrier concentration changed largely in the low injection condition with bias voltage. Once the injection condition changed into high injection mode, band bending was predicted to occur even in the neutral region in n-type layer. Simulated current-voltage (J(V)) characteristics assuming the simple stacking p-n junction structure with  $N_A = 4 \times 10^{17} \text{ cm}^{-3}$  for the p-type layer and  $N_D = 2 \times 10^{19} \text{ cm}^{-3}$  for the n<sup>+</sup>-type layer were compared with the experimentally obtained data. Bias voltage boundary between low and high injection condition,  $\Psi_{bi} = 4.7 \text{ eV}$ , was well reproduced. However, a large discrepancy was observed between the simulated results and experimentally obtained data on the absolute current level and slope of J(V) curve were large, even considering the SRH and Auger recombination models. This means that the other unconsidered factors such as ohmic contact resistivity, carrier tunneling and crystalline defects contributes strongly to the J(V) characteristics of diamond p-n junction remain. However, it is possible to predict the breakdown characteristic of the p-n junction which is evaluated to happen at a reverse bias voltage of 225 V. Also, important factor such as the hopping mobility must be taken into account. In this way, hopping mobility was implemented into the simulation tools. This work is motivated by the increasing number of diamond devices which emerged in the past few years. Recently, it has been demonstrated that different regimes can be controlled in a MOS capacitor [Chicot 2013b] opening the route for the fabrication of a MOS field effect transistor. Thus, it is fundamental to predict as accurately as possible the electrical characteristics of this future diamond device as well as its architecture in order to fabricate power devices showing outstanding electrical performances.

## 3.4 Modelling of a diamond metal-oxide-semiconductor field effect transistor

### 3.4.1 Historical framework of the MOSFET <sup>2</sup>

More than 80 years of development in the field of solid state electronic devices have led to the market of the integrated circuits as we know it. This wouldn't be possible without the pioneering work, in the late 1920's, of Julius E. Lilienfeld who proposed the first patents describing the working principle and structure of amplifying devices based on the field-effect. In fact, he proposed three patents containing five transistor structures among which the metal-oxide-semiconductor field effect transistor (MOSFET) was described. Moreover, in 1935, O. Heil proposed the inversion channel MOSFET. On this basis, the first demonstration of the transistor operation, that is a solid state device (in this case a bipolar transistor) showing a power gain greater than unity, was demonstrated in 1947 by Brattain and Shockley. Furthermore, in 1948 Shockley and Pearson made the demonstration of the field effect, that is a modulation of the conductance takes place in the surface region of a semiconductor [Shockley 1948, Shockley 1956]. However, these first milestones in the development of modern solid state devices, suffered from a lack of reproducibility. Actually, it was shown that the density of interface states was extremely high (about one surface state or dangling silicon bond per ten silicon surface atoms) resulting in a small conductivity modulation. Thus, great efforts were done to stabilize the silicon surface, especially by using thermal oxidation of the silicon surface to produce high quality silicon dioxide. Thus in 1960, the successful operation of a p-type silicon MOSFET using thermally grown SiO<sub>2</sub> gate oxide over an n-type inversion layer between two back to back n<sup>+</sup>-p junctions could be demonstrated by Kahng and Atalla [Kahng 1976]. These developments have led the MOSFET to be the most spread electronic device and also as being of use for power device applications. The next section will describe the working principle of the modern inversion mode MOSFET.

---

<sup>2</sup>this section is based on the extremely detailed review of C. T. Sah [Sah 1988].

### 3.4.2 MOSFET working principle

The MOSFET is a four terminal device where the channel resistance between two suitably located ohmic contacts (the source and the drain) is controlled by the third contact (the gate), the fourth contact acting as the back gate, which role is to control the substrate potential. The source contact is used as the reference (connected to the ground) and the back gate contact is in short circuit with the source. The structure of the MOSFET is depicted in Fig.3.13, in the case of an n-type inversion channel device, NMOSFET.

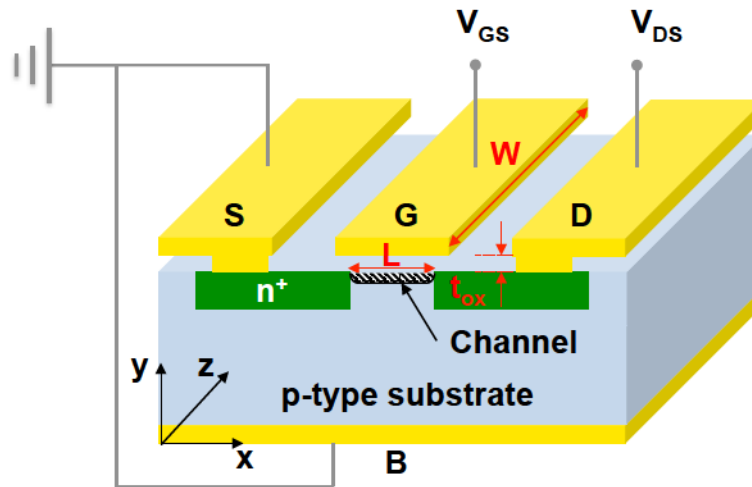


Figure 3.13: Schematic structure of an n-type channel MOSFET.  $L$ ,  $W$  and  $t_{ox}$  represent the gate length, the gate width and the oxide thickness respectively.

The main parameters of the MOSFET are the channel length  $L$ , the channel width  $W$ , the gate oxide thickness  $t_{ox}$  and the doping level of the p-type substrate  $N_A$  [Sze 2007]. When the drain voltage  $V_{DS}$  is small (positive) or ground, and if the gate voltage  $V_{GS} = 0$  V, the two back to back p-n<sup>+</sup> junctions ensure the off state of the device: no current flow through the p-type substrate separating the two electron reservoirs (n<sup>+</sup> regions). This is an important difference if we compare to nitride HEMT (High Electron Mobility Transistor) or hydrogen terminated MOSFET (H-MOSFET) where the off-state is ensured only by channel depletion. By applying a sufficiently high bias voltage to the gate contact  $V_{GS} > V_{th} > 0$ , the p-type substrate can reach the inversion regime, electrons are accumulating in the semiconductor at the oxide/semiconductor interface, thus creating a n-type conducting surface channel. As a result, a current can flow between the drain and source contacts for  $V_{DS} \neq 0$  and the conductance of the channel can be electrostatically controlled by the applied gate voltage  $V_{GS}$ . The operation of the gate

contact is described in section 2.3. The gate voltage at which the transistor is turned on, that is the channel reaches the inversion regime, is called the threshold voltage  $V_t$  and given by [Sze 2007, Baliga 2012] when interface states and oxide fixed charges are neglected:

$$V_{th} = V_{FB} + \frac{2k_B T}{q} \ln\left(\frac{p}{n_i}\right) + \frac{\sqrt{4\varepsilon_{sc} k_B T N_A \ln\left(\frac{p}{n_i}\right)}}{\varepsilon_{ox}/t_{ox}} \quad (3.19)$$

where  $V_{FB}$  is the flat band voltage<sup>3</sup>,  $k_B$  is Boltzmann's constant,  $T$  the temperature,  $q$  the elementary charge,  $N_A$  the doping level in the p-type region,  $p$  the free hole concentration calculated from Eq.2.19,  $n_i$  the intrinsic carrier concentration,  $\varepsilon_{sc}$  the semiconductor relative dielectric constant,  $\varepsilon_{ox}$  the oxide relative dielectric constant and  $t_{ox}$  the oxide thickness. The flat band voltage is calculated from the following equation [Sze 2007]:

$$qV_{FB} = q[\Phi_M - (\chi_{sc} + E_g - \phi_p)] \quad (3.20)$$

with  $\Phi_M = 4.3$  eV corresponding to the titanium work function,  $\chi_{sc} = 1.7$  eV is the O-diamond surface electron affinity and  $\phi_p = 0.37$  eV is the Fermi potential with respect to the valence band edge, approximated to be constant in this analysis. Thus, the flat band voltage is calculated to be -2.5 V in case of a Ti/Al<sub>2</sub>O<sub>3</sub>/O-diamond stack.

A simple analytical calculation allows to estimate the effect of both p-type layer doping concentration and oxide thickness on the threshold voltage of the inversion mode diamond MOSFET, as shown in Fig.3.14. The calculation is performed at 300 K varying the doping concentration from  $10^{13}$  cm<sup>-3</sup> to  $10^{18}$  cm<sup>-3</sup> and the gate oxide thickness from 20 nm to 200 nm. As a result, the threshold voltage ranges from 2.2 V to 24.6 V. However, for practical device realization, the values above 6 V will not be considered and thus the same color level is applied. Recently, Kovi et al. [Kovi 2015] reported the observation of the inversion regime in diamond MOSCAP. However, the MOSCAP suffered from high leakage currents, which might affect the device C(V) properties. Thus, measurement artifacts coming from the high leakage currents should not be discarded. Even if the inversion regime could have been observed, the doping levels reported ( $>10^{19}$  cm<sup>-3</sup>)

<sup>3</sup>its value is constant in this analysis.

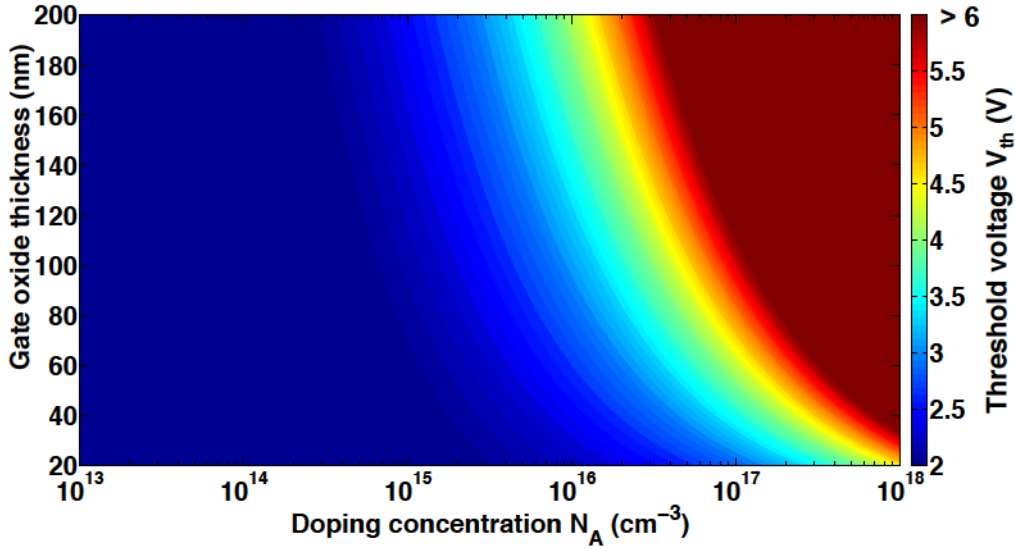


Figure 3.14: Threshold voltage calculated at 300 K from Eq.3.19, showing the p-type doping level  $N_A$  and oxide thickness  $t_{ox}$  influence.

might not be suitable for device applications, since they lead to threshold voltages above 6 V.

In the inversion mode MOSFET, electrons carried along the longitudinal axis (parallel to the  $x$ -direction, see Fig.3.13) by the local electric field due to the Source-Drain bias, give rise to a conduction current. This local conduction current depends on the effective electron mobility  $\mu_n$  together with the width  $W$  of the transistor channel, such that [Vincent 2008]:

$$I_{DS} = \mu_n W Q_{inv} \frac{d\Psi_s}{dx} \quad (3.21)$$

where  $Q_{inv}$  is the local inversion charge, and  $\Psi_s$  is the surface potential as defined in section 2.3.

The local inversion charge as a function of the surface potential is illustrated in Fig.3.15. Then, the integration from the source to the drain, at distance  $L$  gives:

$$I_{DS} \cdot L = \mu_n W \int_{2\Psi_b}^{2\Psi_b + V_{DS}} Q_{inv}(\Psi_s) d\Psi_s \quad (3.22)$$

The integral in the  $Q\Psi$  plane corresponds to the area  $A_{Q\Psi}$ , which is delimited by the two vertical lines  $2\Psi_b$  and  $2\Psi_b + V_{DS}$ , the square root of depletion and the oxide capacitance straight line, as illustrated in Fig.3.15.

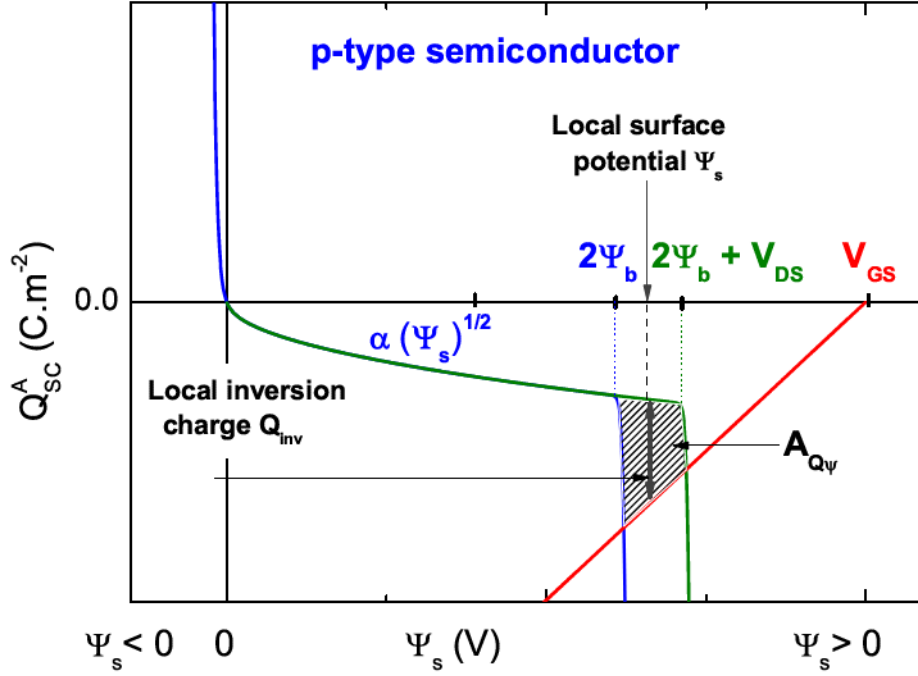


Figure 3.15: Local inversion charge as a function of the surface potential [Vincent 2008]. The current is proportional to the area  $A_{Q\Psi}$  delimited by the two vertical lines  $2\Psi_b$  and  $2\Psi_b + V_{DS}$ , the square root of depletion and the oxide capacitance straight line.

Finally, the current is obtained after integration, knowing that  $Q_{inv} = \frac{\epsilon_{ox}}{t_{ox}}(V_{GS} - \Psi_s) - \sqrt{2\epsilon_{sc}qN_A\Psi_s}$ , thus:

$$I_{DS} = \mu_n \frac{W}{L} \frac{\epsilon_{ox}}{t_{ox}} \left[ \left( V_{GS} - 2\Psi_b - \frac{V_{DS}}{2} \right) V_{DS} - \frac{4}{3} \frac{\epsilon_{sc}}{\epsilon_{ox}} \frac{t_{ox}}{\sqrt{2\epsilon_{sc}2\Psi_b/qN_A}} (2\Psi_b)^2 \left\{ \left( 1 + \frac{V_{DS}}{2\Psi_b} \right)^{3/2} - 1 \right\} \right] \quad (3.23)$$

The above expression can be simplified using power series of  $(1 + V_{DS}/2\Psi_b)^{3/2}$  around  $V_{DS}$ , if  $V_{DS} \ll (V_{GS} - V_t)$  (*linear regime*) [Sze 2007]:

$$I_{DS} = \mu_n \frac{W}{L} \frac{\epsilon_{ox}}{t_{ox}} \left( V_{GS} - V_t - \frac{V_{DS}}{2} \right) V_{DS} \quad (3.24)$$

Now, it is possible to distinguish three working regimes, depending on the Source-Drain bias:

- if  $V_{DS} \ll V_{DSAT}$ , the *linear regime* is described by  $I_{DS} = \mu_n \frac{W}{L} \frac{\epsilon_{ox}}{t_{ox}} (V_{GS} - V_t) V_{DS}$ ;
- if  $V_{DS} \gg V_{DSAT}$ , the *saturation regime* is described by  $I_{DS} = \mu_n \frac{W}{L} \frac{\epsilon_{ox}}{t_{ox}} (V_{GS} - V_t - \frac{V_{DSAT}}{2}) V_{DSAT}$ ;
- the *non-linear regime* links the two aforementioned regimes.

These regimes are illustrated in Fig.3.16.a) where the  $I_{DS}$  vs.  $V_{DS}$  characteristic of the simulated diamond MOSFET (to be described in the next section) with gate oxide thickness  $t_{ox} = 20$  nm and doping concentration  $N_A = 10^{15}$  cm<sup>-3</sup> has been plotted. If the gate bias voltage  $V_{GS}$  is below the threshold voltage  $V_t$ , the drain current  $I_{DS}$  is null. When  $V_{GS} > V_{th}$ , the current first linearly increases and then saturates. In the above description,  $V_{DSAT}$  represents the drain voltage at which the inversion charge near the drain contact reduces to zero. At this specific value  $V_{DSAT} = V_{GS} - V_{th}$ , the transistor is pinched-off and with further increase of the drain voltage  $V_{DS}$ , the area  $A_{Q\Psi}$  remains constant (since  $V_{GS}$  is fixed). As a result the saturation current is:

$$I_{DS} = \frac{1}{2} \mu_n \frac{W}{L} \frac{\epsilon_{ox}}{t_{ox}} (V_{GS} - V_{th})^2 \quad (3.25)$$

The same analysis can be performed when considering a constant value for  $V_{DS}$  and varying  $V_{GS}$ . The resulting curve gives the evolution of  $I_{DS}$  as a function of  $V_{GS}$  for a constant applied  $V_{DS}$ . As shown in Fig.3.16.b), when  $V_{GS} < V_{th}$ ,  $I_{DS}$  (the conduction current) is null. For bias voltages  $V_{GS} \geq V_{th}$ , the MOSFET is in the saturation regime and  $I_{DS}$  follows the relationship given by Eq.3.25. Finally, for  $V_{GS} \gg V_{th}$ , the inversion layer develops under the whole gate length  $L$  and the transistor reaches the linear regime. The details of the device simulation will be given in the next section.

### 3.4.3 Design of a planar inversion MOSFET

In order to validate the implemented diamond models, a simple planar MOSFET structure was simulated using TCAD Silvaco [SILVACO 2010]. The main parameter effects,

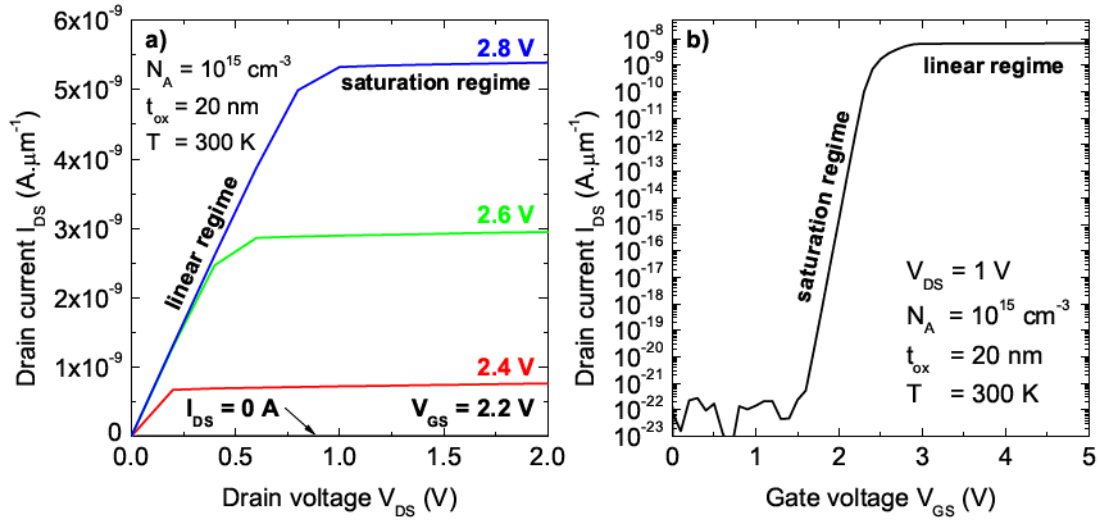


Figure 3.16: a)  $I_{DS}$  vs.  $V_{DS}$  characteristic of the simulated diamond MOSFET with  $N_A = 10^{15} \text{ cm}^{-3}$ ,  $t_{ox} = 20 \text{ nm}$  and  $T = 300 \text{ K}$ . The curve is characterized by the linear increase of  $I_{DS}$  (linear regime), followed by the saturation when  $V_{DS} = V_{DSAT} = V_{GS} - V_{th}$ . b) Corresponding  $I_{DS}$  vs.  $V_{GS}$  characteristic (transconductance) with  $V_{DS} = 1 \text{ V}$ .

namely oxide thickness  $t_{ox}$ , temperature  $T$  and doping level  $N_A$ , on the simulated diamond MOSFET electrical characteristics were investigated. Thus, in a first part the simulated structure will be described. Then, the dc simulation results will be discussed.

### 3.4.3.1 Design using TCAD Silvaco

The structure was inspired by the experimental work performed in AIST (Tsukuba, Japan) described in section 4.6 and is represented in Fig.3.17.

The structure is composed of four terminals, the source, the drain, the gate and the back gate with respective dimensions of 1  $\mu\text{m}$ , 3  $\mu\text{m}$  and 18  $\mu\text{m}$ , which allows separate control of the top and bottom gates potentials. However, in the present case, the back gate contact is short circuited with the source electrode and grounded as a potential reference. The gate contact overlaps the source and drain  $n^+$ -type region by 0.1  $\mu\text{m}$ , in order that when the inversion channel develops, no additional series resistance appears due to non-inverted region. This structure has the advantage of being normally-off due to the presence of the two back to back  $n^+$ -p junctions with built-in potential of approximately 4.7 V. The doping concentration of the source and drain contacts ( $n^+$ -type diamond) was set to  $10^{20} \text{ cm}^{-3}$  and the spacing between them was 2.8  $\mu\text{m}$ , which

corresponds to the inversion channel length  $L$ . In order to simplify the study, the hopping conduction mechanism was neglected. The effect of hopping in the  $n^+$ -type layer would be a decrease of the resistance of both source and drain contacts [Oyama 2009]. The device properties are mainly determined by the channel properties ( $N_A$  and  $L$ ) and the oxide thickness. In the present study, the channel length  $L$  was chosen to be constant.

Finally, the MOSFET performances have been investigated versus p-type layer doping concentration  $N_A$ , oxide thickness  $d_{ox}$  and temperature  $T$ . The effect of these parameters on the electrical properties of the simulated planar inversion diamond MOSFET will be discussed in the next section.

### 3.4.3.2 Electrical simulations

The models implemented for the simulation of the p-n junction electrical properties (see section 3.3) were used for the simulation of the planar MOSFET structure. The oxide layer was considered perfect, corresponding to the ideal MOS capacitor as defined in section 2.3. Moreover, for insulator materials, only the Poisson and lattice heat equations are solved. Therefore, the only adjustable parameter is the oxide relative dielectric constant. This restriction will have a lot of consequences on the simulation of gate leakage currents. However, this difficulty could be overcome by defining the insulating

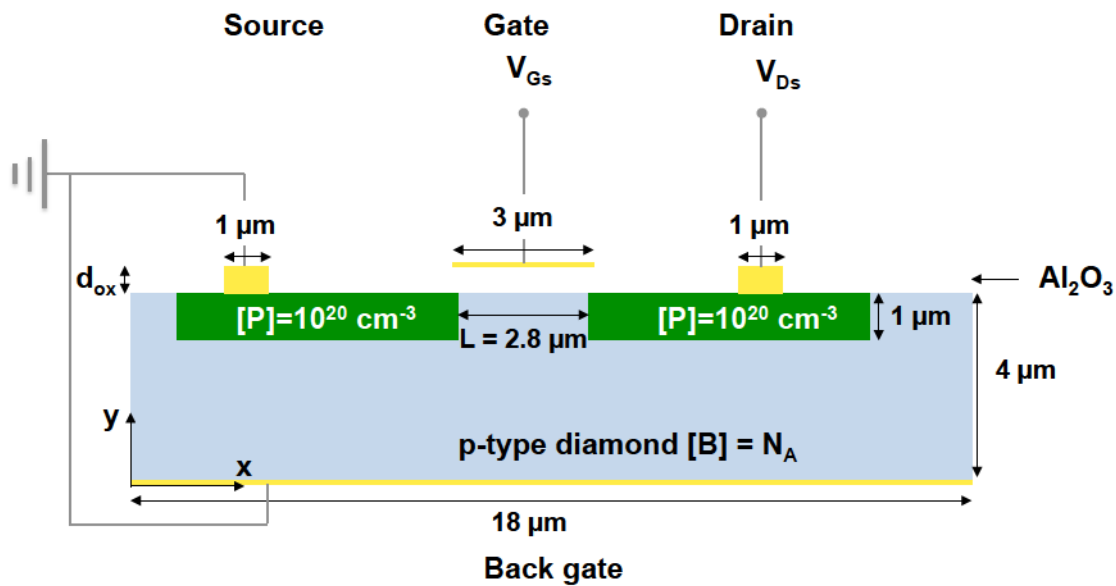


Figure 3.17: Structure of the simulated planar MOSFET. The Source and Back gate contact are short circuited and grounded.

layer as a semiconductor. In this case, the material properties must be specified, such as the electron and hole mobilities, which are difficult to access for dielectric materials, the band gap, the electron affinity and, not to be neglected, generation-recombination models. In the following, the oxide layer was considered as perfect in order to simplify the analysis. In near future, the implementation of material parameters would be a great step forward for the modelling of gate leakage currents.

The drain diffusion current  $I_{DS}$  were calculated as a function of the applied drain bias  $V_{DS}$  for various gate bias  $V_{GS}$  and for different sets of parameters,  $N_A$ ,  $t_{ox}$  and  $T$  in order to study the trends on resulting simulated electrical properties. First, the  $I_{DS}$  vs  $V_{DS}$  characteristics were calculated and then the transconductance was extracted at a constant Source-Drain bias of  $V_{DS} = 1$  V. The threshold voltage was determined using the second derivative method described by [Ortiz-Conde 2002]. The method consists in finding the maximum of the derivative of the transconductance  $d^2I_{DS}/dV_{GS}^2$  [Ortiz-Conde 2002].

### Temperature influence on electrical properties

Fig.3.18.a) shows the  $I_{DS}$  vs.  $V_{GS}$  extracted from the  $I_{DS}$  vs.  $V_{DS}$  characteristic calculated at temperatures ranging from 300 K to 600 K. The temperature mainly influences the current level in the transistor. In fact, when the temperature is increased, the intrinsic carrier concentration increases.

In order to maintain equilibrium conditions, i.e. keeping the  $np = n_i^2$  product constant, the electron concentration increases, as illustrated in Fig.3.19 where the electron concentration is plotted as a function of the depth to the oxide/diamond interface. Moreover, the decrease in mobility with temperature does not compensate the increase in electron concentration, finally resulting in an increase of the current. However, as demonstrated by Fig.3.18.b), the threshold voltage remains almost constant and equal to 2.4 V in opposition to the expected temperature dependency expressed by Eq.3.19. This is a consequence of the shape of the transconductance. In fact, the derivative  $dI_{DS}/dV_{GS}$  (see Fig.3.20.a)) suffers from the presence of a plateau of 0.3 V which prevent from the accurate determination of the threshold voltage temperature dependence from the  $d^2I_{DS}/dV_{GS}^2$  plot as illustrated in Fig.3.20.b).

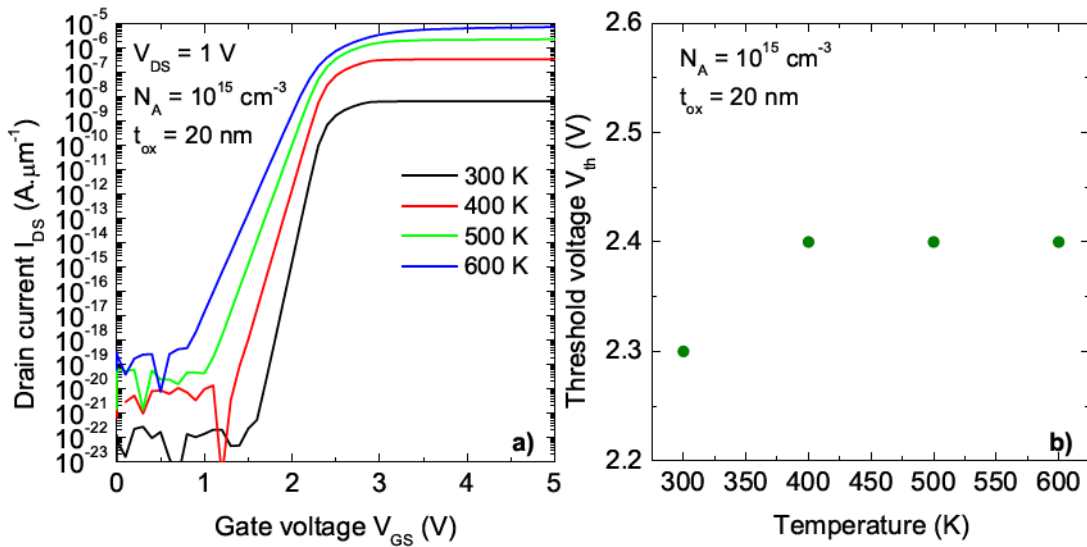


Figure 3.18: a) Transconductance characteristic  $I_{DS}$  vs.  $V_{GS}$  for  $V_{DS} = 1$  V,  $N_A = 10^{15}$   $\text{cm}^{-3}$ ,  $t_{ox} = 20$  nm, simulated for temperatures ranging from 300 K to 600 K. b) Corresponding threshold voltage as a function of temperature.

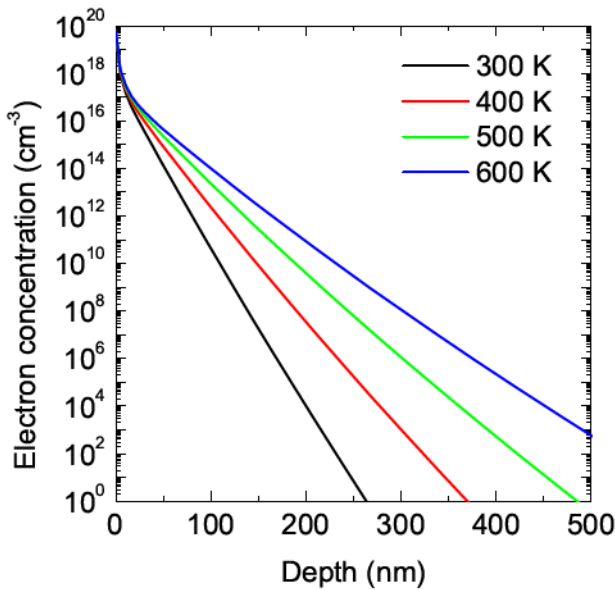


Figure 3.19: Electron concentration as a function of the depth to the oxide/diamond interface extracted at various temperatures. The simulation was performed with  $N_A = 10^{15}$   $\text{cm}^{-3}$ ,  $t_{ox} = 20$  nm,  $V_{DS} = 2$  V and  $V_{GS} = 10$  V.

### Gate oxide thickness influence on electrical properties

From Eq.3.19 and Fig.3.14, the threshold voltage can be expected to follow a linear increase with the gate oxide thickness. This property is confirmed in Fig.3.21, where the  $I_{DS}$  vs.  $V_{GS}$  characteristic and threshold voltage are plotted for the different gate oxide thickness values.

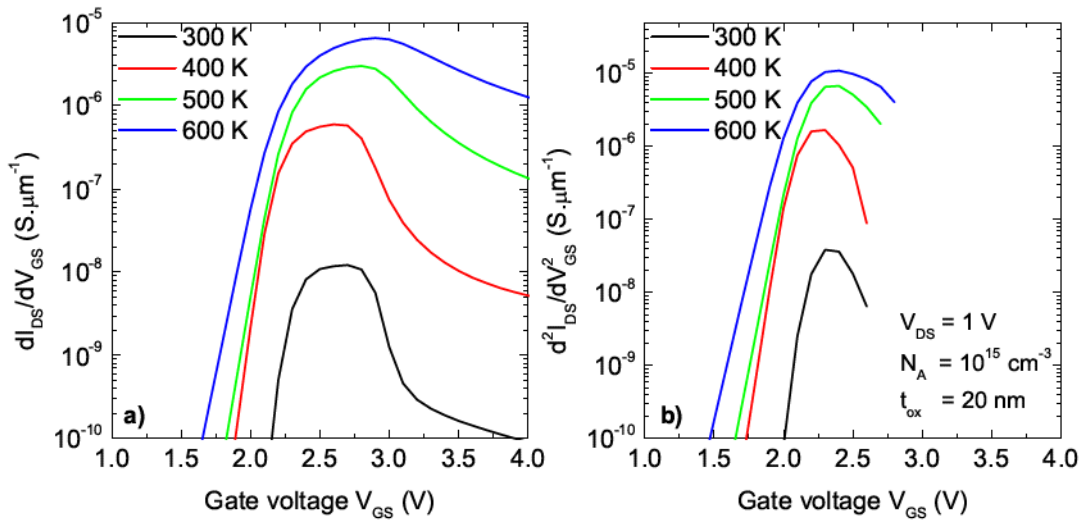


Figure 3.20: a)  $dI_{DS}/dV_{GS}$  vs.  $V_{GS}$  for  $V_{DS} = 1$  V,  $N_A = 10^{15}$  cm $^{-3}$ ,  $t_{ox} = 20$  nm, simulated for temperatures ranging from 300 K to 600 K. b) Corresponding  $d^2I_{DS}/dV_{GS}^2$  vs.  $V_{GS}$ . The threshold voltage is extracted from the maximum value of the  $d^2I_{DS}/dV_{GS}^2$  plot. The negative values of the  $d^2I_{DS}/dV_{GS}^2$  plot are omitted.

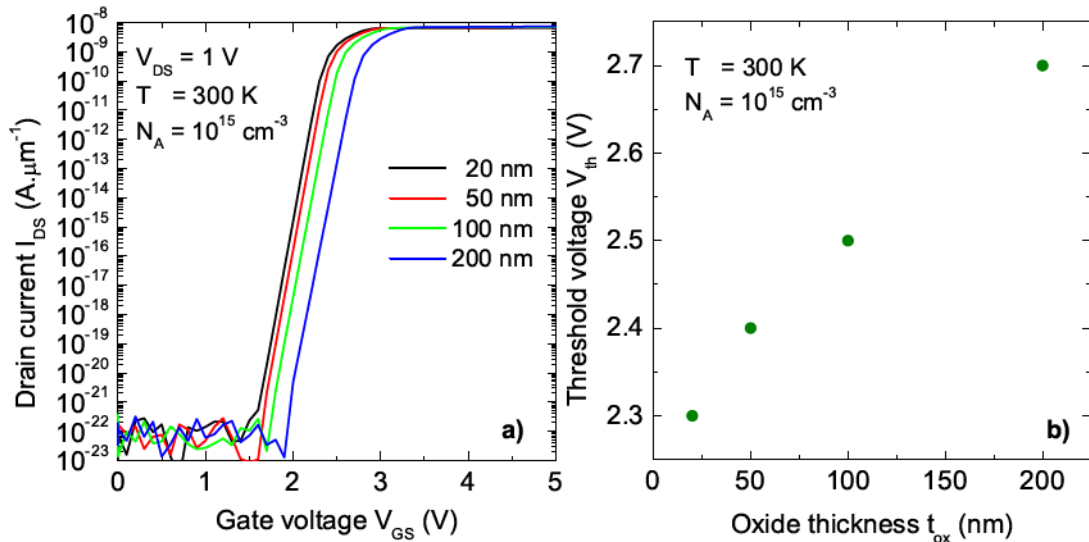


Figure 3.21: a)  $I_{DS}$  vs.  $V_{GS}$  characteristic for  $V_{DS} = 1$  V,  $T = 300$  K,  $t_{ox} = 20$  nm, simulated for gate oxide thicknesses ranging from 20 nm to 200 nm. b) Corresponding threshold voltage as a function of the oxide thickness. The simulation was performed for a doping level of  $10^{15}$  cm $^{-3}$  at a temperature of 300 K.

### Doping concentration influence on electrical properties

An interesting feature, however, is the doping influence of the p-type layer on the simulated diamond MOSFET electrical characteristics. As shown in Fig. 3.22, the channel

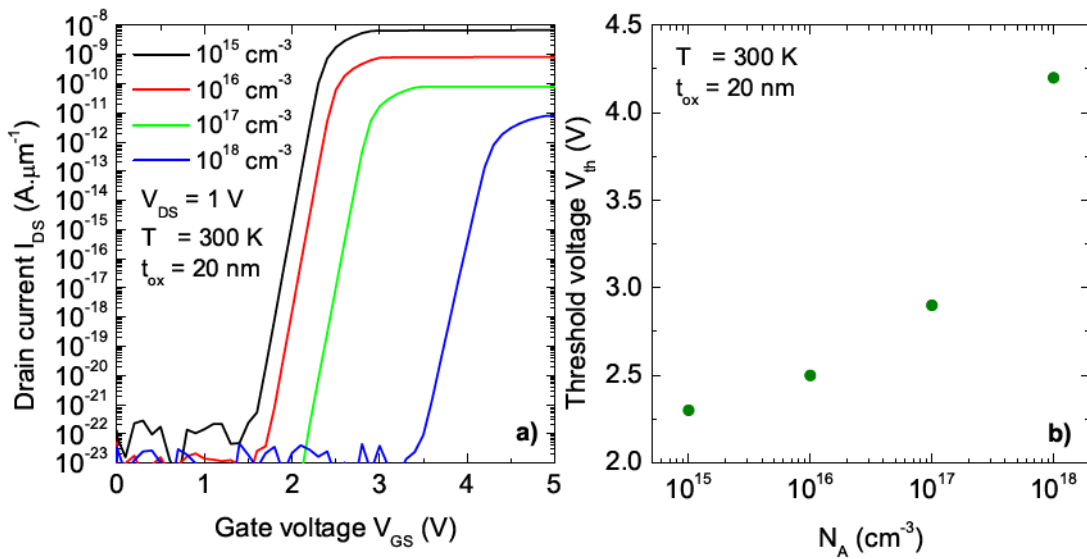


Figure 3.22: a)  $I_{DS}$  vs.  $V_{GS}$  characteristic for  $V_{DS} = 1 \text{ V}$ ,  $T = 300 \text{ K}$ ,  $t_{ox} = 20 \text{ nm}$ , simulated for p-type doping concentrations ranging from  $10^{15} \text{ cm}^{-3}$  to  $10^{18} \text{ cm}^{-3}$ . b) Corresponding threshold voltage as a function of the p-type doping concentration. The simulation was performed for a gate oxide thickness of 20 nm at a temperature of 300 K.

resistance increases with p-type doping concentration (reduced saturation current). In fact, the channel resistance could be negligible as regards to the drain and source series resistance, thus one would have expected that the maximum resistance of the device is fixed by these two last contributions.

In order to elucidate this point, the potential distribution in the 2D structure is required. As exhibited in Fig.3.23, as the p-type doping concentration is increased, the inversion layer becomes thinner. Thus, the electrons will flow in a smaller section from source to drain resulting in the increase of the channel resistance.

It is even more obvious in Fig.3.24, where both electron concentration and band diagrams are shown as a function of p-type doping level. Moving away from the oxide/diamond interface, the electron concentration is greater in the case of low doping concentration (see Fig.3.24.a)), as a consequence of the band bending which takes place deeper in the diamond region in case of  $N_A = 10^{15} \text{ cm}^{-3}$  than for  $N_A = 10^{18} \text{ cm}^{-3}$ , as depicted in Fig.3.24.b and c).

## 3.4.3.3 Blocking characteristics

In order to predict the breakdown characteristic of future diamond MOSFET, several parameters should be considered. Firstly, the p-type diamond layer doping concentration

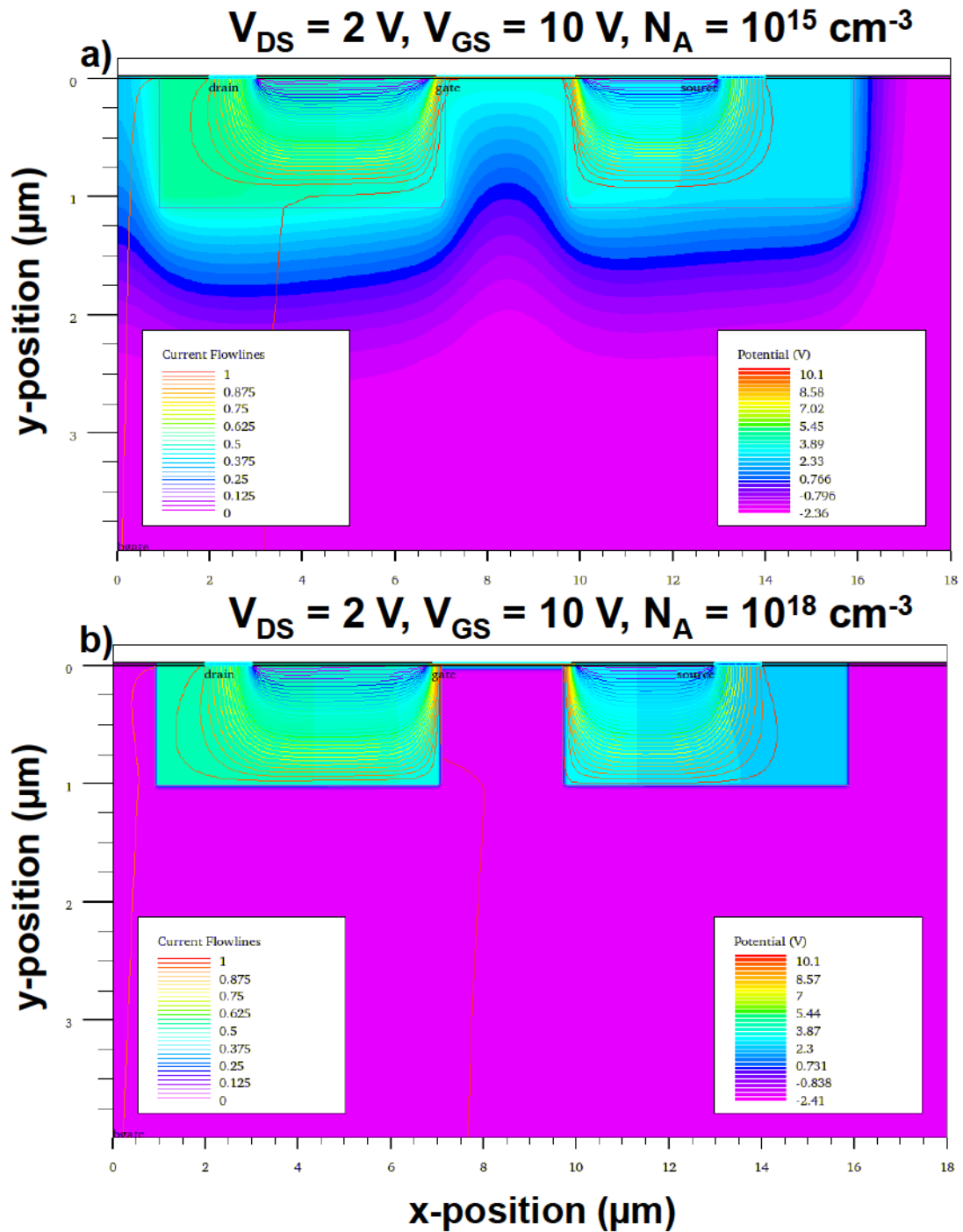


Figure 3.23: 2D simulated diamond MOSFET structure showing the potential distribution (color plot) and the current distribution (current flowlines) for a doping level of a)  $10^{15}\text{ cm}^{-3}$  and b)  $10^{18}\text{ cm}^{-3}$ , a gate oxide thickness of 20 nm and at 300 K.

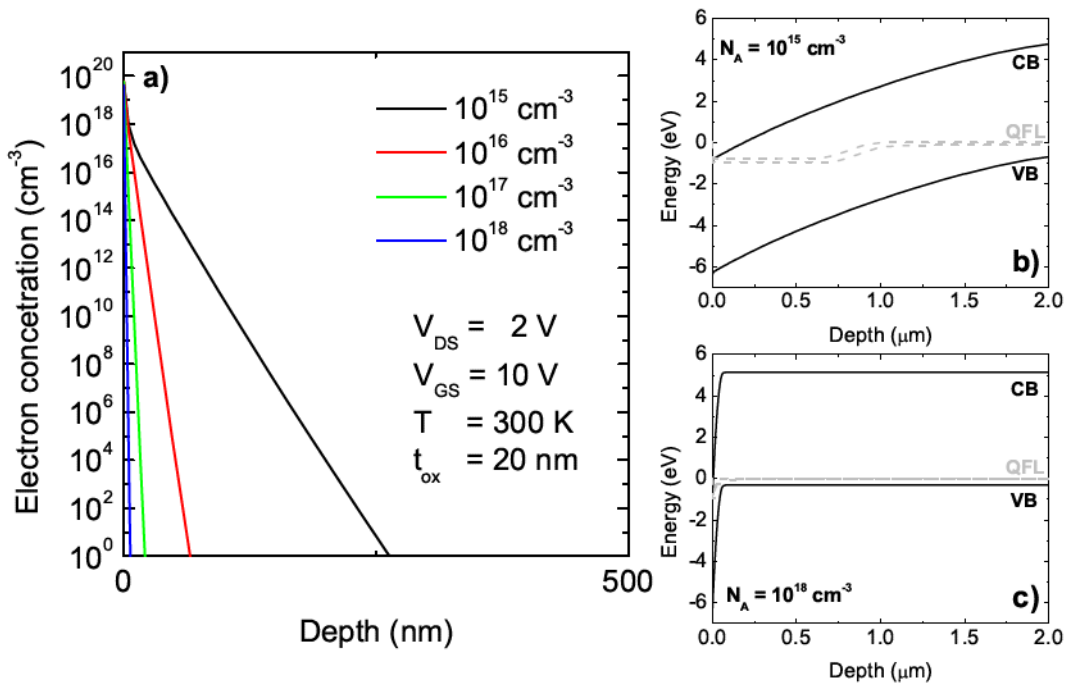


Figure 3.24: a) Electron concentration as a function of the depth to the oxide/diamond interface for p-type doping level ranging from  $10^{15}\text{ cm}^{-3}$  to  $10^{18}\text{ cm}^{-3}$  for  $V_{DS} = 2\text{ V}$ ,  $V_{GS} = 10\text{ V}$ ,  $t_{ox} = 20\text{ nm}$  and  $T = 300\text{ K}$ . b) Corresponding band diagram of the MOS contact in the strong inversion regime for  $N_A = 10^{15}\text{ cm}^{-3}$  and c)  $N_A = 10^{18}\text{ cm}^{-3}$ .

will determine the maximum  $V_{DS}$  that the p-n<sup>+</sup> junction can sustain. For instance, considering a maximum electrical breakdown field of  $10\text{ MV}\cdot\text{cm}^{-1}$  for diamond and a completely depleted region of  $3\ \mu\text{m}$  (for the non-punch-through case), one could expect a maximum  $V_{DS}$  of  $1500\text{ V}$  for the p-n<sup>+</sup> junction breakdown voltage. Secondly, this doping concentration will also influence the parasitic triggering of the parasitic n<sup>+</sup>-p-n<sup>+</sup> bipolar transistor during the MOSFET turn OFF [Simonot 2011]. This mechanism originates from a local increase of the potential in the structure which leads to the parasitic turn on of the transistor. Finally, the oxide thickness will mainly influence the threshold voltage of the MOSFET. However, its value also determines the maximum gate bias  $V_{GS}$  applicable to the gate contact before oxide breakdown. As an example, if  $\text{Al}_2\text{O}_3$  is to be considered as a gate oxide for future diamond MOSFET, the maximum applied electric field could be in the range of  $7\text{ MV}\cdot\text{cm}^{-1}$  [Yota 2013].

The blocking characteristics of the diamond MOSFET structure were obtained by increasing the drain voltage while keeping a zero gate bias for an oxide layer thickness of  $200\text{ nm}$ , a p-type doping concentration of  $10^{15}\text{ cm}^{-3}$  and a temperature of  $300\text{ K}$ ,

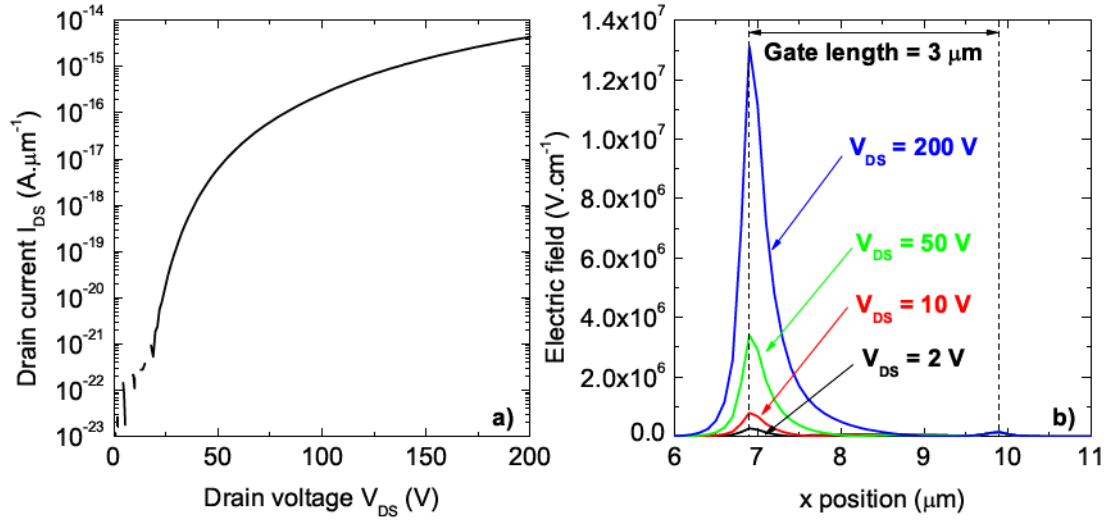


Figure 3.25: a)  $I_{DS}$  vs.  $V_{DS}$  characteristic of the simulated diamond MOSFET with  $V_{GS} = 0$  V and  $T = 300$  K. In this  $V_{DS}$  range, due to the very low intrinsic carrier concentration, the leakage currents are extremely small. b) Electric field at the oxide surface near the gate contact, with  $V_{DS} = 2, 10, 50$  and  $200$  V.

giving a threshold voltage of 2.7 V. This choice is motivated by the comparison to the commercially available 1200 V SiC power MOSFET [CREE]. The diamond breakdown properties were taken into account via the impact ionization model studied in section 3.3.2. As evidenced by Fig.3.25.a), the extremely low intrinsic carrier concentration in diamond, induces a negligibly small leakage current at room temperature. This means that in theory, the Drain-Source bias  $V_{DS}$  could be increased to even higher values than 200 V for a simple planar MOSFET structure. However, one must consider the electric field building up between the drain and gate electrodes. In fact, as exhibited by Fig.3.26, which represents the electric field distribution in the simulated 2D diamond MOSFET, the enhancement of the electric field occurs at the edge of the gate contact. A simple cut line at the oxide layer surface, where the electric field is maximum, reveals that the electric field can be as high as  $13 \text{ MV.cm}^{-1}$  for a bias voltage of  $V_{DS} = 200$  V, as shown in Fig.3.25.b). Obviously, this extracted value is found greater than the reported  $\text{Al}_2\text{O}_3$  maximum breakdown fields [Kawakami 2005, Yota 2013].

In the present case, the  $\text{Al}_2\text{O}_3$  breakdown characteristic was not extracted, the main reason being that the impact ionization models are not available for modeling the oxide breakdown mechanisms, which is not the case if one considers the  $\text{SiO}_2$  as a gate oxide. One possibility would have been to consider the  $\text{Al}_2\text{O}_3$  as a semiconductor and

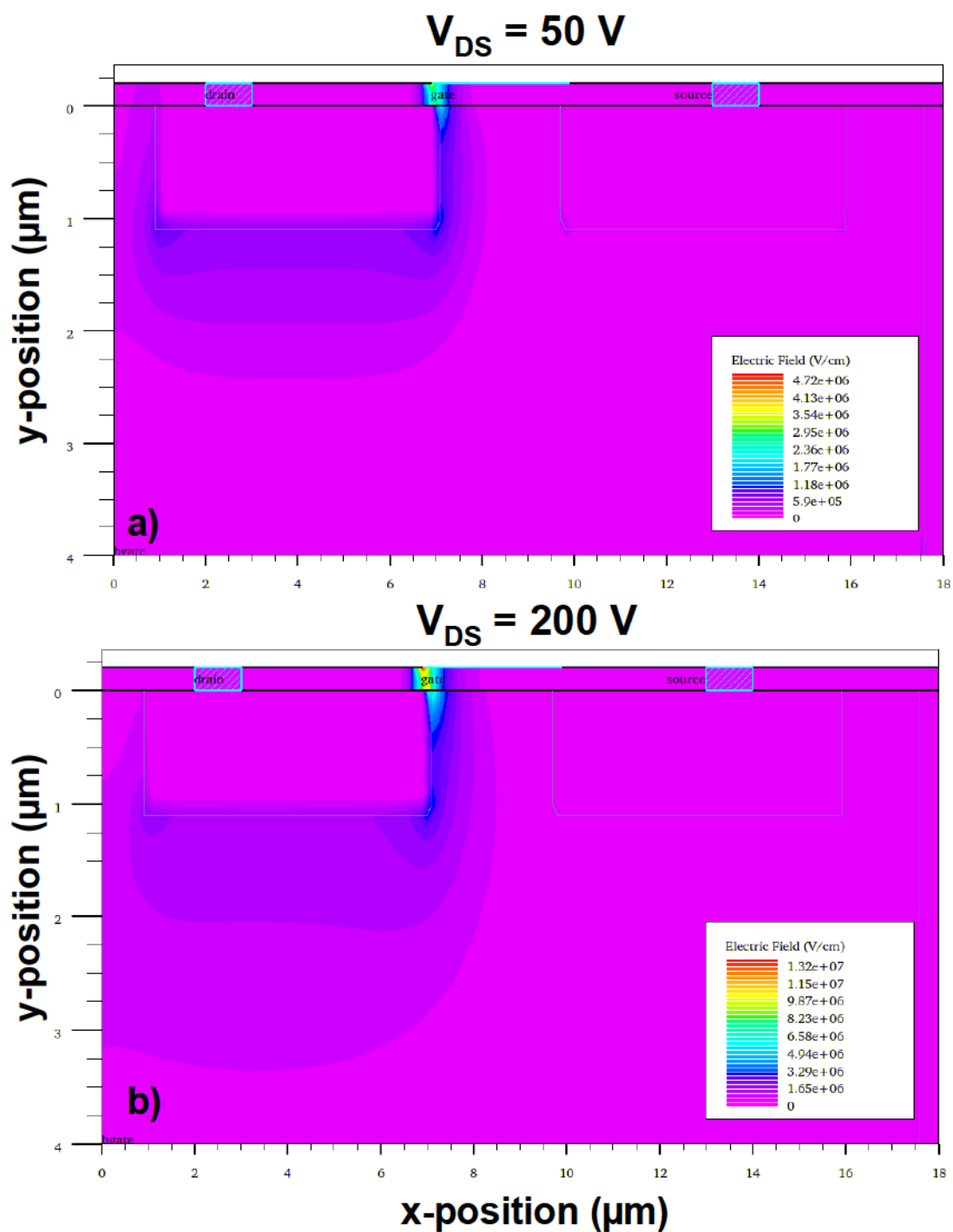


Figure 3.26: Electric field distribution in the simulated 2D diamond MOSFET for an oxide thickness of 200 nm, a p-type doping level of  $10^{15} \text{ cm}^{-3}$  and a temperature of 300 K at a)  $V_{DS} = 50 \text{ V}$  and b)  $V_{DS} = 200 \text{ V}$

to implement the effective masses and mobilities for both holes and electrons. As these informations are not currently available in the literature, to our knowledge, this approach was not investigated. However, the accurate modelling of MOS device breakdown would highly required such kind of informations.

Together with the undesirable oxide breakdown is the punch-through of the n<sup>+</sup>-p junction. In fact, as the electric field in the drain side increases, the depletion layer extends towards the source space charge region. When both space charge regions merge, the leakage current can thus flow between drain and source. This phenomenon is shown in Fig.3.27 which depicts the potential as well as the leakage currents distribution in the 2D MOSFET structure.

As evidenced, when  $V_{DS}$  is increased up to 300 V, the current flow lines start to leak from the drain contact to the source contact, inducing the uncontrolled turn on of the transistor. It is an undesired mechanism since the maximum electric field of diamond is not reached at this bias values, and thus does not correspond to the n<sup>+</sup>-p junction breakdown.

The parasitic mechanism is even clearer when plotting  $I_{DS}$  vs.  $V_{DS}$  as exhibited in Fig.3.28, showing the  $I_{DS}$  vs.  $V_{DS}$  characteristic of the simulated diamond MOSFET with  $V_{GS} = 0$  V and  $T = 300$  K. When  $V_{DS}$  reaches a value of approximately 290 V,  $I_{DS}$  increases, inducing the turn-on of the transistor. This behavior could be avoided when considering a higher p-type doping concentration or a greater channel length.

#### 3.4.4 Summary

Performing diamond MOSFET simulation for the first time allowed to estimate the ideal electrical behavior of this simple planar structure in both ON-state and OFF-state. The implemented diamond models were taken into account as for the p-n junction simulation presented in section 3.3. The channel properties ( $N_A$ ), temperature and gate contact capacitance (through  $t_{ox}$ ) influences on the  $I_{DS}$  vs.  $V_{GS}$  characteristics were investigated. In particular, the temperature effect on the threshold voltage was not reproduced. On the other hand, the oxide thickness had the expected influence on the threshold voltage. A particular feature was evidenced when studying the effect of channel p-type doping concentration on the simulated diamond MOSFET electrical properties:

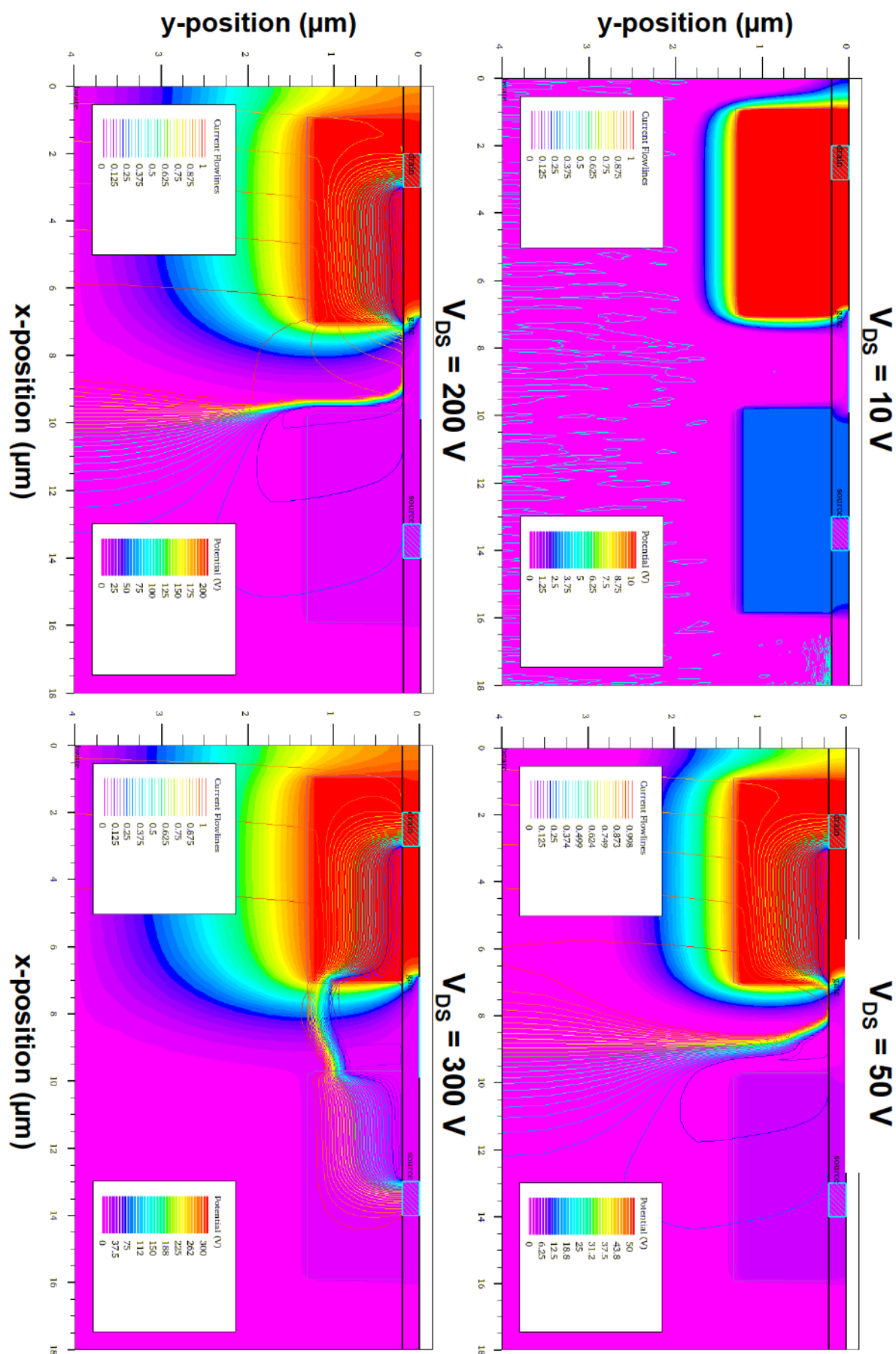


Figure 3.27: Potential and leakage currents flow lines distributions in the 2D diamond MOSFET structure,  $V_{DS}$  ranging from 10 V to 300 V.

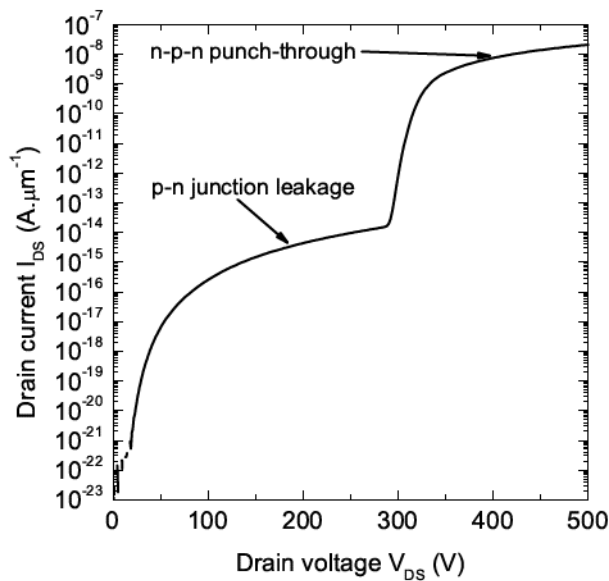


Figure 3.28:  $I_{DS}$  vs.  $V_{DS}$  characteristic of the simulated diamond MOSFET with  $V_{GS} = 0$  V and  $T = 300$  K. When  $V_{DS}$  reaches a value close to 290 V,  $I_{DS}$  increases, inducing the turn-on of the transistor.

the increasing channel resistance with increasing doping concentration. The 2D analysis offers a new perspective for diamond device simulation. In fact, the specific 2D effect, such as the current flow lines, the electric field and potential distributions can be accessed. It evidenced that electric field enhancement takes place near the edge of the gate contact. However, limitations due to the lack of implemented parameters prevent from modeling the gate oxide breakdown, evidenced by the unreasonably high level of electric field in the oxide layer (almost  $10 \text{ MV} \cdot \text{cm}^{-1}$ ). Thus, future effort must be conducted to properly model the dielectric breakdown. As this device is envisioned for future power device integration, the investigation of the dynamic behavior is also of great interest. Finally, the studied diamond MOSFET structure showed that the electrical breakdown was much lower than the expected diamond limit. Thus, new device structures must be explored in order to take advantage of the full potential of diamond for next generation power device applications.

Two examples are given in Fig.3.29, where the specific architectures are evidenced to achieve proper electrical behavior. The V-shape geometry [Lane 1980] proposed in Fig.3.29.a) has the advantage of being a vertical device, where the drift layer and hence the breakdown properties are controlled by the lightly boron-doped diamond layer quality and thickness. On the other hand, the geometry proposed in Fig.3.29.b) represents a planar power MOSFET with a  $n^-$ -type drift region on the drain side. Even though several challenges have to be tackled before the actual device realization, these structures

could be envisioned for future diamond MOSFET developments.

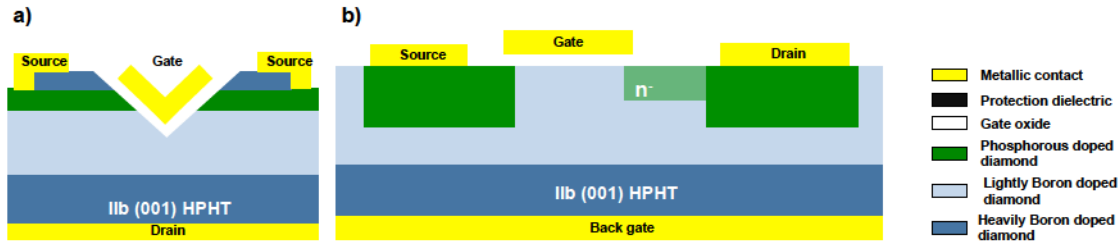


Figure 3.29: Potential diamond MOSFET structures envisioned for next generation power device applications.

### 3.5 Conclusions

In this chapter, the electrical properties of two diamond devices were studied. First, the simulation of the electrical properties of a diamond p-n junction was conducted to verify the implemented models and the effect of parameters value on the simulated electrical properties. Large discrepancies were observed between the simulation results and the experimental data. This means that other factors such as ohmic contact resistivity, carrier tunneling, crystalline defect and potentially specific generation-recombination models for diamond [Makino 2012] strongly contributes to the diamond device electrical characteristics. These factors must be investigated for future diamond device simulations.

On the other hand, the simulation of the diamond MOSFET 2D structure, taking into account the specific diamond properties, allowed to investigate the effect of channel doping concentration, temperature and oxide thickness on the simulated electrical properties. In particular, these simulations demonstrate that the simulated MOSFET is not appropriate in terms of high power device applications. As shown in Fig.3.30, which exhibits the specific on-resistance as a function of the breakdown voltage, the simulated structure suffers from several drawbacks. On one hand, the  $n^+$ -p junction punch-through occurs at a bias voltage of only 290 V, which is, on the other hand, over the oxide breakdown voltage of 140 V. In the end, even with an elevated breakdown voltage of 1500 V for the  $n^+$ -p junction, this diamond MOSFET structure has a lower  $R_{on}S/BV$  figure of merit than the calculated Si limit [Baliga 2012]. As a consequence, specific architectures (see Fig.3.29) must be developed to take advantage of the strong potential of diamond for future power electronic device applications.

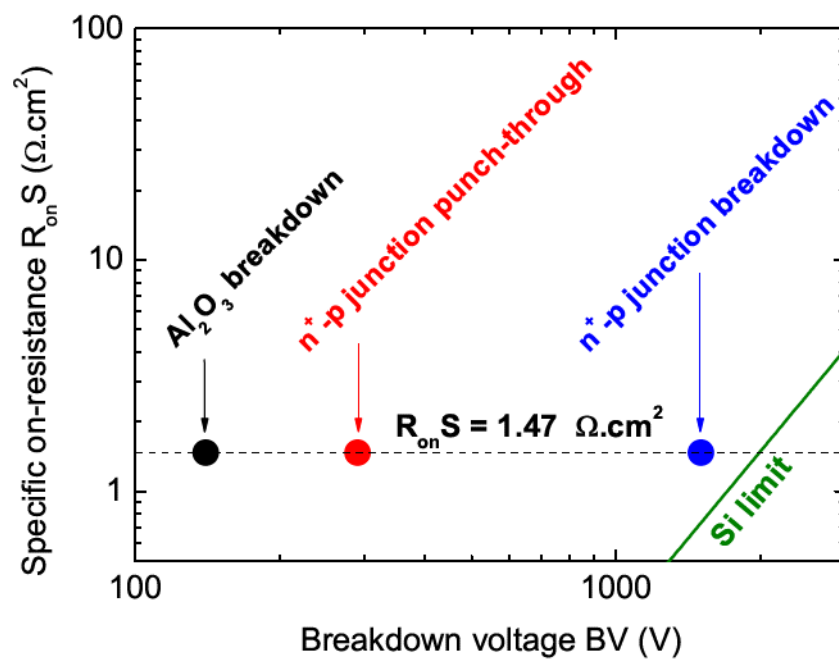


Figure 3.30: Specific on-resistance as a function of the breakdown voltage. The Si limit is calculated through Baliga's law as  $R_{on}S = 8.37 \times 10^{-9} \cdot BV^{2.5}$  [Baliga 2012].



## Chapter 4

# Diamond MOS capacitors fabrication and characterization

### Contents

---

<b>4.1</b>	<b>Introduction</b>	<b>103</b>
<b>4.2</b>	<b>A brief history of diamond metal-oxide-semiconductor capacitors</b>	<b>104</b>
<b>4.3</b>	<b>Fabrication of diamond MOS capacitors</b>	<b>107</b>
4.3.1	Diamond homoepitaxial growth by MPCVD	107
4.3.2	Pseudo vertical diamond MOS capacitor fabrication	113
4.3.3	Summary	116
<b>4.4</b>	<b>Band alignment investigation of Al<sub>2</sub>O<sub>3</sub>/O-terminated diamond heterostructure</b>	<b>117</b>
4.4.1	Xray photoelectron spectroscopy analysis	117
4.4.2	Energy band diagram	120
4.4.3	Summary	122
<b>4.5</b>	<b>Electrical characterization of diamond MOSCAPs</b>	<b>123</b>
4.5.1	Al <sub>2</sub> O <sub>3</sub> /O-terminated diamond MOSCAPs electronic properties	123
4.5.2	Al <sub>2</sub> O <sub>3</sub> /O-terminated diamond MOSCAPs leakage currents analysis	138
4.5.3	Summary	144
<b>4.6</b>	<b>Experimental realization of a n-type channel MOSFET</b>	<b>145</b>

---

4.6.1	Sample structure . . . . .	145
4.6.2	Experimental setup and electrical characterizations . . . . .	147
4.6.3	Summary . . . . .	156
<b>4.7</b>	<b>Conclusions . . . . .</b>	<b>156</b>

---

## 4.1 Introduction

In this chapter, the fabrication steps leading to the realization of the pseudo-vertical  $\text{Al}_2\text{O}_3/\text{O}$ -diamond metal-oxide-semiconductor capacitors (MOSCAPs) are described. A first step of epitaxial growth of the  $\text{p}^+$ -type layer and the p-type layer is performed, starting from a Ib HPHT (001) diamond substrate. Then, the definition of the mesa structure is realized with the use of pure oxygen plasma through ICP etching. The ohmic contact are thus directly deposited on top of the  $\text{p}^+$ -type diamond layer. The vacuum UV light/ozone treatment [Teraji 2009] results in the oxygen termination of the diamond surface prior to the atomic layer deposition of the  $\text{Al}_2\text{O}_3$  layer at 250 °C. Finally, the gate contact is deposited. Fig.4.1 shows the schematic cross section of the sample together with a picture, where the ohmic contact, the metal-oxide-semiconductor (MOS) contacts and the metal-insulator-metal (MIM) contacts are depicted.

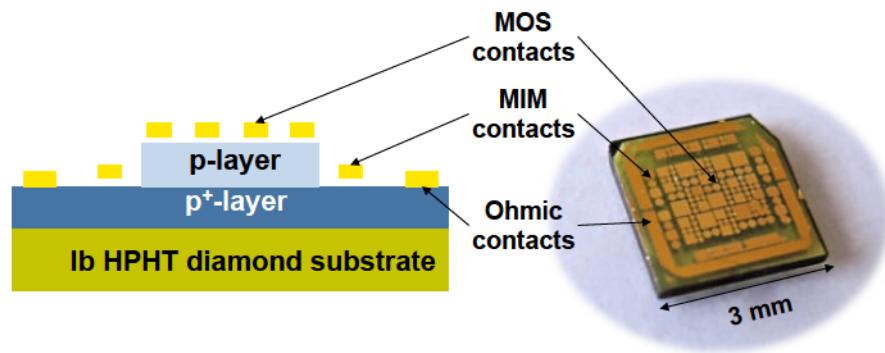


*Figure 4.1:* Schematic cross section (left) of the fabricated diamond MOSCAP and the corresponding actual device (right).

The interfacial band configuration of the  $\text{Al}_2\text{O}_3/\text{O}$ -diamond heterostructure was investigated with X-ray photoelectron spectroscopy (XPS) performed at the Laboratoire des Technologies de la Microelectronique (LTM) by M. Aoukar and C. Vallée. This study allows to establish the energy band diagram of the  $\text{Al}_2\text{O}_3/\text{O}$ -diamond structure thanks to the measurement of the valence band offset [Maréchal 2015].

The electrical characterization of the  $\text{Al}_2\text{O}_3/\text{O}$ -diamond MOSCAP using capacitance and conductance methods revealed the presence of a high density of interface states resulting in the pinning of the Fermi level at the interface preventing the MOSCAP to reach accumulation. Nevertheless, depletion and deep depletion regimes are achieved. On the other hand, leakage currents were observed in the device and investigated in

terms of temperature dependent trap assisted tunneling of holes from the diamond layer to the top gate electrode. Discrepancy between the experimental data and the theoretical model is linked to the presence of hole injection from the p<sup>+</sup>-type layer, resulting in a higher hole concentration in the p-type layer, well above the equilibrium concentration [Muret 2015].

In order to highlight the context of diamond MOSCAP, a brief review will be made showing the last 25 years of effort towards the realization of working devices. Then, the fabrication steps of the device investigated in this work will be shown. The band diagram obtained from XPS analysis will be established and the results from the electrical characterization will be discussed. Finally, the characterization of a diamond MOSFET performed during a four months stay in AIST (Tsukuba, Japan) will be presented.

## 4.2 A brief history of diamond metal-oxide-semiconductor capacitors

In 1991, Geis et al. [Geis 1991] performed the first C(V) measurements of metal-SiO<sub>2</sub>-diamond structure. The structure was composed of a type II natural diamond substrate with boron doping, making it a p-type semiconductor. The oxide deposition was made by chemical vapor deposition of SiO<sub>2</sub> with various thicknesses. The measured C(V) characteristics revealed several interesting features, some illustrated in Fig.4.2 for a SiO<sub>2</sub> layer of  $d_{ox} = 89.5$  nm and summarized as follows:

- accumulation and deep depletion regimes could be clearly identified;
- C(V) curves showed strong temperature dependencies near accumulation but almost no effect in deep depletion;
- interface states and oxide mobile charges were responsible for the hysteresis behavior of the capacitance;
- deep depletion capacitance was influenced by illuminating the sample with UV light, a consequence of electron generation in the diamond depletion layer.

This first contribution demonstrated the feasibility of diamond MOS capacitors (MOSCAP) for developing diamond p-channel's field effect transistors using the hydrogen-terminated

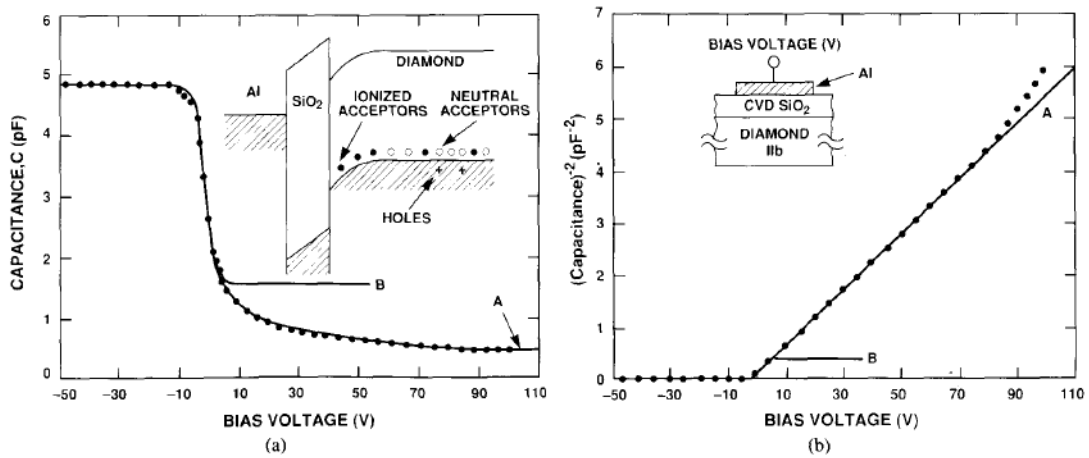


Figure 4.2: a) Capacitance vs. bias voltage and b)  $1/C^2$  vs. bias voltage for the (001) substrate taken from [Geis 1991]. The measurement temperature was 250 °C and the ac signal frequency 10 kHz. The inset of a) shows the energy band diagram of the structure biased into depletion and the one in b) is a schematic of the diamond MOSCAP.

diamond (H-diamond) surface conductive layer properties. In fact, the accumulation capacitance was only  $\sim 20\%$  lower than the expected value, thus leading to a SiO<sub>2</sub> dielectric constant of 3.3 instead of the 3.9 expected. The low leakage currents value of about  $60 \mu\text{A}\cdot\text{cm}^{-2}$  at -40 V was still reasonable to consider this device for practical applications. However, the fabricated devices suffered from several imperfections. First, the boron doping could not be controlled since it was made from type II natural diamond. Furthermore, the bias voltage window required to achieve the surface potential modulation from accumulation to deep depletion was more than 100 V. Finally, the SiO<sub>2</sub> layer suffered from adhesion issues during the deposition process.

This pioneered work was followed by numerous developments, such as the fabrication of diamond MOSCAPs using CVD diamond with controlled boron doping level and high- $\kappa$  oxides to achieve field effect modulation of the majority carrier in the diamond layer [Ariki 1994, Otsuka 1995]. Ariki et al. were able to demonstrate efficient field effect control with only few volts of applied gate bias voltage [Ariki 1994]. However, the capacitance could not be set into accumulation regime and they were not able to attain the flat band condition. Then, Otsuka et al. [Otsuka 1995] evidenced the Fermi level pinning at the BaTiO<sub>3</sub>/diamond interface. Comparing the obtained results with the C(V) characteristic of an unpinned CaF<sub>2</sub>/diamond interface, they concluded that the adsorption of oxygen atoms on the surface was responsible for a large amount of interface states resulting in the Fermi level pinning. These results led to the study of fluorides as gate

insulator [Tanaka 1998]. Later on, H-diamond conductive surface devices were prepared using  $\text{SiO}_x$  as gate oxide deposited on non-intentionally doped diamond and MOSFET operation was evidenced [Hokazono 1999]. Efforts in developing high quality oxide deposition on H-diamond, in particular the development of atomic layer deposition (ALD)<sup>1</sup>, led to the emergence of high quality H-diamond MOSFET using various oxides, such as  $\text{Al}_2\text{O}_3$  [Liu 2013b, Daicho 2014],  $\text{HfO}_2$  [Liu 2013a] or a combination of ALD-oxide together with a high- $\kappa$  material for increasing the field effect [Liu 2014c, Liu 2014b]. Thus, these devices take advantage of the presence of the hydrogen layer at the diamond surface. Specifically, the hole density in this layer is controlled by applying an electric field on a top electrode. The current flow is then modulated between a source contact and a drain contact. This kind of device is referred to as accumulation MOSFET, since the current flows thanks to the accumulated holes at the H-terminated diamond surface. An alternative to the H-diamond MOSFET is the inversion MOSFET, which is based on the control of the diamond band bending from accumulation to inversion, enabling the current to flow between two reservoirs. In this case, there must be a sufficiently high barrier for both electrons and holes to prevent leakage currents in the gate contact. This can be achieved by using oxygen-terminated diamond (O-diamond) with an appropriate gate oxide. However, only few contributions on O-diamond MOSCAPs are reported. This is attributed to the high ionization energy of boron (0.38 eV), which requires very high crystalline quality and boron doping control. Only recently, Cheng et al. [Cheng 2012] used high- $\kappa$   $\text{Ta}_2\text{O}_5$  as gate insulator on O-diamond. The  $C(V)$  characteristics exhibited majority carrier modulation from accumulation to depletion. However, the deep depletion or inversion regime was not achieved and more importantly the gate oxide forbidden bandgap was too small to provide a barrier for both electrons and holes. In our approach, we used ALD of  $\text{Al}_2\text{O}_3$  to stabilize the O-diamond surface [Chicot 2013b]. Thus, the Al/ $\text{Al}_2\text{O}_3$ /O-diamond MOSCAP depletion and deep depletion regimes could be controlled within few volts of applied gate voltage. However, the device suffered from leakage currents in the entire bias voltage range and the measured accumulation capacitance at high frequency ( $f = 1$  MHz) was 10 times smaller than the expected value, a discrepancy which can not be attributed to a smaller oxide dielectric constant  $\epsilon_{ox}$  since it would lead to an unreasonably small value. In this work, efforts have been made to investigate an improved version of the previous  $\text{Al}_2\text{O}_3$ /O-diamond design, which fabrication steps are described in the following section.

---

<sup>1</sup>first demonstration of ALD  $\text{Al}_2\text{O}_3$  on diamond was reported by Kawakami et al. [Kawakami 2005].

## 4.3 Fabrication of diamond MOS capacitors

### 4.3.1 Diamond homoepitaxial growth by MPCVD

This section describes the growth technique used in this work to fabricate both heavily  $p^+$  and slightly  $p$  boron doped diamond layers. These epi-layers were deposited on Ib HPHT (001) diamond substrate provided by Sumitomo company. The substrate was polished by Syntek company which provides nearly atomically flat diamond surfaces. No particular attention was paid on the surface mis-orientation angle. Prior to the growth, a standard process for cleaning the substrate is performed. It consists in a first step of solvent cleaning (acetone and ethanol) combined with ultra-sounds to remove the surface contamination. Then, a hot acid treatment is performed, using a mixture of  $\text{HClO}_4:\text{HNO}_3:\text{H}_2\text{SO}_4$  (1:4:3) at a temperature of 250 °C during 30 minutes.

#### 4.3.1.1 Home-made NIRIM type reactor

In this work, a home-made Microwave Plasma-enhanced Chemical Vapor Deposition (MPCVD) NIRIM type reactor was used to grow both  $p^+$  and  $p$  type layers. Fig.4.3 shows the MPCVD reactor [Fiori 2012]. This is a modified version of the Japanese reactor used in NIRIM (National Institute for Research in Inorganic Materials, at present time named NIMS) developed by Kamo et al. [Kamo 1983]. It is based on generating a plasma glow discharge ball at the intersection between the inner silica tube and the microwave guide. The microwave guide (generator operating at 2.45 GHz) can be tuned by adjusting the impedance in order to minimizing the reflected power and maximizing the energy at the crossing point. The growth chamber is made out of an outer and an inner silica tube, which can be changed depending on the boron doping level targeted. In this way, three exchangeables silica tubes are used in order to minimize the boron contamination when low boron doping is targeted. The gases are injected from the top of the chamber and the plasma glow discharge ball is located at the point where the microwave power is maximum. The diamond sample is located on a non-intentionally doped polycrystalline diamond coated silicon sample holder itself mounted on top of the inner silica tube. The sample can be positioned with respect to the plasma glow discharge ball in order to control the layer properties (doping concentration and surface

homogeneity) and the sample temperature, which is mainly controlled by the micro-wave power. The temperature of the diamond sample is estimated by a single color pyrometer (980 nm), which emissivity is set to 0.4, taking into account the contribution of the silicon sample holder.

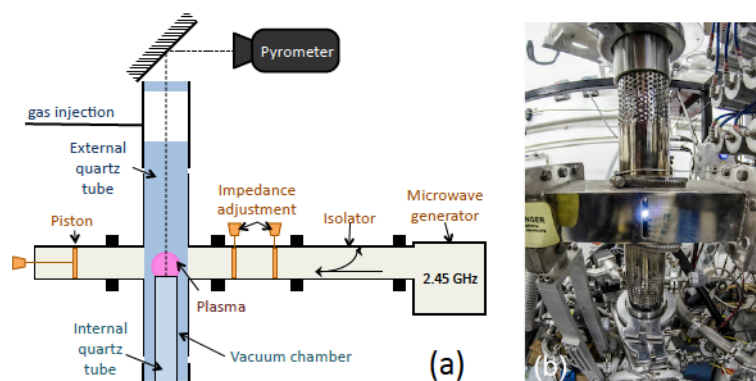


Figure 4.3: a) Schematic view of the home-made NIRIM type MPCVD reactor. b) Picture of the growth chamber [Fiori 2012].

The next section will describe the first step of the diamond MOSCAP fabrication, namely the  $p^+$ -type layer growth, which role being to minimize the series resistance of the device.

#### 4.3.1.2 Heavily boron doped layer

The growth conditions follow the growth procedure established by A. Fiori [Fiori 2012] to get high boron concentration and thus to obtain highly conductive diamond layers. According to the established procedure, the  $p^+$ -type layers were grown using a gas mixture of methane ( $[CH_4]/[H_2] = 4\%$ ), diborane ( $[B]/[C] = 1200$  ppm) and hydrogen at a pressure of 33 Torr and a temperature of 830 °C for 15 min growth duration. These growth conditions were optimized to minimize the defects generation and propagation in the heavily boron doped diamond layer. Moreover, the boron concentration ensures a metallic transition of the diamond layer since the boron incorporation is above  $5 \times 10^{20} \text{ cm}^{-3}$  [Klein 2007] as can be seen in Fig.4.4.

The epi-layer thickness was measured by Spectroscopic Ellipsometry. This method is based on measuring the change in polarization of an electromagnetic wave reflected on a sample surface [Fujiwara 2009]. The difference in optical refractive index between the Ib HPHT diamond substrate and the heavily boron doped layer allows the measurement of the epi-layer thickness, which is evaluated as 470 nm.

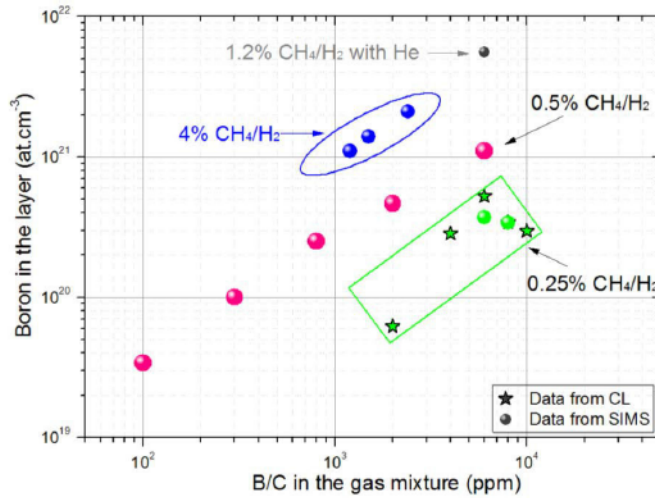


Figure 4.4: Boron incorporation as a function of the  $[B]/[C]$  ratio in the gas mixture for various  $[CH_4]/[H_2]$  ratios, taken from [Fiori 2012]

Optical profilometry using a Veeco 3D optical profiler Contour GT<sup>2</sup> was performed to characterize the surface morphology of the p<sup>+</sup>-layer. A typical surface morphology of the heavily boron doped diamond layer is shown in Fig.4.5. The surface roughness is quantified by the measurement of the mean roughness  $Sa$  and the Root Mean Square (RMS)  $Sq$ . The typical values for the high quality heavily boron doped diamond layers are 0.22 nm and 0.27 nm, respectively (typically measured on a  $127 \times 95 \mu\text{m}^2$  area, see Fig.4.5).

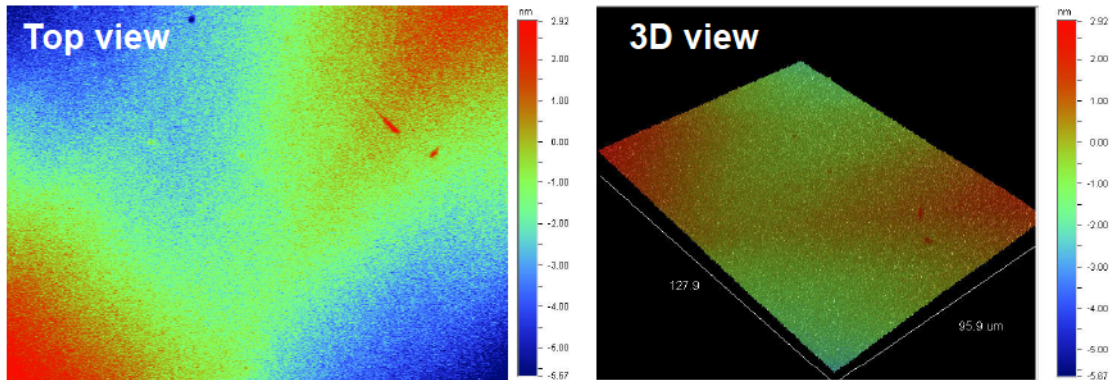


Figure 4.5: Typical surface morphology of the heavily boron doped diamond layer with mean roughness  $Sa = 0.22$  nm and Root Mean Square (RMS)  $Sq = 0.27$  nm.

#### 4.3.1.3 Lightly boron doped layer

Previous to the lightly boron doped layer (denoted as p-type layer), the outer and inner silica tubes are changed in order to avoid a too high contribution of the memory effect due to the adsorption of boron species in the growth chamber during the p<sup>+</sup>-type layer growth.

<sup>2</sup>vertical resolution below 0.1 nm

Moreover, a cleaning procedure using a pure oxygen plasma treatment is performed to reduce the contamination. The growth conditions are a modified version of the one developed by G. Chicot [Chicot 2013a]. More precisely, an oxygen content of 0.25 % was added to the gas mixture in order to improve the crystalline quality of the p-type layer [Omnès 2011]. The counter part is that oxygen decreases the boron incorporation in the layer by two orders of magnitude. Thus a calibration was performed. The calibration sample was processed with a periodic growth of non-intentionally doped (NiD) and doped diamond layers with a constant  $[O_2]/[H_2]$  ratio of 0.25 % at a pressure of 50 Torr. The growth sequence is as follows: first, a hydrogen plasma is performed in order to bring the sample to the desired temperature. Then, the NiD layer was grown during 20 minutes followed by a cleaning of 3 minutes under plasma with 2000 sccm hydrogen flow. The final step consists in growing the boron doped diamond layer during 20 minutes. The growth conditions are summarized in Tab.4.1.

Step	Plasma type	Flow (sccm)	$[CH_4]/[H_2]$ (%)	$[O_2]/[H_2]$ (%)	$[B]/[C]$ (ppm)	Duration (min)
1	H <sub>2</sub>	200				60
2	NiD	200	1	0.5		20
3	H <sub>2</sub>	2000				3
4	p	200	1	0.25	200	20
5	H <sub>2</sub>	2000				3
6	NiD	200	1	0.5		20
7	H <sub>2</sub>	2000				3
8	p	200	1	0.25	600	20
9	H <sub>2</sub>	2000				3
10	NiD	200	1	0.5		20
11	H <sub>2</sub>	2000				3
12	p	200	1	0.25	900	20
13	H <sub>2</sub>	2000				3
14	NiD	200	1	0.5		20

*Table 4.1:* Growth sequences with plasma type, gas flow, gas composition and duration of each step used to calibrate the boron doped diamond layer using oxygen in the gas phase.

The boron concentrations in the different layers were analyzed by secondary ion mass spectroscopy (SIMS). This destructive characterization method is based on the sputtering of the sample surface atoms by a primary ion beam. By collecting the sputtered secondary ions with a mass spectrometer and after a calibration with a boron-implanted diamond

sample, the concentration as a function of depth is reconstructed. This technique allows to detect various elements with concentrations as low as  $10^{15} \text{ cm}^{-3} - 10^{16} \text{ cm}^{-3}$  in diamond. In the present case, the measurements were performed by F. Jomard from GEMAC (Groupe d'Etude de la Matière Condensée, Versailles, France). The incident ions used were  $\text{O}_2^+$  with an energy of 5 keV and an incident angle of  $47^\circ$ . The obtained SIMS profil is shown in Fig.4.6.

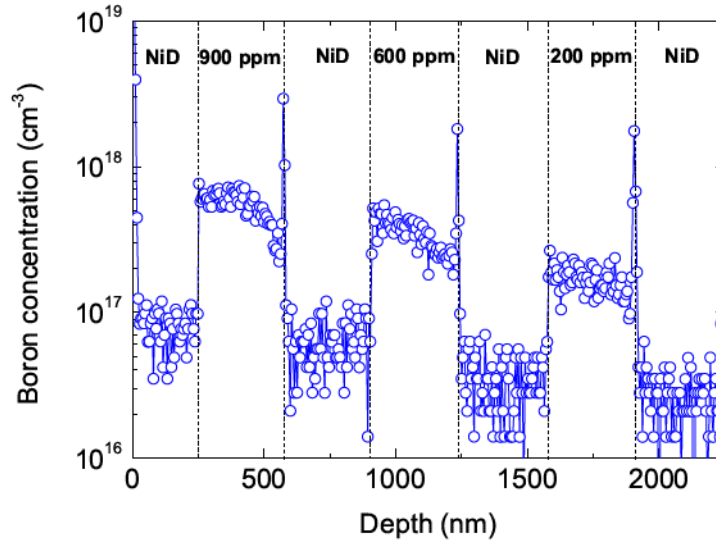


Figure 4.6: Secondary Ion Mass Spectroscopy profile of the sample prepared for the doping concentration calibration.

From the SIMS profile the boron concentration and the growth rate of the layers were extracted. Tab.4.2 summarizes the boron concentrations and growth rates of the layers.

Layer	$[\text{B}]/[\text{C}]$ (ppm)	Boron concentration ( $\text{cm}^{-3}$ )	Growth rate ( $\text{nm}\cdot\text{min}^{-1}$ )
NiD		$<10^{17}$	16.5
p	200	$\approx 2 \times 10^{17}$	16
p	600	$\approx 4 \times 10^{17}$	16
p	900	$\approx 6 \times 10^{17}$	16

Table 4.2: Boron concentration and growth rate of the NiD and doped diamond layers extracted from the SIMS profile.

In the following, the samples were fabricated using a gas mixture of methane ( $[\text{CH}_4]/[\text{H}_2] = 1\%$ ), diborane ( $[\text{B}]/[\text{C}] = 600 \text{ ppm}$ ), oxygen ( $[\text{O}_2]/[\text{H}_2] = 0.25 \%$ ) and hydrogen at

a pressure of 33 Torr and a temperature of 910 °C for 45 min growth duration. The pressure was lowered from 50 Torr to 33 Torr in order to increase the plasma glow discharge ball size. Thus, the plasma interaction surface with the diamond sample is greater leading to a more homogeneous epitaxial layer. The measured thickness estimated using Spectroscopic Ellipsometry was 590 nm. A typical surface morphology is shown in Fig.4.7. The measured  $Sa$  and  $Sq$  parameters are 0.46 nm and 0.82 nm, respectively, measured on the  $127 \times 95 \mu\text{m}^2$  area (it was typically 0.22 and 0.27 nm before p-type growth).

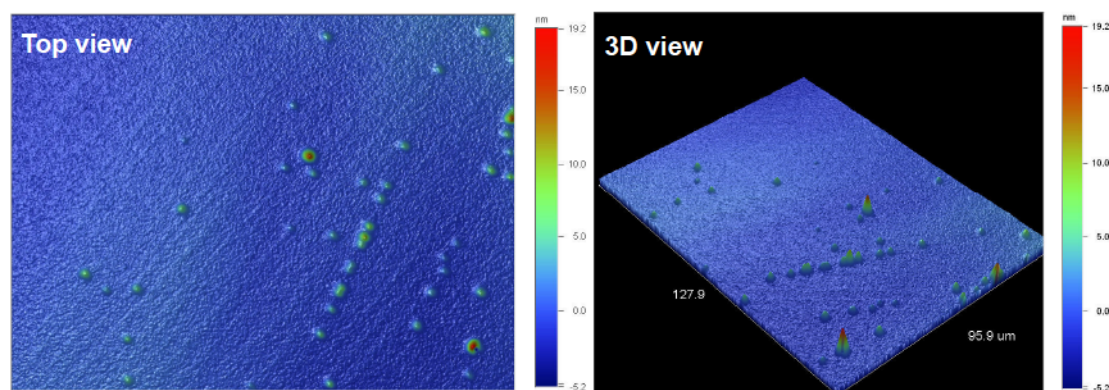


Figure 4.7: Typical surface morphology of the p-type boron doped layer with  $Sa = 0.46$  nm and  $Sq = 0.82$  nm on the  $127 \times 95 \mu\text{m}^2$  area.

#### 4.3.1.4 Summary

Two successive CVD diamond growth steps were performed to produce a 470 nm thick  $\text{p}^+$ -type diamond layer on top of which a 590 nm thick p-type diamond layer was deposited. The  $\text{p}^+$ -type diamond layer was performed using a gas mixture of methane ( $[\text{CH}_4]/[\text{H}_2] = 4\%$ ), diborane ( $[\text{B}]/[\text{C}] = 1200$  ppm) and hydrogen at a pressure of 33 Torr and a temperature of 830 °C for 15 min growth duration. The surface morphology investigated by optical profilometry revealed a high quality epitaxial layer with mean roughness of 0.22 nm and Root Mean Square of 0.27 nm. The p-type diamond layer was performed using a gas mixture of methane ( $[\text{CH}_4]/[\text{H}_2] = 1\%$ ), diborane ( $[\text{B}]/[\text{C}] = 600$  ppm), oxygen ( $[\text{O}_2]/[\text{H}_2] = 0.25\%$ ) and hydrogen at a pressure of 33 Torr and a temperature of 910 °C for 45 min growth duration. These growth conditions lead to a high diamond epitaxial layer quality, as demonstrated by the surface mean roughness and Root Mean Square, measured by optical profilometry as 0.46 nm and 0.82 nm respectively. In the next section, the technological steps for producing the diamond MOSCAP will be described.

### 4.3.2 Pseudo vertical diamond MOS capacitor fabrication

#### 4.3.2.1 Ohmic contacts fabrication

The deposition of a metal on a p-type semiconductor generally leads to the formation of a downward bending of the diamond bands at the metal/semiconductor interface. This results in the formation of a depletion layer which prevents the charge carriers to flow from the semiconductor to the metal electrode. The resulting built-in potential is called the Schottky barrier. Majority carriers can overcome the Schottky barrier through different mechanisms, such as thermionic emission, thermionic-field emission and field emission [Sze 2007]. On the opposite, ohmic contacts are characterized by a low Schottky barrier height or a depletion region so thin that carriers can quantum-mechanically tunnel through the layer, resulting in low contact resistivity. The formation of ohmic contacts on diamond generally involves the deposition of a carbide-forming metal together with the annealing of the deposited metal at temperatures in the range of 400 °C to 1000 °C [Viljoen 1994, Nakanishi 1994]. The formation of a damaged carbide interfacial layer lowers the metal/diamond Schottky barrier height or enhances tunneling or both [Werner 2003]. The choice of material for ohmic contact is driven by requirements, such as low contact resistivity, good adhesion, high thermal stability, high corrosion resistance and bondable top-layer [Werner 2003]. As the depletion layer varies as  $W_D \propto N_A^{-1/2}$ , the low contact resistivity can be achieved by the use of heavily doped diamond layer. The good adhesion requirement is fulfilled by using titanium (Ti), which forms a TiC interfacial layer with diamond [Viljoen 1994]. The strong affinity of Ti with oxygen requires the use of a passivation layer such as Gold (Au). However, the thermal stability is not achieved since Ti diffuses along the Au grain boundaries [Viljoen 1994]. Thus, platinum (Pt) is used as a diffusion barrier to prevent from thermal deterioration.

The ohmic contacts were performed by depositing a Ti/Pt/Au metallic stack on the heavily boron doped diamond layer. The different steps of the ohmic contacts fabrication are summarized in Fig.4.8.

A first step of laser lithography (using a Heidelberg DWL66FS instrument) is performed defining the etching mask area. Then, a 150 nm thick nickel (Ni) layer is deposited by electron beam (e-beam) evaporation on diamond followed by a lift-off process. Inductively Coupled Plasma (ICP) etching step allows to delineate the mesa structure. Pure

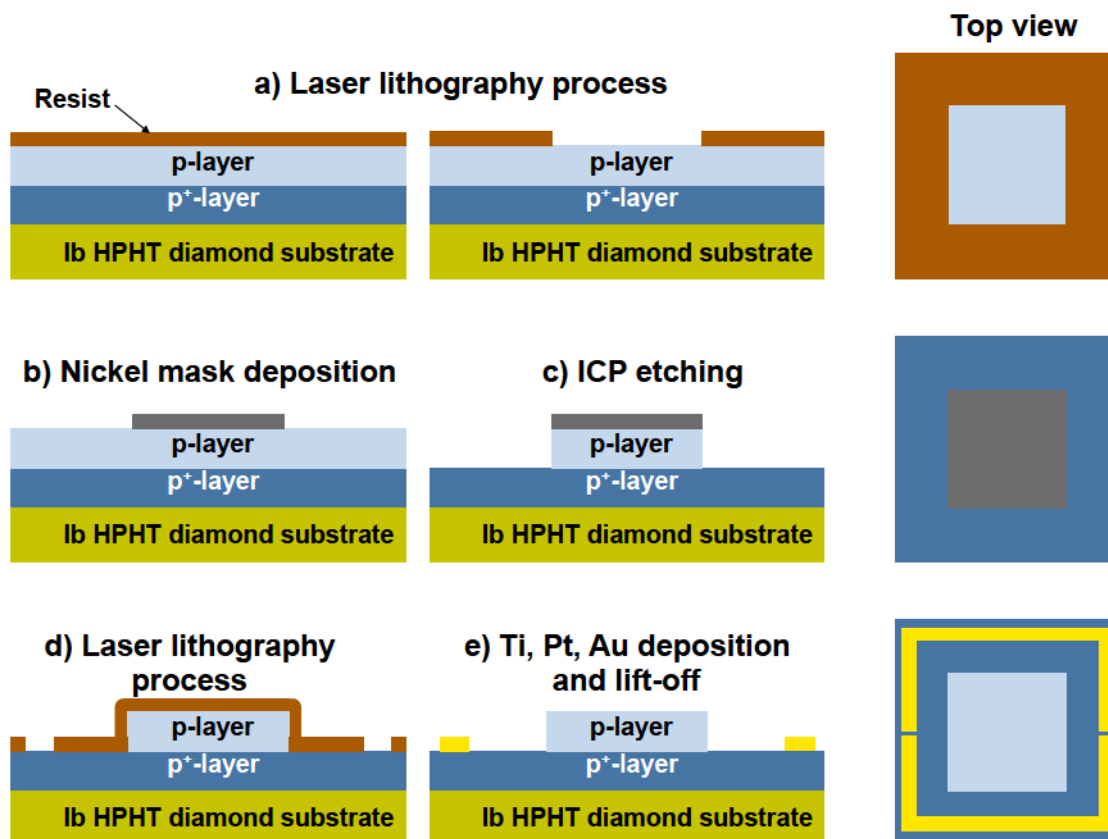


Figure 4.8: Schematic describing the ohmic contacts fabrication process.

oxygen plasma etching was performed with a 1000 W coil power, a 40 W platen power, 100 sccm gas flow and under 10 mTorr pressure<sup>3</sup>. After etching, the Ni mask is removed by hot acid treatment, typically HCl:HNO<sub>3</sub> (3:1) at 150 °C for 1 h. A second laser lithography step is applied to define the ohmic contact area followed by a Ti/Pt/Au e-beam deposition and lift-off process. A small gap has been performed in the ohmic contact square in order to measure the resistance. The ohmic contacts electrical properties are satisfied as shown in Fig.4.9, where the resistance is measured between the two ohmic contacts and is of the order of 25 Ω.

#### 4.3.2.2 MOS gate fabrication

Previous to the ozone treatment of the diamond surface, an acid treatment consisting in a H<sub>2</sub>O<sub>2</sub>:H<sub>2</sub>SO<sub>4</sub> (1:3) mixture is performed to remove any remaining resist and organic contamination.

<sup>3</sup>the etching rate of this recipe is 53 nm.min<sup>-1</sup>.

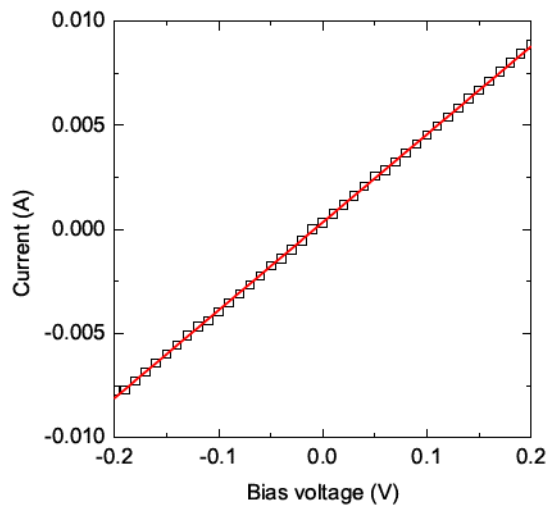


*Figure 4.9:*  $I(V)$  characteristic of the ohmic contact deposited on heavily boron doped diamond. The contact resistance is of the order of  $25 \Omega$ . The value is extracted from the slope of the  $I(V)$  characteristic measured between the two ohmic contacts.

Oxygen termination of diamond surface (O-diamond) is achieved by performing an ozone treatment, a technique first proposed by Teraji et al. [Teraji 2008, Teraji 2009]. This method is based on exposing the sample to vacuum deep ultraviolet (VUV) light in oxygen atmosphere. A xenon lamp centered at 172 nm serves as UV light source. By introducing oxygen in the chamber, ozone is produced and oxygen saturates the diamond surface with hydroxyl (C-O-H), ether (C-O-C) and carbonyl (C=O) group terminations [Boukherroub 2005, Hoeb 2010]. This treatment has proven a great efficiency in surface passivation and in control of the diamond Schottky diode electrical properties [Teraji 2009, Fiori 2014, Traoré 2014]. In practice, the diamond samples were introduced in a chamber under secondary vacuum. Then, oxygen was introduced under a pressure of 500 mbar and exposed to the UV light for 90 minutes at room temperature. Right after the VUV light/ozone treatment, the aluminum oxide  $\text{Al}_2\text{O}_3$  is deposited by atomic layer deposition using a Savannah 100 system from Cambridge NanoTech. This method consists in a sequential exposure of the sample surface to different precursors, namely Trimethylaluminium (TMA), and water as an oxidant. The pulse and exposure duration were 30 s and 15 ms, respectively. The temperature was set to 250 °C and the typical base pressure was  $1.3 \times 10^{-1}$  Torr. A total number of 200 cycles were performed and the  $\text{Al}_2\text{O}_3$  layer thickness was measured by Spectroscopic Ellipsometry giving a deposition rate of 0.1 nm/cycle, resulting in a 20 nm thick layer. Then, a laser lithography step is required to define the gate contacts on top of the oxide layer followed by e-beam deposition of Ti/Pt/Au gate stack and standard lift-off process. Finally, MOS and MIM capacitors are defined on the same sample, allowing independent characterization of the  $\text{Al}_2\text{O}_3$

dielectric layer (MIMCAP) and  $\text{Al}_2\text{O}_3/\text{O}$ -diamond MOSCAPs as shown in Fig.4.10

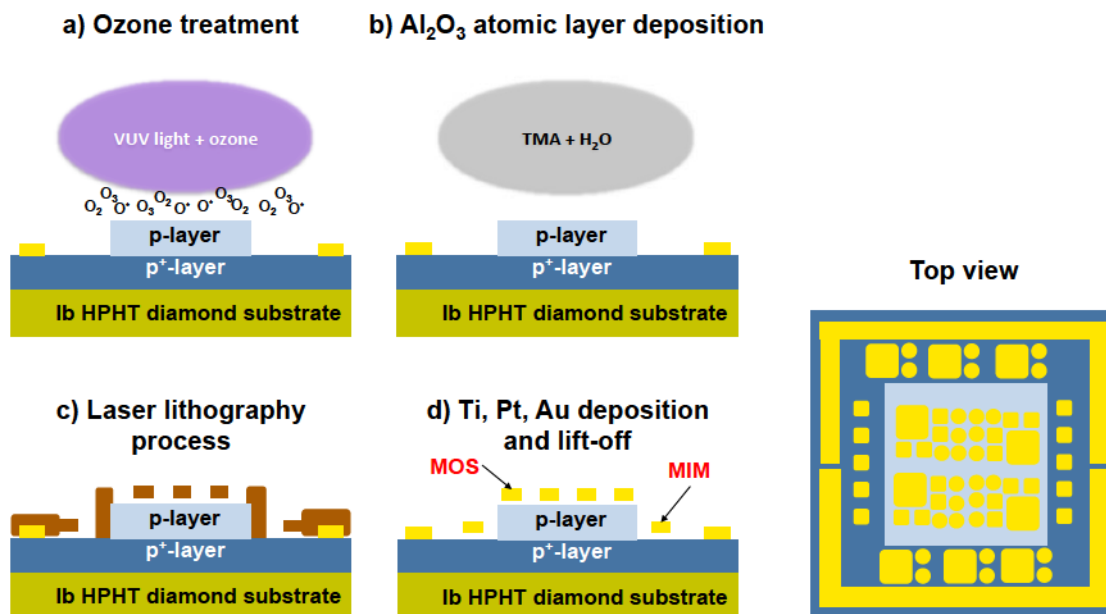


Figure 4.10: Schematic describing the MOS contact fabrication steps.

### 4.3.3 Summary

The pseudo-vertical diamond MOSCAPs were fabricated using standard deposition and liftoff techniques. A first step consisting in defining the mesa structure on the sample was performed followed by the deposition and annealing of the ohmic contacts. Oxygen termination of the diamond surface was achieved using a VUV light/ozone treatment with oxygen pressure of 500 mbar during 90 min at room temperature. The 20 nm  $\text{Al}_2\text{O}_3$  gate dielectric was deposited on the O-diamond surface using atomic layer deposition (ALD), and the definition of the gate contact followed to produce the final pseudo-vertical diamond MOSCAP. In the next section, results on X-ray photoelectron spectroscopy (XPS) measurements will be presented. This study allowed to determine the interfacial energy band diagram configuration of the  $\text{Al}_2\text{O}_3/\text{O}$ -diamond structure.

## 4.4 Band alignment investigation of Al<sub>2</sub>O<sub>3</sub>/O-terminated diamond heterostructure

### 4.4.1 Xray photoelectron spectroscopy analysis

Xray photoelectron spectroscopy (XPS) is a non-destructive characterization technique based on irradiating a sample with monochromatic X-rays and analyzing the energy of the emitted electrons [Moulder 1992]. The typical photons penetration length is of the order of 1-10  $\mu\text{m}$  and the electron mean free path is of the order of 2-8 nm. Thus, surface atoms interact with the beam and electrons are ejected by the photoelectric effect. The kinetic energy  $E_K$  of the emitted electrons is given by:

$$E_K = h\nu - E_B - \phi_s \quad (4.1)$$

with  $h\nu$  the energy of the incident photon,  $E_B$  the electron binding energy and  $\phi_s$  the spectrometer work function. Measuring the electron kinetic energy  $E_K$ , knowing  $h\nu$  and  $\phi_s$  the binding energy  $E_B$  is determined allowing the identification of the chemical environment of the surface atoms.

The XPS analysis was carried out by M. Aoukar and C. Vallée from the Laboratoire des Technologies de la Microelectronique (LTM) in Grenoble using a Thermo Scientific Theta 300 spectrometer. Three samples were prepared as illustrated in Fig.4.11. First, a 2 nm thin ALD-Al<sub>2</sub>O<sub>3</sub> layer deposited at 250 °C on Ib HPHT O-diamond was prepared (see section 4.3.2.2 for details). This layer allowed the XPS signal coming out from the surface of the sample, thus identifying the binding energy between the O-diamond surface and the Al<sub>2</sub>O<sub>3</sub> layer. A second sample with a 20 nm thick Al<sub>2</sub>O<sub>3</sub> layer deposited in the same condition as the first one was prepared as a calibration for the bulk Al atoms. Finally, an oxygen terminated diamond sample was prepared. This sample allows to determine the binding energy of the C atoms.

The experiments were carried out using a high resolution monochromatic Al K $\alpha$  ( $h\nu = 1486.68 \text{ eV}$ ) X-ray source. The core level spectra were recorded using a 0.05 eV step and a 55 eV pass energy as described in [Liu 2013b]. The peak contributions were extracted by combining a Lorentzian and a Gaussian function. The background was subtracted

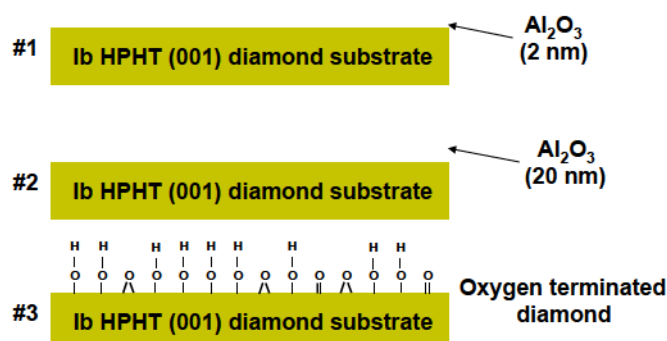


Figure 4.11: Schematic cross section of the samples prepared for the XPS analysis.

using Shirley function. On XPS spectra, the zero energy is usually at the Fermi level. Nevertheless, charge effect and surface contamination can compromise its position. The approach defended here, is to use core level on three samples in order to determine the valence band offset between  $\text{Al}_2\text{O}_3$  and O-diamond. First, considering the mean free path of photoelectrons in a material ( $\sim 2$  nm), a 20 nm  $\text{Al}_2\text{O}_3$  layer serves to infer the energy core level (ECL) for bulk  $\text{Al}_2\text{O}_3$ . The same approach is used for O-diamond. At last, with a 2 nm thick  $\text{Al}_2\text{O}_3$  layer, XPS measurement is sensitive to O-diamond and  $\text{Al}_2\text{O}_3$ . This sample allows to determine the valence band offset. On the 2 nm thick  $\text{Al}_2\text{O}_3$ , C 1s spectrum shows clearly different peak contributions. C-Al contribution is the one which is representative of the interface. Fig.4.12 shows the C 1s spectrum of the 2 nm thick  $\text{Al}_2\text{O}_3$  and the C-Al binding energy of  $284.08 \pm 0.2$  eV. A strong contribution attributed to surface contamination is also present with an energy of  $285.11 \pm 0.2$  eV. This peak was not investigated since its energy is not relevant for the determination of the valence band discontinuity.

Fig.4.13 shows the carbon atoms binding energy for the bulk O-diamond sample. There are number of peaks, which can be attributed to different contributions. For instance, the  $\text{sp}^3$  C-C binding energy is measured as  $284.32 \pm 0.2$  eV, in good agreement with measurements performed on boron doped diamond samples by Ghodbane et al. [Ghodbane 2006] as well as with the values reported in [Liu 2013b]. Other contributions such as the  $\text{CH}_x$ , ether (C-O-C) and carbonyl (C=O) groups are also identified.

As shown in Fig.4.14, the binding energy of Al-O was extracted by measuring Al  $2p_{3/2}$  spectrum of the 20 nm thick  $\text{Al}_2\text{O}_3$  sample. The value of  $74.35 \pm 0.2$  eV is in good agreement with the reported data of [Liu 2013b].

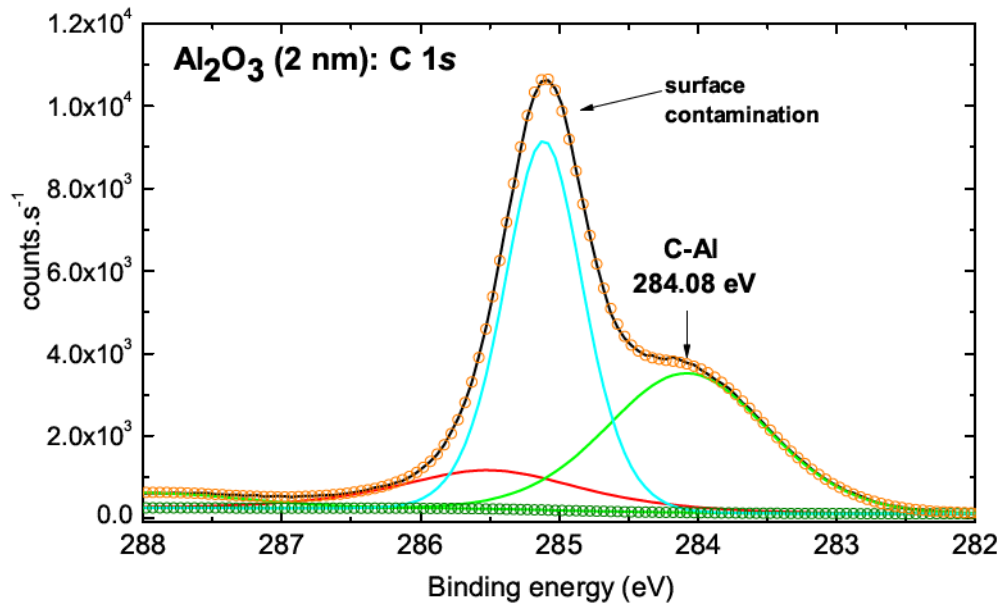


Figure 4.12: C 1s spectrum of the 2 nm thick  $\text{Al}_2\text{O}_3$  layer deposited on O-diamond. The relevant component is the C-Al binding energy which is  $284.08 \pm 0.2$  eV.

Finally, the valence band spectra of both the O-diamond sample and the 20 nm thick  $\text{Al}_2\text{O}_3$  sample are reported in Fig.4.15. The valence band maximum (VBM) is extracted by extrapolating the linear fit to the  $x$ -axis and are  $3.20 \pm 0.2$  eV and  $2.07 \pm 0.2$  eV for  $\text{Al}_2\text{O}_3$  and O-diamond respectively. All the extracted relevant binding energies are summarized in Tab.4.5.

		O-diamond	$\text{Al}_2\text{O}_3$ (2 nm)	$\text{Al}_2\text{O}_3$ (20 nm)
C 1s	C-C	284.32		284.2
	$\text{CH}_x$	284.93		
	C-Al		284.08	
	C-O-C	285.90		
	C=O	287.20		
Al $2p_{3/2}$	Al-O		74.32	74.35
O 1s		530.60	530.46	530.69
VBM		2.07		3.20

Table 4.3: C 1s, Al  $2p_{3/2}$  and O 1s binding energies (eV) of the core level spectra for the O-terminated diamond, the 20 nm  $\text{Al}_2\text{O}_3$  and 2 nm  $\text{Al}_2\text{O}_3$  samples. The valence band maxima (VBM) were recorded for the O-terminated diamond and the 20 nm thick  $\text{Al}_2\text{O}_3$

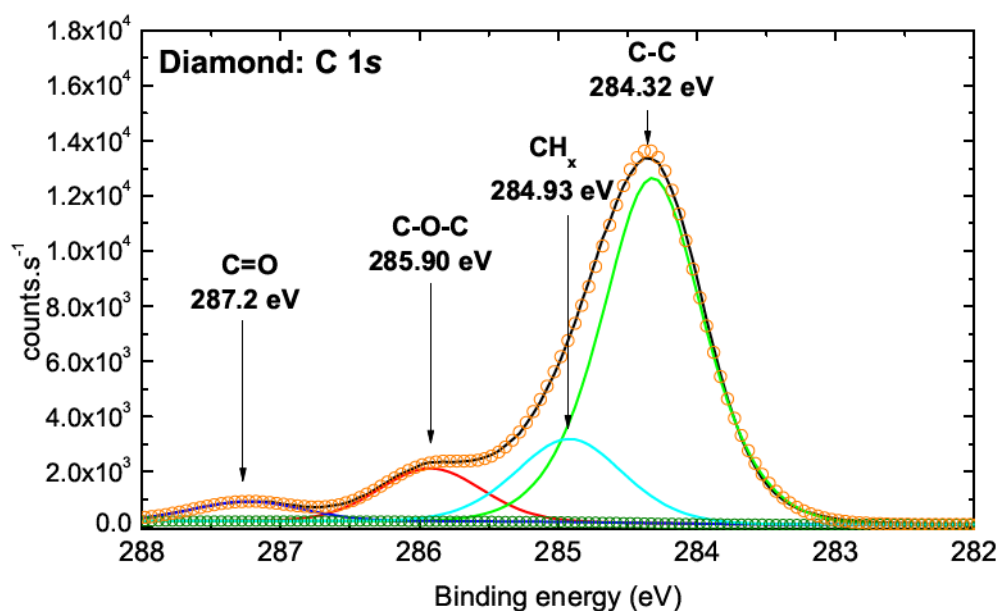


Figure 4.13: C 1s spectrum of the O-diamond sample. The different peaks are attributed to  $sp^3$  (C-C),  $CH_x$ , ether (C-O-C) and carbonyl (C=O) group respectively.

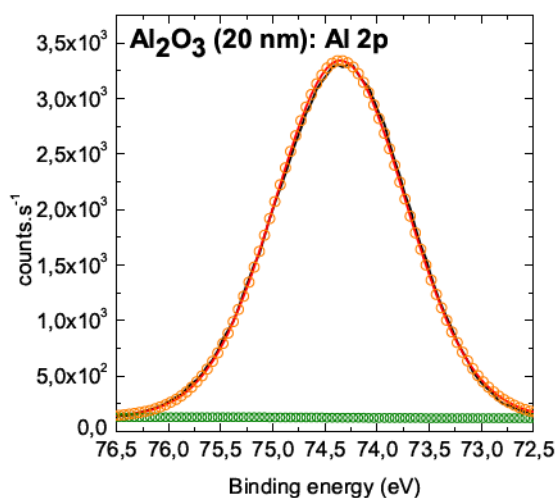


Figure 4.14: Al  $2p_{3/2}$  spectrum of the 20 nm thick  $Al_2O_3$  sample. The binding energy between the aluminum atom and the oxygen atom is measured as  $74.35 \text{ eV} \pm 0.2$ .

#### 4.4.2 Energy band diagram

When the  $Al_2O_3$  is brought in contact with the O-diamond sample, a valence band discontinuity appears at the interface, represented by  $\Delta E_v$ , as exhibited in Fig.4.16.

The valence band discontinuity at the  $Al_2O_3$ /O-diamond interface is calculated using the following formula [Kraut 1980]:

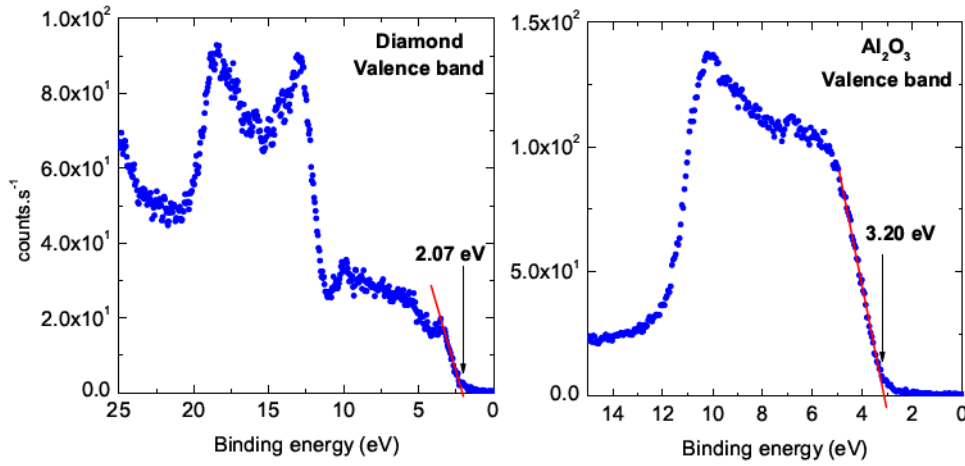


Figure 4.15: Valence band spectra for the O-diamond and the  $\text{Al}_2\text{O}_3$  (20 nm). The valence band maxima are respectively  $2.07 \pm 0.2$  eV and  $3.20 \pm 0.2$  eV.

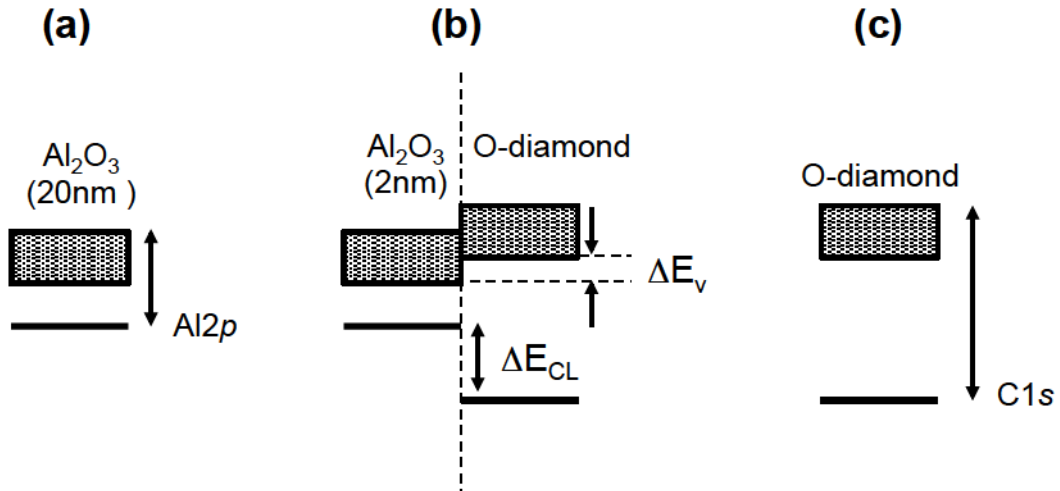


Figure 4.16: a) Al  $2p$  core level and the valence band of the dielectric layer. b) When the 2 nm thin  $\text{Al}_2\text{O}_3$  is brought in contact with the O-diamond surface, the valence band discontinuity  $\Delta E_V$  develops. c) C  $1s$  core level together with the valence band of the O-diamond.

$$\Delta E_V = (E_{\text{CL}} - E_{\text{VBM}})_{\text{O-diamond}} - (E_{\text{CL}} - E_{\text{VBM}})_{\text{Al}_2\text{O}_3} - \Delta E_{\text{CL}} \quad (4.2)$$

where  $(E_{\text{CL}} - E_{\text{VBM}})_{\text{O-diamond}}$  is the difference in binding energy between the C  $1s$  core level and the valence band maximum (VBM) of the O-diamond.  $(E_{\text{CL}} - E_{\text{VBM}})_{\text{Al}_2\text{O}_3}$  is the difference in binding energy between the Al  $2p_{3/2}$  and VBM of the 20 nm thick  $\text{Al}_2\text{O}_3$  film and  $\Delta E_{\text{CL}}$  is the difference in binding energy between the Al  $2p_{3/2}$  and C  $1s$  core level for the 2 nm thick  $\text{Al}_2\text{O}_3$  film. The calculated value  $\Delta E_V$  is often called the valence band offset. It represents the difference in energy between the top of the O-diamond

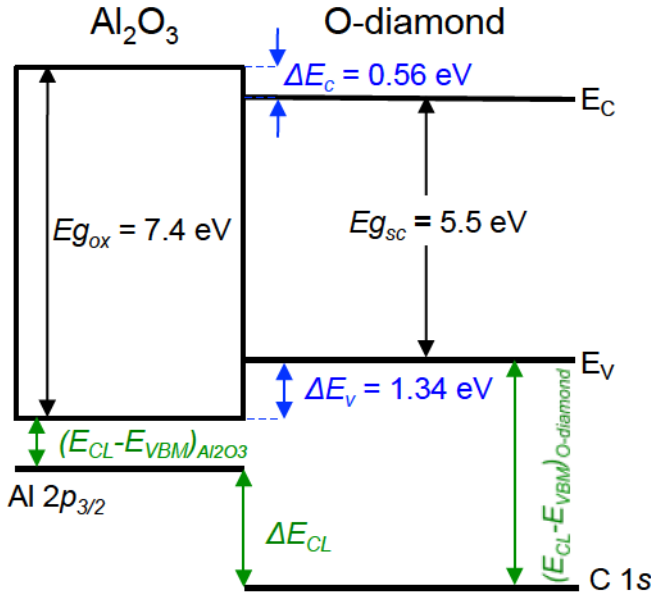


Figure 4.17: Schematic energy band diagram of the Al<sub>2</sub>O<sub>3</sub>/O-diamond with Ti in contact with the oxide layer, deduced from XPS measurement. The valence band offset is  $1.34 \pm 0.2 \text{ eV}$  and the conduction band offset is  $0.56 \pm 0.2 \text{ eV}$ . The oxide band gap value is taken from [Kim 2006].

valence band and the top of the Al<sub>2</sub>O<sub>3</sub> valence band. Using the values of Tab.4.5 and Eq.4.2, the valence band offset between the oxygen-terminated p-type diamond and the Al<sub>2</sub>O<sub>3</sub> layer is calculated as:

$$\Delta E_V = (284.32 - 2.07)_{\text{O-diamond}} - (74.35 - 3.20)_{\text{Al}_2\text{O}_3} - (284.08 - 74.32)\Delta E_{CL} = 1.34 \pm 0.2 \text{ eV} \quad (4.3)$$

Moreover, taking into account an Al<sub>2</sub>O<sub>3</sub> band gap energy of 7.4 eV [Kim 2006], the conduction band offset can be evaluated and finally the energy band diagram of the Al<sub>2</sub>O<sub>3</sub>/O-diamond can be established, as shown in Fig.4.17. Also represented are the energy differences in the core level energy  $E_{CL}$  and valence band energy  $E_{VBM}$  for Al<sub>2</sub>O<sub>3</sub> and O-diamond as well as the core level energy difference  $\Delta E_{CL}$ .

#### 4.4.3 Summary

The interfacial band configuration of the Al<sub>2</sub>O<sub>3</sub>/O-diamond was investigated using X-ray photoelectron spectroscopy (XPS) measurements. In particular, the valence band discontinuity between the Al<sub>2</sub>O<sub>3</sub> valence band and the O-diamond valence band is determined to be  $\Delta E_v = 1.34 \pm 0.2 \text{ eV}$  and the conduction band discontinuity is calculated as  $\Delta E_c = 0.56 \pm 0.2 \text{ eV}$ , taking into account the Al<sub>2</sub>O<sub>3</sub> band gap of 7.4 eV [Kim 2006].

A smaller  $\text{Al}_2\text{O}_3$  band gap would result in a smaller barrier for holes. Thus, the development of high quality  $\text{Al}_2\text{O}_3$  layer is necessary to reach high band gap values, such as 8.8 eV [Robertson 2000]. In conclusion,  $\text{Al}_2\text{O}_3/\text{O-diamond}$  MOS could be suitable for the development of normally-off p-channel MOSFET, since confinement of holes at the interface could be realized thanks to the barrier  $\Delta E_v$ . The lower  $\Delta E_v = 1.34 \pm 0.2$  eV in case of  $\text{Al}_2\text{O}_3/\text{O-diamond}$  than in case of  $\text{Al}_2\text{O}_3/\text{H-diamond}$  interface ( $\Delta E_v = 2.9 \pm 0.2$  eV [Liu 2012]), was expected, even if a rigid application of the electron affinity  $\chi$  difference leads to a value of  $\Delta E_v = 0.8$  eV. At the opposite, n-type channel will result in a too small barrier ( $\Delta E_c = 0.56 \pm 0.2$  eV) between the conduction bands of  $\text{Al}_2\text{O}_3$  and O-diamond, if assuming an energy band gap of  $E_g^{\text{Al}_2\text{O}_3} = 7.4$  eV [Kim 2006]. Thus,  $\text{Al}_2\text{O}_3$  will not be efficient for confining electrons and n-type channel MOSFET will not work using this interface.

## 4.5 Electrical characterization of diamond MOSCAPs

In this section the electrical properties of the  $\text{Al}_2\text{O}_3/\text{O-diamond}$  MOSCAP are investigated. Part of this work was performed in the framework of Chloé Rivière Master 2 internship. Specifically the presence of a high interface states density inducing the Fermi level pinning at the interface  $\text{Al}_2\text{O}_3/\text{O-diamond}$  is evidenced using Terman's method and the conductance method. A tentative to explain the diamond MOSCAP leakage currents is performed using a model of temperature dependent trap assisted tunneling through traps located in the dielectric layer [Svensson 1973].

### 4.5.1 $\text{Al}_2\text{O}_3/\text{O-terminated}$ diamond MOSCAPs electronic properties

#### 4.5.1.1 Experimental setup

The sample electrical characterization was performed in a home-made vacuum probe station with a Keithley electrometer 6517B for the current-voltage  $I(V)$  measurements and an Agilent E4980 A Precision LCR Meter for measuring the capacitance-voltage  $C(V)$  characteristics. The  $I(V)$  measurements were performed under vacuum. Different delays, i.e. duration between two acquisitions, were investigated. No difference was observed between an  $I(V)$  acquired when taking a delay of either 200 ms or 1s. For

better accuracy and to avoid any charge trapping effect a delay of 1 s was used for I(V) measurements. For C(V) measurements, the ac signal amplitude was typically 50 mV and the frequency ranged from 1 kHz to 2 MHz with dc bias ranging from -8 V to 5 V. The measurement time was 110 ms per point at 1 kHz [KeysightTechnologies 2014] (“MED” measurement time setting<sup>4</sup>) and the dc bias sweep rate was set to 100 mV.s<sup>-1</sup>. In the present case, the averaging factor was set to 1. Its influence on the measured data was not studied here. The electrical characterizations were performed using a Linkam cooling system to control the sample temperature (which can be controlled between -196 °C and 600 °C). Fig.4.18 shows a picture of the experimental setup. A binocular microscope allows to accurately locate the probes on the sample (moved either by piezoelectric micro manipulators or manual micro manipulators).



*Figure 4.18:* Picture of the probe station used for I(V) and C(V) characterization of the samples. The sample characterization is made under vacuum ( $<10^{-3}$  Torr) and in the dark to avoid any effects due to optical excitation. The temperature is controlled with a Linkam cooling system from liquid nitrogen temperature to 600 °C.

#### 4.5.1.2 Impedance model

The choice of the impedance model to extract the measured capacitance is strongly affected by the device electrical properties. In particular, the resistivity of diamond for low boron concentration  $\rho \approx 35 \Omega \cdot \text{cm}$  for  $N_A = 2.5 \times 10^{17} \text{ cm}^{-3}$  and a compensation  $N_D = 10^{16} \text{ cm}^{-3}$ , leads to the presence of a significant series resistance  $R_s$  which affects the frequency dependence of the measured C(V) curves. This effect has been reduced by the use of a buried p<sup>+</sup>-type diamond layer as presented in section 4.3. This series resistance will be taken into account in the MOSCAP equivalent circuit through the

<sup>4</sup>This is the time between the trigger and the end of measurement [KeysightTechnologies 2014].

$R_s$  term. Moreover, the non-ideal insulating behavior of the  $\text{Al}_2\text{O}_3$  dielectric layer, i.e. the presence of leakage currents in the gate  $\text{Al}_2\text{O}_3/\text{O-diamond}$  stack, is equivalent to a parallel resistance  $R_p$  (see Fig.4.19) and the parallel capacitance is represented by  $C_p$ . Thus, the complex impedance is accessible through the measurement of the phase difference between an ac current  $I(\omega)$  and an ac voltage  $V(\omega)$  as follows:

$$V(\omega) = Z(\omega) \cdot I(\omega) \quad (4.4)$$

with  $\omega = 2\pi f$  the pulsation of the ac signal proportional to the ac signal frequency  $f$  and  $Z(\omega)$  the complex impedance written as:

$$Z(\omega) = R(\omega) + jX(\omega) \quad (4.5)$$

where  $R(\omega)$  is the frequency dependent impedance real part and  $X(\omega)$  is the frequency dependent impedance imaginary part.

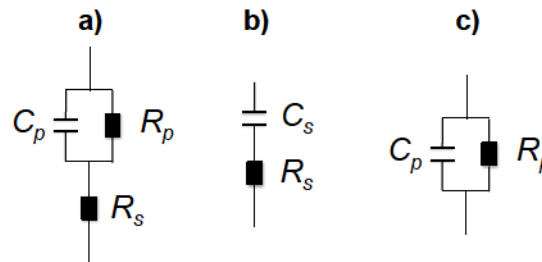


*Figure 4.19:* Equivalent models used to extract the capacitance from the impedance measurement, respectively a) the three elements equivalent circuit, b) the series  $C_s R_s$  equivalent circuit and c) the parallel  $C_p R_p$  equivalent circuit.

In a simple approach, two equivalent circuits are possible depending on which approximations are done [Schroder 2006, Sze 2007]. Firstly, when the oxide leakage currents are small enough such that the parallel resistance  $R_p$  is large as compared to the series resistance, the series equivalent circuit of Fig.4.19.b) is valid. Secondly, if the series resistance is negligible with regard to the parallel resistance, the parallel equivalent circuit of Fig.4.19.c) prevails. As discussed in [Chicot 2013a], the three elements equivalent circuit of Fig.4.19.a) is the most appropriate to extract the capacitance from the measured complex impedance. Thus, the impedance is given by the following expression:

$$Z(\omega) = R_s + \frac{R_p}{1 + (R_p C_p \omega)^2} - j \frac{C_p R_p^2 \omega}{1 + (R_p C_p \omega)^2} \quad (4.6)$$

### Al<sub>2</sub>O<sub>3</sub>/O-diamond metal-insulator-metal capacitors

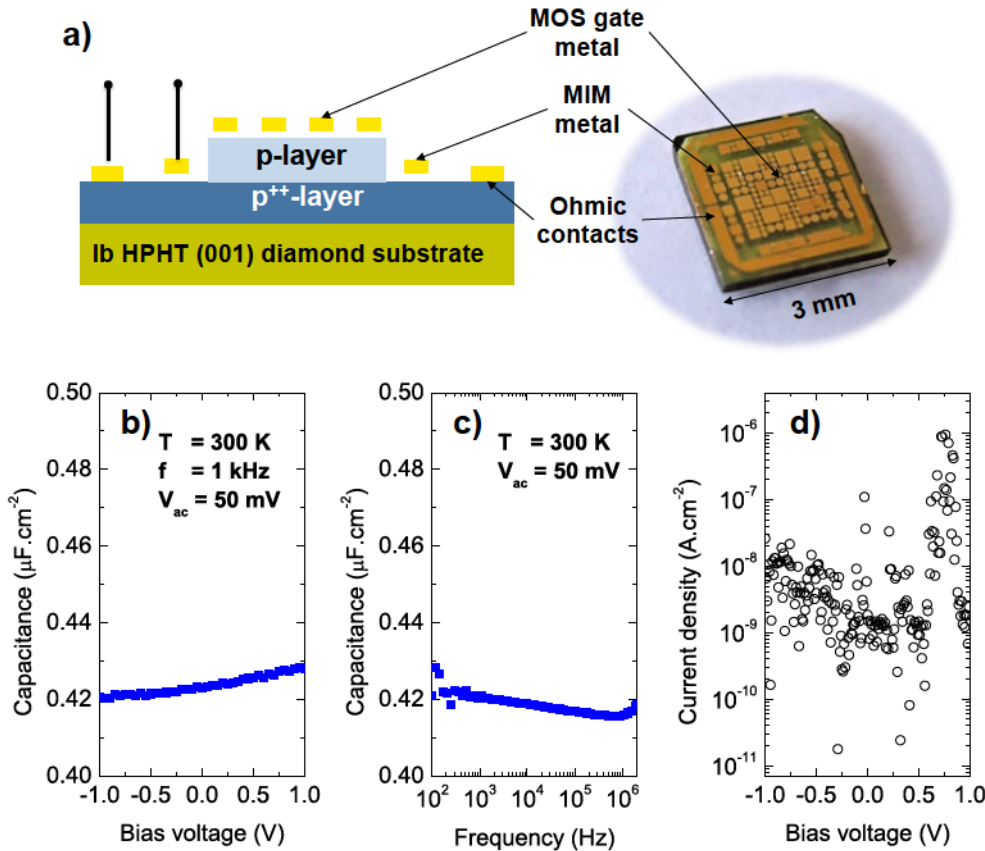


*Figure 4.20:* a) Schematic cross section showing the MIMCAP characterization procedure (left) and picture of the Al<sub>2</sub>O<sub>3</sub>/O-diamond MOSCAP (right) showing the MIM, MOS and ohmic contacts respectively. b) C(V) characteristic of the MIMCAP measured at 300 K with small signal parameters  $f = 1$  kHz and  $V_{ac} = 50$  mV. c) C(f) curve showing no clear frequency dependence of the capacitance over the range 100 Hz to 2 MHz. d) J(V) characteristic of the MIMCAP. These measurements were performed on a circular contact with diameter of 100  $\mu\text{m}$ .

As shown in Fig.4.20.a), the fabricated diamond device includes metal-insulator-metal capacitors (MIMCAPs) where the metal back contact is the metallic p<sup>+</sup>-type diamond layer. Their presence makes possible the electrical characterization of the dielectric layer. Here, the presence of the dielectric on top of the back contact (see Fig.4.20.a), left) is not a problem since it is short circuited as soon as a bias voltage is applied. For measuring the capacitance vs. voltage and vs. frequency, the  $C_p R_p$  equivalent model is used.

Fig.4.20.b) exhibits the  $C(V)$  curve of a MIMCAP with circular contact of  $100 \mu\text{m}$  in diameter. As the bias voltage is changed from  $-1 \text{ V}$  to  $+1 \text{ V}$ , the capacitance remains almost constant, with relative variation of less than 2 %. Moreover, the capacitance does not show clear frequency dependence as exhibited in Fig.4.20.c). This analysis allows to extract the  $\text{Al}_2\text{O}_3$  relative dielectric constant which is calculated to be  $\epsilon_{\text{Al}_2\text{O}_3} \approx 9.5$ . The leakage currents represented in Fig.4.20.d) are lower than  $10^{-6} \text{ A.cm}^{-2}$  at 300 K, which is a reasonable value considered the thickness of the dielectric layer.

### $\text{Al}_2\text{O}_3/\text{O}$ -diamond metal-oxide-semiconductor capacitors

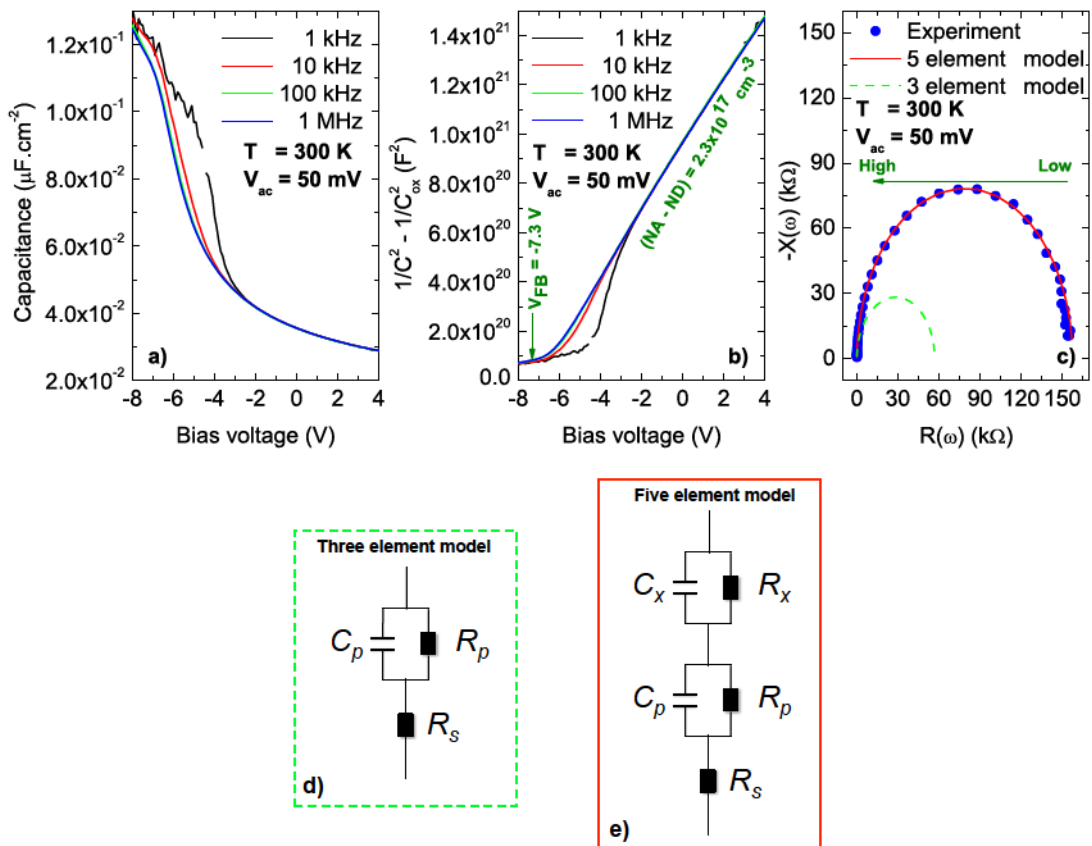


Figure 4.21: a)  $C(V)$  curve measured for frequencies ranging from 1 kHz to 1 MHz at 300 K. b)  $1/C^2$  plot used to extract the flat band voltage and the doping concentration. c) Imaginary part  $-X(\omega)$  as a function of the real part  $R(\omega)$  of the complex impedance, high and low referring to the high and low frequency conditions. The fit corresponds either to the three d) or to the five e) element equivalent circuit.

The independent characterization of the oxide relative dielectric constant allows to estimate the expected accumulation capacitance value for a MOSCAP. As an example, the  $C_{ox} = \epsilon_{ox}\epsilon_0 A/t_{ox}$  for a  $300 \mu\text{m}$  square MOSCAP should be around 360 pF ( $4 \times 10^{-1}$

$\mu\text{F}\cdot\text{cm}^{-2}$ ). As evidenced in Fig.4.21.a) the capacitance value is 70 % lower than the expected one at 300 K. Moreover the capacitance shows frequency dependence in the range -8 V to -4 V. This is related to the presence of interface states, which will be discussed in more details in the next section. The effect of interface states on the measured capacitance is observed for low frequencies, where the traps can follow the ac signal and so contribute to the capacitance signal. Then, increasing the frequency to 100 kHz and 1 MHz, the  $C(V)$  curves show almost no change vs. frequency. The interface traps cannot follow the ac signal anymore and do not contribute to the  $C(V)$  characteristic. Fig.4.21.b) shows the  $1/C^2$  plot, where the oxide capacitance is calculated with  $\epsilon_{ox} = 9.5$ . The flat band voltage is extrapolated and the doping concentration is extracted from fitting the curve with Eq.2.43 [Muret 2014]. From this fit, the flat band voltage is  $V_{FB} = -7.3$  V and the doping concentration  $(N_A - N_D) = 2.3 \times 10^{17} \text{ cm}^{-3}$  are extracted. From the flat band voltage the oxide fixed charge density  $N_f$  can be calculated using the following equation [Schroder 2006]:

$$N_f = \frac{C_{ox} (\phi_{ms} - V_{FB})}{qA} \quad (4.7)$$

where  $C_{ox}$  is the calculated value,  $\phi_{ms} = 2.5$  V is the difference in the metal and semiconductor work functions and  $A$  is the contact area. Then  $N_f$  is found equal to  $1.2 \times 10^{13} \text{ cm}^{-2}$ , i.e.  $6 \times 10^{18} \text{ cm}^{-3}$  for the 20 nm thick  $\text{Al}_2\text{O}_3$  layer. Part of this oxide fixed charge density is at the origin of the trap assisted tunneling current which will be discussed later. Finally, the complex impedance imaginary part  $-X(\omega)$  is plotted as function of the impedance real part  $R(\omega)$  as depicted in Fig.4.21.c). The procedure was to fix the oxide capacitance  $C_{ox} = C_p$  to the expected value and fitting the  $R_p$  and  $R_s$  values. In the case of the aforementioned three elements equivalent model the high frequency part of the  $RX$  plot is not reproduced (left part), only the series resistance can be extracted with value  $R_s = 51 \Omega$ . However, adding a parallel element  $C_x R_x$  to the equivalent circuit (see Fig.4.21.e) five elements model) [Liao 2015], the experimental data are fitted. This means either that the interface states are contributing to the accumulation capacitance and  $C_x = C_{it}$  or that the MOSCAP is still in depletion such that  $C_x = C_{sc} + C_{it}$ . In order to clarify this point, the interface states have been investigated in terms of capacitance and conductance measurements as discussed in the next section.

### 4.5.1.3 Capacitance and conductance analysis of interface states

The presence of interface states at an oxide/semiconductor interface results from the discontinuity in material and lattice at the interface. This discontinuity results in the presence of dangling or unsaturated bonds [Terman 1962]. The unsaturated bonds (lack of oxygen atoms) will impact the energy band diagram in such a way that they allow energy levels within the forbidden band gap at the  $\text{Al}_2\text{O}_3/\text{O}$ -diamond interface. In the presence of interface traps, the ideal  $C(V)$  characteristic presented in section 2.3 will be modified if the traps time constants are in the range of the ac signal frequency. In an ideal MOSCAP, when applying a small bias change, to maintain charge neutrality band bending must change in consequence such that  $\delta Q_G + \delta Q_s = 0$  [Nicollian 1982], with  $\delta Q_G$  the change in gate charge and  $\delta Q_s$  the change in semiconductor surface charge. In the presence of interface traps, the change in gate bias is also accompanied with a change in the interface trap charge density  $\delta Q_{it}$ , such that the charge neutrality is modified as follows:

$$\delta Q_G + \delta Q'_s + \delta Q_{it} = 0 \quad (4.8)$$

Thus, for a given  $\delta Q_G$ ,  $\delta Q'_s < \delta Q_s$  due to the presence of  $\delta Q_{it}$ . The band bending is less for a MOSCAP with interface traps as compared to the one without, making the accumulation to depletion bias window larger. The  $C(V)$  curve is then stretched out along the gate bias axis. The stretch out is predicted from applying Gauss's law to the MOSCAP with interface traps such that the gate charge is given by [Nicollian 1982]:

$$C_{ox}(V_G - \Psi_s) = -Q_{it}(\Psi_s) - Q_s(\Psi_s) \quad (4.9)$$

with  $C_{ox}$  the oxide capacitance,  $V_G$  the gate bias voltage,  $\Psi_s$  the surface potential,  $Q_{it}(\Psi_s)$  the interface charge and  $Q_s(\Psi_s)$  the semiconductor surface charge, both depending on the surface potential. Applying a small gate bias change  $dV_G$  leads to:

$$C_{ox}dV_G = (C_{ox} + C_{it}(\Psi_s) + C_s(\Psi_s))d\Psi_s \quad (4.10)$$

where  $C_{it}(\Psi_s) = -dQ_{it}/d\Psi_s$  and  $C_s(\Psi_s) = -dQ_s(\Psi_s)/d\Psi_s$ . Thus, for a given gate bias voltage variation  $dV_G$ , the surface band bending is smaller inducing the stretch out of the  $C(V)$  curve. In the low frequency regime, such that the majority of interface traps can follow the ac signal, the equivalent circuit of the MOSCAP is shown in Fig.4.22.b). In this case, the interface trap capacitance is frequency dependent, i.e. only the traps able to capture charge carriers within a period of the ac signal will contribute to the  $C(V)$  characteristic. Thus, if the ac signal frequency becomes so high that the traps cannot respond and the interface charge remains constant during the bias voltage sweep, the  $C(V)$  curve will only differ from the ideal one by the stretch out of the capacitance versus bias, and the interface trap density can be investigated. This method is referred as Terman's method and will be discussed in the following.

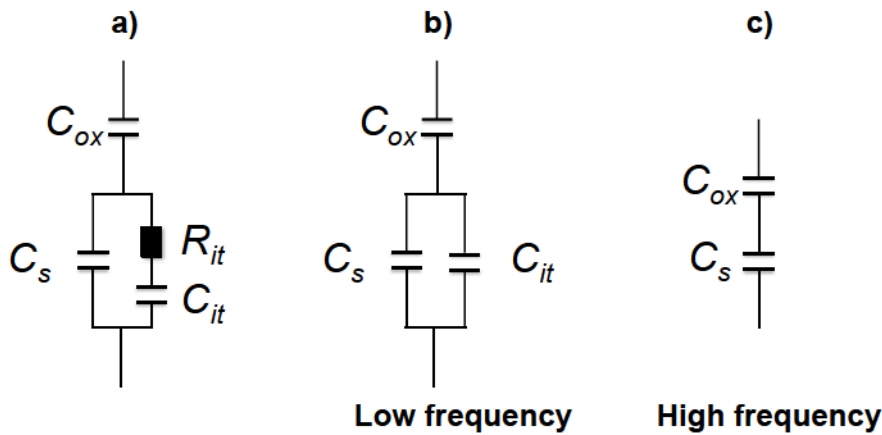


Figure 4.22: a) Equivalent circuit with interface traps. b) At low frequency  $R_{it}$  is set to zero whereas c) at high frequency  $C_{it}$  tends to infinity such that the  $R_{it}C_{it}$  branch of a) is ignored.

### Terman's method

Terman's method is based on the measurement of the high frequency  $C(V)$  characteristic of a MOSCAP which is equivalent to the high frequency circuit of Fig.4.22.c). In this regime, the interface traps cannot respond to the rapidly varying ac signal but can follow the slowly varying dc bias [Schroder 2006]. The interface states will be charged when the Fermi level will sweep the energy level at the interface. In our case, positive charge will appear at the interface, keeping the semiconductor in depletion. This results in the stretch out of the  $C(V)$  curve, a non-parallel shift of the  $C(V)$  characteristic along the gate bias axis. As the only difference between an ideal and an experimental  $C(V)$

curve comes from the presence of interface states, provided that the band bending can be controlled and is the same, a direct comparison allows to extract the interface states density. The procedure is to extract the voltage difference for a constant capacitance (see Fig.4.23) and after differentiation with respect to the band bending  $\Psi_s$  leads to the interface states density  $D_{it}$  as a function of  $\Psi_s$ . The following equation explicits  $D_{it}$  [Schroder 2006]:

$$D_{it} = \frac{C_{ox}}{q^2} \frac{d\Delta V_G}{d\Psi_s} \quad (4.11)$$

Fig.4.23 shows the comparison between the high frequency C(V) with the calculated theoretical one, adjusting the doping concentration from the  $1/C^2$  plot to  $2.3 \times 10^{17} \text{ cm}^{-3}$  and the flat band voltage to -7.1 V such that the deep depletion experimental and theoretical characteristics match. The insert shows a zoom in where the  $\Delta V$  is highlighted. From -8 V to -6 V,  $\Delta V$ , due to the interface states response, is measurable, which is not the case for bias voltages larger than -6 V where  $\Delta V$  is no longer measurable, since traps cannot follow the bias sweep rate, as discussed later.

The interface states distribution in the diamond band gap is then established by calculating the trap energy level  $E_{it}$  as function of the surface potential  $\Psi_s$  as follows:

$$E_{it}(\Psi_s) = q\Psi_s + (E_F - E_v) \quad (4.12)$$

where  $E_F$  is the Fermi level in the bulk semiconductor and  $E_v$  is the valence band energy. This difference is calculated at 300 K for a doping level of  $N_A = 2.3 \times 10^{17} \text{ cm}^{-3}$  with compensation  $N_D = 10^{16} \text{ cm}^{-3}$  and equals to 0.305 eV.

Fig.4.24 exhibits the energy distribution profile of the interface states inside the diamond band gap, where the valence and conduction band edges are depicted. As observed, the interface states density is as high as  $3 \times 10^{13} \text{ cm}^{-2} \cdot \text{eV}^{-1}$  for a trap energy corresponding to 0.6 eV. This trap energy is reached for a bias voltage of -8 V. If one assumes that the density of surface atoms of  $\sim 8 \times 10^{14} \text{ atoms} \cdot \text{cm}^{-2}$  can be uniformly distributed along the diamond bandgap ( $E_g = 5.5 \text{ eV}$ ), the density of  $\sim 1.5 \times 10^{14} \text{ cm}^{-2} \cdot \text{eV}^{-1}$  is calculated. This density of interface states  $D_{it}$  represents 20 % of unsaturated bonds of surface atoms. On the other hand, when increasing the bias voltage, the interface states density

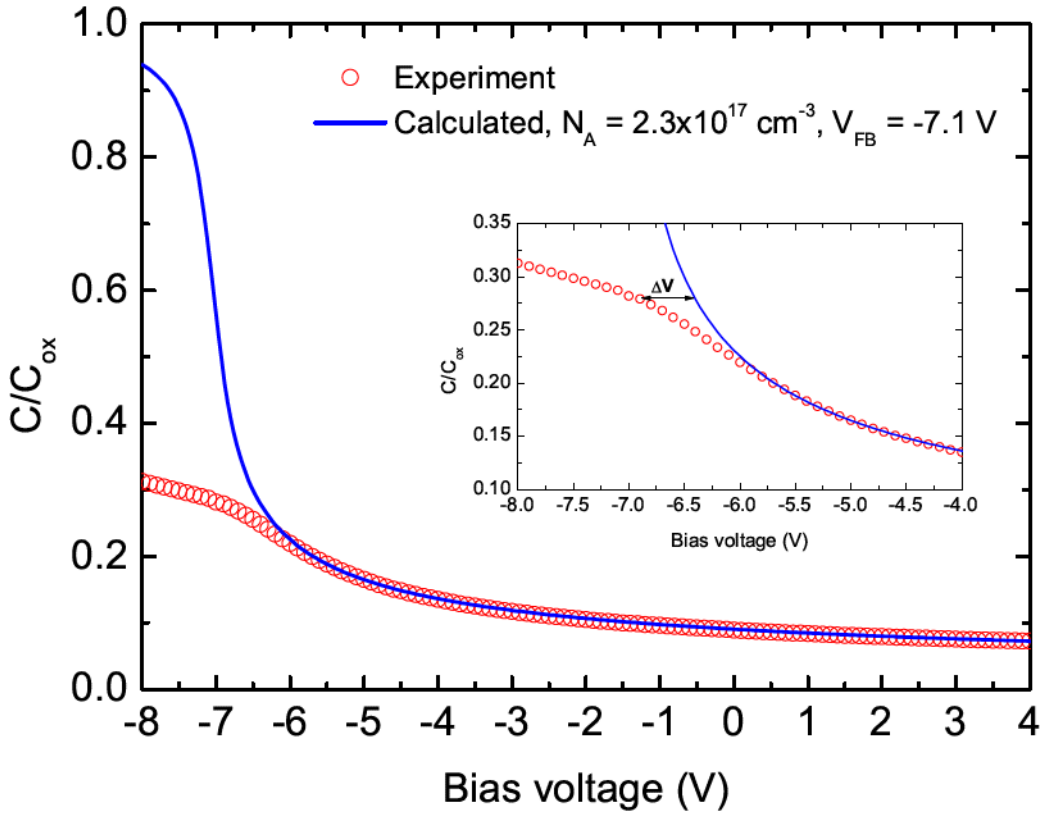


Figure 4.23: Normalized high frequency experimental  $C(V)$  curve (1 MHz) compared to the calculated ideal one with  $N_A = 2.3 \times 10^{17} \text{ cm}^{-3}$ ,  $N_D = 10^{16} \text{ cm}^{-3}$  and  $V_{FB} = -7.1 \text{ V}$ . The insert is a zoom in where  $\Delta V$  is indicated.

decreases and becomes negligible for bias voltages greater than  $-6 \text{ V}$  since the  $\Delta V$  is not anymore measurable.

In this analysis two hypotheses were made, i) the ac signal frequency is high enough so that the interface traps cannot respond to the ac signal and ii) the bias sweep is slow enough so that all the traps can follow. The first assumption is reasonable in this work, as regards to the trapping time constant of holes  $\tau_{it}$  in the diamond band gap, as exhibited in Fig.4.25.b), where the hole generation time is plotted as function of the energy and calculated according to [Engel-Herbert 2010, Muret 2014]:

$$\tau_{it} = \frac{1}{\nu_{th}\sigma_p N_v} \cdot \exp\left(\frac{E_{it} - E_v}{k_B T}\right) \quad (4.13)$$

where  $\nu_{th}$  is the thermal velocity for holes,  $\sigma_p$  is the trap capture cross section for holes,  $N_v$  is the effective density of states in the valence band and  $(E_{it} - E_v)$  is the energy

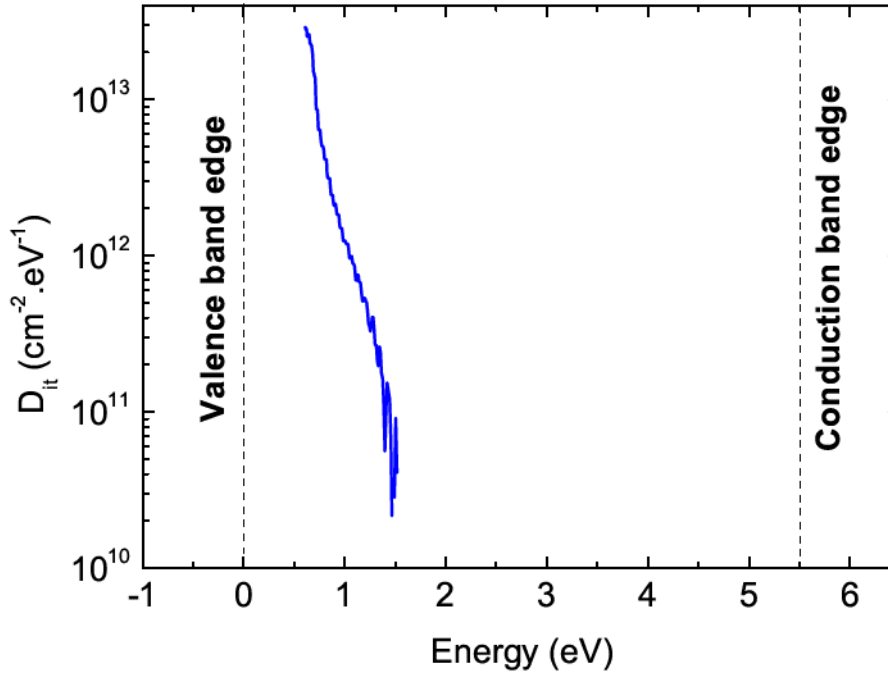
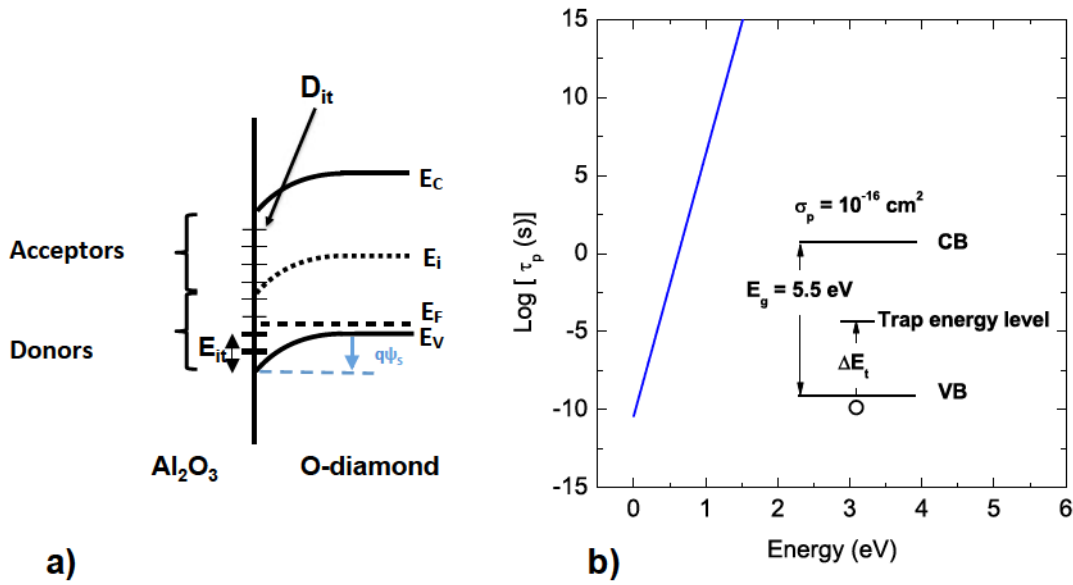


Figure 4.24: Interface states density as function of the energy, distributed inside the diamond band gap, extracted using Terman's method [Schroder 2006].

difference between the trap energy level and the valence band maximum as illustrated in Fig.4.25.a). The donor states below  $E_F$  are occupied by electrons and hence neutral. Those with energies  $E_F < E < E_i$  are unoccupied donors and hence positively charged. Those above  $E_i$  are unoccupied acceptors and hence neutral.

In Fig.4.25.b), it is evidenced that close to the valence band edge the generation time  $\tau_{it}$  is of the order of 8 min for a trap energy of 0.9 eV. As the energy increases the generation time increases exponentially to reach  $10^{80}$  s when the trap is located close to the conduction band edge (5.5 eV). Now the limitation of this method appears. As the second hypothesis implies that the traps can follow the slowly varying bias voltage sweep versus time, the generation time becomes too high as compared to the bias sweep speed. As a consequence, the traps cannot follow the dc bias sweep and the interface states density is underestimated, for trap energies above 0.7 eV. A solution to investigate more accurately the interface traps density would be to modify the dc bias sweep speed as the band are bended towards depletion. However, the interface traps density will not be probed with high accuracy far from the valence band edge due to the high generation time values.



**Figure 4.25:** Energy band diagram of the MOSCAP biased into accumulation in the presence of interface traps density  $D_{it}$ . Electron-occupied interface traps are represented by the small horizontal heavy lines whereas the unoccupied ones are represented by the light lines.

In addition to the interface states density, Terman's method allows to evidence the Fermi level pinning at the Al<sub>2</sub>O<sub>3</sub>/O-diamond interface. As evidenced in Fig.4.23, the experimental  $C(V)$  does not reach the theoretical one in the accumulation regime. The high interface states density prevents the Fermi level to move further with increasing the negative bias voltage, a consequence of the Fermi level pinning. This phenomenon is also evidenced by the conductance method which will be discussed in the following.

### Conductance method

The conductance method is based on measuring the equivalent parallel conductance  $G_p$  as a function of both bias voltage and frequency [Schroder 2006]. It has the advantage of allowing estimation of both the interface traps density  $N_{it}$  and their capture/emission time constant. The equivalent parallel conductance  $G_p$  is related to the measured conductance by the following equation:

$$\frac{G_p}{\omega} = \frac{\omega G_m C_{ox}^2}{G_m^2 + \omega^2 (C_{ox} - C_m)^2} \quad (4.14)$$

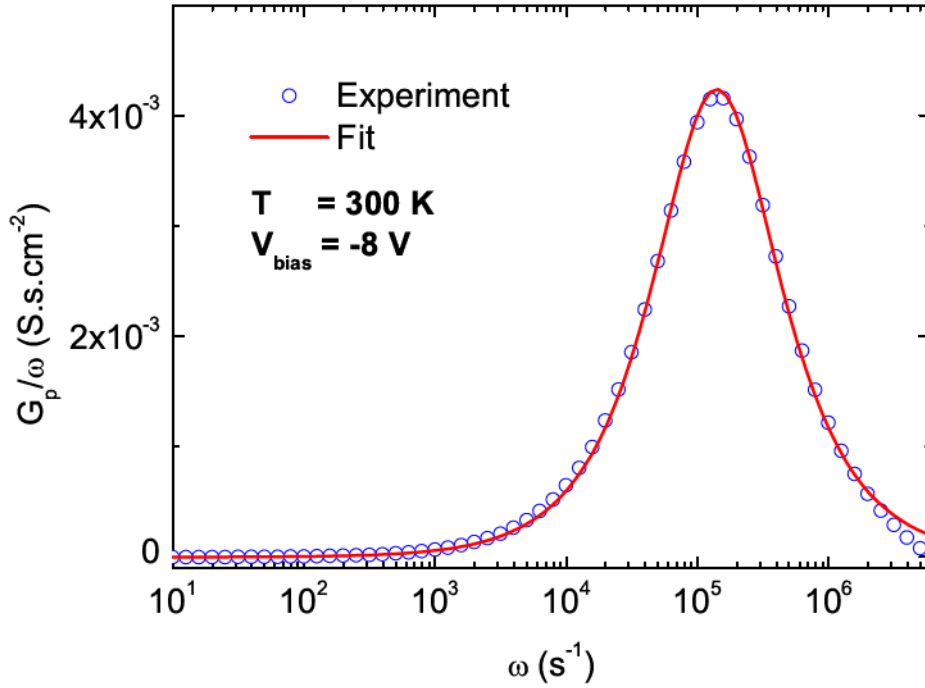


Figure 4.26: Equivalent parallel conductance  $G_p/\omega$  as a function of  $\omega$  measured under bias voltage of -8 V and at a temperature of 300 K.

where  $G_m$  is the measured conductance,  $C_m$  is the measured capacitance and  $\omega = 2\pi f$  is the ac signal pulsation. This method consists in analyzing the loss that is caused by the change in the trap level charge state [Engel-Herbert 2010, Nicollian 1982]. Thus, each time an interface trap is in resonance with the applied ac signal ( $\omega\tau = 1$ ) maximum loss occurs and a peak in the conductance signal is observed as shown in Fig.4.26, which represents the parallel conductance calculated from Eq.4.15 where the leakage currents are taken into account through the  $G_t$  term. The tunnel conductance  $G_t$  was determined as the local slope from the 300 K  $I(V)$  characteristic, such that  $G_t(V) = dI/dV$ .

$$\frac{G_p}{\omega} = \frac{\omega (G_c - G_t) C_{ox}^2}{G_m^2 + \omega^2 (C_{ox} - C_m)^2} \quad (4.15)$$

with  $G_c$  and  $G_m$  given as:

$$G_c = \frac{C_m}{(1 - R_s G_m)^2 + (\omega R_s C_m)^2} \quad (4.16)$$

$$G_m = \frac{\omega^2 R_s C_m C_c - G_m}{R_s G_m - 1} \quad (4.17)$$

with  $R_s$  the series resistance and  $C_c$  as follows:

$$C_c = \frac{C_m}{(1 - R_s G_m)^2 + (\omega R_s C_m)^2} \quad (4.18)$$

Then, comparing equivalent circuit of Fig.4.27.d) with the equivalent circuit of Fig.4.27.b), the following relationship is established [Schroder 2006]:

$$\frac{G_p}{\omega} = \frac{q\omega N_{it}\tau_{it}}{1 + (\omega\tau_{it})^2} \quad (4.19)$$

where  $N_{it}$  is the interface states density and  $\tau_{it}$  the interface states time constant described by Eq.4.13.

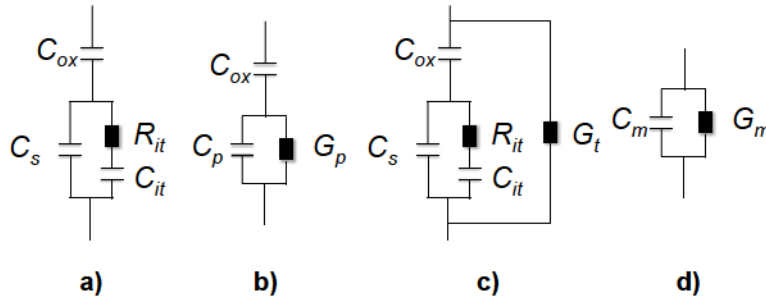


Figure 4.27: Equivalent circuits for conductance measurements.

The experimental procedure consists in measuring the conductance  $G_m$  and capacitance  $C_m$  as a function of bias voltage and frequency and extracting the interface trap density  $N_{it}$ . The trap response is maximum when  $\omega\tau_{it} = 1$ , which results from Eq.4.19 in:

$$N_{it} = \frac{2}{q} \cdot \left( \frac{G_p}{\omega} \right)_{max} \quad (4.20)$$

In this case the interface state density is extracted as  $5 \times 10^{12} \text{ cm}^{-2} \cdot \text{eV}^{-1}$ , which is almost one order of magnitude lower than the value extracted from Terman's method. This is

explained by the fact that the conductance method becomes insensitive to  $N_{it}$  values when  $qN_{it} > C_{ox}$  [Martens 2008]. Here,  $C_{ox}/q = 2.5 \times 10^{12} \text{ cm}^{-2} \cdot \text{eV}^{-1}$ , thus the interface states density is underestimated. However, the map of the parallel conductance as a function of bias voltage and frequency (not shown here) measured at 300 K gives additional information on how much band bending is efficient in response to the applied bias voltage. In particular, if the band bending is efficient  $(G_p/\omega)_{max}$  should move vertically across the map [Engel-Herbert 2010]. The frequency shift was negligible for bias voltage close to -8 V which indicates that the band bending is not efficient, i.e. the Fermi level is pinned at the  $\text{Al}_2\text{O}_3/\text{O-diamond}$  interface. Moreover, the fitting of the experimental  $G_p/\omega$  vs.  $\omega$  with Eq.4.19 leads to an estimation of the trap capture time constant of  $5 \times 10^{-8} \text{ s}$ .

The temperature dependence of the equivalent parallel conductance  $G_p$  was investigated. Fig.4.28 exhibits the dependence of the logarithm of the trap capture cross section as a function of temperature (here in reciprocal axis). The linear behavior indicates the exponential variation of the capture cross section, which is extracted as  $3 \times 10^{-18} \text{ cm}^2$ . The slope gives the trap energy which is  $E_t - E_v = 162 \text{ meV}$  for a bias voltage of -8 V. We can notice that the trap energy level determined from this method is different from the one determined from Terman's method ( $E_t - E_v = 0.6 \text{ eV}$ ) for the same gate bias voltage. More investigations are needed to conclude about the origin of this discrepancy.

#### 4.5.1.4 Summary

Performing interface states characterization on  $\text{Al}_2\text{O}_3/\text{O-diamond}$  MOSCAP allowed to evidence the presence of a high interface states density and more specifically the Fermi level pinning at the  $\text{Al}_2\text{O}_3/\text{O-diamond}$  interface.

- On one hand, Terman's method allowed to establish the interface states energy distribution in the diamond bandgap. Specifically, a  $D_{it} = 3 \times 10^{13} \text{ cm}^{-2} \cdot \text{eV}^{-1}$  at  $\sim 0.6 \text{ eV}$  above the valence band maximum was determined. Moreover, an oxide fixed charge density of  $6 \times 10^{18} \text{ cm}^{-3}$  was determined from the flat band voltage shift. Part of this oxide fixed charge density is at the origin of trap assisted tunneling of holes from the diamond valence band to the top gate electrode and is discussed in the next section.

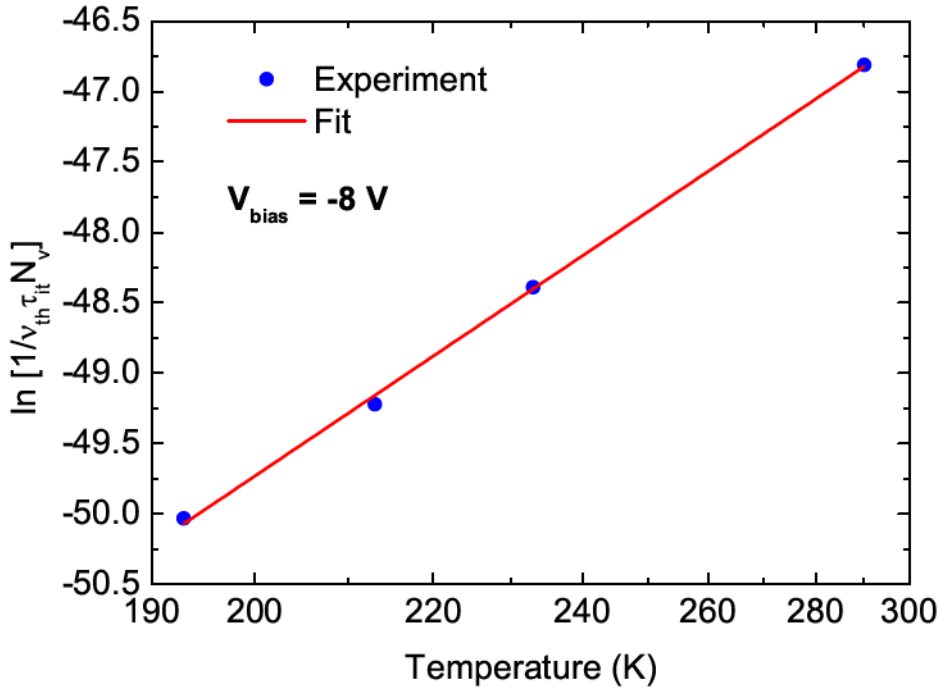


Figure 4.28:  $\ln [1/v_{th}\tau_{it}N_v]$  as a function of temperature (reciprocal axis). The slope of the linear fit is proportional to the trap capture cross section and found to be  $3 \times 10^{-18} \text{ cm}^2$ .

- On the other hand, the conductance method was used to characterize qualitatively the interface state properties. As evidenced, the  $qN_{it} > C_{ox}$  implying that the trap density was under estimated. However, the trap capture cross section was determined by measuring the temperature dependence of the parallel conductance  $G_P$ , which is extracted as  $\sigma_p = 3 \times 10^{-18} \text{ cm}^2$ .

## 4.5.2 Al<sub>2</sub>O<sub>3</sub>/O-terminated diamond MOSCAPs leakage currents analysis

### 4.5.2.1 Temperature dependent trap assisted tunneling

In the previous section the oxide fixed charge density was determined from the flat band voltage shift as  $N_f = 6 \times 10^{18} \text{ cm}^{-3}$ . On the other hand, temperature dependent leakage currents are observed in the Al<sub>2</sub>O<sub>3</sub>/O-diamond MOSCAP as evidenced in Fig.4.29. These measurements were performed under vacuum (typically  $< 10^{-3}$  Torr) and in dark conditions to avoid any optical excitation effects. A Linkam Temperature controller enables to set the sample temperature from -196 °C to 600 °C. However, in order not to

do any thermal treatment to the oxide layer, the temperature was always kept below the deposition temperature of 250 °C. The  $J(V)$  characteristics of a circular MOSCAP with diameter of 150  $\mu\text{m}$  is presented in Fig.4.29 for various temperatures.

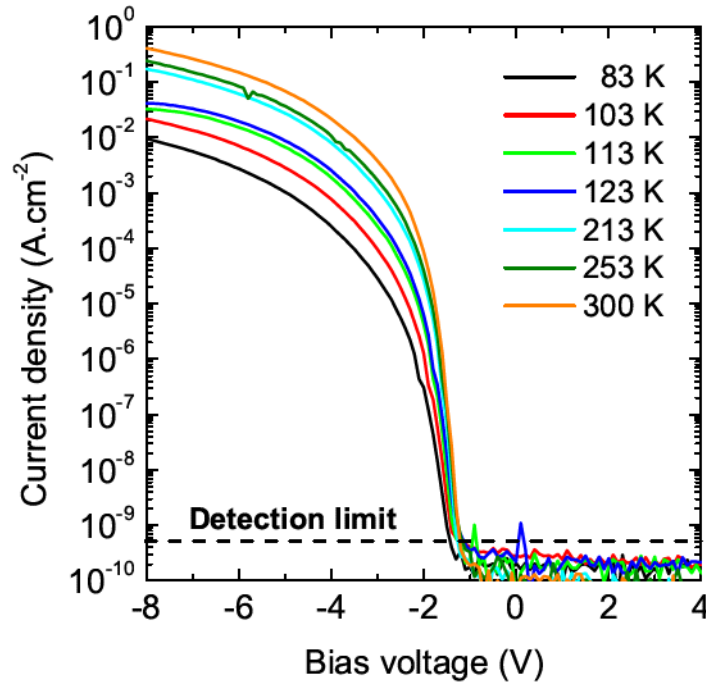


Figure 4.29:  $J(V)$  characteristics of a circular MOSCAP with diameter of 150  $\mu\text{m}$  measured at various temperatures. A specific feature is the absence of leakage currents in the depletion regime.

Several mechanisms have been investigated in order to explain the origin of these leakage currents, such as Fowler-Nordheim (F-N) tunneling [Chiu 2014, Hiraiwa 2013], Pool-Frenkel (P-F) conduction mechanism [Cheong 2007], Schottky emission (S-E) [Sze 2007] and the temperature dependent trap assisted tunneling (TAT) mechanism [Svensson 1973, Houssa 2000].

- F-N tunneling occurs when a thin triangular barrier forms at the oxide/semiconductor interface. It is characterized by a temperature independent tunneling of carrier from the top gate contact to the semiconductor. A plot of  $\ln(J/E^2)$  vs.  $1/E$  where  $E$  is the electric field yields a straight line.
- P-F conduction is dominated by the thermal excitation of carriers under the influence of an external electric field from traps located in the conduction or valence band of the oxide. This mechanism often occurs in amorphous oxides.

- S-E is a conduction mechanism characterized by thermal injection of majority carriers over the barrier formed at the oxide/semiconductor interface. This mechanism is dominant at relatively high temperature.
- Temperature dependent TAT mechanism is a two step process in which a hole from the valence band of the semiconductor is captured by a trap located in the oxide forbidden bandgap and then re-emitted to the top gate electrode. This mechanism is strongly affected by the hole statistics at the oxide/semiconductor interface as well as by the temperature.

However, none of the three first mechanisms were able to take into account the observed temperature dependence nor the fact that the leakage current is due to the tunneling of majority carriers from the diamond layer to the top gate electrode through the oxide. In the case of F-N tunneling, the carriers are injected from the top gate electrode to the semiconductor. For P-F mechanism the transport through the dielectric is the limiting process and for S-E, ideality factor close to 3 were found discarding it for being at the origin of the observed behavior. Thus, the temperature dependent trap assisted tunneling (TAT) model developed by Svensson and Lundström [Svensson 1973] to explain leakage currents in Si/SiO<sub>2</sub>/Si<sub>3</sub>N<sub>4</sub> structures was adjusted to the Al<sub>2</sub>O<sub>3</sub>/O-diamond MOSCAP since this model describes the TAT process of majority carriers from the semiconductor to the top gate electrode through traps located in the dielectric layer.

To illustrate this model the Al<sub>2</sub>O<sub>3</sub>/O-diamond energy band diagram is plotted in Fig.4.30 using nextnano<sup>5</sup>, where the trap energy level of  $\phi_t = 0.7$  eV is indicated as well as the band offsets  $\Delta E_c$  and  $\Delta E_v$  determined from the XPS measurements. In this figure, the MOSCAP is in accumulation regime and the Fermi level is un-pinned at the interface.

The TAT mechanism is a two steps process in which a hole from the valence band of the semiconductor is captured by a trap located in the forbidden band gap of the dielectric layer above the valence band and re-emitted from the trap to the electrode. In the following, the capture time constant  $\tau_{capt}$  of a hole is assumed to be much larger than the emission time constant  $\tau_{emis}$  [Svensson 1973], i.e. the emission is not the limiting process. Thus, within this model, the expression of the gate current is given by the following equation:

---

<sup>5</sup>[www.nextnano.com/nextnano3](http://www.nextnano.com/nextnano3)

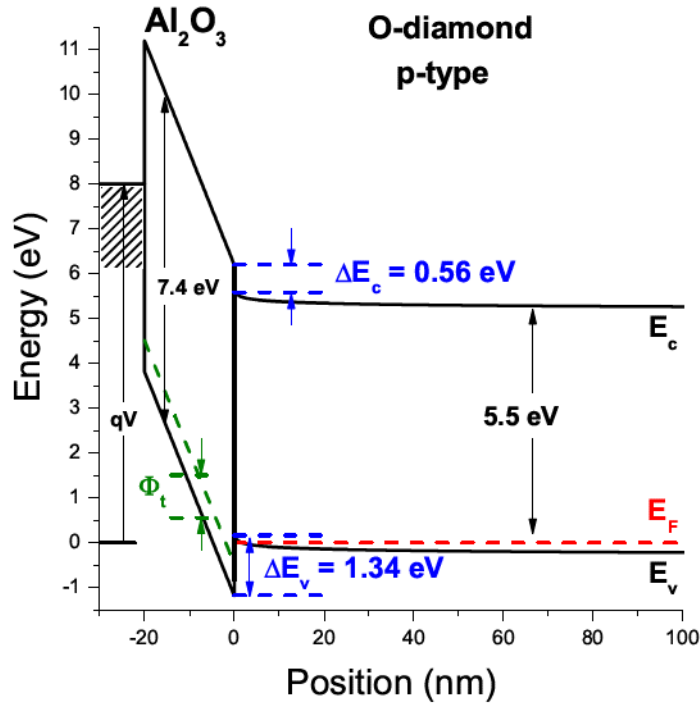


Figure 4.30: Energy band diagram of the  $\text{Al}_2\text{O}_3/\text{O-diamond}$  MOSCAP established using nextnano. The band offsets are adjusted from the XPS measurements [Maréchal 2015]. The trap energy level is depicted and equals 0.7 eV. The top electrode work function is 4.3 eV and corresponds to Ti. A bias voltage of -8 V is applied to the top electrode.

$$J(V, T) = \int_0^{x_m} \frac{qN_t f_s}{\tau_{capt}} dx \quad (4.21)$$

where  $N_t$  is the trap density and the capture time constant is given by:

$$\tau_{capt} = \frac{3m_{ox}^2 H_{ox}}{4\hbar m_{sc} k_0^3 P_{ox}} \quad (4.22)$$

with  $m_{ox} = 2.43m_0$  is the carrier effective mass in the dielectric layer calculated as  $(m_{h\perp}^2 m_{h\parallel})^{1/3}$  [Perevalov 2007],  $m_{sc} = 0.908m_0$  is the hole effective mass in the semiconductor [Pernot 2010],  $H_{ox} = (2qm_{ox}\Delta E_v)/\hbar$  is a constant,  $\hbar$  is the reduced Planck's constant,  $k_0 = (2qm_{sc}V)^2/\hbar$  depends on the oxide electric field as  $V = \Delta E_v - \phi_t - E_{ox} \cdot x$  and  $E_{ox} = V_{ox}/t_{ox}$  with  $V_{ox} = V_{bias} - \Psi_s - V_{FB}$ . The probability of a hole being captured by a trap in the dielectric layer is given by:

$$P_{ox} = \exp \left\{ -\frac{4}{3} \frac{(2qm_{ox})^{1/2}}{\hbar E_{ox}} \left[ (\phi_t + E_{ox}x)^{3/2} - \phi_t^{3/2} \right] \right\} \quad (4.23)$$

Finally, the Fermi factor  $f_s$  is given as follows:

$$f_s = \frac{1}{1 + \exp \left\{ \frac{q(V - V_F)}{k_B T} \right\}} \quad (4.24)$$

where  $V_F$  is the difference between the Fermi level  $E_F$  and the surface potential  $\Psi_s$ . The temperature dependence is carried out by this last term. The integral of Eq.4.21 is performed from the  $\text{Al}_2\text{O}_3/\text{O-diamond}$  interface  $x = 0$  to the position  $x = x_m$ , which corresponds to the  $x$  position where the trap energy is aligned with a hole in the diamond valence band and is explicitly written as  $x_m = (\Delta E_v - \phi_t)/E_{ox}$ . The results are presented and discussed in the following.

#### 4.5.2.2 Results and discussion

Fig.4.31.a) shows the measured current density as a function of the gate bias voltage  $J(V)$  from 83 K to 353 K for a circular gate contact of 150  $\mu\text{m}$  in diameter. For positive bias voltage applied to the gate electrode, the MOSCAP is in depletion and the current density is lower than the detection limit (not depicted here). As the gate bias is decreased towards more negative values, the room temperature current density increases to reach  $4 \times 10^{-1} \text{ A.cm}^{-2}$  at -8 V.

Fig.4.31.b) represents the fit of the experimental and theoretical  $J(V)$  characteristics at 300 K. In this case both the trap density and the trap energy level were adjusted to  $6 \times 10^{14} \text{ cm}^{-3}$  and 0.7 eV respectively. As evidenced, a good agreement with the theory is found for low bias voltages, i.e. below  $\sim -2$  V. As the bias voltage is decreased towards the negative values, discrepancy appears. For bias voltages lower than -2 V, the theoretical current density is lower than the measured one. This could be explained by the fact that the theoretical model did not take into account the Fermi level pinning at the  $\text{Al}_2\text{O}_3/\text{O-diamond}$  interface. In fact, the results were inconsistent when considering the resulting surface potential values. Fermi level pinning would induce an opposite band bending of the diamond bands at the interface, a much stronger electric field in the dielectric layer and a smaller hole concentration at the  $\text{Al}_2\text{O}_3/\text{O-diamond}$  interface. However,

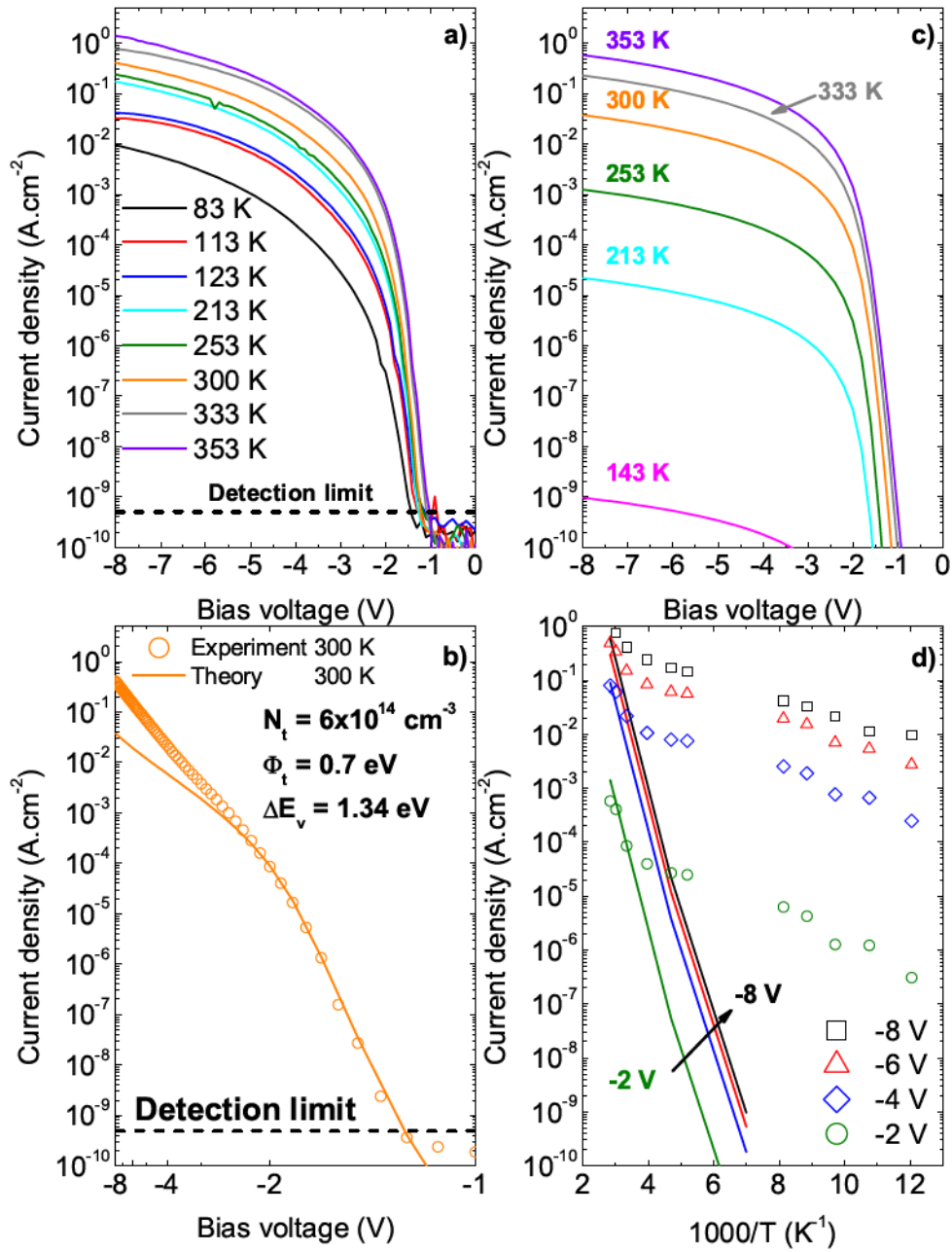


Figure 4.31: a) Experimental  $J(V)$  characteristics measured at various temperatures for a circular contact with diameter of  $150 \mu m$ . b) Calculated  $J(V)$  characteristics at various temperatures using the TAT model described by Eq.4.21. As evidenced the temperature dependence is stronger for the theoretical  $J(V)$  than for the experimental one.

the temperature dependence of the current densities is expected to be stronger, since the ionization rate of boron strongly decreases with decreasing temperature. Thus, it indicates another important phenomenon: hole injection from the buried  $p^+$ -type diamond layer. Specifically, the presence of the  $p^+$ -type diamond layer results in the injection of holes into the p-type layer, increasing the hole concentration far above the equilibrium

concentration at the  $\text{Al}_2\text{O}_3/\text{O}$ -diamond interface strongly influencing the transport properties in the device [Muret 2015]. Fig.4.31.c) exhibits the  $J(V)$  characteristics calculated at various temperatures using Eq.4.21. Comparing the experimental and theoretical  $J(V)$  characteristics, it appears that the temperature dependence is expected to be stronger as regards to the model. Again, effect of the Fermi level pinning as well as hole injection and the presence of oxide charges cannot be discarded.

In Fig.4.31.d), the current density is plotted as function of  $1000/T$  in order to evidence the temperature dependence for different applied bias conditions. In the high temperature range the current density approximately follows a straight line which, indicates that  $J$  varies exponentially with  $1/T$  (represented by the solid line) [Houssa 2000]. This seems to be valid for low bias voltage (-2 V) and is not the case for more negative bias voltage as evidenced by Fig.4.31. This effect could be linked to the Fermi level pinning which would strongly increase the oxide band bending and results from the deviation of the experimental data to the model. Also, effect of hole injection from the  $\text{p}^+$ -type diamond layer must be considered.

### 4.5.3 Summary

In this section the electrical properties of the  $\text{Al}_2\text{O}_3/\text{O}$ -diamond MOSCAP were investigated. Specifically, the interface states characterization using both Terman's method and the conduction method revealed the presence of a high density of interface traps which prevents the MOSCAP to reach the accumulation regime, i.e. the high interface traps density induces the pinning of the Fermi level at the  $\text{Al}_2\text{O}_3/\text{O}$ -diamond interface. Nevertheless, it is shown that the device can be operated in the depletion and deep depletion regimes. On the other hand, the leakage currents observed when negative bias is applied to the gate electrode is explained by the presence of oxide fixed charges which participates to the hole tunneling from the diamond layer to the top electrode through these traps located in the forbidden band of the dielectric layer. However, discrepancy between the predicted current density and the measured data was observed. Hole injection from the  $\text{p}^+$ -type layer could explain this phenomenon since the hole concentration in the p-type layer is brought far above the equilibrium concentration and can strongly influence the hole concentration present at the interface [Muret 2015]. In order to improve the diamond MOSCAP, effect of thermal annealing of the dielectric layer using forming

gas (mixture of H<sub>2</sub> and N<sub>2</sub>) and different surface treatment including Fluor termination of the diamond surface could be envisioned. The control of the dielectric/O-diamond interface is of great importance in order to develop the next generation inversion MOSFET. A first attempt in fabricating diamond inversion MOSFET has been performed very recently in Japan and the electrical characterization will be discussed in the next section.

## 4.6 Experimental realization of a n-type channel MOSFET

This section describes the work performed at the National Institute for Advanced Industrial Science and Technology (AIST) in Tsukuba, during a four months stay, under the supervision of Satoshi Yamasaki<sup>6</sup>. During this stay, the main focus was to characterize an n-type channel MOSFET fabricated in AIST clean rooms. In a first part, the sample structure will be described. Then, the experimental setup and the electrical characterization results will be exposed and discussed.

### 4.6.1 Sample structure

The sample was fabricated in AIST (Tsukuba) under the supervision of H. Kato<sup>7</sup> and T. Makino<sup>8</sup>, a step in which I was not personally involved.

As shown in Fig.4.32.e), the sample is composed of a heavily boron-doped IIb (100) HPHT diamond substrate with typical boron concentration of about 10<sup>20</sup> cm<sup>-3</sup>. A first step consisted in the growth of a 4 μm thick non-intentionally boron-doped diamond layer (p<sup>-</sup>-type layer), with boron content of  $(N_A - N_D) = 2.5 \times 10^{13}$  cm<sup>-3</sup>, as measured by characterizing Schottky diodes on the same structure (not shown here). The fabrication of the n<sup>+</sup>-type reservoirs was performed by using a selective growth process [Kato 2009]. The main point of this technique is to take advantage of the good phosphorous incorporation in the (111) orientation achieved by patterning the sample surface

---

<sup>6</sup>Principal Research Manager, Energy Enabling Technology Group, Energy Technology Research Institute, s-yamasaki@aist.go.jp

<sup>7</sup>Senior Research Scientist, Energy Enabling Technology Group, Energy Technology Research Institute, hiromitsu.kato@aist.go.jp

<sup>8</sup>Chief Senior Researcher, Energy Enabling Technology Group, Energy Technology Research Institute, toshiharu-makino@aist.go.jp

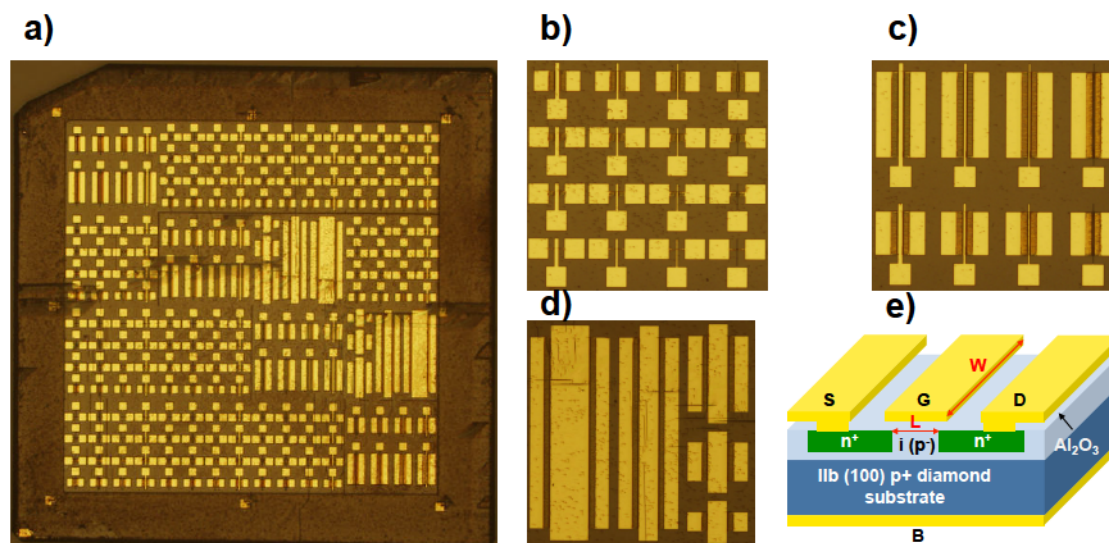


Figure 4.32: a) Optical microscope view of the MOSFET sample and b), c) and d) shows a close up on the three different geometries referred to as A, B and C respectively. e) Schematic 3D view. The MOSFET is composed of 4 terminals, the Source  $S$ , the Drain  $D$ , the Gate  $G$  and the Back gate  $B$ . The channel length  $L$  and width  $W$  are also indicated.

with trenches. This process has proven to be of great efficiency in the fabrication of diamond lateral p-n junctions [Hoshino 2012] and JFETs [Iwasaki 2012, Iwasaki 2013]. The doping concentration of the  $n^+$ -type diamond is expected to be in the range of  $1\text{-}2 \times 10^{20} \text{ cm}^{-3}$ . Oxygen termination of the diamond surface was performed by a standard hot acid treatment which consists of a mixture of  $\text{HNO}_3$  and  $\text{H}_2\text{SO}_4$  (1:3). Then, a 24 nm thin  $\text{Al}_2\text{O}_3$  layer was deposited by ALD at 573 K. The electrical contacts were deposited by electron beam evaporation of Ti/Pt/Au with typical thickness of 30/30/100 nm respectively. Fig.4.32.a) shows an optical microscope view of the final sample. As can be seen in Fig.4.32.b).c).d), three different geometries were defined (referred to as A, B and C respectively), with different gate length  $L$  and gate width  $W$  ranging from 1  $\mu\text{m}$  to 100  $\mu\text{m}$  and from 2  $\mu\text{m}$  to 200  $\mu\text{m}$  respectively. Fig.4.32.e) represents a schematic 3D view of the sample with emphasis on the gate length  $L$  and gate width  $W$ . A single MOSFET device is composed of 4 terminals, the source and drain contacts, the gate contact and the back gate contact to control the substrate bias, namely  $S$ ,  $D$ ,  $G$  and  $B$  in Fig.4.32.e).

## 4.6.2 Experimental setup and electrical characterizations

### 4.6.2.1 Experimental setup

The electrical properties of the MOSFET were investigated with an Agilent Technologies B1500A Semiconductor Device Analyzer. The  $I(V)$  properties were recorded using a Keithley 2636 Dual-channel System SourceMeter instrument and the  $C(V)$  characteristics of the gate were investigated using an Agilent E4980 A Precision LCR Meter with dc bias voltage sweep rate of  $250 \text{ mV}\cdot\text{s}^{-1}$  and "MED" measurement time settings [KeysightTechnologies 2014] as mentioned in section 4.5. All measurements were performed under vacuum ( $< 10^{-7}$  Torr) and in dark conditions. A picture of the probe station is shown in Fig.4.33.

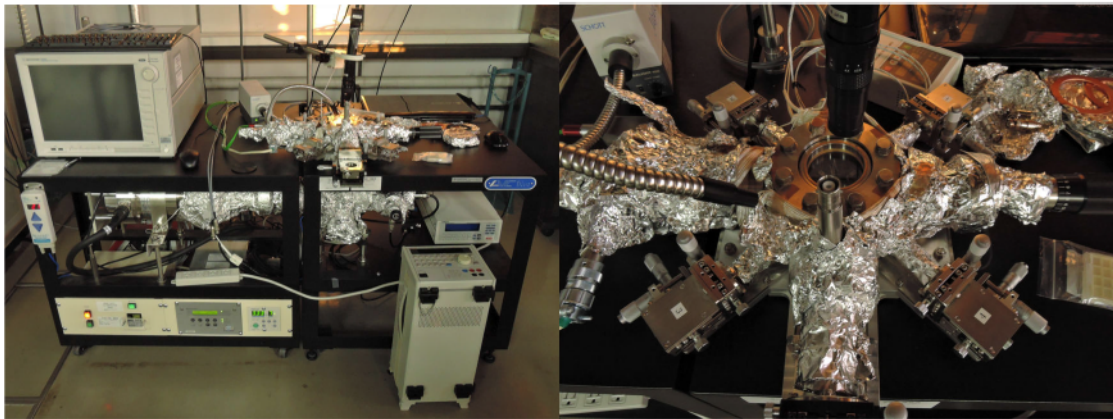


*Figure 4.33:* Experimental setup for the MOSFET characterization. 4 independent probes allow to control the bias voltage of the 4 contacts.

### 4.6.2.2 Electrical characterizations

#### Capacitance-voltage properties

In order to obtain the  $C(V)$  characteristics of the gate contact, the bias voltage was applied between the top gate and the back gate electrodes, while the source and drain contacts were kept as floating, i.e. not connected. The measurements were averaged on a 1 s duration to reduce the signal/noise ratio. Typical ac voltage amplitude of 50 mV has been set. It was noticed that this amplitude did not influence the measured capacitance.

Fig.4.34 presents the  $C(V)$  characteristics of sample BI1\_3\_101 ( $L = 3 \mu\text{m}$ ,  $W = 101 \mu\text{m}$ ) measured at room temperature (about 300 K). In Fig.4.34.a), the frequency was varied from 50 Hz to 1 MHz. In this frequency range, the accumulation capacitance measured at -10 V did not show any pronounced frequency dependence. This is typically the case for a high quality oxide/semiconductor interface, where the interface states density is low enough, so that the surface potential  $\Psi_s$  is not influenced by the presence of defects at the interface. On the other hand, Fig.4.34.b) shows an hysteresis behavior when biasing the MOSCAP from accumulation to deep depletion and coming back to accumulation. The voltage shift  $\Delta V$  between the forward and the backward curve is measured as 1.3 V, for a capacitance value of 3 pF. This hysteresis results from the presence of mobile charges in the dielectric layer or from interface states contribution which can follow the ac signal frequency [Sze 2007] and was observed for the entire frequency range.

The doping level of the  $p^-$ -type layer was investigated by plotting the  $1/C^2$  graph as shown in Fig.4.35.a) for an ac signal frequency of 1 MHz. In principle, a constant doping level would result in a straight line when plotting  $(1/C^2 - 1/C_{ox}^2)$  as a function of the bias voltage in the depletion regime, i.e. for  $V > V_{FB}$  and  $V > 0$ , as obtained by Eq.4.25

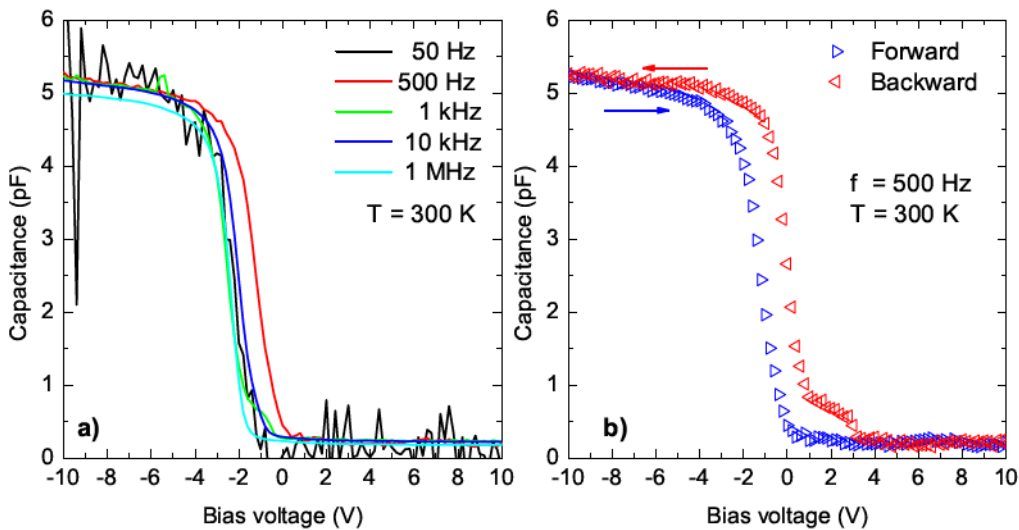


Figure 4.34: a)  $C(V)$  properties of device BI1\_3\_101 measured as a function of the frequency at a temperature of 300 K. In this frequency range, the  $C(V)$  did not show frequency dependence. b) Hysteresis measured on device BI1\_3\_101. The dc bias sweep rate was set to  $250 \text{ mV}\cdot\text{s}^{-1}$  and the ac signal amplitude was 50 mV.

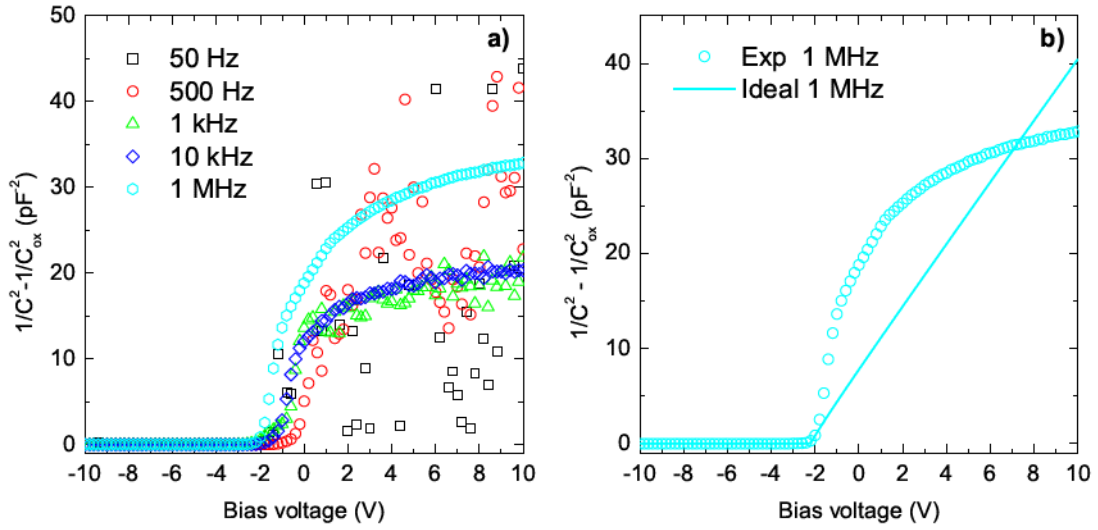


Figure 4.35: a)  $1/C^2$  plot of device BI1\_3\_101 for frequencies ranging from 50 Hz to 1 MHz. b) Comparison between the experimental and ideal  $1/C^2$  plot at 1 MHz with doping concentration of  $8 \times 10^{13} \text{ cm}^{-3}$  and flat band voltage of -2.2 V.

[Schroder 2006]:

$$(N_A - N_D) = \frac{2}{q\epsilon_{sc}\epsilon_0 A^2 d(1/C^2)/dV} \quad (4.25)$$

with  $(N_A - N_D)$  the total impurity concentration,  $\epsilon_{sc}$  the semiconductor relative dielectric constant,  $\epsilon_0$  the permittivity of free space,  $A$  the gate contact area and  $d(1/C^2)/dV$  the derivative of the inverse square capacitance with respect to the bias voltage. The resulting doping concentration as a function of the depletion layer extension (space charge width  $w$ ) is shown in Fig.4.36, where the space charge width was calculated from [Schroder 2006]:

$$W = \epsilon_{sc}\epsilon_0 A \left( \frac{1}{C} - \frac{1}{C_{ox}} \right) \quad (4.26)$$

Moreover, the flat band voltage is determined by the intersection of the linear fit of the depletion region  $1/C^2$  with the  $x$ -axis. However, due to the non-linear behavior of the experimental data, the flat band voltage value is not measurable. It is clear from this graph that the doping concentration of the  $p^-$ -type layer is over-estimated as compared to the expected doping concentration of  $2 \times 10^{13} \text{ cm}^{-3}$ .

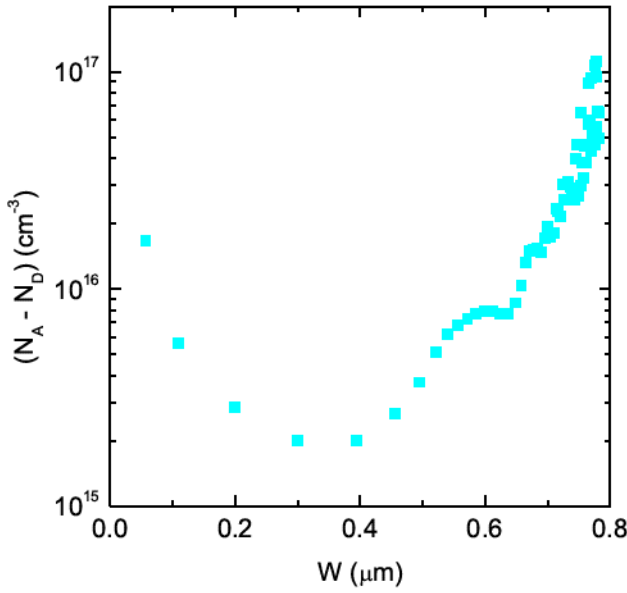


Figure 4.36: Doping profile  $(N_A - N_D)$  as a function of depletion layer width  $W$  extracted from the measured  $C(V)$  at 1 MHz and 300 K.

The  $\text{Al}_2\text{O}_3$  relative dielectric constant was extracted by measuring the accumulation capacitance for a bias voltage of  $-8$  V and found of the order of 4–4.8. This value is much smaller than the one determined from  $C(V)$  measurements on MIMCAP where the  $\text{Al}_2\text{O}_3$  dielectric layer was deposited at  $250^\circ\text{C}$  and  $\epsilon_{ox} = 9$  in agreement with [Kim 2006]. Despite the fact that the experimental data did not allow the determination of the doping level nor the flat band voltage, the comparison between the experimental and the ideal  $C(V)$  curves for device BI1\_3\_101 was made by differentiating Eq.2.36 with respect to  $\Psi_s$  as represented in Fig.4.37. The accumulation capacitance is reached for an  $\text{Al}_2\text{O}_3$  relative dielectric constant of 4 and a contact area of  $2.803 \times 10^{-5}$   $\text{cm}^2$ . Also, the flat band voltage was adjusted to fit the data and found to be  $V_{FB} = -2.2$  V, which is close to the ideal  $V_{FB}$  value of  $-2.5$  V calculated as follows [Sze 2007]:

$$V_{FB} = \phi_m - (\chi + E_g - E_F) \quad (4.27)$$

where  $\phi_m = 4.33$  eV is the metal work function,  $\chi = 1.7$  eV is the electron affinity of the oxygen-terminated diamond,  $E_g = 5.5$  eV is the diamond band gap, and  $E_F = 0.37$  eV is the Fermi level calculated at 300 K and with  $N_A = 8 \times 10^{13}$   $\text{cm}^{-3}$  and  $N_D = 1 \times 10^{12}$   $\text{cm}^{-3}$  in the framework of Boltzmann approximation. On the other hand, the capacitance minimum is fitted with a doping level of  $8 \times 10^{13}$   $\text{cm}^{-3}$ , which is of the order of magnitude of the targeted doping level. The discrepancy between the experimental

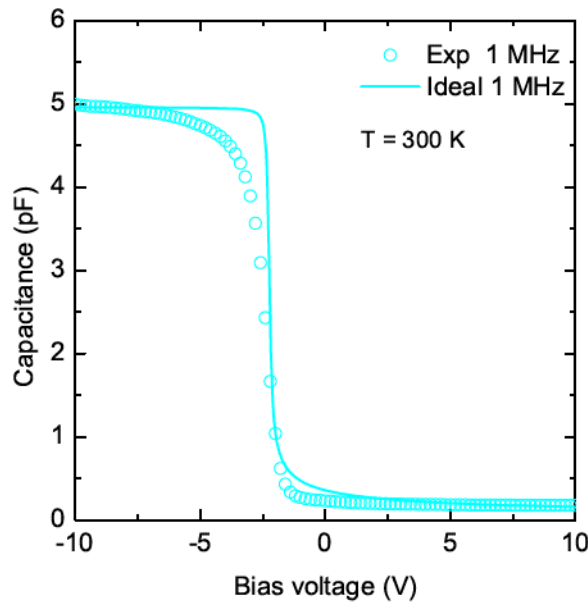


Figure 4.37: Comparison between the experimental 1 MHz  $C(V)$  curve (empty dots) and the corresponding ideal characteristic (solid line) for  $T = 300$  K. The corresponding oxide relative dielectric constant of 4 was set as well as a doping level of  $8 \times 10^{13} \text{ cm}^{-3}$  to fit the accumulation capacitance and the deep depletion capacitance respectively. The flat band voltage was adjusted to  $-2.2$  V.

and ideal  $1/C^2$  plot is emphasized in Fig.4.35.b). As the ideal characteristic leads to a straight line, the experimental one shows a non-constant doping profile, evidenced by the non-linearity of the curve. Nonetheless, the ideal characteristic shows good agreement with the experimental data as shown in Fig.4.37.

### Current-voltage characteristics

The current-voltage characteristics of the MOSFET were recorded with an Agilent Technologies B1500A Semiconductor Device Analyzer at 573 K. As illustrated in Fig.4.38, the measurements consist in applying a constant gate bias  $V_{GS}$  when biasing the Drain-Source contacts ( $V_{DS}$ ) from 0 V to 16 V. The substrate bias was controlled by short circuiting the source and back gate contacts to the ground.

To ensure the proper electrical properties of the gate contact, the leakage current was measured when applying a constant gate voltage  $V_{GS}$  and changing  $V_{DS}$ . The results are presented in Fig.4.39, where the gate current  $I_{GS}$  is represented as a function of the drain voltage  $V_{DS}$  under different gate bias conditions, respectively from 0 V to 10 V. As evidenced, the leakage currents are under the detection limit ( $5 \times 10^{-13}$  A).

The drain characteristics ( $I_{DS}$  vs.  $V_{DS}$ ) are shown in Fig.4.40.a). When  $V_{GS} = 0$  V, the channel is closed and the drain current is always below  $2 \times 10^{-8} \text{ mA.mm}^{-1}$ . Then, increasing the gate bias voltage  $V_{GS}$  up to 10 V, the drain current reaches a value of

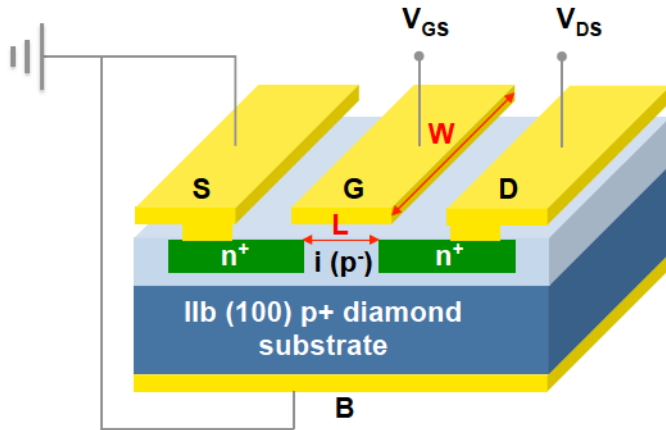


Figure 4.38: Principle of the MOSFET characterization. A bias voltage is applied between the source and drain contacts  $V_{DS}$ , while the source and back gate contacts are short-circuited. The gate bias  $V_{GS}$  is controlled independently.

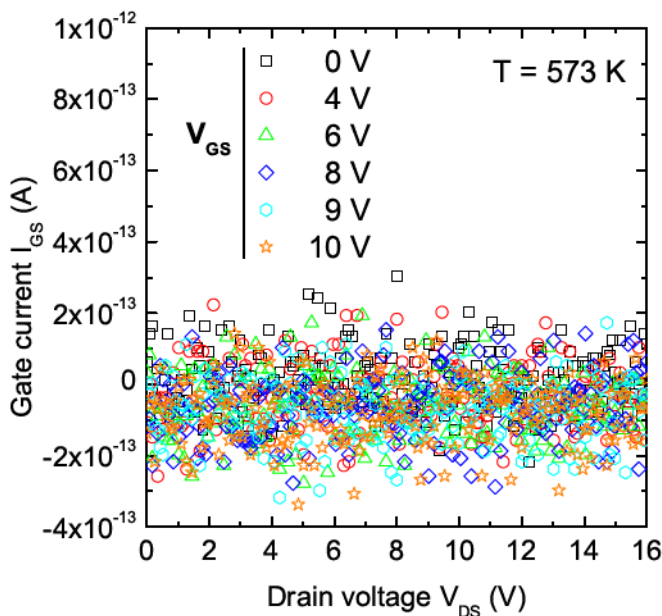


Figure 4.39: Gate leakage currents characteristics of the top gate contact of MOSFET BI1\_3\_101 measured when biasing the gate from 0 V to 10 V during a drain voltage bias from 0 V to 16 V.

$1.77 \times 10^{-7} \text{ mA} \cdot \text{mm}^{-1}$  for  $V_{DS} = 16 \text{ V}$ . In order to keep the electric field in the structure low enough to avoid any breakdown,  $V_{DS}$  and  $V_{GS}$  were always kept below 16 V and 10 V respectively. In fact, a gate voltage of 10 V already induces an electric field of  $4.1\text{-}5 \text{ MV} \cdot \text{cm}^{-1}$ , if one considers that all the potential drop occurs in the dielectric layer. As shown in Fig.4.40.a), a kink in the drain current is observed between 2 V and 4 V, which might be originating from trapped charges either in the dielectric layer or at the  $\text{Al}_2\text{O}_3/\text{O-diamond}$  layer. Also, when plotting the transfer characteristic ( $I_{DS}$  vs.  $V_{GS}$ ), it is obvious that the device operation is not ideal.

The same measurements were performed on device AI3\_1\_50 ( $L = 1 \mu\text{m}$ ,  $W = 50 \mu\text{m}$ ). As shown in Fig.4.41, the gate electrode shows good electrical properties since the leakage current level is of the order of 1 pA.

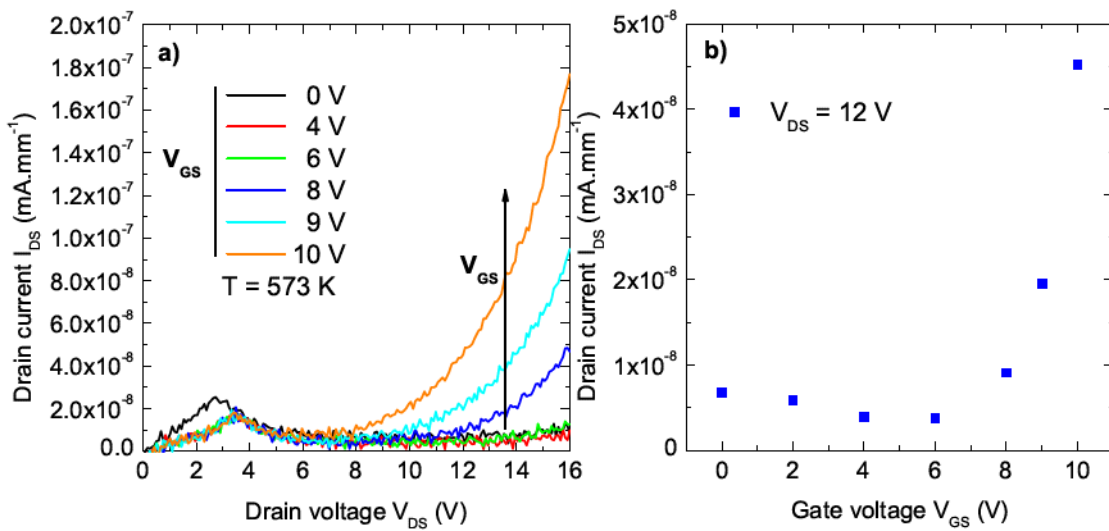


Figure 4.40: a) Drain current as a function of the drain bias for device B11\_3\_101 measured at 573 K. b) Drain current as a function of the gate voltage measured at 573 K and at constant drain bias of 12 V.

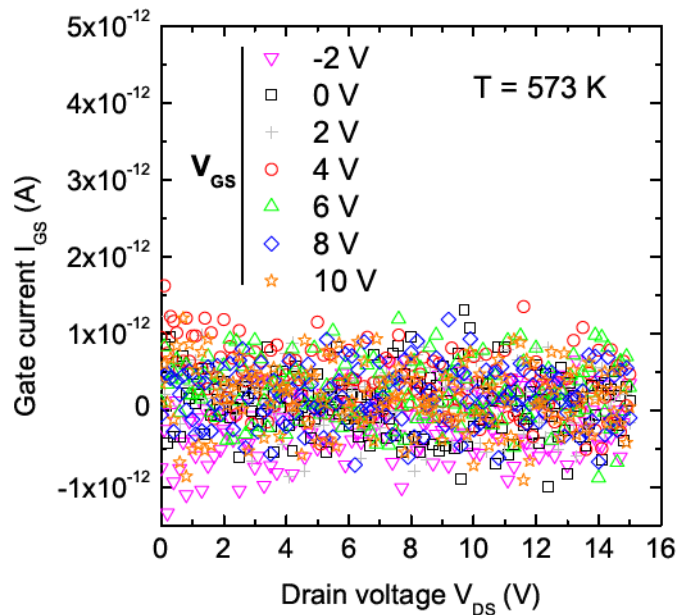


Figure 4.41: Gate leakage currents characteristics of the top gate contact measured when biasing the gate from 0 V to 10 V during a drain voltage bias from 0 V to 15 V for sample A13\_1\_50.

The  $C(V)$  characteristic of this device are shown in Fig.4.42 measured at 500 Hz and 1 kHz and 573 K. Fig.4.42.a) exhibits a positive shift which might be due to fixed negative charges at the  $\text{Al}_2\text{O}_3/\text{O}$ -diamond interface. Hysteresis is also seen and reflects the presence of mobile oxide charges in the  $\text{Al}_2\text{O}_3$  layer as discussed above. On the other hand, the same characteristic measured at 1 kHz (see Fig.4.42.b)) and frequency above, showed extremely noisy behavior. Thus, the high frequency (1 MHz) data could not

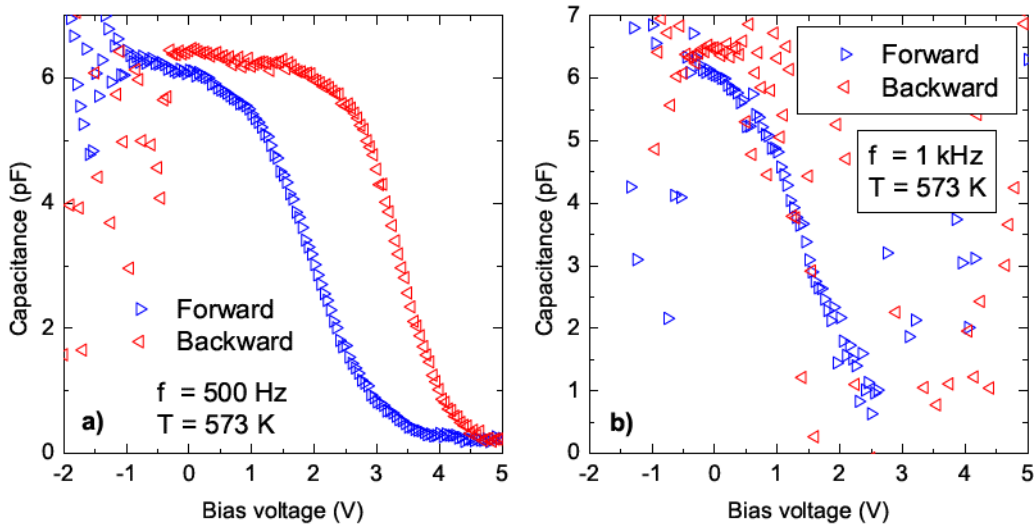


Figure 4.42:  $C(V)$  characteristic of device AI3\_1\_50 measured at a) 500 Hz and b) 1 kHz. Both measurements were performed at 573 K.

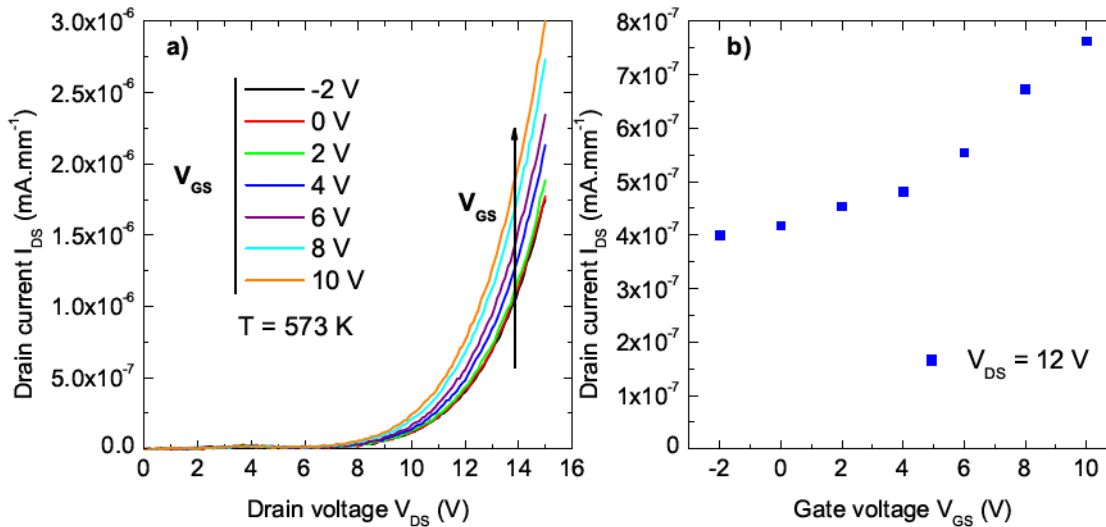


Figure 4.43: a) Drain current as a function of the drain bias for device AI3\_1\_50 measured at 573 K. b) Drain current as a function of the gate voltage measured at 573 K and at constant drain bias of 12 V.

be used to extract the physical parameters of this device. The  $\text{Al}_2\text{O}_3$  relative dielectric constant was extracted from the 500 Hz  $C(V)$  property and found to be in the range 5.7–6.8.

The  $I_{DS}$  vs.  $V_{DS}$  characteristics of device AI3\_1\_50 are shown in Fig.4.43.a). In opposition with device BI1\_3\_101, for  $V_{DS} = 0$  V, current is observed. Even when

biasing the gate contact with negative voltage, the current is still observed. When increasing the gate bias voltage towards positive values, the current is increased and reached  $3 \times 10^{-6} \text{ mA} \cdot \text{mm}^{-1}$  for  $V_{DS} = 15 \text{ V}$  and  $V_{GS} = 10 \text{ V}$ . The transfer characteristic is plotted in Fig.4.43.b) and does not show the expected behavior, as for device BI1\_3\_101.

### Summary on the electrical characterization of diamond MOSFET

Several devices were characterized but none of them presented the desired properties. As evidenced in Fig.4.44, the  $C(V)$  characteristics were very dependent from one device to another. As observed, the  $C(V)$  property shows a non-reproducible shift, different for three different gate contacts. This is probably due to the presence of inhomogeneities of the  $\text{Al}_2\text{O}_3/\text{O}$ -diamond interface quality and/or in the  $\text{Al}_2\text{O}_3$  layer quality deposited by ALD at 573 K. Hysteresis is observed for all tested devices indicating the presence of mobile charges in the dielectric layer. These charges might deteriorate the electrical properties of the MOSFET.

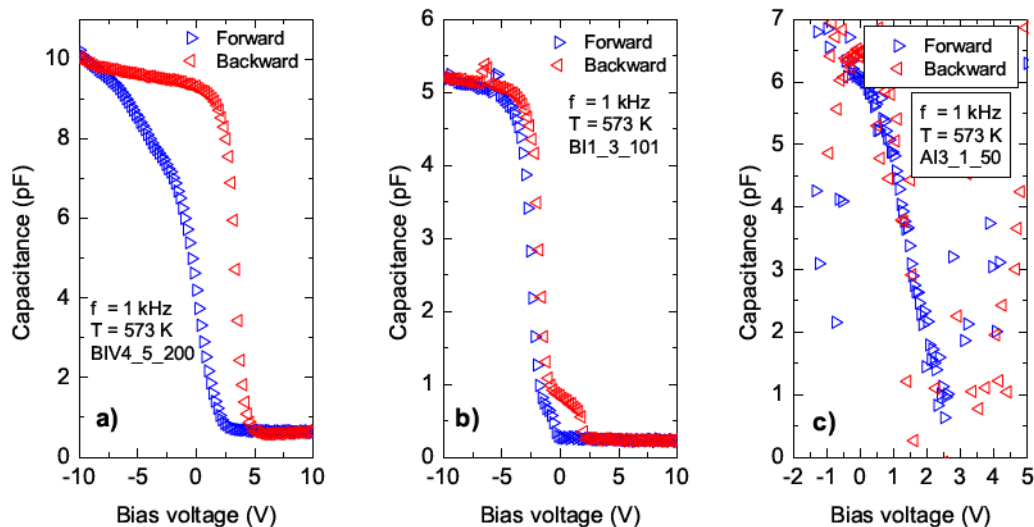


Figure 4.44:  $C(V)$  properties measured at 573 K and 1 kHz ( $V_{ac} = 50 \text{ mV}$ ) for device a) BIV4\_5\_200 ( $L = 5 \mu\text{m}$   $W = 200 \mu\text{m}$ ), b) BI1\_3\_101 ( $L = 3 \mu\text{m}$   $W = 101 \mu\text{m}$ ) and c) AI3\_1\_50 ( $L = 1 \mu\text{m}$   $W = 50 \mu\text{m}$ ).

As evidenced by the simulation results of chapter 3, this structure is not yet optimized. However, improving the geometry, the doping level of the drift layer together with the oxide thickness would pave the way toward a reliable inversion MOSFET. Specifically, several studies for future development could be conducted, such as:

- The study of the amount of overlap of the gate contact over the  $n^+$ -type diamond influence on the electrical properties of the device
- The optimization of the length  $L$  of the gate contact
- The optimization of the ohmic contact on  $n^+$ -type diamond, already under investigation in Japan, as reported in [Matsumoto 2014]
- The optimization of the  $p-n^+$  interface to attain ideal p-n junction properties

As regards to all the above mentioned items, there are still many possible ways for improving the future diamond MOSFET properties.

### 4.6.3 Summary

A n-type channel MOSFET was fabricated for the first time and its electrical properties investigated in terms of capacitance vs. voltage and current vs. voltage measurements. The  $C(V)$  properties of the gate contact revealed that the accumulation and depletion regimes were attained. A discrepancy in the deep depletion regime between the ideal and experimental characteristics was observed with origin not yet understood. Several gate contacts were investigated and large inhomogeneities were observed, possibly coming from inhomogeneities in the O-termination of the diamond surface. The  $I(V)$  characterization of the MOSFET operation did not lead to the expected behavior. Even when measuring the MOSFET properties at high temperature (573 K) only a very weak resistivity modulation of the source-drain channel was observable.

Nevertheless, this first attempt is very promising for the development of the next generation diamond power devices.

## 4.7 Conclusions

In this chapter, the fabrication steps of the pseudo-vertical diamond MOSCAPs was presented. The growths consisted in a p-type layer deposited on a  $p^+$ -type diamond layer itself deposited on a Ib HPHT (001) diamond substrate. The mesa structure was defined by ICP etching using an oxygen plasma. Then, the ohmic contacts were directly

deposited on the  $p^+$ -type diamond layer. The oxygen termination of the diamond surface was realized using a VUV light/ozone treatment and the  $Al_2O_3$  layer was deposited by ALD at a temperature of 250 °C. The device structure allowed to determine the relative dielectric constant of the  $Al_2O_3$  as 9.5. Thus, the expected capacitance of the MOSCAP can be estimated, evidencing a discrepancy which was investigated in terms of capacitance and conductance measurements. Specifically, using Terman's method, a high density of interface states was determined, resulting in the Fermi level pinning at the interface preventing to reach accumulation regime. The Fermi level pinning was further evidenced by the conductance method. Further investigation of the MOSCAP behavior using thermal annealing and/or different surface termination would help in determining the best device processing in order to fabricate a reliable MOS gate contact for the next generation diamond MOSFET.

Moreover, trap assisted tunneling of holes from the diamond layer to the gate contact was evidenced using current vs. voltage measurements at different temperature. Discrepancies between the expected behavior and the experimental characteristics is attributed to the presence of hole injection from the  $p^+$ -type layer to the p-type layer. Further investigations using thicker p-type diamond layer could clarify this point.

On the other hand, the measurement of X-ray photoelectron spectroscopy spectra allowed to establish the interfacial energy band configuration of the  $Al_2O_3$ /O-diamond heterojunction. This analysis revealed a type II band configuration in opposition to the type I band configuration determined for the  $Al_2O_3$ /H-diamond heterojunction. In particular, a valence band offset of 1.34 eV was determined. This value could be suitable for inversion p-type channel diamond MOSFET since the hole barrier is sufficient to prevent injection into the gate contact.

Finally, the experimental realization of a n-type channel MOSFET was performed for the first time and its electrical characterization was performed during a four months stay in AIST (Tsukuba, Japan). Unfortunately this first tentative was unsuccessful since MOSFET operation could not be reached. Nevertheless, the gate contacts showed good electrical properties, i.e. accumulation to depletion regimes were reached within a few volt bias window. This pioneering work is very promising and paves the way toward the realization of next generation diamond MOSFET for power electronic applications.



# General conclusion and outlook

This thesis was driven by two main objectives. One is the development of simulation tools taking into account the specific diamond physical properties, aiming to anticipate the architecture and design of next generation diamond power devices. Specifically, the physical properties of diamond have been implemented into a finite element based software (TCAD Silvaco), in order to reproduce the electrical characteristics of a diamond p-n junction. Here, up to date mobility models, impact ionization coefficients and hopping mobility were implemented. Also, an important point was to consider the effect of generation-recombination (G-R) models on the electrical properties of diamond devices. As the G-R parameters and models are neither well known nor understood in diamond, the influence of Auger and Shockley-Read-Hall G-R models was studied. A first set of parameters has been proposed but effort must be continued on this topic. Concerning the current-voltage characteristics, discrepancies were observed between the experimental and the simulated results. This means that unconsidered factors such as contact resistivity, carrier tunneling and crystalline defects contribute to the  $I(V)$  characteristics of diamond p-n junctions. However, according to the implemented impact ionization coefficient, the breakdown voltage of 225 V, corresponding to a breakdown field of  $7.7 \text{ MV}\cdot\text{cm}^{-1}$  was predicted. Furthermore, the implemented parameters were used to study the design of a diamond MOSFET. Specifically, the effect of channel doping concentration, temperature and oxide thickness on the simulated electrical properties were investigated. It is shown that for this particular design the specific on-resistance is not optimized as compared to the silicon limit. It is concluded that specific architectures must be developed to fully take advantage of the strong potentiality of diamond for power device applications.

Further efforts are needed both on the experimental and on the numerical aspects to develop robust simulation tools which taking into account the specificities of diamond

for the design of future diamond power devices.

On the other hand, the study of diamond metal-oxide-semiconductor capacitors (MOSCAP) using oxygen-terminated surface paves the way towards the fabrication of a MOS field effect transistor (MOSFET). In particular, the interfacial band configuration of the  $\text{Al}_2\text{O}_3/\text{O}$ -diamond was deduced from X-ray Photoelectron Spectroscopy (XPS). Thus, a valence band offset of  $1.34 \pm 0.2$  eV was determined. Assuming an  $\text{Al}_2\text{O}_3$  bandgap of 7.4 eV, the conduction band offset was calculated to be  $0.56 \pm 0.2$  eV. The conclusion of this study is that the  $\text{Al}_2\text{O}_3/\text{O}$ -diamond might be suitable for developing an inversion mode MOSFET using a p-type channel.

Since 2011, Néel Institute is involved in the development of MOSCAP using  $\text{Al}_2\text{O}_3$  as a gate dielectric. In this work, a new design was developed. A pseudo-vertical MOSCAP was thus fabricated, which is composed of a p-type diamond layer grown on top of a  $\text{p}^+$ -type diamond layer. The role of the later is to reduce the series resistance together with the contact resistance. In fact, by using Inductively Coupled Plasma (ICP) etching to define a mesa structure, the ohmic contacts are directly deposited on the  $\text{p}^+$ -type diamond layer. The final device is obtained by several lithography and metal deposition steps. The device electrical properties were studied in terms of capacitance-voltage and current-voltage measurements. As the device includes MOSCAP and metal-insulator-metal capacitor (MIMCAP), the oxide relative dielectric constant was extracted. Then, the expected accumulation capacitance of the MOSCAP were calculated. However, we observed discrepancy between the measured and the expected values. Thus, the interface quality was investigated using capacitance and conductance analysis of the interface states. The conclusion is that Fermi level pinning is responsible for the observed behavior, preventing the device to operate in accumulation regime. Also, high interface states density is observed near the valence band edge. This interface states might originate from the presence of unsaturated carbon bonds at the  $\text{Al}_2\text{O}_3/\text{O}$ -diamond interface. However, no Fermi level pinning was observed in depletion or deep depletion mode, allowing the inversion mode operation.

$\text{Al}_2\text{O}_3/\text{O}$ -diamond MOSCAP  $I(V)$  analysis was performed at various temperatures. The origin of the leakage currents in negative bias voltage conditions were investigated in terms of temperature dependent trap assisted tunneling. This two step process, originating from the presence of traps in the dielectric layer, could be at the origin of the

leakage currents. However, the effect of the Fermi level pinning was not taken into account in the model. This could be a hint to explain the quantitative discrepancy between the experimental and the theoretical  $I(V)$  in the high negative bias regime. Also, the presence of the buried  $p^+$ -type layer might play a role in the amount of hole available at the  $\text{Al}_2\text{O}_3/\text{O-diamond}$  interface since hole injection occurs.

Specific surface treatments (comparison between VUV light/ozone treatment and hot acid treatment for instance) and dielectric annealing under various atmospheres could help to improve both the interface quality and the dielectric layer quality.

Finally, a n-type inversion channel MOSFET was fabricated and characterized for the first time. Despite the fact that the MOSFET did not show ideal characteristics, the MOS gate contact showed reasonably good properties. This first attempt demonstrate that the fabrication of a diamond MOSFET is not a technological issue and is very promising for the development of a diamond power MOSFET. Also, the next step could be to develop a p-type channel MOSFET, since we demonstrated that the interfacial band configuration is favorable for the confinement of holes in the diamond at the  $\text{Al}_2\text{O}_3/\text{O-diamond}$  interface without Fermi level pinning.



# Résumé de thèse en français

Le présent manuscrit résume la sélection de travaux réalisés pendant mes trois années de thèse, passées au sein de l'Institut Néel et du Laboratoire de Génie Electrique de Grenoble (G2Elab), sous la direction d'Etienne Gheeraert (Directeur de Thèse), Nicolas Rouger (co-directeur de thèse) et Julien Pernot (co-encadrant de thèse).

Ce travail s'inscrit dans le cadre de l'électronique de puissance en diamant. Plus précisément, mon travail a consisté à développer une plateforme de simulation par la méthode des éléments finis robuste dans le but de modéliser des composants électronique en diamant. D'autre part, la réalisation expérimentale de capacité métal-oxyde-semiconducteur (MOSCAP) a permis l'étude de la faisabilité de la réalisation d'un transistor MOS en diamant.

## Introduction

La consommation d'énergie électrique et la demande n'ont cessé d'augmenter dans les pays avancés ainsi que dans les pays en développement. Les combustibles fossiles ont récemment vu leurs prix considérablement diminué, passant de près de 100 \$ le baril à la mi-2014 au-dessous de 50 \$ le baril au début de l'année 2015 [IEA 2015]. À l'échelle mondiale cette diminution agit comme un stimulus économique. Toutefois, la combustion d'énergies fossiles à des fins énergétiques représente une grande quantité d'émissions de gaz à effet de serre (environ les deux tiers de toutes les émissions anthropiques de gaz à effet de maison), qui, en raison de leur longue durée de vie résultant de leur accumulation dans l'atmosphère est responsable du réchauffement climatique observé et leur rôle dans le changement climatique est désormais bien établie. Comme la population mondiale ne cesse d'augmenter (par exemple, la population mondiale augmente

de 1,18% par an, soit 83 millions de personnes par an [Eeckhout 2015]) est donc la demande d'électricité. Ainsi, dans le but de limiter les émissions de gaz à effet de serre et plus particulièrement à maintenir le réchauffement climatique en dessous du seuil critique de 2 °C, les gouvernements ont signé un traité international de l'environnement (la Convention-cadre des Nations Unies sur les changements climatiques) sur les objectifs à long terme envers profonde la réduction des émissions mondiales de gaz effet de serre [IEA 2015]. Afin de remplir sa promesse, l'UE doit réduire ses émissions de gaz à effet de serre d'au moins 40% en dessous des niveaux de 1990 d'ici à 2030. La progression vers cet objectif sont évaluées à la conférence annuelle des Nations Unies sur les changements climatiques, tenue cette année à Paris<sup>9</sup>.

Ainsi, la croissance durable dans les deux pays avancés et en développement repose sur la réduction des émissions de gaz à effet de serre. Cette réduction est possible en développant le domaine de l'électronique verte [Ohashi 2012], à savoir des technologies plus propres et plus efficaces sont obligatoires pour obtenir une réduction des émissions de carbone. De cette manière, deux approches peuvent être envisagées [Baliga 2012]. D'une part, la production d'électricité devrait compter sur de plus en plus de sources d'énergie renouvelables, comme l'énergie solaire, l'énergie éolienne, l'énergie marémotrice ou l'énergie hydroélectrique qui utilise l'électronique de puissance pour convertir le courant alternatif généré au pouvoir bien adapté qui pourrait être utilisé par les consommateurs. Les dispositifs à base de semiconducteurs de puissance sont des éléments clés permettant de soutenir une forte tension, une forte densité de courant, une haute température et une haute puissance pendant une telle conversion. La seconde approche consiste à réaliser de faibles pertes et systèmes à haute efficacité pour la gestion et le transfert du pouvoir du point de la production au point de consommation.

Au coeur du système est le semi-conducteur de puissance, ce qui est actuellement principalement à base de silicium. En fait, par rapport à d'autres matériaux, il a un rapport performances / coût qui conduit à une figure de mérite commerciale imbattable à l'heure actuelle [Udrea 2015]. Cependant, même si des architectures spécifiques, tels que les transistors super jonction [Antoniu 2010] sont développés, les dispositifs de puissance à base Si atteignent les limites matérielles. Ainsi, les dispositifs de puissance à base de semiconducteurs à grand gap (WBGSc) tels que SiC, GaN et de diamants émergent. Les propriétés physiques supérieures des WBGSc les rend appropriés pour des applications

---

<sup>9</sup><http://www.cop21.gouv.fr>

de commutation de puissance élevée. Les dispositifs SiC ainsi que des dispositifs à base de GaN sont déjà en commercialisation. Le diamant, quand à lui, est au stade de la recherche et développement et est intensivement étudiée par plusieurs groupes à travers le monde (France, Japon, Etats-Unis, Russie, Espagne, Royaume-Uni ...). Plus de deux décennies de progrès technologiques concernant la qualité de la croissance, le contrôle du dopage et le processing ont conduit à l'émergence de nouvelles potentialités en termes d'applications électroniques. Comme le diamant semiconducteur représente le matériau ultime en raison de ses propriétés physiques supérieures, des efforts ont été réalisés pour développer divers dispositifs électroniques, tels que des diodes Schottky, des transistors à effet de champ, transistor bipolaire, jonctions pin ...

Comme condition préalable à la mise au point de nouveaux dispositifs de puissance en diamant de future génération, d'une part, il est nécessaire de développer des outils capables d'anticiper les propriétés électriques du composant ainsi que son architecture afin de profiter pleinement des propriétés physiques. D'autre part, l'étude expérimentale du contact de grille, la deuxième brique élémentaire du transistor, est fondamentale afin de développer des dispositifs de haute performance. À cet égard, on peut considérer plusieurs questions ouvertes: (i) les outils de simulation sont-ils capables de prendre en compte les spécificités du diamant pour modéliser les appareils électriques? (ii) l'oxyde d'aluminium est-il approprié pour développer un contact de grille de transistor MOSFET? (iii) Si oui, l'interface oxyde/diamant est-elle d'assez bonne qualité? (iv) la fabrication d'un MOSFET en diamant est-elle une question technologique? Afin de répondre à ces questions, ce manuscrit est organisé comme suit:

Chapitre 1: Dans ce premier chapitre, les principaux enjeux pour l'électronique de puissance seront présentés. Pour les technologies à faibles émissions de carbone, les semiconducteurs à bande interdite large (WBGSc) tels que SiC, GaN et le diamant joueront un rôle fondamental dans les applications futures. Insister sur les propriétés physiques du diamant aideront à comprendre pourquoi ce matériau est le semiconducteur ultime. L'état de l'art des dispositifs à base de diamant sera présentée en se concentrant sur des transistors à effet de champ. Un sujet complémentaire pour le développement de nouveaux composant d'électronique de puissance en diamant est l'anticipation des propriétés électriques de l'appareil et de l'architecture du composant grâce à des logiciels de simulation à base d'éléments finis. Ainsi, la nécessité d'une simulation fiable seront présentés.

Chapitre 2: Les principaux modèles mis en œuvre dans les outils de simulation sera présenté et les propriétés électriques du diamant seront donnés. Pour la simulation du transistor en diamant à effet de champ métal-oxyde-semiconducteur (MOSFET), l'étude de deux briques élémentaires est nécessaire: la jonction pn et le contact de grille. Les propriétés idéales du MOSCAP seront présentés tandis que la jonction pn servira comme base pour le calibrage des paramètres physiques mises en œuvre dans le logiciel à éléments finis.

Chapitre 3: Ce chapitre présentera les principaux résultats concernant les simulations de périphériques de diamant. Dans une première partie, les résultats sur la simulation de jonction pn seront présentés. En particulier, l'influence des modèles de génération-recombinaison sur les propriétés électriques simulées de la jonction pn sera discutée. Enfin, la simulation des propriétés électriques d'un métal-oxyde-semiconducteur transistor à effet de champ de diamant (MOSFET) sera présentée.

Chapitre 4: Dans ce dernier chapitre, l'accent sera mis sur la fabrication et la caractérisation du condensateur diamant métal-oxyde-semiconducteur (MOSCAP). Plus précisément, la configuration interfaciale de l'interface  $\text{Al}_2\text{O}_3$ /diamant à terminaison d'oxygène (O-diamant) a été étudiés en utilisant la spectroscopie de photoélectrons à rayons X. Les résultats ont permis d'établir le diagramme de bande de l'hétérostructure  $\text{Al}_2\text{O}_3$ /O-diamant. Ensuite, les propriétés électriques de la MOSCAP de diamant seront présentées. En particulier, l'étude de la densité des états d'interface a révélé l'ancrage du niveau de Fermi à l'interface entre l' $\text{Al}_2\text{O}_3$  et l'O-diamant. En outre, les courants de fuite à travers la couche d' $\text{Al}_2\text{O}_3$  seront discutés en termes de piègeage dépendant de la température assisté tunnel de trous de la couche de diamant à la grille supérieure contact. Enfin, la caractérisation électrique du premier MOSFET O-diamant, effectuée au National Institute for Advanced Industrial Science and Technology (AIST) au Japon, sera présentée. Même si cette première tentative a échoué, il est prometteur pour le développement de diamant MOSFET depuis la démonstration de la réalisation effective de l'appareil est clairement établi.

Une conclusion générale suivra alors et les perspectives de ce travail sera discutées.

## Chapitre 1: Le diamant pour les futures applications en électronique de puissance

Afin d'avoir un meilleur aperçu des performances des WBGSc leurs propriétés physiques sont résumées dans le Tab.4.4. En particulier, le SiC, GaN et le diamant ont de plus grand champ critique et conductivité thermique que le Si. Le diamant est "outrageusement" meilleur que ses concurrents. Plus précisément, son champ de claquage est plus de 30 fois supérieur à celui du Si et 3 fois supérieure à celle du SiC, ce qui convient pour les opérations à tension de blocage élevée. Sa conductivité thermique de 22 W/cm.K en fait un candidat pour des applications à haute température. Sa mobilité supérieure des trous rend approprié pour les dispositifs de fonctionnement à haute fréquence et les applications à courant élevé. Habituellement, la comparaison entre les semi-conducteurs du GBM est faite par le calcul de la figure de mérite (FOM), soit la FOM de Johnson, la FOM de Keyes ou la FOM de Baliga en fonction des applications ciblées.

Property	[unit]	Si	4H-SiC	GaN	Diamond
Band gap	$E_G$ [eV]	1.1 <i>i</i>	3.23 <i>i</i>	3.45 <i>d</i>	5.45 <i>i</i>
Dielectric constant	$\epsilon_r$	11.8	9.8	9	5.7
Critical Field	$E_{crit}$ [MV/cm]	0.3	3	2	10
Thermal conductivity	$\lambda$ [W/cm.K]	1.5	5	1.5	22
Sat. drift velocity e <sup>-</sup>	$v_s$ [ $10^7$ cm/s]	1.0	2.0	2.2	2.7
Sat. drift velocity h <sup>+</sup>	$v_s$ [ $10^7$ cm/s]	1.0			1.1
Electrons mobility	$\mu_e$ [cm <sup>2</sup> /V.s]	1500	1000	1250	1000
Holes mobility	$\mu_h$ [cm <sup>2</sup> /V.s]	480	100	200	2000
Johnson's FOM	$JFM$ [ $10^{23}$ $\Omega.W/s^2$ ]	2	911	490	3064
Keyes' FOM	$KFM$ [ $10^7$ W/K.s]	9	49	16	215
Baliga's FOM	$BFM$ [Si=1]	1	554	188	23017

*Table 4.4:* Les propriétés physiques du silicium (Si), du carbure de silicium (SiC), du nitrure de gallium (GaN) et du diamant utilisés dans l'électronique de puissance et les figures de mérite respectives (FOM) (Johnson, Keyes et Baliga). *i* et *d* désignent respectivement bande interdite directe et indirecte. Les valeurs sont données à température ambiante et les FOM ont été calculés à 300 K pour les électrons à l'exception du diamant pour lequel les trous ont été considérés.

Le diamant est considéré comme le semiconducteur ultime en ce qui concerne la FOM calculée (voir Tab.4.4). En théorie, le diamant doit être adapté à la haute fréquence, haute température et les applications à haute densité de puissance. De plus, son intégration au module d'alimentation devrait réduire considérablement la taille du système d'alimentation en collaboration avec le système de refroidissement. Plus précisément, la

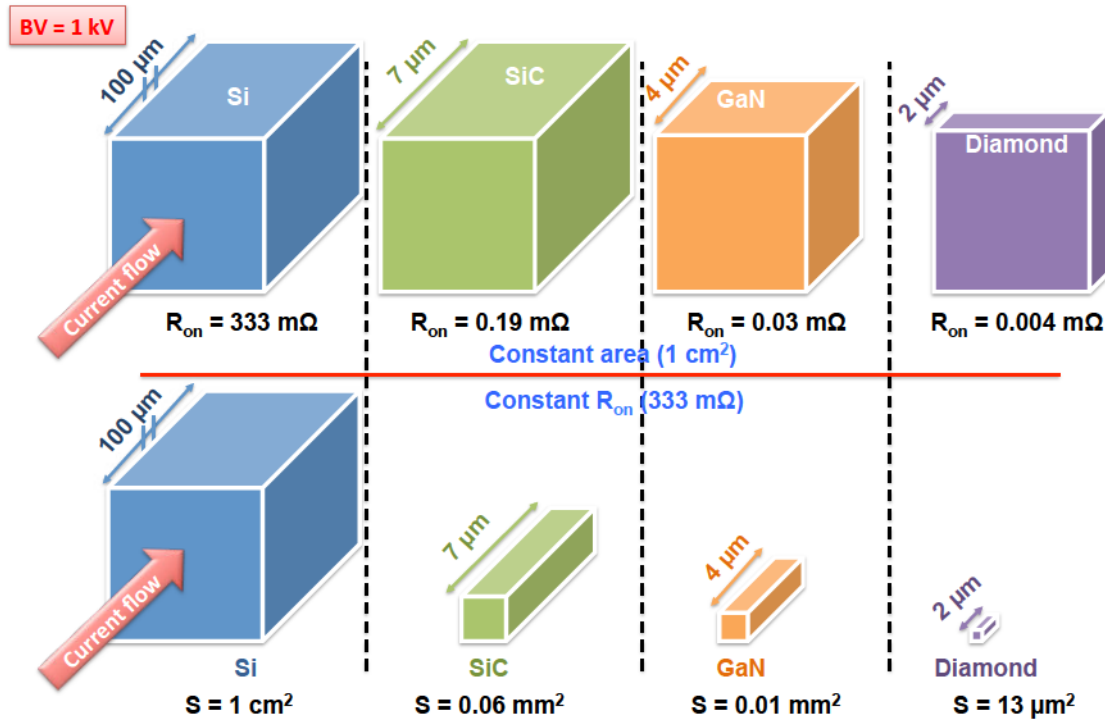


Figure 4.45: Illustration de l'avantage de WBGSc Si en termes de compromis  $R_{ons}$  vs  $BV$  [Rouger 2015]. Les WBGSc montrent les plus petites régions de contact ainsi que mince zone de dérive (représenté par la double flèche).

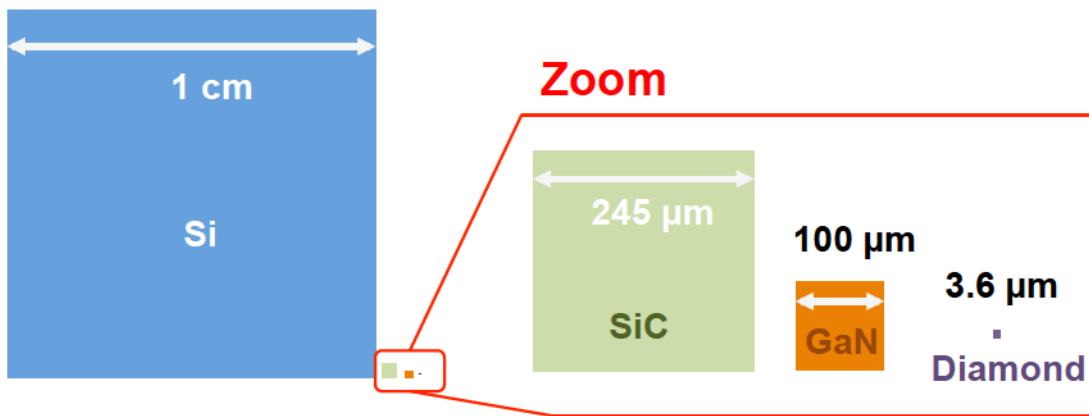


Figure 4.46: Mise à l'échelle de Fig.1.4 en considérant une tension de bloquage de  $1 \text{ kV}$  [Rouger 2015]. Parmi les WBGSc, le diamant est imbattable en termes de taille.

conception d'un semiconducteur de puissance est déterminée par l'épaisseur de la couche de dérive [Rouger 2015]. Ceci est illustré sur les Fig.4.45 et Fig.4.46 qui représentent respectivement pour une surface constante l'impact sur les pertes en conduction et, d'autre part, pour une résistance à l'état passant donnée l'impact sur la surface du composant.

Aussi, en utilisant un modèle simple de calcul de perte total dans un composant, on peut voir l'impact de l'utilisation des WBGSc par rapport au Si, comme l'illustre la Fig.4.47.

Même avec cette approche simple et spécifique plus réaliste sur la résistance  $R_{onS}$  l'avantage des WBGSc sur le Si est frappante. En outre, un modèle simplifié pour le calcul des pertes de commutation et a été utilisé Fig.1.9.b) donne un aperçu de l'avantage de l'utilisation de diamant pour augmenter la fréquence de commutation d'un convertisseur de puissance. Cependant, en même temps que la réduction de la zone de semi-conducteur, la densité de perte et la densité de courant augmente. Ainsi, une attention particulière doit être apportée lors de la conception des dispositifs de puissance WBGSc.

### Etat de l'art de la capacité MOS en diamant

Pour résumer brièvement les connaissances actuelles sur  $Al_2O_3/O$ -diamant MOSCAP, les résultats de G. Chicot thèse de doctorat sont présentés [Chicot 2013a]. La Fig.4.48 représente la structure plane MOSCAP. Le contact ohmique est fait de Ti/Pt/Au et l'empilement MOS est Al/ $Al_2O_3$  déposé sur le diamant terminé oxygène dopé au bore. Les 20 nm d' $Al_2O_3$  ont été déposé par dépôt de couches atomiques (ALD). Les détails sur la fabrication peuvent être trouvés dans [? ].

Comme représenté sur la Fig.4.49, la structure MOS de diamant peut être utilisé sous déplétion et régime de déplétion profonde (mise en évidence par le graphique  $1/C^2(V)$  de Fig.4.49.b)) pour augmenter la tension de polarisation de grille. De plus, la capacité d'accumulation ne dépend pas de la fréquence du signal en courant alternatif, mais le tronçon de la  $C(V)$  caractéristique est prononcée et varie de 1 kHz à 1000 kHz. Dans le même temps, la capacité d'accumulation prévu n'a pas été atteint. Plus précisément, la capacité d'accumulation mesurée était de 10 fois plus petit que la valeur attendue. L'origine de cette différence n'a pas été identifié, mais sera étudiée dans le présent ouvrage en utilisant des méthodes de caractérisation de spectroscopie d'impédance. Le comportement d'hystérésis a été observé sur ce dispositif, comme exposé dans Fig.4.50. Ce problème se produit lorsque des charges mobiles sont présents dans la couche d'oxyde. Ainsi, les propriétés  $I(V)$  du dispositif peuvent être influencées par la présence d'ions mobiles. Le courant par rapport à la tension de grille est tracée dans Fig.4.50. Dans le régime d'accumulation, le courant peut être aussi élevée que  $10^{-2}$  A.cm<sup>-2</sup> à -10 V, tandis que, lorsque la déplétion profonde a lieu, le courant est de l'ordre de  $10^{-7}$  A.cm<sup>-2</sup>

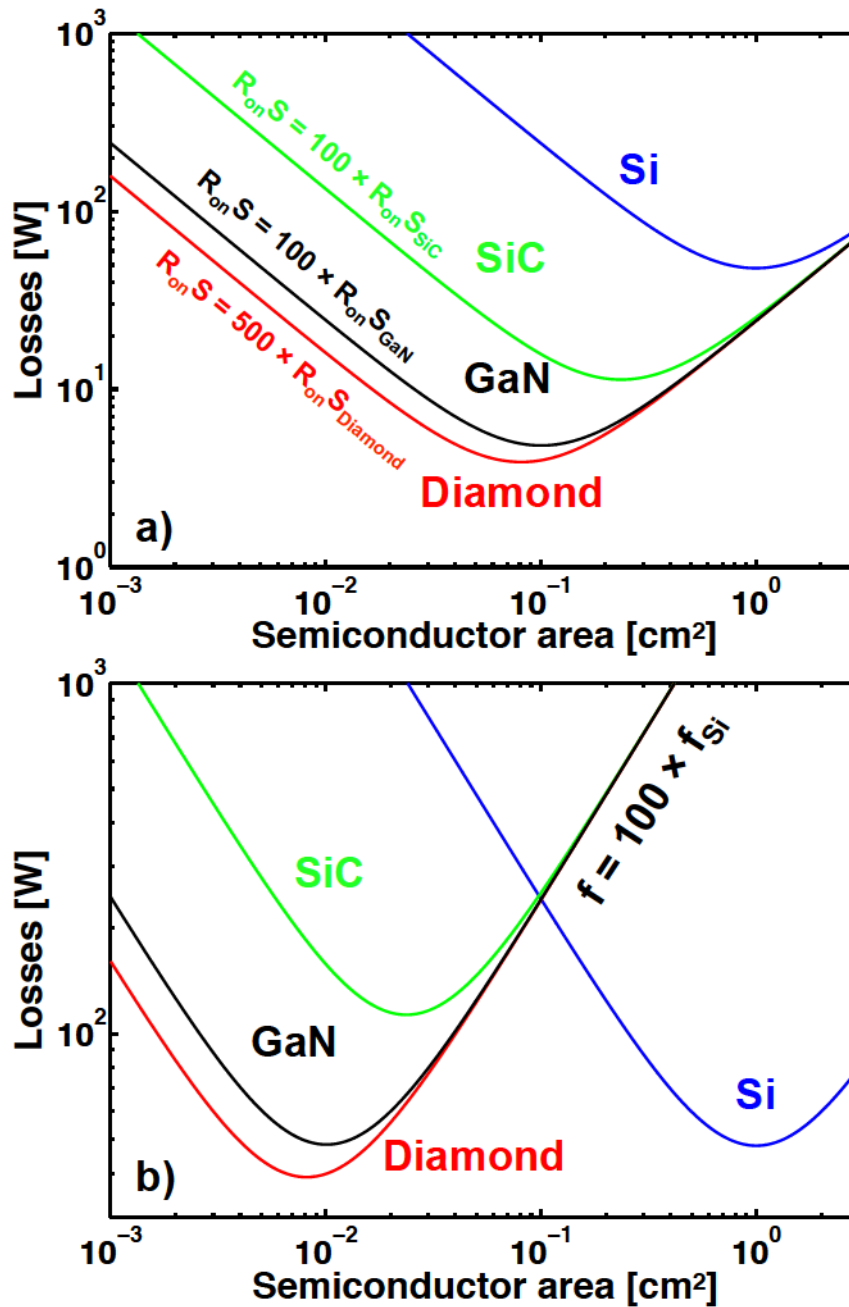


Figure 4.47: Exemple de l'optimisation de la zone de semi-conducteur dans le cas d'un dispositif de puissance unipolaire verticale avec 1200 V/10 A – 35 kHz –  $\alpha = 0.5$ . Une comparaison est faite entre Si, SiC, GaN et le diamant. a) Une réduction dans les  $R_{on}S$  sur les résultats dans une zone de semi-conducteurs réduit et une amélioration des pertes de puissance dans le dispositif d'alimentation. b) Même si une augmentation de la fréquence de commutation ( $f_{WBG} = 100 \times f_{Si}$ ) ne conduit pas à une réduction significative des pertes de puissance, la zone de semi-conducteurs est réduite [Rouger 2015].

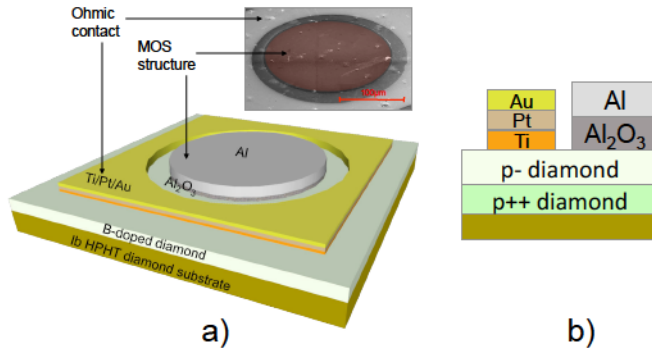


Figure 4.48: a) Al/Al<sub>2</sub>O<sub>3</sub>/O-diamond MOS schematic view and corresponding SEM image and b) cross section showing the stack [Chicot 2013b].

à 10 V. Ces courants peuvent être expliqués par les valeurs théoriques faibles attendues pour les électrons et trous barrière hauteurs à l'interface Al<sub>2</sub>O<sub>3</sub>/O-diamant [? ]. Ainsi, afin d'avoir une meilleure compréhension de l'Al<sub>2</sub>O<sub>3</sub>/O-diamant MOSCAP, une analyse détaillée a été effectuée au cours de cette thèse sur le Al<sub>2</sub>O<sub>3</sub>/O-diamant heterojunction caractériser à la fois la configuration de bande interfaciale et les propriétés électriques du diamant MOSCAP.

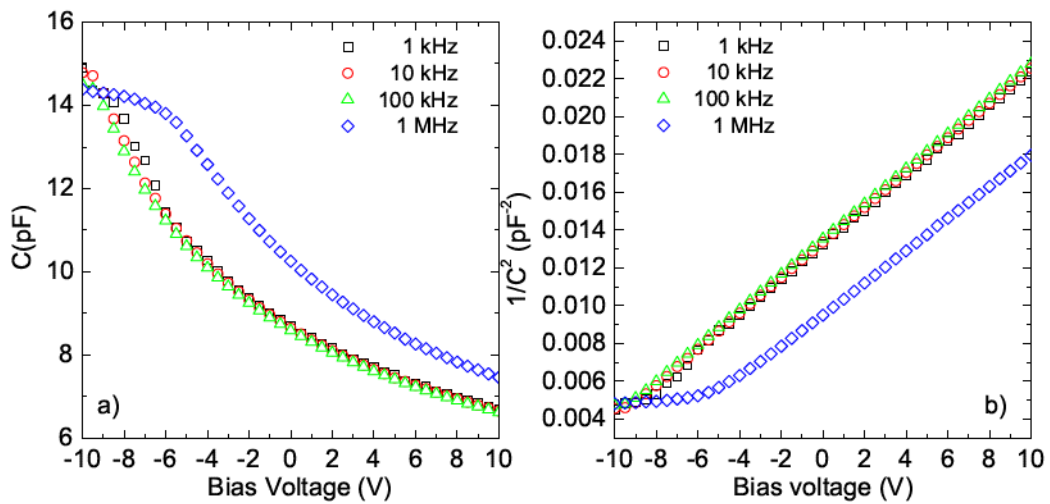


Figure 4.49: a) C(V) characteristic of the Al/Al<sub>2</sub>O<sub>3</sub>/O-diamond MOSCAP for various frequencies. b) 1/C<sup>2</sup>(V) plot showing constant slope for deep depletion regime [Chicot 2013a]. Measurements were performed at 300 K. The 20 nm thin Al<sub>2</sub>O<sub>3</sub> layer was deposited at 100 °C by ALD. The gate contact diameter is 200 μm.

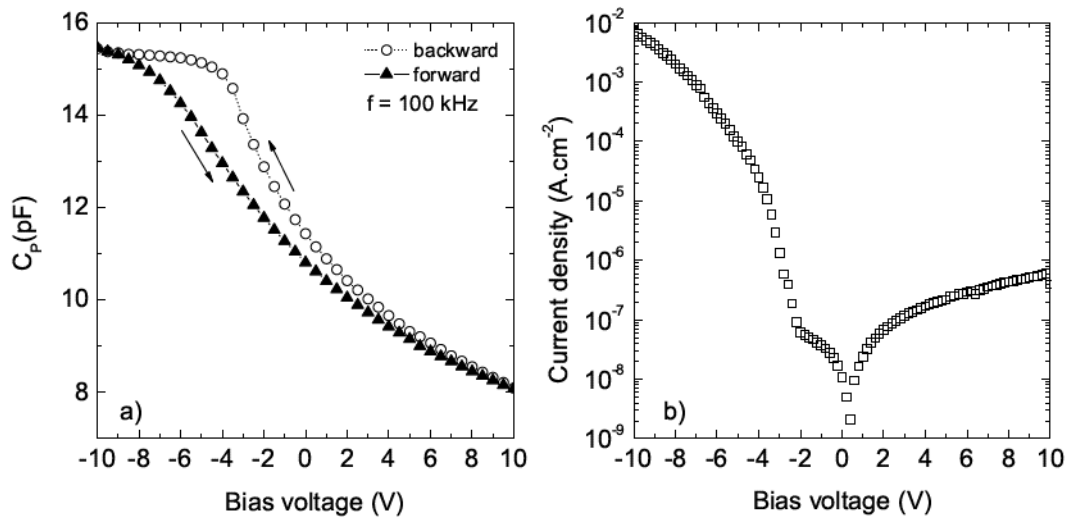


Figure 4.50: a) Hysteresis behavior of the  $C(V)$  characteristic at 100 kHz when biasing the structure from accumulation to deep depletion and from deep depletion to accumulation. b) Current-voltage  $I(V)$  characteristic of the device showing leakage currents [Chicot 2013a]. The 20 nm thin  $\text{Al}_2\text{O}_3$  layer was deposited at 100 °C by ALD.

## Chapitre 2: Propriétés électriques du diamant et concept du MOS idéal

Dans une première partie, les propriétés électriques de diamant principal mis en juvre dans le logiciel des éléments finis à base ont été présentés. Plus précisément, la largeur de bande dépendant de la température, l'ionisation incomplète des dopants, la température et la mobilité dépendant du dopage et les modèles de génération-recombinaison ont été présentés. La plupart des difficultés rencontrées dans les simulations de diamants comptent sur les faits que: i) la valeur intrinsèque concentration support est extrêmement faible dans le diamant et que ii) les paramètres GR sont inconnus. Ainsi, des attentions particulières doivent être payés afin d'éviter les problèmes de convergence et de l'étude de l'influence des paramètres GR est requis pour les simulations de périphériques de diamant fiables. Ces modèles ont été utilisés pour simuler une jonction pn diamant visant à re- produire des données expérimentales [Makino 2008, Koizumi 2013]. Les résultats seront présentés dans le chapitre 3. D'autre part, la simulation du MOSFET de diamant (voir section 3.4), basée sur l'expérience réalisée à l'AIST (voir rubrique 4.6), a examiné les mêmes paramètres que pour la jonction pn mais seulement considéré comme idéal

MOS contact de grille. La description du principe de fonctionnement du MOSCAP idéal est effectuée dans la prochaine partie de ce chapitre.

Dans cette partie, MOSCAP travail idéal équations principales et fondamentales ont été présentés et ses propriétés électriques ont été mis en place grâce à l'utilisation de la notion de graphe  $Q\Psi$ . En particulier, comme représenté sur la Fig.4.51, la charge par unité de surface dans le semi-conducteur par rapport à la surface  $Q_{SC}$  potentiel ( $\Psi_S$ ) et la capacité fonction de la tension  $C(V)$  est facilement reconstitué. Ce chiffre donne une idée de l'ordre de grandeur de  $\Psi_b$  et de la capacité d'accumulation attendue, qui correspond à la capacité d'oxyde calculée pour une superficie de  $A = 1.77 \times 10^{-4} \text{ cm}^2$  et une constante diélectrique relative de  $\epsilon_{ox} = 9$ .

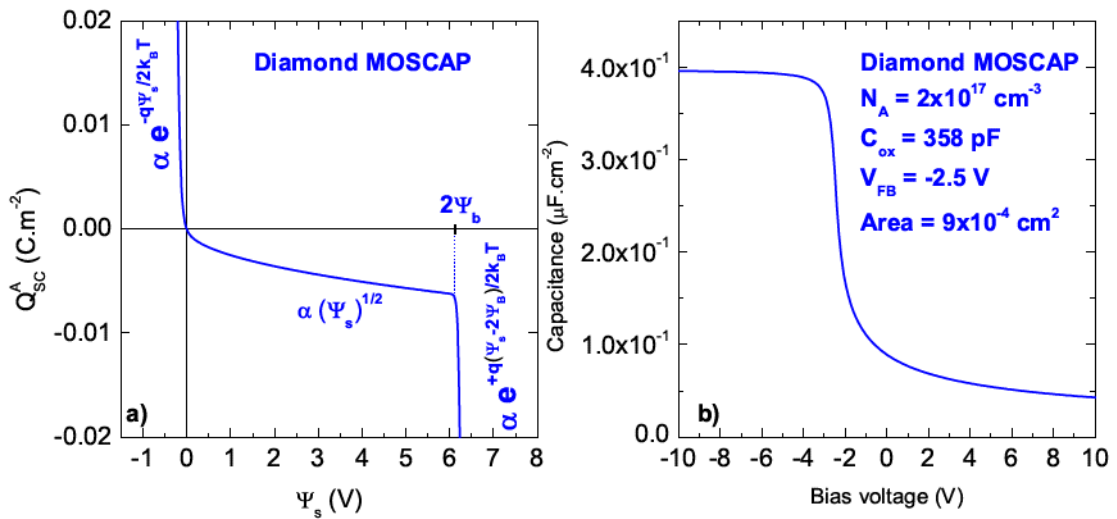


Figure 4.51: a) Charge per unit area  $Q_{SC}^A$  as a function of the surface potential  $\Psi_S$  in the diamond MOSCAP calculated from Eq.2.36. b) Corresponding capacitance vs. voltage ideal characteristic, with  $N_A = 2 \times 10^{17} \text{ cm}^{-3}$ ,  $V_{FB} = -2.5$ ,  $A = 9 \times 10^{-4} \text{ cm}^2$  and  $\epsilon_{ox} = 9$ .

L'anticipation de l'architecture et des propriétés électriques des dispositifs électroniques à base de diamant, en particulier MOSFET, nécessite le développement d'outils d'éléments finis à base de simulations qui prennent en compte les propriétés physiques uniques du diamant. Ainsi, la première partie de ce chapitre présente les principaux paramètres mis en œuvre dans TCAD Silvaco. Dans le chapitre 3, les modèles mis en œuvre seront discutés par la simulation d'une jonction pn. L'influence de la température sur les principaux paramètres sera montré et discuté. En outre, la simulation d'un MOSFET de diamant, sur la base des valeurs des paramètres implémentés utilisés lors des simulations de jonction pn, a été effectuée. Dans cette étude, le contact de porte a été considéré

comme idéal, à savoir l'oxyde est parfait en termes de comportement isolant et de frais fixes. Cependant, les propriétés électriques d'un transistor MOSFET sont influencées par la qualité de son électrode de grille. Ainsi, la deuxième partie de ce chapitre décrit les propriétés de la MOSCAP idéal, la partie la plus critique du MOSFET. MOSCAP réel, encore, peut montrer des anomalies liées à la présence des états d'interface à l'oxyde / semiconducteur interface comme il est le cas pour notre MOSCAP  $\text{Al}_2\text{O}_3/\text{O-diamant}$ . Afin d'étudier la structure  $\text{Al}_2\text{O}_3/\text{O-diamant}$ , chapitre 4 sera consacrée à l'étude de la nouvelle  $\text{Al}_2\text{O}_3/\text{O-diamant}$  architecture MOSCAP permettant dépôt de couche atomique à 250 °C. L'alignement de la bande de hétérostructure et les propriétés électriques de la MOSCAP de diamants fabriqués seront présentés et discutés en termes de MOSFET fabrication. En outre, au cours d'un séjour de quatre mois à l'Institut national de science industrielle avancée et de la technologie, la caractérisation électrique d'un MOSFET de diamant a été effectuée et les résultats seront présentés à la section 4.6.

### Chapitre 3: Modélisation de composants électroniques en diamant

Dans la perspective de l'optimisation de l'architecture et de prédire les caractéristiques électriques de futurs dispositifs de puissance de diamant, la mise en juvre des paramètres physiques et des modèles de diamant dans les logiciels à base d'éléments finis TCAD est nécessaire.

Dans ce contexte, Rashid et al. [Rashid 2008] ont modélisé un 1D diamant Schottky de intrinsèque-p le + (mi-p +) diode et étudié la mode passant et boqué J (V) caractéristiques de la structure. Les auteurs ont présenté les modèles mis en juvre et a souligné le manque de données inhérentes aux matériaux de diamant ainsi que les difficultés rencontrées pour simuler couche de diamant intrinsèque puisque la concentration de porteurs intrinsèques est de l'ordre de  $10^{-27} \text{ cm}^{-3}$  à 300 K. Ils ont trouvé de bonnes corrélations entre diode Schottky simulé et expérience J (V) caractéristiques. L'architecture d'un tel dispositif unipolaire a également été étudié par Thion et al. [Thion 2011]. Les auteurs ont étudié l'effet d'une plaque de champ sur la distribution du champ électrique dans la structure montrant l'importance de simulation numériques pour optimiser l'architecture du dispositif. Nawawi et al. [Nawawi 2011] ont modélisé les caractéristiques statiques et

transitoires d'une diode Schottky diamant afin de démontrer le potentiel des dispositifs unipolaires de diamant pour des applications d'électronique de puissance. Cependant, une approche plus systématique pour la modélisation de dispositifs de diamant soit unipolaire ou bipolaire est nécessaire. Puisque la technologie du diamant est encore très jeune, il ya un manque de valeurs de paramètre dans les outils numériques. Dans la perspective de modéliser avec précision les MOSFET de diamants, il est d'une importance fondamentale pour mettre en juvre les valeurs physiques des paramètres de diamant (impact coefficients d'ionisation, durée de vie des porteurs) et des modèles de mobilité dans les simulateurs de l'appareil, sur une large plage de température. Ainsi, l'étude des blocs de construction de diamant MOSFET, voici la jonction pn, est nécessaire.

Dans ce chapitre, les valeurs des paramètres physiques de diamant ont été mises en juvre dans Silvaco TCAD éléments finis logiciel [? ]. Les modèles mises en juvre ont ensuite été appliquées à une jonction pn diamant, des données tirées de Makino et al. [Makino 2008] et Koizumi et al. [Koizumi 2013]. Ces références ont été utilisés pour comparer les valeurs et les modèles de paramètres mis en juvre. Dans une première partie, les modèles numériques seront décrits. Ensuite, les caractéristiques de la jonction pn diamant simulées seront présentés. L'influence de la température, la durée de vie de Shockley-Read-Hall et les paramètres de recombinaison Auger sur les densités de porteurs et sur les caractéristiques  $J(V)$  sera affiché. En outre, les propriétés électriques d'une structure simple MOSFET plan seront présentés et discutés. Nous concluons sur les perspectives et les principales difficultés en raison du manque de valeurs et de modèles de paramètres mis en juvre dans les outils de simulation numérique.

## Modélisation d'une jonction pn

Propriétés électriques et électroniques de diamant jonction pn ont été simulées pour la première fois en utilisant un logiciel basé Silvaco des éléments finis. En raison d'un effet de grande énergie d'activation dans le système à grande largeur de bande interdite, concentration de porteurs changé en grande partie à l'état d'injection bas avec une tension de polarisation. Une fois que la condition d'injection changé en mode haute injection, la bande de flexion a été prédite se produire même dans la zone neutre en couche de type n. Courant-tension simulée ( $J(V)$ ) caractéristiques en supposant simple empilage p-n structure de jonction avec  $N_A = 4 \times 10^{17} \text{ cm}^{-3}$  à la couche de type p et  $N_D = 2 \times 10^{19} \text{ cm}^{-3}$

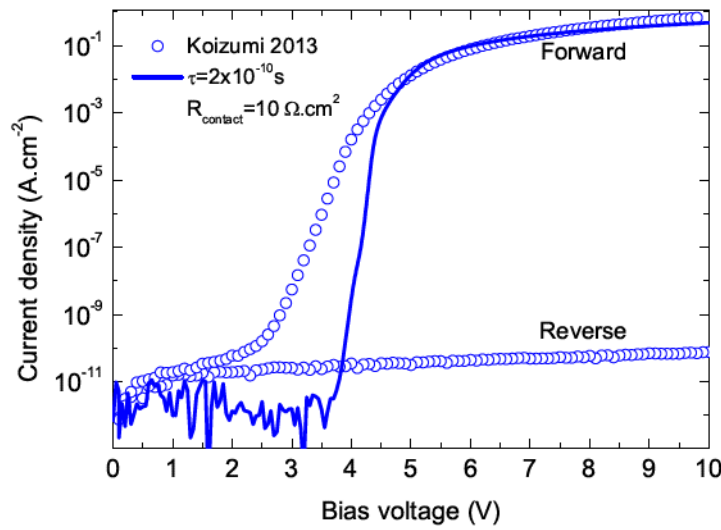


Figure 4.52: Fit of the experimental  $J(V)$  characteristic reported in [Koizumi 2013], at 300 K with a contact resistance  $R_{contact} = 10 \Omega.cm^2$  and  $\tau = \tau_p^{SRH} = \tau_n^{SRH} = 2 \times 10^{-10} s$ . This value is calculated according to the diffusion length of holes reported by Kato et al. [Kato 2013] using  $L_h = \sqrt{D\tau}$ , where  $D$  is the diffusion coefficient,  $D = k_B T \mu / q$ . The ideality factor  $n$  of the experimental  $I(V)$  is 3.5.

pour le type n + couche ont été comparés avec les données obtenues expérimentalement. Limite de tension de polarisation entre basse et haute état d'injection,  $\Psi_{bi} = 4,7 eV$ , était bien reproduit. Cependant, une grande différence n'a été observée entre les résultats simulés et les données obtenues expérimentalement sur le niveau actuel absolu et la pente de  $J(V)$  courbe étaient grandes, même en considérant les modèles de recombinaison de SSR et Auger. Cela signifie que les autres facteurs inconsiderés tels que la résistivité de contact ohmique, porteuse de tunnels et défauts cristallins contribue fortement à la  $J(V)$  caractéristiques de jonction pn diamants restent. Cependant, il est possible de prédire la caractéristique de claquage de la jonction pn qui est évaluée pour arriver à une tension de polarisation inverse de 225 V. En outre, le facteur important, tels que la mobilité de saut doit être prise en compte. De cette façon, la mobilité de saut a été exécuté dans les outils de simulation. Ce travail est motivé par le nombre croissant d'appareils de diamants qui a émergé au cours des dernières années. Récemment, il a été démontré que les différents régimes peuvent être contrôlés dans un condensateur MOS [?] ouvrant la voie pour la fabrication d'un transistor à effet de champ MOS. Ainsi, il est fondamental de prévoir aussi précisément que possible les caractéristiques électriques de ce futur dispositif de diamant ainsi que son architecture afin de fabriquer des dispositifs de puissance montrant performances électriques exceptionnelles.

## Modélisation d'un transistor MOSFET

La structure est composée de quatre terminaux, la source, le drain, la grille et la porte arrière avec des dimensions respectives de  $1\ \mu\text{m}$ ,  $3\ \mu\text{m}$  et  $18\ \mu\text{m}$ , ce qui permet séparé contrôle de la partie supérieure et de vannes de fond potentiels. Toutefois, dans la présente affaire, la porte arrière contact est court-circuité avec l'électrode de source et la terre comme un potentiel de référence. Le contact de grille chevauche la source et le drain de type n + région de  $0,1\ \mu\text{m}$ , de manière que, lorsque le canal d'inversion se développe, pas de résistance en série supplémentaire apparaît du fait de la région non inversée. Cette structure a l'avantage d'être normalement ouvert en raison de la présence des deux dos à dos n + -p jonctions avec haut-potentiel de l'ordre de 4,7 V. La concentration en dopage des contacts de source et de drain (n + - diamant de type) était mis à  $10^{20}\ \text{cm}^{-3}$  et l'espacement entre eux est de  $2,8\ \mu\text{m}$ , ce qui correspond à la longueur de canal d'inversion de  $L$ . Afin de simplifier l'étude, le mécanisme de conduction de saut a été négligée. L'effet de sauter dans la couche de type n + serait une diminution de la résistance des deux contacts source et drain [Oyama 2009]. Les propriétés de l'appareil sont principalement déterminées par les propriétés du canal ( $N_A$  et  $L$ ) et l'épaisseur d'oxyde. Dans la présente étude, la longueur de canal  $L$  a été choisie pour être constante. Enfin, les performances MOSFET ont été étudiées par rapport à de type p concentration de dopage  $N_D$ , l'épaisseur de l'oxyde et de la température  $T$ ,  $d_{ox}$ . L'effet de ces paramètres sur les propriétés électriques de la simulation plane inversion diamant MOSFET sera discuté dans la prochaine section.

Fig.4.54.a) montre l'IDS vs VGS extraite de l'IDS vs VDS calcul caractéristique à des températures allant de 300 K à 600 K. La température influe principalement le niveau de courant dans le transistor. En fait, quand on augmente la température, la concentration de porteurs intrinsèques augmente.

Afin de prédire la caractéristique de répartition de la future MOSFET de diamant, plusieurs paramètres doivent être pris en considération. Tout d'abord, la couche de diamant concentration de dopage de type p détermine le maximum VDS que le p-n + jonction peuvent supporter. Par exemple, en considérant un champ électrique maximale de claquage de  $10\ \text{MV.cm}^{-1}$  pour le diamant et une région complètement déchargée de  $3\ \mu\text{m}$  (pour le cas non-punch-through), on pourrait s'attendre à un VDS maximum de

1500 V pour le p-n+ jonction tension de claquage. Deuxièmement, cette concentration de dopage sera également influencer le déclenchement parasite du parasite n+n + -p-transistor bipolaire au cours de la MOSFET éteindre [Simonot 2011]. Ce mécanisme provient d'une augmentation locale du potentiel dans la structure qui conduit à la tour de parasite du transistor. Enfin, l'épaisseur d'oxyde sera principalement influencer

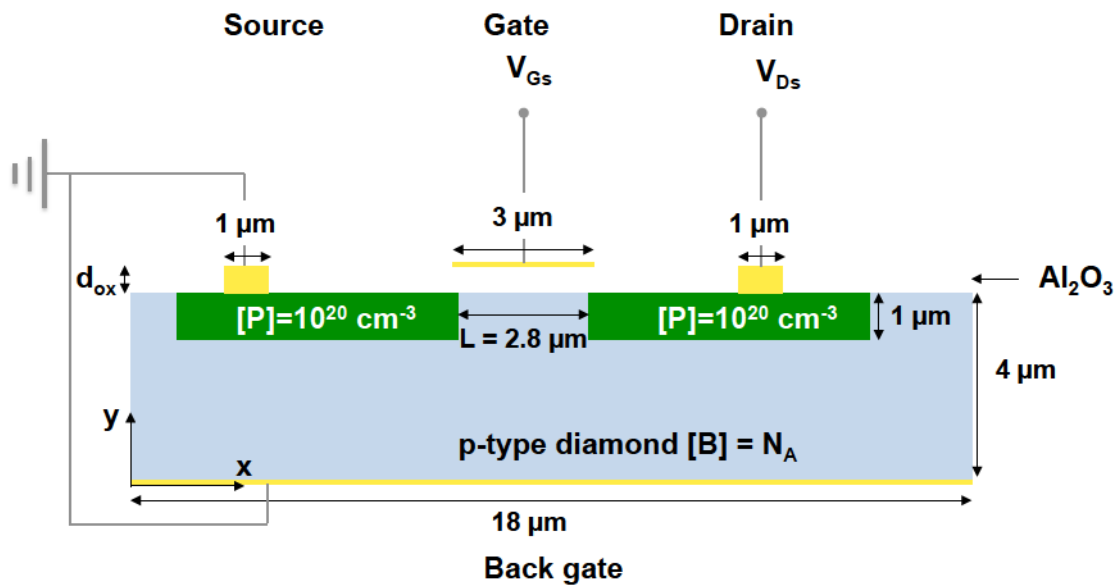


Figure 4.53: Structure of the simulated planar MOSFET. The Source and Back gate contact are short circuited and grounded.

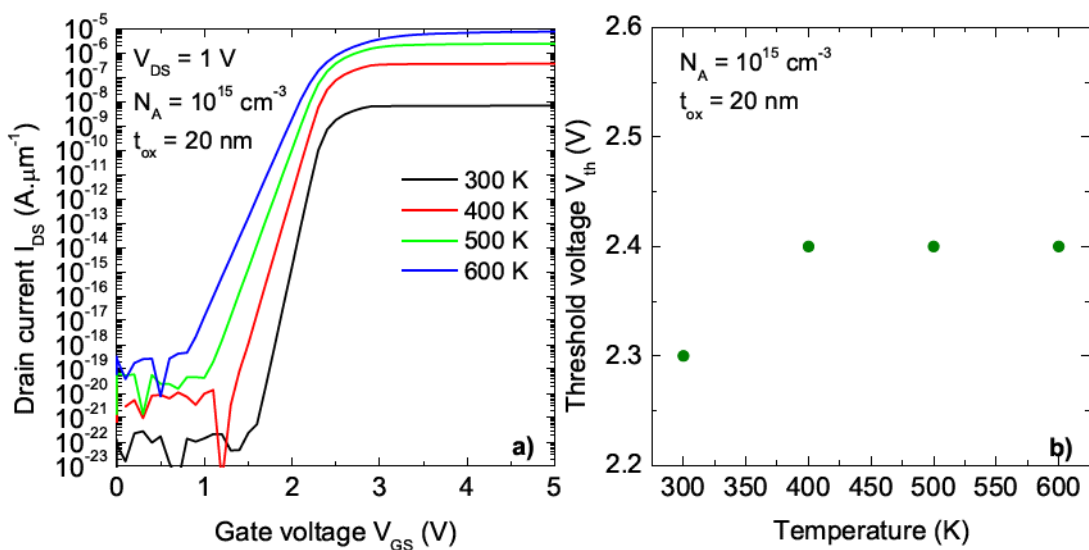


Figure 4.54: a) Transconductance characteristic  $I_{DS}$  vs.  $V_{GS}$  for  $V_{DS} = 1$  V,  $N_A = 10^{15}$  cm $^{-3}$ ,  $t_{ox} = 20$  nm, simulated for temperatures ranging from 300 K to 600 K. b) Corresponding threshold voltage as a function of temperature.

la tension de seuil du transistor MOSFET. Cependant, sa valeur détermine également la polarisation de grille VGS maximale applicable au contact de grille avant claquage d'oxyde. A titre d'exemple, si  $\text{Al}_2\text{O}_3$  est à considérer comme un oxyde de grille pour le transistor MOSFET avenir de diamant, un maximum de champ électrique appliqué peut être de l'ordre de  $7 \text{ MV.cm}^{-1}$  [Yota 2013].

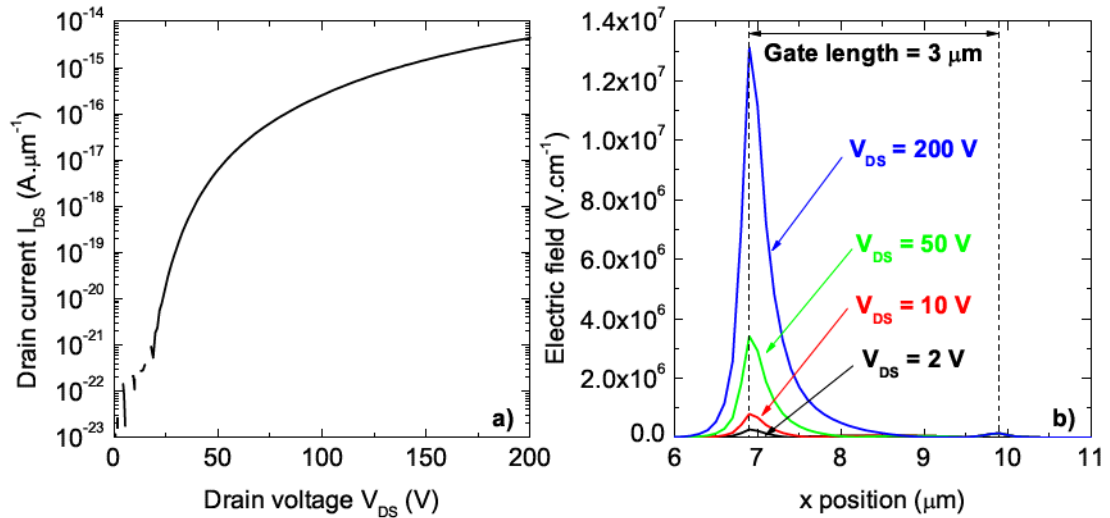


Figure 4.55: a)  $I_{DS}$  vs.  $V_{DS}$  characteristic of the simulated diamond MOSFET with  $V_{GS} = 0 \text{ V}$  and  $T = 300 \text{ K}$ . In this  $V_{DS}$  range, due to the very low intrinsic carrier concentration, the leakage currents are extremely small. b) Electric field at the oxide surface near the gate contact, with  $V_{DS} = 2, 10, 50$  and  $200 \text{ V}$ .

Les caractéristiques de blocage de la structure de diamant MOSFET ont été obtenus par augmentation de la tension de drain tout en maintenant une polarisation de grille nulle pour une épaisseur de couche d'oxyde de  $200 \text{ nm}$ , une concentration de dopage de type p de  $10^{15} \text{ cm}^{-3}$  et une température de  $300 \text{ K}$ , donnant une tension de seuil de  $2,7 \text{ V}$ . Ce choix est motivé par la comparaison à l'commerciallement disponible  $1200 \text{ V SiC MOSFET}$  de puissance [CREE]. Les propriétés de dégradation de diamants ont été prises en compte par le modèle d'ionisation par impact étudié dans la section 3.3.2. Comme le montre Fig.4.57.a), la très faible concentration de porteurs intrinsèques dans le diamant, induit un négligeable du courant de fuite à la température ambiante. Cela signifie que, en théorie, le biais VDS Drain-Source pourrait être augmenté à des valeurs encore supérieures à  $200 \text{ V}$  pour une structure plane de MOSFET simple. Toutefois, il faut considérer le champ électrique construit entre les électrodes drain et de grille. En fait, comme montré par Fig.4.56, qui représente la distribution du champ électrique dans la simulation 2D diamant MOSFET, le renforcement du champ électrique se produit au

niveau du bord du contact de grille. Une ligne de coupe simple à la surface de la couche d'oxyde, où le champ électrique est maximale, révèle que le champ électrique peut être aussi élevée que  $13 \text{ MV.cm}^{-1}$  pour une tension de polarisation de  $V_{DS} = 200 \text{ V}$ , comme représenté sur la Fig.4.56. b). De toute évidence, cette valeur extraite se trouve plus que les champs de décomposition maximales  $\text{Al}_2\text{O}_3$  rapporté [Kawakami 2005, Yota 2013].

En effectuant la simulation de MOSFET de diamant pour la première fois permis d'estimer le comportement électrique idéal de cette structure plane simple à la fois sur l'état et OFF-state. Les modèles de diamants mis en jeu ont été prises en compte pour la simulation de jonction pn présenté dans la section 3.3. Les propriétés du canal (NA), de température et de contact de grille capacité (par  $t_{ox}$ ) influences sur les IDS vs VGS caractéristiques ont été étudiées. En particulier, l'effet de la température sur la tension de seuil n'a pas été reproduite. D'autre part, l'épaisseur d'oxyde était l'influence attendue sur la tension de seuil. Une caractéristique particulière est mise en évidence lorsque l'on étudie l'effet de la concentration de dopage de type p de canal sur les propriétés électriques simulé diamant MOSFET: la résistance du canal augmentant avec l'augmentation de la concentration de dopage. L'analyse 2D offre une nouvelle perspective pour la simulation de dispositif de diamant. En fait, l'effet 2D spécifique, tel que les lignes d'écoulement de courant, le champ électrique et les distributions possibles peut être consulté. Il témoigne que l'amélioration de champ électrique a lieu près du bord de contact de grille. Cependant, les limitations dues à l'absence de paramètres mis en jeu empêchent de modélisation de la répartition d'oxyde de grille, comme en témoigne le niveau excessivement élevé de champ électrique dans la couche d'oxyde (près de  $10 \text{ MV.cm}^{-1}$ ). Ainsi, l'effort avenir doit être menée pour modéliser correctement la rupture diélectrique. Comme ce dispositif est envisagé pour l'avenir de l'intégration du dispositif de puissance, l'enquête sur le comportement dynamique est également d'un grand intérêt. Enfin, la structure de diamant MOSFET étudié a montré que le claquage électrique était beaucoup plus faible que la limite de diamant attendu. Ainsi, de nouvelles structures de l'appareil doivent être explorées afin de profiter de tout le potentiel de diamant pour des applications de dispositifs de puissance de la prochaine génération.

Deux exemples sont donnés dans Fig.4.58, où les architectures spécifiques sont mises en évidence à obtenir un comportement électrique appropriée. La géométrie en forme de V [Lane 1980] proposé dans Fig.4.58.a) a l'avantage d'être un dispositif vertical, où la couche de dérivation et donc les propriétés de dégradation sont contrôlées par la couche de

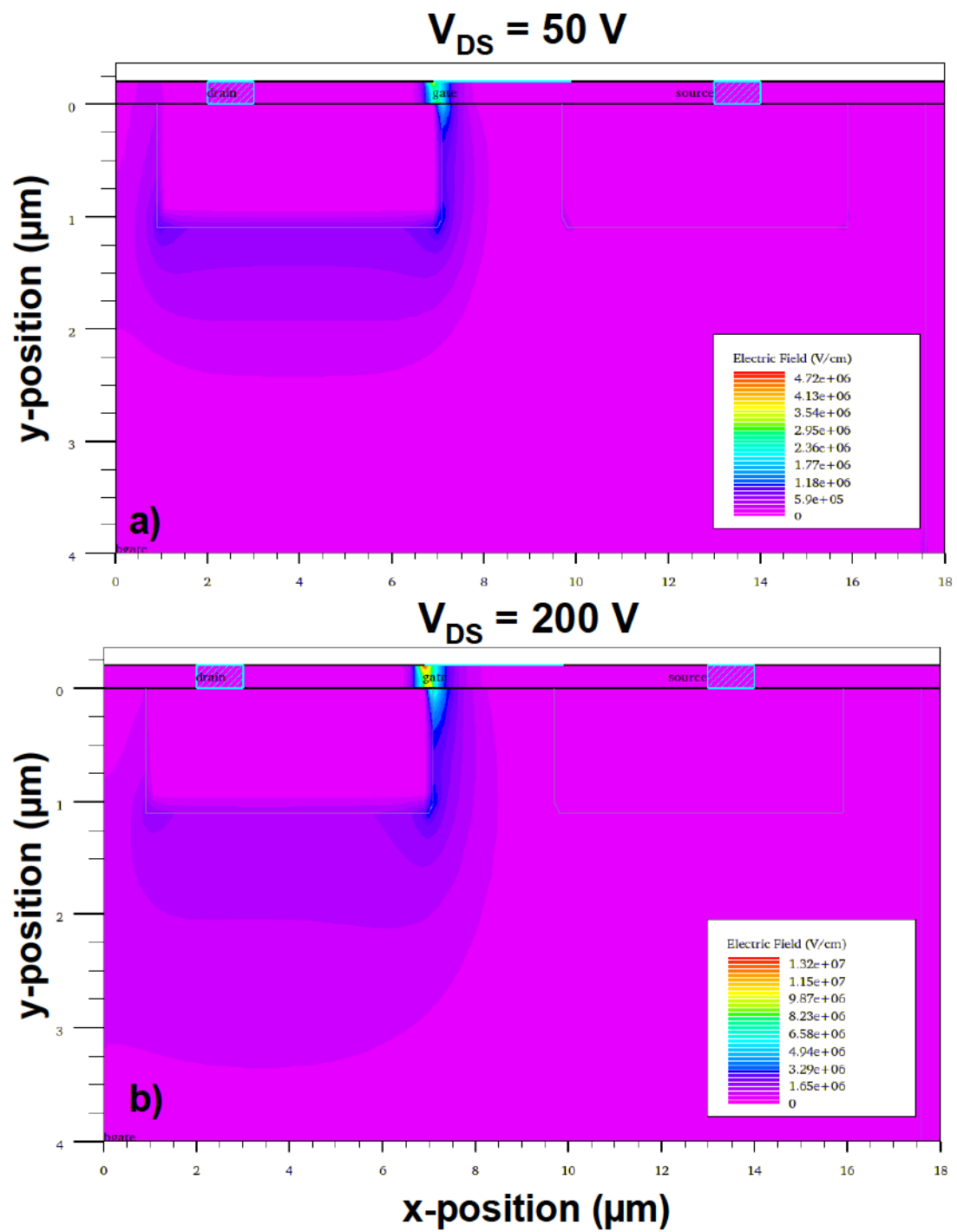
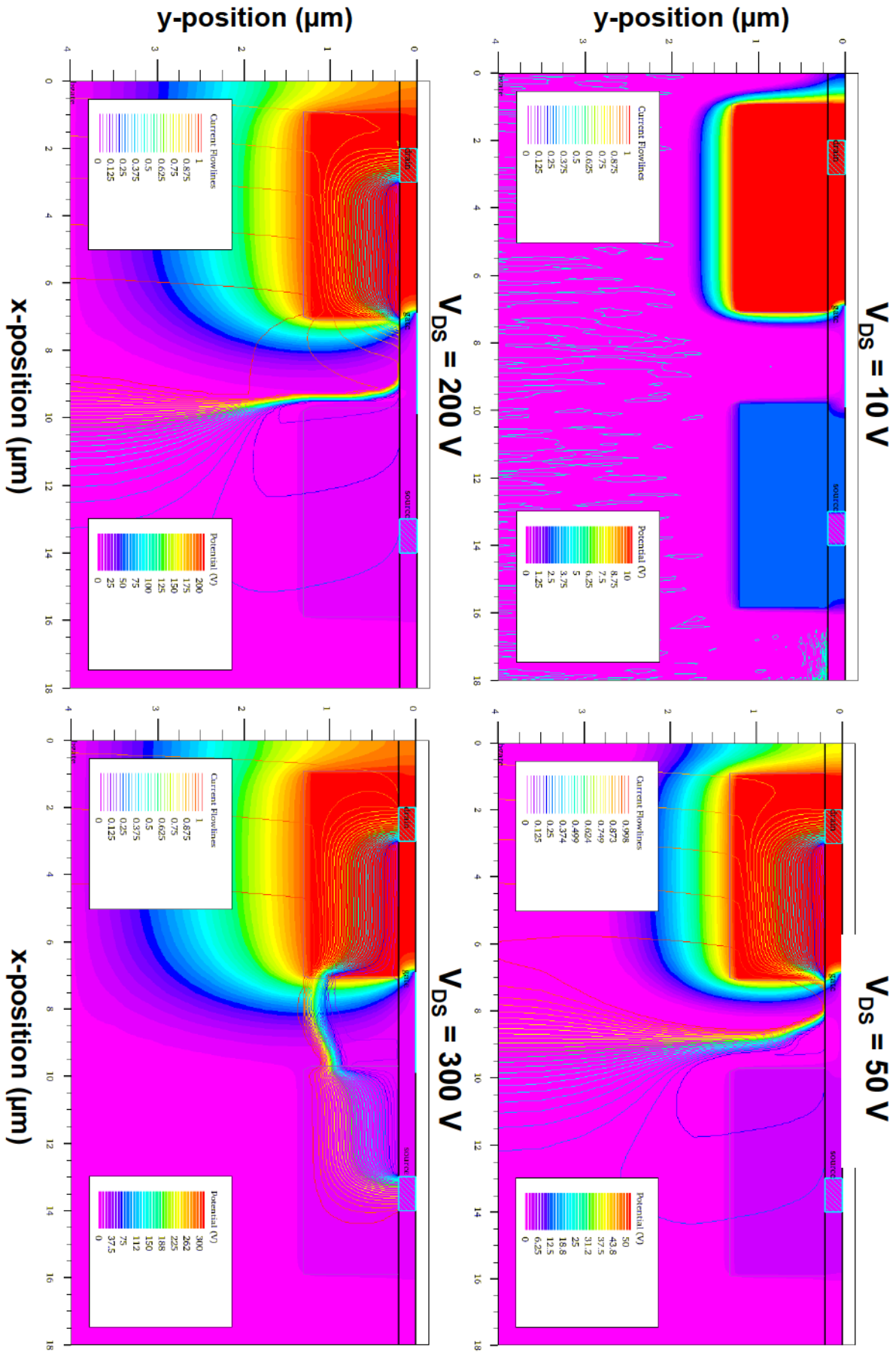


Figure 4.56: Electric field distribution in the simulated 2D diamond MOSFET for an oxide thickness of 200 nm, a p-type doping level of  $10^{15} \text{ cm}^{-3}$  and a temperature of 300 K at a)  $V_{DS} = 50 \text{ V}$  and b)  $V_{DS} = 200 \text{ V}$



diamant dopé au bore légèrement lité et l'épaisseur lité . D'autre part, la géométrie proposée dans Fig.4.58.b) représente un MOSFET de puissance avec un plan - région de dérivation de type sur le côté de vidange. Même si plusieurs défis doivent être abordés avant la réalisation réelle de l'appareil, ces structures pourraient être envisagées pour les futurs développements de diamant MOSFET.

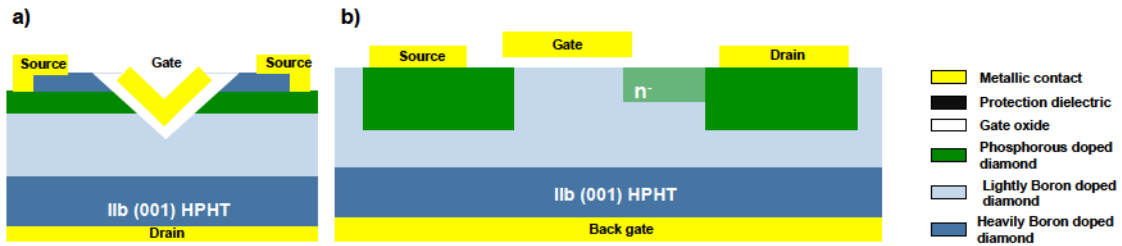


Figure 4.58: Potential diamond MOSFET structures envisioned for next generation power device applications.

Dans ce chapitre, les propriétés électriques des deux dispositifs de diamants ont été étudiés. Tout d'abord, la simulation des propriétés électriques d'une jonction pn diamant a été menée pour vérifier les modèles mis en œuvre et l'effet de la valeur des paramètres sur les propriétés électriques simulées. Des écarts importants ont été observés entre les résultats de simulation et les données expérimentales. Cela signifie que d'autres facteurs tels que la résistivité de contact ohmique, porteuse tunnel, défauts cristallins et des modèles spécifiques potentiellement génération-recombinaison pour le diamant [Makino 2012] contribue fortement à l'appareil de diamant caractéristiques électrique. Ces facteurs doivent être étudiés pour les futures simulations de périphériques de diamant.

D'autre part, la simulation de la structure de diamant en 2D MOSFET, en prenant en compte les propriétés spécifiques du diamant, a permis d'étudier l'effet de la concentration de dopage canal, de la température et de l'épaisseur d'oxyde sur les propriétés électriques simulées. En particulier, ces simulations montrent que le MOSFET simulé est pas approprié en termes d'applications de périphériques haute puissance. Comme représenté sur la Fig.4.59, qui présente la résistance spécifique en fonction de la tension de claquage, la simulation la structure présente plusieurs inconvénients. D'une part, le n + -p jonction punch-through se produit à une tension de polarisation de seulement 290 V, ce qui est, d'autre part, sur l'oxyde percées abaisseur de tension de 140 V. En fin de compte, même avec une ventilation élevée tension de 1500 V pour le n + -p jonction, cette structure de transistor MOSFET de diamant a une baisse des  $R_{ons} / BV$  figure de

mérite à la limite Si calculé [Baliga 2012]. En conséquence, les architectures spécifiques doivent être développés pour profiter du fort potentiel du diamant pour des applications de dispositifs électroniques de puissance future.

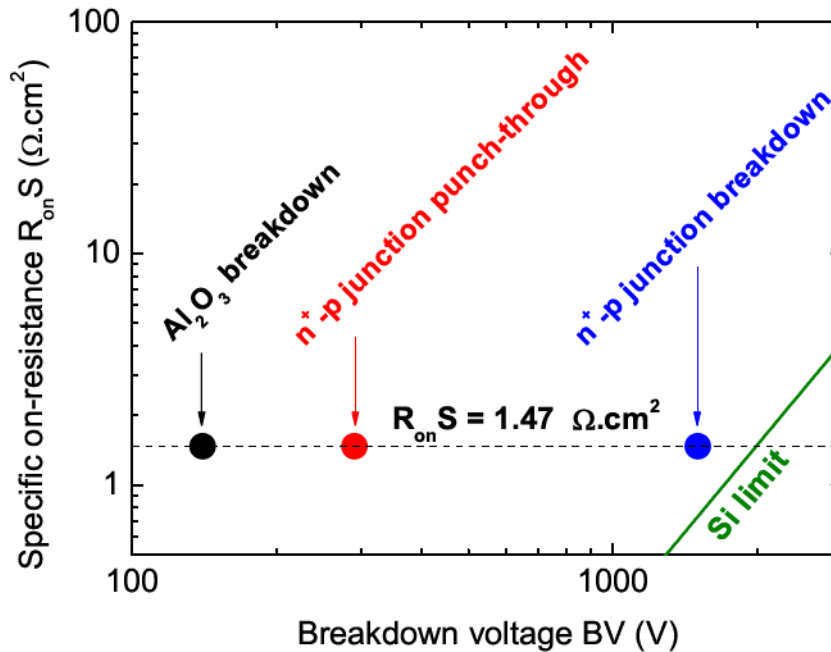


Figure 4.59: Specific on-resistance as a function of the breakdown voltage. The Si limit is calculated through Baliga's law as  $R_{on}S = 8.37 \times 10^{-9} \cdot BV^{2.5}$  [Baliga 2012].

## Chapitre 4: Fabrication et caractérisation de capacité métal-oxyde-semiconducteur en diamant

Dans ce chapitre, les étapes de fabrication menant à la réalisation des  $\text{Al}_2\text{O}_3/\text{O}$ -diamant condensateurs métal-oxyde-semiconducteur pseudo-verticale (MOSCAPs) sont décrits. Une première étape de croissance épitaxiale de la couche de type p + et la couche de type p est réalisée à partir d'un Ib HPHT (001) substrat en diamant. Ensuite, la définition de la structure mesa est réalisée avec l'utilisation d'un plasma d'oxygène pur par ICP gravure. Le contact ohmique sont ainsi directement déposée sur le dessus de la couche de type p + du diamant. La lumière UV sous vide / traitement à l'ozone [Teraji 2009] résultats dans la terminaison de l'oxygène de la surface du diamant avant le dépôt de couche atomique de la couche d' $\text{Al}_2\text{O}_3$  à 250 °C. Enfin, le contact de grille est déposé. Fig.4.60 montre la vue en coupe schématique de l'échantillon avec une image,

où le contact ohmique, les métal-oxyde-semiconducteur (MOS) et des contacts du métal-isolant-métal (MIM) contacts sont représentés.

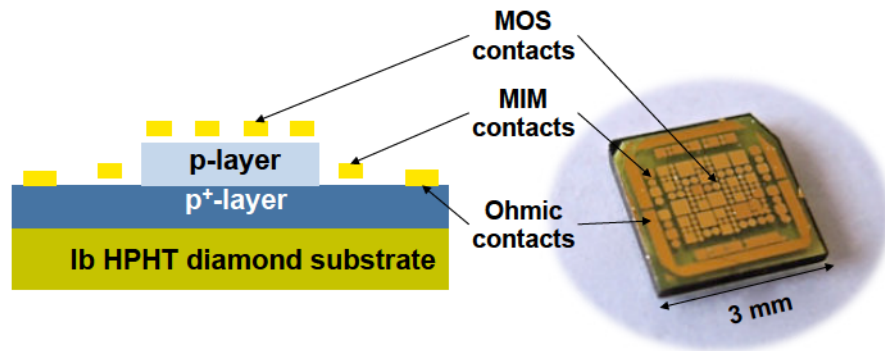


Figure 4.60: Schematic cross section (left) of the fabricated diamond MOSCAP and the corresponding actual device (right).

La configuration de la bande interfaciale de l'hétérostructure  $\text{Al}_2\text{O}_3/\text{O}$ -diamant était étudiée par spectroscopie de photoélectrons X (XPS) effectuée au Laboratoire des Technologies de la Microélectronique (LTM) de M. Aoukar et C. Vallée. Cette étude permet d'établir le diagramme de bande d'énergie de la structure  $\text{Al}_2\text{O}_3/\text{O}$ -diamant grâce à la mesure du décalage de bande de valence [Maréchal 2015]. La caractérisation électrique du MOSCAP  $\text{Al}_2\text{O}_3/\text{O}$ -diamant en utilisant des méthodes de capacité et de la conductance a révélé la présence d'une forte densité d'états d'interface résultant dans le brochage du niveau de Fermi à l'interface empêchant la MOSCAP pour atteindre accumulation. Néanmoins, les régimes d'épuisement et de l'épuisement profond sont atteints. D'autre part, les courants de fuite ont été observés dans le dispositif et étudiés en termes de piège dépendant de la température assisté tunnel de trous de la couche de diamant à l'électrode de grille supérieure. La divergence entre les données expérimentales et le modèle théorique est liée à la présence du trou de l'injection de la couche de type p+, ce qui entraîne une concentration plus élevée de trou dans la couche de type p, bien supérieure à la concentration à l'équilibre [Muret 2015].

Afin de souligner le contexte de diamant MOSCAP, un bref examen sera effectué montrant les 25 dernières années d'efforts vers la réalisation de dispositifs de travail. Ensuite, les étapes de fabrication de l'appareil étudié dans ce travail seront affichées. Le diagramme de bande obtenue à partir de l'analyse XPS sera établi et les résultats de la caractérisation électrique sera discuté. Enfin, la caractérisation d'un MOSFET de diamant effectué pendant un séjour de quatre mois en AIST (Tsukuba, Japon) sera présenté.

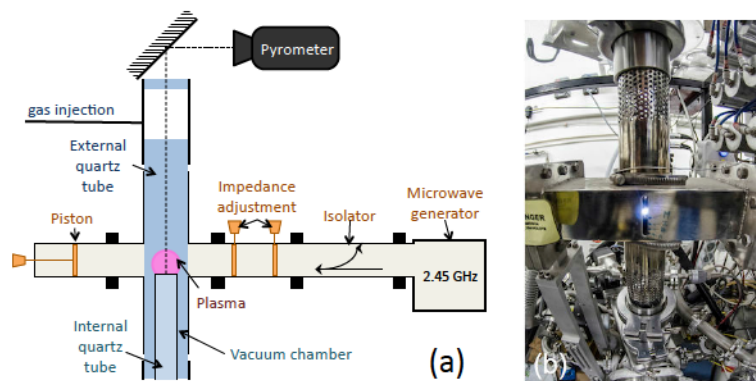


Figure 4.61: a) Schematic view of the home-made NIRIM type MPCVD reactor. b) Picture of the growth chamber [Fiori 2012].

Deux étapes de croissance du diamant CVD successives ont été réalisées pour produire un 470 p nm d'épaisseur + de type couche de diamant sur le dessus de laquelle un nm couche de diamant de type p 590 épaisse a été dé- posé. La couche de type p + diamant a été réalisée en utilisant un mélange gazeux de méthane ( $[CH_4] / [H_2] = 4\%$ ), du diborane ( $[B] / [C] = 1200$  ppm) et de l'hydrogène à une pression de 33 Torr et une température de 830 °C pour une durée de croissance de 15 min. La morphologie de la surface étudiée par profilométrie optique a révélé une couche épitaxiale de haute qualité avec une rugosité moyenne de 0,22 nm et Root Mean Square de 0,27 nm. La couche de diamant de type p est réalisée en utilisant un mélange gazeux de méthane ( $[CH_4] / [H_2] = 1\%$ ), du diborane ( $[B] / [C] = 600$  ppm), d'oxygène ( $[O_2] / [H_2] = 0,25\%$ ) et de l'hydrogène à une pression de 33 Torr et une température de 910 °C pour une durée de croissance de 45 min. Ces conditions de croissance conduisent à une haute qualité de diamant couche épitaxiale, comme démontré par la rugosité de surface et Root Mean Square, mesurée par profilométrie optique 0,46 nm et 0,82 nm respectivement signifier. Dans la section suivante, les étapes technologiques pour produire le MOSCAP de diamant seront décrits.

Les contacts ohmiques sont réalisées par dépôt d'un empilement métallique Ti/Pt/Au sur la couche de diamant fortement dopée au bore. Les différentes étapes de la fabrication de contacts ohmiques sont résumés dans le Fig.4.62.

La terminaison oxygène de la surface de diamant (O-diamant) est obtenue en effectuant un traitement à l'ozone, une première technique proposée par Teraji et al. [Teraji 2008, Teraji 2009]. Cette méthode est basée sur l'exposition de l'échantillon à l'ultraviolet profond de la lumière dans l'atmosphère d'oxygène. Une lampe à xénon centrée à 172

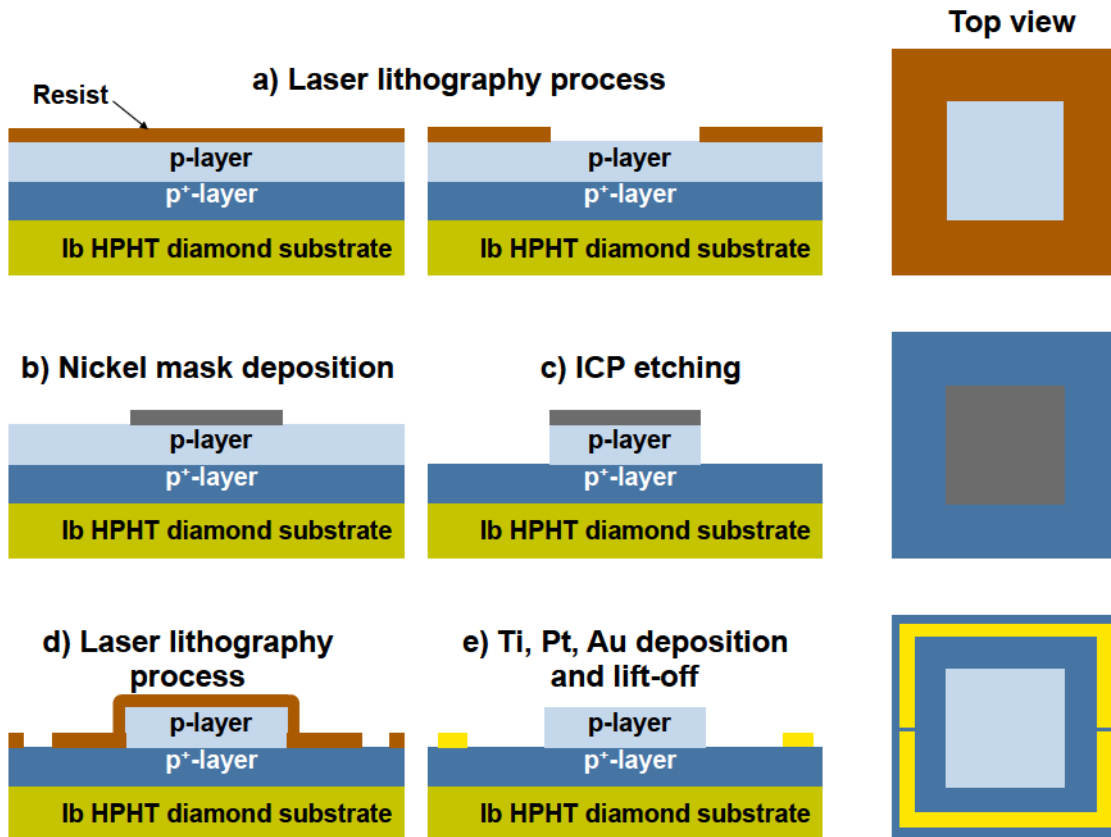


Figure 4.62: Schematic describing the ohmic contacts fabrication process.

nm sert de source de lumière UV. En introduisant l'oxygène dans la chambre, l'ozone est produit et l'oxygène sature la surface de diamant avec hydroxyle (COH), les organisations de l'éther (COC) et carbonyle (C = O) [Boukherroub 2005, Hoeb 2010]. Ce traitement a démontré une grande efficacité dans la passivation de surface et dans le contrôle des propriétés électriques de diodes Schottky diamant [Teraji 2009, Fiori 2014? ]. Dans la pratique, les échantillons de diamants ont été introduits dans une chambre sous vide secondaire. Ensuite, l'oxygène a été introduit sous une pression de 500 mbar et exposé à la lumière UV pendant 90 minutes à température ambiante. Juste après le traitement par la lumière VUV / ozone, l'oxyde d'aluminium Al<sub>2</sub>O<sub>3</sub> est déposé par dépôt de couches atomiques en utilisant un système Savannah 100 de Cambridge NanoTech. Cette méthode consiste en une exposition séquentielle de la surface de l'échantillon à différents précurseurs, à savoir triméthylaluminium (TMA), et l'eau comme un oxydant. La durée de l'impulsion et de l'exposition était de 30 s et 15 ms, respectivement. La température a été réglée à 250 °C et pression de base typique était de  $1,3 \times 10^{-1}$  Torr. Un nombre total de 200 cycles ont été effectués et l'épaisseur de la couche d'Al<sub>2</sub>O<sub>3</sub> a été mesurée par ellipsométrie spectroscopique donnant un taux de dépôt de 0,1 nm /

cycle, résultant en une couche épaisse de 20 nm. Ensuite, une étape de lithographie laser est nécessaire de définir les contacts de grille au-dessus de la couche d'oxyde, suivie par un dépôt par faisceau d'électrons de Ti / Pt / Au empilement de grille et le procédé de lift-off standard. Enfin, MOS et des condensateurs MIM sont définies sur le même échantillon, ce qui permet la caractérisation indépendante de l' $\text{Al}_2\text{O}_3$  couche diélectrique (MIMCAP) et MOSCAPs  $\text{Al}_2\text{O}_3/\text{O}$ -diamant comme représenté sur la Fig.4.63.

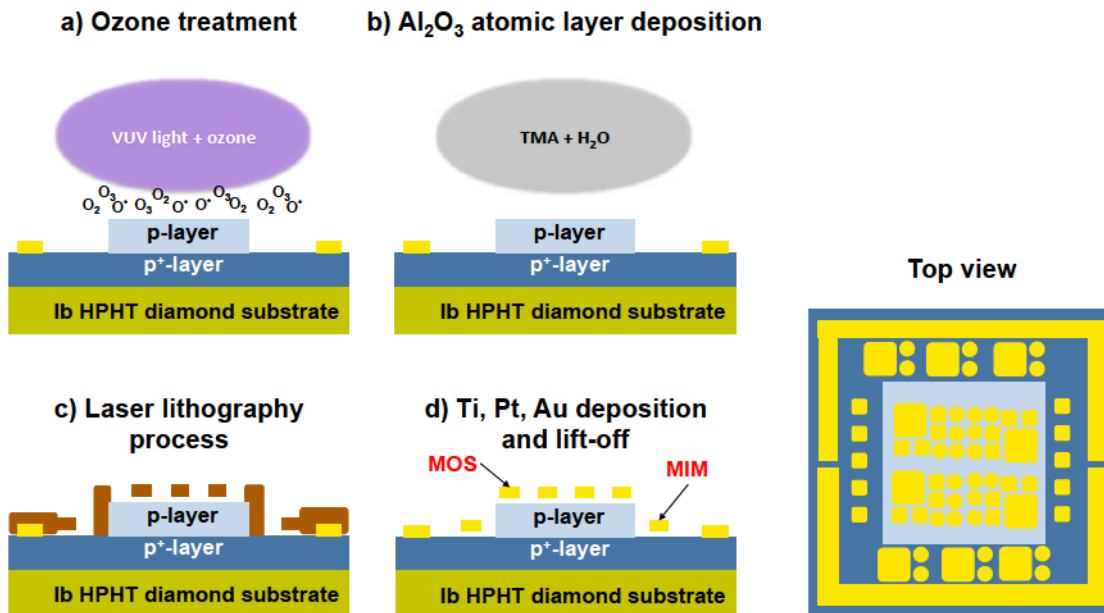


Figure 4.63: Schematic describing the MOS contact fabrication steps.

Les MOSCAPs de diamant pseudo-verticale ont été fabriqués en utilisant des techniques de dépôt et du décollage standard. Une première étape consistant à définir la structure mesa sur l'échantillon a été effectuée suivie par le dépôt et le recuit des contacts ohmiques. Terminaison de l'oxygène de la surface du diamant a été réalisée en utilisant un / traitement à l'ozone lumière dans l'ultraviolet lointain avec une pression d'oxygène de 500 mbar pendant 90 min à température ambiante. Le 20 nm porte  $\text{Al}_2\text{O}_3$  diélectrique a été déposé sur la surface O-diamant en utilisant couche atomique position de dé- (ALD), et la définition du contact de grille suivie pour produire le diamant finale MOSCAP pseudo-verticale. Dans la section suivante, les résultats sur X Spectroscopie de photoélectrons (XPS) des mesures seront présentées. Cette étude a permis de déterminer la configuration du diagramme de bande d'énergie de la structure d'interface  $\text{Al}_2\text{O}_3/\text{O}$ -diamant.

## XPS

Trois échantillons ont été préparés comme illustré sur la Fig.4.11. Tout d'abord, une fine couche ALD- $\text{Al}_2\text{O}_3$  2 nm déposée à 250 °C sur Ib HPHT O-diamant a été préparé (voir la section 4.3.2.2 pour plus de détails). Cette couche a permis aux XPS Signal sortant de la surface de l'échantillon, identifiant ainsi l'énergie de liaison entre la surface O-diamant et la couche d' $\text{Al}_2\text{O}_3$ . Un deuxième échantillon d'une couche de  $\text{Al}_2\text{O}_3$  de 20 nm d'épaisseur déposée dans les mêmes conditions que le premier a été préparé sous forme de calibrage pour les atomes d'Al en vrac. Enfin, un oxygène terminé échantillon de diamant a été préparé. Cet exemple permet de déterminer l'énergie de liaison des atomes de carbone.

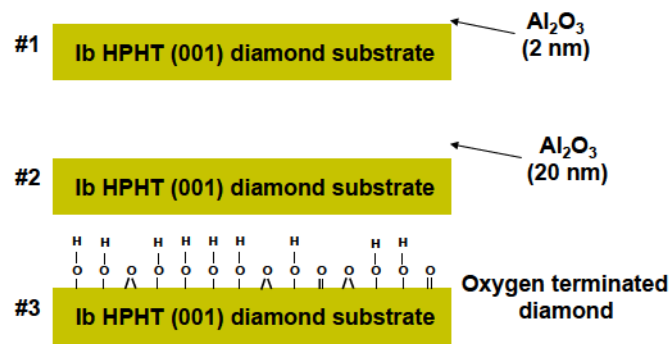


Figure 4.64: Schematic cross section of the samples prepared for the XPS analysis.

Le maximum de bande de valence (VBM) est extrait par extrapolation linéaire à l'ajustement de l'axe x et sont 3,20 ± 0,2 eV et 2,07 eV pour ± 0,2  $\text{Al}_2\text{O}_3$  et O-diamant respectivement. Toutes les énergies de liaison pertinentes extraites sont résumés dans Tab.4.5.

		O-diamond	$\text{Al}_2\text{O}_3$ (2 nm)	$\text{Al}_2\text{O}_3$ (20 nm)
C 1s	C-C	284.32		284.2
	$\text{CH}_x$	284.93		
	C-Al		284.08	
	C-O-C	285.90		
	C=O	287.20		
	Al 2p <sub>3/2</sub>	Al-O		74.32
O 1s		530.60	530.46	530.69
VBM		2.07		3.20

Table 4.5: C 1s, Al 2p<sub>3/2</sub> and O 1s binding energies (eV) of the core level spectra for the O-terminated diamond, the 20 nm  $\text{Al}_2\text{O}_3$  and 2 nm  $\text{Al}_2\text{O}_3$  samples. The valence band maxima (VBM) were recorded for the O-terminated diamond and the 20 nm thick  $\text{Al}_2\text{O}_3$

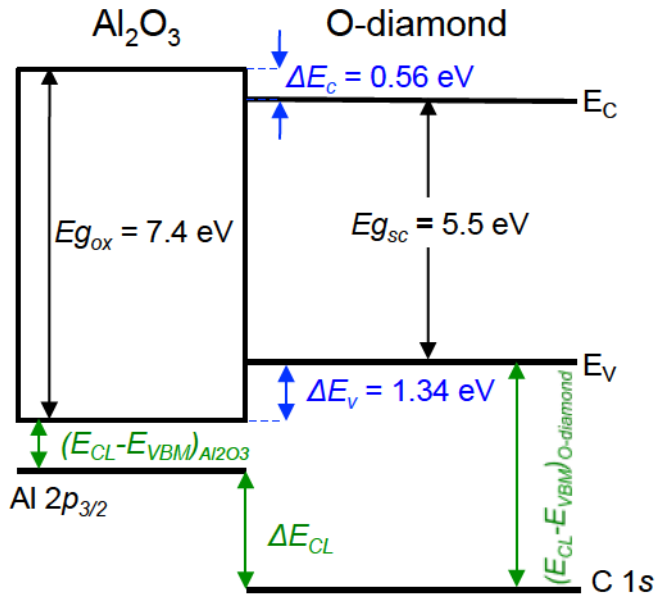


Figure 4.65: Schematic energy band diagram of the  $\text{Al}_2\text{O}_3/\text{O-diamond}$  with Ti in contact with the oxide layer, deduced from XPS measurement. The valence band offset is  $1.34 \pm 0.2$  eV and the conduction band offset is  $0.56 \pm 0.2$  eV. The oxide band gap value is taken from [Kim 2006].

La configuration de la bande interfaciale de l' $\text{Al}_2\text{O}_3$  / O-diamant a été étudiée en utilisant X spectroscopie de photoélectrons (XPS) de mesures. En particulier, la bande de valence discontinuité entre la bande  $\text{Al}_2\text{O}_3$  de valence et la bande de valence O-diamant est déterminées être  $\Delta E_v = 1,34 \pm 0,2$  eV et la discontinuité de bande de conduction est calculé comme  $\Delta E_c = 0,56 \pm 0,2$  eV, en tenant compte de la largeur de bande de  $\text{Al}_2\text{O}_3$  de 7,4 eV [Kim, 2006]. Une largeur de bande interdite plus petite de  $\text{Al}_2\text{O}_3$  se traduirait par une barrière pour les trous plus petits. Ainsi, le développement de la couche d' $\text{Al}_2\text{O}_3$  de haute qualité est nécessaire pour atteindre des valeurs élevées de l'écart de bande, tels que 8,8 eV [Robertson 2000]. En conclusion, MOS  $\text{Al}_2\text{O}_3$  / O-diamant pourrait être approprié pour le développement de normalement ouvert à canal P MOSFET, depuis confinement des trous à l'interface pourrait être réalisé grâce à la barrière  $\Delta E_v$ . Le  $\Delta E_v$  inférieure =  $1,34 \pm 0,2$  eV en cas d' $\text{Al}_2\text{O}_3$  / O-diamant que dans le cas de l'interface  $\text{Al}_2\text{O}_3$  / H-diamant ( $\Delta E_v = 2,9 \pm 0,2$  eV [Liu 2012]), qui était attendu, même si une application rigide de la ? d'affinité électronique différence conduit à une valeur de 0,8  $\Delta E_v =$  eV. A l'opposé, le canal de type n se traduira dans une trop petite barrière ( $\Delta E_c = 0,56 \pm 0,2$  eV) entre les bandes de conduction de  $\text{Al}_2\text{O}_3$  et O-diamant, si l'hypothèse d'un intervalle de bande d'énergie de 7,4 eV [Kim 2006]. Ainsi, g  $\text{Al}_2\text{O}_3$  ne sera pas efficace pour confiner les électrons et les MOSFET canal N de type ne fonctionnera pas en utilisant cette interface.

## Propriétés électriques

La méthode de Terman est basé sur la mesure de la caractéristique haute fréquence  $C(V)$  d'un MOSCAP qui est équivalent au circuit à haute fréquence de Fig.4.66. Dans ce régime, les pièges d'interface ne peuvent pas répondre au signal de courant alternatif variant rapidement, mais peuvent suivre la polarisation continue lentement variable [Schroder 2006]. Les états d'interface seront facturés lorsque le niveau de Fermi va balayer le niveau d'énergie à l'interface. Dans notre cas, la charge positive apparaît à l'interface, en gardant le semi-conducteur dans l'épuisement. Il en résulte dans le tronçon de la courbe  $C(V)$ , un décalage non parallèle de la caractéristique  $C(V)$  le long de l'axe de polarisation de grille. Comme la seule différence entre un idéal et une courbe expérimentale  $C(V)$  est fourni à partir de la présence d'états d'interface, à condition que la bande de recourbement peut être commandé et est le même, une comparaison directe permet d'extraire la densité d'états d'interface. La procédure consiste à extraire la différence de tension pour une capacité constante

Fig.4.66 montre la comparaison entre la haute fréquence  $C(V)$  avec l'un théorique calculée, ajuster la concentration de dopage de la parcelle  $1/C^2$  à  $2,3 \times 10^{17} \text{ cm}^{-3}$  et la tension de bande plate de  $-7,1 \text{ V}$  tels que la profondeur appauvrissement expérimentale et les caractéristiques théoriques correspondance. L'insert montre un zoom où le AV est mis en évidence. De  $-8 \text{ V}$  à  $-6 \text{ V}$ , AV, grâce à l'interface états de réponse, est mesurable, ce qui est pas le cas pour les tensions de polarisation supérieure à  $-6 \text{ V}$  où AV est plus mesurable, car les pièges ne peuvent pas suivre le balayage de polarisation taux, tel que discuté plus tard.

Fig.4.24 présente le profil de distribution d'énergie des états d'interface à l'intérieur de la largeur de bande du diamant, où les bords valence et bande de conduction sont représentés. Comme l'a observé, la densité des états d'interface est aussi élevé que  $3 \text{ CE } 10^{13} \text{ cm}^{-2} \cdot \text{eV}^{-1}$  pour une énergie de piège correspondant à  $0,6 \text{ eV}$ . Cette énergie de piège est atteint pour une tension de polarisation de  $-8 \text{ V}$ . Si l'on suppose que la densité des atomes de la surface de  $8 \times 10^{14} \text{ atoms} \cdot \text{cm}^{-2}$  peut être répartie uniformément le long de la bande interdite diamant ( $E_g = 5,5 \text{ eV}$ ), la densité de  $1,5 \times 10^{14} \text{ cm}^{-2} \cdot \text{eV}^{-1}$  est calculé. Cette densité de l'interface indique D<sub>it</sub> représente 20% des liaisons insaturées des atomes de surface. D'autre part, lorsque l'on augmente la tension de polarisation, la

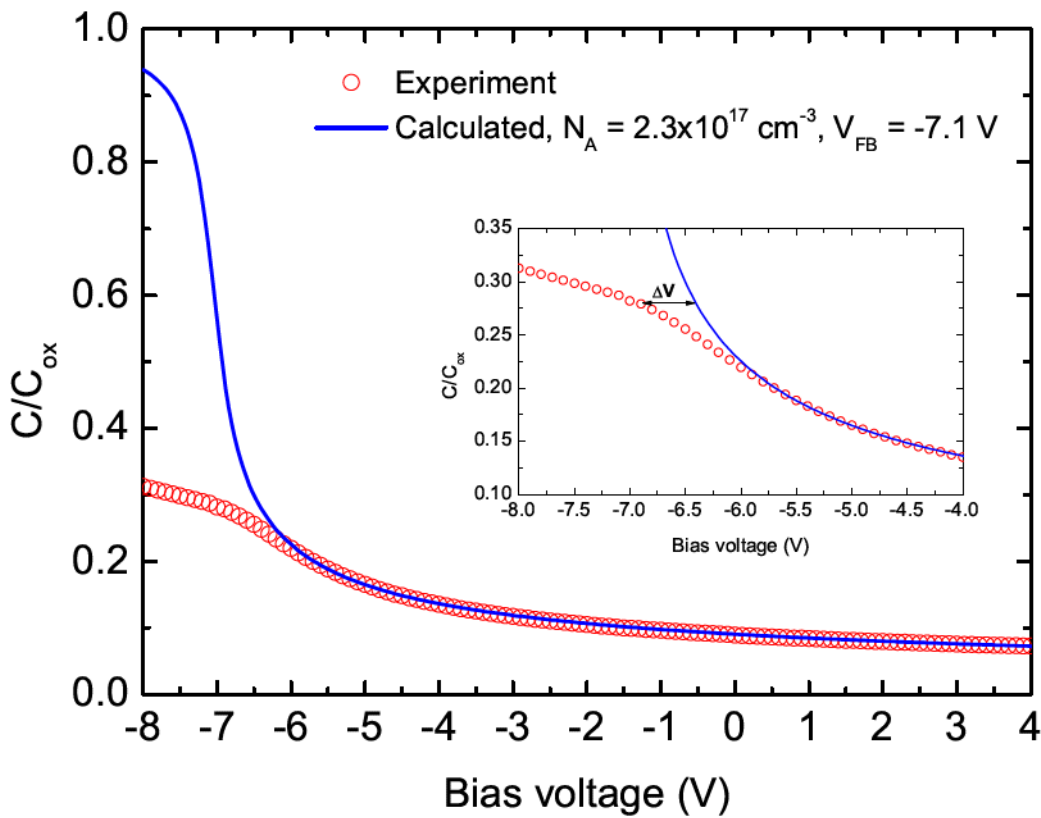


Figure 4.66: Normalized high frequency experimental  $C(V)$  curve (1 MHz) compared to the calculated ideal one with  $N_A = 2.3 \times 10^{17} \text{ cm}^{-3}$ ,  $N_D = 10^{16} \text{ cm}^{-3}$  and  $V_{FB} = -7.1 \text{ V}$ . The insert is a zoom in where  $\Delta V$  is indicated.

densité d'états d'interface diminue et devient négligeable pour les tensions de polarisation supérieure à  $-6 \text{ V}$  depuis le AV est pas plus mesurable.

Fig.4.68 montre la densité de courant mesurée en fonction de la tension de polarisation de grille  $J$  (V) à partir de  $83 \text{ K}$  à  $353 \text{ K}$  pour un contact de grille circulaire de  $150 \mu\text{m}$  de diamètre. Pour une tension de polarisation positive appliquée à l'électrode de grille, la MOSCAP est en épuisement et de la densité de courant est inférieure à la limite de détection (non représenté ici). Comme la polarisation de grille est réduite vers des valeurs plus négatives, la température ambiante augmente de densité de courant pour atteindre  $4 \times 10^{-1} \text{ A.cm}^{-2}$  à  $-8 \text{ V}$ .

Dans cette section, les propriétés électriques de la  $\text{Al}_2\text{O}_3 / \text{O-diamant}$  MOSCAP ont été étudiés. En particulier, la caractérisation des états d'interface utilisant à la fois la méthode de Terman et le procédé de conduction révélé la présence d'une forte densité de pièges d'interface qui empêche la MOSCAP pour atteindre le régime d'accumulation,

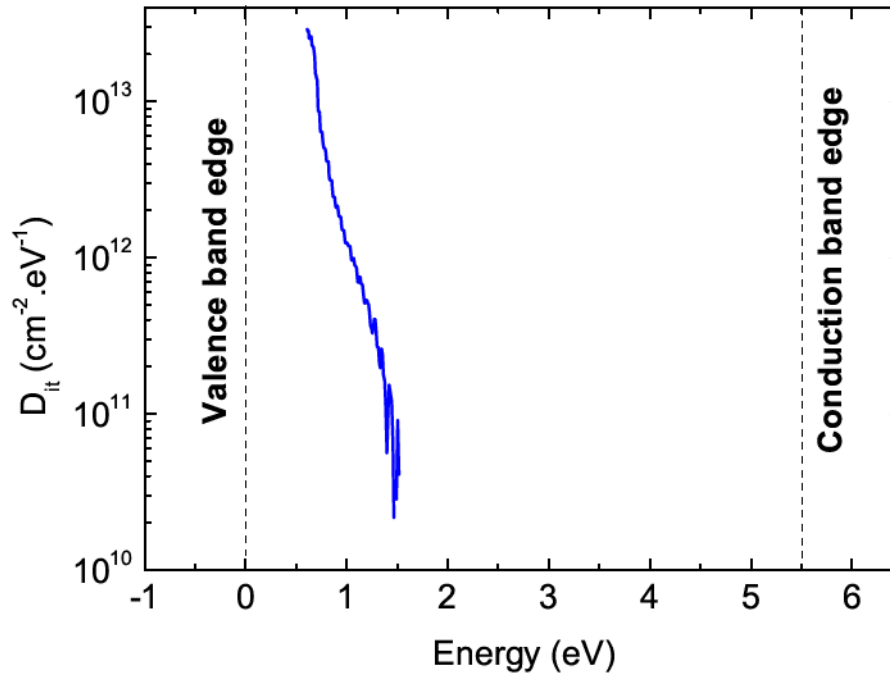


Figure 4.67: Interface states density as function of the energy, distributed inside the diamond band gap, extracted using Terman's method [Schroder 2006].

à savoir la densité élevée des pièges de l'interface provoque le piégeage du niveau de Fermi à la  $\text{Al}_2\text{O}_3$  / O-diamant interface. Néanmoins, il est démontré que l'appareil peut être utilisé dans l'épuisement et les régimes d'épuisement profondes. D'autre part, les courants de fuite observés lors de polarisation négative est appliquée à l'électrode de grille est expliqué par la présence de charges d'oxyde fixe qui participe à l'effet tunnel de trous à partir de la couche de diamant à l'électrode supérieure à travers ces pièges situés dans la bande interdite de la couche diélectrique. Cependant, discordance entre la densité de courant prédite et les données mesurées a été observée. Trou d'injection du type p + couche pourrait expliquer ce phénomène depuis le trou concentration dans la couche de type p est amené au-dessus de la concentration d'équilibre et peut influencer fortement sur la concentration du trou présent à l'interface [Muret 2015]. Afin d'améliorer la MOSCAP de diamant, effet d'un recuit thermique de la couche diélectrique en utilisant un gaz de formage (mélange de  $\text{H}_2$  et  $\text{N}_2$ ) et un traitement de surface différent y compris la terminaison de la surface du diamant pourrait être envisagée. Le contrôle de l'interface diélectrique / O-diamant est d'une grande importance afin de développer la prochaine production d'un MOSFET d'inversion. Une première tentative dans la fabrication de

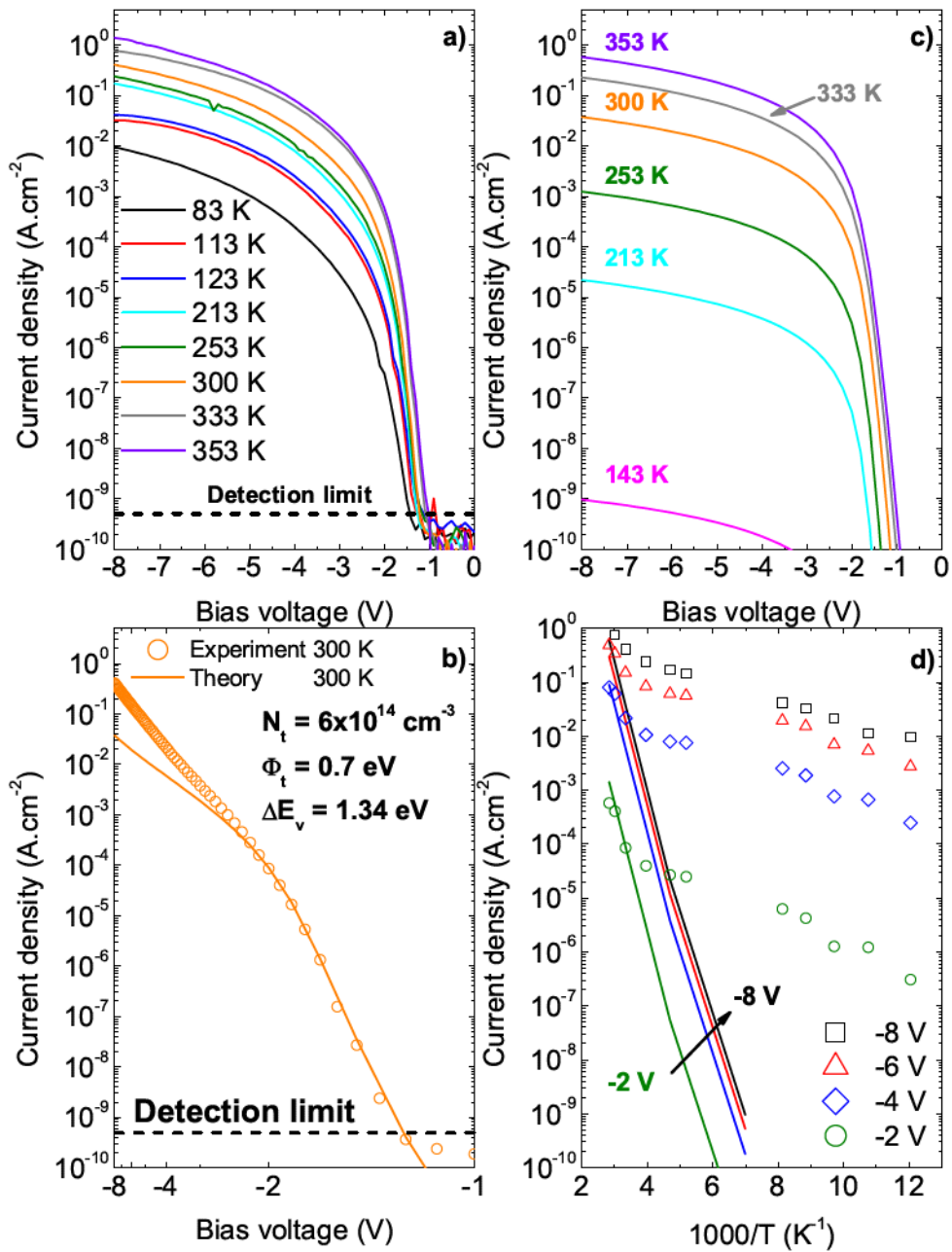
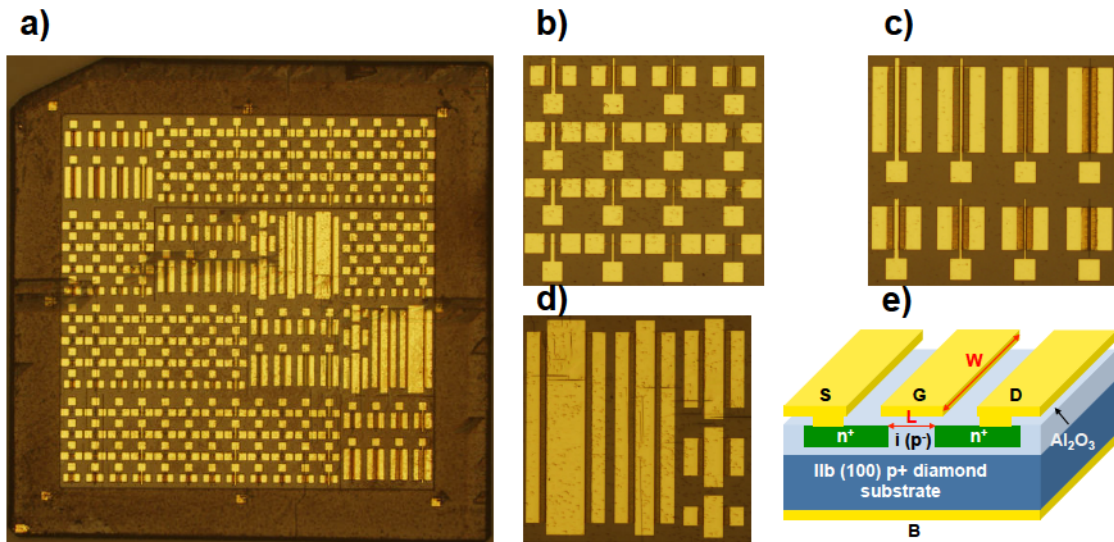


Figure 4.68: a) Experimental  $J(V)$  characteristics measured at various temperatures for a circular contact with diameter of  $150 \mu\text{m}$ . b) Calculated  $J(V)$  characteristics at various temperatures using the TAT model described by Eq.4.21. As evidenced the temperature dependence is stronger for the theoretical  $J(V)$  than for the experimental one.

diamants inversion MOSFET a été effectuée récemment au Japon et la caractérisation électrique sera discuté dans la prochaine section.

## Caractérisation d'un MOSFET

La Fig.4.32 représente la structure de l'échantillon caractérisé.



*Figure 4.69:* a) Optical microscope view of the MOSFET sample and b), c) and d) shows a close up on the three different geometries referred to as A, B and C respectively. e) Schematic 3D view. The MOSFET is composed of 4 terminals, the Source *S*, the Drain *D*, the Gate *G* and the Back gate *B*. The channel length *L* and width *W* are also indicated.

Plusieurs dispositifs ont été caractérisés, mais aucun d'entre eux ont présenté les propriétés souhaitées. Comme en témoigne Fig.4.44, les caractéristiques  $(V) C$  étaient très dépendants d'un périphérique à un autre. Comme l'a observé, la propriété  $C(V)$  montre un changement non reproductible, différent pour trois contacts de grille différentes. Ceci est probablement dû à la présence de défauts d'homogénéité de l' $Al_2O_3 / O$ -diamant qualité de l'interface et / ou de la qualité de la couche d' $Al_2O_3$  déposée par ALD à 573 K. L'hystérésis est observé pour tous les dispositifs testés indiquant la présence de charges mobiles dans la couche diélectrique. Ces frais pourraient détériorer les propriétés électriques du MOSFET. Comme le montrent les résultats de simulation du chapitre 3, cette structure n'a pas encore été optimisée. Toutefois, l'amélioration de la géométrie, le niveau de la dérive de dopage de la couche avec l'épaisseur d'oxyde ouvrirait la voie vers un MOSFET d'inversion fiable.

Un MOSFET à canal de type n est fabriqué pour la première fois et étudié ses propriétés électriques en fonction de la capacité par rapport à la tension et les mesures de tension de contre actuels. Les propriétés du contact de grille  $C(V)$  a révélé que les

régimes d'accumulation et d'épuisement ont été atteints. Une différence dans le régime de l'épuisement profond entre les caractéristiques idéales et expérimentales a été observée avec l'origine pas encore compris. Plusieurs contacts de grille plus ont été étudiés et on a observé de grandes inhomogénéités, éventuellement provenant d'inhomogénéités dans le joint terminaison de la surface du diamant. La caractérisation  $I(V)$  de l'opération de MOSFET n'a pas conduit au comportement attendu. Même lorsque l'on mesure les propriétés de MOSFET à haute température (573 K), seule une très faible résistivité modulation du canal source-drain était observable. Néanmoins, cette première tentative est très prometteuse pour le développement des prochains appareils électriques à base de diamant de nouvelle génération.

Dans ce chapitre, les étapes de fabrication des MOSCAPs de diamant pseudo-verticale ont été présentées. Les croissances ont consisté en une couche de type p déposée sur un type p + couche de diamant lui-même déposée sur un HPHT Ib (001) du substrat de diamant. La structure mesa a été définie par une gravure ICP utilisant un plasma d'oxygène. Ensuite, les contacts ohmiques sont directement déposés sur la couche du type p + du diamant. La terminaison de l'oxygène de la surface du diamant a été réalisée en utilisant une lumière dans l'ultraviolet lointain / traitement à l'ozone et la couche de  $Al_2O_3$  a été déposée par ALD à une température de 250 °C. La structure de dispositif autorisée pour déterminer la constante diélectrique relative de l' $Al_2O_3$  est 9,5. Ainsi, la capacité prévue de l'MOSCAP peut être estimée, constatant un écart qui a été étudié en termes de capacité et de la conductance mesurées. Plus précisément, en utilisant la méthode de Terman, une haute densité d'états d'interface a été déterminée, résultant du niveau de Fermi à l'interface empêchant d'atteindre le régime d'accumulation. Le niveau de Fermi d'ancrage a en outre été mis en évidence par la méthode de la conductance. Une enquête plus approfondie du comportement de MOSCAP utilisant un recuit thermique et / ou la passivation de surface différente aiderait à déterminer le meilleur traitement de l'appareil pour fabriquer un transistor MOS à contact de grille fiable pour le diamant MOSFET de nouvelle génération. En outre, un piège assisté tunnel de trous de la couche de diamant au contact de grille a été démontré en utilisant des mesures de tension de contre-courants à température différente. L'écart entre le comportement attendu et les caractéristiques expérimentales est attribué à la présence d'injection de trous à partir de la couche de type p + à la couche de type p. D'autres investigations utilisant une épaisse couche de diamant de type p pourraient clarifier ce point. D'autre part, la mesure des

rayons X spectroscopie photoélectronique des spectres al mugissaient d'établir la configuration d'interface de bande d'énergie de l'hétérojonction Al<sub>2</sub>O<sub>3</sub> / O-diamant. Cette analyse a révélé une configuration de type II de la bande en opposition à la configuration de bande de type I déterminé pour l'hétérojonction Al<sub>2</sub>O<sub>3</sub> / H-diamant. En particulier, une bande de valence décalage de 1,34 eV a été déterminée. Cette valeur pourrait être approprié pour de type p inversion diamant MOSFET canal depuis la barrière de trou est suffisante pour empêcher l'injection dans le contact de grille. Enfin, la réalisation expérimentale d'un MOSFET à canal de type n a été réalisée pour la première fois et sa caractérisation électrique a été effectuée pendant quatre mois restent dans l'AIST (Tsukuba, Japon). Malheureusement cette première tentative a échoué car le fonctionnement de MOSFET pas pu être atteint. Néanmoins, les contacts de grille ont montré de bonnes propriétés électriques, à savoir l'accumulation de régimes d'épuisement ont été atteints dans quelques fenêtre de polarisation volts. Ce travail de pionnier est très prometteur et ouvre la voie vers la réalisation de la prochaine génération de diamant MOSFET pour des applications d'électronique de puissance.

## Conclusions générales

Cette thèse a été axées autour de deux objectifs principaux. L'un est le développement d'outils de simulation prenant en compte les propriétés physiques de diamant spécifiques, visant à anticiper l'architecture et la conception de dispositifs de puissance de diamant de la prochaine génération. Plus précisément, les propriétés physiques du diamant ont été mises en œuvre dans un logiciel basé éléments finis (TCAD Silvaco), afin de reproduire les caractéristiques électriques d'une jonction pn diamant. Ici, jusqu'à des modèles de mobilité de date, les coefficients d'ionisation par impact et la mobilité trémie de ping ont été mis en œuvre. En outre, un point important était d'examiner l'effet de la génération-recombinaison (GR) les modèles sur les propriétés électriques des dispositifs de diamant. Comme les paramètres et les modèles GR ne sont ni bien connues ni comprises dans le diamant, l'influence de Auger et modèles Shockley-Read-Hall GR a été étudiée. Un premier ensemble de paramètres a été proposée, mais les efforts doivent être continué sur ce sujet. Concernant les caractéristiques courant-tension, des divergences ont été observées entre le tal expérimentation et les résultats simulés. Cela signifie que des facteurs tels que inconsidérées résistivité de contact, support tunnel défauts cristallins

et contribuent aux caractéristiques  $I(V)$  de jonctions pn diamant. Toutefois, selon le coefficient d'ionisation par impact mises en oeuvre, la tension de claquage de 225 V, ce qui correspond à un domaine de 7,7-1 MV.cm ventilation a été prévue. En outre, les paramètres mis en oeuvre ont été utilisés pour étudier la conception d'un MOSFET de diamant. Plus précisément, on a étudié l'effet du canal dopage concentration, de la température et de l'épaisseur d'oxyde sur les propriétés électriques simulées. On montre que cette conception particulière de la résistance spécifique en est pas optimisées par rapport à la limite de silicium. Il est conclu que les architectures spécifiques doivent être développées pour profiter pleinement de la forte potentialité de diamant pour des applications de dispositifs de puissance. Des efforts supplémentaires sont nécessaires, tant sur le expérimentale et sur les aspects numériques de développer des outils de simulation robustes qui prennent en compte les spécificités de diamant pour la conception des futurs dispositifs de puissance de diamant. D'autre part, l'étude de diamant condensateurs métal-oxyde-semi-conducteur (MOSCAP) à l'aide d'oxygène surface à terminaison ouvre la voie à la fabrication d'un champ MOS transistor à effet (MOSFET). En particulier, la configuration de la bande interfaciale de l' $Al_2O_3 / O$ -diamant a été déduite à partir de rayons X spectroscopie photoélectronique (XPS). Ainsi, un décalage de bande de valence de  $1,34 \pm 0,2$  eV a été déterminée. En supposant une bande interdite de  $Al_2O_3$  de 7,4 eV, la bande de conduction de décalage a été calculée à  $0,56 \pm 0,2$  eV. La conclusion de cette étude est que l' $Al_2O_3 / O$ -diamant pourrait être approprié pour développer un mode MOSFET d'inversion en utilisant un canal de type p. Depuis 2011, l'Institut de l'anguille N est impliqué dans le développement de MOSCAP utilisant  $Al_2O_3$  comme un diélectrique de grille. Dans ce travail, un nouveau design a été développé. Un MOSCAP pseudo-verticale est ainsi fabriquée, qui est composé d'une couche de diamant de type p augmenté au-dessus d'une couche de diamant de type P +. Le rôle de la plus tard est de réduire la résistance en série avec la résistance de contact. En effet, à l'aide de plasma à couplage inductif (ICP) gravure pour définir une structure mesa, les contacts ohmiques sont directement déposés sur la couche du type p + du diamant. Le dispositif final est obtenu en plusieurs étapes de lithographie et de dépôt de métal. Les propriétés électriques de l'appareil ont été étudiés en termes de capacité-tension et de courant-tension mesures. Comme le dispositif comprend MOSCAP et le condensateur isolant-métal-métal (MIMCAP), l'oxyde constante diélectrique relative a été extrait. Ensuite, la capacité d'accumulation prévue de l'MOSCAP ont été calculés. Cependant, nous avons observé écart entre la valeur mesurée et les valeurs attendues. Ainsi, la qualité de

l'interface a été étudiée en utilisant la capacité et l'analyse de la conductance des états d'interface. La conclusion est que Fermi niveau brochage est responsable de la comportement observé, empêchant l'appareil de fonctionner en régime d'accumulation. En outre, la densité des états haut de l'interface est observée près du bord de la bande de valence. Cette interface États pourraient prenant leur source de la présence de liaisons carbone insaturés à l'interface Al<sub>2</sub>O<sub>3</sub> / O-diamant. Cependant, aucun niveau de Fermi brochage a été observée chez épuisement ou en mode d'appauvrissement de profondeur, ce qui permet le fonctionnement en mode d'inversion. Al<sub>2</sub>O<sub>3</sub> / O-diamant MOSCAP I (V) a été réalisée à différentes températures. L'origine des courants de fuite dans des conditions négatives de tension de polarisation ont été étudiés en termes de piège dépendant de la température tunnel assistée. Ce procédé en deux étapes, originaires de la présence de pièges dans la couche diélectrique, peut être à l'origine de courants de fuite. Cependant, l'effet du niveau brochage Fermi n'a pas été prise en compte lors de la modèle. Cela pourrait être un indice pour expliquer la différence quantitative entre l'expérimental et théorique I (V) dans le régime de polarisation négative élevée. En outre, la présence du type p + couche enterrée pourrait jouer un rôle dans la quantité de trou disponible à l'Al<sub>2</sub>O<sub>3</sub> d'interface / O-diamant depuis survient injection de trous. Traitements de surface spécifiques (comparaison entre la lumière VUV / traitement à l'ozone et le traitement à l'acide chaud par exemple) et recuit diélectrique sous différentes atmosphères pourraient aider à améliorer la qualité de l'interface et de la qualité de la couche diélectrique.

Enfin, un canal d'inversion MOSFET de type n a été fabriqué et caractérisé pour la première fois. Malgré le fait que le MOSFET ne montre pas des caractéristiques idéales, le contact de grille MOS montré raisonnablement bonnes propriétés. Ce premier essai démontrent que la fabrication d'un MOSFET de diamant est un problème technologique pas et est très prometteur pour le développement d'un MOSFET de puissance du diamant. Aussi, la prochaine étape pourrait être de développer un canal MOSFET de type p, puisque nous avons démontré que la configuration de la bande interfaciale est favorable pour le confinement des trous dans le diamant à l'Al<sub>2</sub>O<sub>3</sub> d'interface / O-diamant sans Fermi niveau brochage.



# Publications

## Metal oxide semiconductor structure using oxygen-terminated diamond

G. Chicot,<sup>1,a)</sup> A. Maréchal,<sup>1</sup> R. Motte,<sup>1</sup> P. Muret,<sup>1</sup> E. Gheeraert,<sup>1</sup> and J. Pernot<sup>1,2,b)</sup>

<sup>1</sup>Institut Néel, CNRS and Université Joseph Fourier, BP166, 38042 Grenoble Cedex 9, France

<sup>2</sup>Institut Universitaire de France, 103 boulevard Saint Michel, 75005 Paris, France

(Received 10 April 2013; accepted 5 June 2013; published online 19 June 2013)

Metal-oxide-semiconductor structures with aluminum oxide as insulator and *p*-type (100) mono-crystalline diamond as semiconductor have been fabricated and investigated by capacitance versus voltage and current versus voltage measurements. The aluminum oxide dielectric was deposited using low temperature atomic layer deposition on an oxygenated diamond surface. The capacitance voltage measurements demonstrate that accumulation, depletion, and deep depletion regimes can be controlled by the bias voltage, opening the route for diamond metal-oxide-semiconductor field effect transistor. A band diagram is proposed and discussed. © 2013 AIP Publishing LLC. [<http://dx.doi.org/10.1063/1.4811668>]

The high breakdown electric field, the elevated mobility, and the outstanding thermal conductivity make diamond the ultimate semiconductor for high power and high frequency applications. Intensive works and important progresses have been done recently in the field of substrate fabrication, epilayer growth, and doping control, but the main problem to make efficient power devices is the large ionization energies of the acceptor and donor impurities: 380 meV for the boron acceptor and 570 meV for the phosphorus donor. The ionization rate of dopants at room temperature is low and the resulting high series resistance of the active layer is not compatible with some device operation (like metal semiconductor field effect transistor (MESFET), bipolar junction transistor (BJT), or junction field effect transistor (JFET)).

In order to overcome this problem, solutions based on two dimensional (2-D) hole gas are under investigation: (i) H-terminated diamond field effect transistor (FET) using hole accumulation layer.<sup>1–3</sup> Such transistors demonstrate high frequency operation but deteriorate under high temperature conditions. (ii) Boron  $\delta$ -FET consisting on a thin heavily doped (metallic) layer between two intrinsic layers resulting theoretically in high mobility (due to delocalisation of carrier away from ionized impurities induced by confinement). However, obtaining a very thin layer<sup>4</sup> (<2 nm needed) is a technological challenge. Delta layers thinner than 2 nm are reported<sup>5</sup> but did not show neither quantum confinement nor enhancement of the mobility, which is yet too low for high frequency applications. (iii) Diamond/nitride heterojunctions FET<sup>6</sup> has been recently proposed and their electronic properties are under investigation at this moment. Concerning more conventional semiconductor devices, the Si metal oxide semiconductor field effect transistor (MOSFET) is ubiquitous in digital and analog integrated electronic systems. The conducting or insulating behavior of the MOSFET is based on the electrostatic control of the band curvature at the oxide/semiconductor interface. Unfortunately, the physical properties of Si semiconductor do not allow to build efficient MOSFET for power electronics applications (generally insulated gate bipolar transistor is preferred but also limited to

4 kV). MOSFET based on other semiconductors, like III-V compounds or SiC, are progressing but the performances of such devices are not competitive with Si devices and anyway will be always lower than that expected for diamond based MOSFET.<sup>7</sup> The main problem to fabricate a MOS structure is to achieve the semiconductor oxide interface with a sufficiently low interface states density. In that case, the different regimes of the MOS can be controlled: accumulation of majority carriers, depletion, deep depletion, or inversion of carrier (minority carrier density larger than majority carrier density at the interface). In most cases and contrary to the Si/Oxide interface, the too large density of interface states within the gap are charging under bias voltage, and the breakdown field of the oxide is reached before deep depletion or inversion regimes. Also, previous MOS structures performed on diamond<sup>1–3,8</sup> exhibited accumulation regime but no deep depletion or inversion regimes. Recent works reported investigation of Al<sub>2</sub>O<sub>3</sub> deposited by Atomic Layer Deposition (ALD) on hydrogen-terminated diamond to stabilize<sup>9</sup> or to study the band offsets<sup>10</sup> related to the hydrogen 2-D gas. MOS structures on diamond using high dielectric constant Ta<sub>2</sub>O<sub>5</sub> oxides were also reported<sup>11</sup> but did not show the deep depletion regime. In our case, in order to reach deep depletion or inversion regimes at the interface of Al<sub>2</sub>O<sub>3</sub>/diamond, we introduce an approach combining an oxygen-terminated diamond with low temperature ALD.<sup>12,13</sup> Using this process, we demonstrate that such MOS capacitor can undergo accumulation, depletion, and deep depletion. The control of the interface regimes reported in this work opens the route for diamond MOSFET and more generally for diamond based electronics. This letter is organized as follows: the first part describes the experimental details and the diamond MOS fabrication using ALD technique for oxide deposition. In the second part, the capacitance measurements are detailed and analyzed in terms of control of the different regimes using the gate metal electrode.

The five structures investigated in this work consist of a stack of Al/Al<sub>2</sub>O<sub>3</sub> gate electrode deposited on a boron-doped epitaxial diamond layer grown in a microwave plasma assisted chemical vapor deposition (MPCVD) reactor on Ib high pressure high temperature (HPHT) (100) diamond

<sup>a)</sup>Electronic mail: [gauthier.chicot@grenoble.cnrs.fr](mailto:gauthier.chicot@grenoble.cnrs.fr)

<sup>b)</sup>Electronic mail: [julien.pernot@grenoble.cnrs.fr](mailto:julien.pernot@grenoble.cnrs.fr)

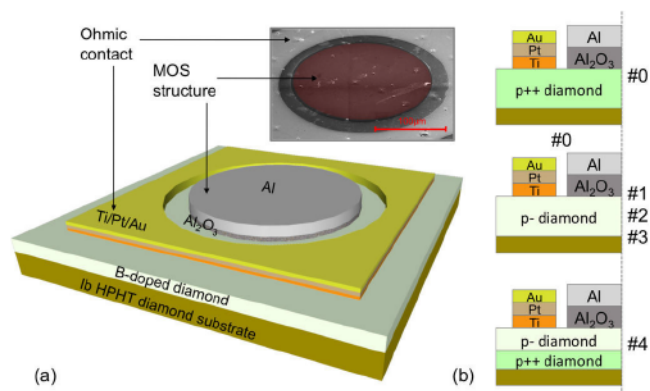


FIG. 1. (a) Schematic of the diamond metal oxide semiconductor structure and SEM image and (b) detailed stacks of each sample.

substrate. A schematic picture of the structure is shown in Fig. 1(a). Sample #0 is composed of a heavily doped diamond layer (named  $p++$  and with boron concentration over the metal insulator transition) in order to fabricate Metal Insulator Metal (MIM) structure. The four other samples #1, #2, #3, and #4 are aimed to be MOS structures. They consist of B-doped diamond layers with a boron concentration of about  $10^{17} \text{ cm}^{-3}$ . The deposition was performed at  $910^\circ\text{C}$  with  $\text{CH}_4/\text{H}_2 = 2\%$  and  $\text{B}/\text{C} = 2 \text{ ppm}$ . In sample #4, a heavily doped layer was grown between the substrate and  $p$ -layer with the same technique but with  $\text{CH}_4/\text{H}_2 = 4\%$ ,  $\text{B}/\text{C} = 1200 \text{ ppm}$  at  $830^\circ\text{C}$ . On each, an ohmic contact (Ti/Pt/Au annealed at  $750^\circ\text{C}$  under high vacuum) was evaporated directly on the epitaxial layer to act as reference contact (see Fig. 1(b)) for capacitance measurement. Photolithography process was used in order to selectively deposit the dielectric oxide. Before that step, diamond surface oxygenation has been performed by two techniques: (i) for samples #0, #1, #3, #4 by deep UV ozone treatment and<sup>14</sup> (ii) for sample #2 by oxygen RF plasma treatment.

Then, the 10 nm for sample #1 and 20 nm for #0, #2, #3, and #4 of  $\text{Al}_2\text{O}_3$  dielectric oxide have been deposited by ALD. In order to preserve the lithography resist, the ALD oxide has been deposited at low temperature ( $100^\circ\text{C}$ ). The ALD system used in the present experiments was Savannah 100 from Cambridge NanoTech. The precursor used was trimethylaluminum (TMA), and the oxidant was  $\text{H}_2\text{O}$ . Using the same window in resist, the dielectric has been covered by a 100 nm thick aluminum metal using electron beam evaporator. After resist removing, the electrical properties of the MOS capacitances have been measured using a Keithley 6517B source-electrometer apparatus for the static current/voltage  $I(V)$  characteristics and a Agilent E4980A Precision LCR Meter for the capacitance/voltage  $C(V)$  measurements. Frequency dependent capacitance measurements have been performed with *a.c.* signal frequency ranging from 100 Hz to 2 MHz and typical amplitude of 50 mV. Nyquist plots have been performed (i) to determine the series and parallel resistances of the stack and (ii) to find the most favorable frequency to measure the imaginary part of the total impedance (where the imaginary part/real part ratio is the highest) in order to determine more accurately the capacitance. The measurements reported in Fig. 2 were done with frequencies in the range of 50 kHz to 200 kHz.

Sample #0 is a MIM structure while the four other samples are MOS structures. In samples #1, #2, and #3, different oxide thicknesses and surface treatments were evaluated (see Table I). In sample #3 (in regards of #1 and #2), the quality of the  $p$ -diamond layer has been improved, principally by reducing its thickness. Sample #4 is the same as #3 with an additional  $p++$  buried layer in order to reduce the series resistance and simplify  $C(V)$  measurements and their interpretation. Thickness and doping of each sample are summarized in Table I.

First of all, using the MIM structure of sample #0 made of a stack of metallic diamond,  $\text{Al}_2\text{O}_3$ , and aluminum metal, the oxide properties were investigated.  $\text{Al}_2\text{O}_3$  oxide thickness value  $d_{ox}$  was measured by ellipsometry and found in good agreement with the targeted values reported in Table I.

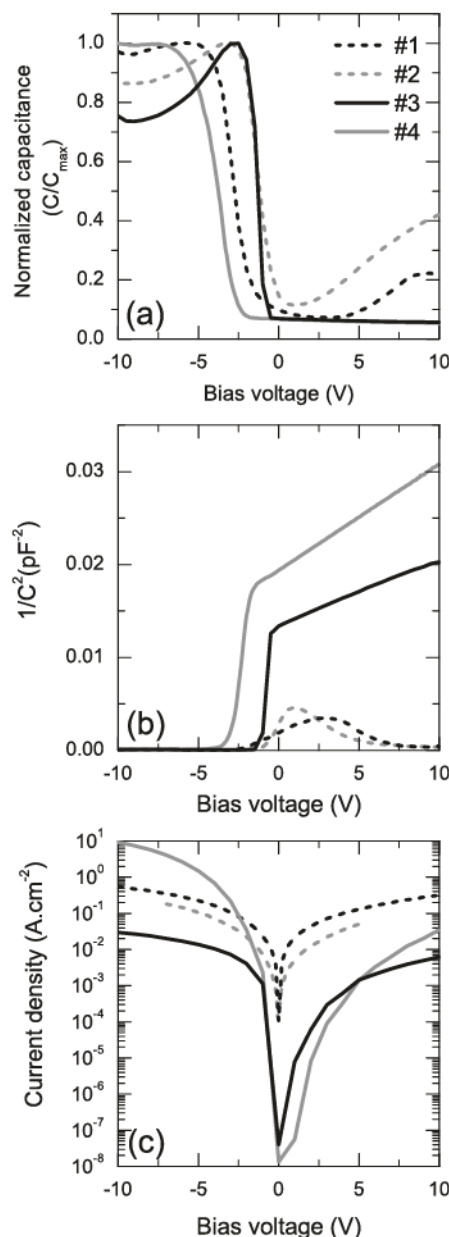


FIG. 2. (a) Capacitance  $C/C_{max}$  versus voltage measurement of the diamond MOS structures, (b)  $1/C^2$  versus voltage which enables us to determine the doping of diamond in case of deep depletion regime (samples #3 and #4) from the slope of the straight line for positive voltage, and (c) static current versus voltage of samples #1, #2, #3, and #4.

TABLE I. Physical properties of metal/oxide/diamond structures.

Samples	Doping (cm <sup>-3</sup> )	d <sub>B-diamond</sub> (nm)	Surface treatment	d <sub>Al<sub>2</sub>O<sub>3</sub></sub> (nm)
#0	>5 × 10 <sup>20a</sup>	50 <sup>a</sup>	DUV O <sub>3</sub>	20 <sup>a</sup>
#1	≈3 × 10 <sup>17b</sup>	1900 <sup>b</sup>	DUV O <sub>3</sub>	10 <sup>a</sup>
#2	≈3 × 10 <sup>17b</sup>	1900 <sup>b</sup>	O <sub>2</sub> plasma	20 <sup>a</sup>
#3	3.6 × 10 <sup>17c</sup>	300 <sup>a</sup>	DUV O <sub>3</sub>	20 <sup>a</sup>
#4	2.2 × 10 <sup>17c</sup> />5 × 10 <sup>20a</sup>	300 <sup>a</sup> /150 <sup>a</sup>	DUV O <sub>3</sub>	20 <sup>a</sup>

<sup>a</sup>Estimated from growth conditions.

<sup>b</sup>Estimated from SIMS measurements.

<sup>c</sup>Measured by C(V) measurements.

The capacitance was measured and found to be constant versus applied voltage (−10 V to 10 V) and versus frequency (100 Hz to 2 MHz). Due to the MIM structure, the resultant capacitance of this stack is equal to the oxide capacitance  $C_{ox}$  given by

$$C_{ox} = \frac{\epsilon_0 \epsilon_{ox} S}{d_{ox}}, \quad (1)$$

where  $\epsilon_0$  is the vacuum permittivity,  $\epsilon_{ox}$  is the relative permittivity of the oxide, and  $S$  is the MOS capacitor area. The measured value of capacitance was 20% lower than the value expected if calculated with the Al<sub>2</sub>O<sub>3</sub> relative permittivity given in literature<sup>12</sup> for similar deposition process (i.e., low temperature ALD except the Si substrate).

In samples #1 and #2, different regimes can be observed on C(V) measurements (see Fig. 2(a)). For negative voltage ( $V \leq -5$  V for #1 and  $V \leq -3$  V for #2), the holes accumulation is observed. This regime is characterized by an almost flat capacitance theoretically equal to that of the oxide capacitance  $C_{ox}$  (Eq. (1)) because the stack is like a planar capacitance (see Fig. 3(a)) composed of the oxide layer in between two electrodes (Al and diamond). But experimental capacitances in the accumulation regime take values above or below  $C_{ox}$  according to the measurement frequency. A three elements circuit has been used to introduce the series resistance effect on the measurement. Indeed, in the ideal case, the capacitance is considered in parallel to the resistance of the oxide (leakage current through the oxide) leading to a

two elements circuits. In our structure, the series resistance of the *p*-type diamond layer cannot be neglected and must be considered in series with the two elements impedance. Even with a two frequency correction method<sup>15</sup> applied to this three element circuits, this frequency dispersion still exists showing that this unexpected behaviour cannot be exclusively attributed to a non negligible series resistance. An additional impedance due to interface states or/and deep levels in the diamond layer close to the Al<sub>2</sub>O<sub>3</sub>/diamond interface (compensating levels in the first hundred nanometers under Al<sub>2</sub>O<sub>3</sub>/diamond interface in a diamond growth without oxygen in the gas phase<sup>16–18</sup>) could be responsible of the phenomenon. While the voltage increases, a space charge region begins to appear in the semiconductor (Fig. 3(c)), and the resultant capacitance is now characteristic of the capacitance measured in accumulation in series with the capacitance of the space charge region resulting in a decrease of the total capacitance. Then, for voltage increasing in positive values ( $V \geq 3$  V for #1 and  $V \geq 2$  V for #2), the capacitance starts to increase again. Usually, an increase in capacitance in this voltage range is characteristic of the strong inversion regime where majority carriers type is locally (near oxide/semiconductor interface) inverted, meaning that electron concentration at the oxide/diamond interface is larger than the hole density in *p*-type diamond region. This regime needs a minority carriers (here electrons) generation mechanism to be observed. Minority carriers can be provided by thermal or optical generation of electron-hole pairs in the neutral part of the semiconductor but frequency of the *a.c* signal used to measured capacitance must be sufficiently low to be comparable to the inverse time constant related to the generation mechanism (approximate maximum value of 10<sup>−20</sup> s<sup>−1</sup> for a mid gap trap level) in order that the charges could follow this *a.c* signal. In our case, no optical excitation was used and the frequency measurement is too high for thermal generation. Diamond *p*-layer of these two samples shows a large amount of defects such as hillocks (due to the large thickness of the layer), which are generally going through the whole depth of the layer. A mechanism providing electrons from neutral regions through these defects up to the oxide/semiconductor interface could be responsible of this electron generation. However, a measurement artifact due to the high

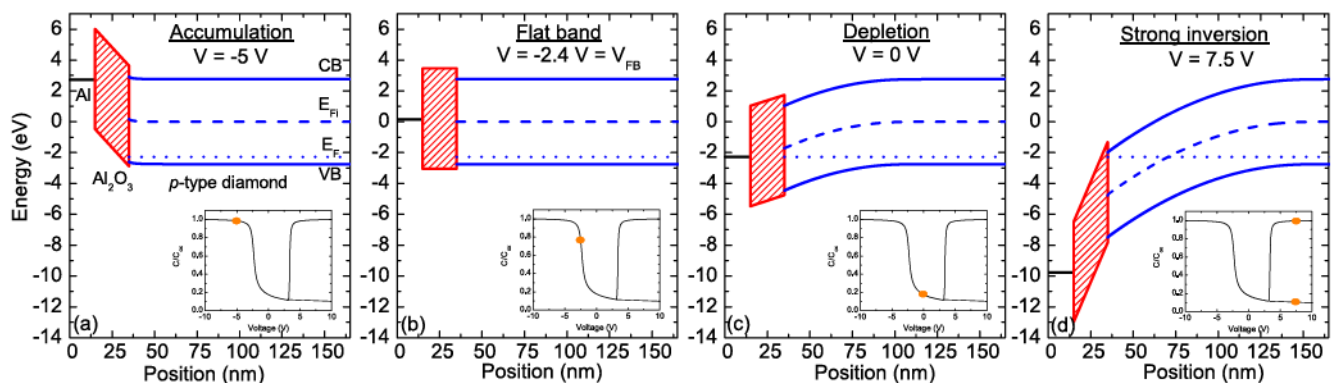


FIG. 3. Band diagram of a theoretical diamond metal oxide at different applied bias voltages with an oxide thickness of 20 nm, a *p*-type diamond doped at  $2.2 \times 10^{17}$  cm<sup>−3</sup>, an affinity of O-terminated diamond of 1.7 eV, and an Al<sub>2</sub>O<sub>3</sub> gap of 6.5 eV. The schematic band diagrams represent (a) the accumulation regime for  $V = -5$  V, (b) the flat band regime for  $V = -2.4$  V, (c) the depletion regime for  $V = 0$  V, and (d) the inversion regime for  $V = 7.5$  V. The inset in each band diagram shows the corresponding capacitance versus voltage measurements (inversion and deep depletion are both plotted).

oxide leakage current or an impedance due to deep levels (as suggested above) cannot be discarded. In order to clarify this point, samples #3 and #4 were fabricated. Diamond layers are thinner, contain less defects, and in sample #4 a buried  $p++$  layer was added in order to reduce the series resistance and avoid measurement artifacts. For these two samples, the hole accumulation (with some frequency dispersion) and depletion are also observable like in samples #1 and #2, but instead of increasing again in the positive voltage range, the capacitance continues to decrease. This decrease is typical of the deep depletion regime. In fact, the  $1/C^2$  versus voltage plot (see Fig. 2(b)) in this voltage range ( $-2\text{ V} \leq V \leq 10\text{ V}$ ) is linear and typical of the depletion of an homogeneous doped semiconductor over the depth. By applying a linear fit to this part, the effective doping of the  $p$ -diamond can be deduced from the slope for these two samples and are  $3.6 \times 10^{17}\text{ cm}^{-3}$  for sample #3 and  $2.2 \times 10^{17}\text{ cm}^{-3}$  for sample #4. These values are consistent with SIMS measurement performed on a similar sample where the boron doping level was measured between  $2 \times 10^{17}\text{ cm}^{-3}$  and  $5 \times 10^{17}\text{ cm}^{-3}$  over the whole depth of the layer ( $1.8\text{ }\mu\text{m}$ ). The good agreement between  $B$ -density determined by  $1/C^2$  and SIMS confirmed that the whole area of the MOS capacitor is active. Moreover, the observation of a deep depletion regime is consistent with the frequency range used for measurement.

Static  $I(V)$  measurements were also performed on these four MOS structures. Surprisingly for a stack containing an insulating layer, the current density is quite high as it can be seen in Fig. 2(c). Moreover, the  $I(V)$  characteristics of samples #1 and #2 are symmetrical while those of samples #3 and #4 are not with more current flowing in the negative voltage (holes accumulation) than in positive voltage (deep depletion). These observations could be related to the large range of the  $\text{Al}_2\text{O}_3$  band gap values  $E_g$  reported in literature: between  $5.4\text{ eV}$  and  $8.8\text{ eV}$ .<sup>19–23</sup> More precisely,  $E_g = 6.7 \pm 0.2\text{ eV}$  (Refs. 19 and 23) for ALD deposited  $\text{Al}_2\text{O}_3$  and even smaller if deposited by other techniques such as e-beam evaporation and spray pyrolysis method ( $E_g = 5.40\text{--}5.55\text{ eV}$  (Ref. 20)). Diamond oxygenated surface electronic affinity is reported between  $1.0\text{ eV}$  and  $1.7\text{ eV}$  (Refs. 24–26). In Fig. 3, theoretical band diagrams are plotted<sup>27</sup> at different applied voltages taking a band gap of  $6.5\text{ eV}$  for  $\text{Al}_2\text{O}_3$ , electronic affinity of  $1.7\text{ eV}$  for oxygenated diamond, and  $2.2 \times 10^{17}\text{ cm}^{-3}$  for  $B$ -doping. As shown, the barrier for holes is very low ( $\approx 0.4\text{ eV}$ ) and could be inexistent if somewhat a smaller  $\text{Al}_2\text{O}_3$  gap value or/and a little bit higher diamond affinity was considered. In that case, we expect a rectifier behavior with a high current limited by the diamond series resistance (and maybe also the contact resistance of the ohmic contact) for  $V < 0\text{ V}$  and a blocking regime for  $V > 0\text{ V}$  as observed for samples #3 and #4. Due to the much lower series resistance resulting from the  $p++$  buried layer in sample #4, the current density in accumulation is higher in comparison to other samples. Moreover, for samples #3 and #4, the current is lower under positive voltage than under the negative ones. Assuming a very small barrier for holes (if any) when the structure is in deep depletion, the current is only limited by the insulating space charge region. On the contrary, for samples #1 and #2, the almost symmetrical current may be due to a parallel leakage

path inside the depletion zone, as previously invoked to explain the capacitance anomalies.

Two different surface treatments (see Table I: DUV  $\text{O}_3$  and  $\text{O}_2$  plasma) to oxidize the diamond surface were tested. Samples #2 and #3 (different treatments with the same oxide deposition) show different behaviours, particularly in positive voltage. But as the crystalline quality of these two samples is different, no clear conclusion can be drawn about a possible influence of the surface treatment type.

The observation of a deep depletion regime in samples #3 and #4 opens the route for the fabrication of diamond MOSFET. In case of an  $n$ -MOSFET, the electrons needed to create inversion channel at the interface will be provided by  $n$ -type diamond boxes (source and drain). Such a transistor would be in off state because of a channel in depletion regime when no bias is applied to the gate (see band diagram in Fig. 3(c)), since the flat band voltage is not strongly negative ( $V_{FB} \approx -2.4\text{ V}$  in Fig. 3). This case is indeed achieved in samples #1, #2, and #3 as it can be seen on  $C(V)$  measurements in Fig. 2, while the more negative flat band voltage in sample #4, which might induce weak inversion, deserves future investigations. The on state (inversion) is expected to be reached for voltage larger than  $V \approx 2.5\text{ V}$ .

In this work, we demonstrated the fabrication of metal oxide diamond structures where different regimes are controlled by bias voltage: accumulation of holes, depletion, and deep depletion. The properties of the different samples have been discussed in order to compare the capacitance increase for positive applied voltages in two of the samples and the capacitance decrease induced by the deep depletion regime in two other ones. Electrical measurements enable us to investigate band offsets of the diamond MOS structures and show that even if no barrier exists for holes, a MOSFET using this stack would be operative since both off and on states could be reached.

The authors would like to thank L. Cagnon, Institut Néel, CNRS, for his expertise on ALD technique. Funding for this project was provided by grants from la Région Rhône-Alpes and from the Laboratoire d'excellence LANEF in Grenoble No. ANR-10-LABX-51-01.

<sup>1</sup>K. Hiram, S. Miyamoto, H. Matsudaira, K. Yamada, H. Kawarada, T. Chikyo, H. Koinuma, K. Hasegawa, and H. Umezawa, *Appl. Phys. Lett.* **88**, 112117 (2006).

<sup>2</sup>K. Hiram, K. Tsuge, S. Sato, T. Tsuno, Y. Jingu, S. Yamauchi, and H. Kawarada, *Appl. Phys. Express* **3**, 044001 (2010).

<sup>3</sup>M. Kasu, H. Sato, and K. Hiram, *Appl. Phys. Express* **5**, 025701 (2012).

<sup>4</sup>A. Fiori, J. Pemot, E. Gheeraert, and E. Bustarret, *Phys. Status Solidi A* **207**, 2084 (2010).

<sup>5</sup>G. Chicot, T. N. Tran Thi, A. Fiori, F. Jomard, E. Gheeraert, E. Bustarret, and J. Pemot, *Appl. Phys. Lett.* **101**, 162101 (2012).

<sup>6</sup>M. Imura, R. Hayakawa, E. Watanabe, M. Y. Liao, Y. Koide, and H. Amano, *Phys. Status Solidi RRL* **5**, 125 (2011).

<sup>7</sup>H. Umezawa, M. Nagase, Y. Kato, and S.-i. Shikata, *Diamond Relat. Mater.* **24**, 201 (2012).

<sup>8</sup>N. Kawakami, Y. Yokota, T. Tachibana, K. Hayashi, and K. Kobashi, *Diamond Relat. Mater.* **14**, 2015 (2005).

<sup>9</sup>A. Hiraiwa, A. Daicho, S. Kurihara, Y. Yokoyama, and H. Kawarada, *J. Appl. Phys.* **112**, 124504 (2012).

<sup>10</sup>J. W. Liu, M. Y. Liao, M. Imura, and Y. Koide, *Appl. Phys. Lett.* **101**, 252108 (2012).

<sup>11</sup>S. Cheng, L. Sang, M. Liao, J. Liu, M. Imura, H. Li, and Y. Koide, *Appl. Phys. Lett.* **101**, 232907 (2012).

<sup>12</sup>M. D. Groner, F. H. Fabreguette, J. W. Elam, and S. M. George, *Chem. Mater.* **16**, 639 (2004).

- <sup>13</sup>G. Chicot, A. Maréchal, P. Muret, and J. Pernot, Patent No. FR2012053026 (20 December 2011).
- <sup>14</sup>T. Teraji, S. Koizumi, and Y. Koide, *J. Appl. Phys.* **104**, 016104 (2008).
- <sup>15</sup>K. J. Yang and C. Hu, *IEEE Trans. Electron Devices* **46**, 1500 (1999).
- <sup>16</sup>P. Muret, J. Pernot, T. Teraji, and T. Ito, *Appl. Phys. Express* **1**, 035003 (2008).
- <sup>17</sup>P. Muret, J. Pernot, A. Kumar, L. Magaud, C. Mer-Calfati, and P. Bergonzo, *Phys. Rev. B* **81**, 235205 (2010).
- <sup>18</sup>P. Muret, P.-N. Volpe, J. Pernot, and F. Omnès, *Diamond Relat. Mater.* **20**, 722 (2011).
- <sup>19</sup>H. Nohira, W. Tsai, W. Besling, E. Young, J. Petry, T. Conard, W. Vandervorst, S. De Gendt, M. Heyns, J. Maes, and M. Tuominen, *J. Non-Cryst. Solids* **303**, 83 (2002).
- <sup>20</sup>K. S. Shamala, L. C. S. Murthy, and K. Narasimha Rao, *Mater. Sci. Eng., B* **106**, 269 (2004).
- <sup>21</sup>H. J. Kim, S. Y. No, D. Eom, and C. S. Hwang, *J. Korean Phys. Soc.* **49**, 1271 (2006).
- <sup>22</sup>R. H. French, *J. Am. Ceram. Soc.* **73**, 477 (1990).
- <sup>23</sup>M. L. Huang, Y. C. Chang, Y. H. Chang, T. D. Lin, J. Kwo, and M. Hong, *Appl. Phys. Lett.* **94**, 052106 (2009).
- <sup>24</sup>S. J. Sque, R. Jones, and P. R. Briddon, *Phys. Rev. B* **73**, 085313 (2006).
- <sup>25</sup>P. Muret and C. Saby, *Semicond. Sci. Technol.* **19**, 1 (2004).
- <sup>26</sup>F. Maier, J. Ristein, and L. Ley, *Phys. Rev. B* **64**, 165411 (2001).
- <sup>27</sup>R. G. Southwick, A. Sup, A. Jain, and W. B. Knowlton, *IEEE T. Device Mat. Re.* **11**, 236 (2011).

# Diamond bipolar device simulation

A. Maréchal *Univ. Grenoble Alpes, Inst NEEL, F-38042 Grenoble, France*

N. Rouger *Univ. Grenoble Alpes, G2Elab, F-38042 Grenoble*

J.-C. Créber *Univ. Grenoble Alpes, G2Elab, F-38042 Grenoble*

J. Pernot *Univ. Grenoble Alpes, Inst NEEL, F-38042 Grenoble, France*

S. Koizumi *Sensor Materials Center, National Institute for Materials Science, 1-1 Namiki, Tsukuba, Ibaraki 305-0044, Japan*

T. Teraji *Sensor Materials Center, National Institute for Materials Science, 1-1 Namiki, Tsukuba, Ibaraki 305-0044, Japan*

E. Gheeraert *Univ. Grenoble Alpes, Inst NEEL, F-38042 Grenoble, France*

**Abstract**—Diamond is not only known for being the hardest gemstone but also for being the semiconductor having the highest calculated figures of merit (FOM). This comes from the unique physical properties of this material. Thus, it is predicted that diamond should exceeds silicon carbide (SiC) and gallium nitride (GaN) in terms of low loss device and better compromises for on-state resistance versus breakdown voltage. However, in practice the applications of diamond devices are still limited and the performances are still not reaching the theoretical predictions. The question is then how to predict and evaluate diamond device performances themselves and in their environment. One of the possible answer is by using finite element based softwares. Few reports exist on unipolar diamond device modeling, and none on diamond bipolar device. The main limitations come from the lack of parameters implemented in the simulation tools together with the difficulties for modeling wide band gap semiconductor, i.e. extremely low carrier concentrations. In this study, we present the results on the first simulation of a diamond bipolar junction transistor electrical characteristics. The validation of the simulation is the first step towards the prediction of the architecture and behavior of future diamond devices.

**Index Terms**—Numerical simulation, TCAD software, diamond bipolar device

## I. INTRODUCTION

During the last two decades, achievements in controlling both growth quality and doping concentration in CVD diamond have led to the emergence of electronic devices, in particular the recent work on bipolar junction transistors have been fabricated either on (111)-oriented IIb diamond or (001)-oriented IIb diamond using the selective growth technique [1], [8]. The physical properties of diamond, summarized in Tab. I, lead to the highest calculated FOM [7], making diamond an ideal semiconductor for high power and high frequency electronic applications. However, the predicted FOM are not reached experimentally, thus, it is necessary to study the architecture and predict the electrical characteristics of the devices. In this work we used Silvaco finite element based software to validate the approach and study the influence of base width on the electrical characteristics of the bipolar junction transistor reported in Ref. [8].

TABLE I

PHYSICAL PROPERTIES AT 300 K OF Si, 4H-SiC, GaN AND DIAMOND AND RELATED FIGURES OF MERIT (JOHNSON, KEYES AND BALIGA).<sup>1</sup>

[unit]	Si	4H-SiC	GaN	Diamond
$E_G$ [eV]	1.12 <i>i</i>	3.23 <i>i</i>	3.39 <i>d</i>	5.47 <i>i</i>
$\epsilon_r$	11.7	9.66	8.9	5.7
$E_B$ [MV/cm]	0.3	3	5	10
$\lambda$ [W/cm.K]	1.3	3.7	1.3	22
$v_s$ [ $10^7$ cm/s]	1.0	2.0	2.2	2.7
$\mu_e$ [ $\text{cm}^2/\text{V.s}$ ]	1400	900	1000	1000
$\mu_h$ [ $\text{cm}^2/\text{V.s}$ ]	450	100	350	2000
$JFM$ [ $10^{23}$ $\Omega.W/s^2$ ]	2.3	900	490	2530
$KFM$ [ $10^7$ W/K.s]	10	53	17	218
$BFM$ [Si=1]	1	554	188	23068

## II. IMPLEMENTED MODELS

Three models were used in order to take into account the specific properties of diamond, i.e. the incomplete ionization of dopants, the carrier mobility and the recombination processes.

### A. Incomplete ionization

The large activation energies of dopants in diamond lead to incomplete dopant ionization at room temperature. As the physics leading to the reduction of the ionization energy is quite complex, an empirical law has been used, inspired from the Pearson and Bardeen model [9]. Parameters have been adjusted for boron acceptor in order to get 0.38 eV ionization energy at low dopant concentration [10] and zero at the insulator-metal transition of  $4.5 \times 10^{20}$   $\text{cm}^{-3}$  [11]:

$$E_a(\text{eV}) = 0.38 - 4.7877 \times 10^{-8} \times N_a^{\frac{1}{3}} \quad (1)$$

where  $E_a(\text{eV})$  is the thermal activation energy of the boron acceptor in electron-volt and  $N_a$  is the boron concentration in  $\text{cm}^{-3}$ . In the case of phosphorus donor, a constant value of  $E_d=0.57$  eV for the activation energy has been assumed [12], [13] since reports indicate no measurable reduction up

<sup>1</sup>Johnson's FOM:  $JFM = \frac{E_B v_s}{2\pi}$ —Frequency and power products of transistor.

Keyes' FOM:  $KFM = \lambda \left( \frac{c v_s}{2\pi \epsilon_r} \right)^{\frac{1}{2}}$ —Thermal limitation on high-frequency performance.

Baliga's FOM:  $BFM = \epsilon_r \mu E_B^3$ —Loss in high power and high-frequency operation.

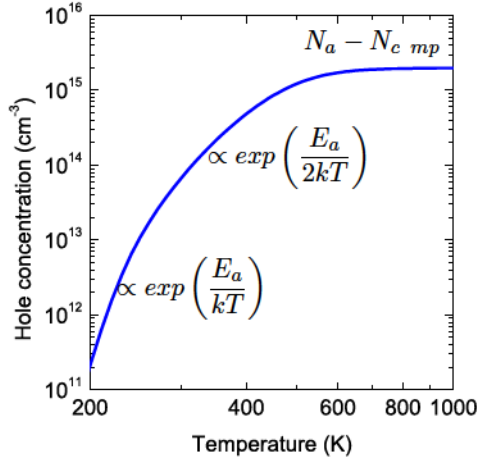


Fig. 1. Hole concentration as a function of temperature. The doping concentration is  $N_a=2 \times 10^{15} \text{ cm}^{-3}$  and the compensation is  $N_{comp}=1 \times 10^{13} \text{ cm}^{-3}$ . The ionization ratio  $p/N_a$  is about 3% at 300 K and increasing until it reaches the saturation regime where the free hole concentration  $p=N_a-N_{comp}$ .

to  $10^{19} \text{ cm}^{-3}$ , and hopping conduction above. The incomplete ionization of boron in diamond is illustrated by Fig. 1 which represents the free hole concentration as a function of temperature, calculated from equation 2.

$$p + N_d = \frac{N_a}{1 + \frac{p}{\phi_a}}, \quad \phi_a = g_h N_v T^{3/2} \exp\left(-\frac{E_a}{kT}\right) \quad (2)$$

where  $p$  is the free hole concentration,  $N_a$  is the acceptor concentration,  $N_d$  is the donor concentration,  $E_a$  is the acceptor thermal activation energy,  $k$  is the Boltzmann constant,  $h$  is the Planck constant and  $T$  is the temperature. The valence band effective density of state is  $N_v=2(2\pi m_h^* k)^{3/2}/h^3$ . The degeneracy factor is  $g_h=1/4$  for holes [14] and the hole density-of-state effective mass is  $m_h^*=0.908m_0$ . The density-of-state effective mass value is taken from Willatzen et al. in Ref. [15] and calculated by the procedure described by Pernot et al. in Ref. [16].

### B. Mobility model

Another parameter which influences diamond electronic device performances is the electron and hole mobility. The empirical model used to fit the experimental Hall effect measurements reported in Ref. [5], [17] (see Eq. 3 to 5) has been implemented into Silvaco finite element based software via a built-in C language interpreter, in order to take into account the doping concentration and temperature dependence of the mobility. The parameter values are summarized in Table II.

$$\mu(T, N_{imp}) = \mu(300, N_{imp}) \times \left(\frac{T}{300}\right)^{-\beta(N_{imp})} \quad (3)$$

$$\beta(N_{imp}) = \beta_{min} + \frac{\beta_{max} - \beta_{min}}{1 + \left(\frac{N_{imp}}{N_\beta}\right)^{\gamma_\beta}} \quad (4)$$

$$\mu(300, N_{imp}) = \mu_{min} + \frac{\mu_{max} - \mu_{min}}{1 + \left(\frac{N_{imp}}{N_\mu}\right)^{\gamma_\mu}} \quad (5)$$

where  $N_{imp}=(N_a+N_d)$  represents the total number of dopants.

### C. Shockley-Read-Hall recombination model

In bipolar devices, an electron-hole pair has different ways to recombine. It can recombine through a trap which energy lies in the forbidden gap. This process is described by Shockley-Read-Hall (SRH) statistics and depends on the injected carrier lifetimes. Eq. 6 describes the recombination rate of this process,  $R_{srh}$  in  $\text{cm}^{-3}.\text{s}^{-1}$ .

$$R_{srh} = \frac{pn - n_i^2}{a\tau_p^{srh} + b\tau_n^{srh}} \quad (6)$$

$$a = n + n_i \exp\left(\frac{E_t}{kT}\right), \quad b = p + n_i \exp\left(-\frac{E_t}{kT}\right) \quad (7)$$

with  $\tau_{p(n)}^{srh}$  being the hole (electron) lifetime,  $E_t$  the energy difference between the trap energy and the intrinsic Fermi level energy. For the simulations we chose the value of  $E_t=0 \text{ eV}$  which corresponds to the most efficient recombination center, located near the middle of the forbidden band gap.

### D. Impact ionization model

In order to predict breakdown characteristics of diamond device, impact ionization process have to be taken into account. In this way, we used Selberherr's impact ionization model and implemented the values reported in Ref. [18]. Table III presents the values used in equation 8.

TABLE III  
IMPACT IONIZATION VALUES IMPLEMENTED FROM REF. [18].

$a_p$	$b_p$	$a_n$	$b_n$
$\text{cm}^{-1}$	$\text{V.cm}^{-1}$	$\text{cm}^{-1}$	$\text{V.cm}^{-1}$
$6.1 \times 10^4$	$13.94 \times 10^6$	$1.46 \times 10^5$	$24 \times 10^6$

$$\alpha_p = a_p \exp\left(-\frac{b_p}{|E|}\right), \quad \alpha_n = a_n \exp\left(-\frac{b_n}{|E|}\right) \quad (8)$$

with  $a_p, b_p, a_n, b_n$  being constants and  $E$  is the electric field.

## III. BIPOLAR JUNCTION TRANSISTOR STRUCTURE

Fig. 2 represents the 2D structure of the simulated diamond bipolar junction transistor, following the reported work of Kato et al. [8]. The simulated device is composed of an n-type base with  $N_d=10^{18} \text{ cm}^{-3}$  and thickness of 600 nm. To take into account the effect of the selectively grown  $n^+$  diamond, a uniform phosphorus doped diamond layer was defined in the n-type layer with doping concentration of  $N_d=10^{20} \text{ cm}^{-3}$  and thickness of 300 nm. The  $p^+$ -type emitter with  $N_a=10^{21} \text{ cm}^{-3}$  and thickness of 250 nm was defined on top of the n-type layer. The intrinsic layer with concentration  $N_d=10^{15} \text{ cm}^{-3}$  and thickness of  $4 \mu\text{m}$  was defined between the base and the substrate. The later having a thickness of  $1 \mu\text{m}$  and a doping

TABLE II  
EMPIRICAL MOBILITY MODEL PARAMETERS IMPLEMENTED IN SILVACO FINITE ELEMENT BASED SOFTWARE.

Symbol	$\beta_{min}$	$\beta_{max}$	$N_{\beta}$	$\gamma_{\beta}$	$\mu_{min}$	$\mu_{max}$	$N_{\mu}$	$\gamma_{\mu}$
Unit			$\text{cm}^{-3}$		$\text{cm}^2 \cdot \text{V}^{-1} \cdot \text{s}^{-1}$	$\text{cm}^2 \cdot \text{V}^{-1} \cdot \text{s}^{-1}$	$\text{cm}^{-3}$	
Hole	0	3.11	$4.1 \times 10^{18}$	0.617	0	2016	$3.25 \times 10^{17}$	0.73
Electron	0	2.17	$3.75 \times 10^{17}$	0.585	0	1030	$9.9 \times 10^{16}$	0.564

concentration of  $N_a = 6 \times 10^{19} \text{ cm}^{-3}$ . The collector contact is define at the bottom of the p-type substrate and the base width  $W$  is estimated to be  $40 \mu\text{m}$  and the number of cells is 12. Due to numerical convergence problems, the compensation ratios were not taken into account. The lifetimes of carriers ( $\tau_{p(n)}^{srh} = \tau$ ) implemented in the SRH recombination model have been calculated from the diffusion length of holes  $L_h$  reported in Ref. [8]. These lifetimes were evaluated from the diffusion length From  $L_h = 4.2 \times 10^{-5} \text{ cm}$  using  $L_h = \sqrt{D\tau}$ , where  $D = (kT\mu)/q$  is the diffusion coefficient, we find  $\tau = 2 \times 10^{-10} \text{ s}$ . Since no reports exist on the determination of the diffusion length of electron in diamond, we assumed that  $L_h = L_e$ , where  $L_e$  is the diffusion length of electrons.

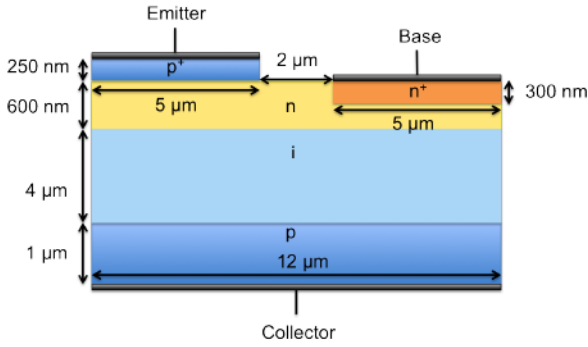


Fig. 2. Structure of the simulated diamond bipolar junction transistor structure after Kato et al. [8]. The base width  $W$  was evaluated to  $40 \mu\text{m}$ .

#### IV. RESULTS

Fig. 3 shows the collector current as a function of the collector voltage for four different emitter current values and compared with the experimental data reported in Ref. [8], using the common-base configuration at 300 K. Clear transistor action is seen on Fig. 3. The simulated collector currents are about two times higher than the experimental data reported in Ref. [8] for an emitter current of  $3 \mu\text{A}$ . Nevertheless, these first results are promising for simulating diamond bipolar devices, for estimating their electrical characteristics and for investigating trends and various dependencies (physical, geometrical, material). The poor injection coefficient is shown on Fig. 4, as the authors in Ref. [8] described.

If the base thickness is smaller than the diffusion length of injected minority carriers, the recombination can be neglected and the electrical characteristics of the transistor are improved. Thus, as mentioned in Ref. [8], we varied the geometry of the device by changing the base thickness from 600 nm to 60 nm and kept the doping concentration unchanged in order to predict the characteristics of the device. Fig. 4 shows the

$I_c(I_e)$  characteristic of the device with base thickness of 60 nm. The current gain  $\alpha = I_C/I_E$  of this device is extremely close to one. The second parameter which influences the device characteristics is the carrier diffusion length. Fig. 5 demonstrate the influence of the carrier lifetimes on the current flowlines (grey lines) distribution in the structure for an emitter current of  $5 \mu\text{A}$  and collector voltage of 10 V. Clear

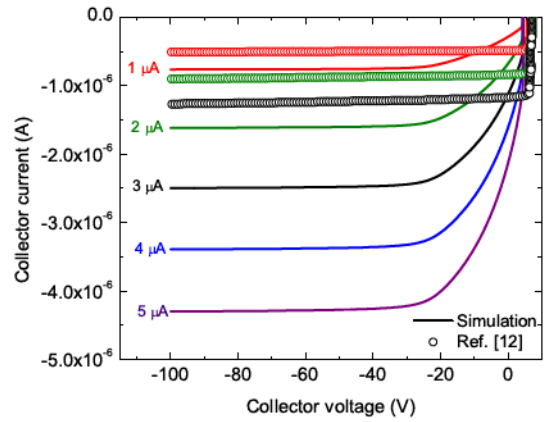


Fig. 3. DC output characteristics of the simulated diamond bipolar junction transistor at 300 K in the common-base configuration. The open circles represent the experimental datas reported in Ref. [8].

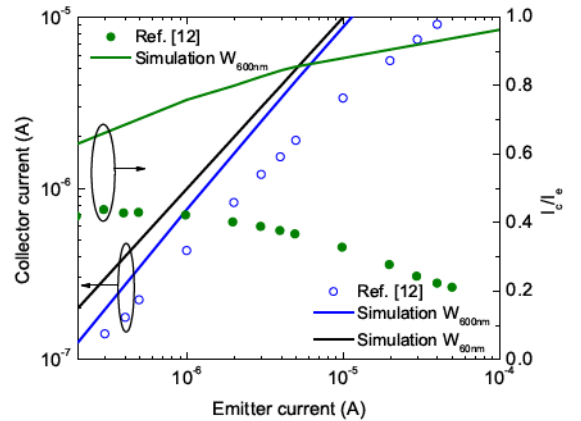


Fig. 4. Simulated collector current ( $I_C$ ) as a function of the emitter current ( $I_E$ ) under a collector bias of -60 V for the base thickness of 600 nm and 60 nm,  $W_{600nm}$  and  $W_{60nm}$  respectively. The simulated gain  $\alpha = I_C/I_E$  is between 0.63 and 0.96. The experimental data are plotted as a comparison, showing the poor injection coefficient.

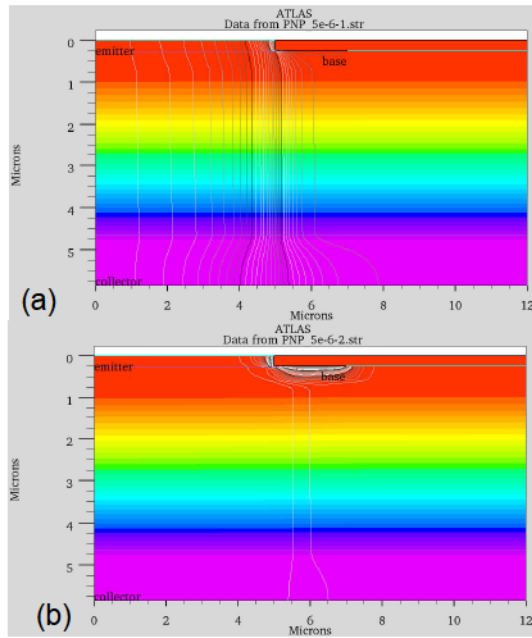


Fig. 5. Color plot showing the potential in the diamond bipolar junction transistor in the case of (a)  $\tau=10^{-9}$  s and (b)  $\tau=10^{-11}$  s. The grey lines represent the current flowline in the device.

improvement of the transistor action is seen when the lifetime is increased from  $10^{-11}$  s to  $10^{-9}$  s.

The breakdown voltage of the collector-base PIN junction related to the specified ionization rates was estimated to approximately 2000 V (see Fig. 6), based on a numerical calculation of avalanche ionization integral as presented in [19]. The predicted breakdown field is 5 MV/cm.

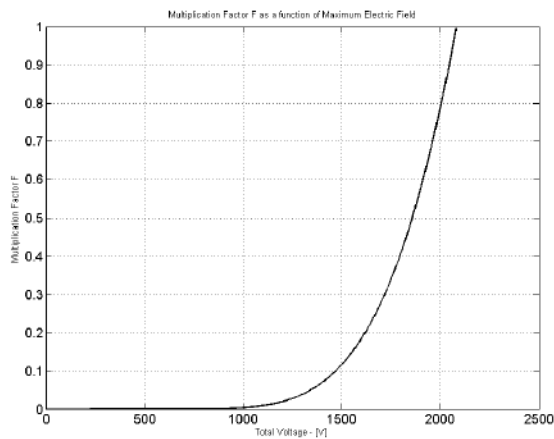


Fig. 6. Multiplication factor as a function of the total voltage calculated from the reported values of Ref. [18].

## V. CONCLUSION

Electric and electronic properties of diamond bipolar transistor were simulated for the first time using Silvaco finite element based software. Due to an effect of large activation

energy in the large band gap system, carrier concentration is extremely low. The carrier lifetimes were estimated from the diffusion length reported in Ref. [8] and implemented in SRH recombination model. Simulated current-voltage (I(V)) characteristics assuming the simple 2D structure with base doping of  $N_d = 10^{18}$  cm $^{-3}$  and thickness of 600 nm were compared with the experimental data. Large discrepancy was observed between the simulated results and experimental data on the slope of I(V) curve. This means that the other unconsidered factors such as ohmic contact resistivity, carrier tunneling and crystalline defects contributes strongly to the I(V) characteristics of diamond bipolar junction transistor. This work is motivated by the increasing number of diamond devices which emerged in the past few years. Recently, it has been demonstrated that different regimes can be controlled in a MOS capacitor [20] opening the route for the fabrication of a MOS field effect transistor. Thus, it is fundamental to predict as accurately as possible the electrical characteristics of this future diamond device as well as its architecture in order to fabricate power devices showing outstanding electrical performances.

## ACKNOWLEDGEMENTS

This work is supported by French state funds ANR-10-LABX-51-01 (Labex LANEF du Programme d'Investissements d'Avenir).

## REFERENCES

- [1] H. Kato, K. Oyama, T. Makino, M. Ogura, D. Takeuchi, and S. Yamasaki, *Diam. Relat. Mater.* 27-28, 19 (2012).
- [2] H. Kato, T. Makino, M. Ogura, D. Takeuchi, and S. Yamasaki, *Diam. Relat. Mater.* 34, 41 (2013).
- [3] S. Koizumi, C. E. Nebel and M. Nesladek, *Physics and Applications of CVD Diamond*, Wiley-VCH, 2008, ISBN: 978-3-527-40801-6.
- [4] J. Pernot, C. Tavares, E. Gheeraert, E. Bustarret, M. Katagiri, and S. Koizumi, *Appl. Phys. Lett.* 89, 122111 (2006).
- [5] J. Pernot and S. Koizumi, *Appl. Phys. Lett.* 93, 052105 (2008).
- [6] J. Pernot, P.N. Volpe, F. Omnès, P. Muret, V. Mortet, K. Haenen, and T. Teraji, *Phys. Rev. B* 81, 205203 (2010).
- [7] C.J.H. Wort and R.S. Balmer, *Mater. Today* 11, 22 (2008).
- [8] H. Kato, T. Makino, M. Ogura, D. Takeuchi, and S. Yamasaki, *Diam. Relat. Mater.* 34, 41 (2013).
- [9] G.L. Pearson and J. Bardeen, *Phys. Rev.* 75, 865 (1949).
- [10] J.-P. Lagrange, A. Deneuve, and E. Gheeraert, *Diam. Relat. Mater.* 7, 1390 (1998).
- [11] T. Klein, P. Achatz, J. Kacmarcik, C. Marcenat, F. Gustafsson, J. Marcus, E. Bustarret, J. Pernot, F. Omnès, B.E. Sernelius, C. Persson, A. Ferreira da Silva, and C. Cytermann, *Phys. Rev. B* 75, 165313 (2007).
- [12] E. Gheeraert, S. Koizumi, T. Teraji, H. Kanda, and M. Nesladek, *Diam. Relat. Mater.* 9, 948 (2000).
- [13] S. Koizumi, T. Teraji, and H. Kanda, *Diam. Relat. Mater.* 9, 935 (2000).
- [14] David C. Look, *Electrical Characterization of GaAs Materials and Devices* (Wiley, New York, 1989).
- [15] M. Willatzen, M. Cardona, and N.E. Christensen, *Phys. Rev. B* 50, 18054 (1994).
- [16] J. Pernot, P.N. Volpe, F. Omnès, P. Muret, V. Mortet, K. Haenen, and T. Teraji, *Phys. Rev. B* 81, 205203 (2010).
- [17] P.-N. Volpe, J. Pernot, P. Muret, and F. Omnès, *Appl. Phys. Lett.* 94, 092102 (2009).
- [18] A. Hiraiwa and H. Kawarada, *J. Appl. Phys.* 114, 034506 (2013).
- [19] Analytic and semi-analytic modeling for double Gaussian and any PN junction, submitted to *IEEE T. Electron Dev.* Not published
- [20] G. Chicot, A. Maréchal, R. Motte, P. Muret, E. Gheeraert, and J. Pernot, *Appl. Phys. Lett.* 102, 242108 (2013).



Contents lists available at ScienceDirect

## Diamond &amp; Related Materials

journal homepage: [www.elsevier.com/locate/diamond](http://www.elsevier.com/locate/diamond)

# Model implementation towards the prediction of J(V) characteristics in diamond bipolar device simulations



A. Maréchal<sup>a,b,c,d,\*</sup>, N. Rouger<sup>c,d</sup>, J.-C. Crébier<sup>c,d</sup>, J. Pernot<sup>a,b</sup>, S. Koizumi<sup>e</sup>, T. Teraji<sup>e</sup>, E. Gheeraert<sup>a,b</sup>

<sup>a</sup> Univ. Grenoble Alpes, Inst. NEEL, F-38042 Grenoble, France

<sup>b</sup> CNRS, Inst. NEEL, F-38042 Grenoble, France

<sup>c</sup> Univ. Grenoble Alpes, G2Elab, F-38042 Grenoble, France

<sup>d</sup> CNRS, G2Elab, F-38042 Grenoble, France

<sup>e</sup> Sensor Materials Center, National Institute for Materials Science, 1-1 Namiki, Tsukuba, Ibaraki 305-0044, Japan

## ARTICLE INFO

## Article history:

Received 8 October 2013

Received in revised form 13 January 2014

Accepted 13 January 2014

Available online 23 January 2014

## Keywords:

Numerical simulation

Silvaco TCAD

Diamond p–n junction

Hopping conduction

## ABSTRACT

In the view of predicting the performances as well as anticipating the architecture of the future diamond devices, it is of fundamental importance to accurately implement the physical properties of diamond into finite element based software. In this context, we used Silvaco to model a diamond p–n junction and studied the carrier densities responsible for the electrical characteristics of the devices. The simulated electrical characteristics are compared to experimental data and the influence of Shockley–Read–Hall and Auger recombination models on the carrier densities and J(V) characteristics was investigated. The bias voltage boundary between low and high injection conditions,  $\Psi_{bi} = 4.7$  eV, was well reproduced. However, the extremely low calculated carrier densities lead to extremely low current densities in the low injection regime, reaching the numerical precision limit. The simulation of the reverse characteristic predicts a breakdown voltage of 225 V. Preliminary results on hopping conductivity implementation into the simulation tool are presented. Eventually, these results will be used to predict the architecture and behavior of future devices, such as bipolar junction transistor and metal–oxide–semiconductor field effect transistor.

© 2014 Elsevier B.V. All rights reserved.

## Contents

1. Introduction . . . . .	34
2. Numerical models . . . . .	35
2.1. Incomplete ionization . . . . .	35
2.2. Empirical mobility model . . . . .	35
2.3. Shockley–Read–Hall and Auger recombination models . . . . .	36
2.4. Temperature dependent band gap . . . . .	36
3. Basic equations . . . . .	36
4. Modelization of a diamond p–n junction . . . . .	36
4.1. p–n junction characteristics . . . . .	36
4.2. Carrier density profiles . . . . .	37
4.2.1. Low injection regime . . . . .	37
4.2.2. High injection regime . . . . .	38
4.2.3. SRH lifetimes and Auger recombination parameter influence . . . . .	39
5. Limitations and perspectives . . . . .	40
5.1. Avalanche impact ionization coefficients . . . . .	40
5.2. Hopping mobility model . . . . .	41
6. Conclusion . . . . .	41
Prime novelty statement . . . . .	42
Acknowledgments . . . . .	42
References . . . . .	42

\* Corresponding author at: Univ. Grenoble Alpes, Inst. NEEL, F-38042 Grenoble, France.  
E-mail address: [aurelien.marechal@grenoble.cnrs.fr](mailto:aurelien.marechal@grenoble.cnrs.fr) (A. Maréchal).

## 1. Introduction

The last twenty years of development in controlling both growth quality and doping concentration in CVD diamond has led to the emergence of electronic devices such as Schottky diodes withstanding high breakdown field ( $7.7 \text{ MV}\cdot\text{cm}^{-1}$ ) [1], lateral p–n junctions with extremely low leakage current ( $<2.10^{-6} \text{ A}\cdot\text{cm}^{-2}$  under a reverse bias voltage of 30 V) [2], H-terminated field effect transistors showing high cutoff frequency (53 GHz) [3], junction field effect transistors using selectively grown n-type diamond having high current on/off ratios ( $10^7$ – $10^8$ ) [4] and more recently bipolar junction transistors fabricated either on (111)-oriented IIb diamond or (001)-oriented IIb diamond using the selective growth technique [5,6]. The physical properties of diamond, such as high breakdown field ( $10 \text{ MV}\cdot\text{cm}^{-1}$  [7]), high electron and hole mobilities ( $1000 \text{ cm}^2\cdot\text{V}^{-1}\cdot\text{s}^{-1}$  and  $2000 \text{ cm}^2\cdot\text{V}^{-1}\cdot\text{s}^{-1}$  respectively, for doping levels below  $10^{17} \text{ cm}^{-3}$  at room temperature [8–10]), high thermal conductivity ( $22 \text{ W}\cdot\text{cm}^{-1}\cdot\text{K}^{-1}$ ) and extremely low intrinsic carrier concentration at room temperature ( $n_i \approx 10^{-27} \text{ cm}^{-3}$ ) lead to the highest calculated figures of merit [11], making diamond the ultimate semiconductor for high power and high frequency electronic applications.

In this context, the prediction of the device electrical characteristics is needed in order to reach the predicted material limits. This prediction is possible by implementing the physical parameters and models of diamond in TCAD finite element based software. For instance, Rashid et al. [12] have modeled a 1D Schottky m–i–p+ diode and studied the forward and reverse J(V) characteristics of the structure. They presented the implemented models and pointed out the lack of data inherent to diamond material as well as the difficulties encountered to simulate intrinsic diamond layer since the intrinsic carrier concentration is of the order of  $10^{-27} \text{ cm}^{-3}$  at 300 K. They found good correlations between simulated and experimental Schottky diode J(V) characteristics. The architecture of such a unipolar device has also been studied in Ref. [13]. The authors studied the effect of a field plate on the electric field distribution in the structure showing the importance of numerical simulation for optimizing the device architecture. Nawawi et al. [14] modeled the static and transient characteristics of a diamond Schottky diode in order to demonstrate the potential of diamond unipolar devices for power electronic applications. However, a more systematic approach for modeling either unipolar or bipolar diamond devices is needed. Since diamond technology is still very young, there is a lack of parameter values in the numerical tools. In the perspective of accurately modeling diamond devices, it is of fundamental importance to implement the physical parameter values of diamond (impact ionization coefficient, carrier life-times) and mobility models into the device simulators, over a wide range of temperature. In this paper the physical parameter values of diamond have been implemented into Silvaco TCAD finite element based software. The implemented models have then been applied to a diamond p–n junction after Makino et al. [35] and Koizumi and Makino [33]. These references were used to compare the implemented parameter values and models.

In the first part of the present work, the numerical models will be described. Then, the simulated diamond p–n junction characteristics will be presented. The influence of temperature, Shockley–Read–Hall lifetimes and Auger recombination parameters on the carrier densities and on the J(V) characteristics will be shown. We will conclude on the perspectives and the main difficulties due to the lack of parameter values and models implemented in the numerical simulation tools.

## 2. Numerical models

Three models were used in order to take into account the specific properties of diamond, i.e. the incomplete ionization of dopants, the carrier mobility and the recombination processes.

### 2.1. Incomplete ionization

The free carrier concentrations are calculated by solving the neutrality equations:

$$p + N_d = \frac{N_a}{1 + \frac{p}{g_h}}, \phi_a = g_h N_v T^{3/2} \exp\left(-\frac{E_a}{kT}\right) \quad (1)$$

$$n + N_a = \frac{N_d}{1 + \frac{n}{g_e}}, \phi_d = g_e N_c T^{3/2} \exp\left(-\frac{E_d}{kT}\right) \quad (2)$$

where  $p(n)$  is the free hole (electron) concentration,  $N_{a(d)}$  is the acceptor (donor) concentration,  $E_{a(d)}$  is the acceptor (donor) thermal activation energy,  $k$  is the Boltzmann constant,  $h$  is the Planck constant and  $T$  is the temperature. The effective densities of state are  $N_v = 2(2\pi m_h^* k)^{3/2}/h^3$  and  $N_c = 2(2\pi m_e^* k)^{3/2}/h^3$ . The degeneracy factor is either  $g_h = 1/4$  for holes or  $g_e = 2$  for electrons [15] and the density-of-state effective masses are  $m_h^* = 0.908 m_0$  and  $m_e^* = 0.55 m_0$  for holes and electrons respectively. The hole density-of-state effective mass value is taken from Willatzen et al. in Ref. [16] and calculated by the procedure described by Pernot et al. in Ref. [10]. The electron density-of-state effective mass is calculated from the experimental values of Ref. [17] as  $m_e^* = (m_{\perp}^* m_{\parallel})^{1/3}$ , with  $m_{\perp} = 0.306 m_0$  and  $m_{\parallel} = 1.81 m_0$ . These implemented values are in close agreement with the recent experimental report of Naka et al. [18].

The large activation energies of dopants in diamond lead to incomplete dopant ionization at room temperature. This is the main reason why regular devices such as junction field effect transistor (FET) have poor electrical performances, and specific architectures have been developed such as delta-doped FET [19,20] or hydrogen-terminated FET [3]. As the physics leading to the reduction of the ionization energy is quite complex, an empirical law has been used, inspired from the Pearson and Bardeen model [21]. Parameters have been adjusted for boron acceptor in order to get 0.38 eV ionization energy at low dopant concentration [22] and zero at the insulator–metal transition of  $4.5 \times 10^{20} \text{ cm}^{-3}$  [23]:

$$E_a(\text{eV}) = 0.38 - 4.7877 \times 10^{-8} \times N_a^{\dagger} \quad (3)$$

where  $E_a(\text{eV})$  is the thermal activation energy of the boron acceptor in electron-volt and  $N_a$  is the boron concentration in  $\text{cm}^{-3}$ . In the case of phosphorus donor, a constant value of  $E_d = 0.57 \text{ eV}$  for the activation energy has been assumed [24,17] since reports indicate no measurable reduction up to  $10^{19} \text{ cm}^{-3}$ , and hopping conduction above. However, a recent report [25] indicates a decrease of the activation energy of phosphorus in the presence of high concentration of compensating impurities. In the present work, we only consider low compensated n-type diamond, thus the ionization energy of phosphorus is set to  $E_d = 0.57 \text{ eV}$ .

It results that, at room temperature, about one acceptor in one thousand is ionized and only one donor in one million is ionized for a doping level of  $10^{17} \text{ cm}^{-3}$  (obviously lower values will be achieved when taking into account the compensation).

### 2.2. Empirical mobility model

Another parameter which influences diamond electronic device performances is the electron and hole mobility. The empirical model used to fit the experimental Hall effect measurements reported in Refs. [26,9] (see Eqs. (4) to (6)) has been implemented into Silvaco finite element based software via a built-in C language interpreter, in order to take into account the doping concentration and temperature dependence of the mobility. This method has been adopted, instead of the proposed Masetti model [27], in order to implement in a second time the hopping mechanism, presented in Section 5.2. The parameter values are summarized in Table 1.

**Table 1**  
Empirical mobility model parameters implemented in Silvaco finite element based software.

Symbol	$\beta_{min}$	$\beta_{max}$	$\frac{N_\beta}{\text{cm}^{-3}}$	$\gamma_\beta$	$\frac{\mu_{min}}{\text{cm}^2 \cdot \text{V}^{-1} \cdot \text{s}^{-1}}$	$\frac{\mu_{max}}{\text{cm}^2 \cdot \text{V}^{-1} \cdot \text{s}^{-1}}$	$\frac{N_\mu}{\text{cm}^{-3}}$	$\gamma_\mu$
Hole	0	3.11	$4.1 \times 10^{18}$	0.617	0	2016	$3.25 \times 10^{17}$	0.73
Electron	0	2.17	$3.75 \times 10^{17}$	0.585	0	1030	$9.9 \times 10^{16}$	0.564

$$\mu(T, N_{imp}) = \mu(300, N_{imp}) \times \left(\frac{T}{300}\right)^{-\beta(N_{imp})} \quad (4)$$

$$\beta(N_{imp}) = \beta_{min} + \frac{\beta_{max} - \beta_{min}}{1 + \left(\frac{N_{imp}}{N_\beta}\right)^{\gamma_\beta}} \quad (5)$$

$$\mu(300, N_{imp}) = \mu_{min} + \frac{\mu_{max} - \mu_{min}}{1 + \left(\frac{N_{imp}}{N_\mu}\right)^{\gamma_\mu}} \quad (6)$$

where  $N_{imp} = (N_a + N_d)$  represents the total number of dopants. This empirical mobility model shows good agreement with the experiments over a wide range of doping concentration, from  $N_a = 10^{14} \text{ cm}^{-3}$ , where the mobility is equal to  $2016 \text{ cm}^2 \cdot \text{V}^{-1} \cdot \text{s}^{-1}$ , to  $N_a = 10^{21} \text{ cm}^{-3}$  where the mobility falls down to unity. Concerning the phosphorus donor, the mobility is maximum ( $\mu_{max} = 1030 \text{ cm}^2 \cdot \text{V}^{-1} \cdot \text{s}^{-1}$ ) for  $N_d = 10^{14} \text{ cm}^{-3}$ , and close to unity when  $N_d = 10^{20} \text{ cm}^{-3}$ .

### 2.3. Shockley–Read–Hall and Auger recombination models

The carrier dynamics and distribution in a p–n junction are strongly influenced by recombination processes. In bipolar devices, an electron–hole pair has different ways to recombine. A first way is to recombine through a trap which energy lies in the forbidden gap. This process is described by Shockley–Read–Hall (SRH) statistics and depends on the injected carrier lifetimes. Eq. (7) describes the recombination rate of this process,  $R_{srh}$  in  $\text{cm}^{-3} \cdot \text{s}^{-1}$ .

$$R_{srh} = \frac{pn - n_i^2}{a\tau_p^{srh} + b\tau_n^{srh}} \quad (7)$$

$$a = n + n_i \exp\left(\frac{E_t}{kT}\right), b = p + n_i \exp\left(-\frac{E_t}{kT}\right) \quad (8)$$

with  $\tau_{p(n)}^{srh}$  being the hole (electron) lifetime,  $E_t$  the energy difference between the trap energy and the intrinsic Fermi level energy. During the simulations the value of  $E_t = 0 \text{ eV}$  has been set and corresponds to the most efficient recombination center, located near the middle of the forbidden band gap.

The second recombination process considered was the Auger recombination process occurring at high doping concentration, described in Eq. (9). This process occurs through a non-radiative recombination process in which an electron–hole pair recombines and gives its energy to a third particle.

$$R_{Auger} = I_p^{Auger} n(pn - n_i^2) + I_n^{Auger} p(np - n_i^2) \quad (9)$$

with  $I_{p(n)}^{Auger}$  being the hole (electron) recombination coefficient in  $\text{cm}^6 \cdot \text{s}^{-1}$ . These coefficients have been studied for silicon based devices and do not show temperature dependence [28].

SRH and Auger recombination models have been widely studied for silicon based devices. Even if their values are unknown for diamond, their influences on the carrier densities and on the simulated J(V)

characteristics have been studied in the view of reproducing experimental electrical characteristics.

### 2.4. Temperature dependent band gap

The dependence of the diamond band gap with temperature can be modeled by using Eq. (10).

$$E_g(T) = E_g(300 \text{ K}) + \alpha \frac{300^2}{\beta + 300} - \alpha \frac{T^2}{\beta + T} \quad (10)$$

with  $E_g(300 \text{ K}) = 5.46 \text{ eV}$  the diamond band gap at 300 K,  $\alpha = 1.01007 \text{ eV} \cdot \text{K}^{-1}$ ,  $\beta = 3.95198 \times 10^6 \text{ K}$  fitting parameters determined from the experimental data reported on Ref. [29].

## 3. Basic equations

In a semiconductor, free carrier displacement induces a current. This current can be caused either by an applied electric field (carrier drift) or by a difference in carrier concentration between two regions (carrier diffusion). These two phenomena are taken into account by solving Poisson's equation together with the carrier continuity equation and drift-diffusion transport equations [30,31]. All the equations can be solved analytically by knowing the boundary conditions using Boltzmann approximation. However, when the Fermi–Dirac statistic is considered, one needs to use a numerical tool for solving the equations. Furthermore, when recombination–generation processes are taken into account, or when 2D and 3D structures are studied, numerical tools begin to be mandatory. The following section presents the p–n junction characteristics studied to check the validity of the parameter values and models implemented into Silvaco software. Newton's finite element method is used for solving the equations at each mesh point of the structure.

## 4. Modelization of a diamond p–n junction

Due to the large dopant ionization energies, the characteristics of the diamond p–n junctions are expected to be different from classical silicon p–n junctions, mainly due to the deep-dopant effect [32]. In order to verify the properties of the diamond p–n junction simulated by Silvaco finite element based software, we studied the electrostatic features of the structure as well as the carrier concentrations. The simulation of the mobility neglected the effect of the electric field in the structure as well as the hopping mobility. The effect of the first one would be a decrease of the mobility in the regions of high electric field leading to a decrease of the current density. On the contrary, the hopping mechanism would increase the mobility and hence increase the current density in the p–n junction.

### 4.1. p–n junction characteristics

The simulated p–n junction was inspired by the work of Koizumi et al. [33,34] and Makino et al. [35,36]. For simplicity, we considered a 1D equation resolution to check the validity of the different parameter values and models implemented in the numerical simulation tool. The structure of the simulated diode consists in an  $n^+$ -type diamond layer with phosphorus concentration  $N_d = 2 \times 10^{19} \text{ cm}^{-3}$  and thickness of  $1 \mu\text{m}$  defined on top of the p-type diamond layer

with boron concentration  $N_a = 4 \times 10^{17} \text{ cm}^{-3}$  and thickness of  $1 \mu\text{m}$ . This structure has been chosen to be vertical in opposition to the pseudo-vertical structure presented in Ref. [33] for simplicity. The temperature has been set to 300 K. Ohmic boundary conditions were applied by sandwiching the junction between two metallic electrodes covering the entire surface. The compensation ratios are  $c_n = 10\%$  [9] and  $c_p = 1.25\%$  in the  $n^+$ -type and p-type layers respectively. The models presented in Section 2 were applied to the p–n junction. Particular attention was paid when defining the mesh of the structure to prevent numerical convergence problems. Fig. 1.(a) shows the simulated electric field as a function of the position centered at the p–n junction, for different biasing conditions. The maximum electric field value at the p–n junction is linked to the built-in potential according to Eq. (11).

$$|E_m| = \sqrt{\frac{2qN_aN_d(\Psi_{bi}-V)}{\epsilon_s(N_a+N_d)}}, \quad (11)$$

where  $\Psi_{bi} = E_g - E_a - E_d$  is the built-in potential,  $q = 1.602 \times 10^{-19} \text{ C}$  the elementary charge,  $V$  is the applied voltage and  $\epsilon_s = 5.7\epsilon_0$ . By applying a forward bias voltage to the junction, the width of the space charge region is reduced leading to a decrease in the electric field intensity. The slope of the electric field versus depth in the p-type region, near to the junction, gives the doping concentration in the space charge region according to  $dE/dx = -qN_a / \epsilon_s$ . The ionized dopant concentration is shown in Fig. 1.(b). In the space charge region, which mainly extends in the lowest doped region, the dopants are fully ionized. Moving away from the junction, the ionized dopant concentration reaches the compensation concentration. Fig. 1.(c) shows the band alignment at zero bias voltage and 300 K. These first DC simulations clearly demonstrate that the specificities of diamond devices are correctly implemented, and more precisely the incomplete ionization is verified.

#### 4.2. Carrier density profiles

For calculating the current densities in the p–n junction, it is necessary to solve the drift-diffusion transport equations which depend on the carrier densities in the device. The carrier densities are affected by the applied voltage as well as the recombination-generation processes. Depending on the bias condition, the structure can be either in the low or high injection regime. The following carrier densities result from the simulation of the diamond p–n junction without activating neither SRH nor Auger models to limit the effects of these recombination models. Their influences will be studied in the next section.

##### 4.2.1. Low injection regime

In the low injection regime, the hole concentration in the  $n^+$ -type region (minority carriers), is well below the electron concentration (majority carriers). The hole concentration in the  $n^+$ -type region is increased by increasing the applied forward voltage. The effect of the applied forward voltage on the carrier concentrations is presented in Fig. 2.(a). The calculated carrier concentrations are extremely low, of the order of  $10^{-63} \text{ cm}^{-3}$  at  $V_{bias} = 0.1 \text{ V}$ , but even with such low concentrations, the results are consistent.

The hole and electron concentrations are related to the quasi-Fermi level ( $q$ -FL) position relative to the intrinsic Fermi level ( $E_i \approx E_g/2$ ), as shown in Eq. (12) [31].

$$p = n_i \exp\left(\frac{E_i - E_{fp}}{kT}\right), n = n_i \exp\left(\frac{E_{fn} - E_i}{kT}\right) \quad (12)$$

where  $n_i$  is the intrinsic carrier concentration,  $E_{fp}$  and  $E_{fn}$  are the  $q$ -FL for holes and electrons respectively.

When the difference in energy between the  $q$ -FL for holes and the intrinsic Fermi level is constant, the hole concentration remains constant

in the structure. The same holds for the  $q$ -FL for electrons. This is illustrated in Fig. 2.(b), which represents the simulated band diagram of the p–n junction for  $V_{bias} = 4 \text{ V}$ .

The extremely low carrier concentrations result in extremely low diffusion currents in the low injection regime, and reach the numerical precision limit which is one of the main limitations of diamond device simulations. However, this is not a problem because, at low bias the leakage current is mainly governed by the carrier generation within the space charge region rather than diffusion. The leakage current due to carrier diffusion (saturation current) would indeed represent a negligible part of the measured reverse current [31]. As it will be shown hereinafter, a more detailed model of generation is required for a precise model of leakage currents.

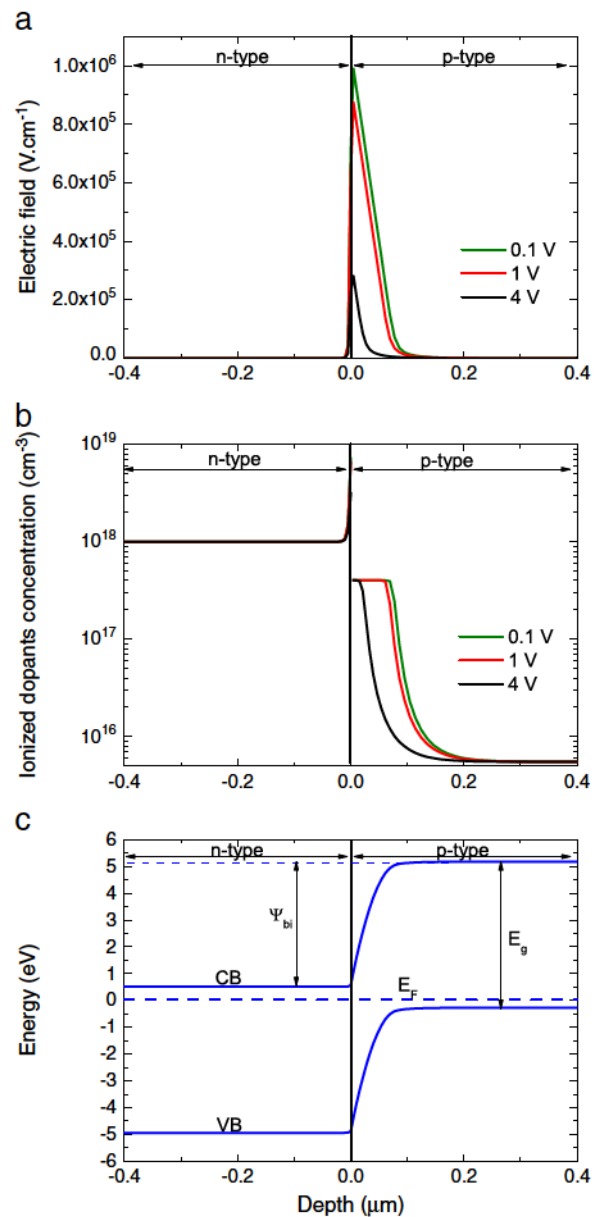


Fig. 1. (a) Electric field calculated across the junction at different forward bias voltages. (b) Ionized dopant concentration as a function of the position at different forward bias voltages. The transition between the space charge region and the neutral regions is correctly modeled. (c) Band structure corresponding to the junction at zero bias and  $T = 300 \text{ K}$ , where CB and VB correspond to the conduction band minimum and valence band maximum respectively.

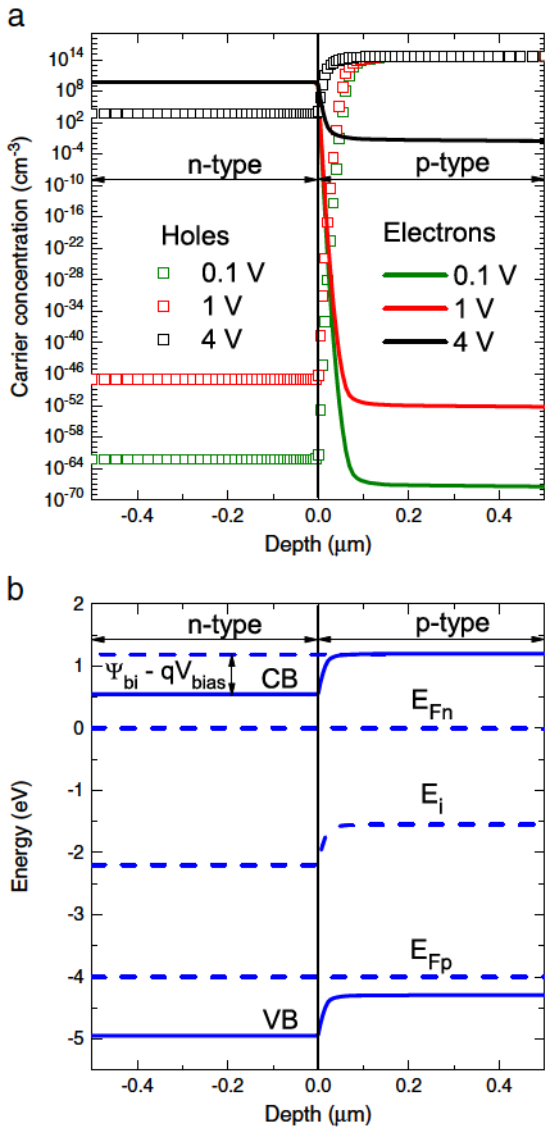


Fig. 2. (a) Hole and electron concentrations for different low forward bias conditions. (b) Band diagram of the simulated p–n junction at 300 K for  $V_{bias} = 4$  V, showing constant  $q\text{-}FL$ ,  $E_{Fp}$  and  $E_{Fn}$ , respectively.

#### 4.2.2. High injection regime

The high injection regime appears at higher bias voltage, which threshold is given by  $\Psi_{bi} = 4.7$  eV, deduced from Fig. 1.(c), at room temperature. Consequently, the hole concentration in the n<sup>+</sup>-type region becomes greater than the electron concentration. Fig. 3.(a) shows the hole and electron concentrations in the structure. It can be seen that the hole and electron concentrations are no more constant in the neutral regions. This is due to the fact that the injected charges induce the bending of the conduction and valence bands as it is shown on the band diagram presented in Fig. 3.(b). This bending causes a potential drop at the origin of the series resistance of the p–n junction and the resistivity modulation.

Fig. 4 shows the simulated  $J(V)$  characteristics of the diode reported in Ref. [33] at three different temperatures. The experimental data are plotted as a comparison. For bias voltage lower than the built-in potential, the simulated current level is of the order of  $10^{-10}$ – $10^{-11}$  A.cm<sup>-2</sup>, and strongly limits the simulations because it reaches the numerical precision limit of approximately  $10^{-11}$  A.cm<sup>-2</sup>.

The comparison between the experimental and simulated  $J(V)$  characteristic shows that the simulated low injection regime current

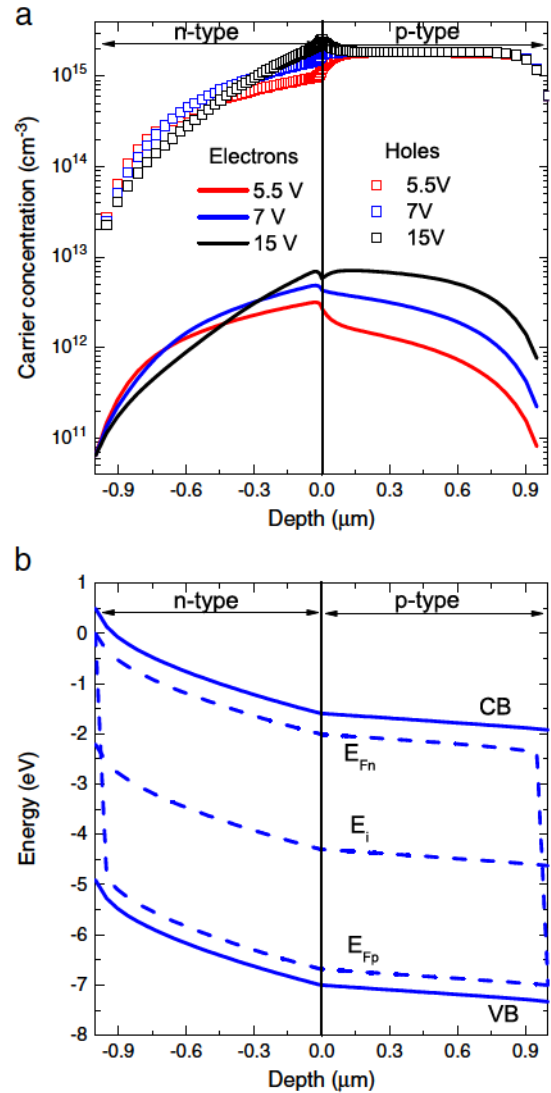


Fig. 3. (a) Hole and electron concentrations for different high forward bias conditions. In the n<sup>+</sup>-type region, the hole concentration is higher than the electron concentration. (b) Band diagram of the simulated p–n junction at 300 K for  $V_{bias} = 7$  V, showing band bending in the structure.

densities do not correspond to the measured one. This is possibly due to parallel leakage conduction paths which are not taken into account during the simulations, and it is also a consequence of material

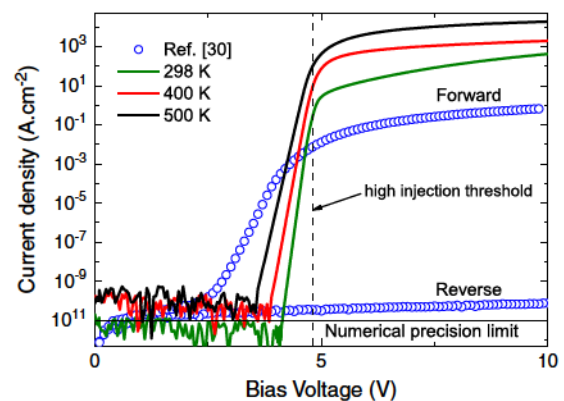


Fig. 4. Simulated  $J(V)$  characteristics at different temperatures without using SRH nor Auger models. The experimental  $J(V)$  characteristic (open circles), measured at room temperature and reported in Ref. [33], was used to validate the models and parameter values.

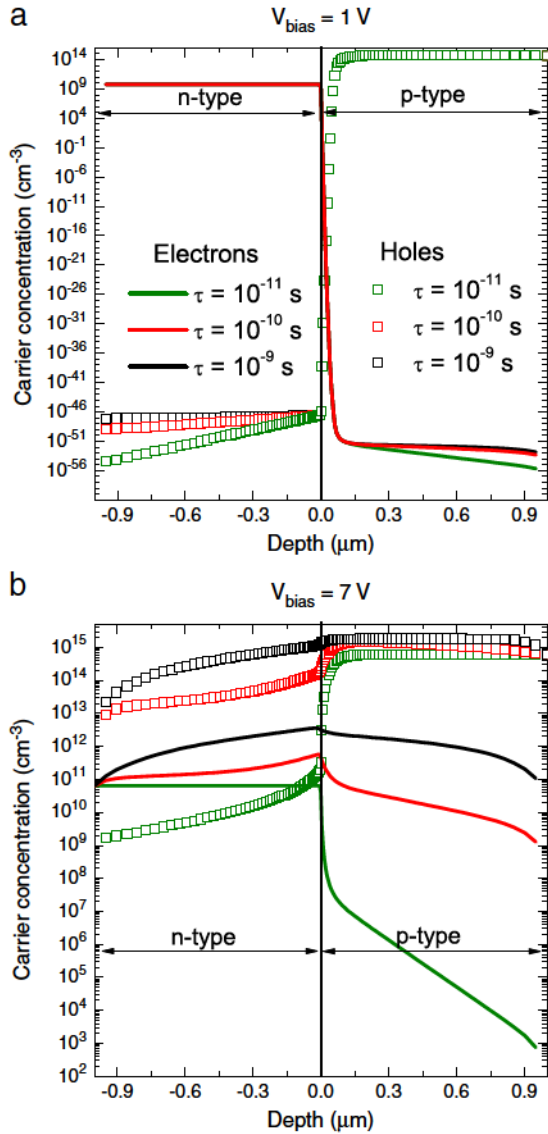


Fig. 5. Effect of the SRH lifetimes ( $\tau = \tau_p^{srh} = \tau_n^{srh}$ ) on the carrier concentrations in the (a) low ( $V_{bias} = 1$  V) and (b) high ( $V_{bias} = 7$  V) injection regimes. The simulations were done at 300 K and for a constant value of  $\alpha_p^{Auger} = \Gamma_n^{Auger} = 10^{-30} \text{ cm}^6 \cdot \text{s}^{-1}$ .

impurities and defects which affects carrier generation. In the high injection regime there is a difference between experimental and simulated current densities which can be adjusted either by adding a contact/access resistance to the electrodes or by tuning the carrier lifetimes of the recombination models. In order to better fit the experimental J(V) characteristics, we investigated on the effects of SRH and Auger recombination models. The results are presented and discussed in the next section.

#### 4.2.3. SRH lifetimes and Auger recombination parameter influence

To study the influence of SRH lifetime values on the simulated p–n junction characteristics, we chose the value of  $E_b = 0$  eV which maximizes the SRH recombination rate,  $R_{srh}$ . Fig. 5 presents the carrier concentrations in the low ( $V_{bias} = 1$  V) and high ( $V_{bias} = 7$  V) injection regime for three SRH lifetimes,  $\tau_p^{RSH} = \tau_n^{RSH} = 10^{-9}$  s,  $10^{-10}$  s and  $10^{-11}$  s with the constant Auger coefficients  $\Gamma_p^{Auger} = \Gamma_n^{Auger} = 10^{-30} \text{ cm}^6 \cdot \text{s}^{-1}$ . It can be noticed that, by increasing the carrier lifetimes up to  $10^{-9}$  s, the carrier concentrations are closer to the concentrations calculated when the SRH and Auger recombination models are not implemented. The influence of the Auger recombination parameter on the carrier concentrations is shown in Fig. 6. For this study, the value

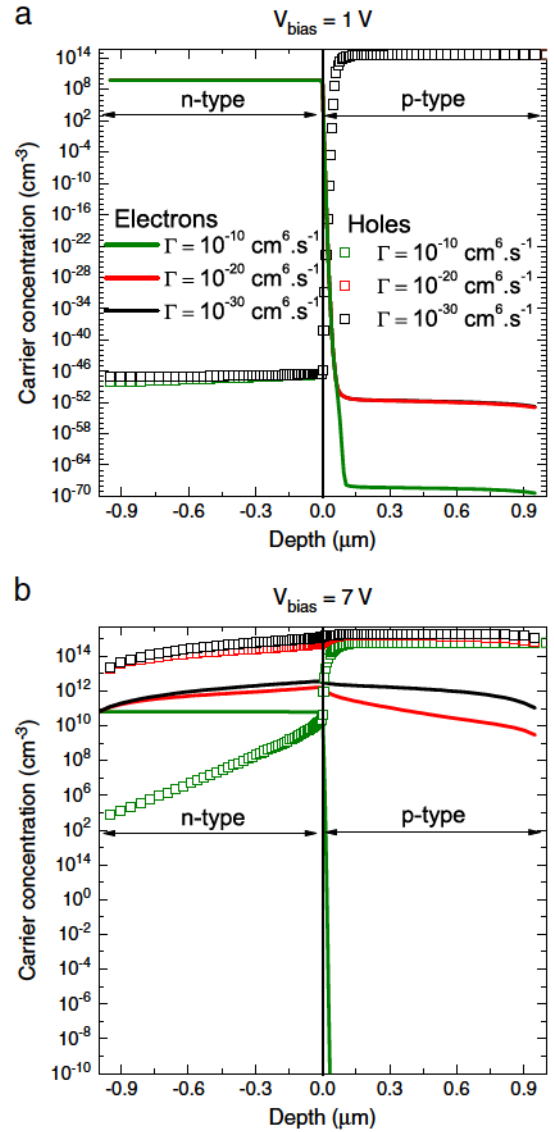


Fig. 6. Effect of the Auger recombination parameter ( $\Gamma = \Gamma_p^{Auger} = \Gamma_n^{Auger}$ ) on the carrier concentrations in the (a) low ( $V_{bias} = 1$  V) and (b) high ( $V_{bias} = 7$  V) injection regimes. The temperature was set to 300 K and the SRH lifetimes were  $\tau_p^{SRH} = \tau_n^{SRH} = 10^{-9}$  s.

of the SRH carrier lifetimes was  $\tau_p^{RSH} = \tau_n^{RSH} = 10^{-9}$  s. When decreasing the Auger recombination parameter down to  $10^{-30} \text{ cm}^6 \cdot \text{s}^{-1}$ , the carrier concentrations are close to the calculated one without recombination models. The simulations reveal that most of the influence appears in the high injection regime.

The influence of the recombination–generation parameters on the J(V) characteristics is presented in Fig. 7. Related to the carrier concentrations, the main influence of the parameter values appears in the high injection regime. In the low injection regime, the minority carrier concentrations are too low to have a significant influence on the current densities.

The study of the influence of the SRH lifetimes and the Auger recombination parameter values shows a significant influence on the current densities. For instance, going from  $\tau = 10^{-11}$  s to  $\tau = 10^{-10}$  s leads to an increase of a factor 728 in the current density at 10 V.

Even though the recombination models have an influence on the current densities, the different parameter values do not lead to a better fit of the experimental J(V) characteristic in the low injection regime (see Fig. 8). However, in the high injection regime the contact resistance can be tuned to fit the experimental J(V) as shown in Fig. 8. A combination of generation–recombination

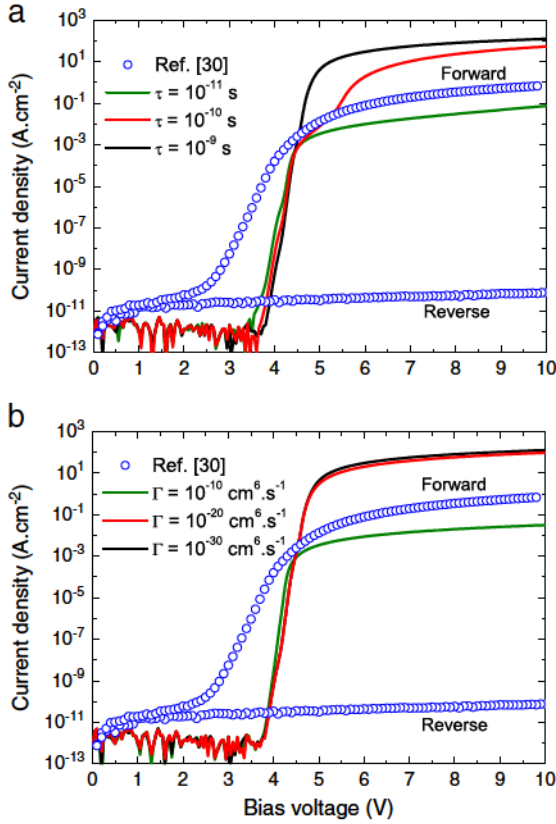


Fig. 7. (a) Influence of the SRH lifetimes ( $\tau = \tau_p^{SRH} = \tau_n^{SRH}$ ,  $\Gamma = 10^{-30}$  cm<sup>6</sup>.s<sup>-1</sup>) on the simulated J(V) characteristics. (b) Simulated J(V) characteristics for different Auger parameter values ( $\Gamma = \Gamma_p^{Auger} = \Gamma_n^{Auger}$ ,  $\tau = 10^{-9}$  s), T = 300 K.

models and series/contact resistance must be added, with a particular attention on carrier generation at low forward bias and reverse bias.

### 5. Limitations and perspectives

As shown in Section 4, the carrier concentrations are extremely low. As a consequence, when the applied forward voltage is lower than the built-in potential, the current density in the p–n junction is too low to be accurately calculated, as it reaches the numerical precision limit. Impurities and defects must also be introduced and modeled in order to correctly represent the specificities of novel diamond devices. These are some of the main limitations for diamond device simulation, since the intrinsic carrier density is extremely low as well as the free carrier

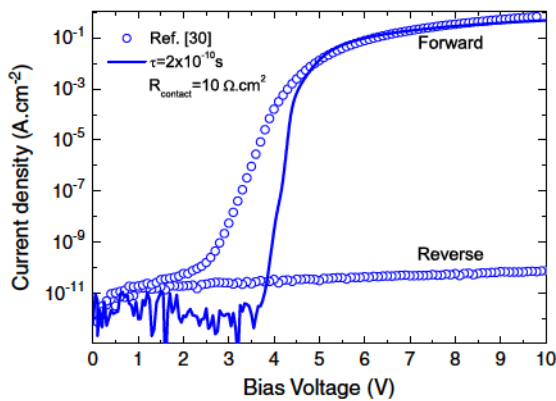


Fig. 8. Fit of the experimental J(V) characteristic reported in Ref. [33], at 300 K with a contact resistance  $R_{contact} = 10 \Omega \cdot cm^2$  and  $\tau = \tau_p^{SRH} = \tau_n^{SRH} = 2 \times 10^{-10}$  s.

concentrations. Furthermore, prediction of the electrical device characteristics needs the implementation of avalanche impact ionization parameter values as well as hopping conductivity models into the simulation tools.

#### 5.1. Avalanche impact ionization coefficients

To predict the breakdown voltage of the simulated devices, one needs to know the avalanche impact ionization coefficients for holes and electrons,  $\alpha_p$  and  $\alpha_n$  respectively shown in Eq. (13) [37].

$$\alpha_p = a_p \exp\left(-\frac{b_p}{|E|}\right), \alpha_n = a_n \exp\left(-\frac{b_n}{|E|}\right) \quad (13)$$

where  $|E|$  is the electric field in the structure,  $a_p$  ( $a_n$ ) and  $b_p$  ( $b_n$ ) are constants for holes (electrons), or electric field and temperature dependent depending on the implemented impact ionization model. The avalanche impact ionization coefficients are used to calculate the multiplication coefficients for electrons and holes ( $M_n$ ,  $M_p$ ) playing a role in the calculation of the total current density [31]. At the present time, there are no experimental reports concerning these parameter values. However, theoretical values extrapolated from silicon and silicon carbide are reported in Refs. [12,37,38]. For instance, the values of  $a_{p,n} = 1.935 \times 10^8$  cm<sup>-1</sup> and  $b_{p,n} = 7.749 \times 10^6$  V.cm<sup>-1</sup> implemented in the models reported in Ref. [38] led to a breakdown field of  $E_{max} = 1.23$  MV.cm<sup>-1</sup> for a doping level  $N_a = 1.23 \times 10^{17}$  cm<sup>-3</sup>. The same parameter values used for estimating the breakdown field of the Schottky diode reported in Ref. [1], led to a decrease of a factor 10 of the simulated breakdown field as compared to the measured  $E_{max} = 7.7$  MV.cm<sup>-1</sup> for a boron concentration of  $N_a = (1.4\text{--}2.8) \times 10^{16}$  cm<sup>-3</sup>. Furthermore, this value is much lower than the predicted 10 MV.cm<sup>-1</sup> breakdown field. Due to this low breakdown field value, the author of Ref. [38] used another simulation method which consisted to stop the simulations when the electric field in the Schottky diode reached 5.6 MV.cm<sup>-1</sup>, a method open to criticism but justified by the lack of impact ionization data related to diamond.

Recently, Hiraiwa and Kawarada [39] theoretically reproduced the breakdown voltage as a function of the doping concentration of diamond diodes by estimating accurately the ionization coefficients. These coefficients were implemented in the simulation tool. Particular attention was paid for simulating the reverse breakdown characteristic

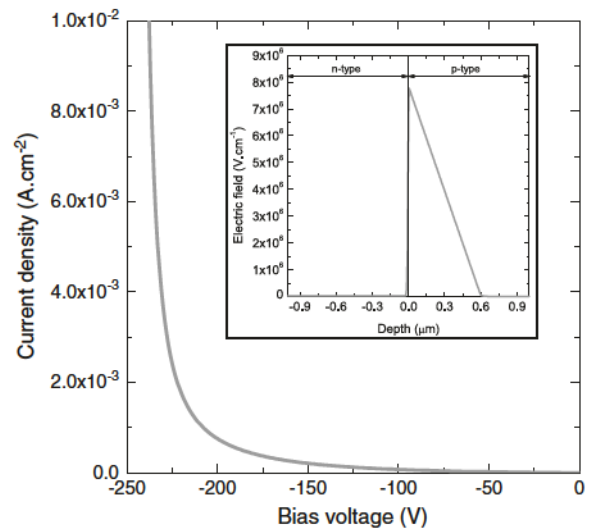


Fig. 9. Theoretical reverse J(V) breakdown characteristic of the simulated diamond p–n junction. The simulation end condition was chosen by setting a compliance current of  $1 \times 10^{-2}$  A.cm<sup>-2</sup>. The inset represents the electric field as a function of the depth at breakdown. The maximum electric field is 7.7 MV.cm<sup>-1</sup>.

because of the extremely low calculated diffusion currents. Thus, an arbitrary value to the leakage diffusion current was defined before modeling the reverse breakdown characteristic by using the impact ionization model. Fig. 9 presents the theoretical reverse characteristic of the simulated diamond p–n junction diode. It predicts a breakdown voltage of approximately 225 V. The inset shows the theoretical electric field as a function of the depth at breakdown, the maximum field being  $7.7 \text{ MV}\cdot\text{cm}^{-1}$ .

Ongoing work on the implementation of trap assisted tunneling [40] and band to band tunneling in order to model the low injection current and the reverse current of the bipolar devices will eventually lead to a better estimation of the current density in the low injection regime.

## 5.2. Hopping mobility model

At doping levels of the order of  $10^{18}$ – $10^{19} \text{ cm}^{-3}$ , below the metal–insulator transition, the conductivity is dominated by carrier hopping from neutral to ionized impurities. Unlike silicon, at room temperature, this conduction mechanism plays an important role in diamond. The nearest neighbor hopping (NNH) experimentally observed in an  $n^+$ -type diamond leads to a decrease of the resistivity, and hence improves the performance of the device as shown in Ref. [41]. In order to take this mechanism into account during the simulations, the NNH formula has been implemented into Silvaco via a built-in C language interpreter. The equivalent mobility ( $\mu_{eq}$ ) is calculated as follows:

$$\sigma_n = q(n_B \mu_B + n_{Hop} \mu_{Hop}) \quad (14)$$

$$\sigma_n = q n_B \mu_{eq} \quad (15)$$

$$\mu_{eq} = \mu_B + \frac{n_{Hop}}{n_B} \mu_{Hop} \quad (16)$$

$$\mu_{Hop} = \frac{1}{6} \frac{q R_{Hop}^2}{kT} \nu_{ph} \exp\left(-2\alpha R_{Hop} - \frac{qW_{Hop}}{kT}\right) \quad (17)$$

where the term  $\mu_B$  represents the band conduction mobility, described in Section 2.2, and the term  $\mu_{Hop}$  represents the nearest neighbor hopping mobility [42].  $n_B$  is the electron concentration in the conduction band calculated from Eq. (2) and  $n_{Hop}$  is the hopping carrier concentration given by  $n_{Hop} = N_d - n_B$ , which represents the non-ionized carrier concentration. Since the thermal ionization energy of the phosphorus donor is high in diamond, the number of non-ionized donor  $n_{Hop}$  is assumed to be  $N_d$ . In this approach, we assumed that all the non-ionized impurities participate to the hopping mechanism. According to Ref. [43],  $\alpha^{-1} = 1.8 \text{ nm}$  is the localization length of the wave function [44,45],  $W_{Hop}$  is

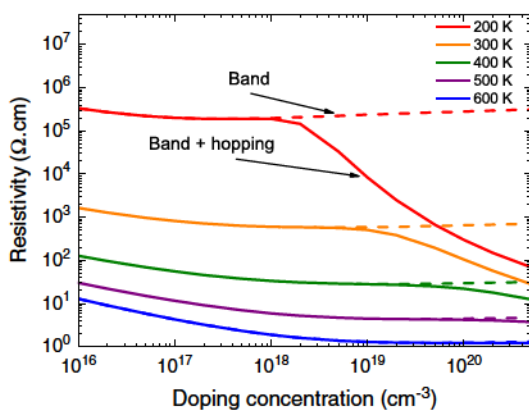


Fig. 10. Resistivity calculated from a uniform 1D n-type diamond layer taking into account the combined effect of band and hopping mechanisms (solid line) compared to the band conduction mechanism (dashed line).

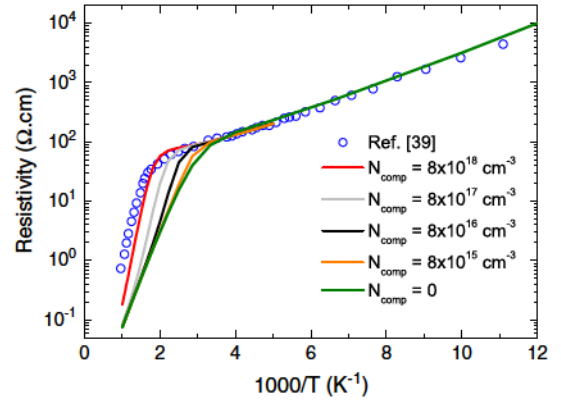


Fig. 11. Calculated resistivity as a function of  $1000/T$  for  $N_d = 8 \times 10^{19} \text{ cm}^{-3}$  at different compensation values. The open circles represent the experimental data reported in Ref. [41].

the thermal activation energy for the hopping process,  $R_{Hop} \approx N_d^{-1/3}$  is the mean distance between impurities and  $\nu_{ph} = 2 \times 10^{11} \text{ s}^{-1}$  is related to the phonon frequency [43]. In the case of boron-doped diamond, the conductivity is governed by a combination of band conduction and variable range hopping (VRH) mechanism [23,46].

In order to validate the approach and the possibility of hopping mobility implementation, a uniform 1D n-type diamond layer with a top and a bottom ohmic electrode was simulated in Silvaco using the equivalent mobility formula (see Eq. (16)) implemented via the C language interpreter. The procedure was to apply a small voltage bias between the two electrodes, then from the  $J(V)$  characteristics we extracted the total resistance ( $dv/di$ ) to finally get the resistivity of the n-type diamond layer. Preliminary results are presented in Fig. 10, which shows the resistivity as a function of the doping concentration. The decrease in resistivity due to hopping conductivity mechanism appears clearly at 200 K for a doping level of  $N_d = 2 \times 10^{18} \text{ cm}^{-3}$ , and at 300 K for a doping level of  $N_d = 10^{19} \text{ cm}^{-3}$ . At higher temperature, the effect of hopping mechanism tends to vanish, as it can be seen for 500 K and 600 K.

The reliability of the hopping mobility formula implementation is confirmed in Fig. 11, which presents the simulated resistivity as a function of  $1000/T$  for different compensation values and a doping concentration of  $N_d = 8 \times 10^{19} \text{ cm}^{-3}$ . The compensation was taken as a fitting parameter, in order to reproduce the experimental data reported by Oyama et al. in Ref. [41] (blue open circles). It appears that the compensation affects the high temperature region of the curve, which corresponds to the band conduction mechanism. However, from 50 K to 200 K, when taking into account the different compensation values, the resistivity cannot be calculated consequently to the extremely low carrier concentrations. The hopping resistivity is not affected by the compensation values as the author in Ref. [47] reported for boron doped diamond.

This model successfully takes into account the hopping conduction mechanism and reproduces the experimental resistivity reported in Ref. [41]. Furthermore, it will be used to predict the effect of hopping conduction on the device electrical characteristics, without falsely contributing to other phenomena.

## 6. Conclusion

Electric and electronic properties of diamond p–n junction were simulated for the first time using Silvaco finite element based software. Due to an effect of large activation energy in the large band gap system, carrier concentration changed largely in the low injection condition with bias voltage. Once the injection condition changed into high injection mode, band bending was predicted to occur even in the neutral region in the n-type layer. Simulated

current–voltage ( $J(V)$ ) characteristics assuming the simple stacking p–n junction structure with  $N_a = 4 \times 10^{17} \text{ cm}^{-3}$  for the p-type layer and  $N_d = 2 \times 10^{19} \text{ cm}^{-3}$  for the n<sup>+</sup>-type layer were compared with the experimentally obtained data. Bias voltage boundary between low and high injection conditions,  $\Psi_{bi} = 4.7 \text{ eV}$ , was well reproduced. However, a large discrepancy was observed between the simulated results and experimentally obtained data on the absolute current level and slope of  $J(V)$  curve were large, even considering the SRH and Auger recombination models. This means that the other unconsidered factors such as ohmic contact resistivity, carrier tunneling and crystalline defects contributing strongly to the  $J(V)$  characteristics of diamond p–n junction remain. However, it is possible to predict the breakdown characteristic of the p–n junction which is evaluated to happen at a reverse bias voltage of 225 V. This work is motivated by the increasing number of diamond devices which emerged in the past few years. Recently, it has been demonstrated that different regimes can be controlled in a MOS capacitor [48] opening the route for the fabrication of a MOS field effect transistor. Thus, it is fundamental to predict as accurately as possible the electrical characteristics of this future diamond device as well as its architecture in order to fabricate power devices showing outstanding electrical performances.

### Prime novelty statement

Up to now, reports on the simulations of diamond devices are only done for unipolar devices. In this work, we modeled for the first time a diamond bipolar p–n junction. This is a first step for predicting the electrical characteristics of the future diamond bipolar devices.

### Acknowledgments

This work is supported by French state funds ANR-10-LABX-51-01 (Labex LANEF du Programme d'Investissements d'Avenir). The authors thank Dr. Takeuchi (AIST) for fruitful discussions.

### References

- [1] P.-N. Volpe, P. Muret, J. Pernot, F. Omnès, T. Teraji, Y. Koide, F. Jomard, D. Planson, P. Brosseard, N. Dheilily, B. Vergne, S. Scharnholz, Extreme dielectric strength in boron doped homoepitaxial diamond, *Appl. Phys. Lett.* 97 (2010) 223501.
- [2] Y. Hoshino, H. Kato, T. Makino, M. Ogura, T. Iwasaki, M. Hatano, S. Yamasaki, Electrical properties of lateral p–n junction diodes fabricated by selective growth of n<sup>+</sup> diamond, *Phys. Status Solidi A* 209 (9) (2012) 1761–1764.
- [3] S.A.O. Russell, S. Sharabi, A. Tallaire, D.A.J. Moran, Hydrogen-terminated diamond field-effect transistors with cutoff frequency of 53 GHz, *IEEE Electron Device Lett.* 33 (2012) 10.
- [4] T. Iwasaki, Y. Hoshino, K. Tsuzuki, H. Kato, T. Makino, M. Ogura, D. Takeuchi, T. Matsumoto, H. Okushi, S. Yamasaki, M. Hatano, Diamond junction field-effect transistors with selectively grown n<sup>+</sup>-side gates, *Appl. Phys. Express* 5 (2012) 091301.
- [5] H. Kato, K. Oyama, T. Makino, M. Ogura, D. Takeuchi, S. Yamasaki, Diamond bipolar junction transistor device with phosphorus-doped diamond base layer, *Diamond Relat. Mater.* 27–28 (2012) 19.
- [6] H. Kato, T. Makino, M. Ogura, D. Takeuchi, S. Yamasaki, Fabrication of bipolar junction transistor on (001)-oriented diamond by utilizing phosphorus-doped n-type diamond base, *Diamond Relat. Mater.* 34 (2013) 41–44.
- [7] S. Koizumi, C.E. Nebel, M. Nesladek, *Physics and Applications of CVD Diamond*, Wiley-VCH, 2008, ISBN 978-3-527-40801-6.
- [8] J. Pernot, C. Tavares, E. Gheeraert, E. Bustarret, M. Katagiri, S. Koizumi, Hall electron mobility in diamond, *Appl. Phys. Lett.* 89 (2006) 122111.
- [9] J. Pernot, S. Koizumi, Electron mobility in phosphorus doped 111 homoepitaxial diamond, *Appl. Phys. Lett.* 93 (2008) 052105.
- [10] J. Pernot, P.N. Volpe, F. Omnès, P. Muret, V. Mortet, K. Haenen, T. Teraji, Hall hole mobility in boron-doped homoepitaxial diamond, *Phys. Rev. B* 81 (2010) 205203.
- [11] C.J.H. Wort, R.S. Balmer, Diamond as an electronic material, *Mater. Today* 11 (2008) 22.
- [12] S.J. Rashid, A. Tajani, D.J. Twitchen, L. Coulbeck, F. Udrea, T. Butler, N.L. Rupesinghe, M. Brezeanu, J. Isberg, A. Garraway, M. Dixon, R.S. Balmer, D. Chamund, P. Taylor, G.A.J. Amaratunga, Numerical parameterization of chemical-vapor-deposited (CVD) single-crystal diamond for device simulation and analysis, *IEEE Trans. Electron Devices* 55 (2008) 10.
- [13] F. Thion, K. Isoird, D. Planson, M.-L. Locatelli, H. Ding, Simulation and design of junction termination structures for diamond Schottky diodes, *Diamond Relat. Mater.* 20 (2011) 729–732.
- [14] A. Nawawi, King Jet Tseng, Rusli, G. Amaratunga, Switching characteristics of diamond-based m–i–p<sup>+</sup> diodes in power electronic applications, *Energy Conversion Congress and Exposition (ECCE)*, 2011, pp. 2676–2680.
- [15] David C. Look, *Electrical Characterization of GaAs Materials and Devices*, Wiley, New York, 1989.
- [16] M. Willatzen, M. Cardona, N.E. Christensen, Linear muffin-tin-orbital and  $k \cdot p$  calculations of effective masses and band structure of semiconducting diamond, *Phys. Rev. B* 50 (1994) 18054.
- [17] E. Gheeraert, S. Koizumi, T. Teraji, H. Kanda, M. Nesladek, Electronic states of phosphorus in diamond, *Diamond Relat. Mater.* 9 (2000) 948.
- [18] N. Naka, K. Fukai, Y. Handa, I. Akimoto, Direct measurement via cyclotron resonance of the carrier effective masses in pristine diamond, *Phys. Rev. B* 88 (2013) 035205.
- [19] H. El-Hajj, A. Denisenko, A. Kaiser, R.S. Balmer, E. Kohn, Diamond MISFET based on boron delta-doped channel, *Diamond Relat. Mater.* 17 (2008) 1259.
- [20] G. Chicot, T.N. Tran Thi, A. Fiori, F. Jomard, E. Gheeraert, E. Bustarret, J. Pernot, Hole transport in boron delta-doped diamond structures, *Appl. Phys. Lett.* 101 (2012) 162101.
- [21] G.L. Pearson, J. Bardeen, Electrical properties of pure silicon and silicon alloys containing boron and phosphorus, *Phys. Rev.* 75 (1949) 865.
- [22] J.-P. Lagrange, A. Deneuille, E. Gheeraert, Activation energy in low compensated homoepitaxial boron-doped diamond films, *Diamond Relat. Mater.* 7 (1998) 1390.
- [23] T. Klein, P. Achatz, J. Kacmarcik, C. Marcenat, F. Gustafsson, J. Marcus, E. Bustarret, J. Pernot, F. Omnès, B.E. Sernelius, C. Persson, A. Ferreira da Silva, C. Cytermann, Metal–insulator transition and superconductivity in boron-doped diamond, *Phys. Rev. B* 75 (2007) 165313.
- [24] S. Koizumi, T. Teraji, H. Kanda, Phosphorus-doped chemical vapor deposition of diamond, *Diamond Relat. Mater.* 9 (2000) 935.
- [25] I. Stenger, M.-A. Pinault-Thaury, T. Kociniowski, A. Lusson, E. Chikoidze, F. Jomard, Y. Dumont, J. Chevallier, J. Barjon, Impurity-to-band activation energy in phosphorus doped diamond, *J. Appl. Phys.* 114 (2013) 073711.
- [26] P.-N. Volpe, J. Pernot, P. Muret, F. Omnès, High hole mobility in boron doped diamond for power device applications, *Appl. Phys. Lett.* 94 (2009) 092102.
- [27] G. Masetti, M. Severi, S. Solmi, Modeling of carrier mobility against carrier concentration in arsenic-, phosphorus-, and boron-doped silicon, *IEEE Trans. Electron Devices* 30 (1983) 764.
- [28] J. Dziejewicz, W. Schmid, Auger coefficients for highly doped and highly excited silicon, *Appl. Phys. Lett.* 31 (1977) 346.
- [29] <http://www.ioffe.ru/SVA/NSM/Semicond/Diamond/bandstr.html>.
- [30] Atlas User's Manual 2010.
- [31] S.M. Sze, K.K. Ng, *Physics of Semiconductor Devices*, third ed. John Wiley and Sons, 2007.
- [32] Y. Koide, Depletion layer in pn-junction of diamond with phosphorus donor and boron acceptor, *Diamond Relat. Mater.* 13 (2004) 1963.
- [33] S. Koizumi, T. Makino, in: R.P. Mildren, J.R. Rabeau (Eds.), *Optical Engineering of Diamond*, Wiley-VCH Verlag GmbH & Co. KGaA, Weinheim, Germany, 2013, pp. 177–208.
- [34] S. Koizumi, K. Watanabe, M. Hasegawa, H. Kanda, Formation of diamond p–n junction and its optical emission characteristics, *Diamond Relat. Mater.* 11 (2002) 307.
- [35] T. Makino, H. Kato, S.-G. Ri, S. Yamasaki, H. Okushi, Homoepitaxial diamond p–n<sup>+</sup> junction with low specific on-resistance and ideal built-in potential, *Diamond Relat. Mater.* 17 (2008) 782.
- [36] T. Makino, H. Kato, M. Ogura, H. Watanabe, S.-G. Ri, Y.G. Chen, S. Yamasaki, H. Okushi, Electrical and optical characterizations of (001)-oriented homoepitaxial diamond p–n junction, *Diamond Relat. Mater.* 15 (2006) 513.
- [37] C. Raynaud, D. Tournier, H. Morel, D. Planson, Comparison of high voltage and high temperature performances of wide bandgap semiconductors for vertical power devices, *Diamond Relat. Mater.* 19 (2010) 1.
- [38] H. Ding, K. Isoird, H. Schneider, S. Kone, G. Civrac, Basic parameters and models in simulation of CVD diamond devices, *Diamond Relat. Mater.* 19 (2010) 500.
- [39] A. Hiraiwa, H. Kawarada, Figure of merit of diamond power devices based on accurately estimated impact ionization processes, *J. Appl. Phys.* 114 (2013) 034506.
- [40] Y. Garino, T. Teraji, A. Lazea, S. Koizumi, Forward tunneling current in (111)-oriented homoepitaxial diamond p–n junction, *Diamond Relat. Mater.* 21 (2012) 33.
- [41] K. Oyama, S.-G. Ri, H. Kato, M. Ogura, T. Makino, D. Takeuchi, N. Tokuda, H. Okushi, S. Yamasaki, High performance of diamond p<sup>+</sup>–i–n<sup>+</sup> junction diode fabricated using heavily doped p<sup>+</sup> and n<sup>+</sup> layers, *Appl. Phys. Lett.* 94 (2009) 152109.
- [42] B. Massarani, J.C. Bourgoin, R.M. Chrenko, Hopping conduction in semiconducting diamond, *Phys. Rev. B* 17 (1978) 1758.
- [43] M. Hosoda, K. Kakushima, K. Natori, S. Yamasaki, H. Ohashi, H. Iwai, On the Electron Conduction in N-diamond, *Ieee*, New York, 2013.
- [44] B.I. Shklovskii, A.L. Efros, *Electronic Properties of Doped Semiconductors*, Springer-Verlag, Berlin; New York, 1984.
- [45] N.F. Mott, *Conduction in Non-crystalline Materials*, Clarendon Press; Oxford University Press, Oxford; New York, 1987.
- [46] T. Sato, K. Ohashi, H. Sugai, T. Sumi, K. Haruna, H. Maeta, N. Matsumoto, H. Otsuka, Transport of heavily boron-doped synthetic semiconductor diamond in the hopping regime, *Phys. Rev. B* 61 (2000) 12970.
- [47] M. Werner, R. Locher, W. Kohly, D.S. Holmes, S. Klose, H.J. Fecht, The diamond Irvin curve, *Diamond Relat. Mater.* 6 (1997) 308.
- [48] G. Chicot, A. Maréchal, R. Motte, P. Muret, E. Gheeraert, J. Pernot, Metal oxide semiconductor structure using oxygen-terminated diamond, *Appl. Phys. Lett.* 102 (2013) 242108.



# Temperature and density dependence metal–oxide–diamond interface investigation by TEM: Toward MOS and Schottky power device behavior

J. C. Piñero<sup>\*1</sup>, D. Araujo<sup>1</sup>, A. Traoré<sup>2</sup>, G. Chicot<sup>2</sup>, A. Maréchal<sup>2</sup>, P. Muret<sup>2</sup>, M. P. Alegre<sup>1</sup>, M. P. Villar<sup>1</sup>, and J. Pernot<sup>2</sup>

<sup>1</sup> Departamento Ciencia de los Materiales, Universidad de Cádiz, 11510 Puerto Real, Cadiz, Spain

<sup>2</sup> Institut Néel, CNRS-UJF, av. des Martyrs, 38042 Grenoble, France

Received 14 March 2014, revised 26 May 2014, accepted 26 May 2014

Published online 23 June 2014

**Keywords** diamond, oxide characterization, power device, Schottky, TEM

<sup>\*</sup> Corresponding author: e-mail josecarlos.pinero@uca.es, Phone: +34 660 584 895, Fax: 956016288

Metal and oxide distribution in diamond metal–oxide–semiconductor (MOS) structures are characterized using several transmission electron microscopy (TEM) modes at nanometric scale. To understand their electrical behavior, oxygen distribution using electron energy loss spectroscopy (EELS) through the layer structure, high-resolution electron

microscopy (HREM), and annular dark field (ADF) observations are reported. Oxide thickness variations, as well as oxygen content variations have been identified and characterized at an atomic resolution. The latter allows to understand the related electrical behavior as, for example, leakages or shortcuts.

© 2014 WILEY-VCH Verlag GmbH & Co. KGaA, Weinheim

**1 Introduction** Diamond is the ultimate semiconductor for high power and high frequency applications due to his high breakdown electric field [1], elevated mobility [2], and the outstanding thermal conductivity. Among such perspectives, diamond-based MOSFET and Schottky diodes are attractive architectures where the conducting or insulating behavior of the device is based on the electrostatic control of the band curvature at the oxide/semiconductor interface.

Previous metal–oxide–semiconductor (MOS) structures performed on diamond exhibited accumulation regime, but no deep depletion or inversion regimes [3–5]. Recent works report investigation of Al<sub>2</sub>O<sub>3</sub> with hydrogen-terminated [6, 7] and oxygen-terminated diamond [8]. The latter demonstrates that such MOS capacitors can undergo accumulation, depletion, and deep depletion, but some structures are still presenting some undesired electric behavior.

On the other hand, Schottky diodes, compared to other diamond power devices (bipolar transistor [9], junction field effect transistor [10], Schottky-pn diode [11], etc.) is the most promising because of a very simple structure and a highest breakdown voltage [1, 12]. However, still architectural progress are required to minimize its serial resistance.

Surface pretreatment and Schottky metal selection are crucial on the development of diamond Schottky power diodes, insofar that is affecting to the barrier heights, the thermal stability and defect density at the interface.

Recently, it has been assumed that the modification of the electrical behavior with thermal treatment of Schottky diodes [13] or with the atomic layer deposition (ALD) Al<sub>2</sub>O<sub>3</sub> growth conditions in MOS [8] are related with the oxide layer modifications. In particular, leakage currents either in Schottky diodes or in MOSFETs motivates the present nanostructural study of the diamond/oxide interface by scanning transmission microscopy (STEM). Indeed, the electrically measured behavior can be attributed to variations in the oxide thickness as well as differences in the oxygen distribution in the interface. The impact of the oxide layer highlights the importance of a nanostructural characterization of the oxide/diamond interface.

The present contribution analyses the latter interfaces by annular dark field (ADF), conventional transmission electron microscopy (CTEM), high-resolution electron microscopy (HREM), and electron energy loss spectroscopy (EELS) to determine their roughness and sharpness, as well as the oxygen distribution along the oxide layer.

**2 Experimental procedure** Samples were prepared using FIB polishing to get electron-transparent specimens with a Quanta 200 3D FIB dual-beam system. Both faces of the specimens were irradiated, at 4° of incidence, during 45 s with a 5 kV/14 pA beam during the last polish in order to reduce the contribution of the amorphous carbon. The fast diamond tendency to graphitize as well as the effect of the FIB implantation of diamond has been previously studied in literature [14, 15].

To evaluate the influence of the oxide variations in power devices, two different structures were analyzed:

- (1) Sample A consists in an Al/Al<sub>2</sub>O<sub>3</sub>/diamond structure whose electrical behavior was attributed to the possibility of leakages and is corresponding to #1 in Ref. [8].
- (2) Sample B consists in a metallic stack, whose Zr layer is in contact with an oxygen-terminated low-doped diamond substrate [13].

Samples were observed by CTEM for a first visual characterization of the diamond/oxide interface. Then, EELS profiles and maps were used to identify and characterize the thickness and the relative composition variations of the oxide layers, these profiles were acquired along oxide/diamond interface for an accurate characterization of the thickness variations. Finally, HREM imaging allows characterizing the previously identified oxide layer with atomic resolution. To realize such characterization, a JEOL 2010F transmission electron microscope (with point-to-point resolution of 0.2 nm) was used.

The previously discussed procedure allows the nano-characterization of oxide structures, whose thickness variations may lead to leakages, shortcuts, and undesired electric behavior. Here are studied samples #A and #B. Sample #A is corresponding with #1 in Ref. [8], an Al/Al<sub>2</sub>O<sub>3</sub>/diamond structure consisting in a B-doped diamond layer with a boron concentration of about few 10<sup>17</sup> cm<sup>-3</sup>. The deposition was performed at 910 °C with CH<sub>4</sub>/H<sub>2</sub> = 2%, B/C = 1200 ppm at 830 °C. Diamond surface oxygenation was performed by deep UV ozone treatment. Then, low temperature (100 °C) atomic layer deposition (ALD) was used for the creation of the oxide layer, the precursor used was trimethylaluminum (TMA), and the oxidant was H<sub>2</sub>O. After this, the dielectric was covered by a 100 nm thick aluminum metal using electron beam evaporator.

On the other hand, sample #B consists in a metallic stack with a Zr contact in a boron-doped oxygen-terminated diamond surface, whose electrical behavior has been recently published by Traoré et al. [13]. The boron-doped diamond layer was grown by microwave plasma-enhanced chemical vapor deposition (MPCVD) with 0.75% of CH<sub>4</sub> and 0.5% of O<sub>2</sub> in hydrogen gas, using a 50 Torr pressure and a temperature of 910 °C.

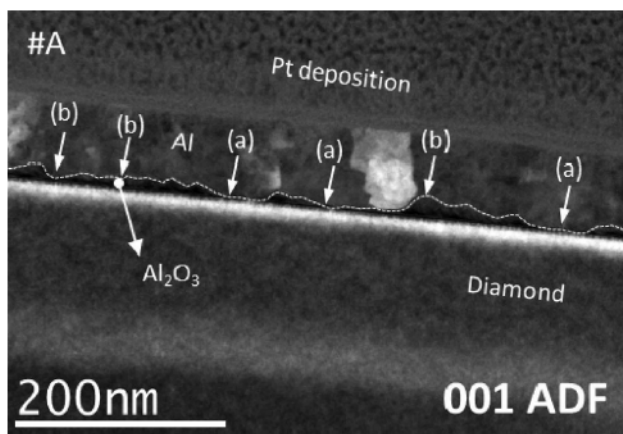
An electron beam evaporator was used to deposit Zr contacts and the first metallic material was subsequently covered with different cap layers. Tin-doped ITO were

deposited to fabricate Schottky contacts. ITO contacts were deposited by sputtering and annealed at 200 °C during 30 min, allowing crystallization.

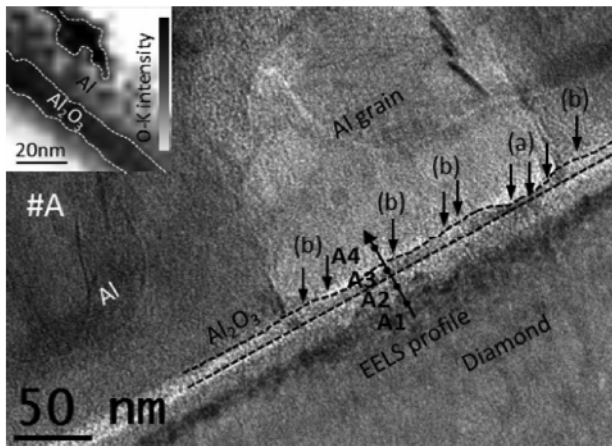
**3 Al<sub>2</sub>O<sub>3</sub> for MOS structures** Al<sub>2</sub>O<sub>3</sub> for MOS structures is a wise choice, due to the relative band-gap difference. Al/Al<sub>2</sub>O<sub>3</sub>/diamond structure investigations have been recently reported [6, 7], particularly, sample #A was previously studied by Chicot et al. [8], showing field effect in most of the structures. However, some capacitors still presents a peculiar C(V), that can be attributed to leakages inside the MOS structure. Indeed, the structure developed for such measurement avoid surface leak. Then, imaging techniques are used to reveal the oxide layer configuration. First, ADF (Fig. 1) and CTEM (Fig. 2) observations shows the Al/Al<sub>2</sub>O<sub>3</sub>/diamond structure. And second, EELS spectra and profiles (Fig. 3) were acquired in different points of the oxide/diamond interface (corresponding with the numbered positions).

Figure 1 shows an ADF micrograph of sample #A, revealing the presence of Al grains over the oxide layer. Furthermore, as contrast in ADF imaging is due to the joint contribution of the relative Z number difference and the diffraction effects, Al<sub>2</sub>O<sub>3</sub> layer appear as a dark contrast. This is not only due to the fact that Al<sub>2</sub>O<sub>3</sub> is lighter than Al, but is also dependent on diffraction contrast (as can be seen in the Al layer). The dark contrast of the Al<sub>2</sub>O<sub>3</sub> is probably largely also due to the amorphous nature of the layer. Additionally, white dashed line in Fig. 1 is used to guide the eyes along the metal–oxide interface, (b)-labeled arrows are used to highlight local oxide thickness variations, finally, (a)-labeled arrows in Fig. 1 shows possible metal–semiconductor contact points.

As can be observed in Fig. 2, oxide's mean thickness is altered in the vicinity of the Al grains. Such behavior can lead to leakages or to shortcuts (if contacting the Al layer with the diamond substrate). Black arrows in Fig. 2 are used to highlight the oxide thickness variations along the



**Figure 1** Annular dark field (ADF) micrograph of sample #A that reveals both, the grain structure along the Al layer and oxide thickness variations.



**Figure 2** Bright field micrograph of sample #A, using the 001 reflection. A polycrystalline grain structure is observed in the Al layer. In the  $\text{Al}_2\text{O}_3$  layer, thickness variations are revealed. Electron energy loss spectroscopy mapping (inset) in another region allows identifying the oxide layer through the observation of the O–K peak.

interface. A black dashed line is superimposed to guide the eyes at both diamond/oxide and oxide/Al interfaces.

As the nominal diamond substrate's surface is very smooth, the first interface shows a similar behavior along the structure. In contrary, despite the oxide layer is deposited by low temperature ALD, a relatively rough interface is revealed between oxide/Al.

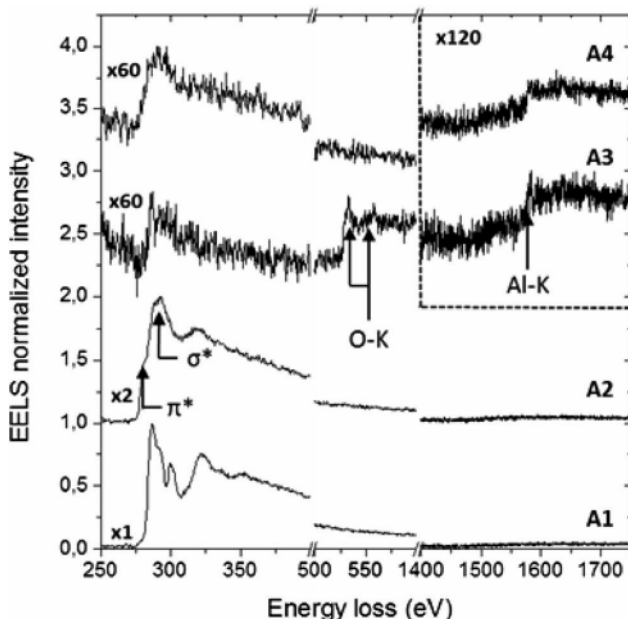


**Figure 3** Electron energy loss spectra recorded along the diamond/oxide structure of #A (see Fig. 2).  $\pi^*$  and  $\sigma^*$  peaks of the carbon K-transition are observed, revealing diamond structure in the substrate (spectrum 1). The C signal in spectra A2, A3, and A4 may be due to C contamination produced during the FIB operation. The oxygen-K peak transition is observed in spectrum A3.

Variations of the  $\text{Al}_2\text{O}_3$  thickness are shown to have some impact on the further synthesis of the device, insofar that Al/diamond electric contacts can be produced, leading to shortcuts and undesirable electrical behavior. For example, (b)-labeled arrows in Fig. 2 mark the presence of local maximums of the  $\text{Al}_2\text{O}_3$  thickness corresponding with an Al grain boundary. Using EELS profiling, a minimum oxide thickness of 4.8 nm as well as a maximum alumina thickness of 20.4 nm were measured in the Al grain/alumina interface. The previously discussed behavior is coherent with the EELS map recorded at 532 eV (color-inverted, oxygen in black) shown in the inset of Fig. 2, which was acquired on a different region of the sample. EELS maps acquired along the interface allow verifying the oxide thickness variations, evidencing also the presence of  $\text{Al}_2\text{O}_3$  islands into the Al layer, as were shown in inset of Fig. 2.

Figure 3 shows EELS profiles that confirm the presence of the oxide layer. Electron energy loss spectra were acquired in substrate, oxide, and metal layers following the numbered profile of Fig. 2. Spectra were acquired over a  $3 \times 3 \text{ nm}^2$  area to improve the signal-to-noise relation. It can be observed that the  $\text{sp}^3$  C-related signal at 285–292 eV is defined only in the diamond substrate, while some lower carbon contamination ( $\text{sp}^2$  shape) is observed at A3 and A4. C redeposition during FIB operation and carbon contamination due to long-time EELS data acquisition can also explain the slight presence of the C-related signal in spectra A3 and A4. Spectrum A1 in Fig. 3 shows C–K peak with typical diamond signature, but spectrum A2 in Fig. 3 is presenting graphitization ( $\pi^*$  and  $\sigma^*$  are revealed near the diamond/oxide interface). Likewise, the oxygen-K signal showed in spectrum A3 of Fig. 3 is confined on the oxide layer. By using this last result, EELS profiling has been used to explore the oxide layer's homogeneity. A series of profiles were acquired along  $1.5 \mu\text{m}$  of the oxide/diamond interface. One of these EELS profiles is shown in Fig. 4, this allows studying the oxygen peak evolution along the oxide layer, revealing an asymmetric oxygen distribution. The relative

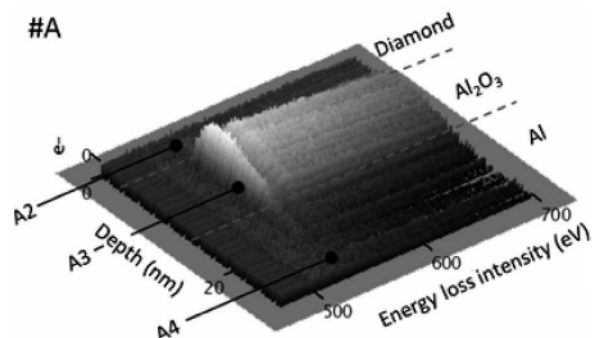


**Figure 4** Electron energy loss spectroscopy (EELS) profile in a specific point of the diamond/ $\text{Al}_2\text{O}_3$ /Al interface (sample #A). The O–K peak is revealed, the peak intensity along the alumina layer is asymmetrically distributed. The numbered positions are corresponding with the spectra presented in Fig. 3 and with the spatial distribution already shown in Fig. 2.

intensity of the O-K peak is different depending on the point of the interface, that is an indirect evidence of the oxide thickness inhomogeneity (insofar that the e-beam is passing through a different oxide thickness point by point). These EELS profiles reveal a maximum oxide thickness of 20.4 nm and a mean thickness of 11.2 nm, as stated above.

EELS profiling and mapping are coherent with CTEM imaging, revealing oxide thickness variations in the Al grain vicinities. Such behavior could mean a mixture of alumina and aluminum in the metal/oxide interface, and can explain the undesired electrical behavior [8].

**4 Zr for diamond Schottky power diode** An outstanding power diode using oxygen-terminated diamond was presented in Ref. [13]. Such device is presenting a high current density and a reverse current that was below the detection threshold. The good electrical behavior of such device was attributed to the possibility of the formation of a thin zirconia film between the oxygen-terminated diamond and the zirconium layer. To verify this assumption, HREM and EELS are here carried out to evidence the presence of oxide in the state of  $ZrO_2$  and show its spatial distribution. The latter is evidenced by HREM with EELS certifying the presence of  $ZrO_2$ .

Figure 5 shows an HREM micrograph of the MOS structure in sample #B and allows measuring the thickness of the  $ZrO_2$  layer with atomic resolution, leading to the detection of an about 4 Å thick oxide layer. Distance between atomic columns of approximately 3 Å can be extracted from an HREM intensity profile. EELS profiling allows identifying the white contrast presented in Fig. 5 as the oxide layer. Squared-dashed line regions in Fig. 5 shows HREM filtered images, revealing [022]-type diamond planes. Fourier transform in the squared regions reveals

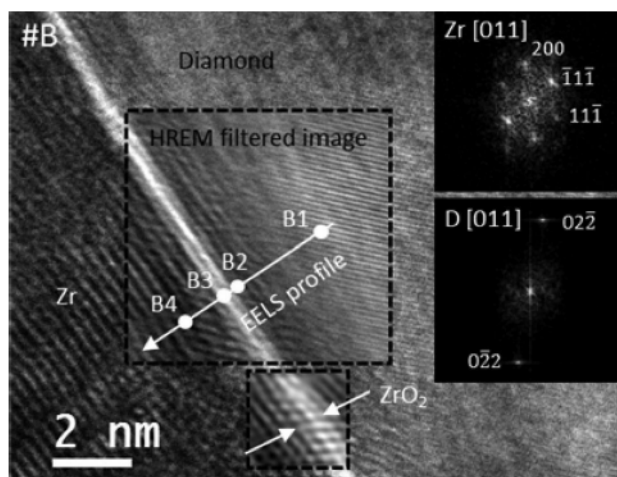


**Figure 5** Wiener filtered HREM micrograph of sample #B. Atomic columns are revealed. Oxide thickness remains constant along the interface. EELS allows identifying a 4 Å  $ZrO_2$  layer. Inset shows Fourier transform of the selected filtered area, revealing the [011] pole.

[011] pole. Fourier transform was carried out in the Zr layer and in the diamond substrate, both are shown as insets in Fig. 5.

By combining the identified [011] pole in the diamond's Fourier transform, the already known diamond's lattice parameter of 3.56 Å and the zirconium's [011]-oriented Fourier transform, a 5 Å Zr lattice parameter has been calculated. This result is coherent with the lattice parameter of a cubic Zr structure [16].

On the other hand, EELS spectra were recorded along the white line indicated in Fig. 5, corresponding results are shown in Fig. 6. Spectra B1 and B2 in Fig. 6 have the typical  $sp_3$ -related shape. The latter shows also a weak Zr- $M_{4,5}$  signal due to the spot extension. Presence of  $ZrO_2$  layer is demonstrated in spectrum B3 of Fig. 6, with the simultaneous presence of the O-K line with the  $M_{4,5}$  and  $M_3$  Zr lines. It also confirms that the white contrast observed in Fig. 5 is, in fact, the zirconia layer.

Using this procedure, three regions are defined in Fig. 5:

- (1) Zr layer, confirmed by spectrum B4 in Fig. 6.
- (2) Four Angstrom thick  $ZrO_2$  layer, identified by EELS (spectrum B3 in Fig. 6).
- (3) Diamond substrate.

Thickness of the zirconia layer was homogeneous along the studied interface. This result is in agreement with the assumption of the formation of a thin zirconia layer in the interface of the Zr deposition with the oxygen-terminated diamond and it can explain the good electric behavior of the associated device [13].

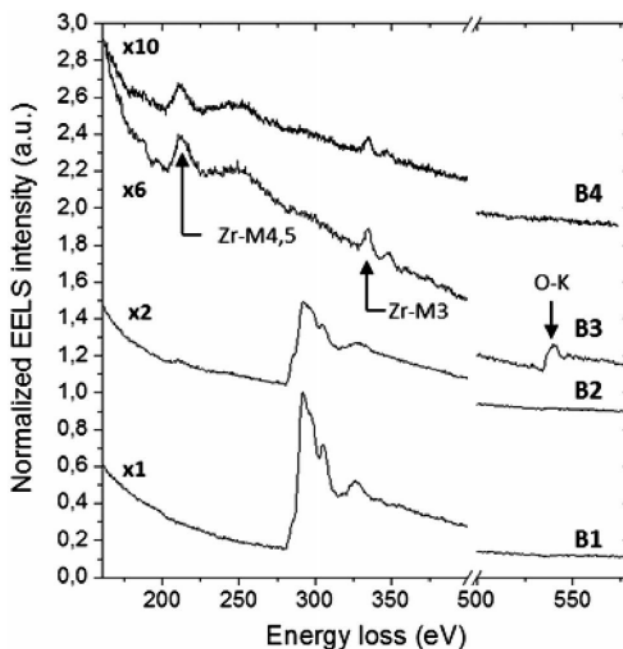


**Figure 6** EELS profile of the metal-oxide-semiconductor interface of #B acquired as shown in Fig. 5.  $ZrO_2$  layer is identified.

**5 Conclusions** The electrical behavior of the Al/Al<sub>2</sub>O<sub>3</sub>/diamond MOS structure (sample #A), that was previously studied by Chicot et al. [8], has been explained in terms of thickness variations of the oxide layer. Not only the oxide thickness, but also the oxygen distributions inside the oxide layer are varying. This behavior can lead to leakages or to shortcuts (Al/diamond contacts) in the associated device.

On the other hand, the electrical behavior of the Schottky diode with a Zr/ZrO<sub>2</sub>/diamond interface (sample #B), has been explained. The hypothesis of Traoré et al. [13] about the formation of a 4 Å thick zirconia layer has been demonstrated. The stability and homogeneity of such layer along the metal/oxide interface remains constant, explaining the electrically measured behavior.

Variations in the oxygen distribution, oxide/metal mixtures and oxide thickness variations have been characterized. These alterations can lead to undesired electric behavior in the associated electric device. Finally, oxide thickness variations have been identified with atomic resolution.

**Acknowledgements** The authors thank “Ministerio de Ciencia e Innovación” for the grants BES-2010-039524 and EEBB-I-13-07696 of the project TEC2009-11399.

## References

- [1] T. P. Chow, W. Huang, J. Yang, and J. E. Butler, *Int. J. High Speed Electron. Syst.* **14**, 872 (2004).
- [2] J. Hammersberg, J. Isberg, E. Johansson, T. Wikstrom, D. J. Twitchen, A. J. Whitehead, S. E. Coe, and G. A. Scarsbrook, *Science* **297**, 1670 (2002).
- [3] M. Imura, R. Hayakawa, E. Watanabe, M. Y. Liao, Y. Koide, and H. Amano, *Phys. Status Solidi RRL* **5**(3), 125 (2011).
- [4] H. Sato, M. Kasu, and K. Hirama, *Appl. Phys. Lett.* **5**, 025701 (2012).
- [5] Y. Yokota, N. Kawakami, T. Tachibana, K. Hayashi, and K. Kobashi, *Diamond Relat. Mater.* **14**, 2015 (2005).
- [6] A. Daicho, A. Hirawira, S. Kurihara, Y. Yokoyama, and H. Kawarada, *J. Appl. Phys.* **112**, 124504 (2012).
- [7] M. Y. Liao, J. W. Liu, M. Imura, H. Li, and Y. Koide, *Appl. Phys. Lett.* **101**, 232907 (2012).
- [8] G. Chicot, A. Marechal, R. Motte, P. Muret, E. Gheeraert, and J. Pernot, *Appl. Phys. Lett.* **102**, 242108 (2013).
- [9] K. Oyama, H. Kato, T. Makino, M. Ogura, D. Takeuchi, and S. Yamasaki, *Diamond Relat. Mater.* **27–28**, 19 (2012).
- [10] Y. Hoshino, T. Iwazaki, K. Tsuzuki, H. Kato, T. Makino, M. Ogura, D. Taekuchi, T. Matsumoto, H. Okushi, S. Yamasaki, and M. Hatano, *Appl. Phys. Express* **5**, 091301 (2012).
- [11] S. Tanimoto, T. Makino, Y. Hayashi, H. Kato, N. Tokuda, M. Ogura, D. Takeuchi, K. Oyama, H. Ohashi, H. Okushi, and S. Yamasaki, *Appl. Phys. Lett.* **94**, 262101 (2009).
- [12] P. Muret, P. N. Volpe, J. Pernot, F. Omnès, T. Teraji, F. Jomard, D. Planson, P. Brosselard, N. Dheilily, B. Vergne, and S. Scharnholtz, *Appl. Phys. Lett.* **97**, 223501 (2010).
- [13] A. Traoré, P. Muret, A. Fiori, D. Eon, E. Gheeraert, and J. Pernot, *Appl. Phys. Lett.* **104**, 052105 (2014).
- [14] W. R. McKenzie, M. Z. Quadir, M. H. Gass, and P. R. Munroe, *Diamond Relat. Mater.* **20**, 1125 (2011).
- [15] Y. Q. Chen, F. Z. Tang, and L. C. Zhang, *J. Mater. Sci. Nanotechnol.* **531–532**, 592 (2013).
- [16] R. A. Ploc, *J. Nucl. Mater.* **99**, 124 (1981).

# Hole injection contribution to transport mechanisms in metal/p<sup>-</sup>/p<sup>++</sup> and metal/oxide/p<sup>-</sup>/p<sup>++</sup> diamond structures

P. Muret<sup>\*1,2</sup>, D. Eon<sup>1,2</sup>, A. Traoré<sup>1,2</sup>, A. Maréchal<sup>1,2</sup>, J. Pernot<sup>1,2,3</sup>, and E. Gheeraert<sup>1,2</sup>

<sup>1</sup> Université Grenoble Alpes, Institut Néel, 38042 Grenoble, France

<sup>2</sup> CNRS, Institut Néel, 38042 Grenoble, France

<sup>3</sup> Institut Universitaire de France, 103 Boulevard Saint-Michel, 75005 Paris, France

Received 16 March 2015, revised 14 July 2015, accepted 15 July 2015

Published online 7 August 2015

**Keywords** charge carrier transport, diamond, electronic devices, metal–oxide–semiconductor structures

\* Corresponding author: e-mail pierre.muret@neel.cnrs.fr, Phone: +33-476-881193, Fax: +33-476-881191

Heterostructures such as Schottky diodes and metal/oxide/semiconductor structures are the building blocks of diamond electronic devices. They are able to carry large current densities, up to several  $\text{kA cm}^{-2}$ , if a heavily boron-doped layer ( $\text{p}^{++}$ ) is included in the semiconducting stack, thus affording a metallic reservoir of mobile holes close to the lightly doped layer ( $\text{p}^-$ ). In this work, hole injection effects are evidenced experimentally in the two previously mentioned devices and also simulated numerically. Although the potential barrier height at metal/semiconductor interfaces is a fundamental parameter, a more general approach consists in defining the current density from the product of an effective velocity and carrier concen-

tration at interface. In accordance with experimental results, such a view permits to describe both depletion and accumulation regimes, which indeed can exist at the metallic or oxide interface, and to take into account the increase of the hole concentration above the thermal equilibrium one in the  $\text{p}^-$  layer. The lower the temperature, the larger is this second effect. For sufficiently thin  $\text{p}^-$  layers, typically below  $2 \mu\text{m}$ , this effect frees device operation from the limitation due to incomplete ionization of acceptors and allows a strong decrease of the specific resistance and forward losses while preserving breakdown voltages in the range of 1.4–2 kV.

© 2015 WILEY-VCH Verlag GmbH & Co. KGaA, Weinheim

**1 Introduction** Diamond heterostructures show huge potentialities for high-power and high-temperature electronic devices due to the astounding physical and electrical properties of this semiconductor such as wide band gap ( $E_G = 5.45 \text{ eV}$ ), high thermal conductivity ( $22 \text{ W cm}^{-1} \text{ K}^{-1}$ ), room temperature mobility of holes close to  $2000 \text{ cm}^2 \text{ V}^{-1} \text{ s}^{-1}$ , and high breakdown field ( $F > 7.7 \text{ MV cm}^{-1}$ ) as already demonstrated recently [1, 2]. P-type device operation can also gain benefit from the ability of diamond to be heavily doped with boron, above the metallic conductivity limit. However, the ionization energy of boron acceptors, near 0.37 eV, induces complete ionization only around 550 K and above in lightly doped layers, which are necessary to lower electric fields in depletion zones. Accordingly, the hole concentration is one to two orders of magnitude smaller than the acceptor concentration at room temperature, making the conductivity somewhat insufficient. With a lightly doped layer ( $\text{p}^-$ ) thicker than  $10 \mu\text{m}$ , the current–voltage characteristics

become strongly temperature dependent [3, 4] and the specific electrical resistance hardly smaller than  $1 \Omega \text{ cm}^2$  at room temperature [4]. Conversely, with an n-type layer not exceeding a few hundred nanometers, the operation of such a Schottky p–n junction [5] becomes completely governed by carrier injection, which permits to reach several  $\text{kA cm}^{-2}$  in the forward regime, but at the expense of a very limited breakdown voltage in the reverse regime. Here, we show that stacking a lightly doped layer ( $\text{p}^-$ ) with a well-designed thickness onto a heavily doped layer ( $\text{p}^{++}$ ) or substrate can circumvent all these drawbacks. In lightly doped diamond layers with thicknesses up to  $2 \mu\text{m}$ , the heavily doped layer or substrate is able to inject holes, thus increasing the hole concentration well above the equilibrium one down to the interface with the oxide or metal, as demonstrated both experimentally and from simulation in this work. Calculations relying either on the numerical solutions of the complete basic equations set or on transport equations relevant only for holes are developed

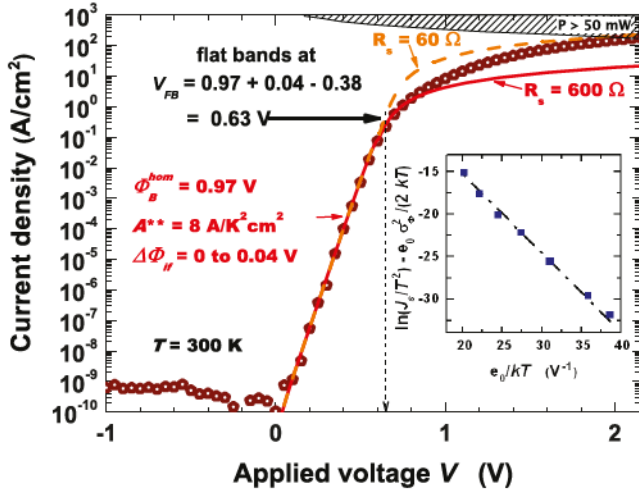


**Figure 1** Experimental current density of the diode as a function of total voltage displayed with open symbols and fitting curves based on the parameters indicated in the figure and determined by the method described in the text; the Richardson plot is shown in the inset. The hatched area close to upper right corner delineates a constant dissipated power of 50 mW below which estimated self-heating remains smaller than 5 K.

in order to attempt predicting the optimal thickness of the p<sup>-</sup> layer. In all the structures, at sufficiently high injection level, the interface with the metal or oxide comes into accumulation regime, including the case of Schottky diodes. Hence, the diode current relies more generally on the transport model based on the majority carrier population and effective velocity at interface rather than on the potential barrier height of the junction. Finally, indications can be derived for the design of devices based on vertical and pseudo-vertical heterostructures in order to maintain an optimal trade-off between lowest forward losses, minimal specific resistance at room temperature, and highest breakdown voltages.

**2 Experimental transport characteristics of devices** The current–voltage characteristics of Zr-oxidized diamond diodes annealed at 450 °C are firstly presented (Fig. 1) and analyzed. The diamond stack comprises a lightly doped layer, 1.3 μm thick and containing  $5 \times 10^{15} \text{ B cm}^{-3}$ , on a heavily doped layer, 0.2 μm thick and containing  $(2 - 4) \times 10^{20} \text{ B/cm}^3$ , epitaxially grown on an Ib substrate. More detailed properties have been already presented in [6], specially the fabrication recipes and the breakdown field in excess of  $7.7 \text{ MV cm}^{-1}$  under reverse bias, confirming older results [2]. Fair uniformity and reproducibility of the electrical characteristics of the diodes fabricated on one or several substrates have been demonstrated [6]. A complete analysis of the transport mechanisms at stake in these Schottky junctions in the depletion regime at various temperatures is currently under submission [7]. In this later study, different methods able to extract the true homogeneous potential barrier height  $\Phi_B^{\text{hom}}$ , free of the random barrier lowering due to interface inhomogeneities and described by its standard deviation  $\sigma_\phi$  [8, 9], are demonstrated and applied. The derivation

of parameters displayed in Fig. 1 is done here along three steps: (i) the derivation of  $\sigma_\phi$  from the adjustment of the apparent barrier got from the current density  $J_s$  extrapolated at zero junction voltage as a function of temperature  $T$  (not shown here); secondly, the Richardson plot of  $J_s/T^2$  corrected by the term proportional to  $\sigma_\phi^2$  shown in the inset of Fig. 1 which permits to derive the effective Richardson constant  $A^{**}$ ; thirdly, the final adjustment of the homogeneous barrier height  $\Phi_B^{\text{hom}}$  and ideality factor  $n$  (here 1.07) to the experimental current density as a function of voltage in the linear part of the characteristics plotted in a semi-logarithmic scale as in Fig. 1, taking the image force lowering  $\Delta\Phi_{\text{if}}$  into account.

In the present case, with an ideality factor  $n$  decreasing from 1.07 at 300 K down to 1.04 at 600 K, the homogeneous barrier height of these almost perfect junctions turns out to be  $0.97 \pm 0.02 \text{ V}$ , in good agreement with an other determination for Zr on oxygenated diamond [10]. Taking into account the image force effect which adds 0.04 V to the barrier at flat bands [7, 9] and the calculated energy difference between the bulk Fermi level and valence band top of 0.38 eV from data in [1], the applied voltage needed to induce flat bands amounts to 0.63 V, as indicated in Fig. 1. For larger junction voltages  $V$ , which are necessary to reach current densities  $J_p$  higher than  $0.4 \text{ A cm}^{-2}$ , band bending is inverted, the interface turns into accumulation regime and the apparent barrier for holes vanishes. Consequently, it is advisable to describe the current density in the Schottky junction as the product of a collection velocity  $v_{\text{coll}}$ , hole concentration  $p(z_0)$  at the metallic interface and elementary charge  $e_0$  [11, 12]. This hole collection velocity  $v_{\text{coll}}$  is the same as the thermionic one,  $v_{\text{coll}} = \alpha \sqrt{\frac{k_B T}{2\pi m^*}}$ ,  $k_B$  being the Boltzmann constant and  $\alpha$  the attenuation coefficient of the reduced thermionic emission due to the oxide interlayer which can be evaluated from the ratio of the effective Richardson constant (see the inset in Fig. 1) to the standard one ( $96 \text{ A K}^{-2} \text{ cm}^{-2}$ ) in diamond. This approach remains valid in the depletion regime where  $p(z_0)$  is merely the product of the equilibrium hole concentration  $p_0$  in the bulk lightly doped layer and the factor  $\exp [(-\Phi_B^{\text{hom}} + V_j/n)/(k_B T)]$ , but is now essential when  $p(z_0)$  deviates in excess from the previous quantity because of the hole injection from the heavily doped layer. Such an effect is firstly evidenced from the deviation existing between experimental data and the full voltage of the  $J_p - V$  characteristic taking into account the effect of the 600 Ω series resistance  $R_s$  due the resistivity of the lightly doped layer calculated at room temperature and thermodynamic equilibrium (Fig. 1). The same characteristics simulated with  $R_s = 60 \Omega$  matches somewhat better the measured points at current densities higher than  $10^2 \text{ A cm}^{-2}$  but very badly in the range  $1 - 50 \text{ A cm}^{-2}$ . This discrepancy shows firstly that the voltage drop in the lightly doped layer is not linear with the current and secondly that it is lower than predicted from the equilibrium concentration of holes which would induce a 600 Ω series resistance. An even more illuminating property emerges from the plot of the derivative of  $J_p - V$ , which is nothing

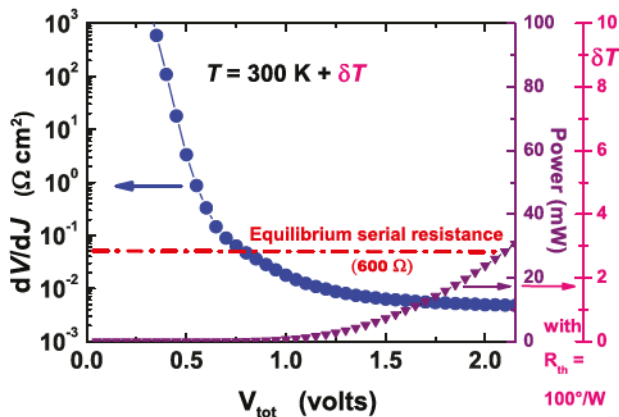


**Figure 2** Specific resistance of the diode as a function of total voltage displayed with full circles. Downward triangles feature both dissipated power and temperature increase  $\Delta T$  sketched in K on the right vertical scale.

other than the specific resistance of the diode, shown in Fig. 2. In this graph, it clearly appears that this specific resistance decreases by a factor larger than 10 below  $R_s = 600 \Omega$  well before any significant increase of the temperature due to self heating, calculated with a largely overestimated thermal resistance of  $100 \text{ K W}^{-1}$  because of the intimate contact of the rear side of the diamond substrate with the silver heat sink of our sample holder.

In metal/oxide/semiconductor (MOS) heterostructures made on diamond [13], the forbidden bandgap of the oxide is often very similar to that of diamond or it overcomes it by only one or two eV. Consequently, band offsets on oxygenated diamond surfaces are almost systematically close to 1 eV or lower, leaving the thermionic currents over the oxide barrier at an easily detectable level when a sufficient forward polarization is applied. This is the case in our MOS structures consisting of Al on  $\text{Al}_2\text{O}_3$ , 25 nm thick, on a  $p^-/p^+$  diamond stack, with an acceptor concentration of  $3 \times 10^{17} \text{ B cm}^{-3}$  in the lightly doped layer which is 500 nm thick. Current density–voltage characteristics over a large range of temperatures (103–353 K) of such an MOS capacitor are displayed in Fig. 3 as a function of bias voltage applied on the metal electrode. Thermionic current over the barrier of 1.34 eV due to the band offset between the valence band edges [14] and determined like in reference [15] but for an oxygenated diamond surface is responsible for the highest slope in the characteristics. If the current was controlled by the equilibrium concentration of holes at the oxide/diamond interface, it would experience more than 15 decades of variation over the whole temperature range, relying on a calculation by the formula (1) in [1]. Conversely, current density at a given voltage changes by at most two decades (see Fig. 3), firmly indicating that the hole concentration is not governed by its equilibrium value but rather by a concentration which is strongly dependent of that in the  $p^+$  layer, practically independent of temperature since diamond is a degenerate semiconductor in this layer. This is the second evidence which demonstrates that current–voltage characteristics in heterostructures comprising a buried heav-

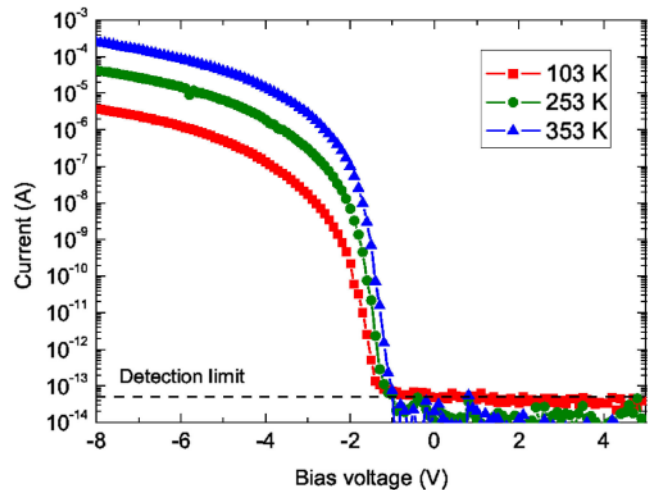


**Figure 3** Current–voltage characteristics in an MOS heterostructure for several temperatures.

ily doped layer must take hole injection from this  $p^+$  layer into account.

**3 Simulation of the hole transport** In order to check the properties previously evidenced and to gain quantitative insight into the transport mechanisms, simulations and calculations are performed. Firstly, using the finite elements software COMSOL Multiphysics, profiles of the valence band top and quasi-Fermi level of holes are simulated at 300 K in a stack  $p^+/p^-/\text{metal}$ , with a Schottky barrier of 1 V, for applied forward voltages spanning the range 0–5 V, each 0.5 V (Fig. 4). The software makes use of all the basic equations which describe semiconductor junctions, as one can find in textbooks like [16], including both minority and majority carriers transport although the former are unnecessary

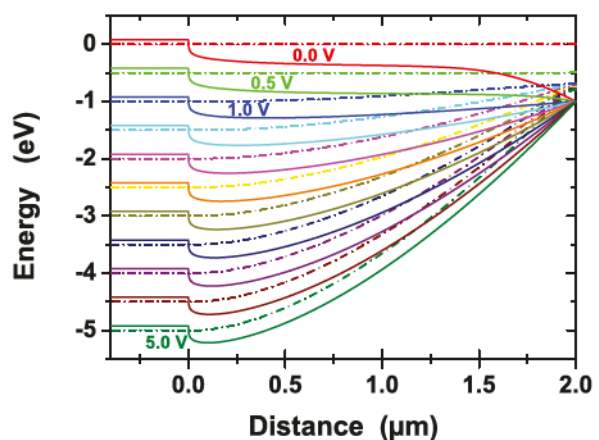


**Figure 4** Energy of the valence band top in full lines and quasi-Fermi level of holes in dotted lines, along the depth of a stack  $p^+/p^-/\text{metal}$  measured from the  $p^+/p^-$  interface, with a Schottky barrier of 1 eV, for applied forward voltages spanning the range 0–5 V, each 0.5 V. Data are obtained from a simulation performed with the software COMSOL Multiphysics for a temperature of 300 K. See text for other conditions.

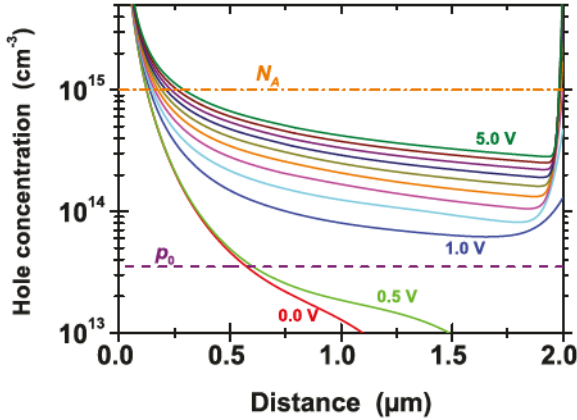


**Figure 5** Hole concentration at 300 K as a function of the distance measured from the  $p^{++}/p^-$  interface for forward applied voltages from 0–5 V, each 0.5 V. The equilibrium hole concentration  $p_0 = 3.5 \times 10^{13} \text{ cm}^{-3}$  and acceptor concentration  $N_A = 10^{15} \text{ cm}^{-3}$  are, respectively, indicated by dashed and dash-dotted lines. Accumulation regime is clearly visible near the Schottky interface, at the 2  $\mu\text{m}$  abscissa.

in the case we are dealing with. The doping concentrations are respectively  $2 \times 10^{20}$  and  $10^{15} \text{ B/cm}^{-3}$  in the  $p^{++}$  and the  $p^-$  layers, the latter being 2  $\mu\text{m}$  thick. Other boundary conditions are defined on the figure for the electric potentials while the field at the beginning of the  $p^{++}$  layer is assumed to be zero because of a perfect ohmic contact, and the carrier velocities at the Schottky contact (at abscissa 2  $\mu\text{m}$ ) are given by the product of the mobility [1] and electric field. Saturation of the hole velocity which happens for fields larger than  $10^4 \text{ V cm}^{-1}$  [17] is ignored, involving a shift of the curves in Figs. 4 and 5 of only a few nanometers toward larger abscissa as estimated from following equations. Depletion regime can be observed close to the metallic interface (at abscissa 2  $\mu\text{m}$ ) for applied voltages 0 and 0.5 V. But for 1 V and above, band curvature near the metallic interface is inverted and the depletion regime is replaced by accumulation, fully confirming the observations detailed in the previous section. The corresponding hole concentrations are plotted in Fig. 5. Here again, one can see that the hole concentration falls below the equilibrium one  $p_0 = 3.5 \times 10^{13} \text{ cm}^{-3}$  near the Schottky interface for applied voltages zero and 0.5 V, while it increases and stays above and above  $p_0$  for larger and larger voltages. Due to this behavior, it is clear that the voltage drop inside the  $p^-$  layer can neither follow linearly the current nor be determined by the equilibrium hole concentration  $p_0$ , the real one remaining several times larger up to distances typically near 2  $\mu\text{m}$  from the  $p^{++}$  layer boundary.

An other approach relies on usual equations describing transport of charge by majority carriers [16] in the  $p^-$  layer. Along the  $z$  direction, perpendicular to interface, the hole current density equation is the sum of the drift and diffusion components,  $\mathcal{E}_z(z)$  being the electric field and  $p(z)$  the hole concentration, with  $\beta = e_0/k_B T$  and a constant mobility  $\mu_p$

as previously assumed:

$$J_p = e_0 \mu_p \left[ p(z) \mathcal{E}_z(z) - \frac{1}{\beta} \frac{dp(z)}{dz} \right]. \quad (1)$$

In accordance with the results of the simulation, the two currents have similar magnitudes but opposite direction close to the origin ( $p^{++}$  layer edge) because the very strong diffusion current must be partially compensated by an opposite conduction current so that the constraint imposed by the effective current  $J_p$  can be satisfied. Consequently, no terms can be neglected in the previous equation. Moreover, Poisson equation must be satisfied:

$$\frac{d\mathcal{E}_z(z)}{dz} = e_0 [p(z) - N_{\text{ion}}^-] / (\varepsilon_0 \varepsilon_{\text{SC}}), \quad (2)$$

where  $N_{\text{ion}}^-$  is the net, negatively charged, ionized impurity concentration. Elimination of the hole concentration in Eq. (1) with help of Eq. (2) gives the following second-order field equation:

$$-\frac{d^2 \mathcal{E}_z(z)}{dz^2} + \beta \mathcal{E}_z(z) \left[ \frac{d\mathcal{E}_z(z)}{dz} + \frac{e_0 N_{\text{ion}}^-}{\varepsilon_0 \varepsilon_{\text{SC}}} \right] = \frac{\beta J_p}{\varepsilon_0 \varepsilon_{\text{SC}} \mu_p}, \quad (3)$$

where the second member is a constant because the current is conservative since there is no recombination. It will be named  $C$  in the following.

The two boundaries conditions are: (i)  $p(0) = p^+$  at  $z = 0$ , the interface between the heavily and lightly doped layers and  $p^+$  the hole concentration in the heavily doped layer; (ii) at the interface with the metal supposed to be located at  $z = z_0$ , the carrier collection velocity  $v_{\text{coll}}$  must be equal to the thermionic one, so that  $p(z_0) = J_p / (e_0 v_{\text{coll}})$ . In terms of the first derivative of the electric field, these two boundary conditions can be read as follows:

$$(i) \frac{d\mathcal{E}_z(0)}{dz} = \frac{e_0}{\varepsilon_0 \varepsilon_{\text{SC}}} [p^+ - N_{\text{ion}}^-]$$

and

$$(ii) \frac{d\mathcal{E}_z(z_0)}{dz} = \frac{e_0}{\varepsilon_0 \varepsilon_{\text{SC}}} [J_p / (e_0 v_{\text{coll}}) - N_{\text{ion}}^-].$$

As we are interested primarily by the extension of the region where the hole concentration largely exceeds the ionized impurity one, the last term of the first member of Eq. (3) is neglected and this equation can then be integrated one time:

$$\frac{e_0}{\varepsilon_0 \varepsilon_{\text{SC}}} [p^+ - p(z)] + \frac{\beta}{2} [\mathcal{E}_z(z)^2 - \mathcal{E}_z(0)^2] = Cz. \quad (4)$$

Because the concentration  $p(z)$  and the square electric field  $\mathcal{E}_z(z)^2$  decrease very rapidly from the origin  $z = 0$ , a good

approximation consists to neglect the terms depending on  $z$ , so that  $\mathcal{E}_z(0)^2 = (2e_0 p^+) / (\beta \epsilon_0 \epsilon_{SC})$ , resulting in the approximated initial condition:  $\mathcal{E}_z(0) = -\sqrt{\frac{2e_0 p^+}{\beta \epsilon_0 \epsilon_{SC}}} = \frac{-1}{\beta L_D} \sqrt{\frac{2p^+}{p_0}}$  where  $L_D$  is the appropriate Debye length in the lightly doped layer. For other abscissa, the remaining differential equation to be solved reads as

$$\frac{\beta}{2} \mathcal{E}_z(z)^2 - \frac{d\mathcal{E}_z(z)}{dz} = Cz, \quad (5)$$

where the first and second terms are respectively due to drift and diffusion components of the current. An exact solution can be found for a vanishing second member, rigorously valid near zero voltage bias:  $\mathcal{E}_z(z) = -\frac{2}{\beta} \frac{1}{z+z_1}$ , where  $z_1 = 2L_D \sqrt{p_0/(2p^+)} = 2\sqrt{\epsilon_0 \epsilon_{SC}/(2e_0 \beta p^+)}$  close to 0.3 nm here. This solution shows that the Debye length has still a significance in terms of attenuation distance, despite a non-exponential damping law. It still describes satisfactorily the field and hole concentration as long as each of the two terms in the first member of Eq. (5) has a comparable absolute value, much larger than the second member, at abscissa  $z < z_c$  of few  $z_1$ . With the help of Eq. (2), one gets  $p(z) \approx \frac{2e_0 \epsilon_{SC}}{e_0 \beta} \frac{1}{(z+z_1)^2}$ , which therefore can be retained for the initial hole concentration close to the  $p^{++}$  layer till  $z_c$ . If  $p(z_c) = 2 \times 10^{14} \text{ cm}^{-3}$ , where  $z_c$  is the distance where the hole concentration has dropped from its initial value  $p(0)$  by a factor of  $10^6$ , a fairly good estimate of 0.3  $\mu\text{m}$  is derived, in agreement with the curves plotted in Fig. 5. Beyond such an abscissa, one of the two terms in the first member of Eq. (5) may become dominant and of the same magnitude as  $Cz$ . Then, assuming that either the first or the second term can be neglected, solutions based on fractions depending of  $z$  and  $\sqrt{z}$  could be found. If only the first term, related to the drift component, is retained,  $\mathcal{E}_z(z) \approx \frac{1}{\beta z_2^{3/2}} \sqrt{z+z_1}$  and  $p(z) \approx \frac{\epsilon_0 \epsilon_{SC}}{e_0 \beta z_2^2} \frac{1}{\sqrt{z+z_1}}$  can be derived, in agreement with the law given in [5] without justification. But this solution is not correct because the order of magnitude of the constant  $z_2 = (2\beta C)^{-1/3}$  makes the second term dominant, contrary to the hypothesis. Similarly, if only the second term, related to the diffusion component, is retained, nonphysical solutions can be obtained. Such steps show firstly that the drift and diffusion components of the whole hole current remain intimately linked and secondly that Eq. (4) in which the last term of Eq. (3), due to ionized impurities, has been neglected, is no longer appropriate. However, the previous solution obtained for a vanishing second member of Eq. (5) cannot be used because the decrease of the hole concentration would be far too steep in comparison with simulated concentrations in Fig. 5. Consequently, only a numerical solution is able to match the physics of the hole transport in the abscissa range where the hole concentration is close to doping one and decreases in a much softer way. The variation law could resemble better the inverse square root law, leading finally to an estimate of several times  $z_c$  for the length where the hole injection affects seriously the equilibrium hole concentration.

A solution valid also near the interface with the Schottky metal or oxide must depend on the current density like what is seen in Fig. 5, or total applied voltage and on boundary conditions at this second interface. It would rely on the same equations using in addition the pseudo-Fermi level of holes  $\phi_p(z)$  in  $p(z) = N_V \exp[\beta(\phi_p(z) - \Psi(z))]$  and potential  $\Psi(z)$ , with  $N_V$  the effective density of states in the valence band:

$$\frac{d\phi_p(z)}{dz} = -\frac{J_p}{e_0 \mu_p N_V} \exp[\beta(\Psi(z) - \phi_p(z))], \quad (6)$$

$$\frac{d\mathcal{E}(z)}{dz} = \frac{1}{\beta L_D^2} \frac{N_V \exp[\beta(\phi_p(z) - \Psi(z))] - N_{\text{ion}}^-}{p_0}, \quad (7)$$

$$\frac{d\Psi(z)}{dz} = -\mathcal{E}(z). \quad (8)$$

Boundary conditions must define the differences  $\phi_p(z) - \Psi(z)$  at  $z = 0$  and  $z = z_0$ :

$$(i) \phi_p(0) - \Psi(0) = (1/\beta) \ln(p^+/N_V)$$

and

$$(ii) \phi_p(z_0) - \Psi(z_0) = (1/\beta) \ln[J_p/(e_0 v_{\text{coll}} N_V) - N_{\text{ion}}^-/N_V],$$

where  $\Psi(z_0)$  can be chosen as the origin of electrical potentials for example. The numerical solver of the COMSOL software solves in fact this set of equations, however, taking the current due to minority carriers into account in addition. But because they have a completely negligible influence since the barrier height is much less than half the diamond band gap and no recombination centers are included, the results obtained by an other solver would not be different than those presented at the beginning of this section.

**4 Conclusion** In vertical or pseudo-vertical Schottky diodes and MOS heterostructures comprising a stack of lightly doped on heavily doped layers, injection of holes plays a very significant role in the transport mechanism. Combined with the advent of accumulation regime at sufficiently high forward bias, this effect induces both the decrease of the forward losses and specific resistance when the current density increases, provided the lightly doped layer is less than about 2  $\mu\text{m}$  for doping concentration below  $10^{16} \text{ B cm}^{-3}$  like usual for high-voltage devices. It allows high current densities higher than  $1 \text{ kA cm}^{-2}$  under a few volts even at room temperature because the hole concentration in the lightly doped layer becomes largely independent of the temperature, thus alleviating the limitation due to incomplete ionization of acceptors in diamond. However, reverse operation would be preserved with breakdown voltages in the range 1.4–2 kV as long as breakdown fields in the range 7–10  $\text{MV cm}^{-1}$  like already achieved [2, 6] are implemented in  $p^-$  layers 1.4–2  $\mu\text{m}$  thick because they are fully depleted and bear the whole reverse voltage. These advantages may have a very positive impact on the performance of high-power diamond devices

in comparison to components made with other wide bandgap semiconductors.

**Acknowledgements** This work is partially supported by French state funds ANR-10-LABX-51-01 (Labex LANEF du Programme d'Investissements d'Avenir).

## References

- [1] P.-N. Volpe, J. Pernot, P. Muret, and F. Omnès, *Appl. Phys. Lett.* **94**(9), 092102 (2009).
- [2] P.-N. Volpe, P. Muret, J. Pernot, F. Omnès, T. Teraji, Y. Koide, F. Jomard, D. Planson, P. Brosselard, N. Dheilily, B. Vergne, and S. Scharnholtz, *Appl. Phys. Lett.* **97**(22), 223501 (2010).
- [3] H. Umezawa, S. I. Shikata, and T. Funaki, *Jpn. J. Appl. Phys.* **53**, 05FP06 (2014).
- [4] V. D. Blank, V. S. Bormashov, S. A. Tarelkin, S. G. Buga, M. S. Kuznetsov, D. V. Teteruk, N. V. Kornilov, S. A. Terentiev, and A. P. Volkov, *Diam. Relat. Mater.*, in press, doi 10.1016/j.diamond.2015.01.005 (2015).
- [5] T. Makino, H. Kato, D. Takeuchi, M. Ogura, H. Okushi, and S. Yamasaki, *Jpn. J. Appl. Phys.* **51**, 090116 (2012).
- [6] A. Traoré, P. Muret, A. Fiori, D. Eon, E. Gheeraert, and J. Pernot, *Appl. Phys. Lett.* **104**(5), 052105 (2014).
- [7] P. Muret, A. Traoré, A. Maréchal, D. Eon, J. Pernot, J. Piñero, M. P. Villar, and D. Araujo, Potential Barrier Heights at Metal on Oxygen-Terminated Diamond Interfaces, arxiv:1501.04790.
- [8] J. H. Werner and H. H. Güttler, *J. Appl. Phys.* **69**(3), 1522 (1991).
- [9] W. Mönch, *Electronic Properties of Semiconductor Interfaces*, Surface Sciences (Springer-Verlag, Berlin, Heidelberg, 2004).
- [10] P. K. Baumann and R. J. Nemanich, *J. Appl. Phys.* **83**(4), 2072 (1998).
- [11] C. R. Crowell and S. M. Sze, *Solid-State Electron.* **9**(11–12), 1035 (1966).
- [12] E. H. Rhoderick and R. H. Williams, *Metal-Semiconductor Contacts*, 2nd edition (Clarendon Press, Oxford, 1988).
- [13] G. Chicot, A. Maréchal, R. Motte, P. Muret, E. Gheeraert, and J. Pernot, *Appl. Phys. Lett.* **102**, 242108 (2013).
- [14] A. Maréchal, M. Aoukar, C. Valle, C. Rivière, D. Eon, J. Pernot, and E. Gheeraert, Energy-Band Diagram Configuration of Alumina/Oxygen-Terminated p-Diamond Metal–Oxide–Semiconductor, submitted to *Appl. Phys. Lett.*
- [15] J. W. Liu, M. Y. Liao, M. Imura, and Y. Koide, *Appl. Phys. Lett.* **101**, 252108 (2012).
- [16] S. M. Sze, *Physics of Semiconductor Devices*, 2nd edition (John Wiley & Sons, New York, Chichester, Brisbane, Toronto, Singapore, 1981).
- [17] P. Muret, P.-N. Volpe, T.-N. Tran-Thi, J. Pernot, C. Hoarau, F. Omnès, and T. Teraji, *Diam. Relat. Mater.* **20**, 285 (2011).

## Potential barrier heights at metal on oxygen-terminated diamond interfaces

P. Muret,<sup>1,a)</sup> A. Traoré,<sup>1</sup> A. Maréchal,<sup>1</sup> D. Eon,<sup>1</sup> J. Pernot,<sup>2</sup> J. C. Pinêro,<sup>3</sup> M. P. Villar,<sup>3</sup> and D. Araujo<sup>3,b)</sup>

<sup>1</sup>*Inst. NEEL, Univ. Grenoble Alpes, F-38042 Grenoble, France and CNRS, Inst. NEEL, F-38042 Grenoble, France*

<sup>2</sup>*Univ. Grenoble Alpes, Inst. NEEL, F-38042 Grenoble, France; CNRS, Inst. NEEL, F-38042 Grenoble, France; and Institut Universitaire de France, 103 Boulevard Saint-Michel, F-75005 Paris, France*

<sup>3</sup>*Dpto. Ciencias de los Materiales, Universidad de Cádiz, 11510 Puerto Real (Cádiz), Spain*

(Received 16 June 2015; accepted 10 November 2015; published online 25 November 2015)

Electrical properties of metal-semiconductor (M/SC) and metal/oxide/SC structures built with Zr or ZrO<sub>2</sub> deposited on oxygen-terminated surfaces of (001)-oriented diamond films, comprised of a stack of lightly p-doped diamond on a heavily doped layer itself homoepitaxially grown on an Ib substrate, are investigated experimentally and compared to different models. In Schottky barrier diodes, the interfacial oxide layer evidenced by high resolution transmission electron microscopy and electron energy losses spectroscopy before and after annealing, and barrier height inhomogeneities accounts for the measured electrical characteristics until flat bands are reached, in accordance with a model which generalizes that by Tung [Phys. Rev. B **45**, 13509 (1992)] and permits to extract physically meaningful parameters of the three kinds of interface: (a) unannealed ones, (b) annealed at 350 °C, (c) annealed at 450 °C with the characteristic barrier heights of 2.2–2.5 V in case (a) while as low as 0.96 V in case (c). Possible models of potential barriers for several metals deposited on well defined oxygen-terminated diamond surfaces are discussed and compared to experimental data. It is concluded that interface dipoles of several kinds present at these compound interfaces and their chemical evolution due to annealing are the suitable ingredients that are able to account for the Mott-Schottky behavior when the effect of the metal work function is ignored, and to justify the reverted slope observed regarding metal work function, in contrast to the trend always reported for all other metal-semiconductor interfaces. © 2015 AIP Publishing LLC.

[<http://dx.doi.org/10.1063/1.4936317>]

### I. INTRODUCTION

Metal-semiconductor interfaces are necessary to implement sensors and electronic devices, and diamond does not escape to this need. Building well defined interfaces at nanometer scale is specially necessary for electrical rectifiers, which can gain high benefits from the bulk properties of boron doped diamond like its very high thermal conductivity, hole mobility, and electrical breakdown field,<sup>1,2</sup> if specific properties of the interface are also fulfilled. These are mainly good adhesion, thermal and chemical stability at elevated temperatures, compatible with the superior possibilities of diamond, and potential barriers ensuring both low electrical losses under forward voltage and minimal reverse currents even at high temperatures. Several attempts have been proposed, relying either on materials which react with the bare surface of diamond to form carbides, such as silicon<sup>3</sup> or refractory metals and compounds,<sup>4–6</sup> even hetero-epitaxially grown on diamond,<sup>7</sup> or metals on either the oxygenated or hydrogenated surface of diamond.<sup>8–12</sup> On bare diamond surfaces, potential barriers close to 2 V and stable at temperatures higher than 500 °C have been obtained but reverse current densities and ideality factors were much greater than expected from the thermionic mechanism alone at least at

room and moderate temperatures, and some of these contacts were ohmic. These poor rectifying current-voltage characteristics have been assigned to inhomogeneous and defective interfaces, especially with carbide forming metals.<sup>8,13</sup> Lower potential barriers are implemented on the hydrogen-terminated diamond surfaces due to the dipole  $H^{+\vartheta} - C^{-\vartheta}$  responsible for the negative electron affinity of these surfaces, where  $\vartheta$  is the averaged fraction of the elementary charge per atom. But the chemical stability is not guaranteed at temperatures as high as in other interfaces and reverse current densities turn out not to be lower than  $10^{-7}$  A/cm<sup>2</sup> at room temperature, still higher than the thermionic limit. Improvement has been achieved with the help of an oxide layer deposited on the H-terminated surface to build field effect transistors<sup>14,15</sup> but this solution is not relevant for Schottky barrier diodes first because it is very difficult to control accurately and in a reproducible way an oxide interlayer made of foreign species with thickness in the subnanometer range. Second, the Schottky barrier heights are known to be much smaller than 1 V and even zero for noble metals<sup>16</sup> on the hydrogenated diamond surface, thus inducing far too high reverse currents in rectifiers. Because of an inverted electric dipole at the oxygenated surface of diamond, the largest potential barriers are generally obtained with either noble (Au) or transition metals deposited on this type of surface,<sup>9</sup> but some authors have shown that thermal treatments up to 500 or 600 °C are able to decrease the

<sup>a)</sup>pierre.muret@neel.cnrs.fr

<sup>b)</sup>daniel.araujo@uca.es

barrier height down to 1.2 V,<sup>17,18</sup> probably because of the cancellation of the electric dipole  $O^{-\delta} - C^{+\delta}$ , still preserving a good adhesion of the metallic layer. More recently, we have shown that a less electronegative and more easily oxidizable metal like Zr was able to reach even more beneficial properties for the Schottky contact, namely, an even lower potential barrier height while maintaining the reverse current density after an anneal at 450 °C close to  $3 \times 10^{-10}$  A/cm<sup>2</sup> at room temperature<sup>19</sup> and an ideal current-voltage behavior for most diodes. However, a comprehensive picture of metal oxygenated-diamond interfaces did not emerge clearly in the last fifteen years, neither for the transport properties of carriers through interfaces nor for the question of how the potential barrier height is determined, contrary to the case of hydrogen-terminated diamond surfaces.<sup>16</sup> In the present paper, mechanisms of carrier flow and significance of barrier heights are investigated, on the one hand, with more details and analysed with the help of several models.

On the other hand, the set of works quoted above demonstrates that both chemistry and physics must be both considered when dealing with the Schottky barriers. This is especially true in the case of diamond where a large dispersion of barrier heights occurred for any metal<sup>8</sup> the in literature. Much work was devoted in the past to general models that are able to explain and predict band misalignments at interfaces compounded of various materials, and a recent review of the various approaches, including a mixed physical-chemical point of view, has been published by Tung.<sup>20</sup> But, as often the case for more than one decade in the literature excepted in Ref. 16, no experimental data regarding diamond interfaces has been brought and discussed. The present study aims at filling this gap, giving evidence of the presence of an oxide interfacial layer and discussing the relevance of various models of barrier height regarding data presented in this article and others available in literature for oxygenated diamond interfaces. In Sec. II, a detailed study by high resolution transmission electron microscopy (HRTEM) and electron energy loss spectroscopy (EELS) is developed to show the characteristics of the interfacial layer at a sub-nanometer scale, the more noticeable being the systematic presence of oxygen at interface before and after annealing. In Sec. III, a first level analysis of the current-voltage characteristics relevant to the depleted semiconductor interface is presented and representative parameters of the junction are derived, confirming the presence of an interfacial layer in-between Zr and diamond and the large decrease of the barrier height after annealing. In Sec. IV, potential barrier inhomogeneities at different scales are analyzed and evidence of positively charged centers in the interfacial oxide is given. The consequences upon current-voltage characteristics are discussed and it is demonstrated that the junctions experience a change from depletion to accumulation regime at sufficient forward bias. Two models are able to take into account the influence of the barrier height inhomogeneities are developed and matched to experimental data, allowing to derive meaningful parameters of each interface which indicate that large barrier inhomogeneities prevail before

annealing while they almost completely vanish after sufficient annealing. The previous results are used in Sec. V to address the problem of whether such an accurate control of the interface and metal choice can allow to tailor and predict the potential barrier heights of Schottky junctions on diamond. Gathering all the data available for well characterized interfaces of various metals on oxygen-terminated diamond permits to unveil a completely unusual relationship between potential barrier heights and metal work functions. Modeling this new result needs to consider the contribution of all electrical dipoles which may be present at these compound interfaces. Conclusions are drawn in Sec. VI.

## II. NANOSTRUCTURE OF ZIRCONIUM ON OXYGEN-TERMINATED DIAMOND INTERFACES

Schottky junctions are implemented by electron-gun deposition in ultra high vacuum of Zr on a stack comprising a lightly boron doped homoepitaxial diamond layer grown on a heavily doped one, itself grown on an Ib substrate. The surface of the lightly doped layer is submitted to a photochemical UV-ozone treatment for two hours at room temperature, so that oxygen terminations prevail on the diamond surface. Other details of the diamond growth and interface preparation are given in Ref. 19. Three types of samples are elaborated, the first one being annealed at temperatures not exceeding 300 °C, while the second and third ones are annealed, respectively, at 350 °C and 450 °C; and the respective interfaces are labeled (a), (b), and (c). Identification of the oxide layer and evaluation of its thickness are carried out by a combination of HRTEM, EELS, and high angle angular dark field-TEM (HAADF-TEM) techniques. HRTEM, HAADF, and EELS measurements were performed using the beam of a JEOL 2010F STEM microscope directed on electron-transparent specimens of the interfaces labeled (a) and (c), fabricated by a lift-off technique in a focused ion beam (FIB) FEI Quanta 200-3D dual beam microscope.

The characterization of the oxide layer has been carried out in three steps: chemical contrast TEM (CTEM) identification of the metal/oxide/diamond interface, scanning TEM-EELS study of the previously identified oxide layer, and HRTEM imaging of the interface. In a first approach, bright-field (BF) images in the CTEM mode are used to identify the interface. BF imaging variations in the electron absorption and dependence on the diffraction angles allow to distinguish between diamond and Zr material. In a second step, EELS spectra are acquired to chemically identify the oxide layer. During EELS spectra acquisition, HAADF-TEM operation mode is used to identify the diamond/Zr interface, insofar contrasts in the HAADF imaging are due to different Z-number of the elements in the sample. Second, EELS profiles are carried out, revealing the oxide layer through the observation of the EELS oxygen-related peak (see Fig. 1(b)). Third, once CTEM and EELS techniques have been applied, HRTEM images of the previously identified oxide layer are acquired. Fig. 1(a) shows EELS spectra recorded across the diamond/Zr interface after the thermal treatment, at the

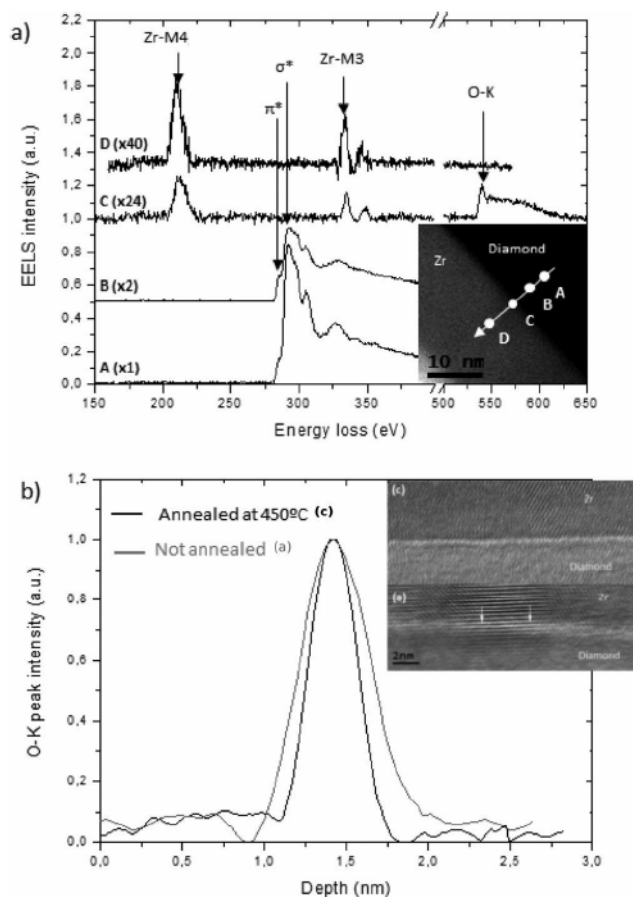


FIG. 1. (a) EELS spectra recorded in an interface of kind (c) along the linescan drawn in the HRTEM image shown in the inset. The peak Zr-M2 is also visible near 345 eV but Zr-M5 normally detected in a 10 nm thick ZrO<sub>2</sub> layer near 190 eV is missing in the interfacial layer. (b) Normalized intensity profile of the oxygen related peak across the Zr/diamond interface before (grey curve) and after annealing at 450 °C for 30 min (black curve), corresponding to interfaces of kinds (a) and (c) as labeled, respectively, in the text. In the inset, HRTEM filtered images of the Zr/oxygen-terminated diamond interfaces of kind ((a), unannealed) and ((c), annealed at 450 °C) are shown. Superimposed contrasts of diamond and Zr can be observed in the Zr/diamond interface of kind (a), with white arrows to guide the eyes through the diamond/Zr interface.

positions indicated in the inset. Presence of oxygen is revealed at the diamond/Zr interface (position C). Moreover, the simultaneous observation of the Zr-M2 to 4 and the O-K peaks at position C discloses the formation of an oxide layer at interface; however, slightly different from bulk ZrO<sub>2</sub> since the peak Zr-M5 is missing. On the one side of the interface, a diamond-related shape of the carbon core-loss is evidenced, while typical Zr-related peaks are observed on the other side. Fig. 1(b) shows normalized intensity profiles of the oxygen-related peak (see spectra at position C) acquired across the diamond/oxide/metal interfaces before and after thermal treatment. To improve signal/noise ratio, ten spectra were averaged. The latter profile exposes how oxygen distribution changes after thermal treatment, showing a real oxide thickness reduction (FWHM varies from 0.6 nm to 0.3 nm) while the amplitude is increased by a factor 1.5, suggesting an augmented oxygen density. Note that the FWHM of the EELS linescan results from the convolution with the probe

size of 0.2 nm. Simultaneously, the EELS analysis of the oxygen content in the Zr layer indicates an averaged concentration of 5% in the as-deposited metal while it decreases to 1% after annealing. Finally, analysis of HRTEM images as shown in the inset of Fig. 1(b) indicates some in-depth roughness in the interfaces of kind (a), whereas a smoother interface takes place after annealing in contacts of kind (c), leaving however an abrupt transition across the interface between carbon atoms and those of the interlayer in both cases.

Titanium and Zirconium are well known to incorporate oxygen and possibly nitrogen when they condense onto a substrate after evaporation in vacuum, an effect which is clearly evidenced by a pressure decrease by about one order of magnitude inside the deposition chamber. Consequently, it is not surprising to find 5% of oxygen in the as-deposited Zr layer. Nitrogen is not detected. Increasing the temperature leads to augmented internal pressure and elastic energy of the Zr lattice, so that it becomes less expensive in terms of total internal energy to form an oxide at the metal interfaces, both because the internal pressure is decreased and the enthalpy of oxide formation is negative. Such effects explain why the oxygen content of the Zr layer is decreased after annealing. More paradoxical is the sharpening of the oxide interlayer shown by the EELS spectra because an increase in the oxygen content at the interface should be expected from the evolutions described previously. At least three reasons can reconcile this apparent contradiction: (i) the beam spot (with an approximate size of 0.2 nm) averages in-depth roughness during the EELS capture and, as a consequence, the recorded O-K profile of Fig. 1(b) shows a widened profile in the interface of kind (a) before thermal treatment; (ii) we know that oxygen termination coverage has a lower density than the last carbon atom layer of the diamond lattice even after the most efficient treatment like UV-ozone oxidation used in this study,<sup>21</sup> a fact which correlates very well with the previous statement since a natural non-uniformity results before annealing; (iii) as demonstrated in Sections III and IV, a strong change in electronic properties of the interface follows the 450 °C anneal, correlated with the electron affinity variation of the diamond surface induced by the cancellation of the oxygen terminations. However, because oxygen is still present at interface after annealing, one is forced to conclude that bonding has been deeply modified, with a probable transformation from a physisorbed metal layer on the oxygen terminated diamond surface likely through the hydroxyl terminations (see Subsection IV A), towards stronger bonds between carbon and oxygen atoms, characterized both by shorter bond lengths and a higher and more uniform density. Taking into account the convolution with the probe size, the oxygen thickness detected by EELS after 450 °C anneal in interfaces of kind (c) suggests that the oxide interlayer comprises two planes of oxygen atoms separated by a Zr atom plane, since the distance between two oxygen planes is 0.256 nm in cubic zirconia, thus defining a full unit cell of ZrO<sub>2</sub> as the whole interlayer thickness. Secs. III and IV are devoted to determine and understand how oxygen species at the interface influence the electrical properties.

### III. CURRENT-VOLTAGE CHARACTERISTICS OF THE ZIRCONIUM-OXYGEN-TERMINATED DIAMOND INTERFACES

#### A. Theoretical background of the relationship between current and voltage

Current-voltage characteristics and mechanisms of carrier transport through the potential barrier present in metal-semiconductor junctions have been discussed extensively in the review articles and textbooks.<sup>20,22–24</sup> The  $z$  direction being perpendicular to the  $x - y$  plane of the interface, the current can be calculated in the semi-classical framework of the Maxwell-Boltzmann distribution of majority carrier velocities by

$$I_z = \iint \int e_0 v_z(E) D(E) dE dx dy, \quad (1)$$

$e_0$  being the elementary charge,  $v_z(E)$  is the carrier velocity in the  $z$  direction, and  $D(E)$  is the majority carrier distribution just at energies  $E$  above the point where the potential barrier culminates. If the barrier is homogeneous, at a constant potential  $\Phi_B$  throughout the  $x$ - $y$  plane, the current density can be written from the previous expression, in the case of a voltage  $V_j$  applied to the junction,<sup>22,25</sup>

$$J_{z,2} = \frac{e_0 N_M v_{coll}}{1 + v_{coll}/v_{diff}} \exp(-e_0 \Phi_B / k_B T) [\exp(e_0 V_j / k_B T) - 1], \quad (2)$$

with  $N_M$  being the effective density of states at the majority carrier band edge,  $k_B$  is the Boltzmann constant,  $T$  is the absolute temperature,  $v_{coll}$  is the collection velocity at interface  $\sqrt{\frac{k_B T}{2\pi m^*}}$ , due to the thermionic effect and equal to one quarter of the thermal velocity,  $m^*$  is the conduction effective mass of majority carriers, and  $v_{diff}$  is their diffusion velocity. The previous expression takes into account the two transport mechanisms of majority carriers which work in series, due, respectively, to the thermoionic velocity at interface and diffusion velocity inside the depletion zone, whereas it neglects bulk recombination. The diffusion velocity simplifies into the product of the majority carrier mobility by the electric field at interface if the band bending exceeds some  $k_B T / e_0$  units and is generally not the limiting factor for the direct current, as confirmed in the samples under study from the comparison of the two velocities. The numerator of the first factor in Eq. (2) can be rewritten  $A^* T^2$  where  $A^* = (4\pi e_0 k_B^2 m_0 / h^3) \times (m^* / m_0)$ , the first quantity inside the parenthesis being the Richardson constant for emission of electrons into vacuum with a mass  $m_0$  at rest,  $A_R = 120 \text{ A cm}^{-2} \text{ K}^{-2}$ . Because  $v_{diff}$  decreases with the increase of the forward bias voltage  $V_j$ , the pre-exponential factor of Eq. (2) becomes voltage dependent. Other reasons for such an effect involving also the factor  $\exp(-e_0 \Phi_B / k_B T)$  are (i) the image force lowering of the barrier, (ii) tunneling through the top of the barrier possibly assisted by the electric field, (iii) voltage drop inside an interfacial layer between the metal and semiconductor, (iv) charging interface states in equilibrium with the semiconductor, and (v) a spatially inhomogeneous barrier

as discussed further. However, the second effect is noticeable only in heavily doped semiconductors, a case which is not achieved in this study since the boron concentration of the lightly doped layer is close to  $N_A = 5 \times 10^{15} \text{ cm}^{-3}$ . As one almost always wants to characterize the Schottky contact with a single potential barrier, the more common approximation consists of keeping only the zero bias voltage barrier height  $\Phi_B^0$  in the first exponential factor of Eq. (2) and gathering all the voltage dependent effects into the last factor. Since all these effects contribute to a slope of the logarithm of the current which is smaller than  $e_0 / k_B T$ , an ideality factor  $n$  larger than one is introduced in the denominator of the exponent of  $\exp(e_0 V_j / k_B T)$  and often considered as a constant at least for a given temperature. Such an hypothesis is strictly valid in the case of an interfacial layer where the voltage drop is a constant fraction  $1 - 1/n$  of the band bending  $U = \Phi_B^0 - V_j - V_{dop}$  (with  $e_0 V_{dop}$  being the energy difference between the Fermi level and majority carrier band edge in the bulk semiconductor) mainly determined by the oxide capacitance and density of interface states<sup>26</sup> when mechanisms (ii) and (iii) are combined. But it is not adequate if the interfacial layer either allows tunneling of carriers as the main transport mechanism or does not display any additional barrier for majority carriers because of band alignments similar to those occurring in type II heterostructures, or in the case of barrier inhomogeneities and even with image force lowering. Other effects, which are due to quantum reflexion, transmission, and phonon scattering of carriers at the interface, are voltage independent and generally very weakly temperature dependent so that it is convenient to lump them into an effective Richardson constant  $A^{**}$  which is weaker than  $A^*$  by some tens of percent in the case of intimate Schottky contacts,<sup>27</sup> yielding the standard value of  $90 \text{ A cm}^{-2} \text{ K}^{-2}$  usually considered for diamond. This effective Richardson constant can be further severely decreased because of the attenuation by a factor  $\alpha$  of the collection velocity  $v_{coll}$  due to additional scattering of carriers by charged centers and roughness, and transport mechanisms through the interfacial layer when they exist. Finally, the non ideal current density is rewritten as

$$J_{z,3} = \alpha A^{**} T^2 \exp\left(-\frac{e_0 \Phi_B^0}{k_B T}\right) \left[\exp\left(\frac{e_0 V_j}{n k_B T}\right) - 1\right]. \quad (3)$$

Experimental current-voltage characteristics can then be accounted for by such an expression with the ideality factor  $n$  as an adjustable parameter, provided  $\alpha A^{**}$  is known and the series resistance  $R_s$  is adjusted in order to fit the additional voltage drop  $R_s I_z$  appearing in the total measured voltage  $V = V_j + R_s I_z$ . This is done in Fig. 2 for the three interfaces near room temperature. Two kinds of deviation between experimental data and the theoretical laws may appear as it can be seen in Fig. 2; the first one is due to a nonconstant ideality factor as long as the voltage drop in the series resistance is negligible (typically below  $0.5 \text{ A/cm}^2$  in these diodes at room temperature) and the second one is due to less common transport mechanisms which are discussed in the following. It is worthwhile to notice that the

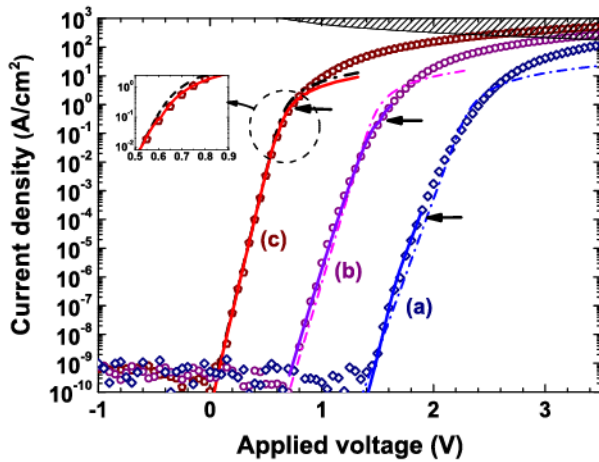


FIG. 2. Current density as a function of applied voltage at 300K in the three interfaces made of Zr deposited on oxygen terminated diamond (a) with annealing temperature not exceeding 300 °C; (b) annealed at 350 °C; (c) annealed at 450 °C. Dashed-dotted lines are calculated with the help of Eq. (3),  $\alpha A^{**}$  values included in Table I which are obtained from fits achieved in the two following figures, and adjusted constant values of the apparent barrier height and ideality factor in each case, that are, respectively: (a) 1.83 V and 1.57; (b) 1.47 V and 1.29; (c) 0.97 V and 1.05. Voltage takes into account the voltage drop in a constant series resistance of 600  $\Omega$  in case (a) and 300  $\Omega$  in cases (b) and (c), in good agreement with the theoretical ones, but current densities above a few A/cm<sup>2</sup> turn out to be higher because of the conductivity increase due to hole injection from the heavily doped layer. Full lines rely on models which incorporate barrier height lowering and are described in Section IV, with Eq. (7) for cases (b) and (c), while Eq. (14) is used for case (a). Horizontal arrows mark the flat band situation in each junction. The effect of image force lowering is displayed in the inset for the case (a). In the hatched area, self-heating becomes important.

rectification ratios are more than twelve decades and that no generation-recombination current is detected on these current-voltage characteristics, which would have involved a symmetrical behavior of the absolute value of the current around the origin at low voltages. Such an almost ideal behavior strongly suggests that the oxygen terminated surface of diamond passivates very efficiently the interface defects able to develop leakage currents.<sup>28</sup> The determination of  $\alpha A^{**}$  needs temperature variations in such a way that the saturation current density over  $T^2$ , namely,  $\alpha A^{**} \exp\left(-\frac{e_0 \Phi_B^0}{k_B T}\right)$ , obtained from the extrapolated value of the current-voltage characteristic at  $V_j = 0$ , can be drawn. Such Richardson plots are displayed in Fig. 3. The effective Richardson constants  $\alpha A^{**}$ , ideality factors at room temperature and parameters described in the following are indicated in Table I. It must be stressed first that the  $\alpha A^{**}$  values are at least ten times lower than the standard value  $A^{**}$  and second that a careful inspection of the Fig. 3 shows that the data points follow systematically a slight upward curvature, indicating a barrier height increase with temperature. The first result confirms indubitably the presence of an insulating interfacial layer, which is able to increase considerably the quantum reflection coefficient and decrease the effective velocity of carriers, mainly because of scattering due to roughness, chemical disorder, and differential dielectric response. The second one is the preliminary indication of the presence of barrier inhomogeneities, a conclusion similar to that obtained in Ref. 29 about silicides-silicon interfaces, also

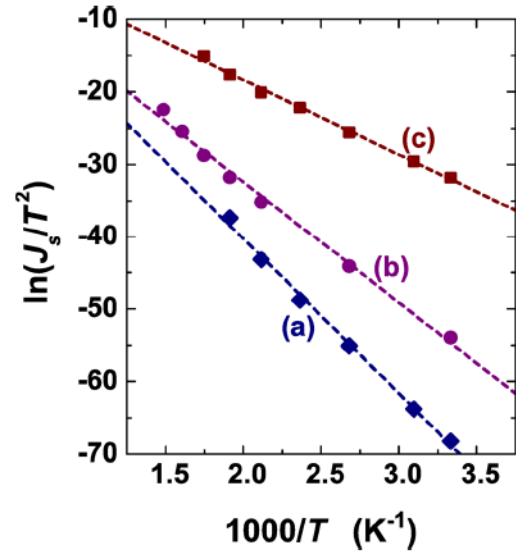


FIG. 3. Richardson plot for the three same interfaces as in Fig. 2. Averaged barrier heights deduced from the slope of each straight line are, respectively: (a) 1.84 V; (b) 1.47 V; (c) 0.95 V; very close to that used in Fig. 2.

implying additional consequences which have to be analyzed more thoroughly.

## B. Richardson constant, ideality factor, and potential barrier behaviors

Zero voltage barrier heights and averaged ideality factors are displayed in Fig. 4 as a function of temperature. On the one hand, the former quantities experience indeed an increase with temperature with generally an asymptotic behavior towards highest temperatures, while the latter ones are decreasing, starting from very different values at room temperature (which are reported in Table I) and displaying very different negative slopes. As noticed previously, such variable ideality factors cannot be ascribed to a voltage drop within an interfacial layer bearing an additional barrier to that built in the semiconductor, because they would not be coherent with oxide interfacial layers which still exist at the three interfaces. On the other hand, experimental data plotted in Fig. 2 deviate from the simulated curves drawn in dashed-dotted lines on the basis of a constant ideality factor when voltage drop in the series resistance and other effects remain negligible. A first attempt to fit more accurately experimental results uses an alternative definition of the current density, which is also more physically meaningful. It consists of using a temperature and voltage dependent barrier height

TABLE I. Parameters of the Schottky barrier in the three interfaces according to the model of Section III.

Sample type and annealing temperature (°C)	$\alpha A^{**}$ (A cm <sup>-2</sup> K <sup>-2</sup> )	$n$ (at 300K)	$\overline{\Phi_{B,\infty}^0}$ (V)	$\sigma_{\Phi}^0$ (mV)
(a) <300	11	1.52	1.93	71
(b) 350	2.8	1.29	1.57	87
(c) 450	8.5	1.00–1.07	0.93	54

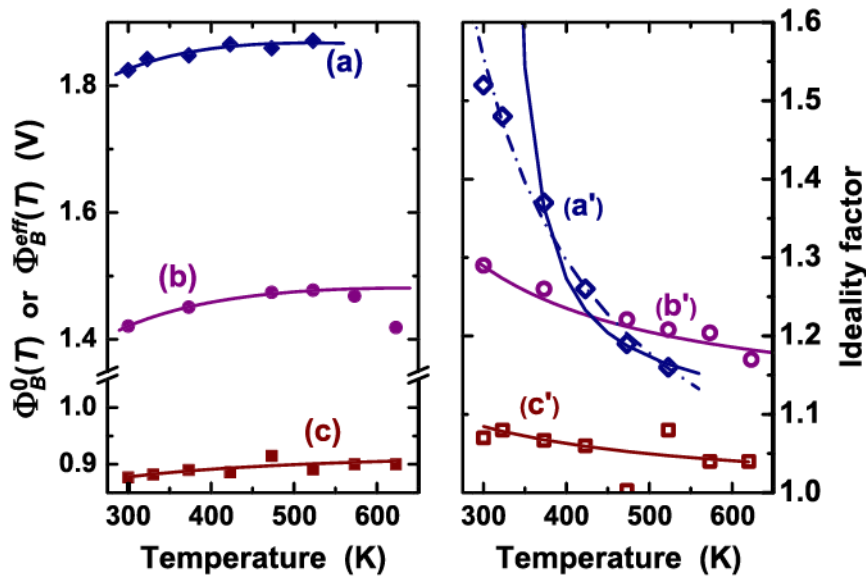


FIG. 4. At left, effective barrier heights as a function of temperature in (a) diodes not annealed at temperatures higher than 300 °C; (b) annealed at 350 °C; (c) annealed at 450 °C; full curves are the best fits according, respectively, to Eq. (5) or Eq. (9) which results essentially in the same behavior for the effective barrier. The point at the highest temperature in data (b) must be discarded because it has been measured at the same temperature as the annealing one, involving an additional annealing time which has induced a further evolution of the interface towards its final state (c). At right, ideality factors for the same diodes after the same respective post-treatments in (a'), (b'), and (c'); the best fits to the ideality factor data obtained with the help of Eq. (11) are displayed in full curves for (b') and (c') and as a dashed-dotted curve for (a'), but using a nonphysical parameter in the last case. The full curve adjusted on (a') data exploits Eq. (17) and related ones with more meaningful parameters at the expense of a worse agreement with data at the lowest temperature (see text).

$\Phi_B(T, V_j)$ , so that the current density can be rewritten more usefully for the homogeneous barrier case

$$J_{z,4} = \alpha A^{**} T^2 \exp\left(-\frac{e_0 \Phi_B(T, V_j)}{k_B T}\right) \left[\exp\left(\frac{e_0 V_j}{k_B T}\right) - 1\right]. \quad (4)$$

Introducing an inhomogeneous barrier which follows a Gaussian spatial distribution in the  $x - y$  plane of the interface, characterized by an average value  $\overline{\Phi_B}(T, V_j)$  and a standard deviation  $\sigma_\Phi(V_j)$ , permits to derive<sup>24,29</sup> a law similar either to Eq. (3) or Eq. (4), with an effective barrier given in the second case by

$$\Phi_B(T, V_j) = \overline{\Phi_B}(T, V_j) - \frac{e_0 \sigma_\Phi^2(V_j)}{2k_B T}. \quad (5)$$

For each temperature, it is always possible to convert Eq. (4) into Eq. (3) through the definition of a voltage independent barrier height, conveniently taken at  $V_j = 0$ , and a voltage dependent ideality factor  $n(T, V_j)$ , valid in all situations, the inverse of which being evaluated from the derivative of the logarithm of the current density given by Eqs. (3) and (4) when the reverse saturation current is neglected

$$\frac{k_B T}{e_0} \frac{d(\ln J_z)}{dV_j} = \frac{1}{n(T, V_j)} = 1 - \frac{d\Phi_B(T, V_j)}{dV_j} = 1 + \frac{d\Phi_B(T, U)}{dU}. \quad (6)$$

However, in this first level model, no explicit dependence of the parameters is given as a function of junction voltage  $V_j$  or band bending  $U$ . Some cases of potential barrier distributions have been analyzed analytically by Tung,<sup>30</sup> who showed that the dependence of the parameters on Eq. (5)

was not linear with the band bending and hence with the junction voltage, on the basis of a physical representation of the barrier lowering by a fictitious dipole located at interface. An additional source of nonideality may be present if a spreading resistance effect occurs, involving inhomogeneous current density inside the semiconductor because of current crowding near the pinch-off patches with a lowered barrier and located close to the interface.<sup>31,32</sup> This effect is normally expected to be relevant at current levels where the series resistance voltage becomes larger than some  $k_B T/e_0$ . But the combination of multiple barriers and incomplete ionization of doping impurities may induce deviation from the ideal current-voltage characteristic at much smaller currents because of severe weakening of the carrier concentration and narrowing of the current paths in the lowest barrier patches which cannot be assessed easily from the comparison to a voltage drop in an averaged series resistance. This kind of nonideality will be discussed Sec. IV.

In the simple model presented above, the barrier fluctuations are characterized by their average and standard deviation but are not supported by any physical model, thus preventing the derivation of any relationship between physical properties of the interface and electrical ones. Moreover, the behaviors of the barrier lowering and ideality factor with voltage and temperature cannot be deduced. Therefore, the reasons for these barrier inhomogeneities have to be analyzed more accurately and an analytical model which will generalize that developed by Tung<sup>30</sup> will be implemented in Sec. IV, concurrently with a realistic simulation of some potential fluctuations at interface. But within the framework of the simple approach developed in the present section, it is already possible to derive the two parameters  $\overline{\Phi_B}(\infty, 0)$  and

$\sigma_{\Phi}(0)$  at zero voltage from the fit of these quantities according to Eq. (5), which are renamed, respectively,  $\overline{\Phi_{B,\infty}^0}$  and  $\sigma_{\Phi}^0$  for the sake of simplicity and displayed in Table I, for the three types of interface. The average barrier height at infinite temperature  $\overline{\Phi_{B,\infty}^0}$  decreases by about 0.5 V after each anneal while the standard deviation  $\sigma_{\Phi}^0$  of the barrier fluctuations goes through a maximum after annealing the interface at 350 °C. But the deficiency of the present model is confirmed by the different behaviors of the ideality factor with temperature plotted in Fig. 4 which cannot be explained. These discrepancies confirm the need for a more accurate model of the effect of potential fluctuations at interface upon current-voltage characteristics.

Meanwhile, an unusual result which ensues from the calculation of the current densities necessary to draw the fitting curves in Fig. 2 can be already pointed out. At some current threshold, flat bands are reached (see the arrows in the same figure) and it is necessary to consider that accumulation occurs at the interface to explain the continuous increase of the current densities beyond this threshold. Such a behavior matches Eq. (1) which states the proportionality of the current to a velocity and carrier concentration at interface. For example, in the case (c), flat bands are reached at a voltage of 0.63 V, corresponding to an initial band bending of  $0.97 - 0.38 = 0.59$  V (here  $V_{dop} = 0.38$  V) plus the barrier increase of 0.04 V demonstrated in Sec. IV. The corresponding current density calculated directly with the hole concentration given by formula (1) in Ref. 1, assuming a compensation of 20% (donor concentration  $N_D = 10^{15} \text{ cm}^{-3}$ ) and Eq. (1), with a collection velocity ten times smaller than that for an intimate contact, yields  $0.4 \text{ A/cm}^2$ , very close both to the experimental one and that calculated by Eq. (4). In cases (b) and (a), still at 300 K, flats bands are reached, respectively, at lower current densities indicated in Fig. 2, which cannot be calculated with the help of the initial model because the apparent barrier heights deduced presently are largely underestimated and would produce irrelevant band bending. Therefore, assessing these values needs to wait for more accurate and physically relevant models which will be developed in Sec. IV. In Eq. (2) and subsequent ones, the barrier height has been introduced for convenience and it was often believed as an impassable limit in Schottky diodes. Such a statement is not true as everyone can be convinced if he realizes that Eq. (2) and subsequent ones all derive from Eq. (1) where the current is controlled by a carrier concentration. Band curvature reversal and occurrence of accumulation regime are possible and even necessary to reach high currents, up to more than thousand times those got at flat bands, in these interfaces made on oxygen-terminated diamond, because first of the low values of the effective Richardson constant, second of the wide forbidden bandgap of diamond and third of the large ionization energy of acceptors. In such a regime, diffusion flow is inverted close to the interface, the barrier seen by majority carriers is canceled and consequently, the models relying on Eq. (2) and following ones, and on the properties of barrier height inhomogeneities, especially their voltage dependence, become inappropriate. Conversely, current crowding near the

pinch-off patches with a lowered barrier may become a major source of nonideality. These mechanisms will be either incorporated into the forthcoming models or else, kept in mind to assess the applicability of the following developments.

#### IV. POTENTIAL BARRIER INHOMOGENEITIES AND IDEALITY FACTOR

##### A. Potential fluctuations due to randomly distributed discrete charges and dipoles

The electrostatic potential experienced by mobile carriers originates from fixed charges scattered inside the space charge zone and interface. For modeling purposes, it is often derived from constant bulk charge concentration in the space charge zone and homogeneous charge density at interface. This view is correct for mechanisms characterized by lengths larger than the Debye length  $\lambda_D = \sqrt{\epsilon_{SC}\epsilon_0 k_B T / (e_0^2 N_A)}$ , where  $\epsilon_{SC}$  and  $\epsilon_0$  are, respectively, the relative permittivity of the semiconductor and the vacuum permittivity, and when average laws are evaluated, but may fail if some physical property of carriers experiences microscopic fluctuations. Indeed, when the effects of potential inhomogeneities are at stake, the discrete nature of fixed charges accommodated within the metal/semiconductor or metal/oxide/semiconductor (MOS) structure must be taken into account and the average distance between these discrete charges have to be compared to  $\lambda_D$ . Here,  $\lambda_D$  amounts to 40 nm at 300 K and 52 nm at 500 K. Three locations have to be considered: (i) inside the depletion zone, the average distance between ionized acceptors is 58 nm, very close to  $\lambda_D$ . Only those which are at such comparable distances from the interface influence the potential barrier height, as clearly evidenced in a following subsection. (ii) The oxygen terminations bonded to the carbon atoms of the (001) diamond surface are making up the negative part of the interface dipole, really present at the interface up to some annealing temperature, an inverted situation in comparison to what happens on the hydrogenated diamond surface, due to the sign change of the electronegativity difference between carbon and oxygen or hydrogen, respectively. The positive counterpart of this dipole lies within the first and second carbon layers just below the surface, resulting in a potential jump through the surface of  $\Delta q d_{di} N_{di} / (\epsilon_i \epsilon_0)$  where  $\Delta q$  is the charge transfer,  $d_{di}$  is the dipolar distance,  $N_{di}$  is the site density, and  $\epsilon_i$  is the relative interface permittivity.<sup>24</sup> This potential jump is directly reflected by the electron affinity change provided by oxygen terminations. On average, it can be estimated close to 1.7 V because the smaller difference between electron affinities of the free ( $2 \times 1$ ) reconstructed surface and the oxygenated surface<sup>33</sup> is probably due to already electron depleted bonds in the last carbon layer of the former one. Taking into account the 30% coverage measured by X-rays photoelectron spectroscopy<sup>21</sup> on our samples treated by UV-ozone, equivalent to  $5 \times 10^{14}$  sites per  $\text{cm}^2$ , a whole distance normal to the interface of roughly  $d_{di} = 0.1 + 0.2 = 0.3$  nm and  $\epsilon_i = 2$ , the estimated charge transfer turns out to be  $2 \times 10^{-20}$  C, that is  $\vartheta' = 0.13$  electronic charge. However, it is known first that there are several oxygen terminations, at least either (C–O–C), carbonyl or ketone (C=O), hydroxyl (C–OH),

and carboxyl (O=C-OH) groups<sup>34–37</sup> as individual adsorbates which can be simultaneously present on the diamond surface, and possibly epoxide (bridged oxygen between two adjacent carbons)<sup>38</sup> in case of UV-ozone treatment as done on our samples. The electron affinities calculated theoretically for the first three terminations are different.<sup>36,39</sup> Second, all the sites are not occupied by ether or ketone terminations (in our case, about 30%,<sup>21</sup> like when oxygen plasma treatment is applied to the diamond surface) but when adjacent sites are provided with an oxygen termination, polymerization along chains may occur.<sup>34</sup> Third, comparison between the experimental electron affinity of the oxygen terminated (100)-oriented diamond surface,<sup>33,40</sup> near 1.6 eV or 1.7 eV, and those calculated theoretically<sup>36,39</sup> (the “bulk” one in the sense of the Sque publication, that is, the difference between the bottom of the conduction band and vacuum level at the surface) shows that the latter are about twice the experimental ones for ether and carbonyl terminations and close to zero or negative like for the hydrogen termination in the case of hydroxyl. It is therefore quite clear that a mixing of at least these three types of terminations is necessary to reconcile experimental and theoretical electron affinities as long as those measured by photo-electron spectroscopy are averaged values. Therefore, the dipole strength resulting from these various adsorbates is able to modify the potential barrier height that is far from being homogeneous at least over a scale length of few nanometers and also along a much larger scale if the various terminations are arranged in the macroscopic domains, resulting in a non-uniform local electron affinity. An other reason which may lead to scattered patches with different barrier heights would be the chemical inhomogeneities as often present when carbide formation occurs,<sup>13</sup> which might also happen if the chemical composition of the interfacial oxide layer or its thickness were not homogeneous throughout the interface. And last but not least, extrinsic defects such as emerging dislocations cannot be excluded as sources of locally lowered barrier height like revealed at CoSi<sub>2</sub>/n-Si(001) interfaces by ballistic electron energy microscopy.<sup>41</sup> On the contrary, the intrinsic dipole due to charge transfer across the interface because of a possible misalignment of the charge neutrality levels in the two materials is supposed to be homogeneous because it results from the occupation of gap states which are delocalized in the plane of the interface and will not participate in potential fluctuations. (iii) As evidenced in the following, discrete charged centers exist inside the oxide of MIS structures and are expected to be also present in the thin interfacial oxide of the Schottky contacts. These cases are treated quantitatively in Subsections IV B–IV E and are brought face to face to experimental and simulation results.

## B. Evidence of charged centers in oxide layers

To check quantitatively the presence of discrete charged centers inside the oxide, an MIS structure Al/ZrO<sub>2</sub>/p-type (001) oriented diamond has been fabricated. The 25 nm oxide layer has been prepared by atomic layer deposition at 100 °C. The p-layer has a thickness of 2 μm, contains some 10<sup>17</sup> B/cm<sup>3</sup>, and has been epitaxially grown on top of a 200 nm p<sup>++</sup> diamond layer itself in epitaxial relationship on a (001) oriented Ib substrate. After etching the p-layer and

before the deposit of the last stack Al/ZrO<sub>2</sub>, an ohmic contact is fabricated around the sample on the heavily doped (p<sup>++</sup>) layer, ensuring a series resistance close to a few kΩ. Similarly, the proper time constant of the MIS structure is inferior to 1 μs. Such a property allows safe measurements of the static, pulsed and transient capacitances at a frequency of 1 MHz, as described in Ref. 42. Results of the reciprocal square capacitance as a function of voltage and the isothermal spectra of projected interface states as a function of the hole emission time constant deduced from the first real Fourier coefficient of the capacitance transients at two time window durations are displayed, respectively, in Figs. 5(a)–5(c). From the extrapolation of the linear part of the curve in Fig. 5(a) to zero ordinates, a flat band voltage  $V_{FB}$  of -4.1 V is deduced whereas a value equal to  $\Phi_{MS} = \Phi_M - \chi_{SC} - E_G/2e_0 - (E_i - E_F)/e_0 = -2.4$  V would be calculated with the help of the electron affinity model and  $\Phi_M = 4.28$  V for the Al work function,<sup>43</sup>  $\chi_{SC} = +1.6$  eV for the electron affinity of oxygen-terminated p-type diamond,<sup>33,40</sup>  $E_G = 5.45$  eV for the diamond band gap and  $\phi_F = (E_i - E_F)/e_0 = 2.35$  V deduced from the difference between intrinsic and Fermi energy levels in bulk boron-doped diamond, assuming no charge in the oxide. The discrepancy comes from this last hypothesis which is not verified, implying that the real situation comprises a positive charge inside the parenthesis of the last term in  $V_{FB} = \Phi_{MS} - (Q_{is}(0) + \overline{Q}_{ox})/C_{ox}$ , where  $C_{ox}$  is the oxide capacitance density,  $Q_{is}(0)$  and  $\overline{Q}_{ox}$  being, respectively, the charge per unit area in interface states at flat bands and the product of the total charge per unit area within the insulator by the ratio of the barycenter of this charge to the insulator thickness.<sup>42</sup> To reconcile the two values, a total number of positive charges per unit area must amount to  $2 \times 10^{13}$  cm<sup>-2</sup> within the 25 nm thick oxide layer.

The centers which accommodate charge may experience change of their charge state if some mechanisms are occurring, like carrier emission from interface states lying in the common forbidden gap of the two materials, and also transport by hopping and tunneling across some thickness of the

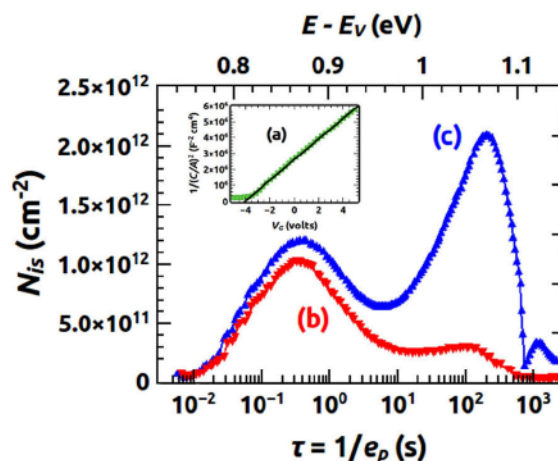


FIG. 5. (a) Square of the inverse capacitance density as a function of the gate voltage; (b) and (c) curves are isothermal transient capacitance spectra, respectively, after a 1 ms and a 100 ms filling pulse, recorded at a gate voltage of 3 V and temperature of 362 K.

insulator. Such effects give rise to transient capacitances in the MIS structure because of the rearrangement of all the individual electric dipoles necessary to comply with the rule of a constant whole electric dipole if the MIS is submitted to a constant voltage.<sup>42</sup> Isothermal spectra are displayed in Figs. 5(b) and 5(c) as a function of the characteristic emission time. They are obtained from the Fourier transform of the transients which are recorded after two filling pulses lasting, respectively, 1 ms and 100 ms. They show a two peak structure, the slower peak being higher for the longer filling pulse. This response can be viewed as the projected spectrum of states on the interface energy scale inasmuch both states located at interface and some oxide states as well may exchange holes with the valence band of diamond. Differential spectroscopy is here unnecessary just because emission from discrete interface states in the common bandgap largely dominates that from a hypothetical continuum since peaked structures clearly appear in Fig. 5, and an accurate calibration of the energy scale is not needed. The smaller filling pulse duration  $t_p = 1$  ms has been chosen to ensure complete filling of interface states even with capture cross sections as low as  $10^{-19}$  cm<sup>2</sup>, whereas the larger  $t_p = 100$  ms is able to involve additionally either injection or extraction of carriers trapped in discrete states localized within the insulator at some distance from the interface. The important point consists of the different behaviors followed by the two peaks as a function of  $t_p$ : the first occurring at the shorter emission time is very weakly sensitive to  $t_p$  and consequently related to an interface state whereas the second one increases with  $t_p$ , involving carrier transport through some insulator slice. This is the demonstration that at least one discrete state exists inside the oxide. An order of magnitude of the distance  $d$  of these centers from the interface can be estimated from the inverse of the attempt-to-escape time checked by Jain and Dahlke for traps in Si/SiO<sub>2</sub> interfaces<sup>44</sup> and given by  $\nu_0 \exp(-qd)$ , with  $\nu_0 \simeq 10^{16}$  s<sup>-1</sup> and  $\alpha \simeq 1.05$  Å<sup>-1</sup>, yielding roughly  $d \simeq 3$  nm. The reciprocal attempt-to-escape time at zero insulator thickness  $\nu_0$  and the quantum transmission coefficient  $q$  are conditioned, respectively, by the quantum uncertainty about the potential well or barrier height, also close to  $2\hbar/G$  where  $G$  is the line width of the resonance,<sup>45</sup> and tunneling transmission coefficient which depends on the square root of the previous quantities. Because the relevant energies are still about 1 eV, the order of magnitude of  $\nu_0$  and  $q$  are expected not to be largely different in the present case. The evaluated distance  $d$  is close to one tenth of the whole insulating layer thickness, a ratio similar to that of the center densities deduced by the transient and static capacitance methods in the MIS structure. Consequently, these point defects behaving as repulsive centers for holes and located inside the oxide layer at the Schottky interfaces under study might not be ignored unless other charged centers or dipoles prevail.

### C. Effects of local barrier enhancement due to random elementary charges and dipoles close to the interface

Electrostatic potential along  $x$  and  $y$  directions, parallel to the interface, and  $z$ , normal to the interface, can be

calculated by adding three terms as a function of normalized distances  $\xi = x/\lambda_D$ ,  $\nu = y/\lambda_D$ , and  $\zeta = z/\lambda_D$ , and band curvature  $U$  in volt: the average potential of the depletion zone  $(\sqrt{U - k_B T/e_0} - \zeta \sqrt{k_B T/(2e_0)})^2$ ; the image force potential  $-u_{im}/\zeta$  with  $u_{im} = e_0/(16\pi\epsilon_S\epsilon_C\epsilon_0\lambda_D)$  and the potential due to either repulsive elementary charges positioned symmetrically at  $\xi = \pm\xi_0$ ,  $\nu = 0$ , and beyond the interface plane by a distance  $\zeta_0$ , that is,

$$\frac{4u_{im}}{\sqrt{(\xi - \xi_0)^2 + \nu^2 + (\zeta + \zeta_0)^2}} + \frac{4u_{im}}{\sqrt{(\xi + \xi_0)^2 + \nu^2 + (\zeta + \zeta_0)^2}}$$

or replacing either one or two of the previous terms by

$$- \frac{4u_{im}}{\sqrt{(\xi \mp \xi_0)^2 + \nu^2 + (\zeta + \zeta_0)^2}} + \frac{4u_{im}}{\sqrt{(\xi \mp \xi_0)^2 + \nu^2 + (\zeta - \zeta_0)^2}}$$

at either one location  $+\xi_0$  or both locations  $\pm\xi_0$  to simulate either one or two elementary dipole due to negative oxygen termination beyond the interface and its positive counterpart on the diamond side. A 3-dimensional view of potential barriers in several cases is given in Fig. 6, the last one being obtained with an inverted sign before  $\zeta_0$  and four random locations of elementary charges within the depletion zone. The three first cases are, respectively, devised to mimic the mechanisms assumed to be at stake in the transport of carriers at interface, resulting from the repulsive effect of charges located just at interface or close to it inside diamond: (a) with negative oxygen terminations inducing interface dipoles which are supposed to dominate; (b) with a mixed influence of repulsive oxide charges and dipoles similar to those of the previous case; (c) with only repulsive oxide charges. In these three cases, elementary charges or dipoles enhance the barrier locally. On the contrary, in the fourth case (d), barrier lowering  $\delta\Phi_{B,1}^{sad}$  may occur with a saddle point at normalized distance  $\zeta_{sad}$  from the interface which can be calculated exactly from the solutions of a quartic equation resulting from the cancellation of the potential derivative along the  $\zeta$  direction. However, a rough estimate, easier to derive, relies on the geometric mean of the two extreme solutions of the quartic equation, and can be expressed as  $\zeta_{sad} \approx \sqrt{\chi(U)[\zeta_0 - 2\chi(U)]}$  with  $\chi(U) = u_{im}^{1/2} \left(\frac{2k_B T}{e_0}\right)^{-1/4} \left(U - \frac{k_B T}{e_0}\right)^{-1/4}$ , and results in  $\delta\Phi_{B,1}^{sad} \approx 4u_{im}/(\zeta_0 - \zeta_{sad})$ . The resulting effects of this barrier height lowering will not be treated in detail here. In the three first cases, the distribution function of potential barrier heights is then calculated with a fixed value of  $\zeta_0$  and random values of  $\xi_0$  around a mean  $\bar{\xi}_0$  according to a normal law with a standard deviation  $\sigma_{\xi}$ , to assess the possible values of  $\overline{\Phi_B}(T, V_j)$  and  $\sigma_{\Phi}(V_j)$ , the characteristic parameters of the inhomogeneous barrier.

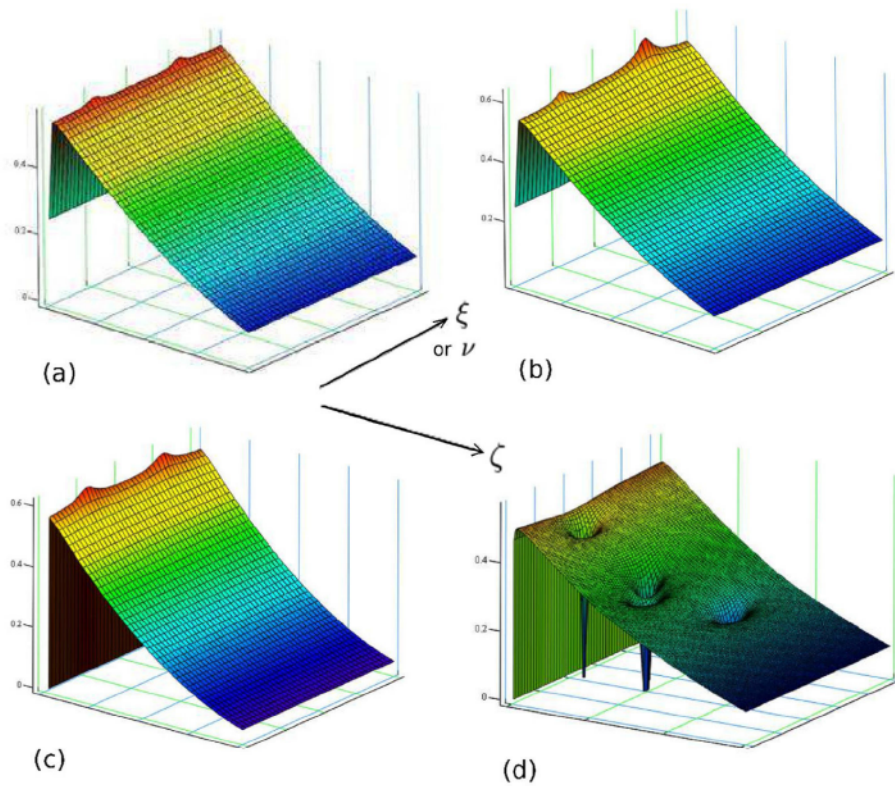


FIG. 6. Sketch of the potential barrier experienced by majority carriers with (a) two dipoles across the interface with a repulsive elementary charge on the semiconductor side; (b) one dipole of the same kind across the interface and one repulsive elementary charge beyond it; (c) two repulsive elementary charges beyond the interface; (d) randomly scattered attractive elementary charges inside the depletion zone, inducing a saddle point of the potential energy, visible as a lowered profile of the top of the barrier near the potential well which is the closest to the summit.

In a first step, the parameter  $\sigma_{\Phi}(0)$  is adjusted to match the values displayed in Table I at a medium temperature, typically 500 K with realistic values of  $\zeta_0$ ,  $\bar{\xi}_0$  and  $\sigma_{\xi}$ . More specifically,  $\zeta_0\lambda_D$  spans the range 0.2 to 0.46 nm and  $(\bar{\xi}_0\lambda_D)^{-2}$  the range  $1.5 \times 10^{12} \text{ cm}^{-2}$  to  $3 \times 10^{14} \text{ cm}^{-2}$ , the two later limits featuring, respectively, a positive charge density inside the oxide layer and the dipole density at the oxygen terminated surface. Accordingly, the average distances  $\bar{\xi}_0$  between point charges or dipoles span a range limited by 0.08 and 0.007 (in  $\lambda_D$  units), respectively. Therefore, the barrier height fluctuations are occurring along a microscopic scale, well below the Debye length. In a second step, the band bending is changed and the values of  $\bar{\Phi}_B(T, U)$  and  $\sigma_{\Phi}(U)$  are evaluated as a function of the band bending  $U$ . In all the cases and whatever the temperature, as suggested in Ref. 29, the increase in the average barrier height  $\bar{\Phi}_B(T, V_j)$  and the decrease in the standard deviation  $\sigma_{\Phi}(V_j)$  with the increasing forward voltage and correlative decreasing band bending is fully confirmed, although the barrier height distribution is not symmetric and cannot be strictly depicted by a normal law. The trends followed by the two terms of Eq. (5) both contribute to an increase in the barrier height with forward voltage which can be also interpreted as an increase in the ideality factor, thus inducing a lower current density in comparison with that anticipated with the help of a constant ideality factor like sketched with dashed-dotted lines in Fig. 2. At variance with the hypothesis used in Ref. 29, neither the variation of  $\bar{\Phi}_B(T, V_j)$  nor that of  $\sigma_{\Phi}(V_j)^2$  is linear with  $V_j$  or  $U$ , a law which would have resulted in a constant ideality factor, in contradiction both with experimental and simulation results. Another major feature is the relative

insensitivity of the ideality factor to the density of point charges or dipoles  $(\bar{\xi}_0\lambda_D)^{-2}$ , the former starting from 1.01–1.02 for band bending corresponding to zero voltage bias and growing up to 1.05–1.15 when the band bending  $U$  becomes close to a few  $k_B T/e_0$ , as shown in Fig. 7, irrespective of the temperature. The barrier height variations which are deduced from the ideality factor match very well with those of the image force lowering as clear in Fig. 7 too. This result coming from the simulated inhomogeneous barrier height with repulsive elementary charges or dipoles demonstrates that the image force lowering and its changes with the

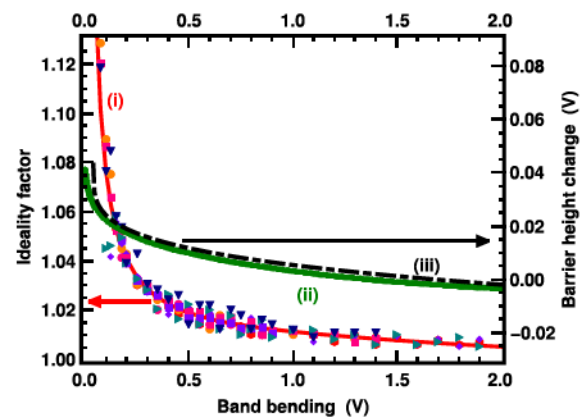


FIG. 7. Ideality factors deduced from the microscopic barrier inhomogeneities model for the three types of interface at 300 K (triangles), 400 K (squares), and 500 K (circles) as a function of the band bending  $U$ . Curve (i) is the best fit of data points by  $1 + 1/P(U)$  with  $P(U) = 136.8 U - 76.4 U^2 + 28.4 U^3$ . The curve (ii) displays the barrier height variation deduced from (i) with the help of Eq. (6) which implies that  $d\Phi_B/dU = -1/[1 + P(U)]$ . Dashed-dotted curve (iii) shows the image force lowering variations.

band bending is the main source of the variation of the average barrier height with the applied voltage, because barrier height enhancement does not contribute significantly to the whole barrier experienced by carriers responsible for the current, except for a reduced effective area. Such a result validates this hypothesis already done in Ref. 30. The whole variation amounts to about 40 mV like inferred in Ref. 24 for the image force lowering alone. It is thus possible to derive a universal law featured by a solid line in Fig. 7 that may be used to derive current density-voltage characteristics with the help of Eqs. (4) and (6). The first important result coming out from this simulation turns out to be the better agreement of the simulated current density sketched in solid line in the inset of Fig. 2 in the case (c) where the barrier height correction has been taken into account. The second one is the insensitivity of the ideality factor to temperature, a property which matches rather well the behavior of the interface (c) in Fig. 4(c'), in contrast to the absolute variations in data (a') and (b'), although the ideality factor (c') remains slightly higher than the values evaluated from the image force lowering alone. Taking all the arguments evidenced and discussed in this subsection, one must conclude that microscopic barrier inhomogeneities resulting from repulsive elementary point charges or dipoles which have been, however, experimentally evidenced, cannot account for most of the properties of the interfaces presently studied, and that another type of barrier inhomogeneity must be present.

#### D. Barrier height and ideality factor of interfaces with lowered barrier patches of size either comparable to or smaller than the Debye length

The calculation of barrier height fluctuations due to barrier height lowering  $\Delta_p$  at circular patches with radius  $R_0$  or linear ones with width  $L_0$  and their effect on the current-voltage characteristics relies on the same principle as previously, except for the weight of each dipole which has to be  $2\pi\epsilon_{SC}\epsilon_0\Delta_p R_0^2$  to induce the desired barrier change at circular patches which will be only considered in the following because close to those happening naturally in inhomogeneous interfaces. Additionally, only patches with a lowered barrier are considered as demonstrated in Subsection IV C. This method, known as the dipole-layer approach, has been implemented analytically by Tung<sup>30</sup> and summarized later by Mönch.<sup>24</sup> For a single circular patch with radius  $R_0$  and barrier lowering  $\Delta_p$  embedded into a homogeneous area characterized by a constant barrier height  $\Phi_B^{hom}$ , a single parameter containing the two characteristic quantities  $R_0$  and  $\Delta_p$ , which is called the patch parameter  $\gamma_p = 3(\Delta_p R_0^2/4)^{1/3}$ , can be defined. Integrating Eq. (1) over the whole area  $A$  with the hypothesis of a parabolic shape of the potential around the saddle point, which is the lowest potential of the patch, restores the form of Eq. (3). But the new barrier height is  $\Phi_B^{hom}$  minus an effective barrier lowering  $\delta\Phi_p^{sad}$  at the potential saddle point, the ideality factor  $n$  is replaced by 1 and an effective area  $A_{eff} = 4\pi\lambda_D^2\Gamma/3$  affects the current expression. The weight of the patch is proportional to the dimensionless parameter  $\Gamma = \frac{\gamma_p}{3}\frac{1}{\eta^{1/3}U^{2/3}}$  where  $\eta = \epsilon_{SC}\epsilon_0 / (e_0 N_A)$ . Both the effective barrier lowering

$3\Gamma U = \gamma_p[U/\eta]^{1/3}$  and area  $A_{eff} = \frac{4\pi\gamma_p k_B T}{9e_0}[\eta/U]^{2/3}$  are dependent on the band bending  $U = \Phi_B^{hom} - V_j - V_{dop}$ , while the ideality factor is approximately  $1 + \Gamma$ , therefore increasing with the forward voltage. The final step consists of introducing a distribution of a variable patch parameter. In the Tung's original work,<sup>30</sup> two cases were worked out: (i) a sharp distribution of lowered barrier patches approximated by a single patch parameter  $\gamma_0$  and (ii) a broad distribution featured by half a Gaussian law which limited the  $\gamma_p$  range to the values pertaining to barrier height lowering alone, which are  $\gamma_p \geq 0$ . This choice was justified by the negligible contribution of patches characterized by a barrier height enhancement to the whole current as we checked in Subsection IV C. In order to generalize such an approach, allowing to match continuously any intermediate behavior between the two previous cases, the patch parameter distribution function will be chosen as

$$N(\gamma_p) = \frac{D_p}{\sqrt{2\pi}\sigma_p} \exp\left(-\frac{(\gamma_p - \gamma_0)^2}{2\sigma_p^2}\right),$$
 characterized by a standard deviation  $\sigma_p$  of the patch parameter around the central value  $\gamma_0$  and an areal density  $D_p$ . Depending on  $\gamma_0$ , the function  $N(\gamma_p)$  depicts either a peaked distribution around the central patch parameter, or half a Gaussian law decreasing from its maximum at  $\gamma_p = 0$  when  $\gamma_0 = 0$  or even a decreasing Gaussian tail with a nonzero initial slope if  $\gamma_0 < 0$ . After summation of all the currents dependent on any positive value of  $\gamma_p$  from zero to infinite, this procedure further allows to derive the following expression where only the last factor inside braces contains the effects of inhomogeneities while the others give the ideal thermionic current density of a homogeneous barrier height  $\Phi_B^{hom}$

$$\begin{aligned} J_z^{patchy} = & \alpha A^{**} T^2 \exp\left(-\frac{e_0\Phi_B^{hom}}{k_B T}\right) \left[ \exp\left(\frac{e_0 V_j}{k_B T}\right) - 1 \right] \\ & \times \left\{ 1 + \frac{2\sqrt{2\pi} k_B T D_p \sigma_p \eta^{2/3}}{9 e_0 U^{2/3}} \exp\left(-\frac{\gamma_0^2}{2\sigma_p^2}\right) \right. \\ & \times \left[ 1 + \frac{\sqrt{2\pi} e_0 \langle \delta\Phi_{p,0}^{sad} \rangle}{k_B T} \right. \\ & \left. \left. \times \exp\left(\frac{1}{2} \left(\frac{e_0}{k_B T} \langle \delta\Phi_{p,0}^{sad} \rangle\right)^2\right) \right] \right\}, \end{aligned} \quad (7)$$

where the standard deviation  $\langle \delta\Phi_{p,0}^{sad} \rangle$  of the distribution of the saddle points of the barrier  $\Phi_p^{sad}$  is

$$\langle \delta\Phi_{p,0}^{sad} \rangle = \sigma_p \left[ \frac{U}{\eta} \right]^{1/3} + \frac{k_B T \gamma_0}{e_0 \sigma_p}. \quad (8)$$

But the current density deviates notably from the ideal thermionic law only if the factor inside the braces of Eq. (7) is larger than unity. As one is interested in this case, a reasonable approximation consists of neglecting the unity terms inside the braces, so that the effective barrier height can be deduced from the exponent of the exponential factors, which turns out to be  $\frac{1}{2} \left[ \frac{e_0}{k_B T} \langle \delta\Phi_{p,0}^{sad} \rangle \right]^2 - \frac{\gamma_0^2}{\sigma_p^2}$  inside the braces of Eq. (7) and logarithm of the pre-exponential factor

$$\Phi_B^{eff}(T, U) = \Phi_B^{hom} - \left[ \frac{e_0}{2k_B T} \sigma_p^2 \left( \frac{U}{\eta} \right)^{2/3} + \gamma_0 \left( \frac{U}{\eta} \right)^{1/3} \right] - \frac{k_B T}{e_0} \ln \left[ \frac{4\pi D_p \sigma_p \eta^{2/3}}{9 U^{2/3}} \langle \delta \Phi_{p,0}^{sad} \rangle \right]. \quad (9)$$

This last equation is similar to Eq. (5) with the new quadratic average  $\langle \delta \Phi_B \rangle$  of barrier fluctuations

$$\langle \delta \Phi_B \rangle = \left[ \sigma_p^2 \left( \frac{U}{\eta} \right)^{2/3} + \frac{2k_B T}{e_0} \gamma_0 \left( \frac{U}{\eta} \right)^{1/3} \right]^{1/2} \quad (10)$$

and an additional term which has a little influence due to the logarithm and a null value for  $D_p$  in the  $10^{10} \text{ cm}^{-2}$  range, but may give a nonnegligible contribution to the ideality factor appearing in next formula when the barrier inhomogeneity level is low. But the main issue is the dependence of  $\langle \delta \Phi_B \rangle$  on temperature which is different from that given by Eq. (5) and results in a shift of the high temperature asymptote of the effective barrier in comparison with  $\Phi_B^{hom}$  by a quantity proportional to  $\gamma_0$ , leading to an apparent extrapolated barrier  $\Phi_B^{app} = \Phi_B^{hom} - \gamma_0 \left( \frac{U}{\eta} \right)^{1/3}$ .

From Eqs. (6), (8), and (9), the ideality factor can be calculated as

$$\begin{aligned} \frac{n(T, U) - 1}{n(T, U)} &= \frac{e_0}{3k_B T U} \left[ \sigma_p^2 \left( \frac{U}{\eta} \right)^{2/3} + \frac{k_B T}{e_0} \gamma_0 \left( \frac{U}{\eta} \right)^{1/3} \right] \\ &\quad - k_\Phi \frac{k_B T}{e_0 U} \\ &= \frac{e_0}{3k_B T U} \langle \delta \Phi_B \rangle^2 - \frac{\gamma_0}{3\eta^{1/3} U^{2/3}} - k_\Phi \frac{k_B T}{e_0 U}, \end{aligned} \quad (11)$$

where  $k_\Phi$  is between 1/3 and 2/3 according to the respective dominance of either the first or the second term in  $\langle \delta \Phi_B \rangle$ . This ideality factor increases with decreasing band bending and therefore with increasing applied voltage as long as flat bands are not reached, so that current-voltage characteristics plotted in a semilogarithmic diagram experience a downwards curvature, as in Figs. 2(a) and 2(b). This model ceases to be valid for neat flat bands and beyond because the current calculation relies only on the carrier flow at the saddle points of the potential barrier, neglecting the areas where the barrier is  $\Phi_B^{hom}$  or higher. It must be also stressed that these ideality factor and effective barrier height must be evaluated around the same band bending  $U = U_b$  if comparison at different temperatures or in different diodes is made. This is often done by assessing the corresponding ideality factor  $n_b$  at the same current density, although such a rule is almost true only at vanishing band bending. It is important to notice that various behaviors of the ideality factor as a function of temperature can result from Eq. (11), with a trend toward a constant value when the second term inside the brackets dominates at elevated temperatures as one can see in Fig. 3(b'), the last term in Eq. (11) being negligible except near flat bands and for ideality factors below 1.1. Either neglecting the last term in Eq. (9) or lumping it into  $\Phi_B^{hom}$ , a relationship between the effective barrier height and ideality factor

$n_b$  at the same band bending  $U_b$  for all the diodes investigated at a given temperature among a set of diodes, comes from Eqs. (9), (10), and (11)

$$\Phi_B^{eff} \approx \Phi_B^{hom} - \frac{3U_b n_b - 1}{2} \frac{\gamma_0}{n_b} - \frac{\gamma_0}{2} \left( \frac{U_b}{\eta} \right)^{1/3} - k_\Phi \frac{k_B T}{e_0 U_b}. \quad (12)$$

Therefore, the difference between the effective barrier height  $\Phi_B^{eff}$  and a quantity shifted from the homogeneous barrier  $\Phi_B^{hom}$  mainly by a term proportional to the central patch parameter  $\gamma_0$ , follows a linear relationship regarding the ideality function  $(n_b - 1)/n_b$ . It does not depend on the standard deviation  $\sigma_p$  of the patch distribution, except for the last term including the factor  $k_\Phi$  which is roughly constant for a given patch distribution. At constant temperature, this last term is indistinguishable from  $\Phi_B^{hom}$  and adds a minor error to it. Conversely, the term proportional to  $\gamma_0$  may contribute to an important shift of the apparent extrapolated barrier at unity ideality factor in comparison to  $\Phi_B^{hom}$ , since this apparent barrier turns out to be  $\Phi_B^{app} = \Phi_B^{hom} - \frac{\gamma_0}{2} \left( \frac{U}{\eta} \right)^{1/3}$  and this correction might not be ignored in general. It can also introduce some dispersion of the data when a family of diodes is studied. The effective barrier height  $\Phi_B^{eff}$  is approximately linear with  $n_b$  only for typical values smaller than 1.4 like noticed in Ref. 24 so that it is better to make plots of the apparent barriers as a function of  $(n_b - 1)/n_b$  for sake of generality, as done in Fig. 8, which will be commented in Subsection IV F. However, it must be stressed that all the expressions derived for the effective barrier height and ideality factor within the framework of the present model, which are Eqs. (9)–(12), assumed that the factor inside the braces of Eq. (7) is largely greater than one. Such a condition implies that the patch density  $D_p$  must be typically much larger than  $10^7 \text{ cm}^{-2}$ , so that one has to wonder whether the value deduced from adjustments has really a physical meaning in each situation.

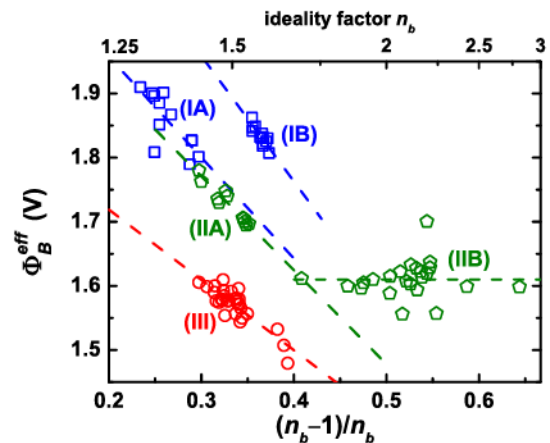


FIG. 8. Effective barrier height as a function of  $(n_b - 1)/n_b$ , where  $n_b$  is the ideality factor at band bending  $U_b$  for 95 diodes fabricated on three distinct diamond stacks elaborated like described in Section II, respectively, identified by squares (I), pentagons (II), and circles (III). Samples I and II have not been intentionally annealed while sample III has been annealed at 350°C. Dashed lines are best linear fits of grouped data IA, IB, IIA, IIB, and III according to Eq. (12).

In one diode alone, the fingerprint of the kind of barrier inhomogeneities breaks out in the behaviors of the ideality factor and to a smaller extent of the effective barrier height as a function of temperature, as shown in Fig. 4, where evolutions of the ideality factor are markedly different for the three interfaces in Figs. 4(a')–4(c'). All these features can be reproduced by the laws demonstrated above, especially the ideality factor variations with temperature which are strongly influenced by the central patch parameter  $\gamma_0$  in Eq. (11). In the case (a), a good agreement with Eq. (11) can be obtained as depicted by the dashed-dotted curve in Fig. 4(a') at the expense of a negative central patch parameter which would induce an apparent barrier  $\Phi_B^{app}$  larger than the homogeneous one  $\Phi_B^{hom}$ , obviously leading to an incoherent physical situation. Moreover, the direct adjustment of the current density according to Eq. (7) turns out to be impossible because this expression is unable to account for the curvature of the current density-voltage characteristic (a) in Fig. 2 below the flat band voltage. An alternative model able to involve a more appropriate physical picture is discussed below for interfaces of kind (a). Data collected in 95 diodes prepared on three distinct diamond stacks, which underwent the same pre-treatment before metal deposition and displayed in Fig. 8, give a first indication: if so different groups of data are possible for diodes whose diameter is  $100\ \mu\text{m}$ , specially the IB against IA and IIA, related to interfaces of kind (a), barrier heights extrapolated at unity ideality factor and averaged on such area must be different. Consequently, the lateral scale of barrier inhomogeneities may no longer be the Debye length but much more, and the approximations of a parabolic potential at the bottom of the lowered barrier patches depicted by the patch parameter  $\gamma_p$  would cease to be valid. Second, strong variations of the ideality factor with temperature as in Fig. 4(a') suggest that diamond resistivity may play a role because acceptors are progressively ionizing in this temperature range.

### E. Barrier domains with multiple sizes and inhomogeneities of the current density

When the lateral size of barrier inhomogeneities largely exceeds the Debye length, the previous model relying on a parabolic potential at the bottom of the patches with a lowered barrier is no longer relevant. These different areas with distinct barrier height can be treated as independent of the band curvature because the pinch-off of the channels where the current flows becomes negligible. Then, the total current is simply obtained by summation of all the currents as in a parallel circuit of the corresponding paths. But such a model is unable to fit the downward curvature experienced by the logarithm of the current density as a function of voltage in interfaces of kind (a) and yields merely an ideal behavior as soon as the lowest barrier is shifted below the others by some  $k_B T/e_0$  because the corresponding current flow dominates the others. In fact, this current inhomogeneity due to carrier crowding at the saddle points and lowest barrier domains remains when the  $z$  coordinate move away from the interface and therefore have a dramatic influence on the total voltage applied to the junction for a given current, specially when carrier freeze-in occurs, inducing large variations of

the ideality factor with temperature. This effect is relevant both for barrier domains much larger than the Debye length where no pinch-off occurs and for pinched-off patches, and the voltage drops in these shrunk channels must be subtracted from the total applied voltage. In the pinched-off case, the diameter of patches is always much smaller than the lightly doped layer thickness  $t_l$  so that the spreading resistance can be approximated by  $\frac{\rho(T)}{4\sqrt{\mathcal{A}_{eff,i}^{p-o}/\pi}}$  with a good accuracy,<sup>46</sup>  $\rho(T)$  being the resistivity of the lightly doped diamond layer. Therefore, the nonpinched-off and pinched-off forward currents which flow, respectively, through individual areas  $\mathcal{A}_i$  and  $\mathcal{A}_{eff,i}^{p-o}$  under an applied voltage  $V_a$  can be derived from the generic thermoionic law but with band bending equal to the homogenous potential barrier minus the relevant barrier lowering and applied voltage  $V_a$  from which the ohmic voltage drop along either non pinched-off or pinched-off channels inside the depletion zone is subtracted

$$I_i^{non-p-o} = \mathcal{A}_i \alpha A^{**} T^2 \exp\left[-\frac{e_0}{k_B T} (\Phi_B^{hom} - \Delta\Phi - V_a + I_i^{non-p-o} \rho(T)/\lambda_i)\right], \quad (13a)$$

$$I_i^{p-o} = \mathcal{A}_{eff,i}^{p-o} \alpha A^{**} T^2 \exp\left[-\frac{e_0}{k_B T} \left(\Phi_B^{hom} - \gamma_p \left(\frac{U_i}{\eta}\right)^{1/3} - V_a + \frac{\rho(T)}{4\sqrt{\mathcal{A}_{eff,i}^{p-o}/\pi}} I_i^{p-o}\right)\right] \quad (13b)$$

with  $\mathcal{A}_{eff,i}^{p-o} = \frac{4\pi k_B T \gamma_p}{9e_0} \left(\frac{\eta}{U_i}\right)^{2/3}$  and  $U_i = \Phi_B^{hom} - \gamma_p \left(\frac{U_i}{\eta}\right)^{1/3} - V_a - V_{dop} + \frac{\rho(T)}{4\sqrt{\mathcal{A}_{eff,i}^{p-o}/\pi}} I_i^{p-o}$ ; the lowest barrier spreading over the areas  $\mathcal{A}_i$  with size much larger than the Debye length being  $\Phi_B^{hom} - \Delta\Phi$ . If the current inhomogeneity remains the same along the whole depth of the lightly doped layer like assumed in Ref. 31 the voltage drop along the  $i^{th}$  non pinched-off channel is simply proportional to a resistance  $\rho(T)/\lambda_i$  where  $\lambda_i = \mathcal{A}_i/t_l$ . This hypothesis is true in the limit of a diameter of the area with a lowered barrier height well larger than  $t_l$ , a condition equivalent to  $\sqrt{\mathcal{A}_i/\pi} \gg t_l/2$ . But because this diameter can span a large range, from values well below  $t_l$  up to much wider ones, the corresponding spreading resistance should take the general form<sup>46</sup>  $\frac{\rho(T)}{2\sqrt{\pi\mathcal{A}_i}} \arctan(2t_l/\sqrt{\mathcal{A}_i/\pi})$  and  $\lambda_i$  should become  $2\sqrt{\pi\mathcal{A}_i}/\arctan(2t_l/\sqrt{\mathcal{A}_i/\pi})$ . It must be noticed that the last term in the exponent of the expression of  $I_i^{p-o}$  and in  $U_i$  is added to  $\Phi_B^{hom}$  and therefore plays the same role as a negative central patch parameter  $\gamma_0$  in the effective barrier experienced by the whole current flowing through the pinched-off patches and given in Eq. (9). This fact explains why neglecting the confinement of current in channels which stretch out along some part of the lightly doped layer thickness had to be compensated by the occurrence of a negative figure for  $\gamma_0$  in the simulation results of Subsection IV D, leading to an incorrect value because of an inappropriate model applied to interfaces of kind (a). Such a fictitious negative figure for  $\gamma_0$  was necessary

to obtain an acceptable, but misleading, agreement of the experimental data with the model developed in Subsection IV D since first, the resulting  $\Phi_B^{app}$  value larger than  $\Phi_B^{hom}$  would contradict the hypothesis which assumed lowered barrier patches and second, the same model was unable to match the curvature of the current-voltage characteristics.

Averaging all the currents over the whole diode area  $\mathcal{A}_d$  is not tractable analytically. A reasonable approximation consists of calculating separately the total current and an estimate of the whole conductance within the shrunk channels from the integration of all the parallel conductances  $\lambda_i/\rho(T)$  or  $4\sqrt{\mathcal{A}_{eff,i}^{p-o}/\pi}/\rho(T)$  appearing in the last term of the exponent of each expression (13a) or (13b), weighted by the distribution  $N(\gamma_p) = \frac{D_p}{\sqrt{2\pi}\sigma_p} \exp(-\frac{(\gamma_p-\gamma_0)^2}{2\sigma_p^2})$  in the later case. It is also assumed like previously that only the lowest barrier for the current flow is efficient and that the barrier lowering is approximated by its quadratic average. For nonpinched-off channels, the total conductance would result from the integral of  $\lambda_i/\rho(T)$  weighted by an unknown distribution, so that it is more convenient to introduce a fictitious area  $\mathcal{A}_{\Delta V}^{non-p-o}$  allowing to write the corresponding voltage drop  $\Delta V^{non-p-o}$ . In the case of the pinched-off currents, two integrals must be evaluated numerically as a function of  $\gamma_0/(\sqrt{2}\sigma_p)$ . Their ratio appears as a fraction in the next formula and gives the exact value within an error smaller than 10%. With  $\mathcal{A}^{non-p-o} = \sum_i \mathcal{A}_i$  representing the true area of the non pinched-off zones, the average current densities in the whole diode area become, respectively, for the non pinched-off and pinched-off channels

$$J_z^{non-p-o} \approx \frac{\mathcal{A}^{non-p-o}}{\mathcal{A}_d} \alpha A^{**} T^2 \exp \left[ -\frac{e_0}{k_B T} (\Phi_B^{hom} - \Delta\Phi - V_a + \Delta V^{non-p-o}) \right] \quad (14a)$$

with

$$\Delta V^{non-p-o} \approx \frac{\rho(T) \mathcal{A}^{non-p-o}}{(\mathcal{A}_{\Delta V}^{non-p-o})^{1/2}} \alpha A^{**} T^2 \exp \left[ -\frac{e_0}{k_B T} (\Phi_B^{hom} - \Delta\Phi - V_a + \Delta V^{non-p-o}) \right] \quad (14b)$$

and  $J^{p-o} = J_z^{patchy}$  from Eq. (7), with  $V_j = V_a - \Delta V^{p-o}$  where

$$\Delta V^{p-o} \approx \frac{\pi}{6} \rho(T) \left( \frac{k_B T}{e_0} \right)^{1/2} \left( \frac{\eta}{U} \right)^{1/3} \frac{1.77\gamma_0 + \sigma_p^2 / (\gamma_0 + \sqrt{2}\sigma_p)}{\sqrt{\pi\gamma_0 + \sqrt{2}\sigma_p/3}} \times \alpha A^{**} T^2 \exp \left[ -\frac{e_0}{k_B T} \left( \Phi_B^{hom} - \frac{e_0}{2k_B T} \langle \delta\Phi_B \rangle^2 - V_a + \Delta V^{p-o} \right) \right] \quad (14c)$$

and

$$U \approx \Phi_B^{hom} - \frac{e_0}{2k_B T} \langle \delta\Phi_B \rangle^2 - V_a - V_{dop}. \quad (14d)$$

It must be noticed that the patch density  $D_p$  does not appear in  $\Delta V^{p-o}$  because both the conductance and current are proportional to it, so that it is canceled in the framework of the previous approximation. From these expressions, it is easy to guess that the lower the temperature, the higher the effect of the smallest barrier, like in previous models. If the nonpinched-off current dominates, the apparent barrier lowering would be  $\Delta\Phi - \frac{k_B T}{e_0} \ln(\mathcal{A}_d/\mathcal{A}^{non-p-o})$ , inducing a linear decrease of the effective barrier as temperature is lowered, whereas alternatively Eq. (9) would be valid, at least when  $\Delta V$  remains small regarding  $V_a$ . At sufficiently high temperature, the increase in the effective barrier would be linear with temperature when the nonpinch-off current dominates, an effect which is not clearly detected in Fig. 4(a), indicating that the pinch-off current might stay as the major one. Such a view is confirmed by the absence of any ‘‘S-shaped’’ current-voltage characteristic in Fig. 2(a), which otherwise would reveal the existence of two parallel nonpinched-off channels like happening in some Ti/4H-SiC diodes,<sup>47</sup> each of the ones having its own barrier height and series resistance with the corresponding condition  $\sqrt{\mathcal{A}_i/\pi} \gg t_l/2$  indeed achieved.

From experimental data displayed in Fig. 8, it seems that the general trend involving a linear relationship between effective barrier height and ideality function is still valid. Such a property can be checked from the integration of the central expression in Eq. (6) where the total applied voltage  $V_a$  replaces the junction voltage  $V_j$  since the current density is now dependent on  $V_a$  if one relies on the last expressions (14). It results in a linear relationship between the effective barrier and ideality factor function if the ideality factor does not depend on the band bending  $U_b$ . Such a condition is only approximately achieved, but better and better when higher and higher band bending is used, like those deduced from these data and reported in Table III, because the voltage drop  $\Delta V$  remains negligible in this range. It is therefore possible to find a range of voltage and corresponding band bending extending over an interval  $U_b/K$  ( $K$  being a unitless constant) where the ideality factor is constant around  $U_b$  and integration of the second and fourth members of Eq. (6) gives the apparent barrier height in non ideal interfaces

$$\Phi_B^{app}(T, U_b) = \Phi_B^{ideal} - \frac{U_b}{K} \frac{n(T, U_b) - 1}{n(T, U_b)}, \quad (15)$$

where  $n(T, U_b)$  is the ideality factor at temperature  $T$ , around the peculiar band bending  $U_b$ .  $\Phi_B^{ideal}$  is the barrier height at unity ideality factor, which matches accurately  $\Phi_B^{hom} - \frac{\gamma_0}{2} (\frac{U}{\eta})^{1/3}$  for pure pinched-off barrier inhomogeneities as demonstrated in Subsection IV D in formula (12) where the last term can be neglected, and is only close to  $\Phi_B^{hom}$  without a precise knowledge of the deviation in other cases. Therefore, the observed linear correlations in Fig. 8 can still be justified. When the voltage drop inside the lightly doped layer is not negligible, approximate expressions of the

ideality function  $Y$  can be drawn separately from the previous equations when either  $I^{non-p-o} = A_d J_z^{non-p-o}$  or  $I^{p-o} = A_d J_z^{p-o}$  dominates, which turns out to be, respectively, with either the ideality factor  $n_a(T, V_a)$  under applied voltage  $V_a$  or the ideality factor  $n_b(T, V_a)$

$$Y^{non-p-o} = \frac{n_a(T, V_a) - 1}{n_a(T, V_a)} \approx \frac{e_0}{k_B T} \Delta V^{non-p-o} \quad \text{or} \quad Y^{p-o} = \frac{n_b(T, V_a) - 1}{n_b(T, V_a)} \quad (16a)$$

$$\approx \left[ \frac{e_0}{3k_B T U} \sigma_p^2 \left( \frac{U}{\eta} \right)^{2/3} + \frac{\gamma_0}{3U} \left( \frac{U}{\eta} \right)^{1/3} \right] \times \left( 1 + \frac{e_0}{k_B T} \Delta V^{p-o} \right) + \frac{e_0}{k_B T} \Delta V^{p-o}. \quad (16b)$$

When the ideality factor has to be studied as a function of temperature, measurements should be done at constant current density, because in such a case the product of  $\alpha A^{**} T^2$  and exponential factors in Eq. (16a) and in terms  $\Delta V^{p-o}$  of Eq. (16b) can be considered as almost invariant, making any parameter adjustment much easier. In each case, these expressions show that the ideality factor may become very sensitive to temperature, especially because it follows the variations of the resistivity  $\rho(T)$  which are very important in the range where freezing out of carrier occurs, typically from 300 K to 550 K in this study. Involvement of the voltage drop due to the flow of current through the narrow bottlenecks, which lengthen the lowered barrier regions inwards the lightly doped layer, is able to explain qualitatively the strong negative slope of the ideality factor in Fig. 4(a'). The general case relies on the combination of the two kinds of current with a proportion  $P = I^{p-o} / (I^{p-o} + I^{non-p-o})$  and on Eq. (6), giving the global ideality function:

$$Y = \frac{n(T, V_a) - 1}{n(T, V_a)} = P Y^{p-o} + (1 - P) Y^{non-p-o}. \quad (17)$$

The best match to the four data at highest temperatures is obtained with  $P = 72\%$  and plotted as a full curve in Fig. 4(a'), confirming the previous hypothesis about the dominance of the pinched-off current. The discrepancy at the lowest temperatures is commented in the following. But it must be stressed that the first term in Eq. (17) is unable to account for the ideality factor variations, which are mainly due to the second term despite its smaller weight. It is thus confirmed that the nonpinched-off currents contribution is necessary to

explain both the current density-voltage curvature and the ideality function shape with temperature in interfaces of kind (a). The more important voltage drop  $\Delta V^{non-p-o}$  in these interfaces is also able to explain why flat bands are reached at a lower current density (see Fig. 2) in comparison to interfaces of kinds (b) and (c) in which the patch and channel densities are so high (see Table II) that the voltage drop remains negligible in this bias range.

At sufficiently high forward bias, band curvature can be inverted in some areas or even in the whole diode, as the readers can understand from the comparison of  $\Phi_B^{hom}$  (in Table II) minus  $V_{dop} = 0.38$  V to the applied voltage in Fig. 2, so that the previous expressions can no longer be used. In other words, energy bands bend upward near the interface when the flat band voltage is exceeded. From Eq. (10), barrier lowering vanishes at flat bands for  $I^{p-o}$  while it stays constant for  $I^{non-p-o}$  and one can think that the effective barrier height remains more or less at the value obtained at flat bands beyond this threshold. But previous models which rely only on barrier lowering are unable to take into account the progressive disappearance of current inhomogeneities in the lightly doped layer due to the general increase of the carrier concentration at the whole interface. Such a behavior would finally lead to a more homogeneous current density and a voltage drop within the lightly doped layer expected to be simply the product of a series resistance and total current. But even this view fails because voltage drop turns out to be lower in Fig. 2 as if the resistivity were smaller than the predicted one. This discrepancy is neither an artifact of the adjustment procedure nor a self-heating effect which would hardly be justified because of the low dissipated power (typically one to some tens of mW in the range of interest), but is rather due to the injection of carrier by the heavily doped layer, involving a conductivity modulation due to the increase of carrier concentration above the equilibrium one and occurrence of a diffusion current starting from this heavily doped layer. This effect is evidenced from the comparison of the current-density data and curves simulated with a constant series resistance in Fig. 2 and it can also be checked because of the lower value of the current-density voltage derivative compared to the theoretical specific resistance (not shown) at sufficiently high current. A detailed study relying both on experiment and simulation is published elsewhere<sup>48</sup> and demonstrates that the injection effect is more and more important as the temperature is lowered below the freeze out of carriers and the active layer thickness is smaller than  $2 \mu\text{m}$ , two conditions which are fulfilled here. It had been

TABLE II. Parameters of the Schottky barrier in the three interfaces according to the models detailed in Section IV, with  $\Phi_{B,1}^{app}$  and  $\sigma_p$  deduced from the adjustment of barrier height as a function of temperature according to Eq. (9). Then,  $\gamma_0$ , and  $\Phi_{B,1}^{hom}$  are derived from ideality factors fitted as a function of temperature with respective help of Eq. (11) in the case of interfaces (b) and (c), and Eq. (16b) for interface of kind (a), while  $D_p$  and  $\Phi_{B,2}^{hom}$  come from the direct adjustment of the current densities shown in Fig. (2), respectively, to Eq. (7) for interfaces of kind (b) and (c) and Eq. (14) for interface of kind (a) as a function of voltage.

Sample type and annealing temp. ( $^{\circ}\text{C}$ )	$\Phi_{B,1}^{app}$ (V)	$\sigma_p$ ( $\text{V}^{1/3} \text{cm}^{2/3}$ )	$\gamma_0$ ( $\text{V}^{1/3} \text{cm}^{2/3}$ )	$\Phi_{B,1}^{hom}$ (V)	$D_p$ ( $\text{cm}^{-2}$ )	$\Phi_{B,2}^{hom}$ (V)
(a) <300	$2.04 \pm 0.14$	$(9 \pm 3) \times 10^{-5}$	$(1.6 \pm 0.4) \times 10^{-4}$	$2.26 \pm 0.16$	$(3 \pm 1) \times 10^6$	$2.38 \pm 0.02$
(b) 350	$1.68 \pm 0.1$	$(9.0 \pm 1) \times 10^{-5}$	$(1.85 \pm 0.3) \times 10^{-4}$	$1.87 \pm 0.1$	$(6 \pm 2) \times 10^9$	$1.90 \pm 0.02$
(c) 450	$0.93 \pm 0.04$	$(5.5 \pm 1.5) \times 10^{-5}$	$(1.3 \pm 1.2) \times 10^{-5}$	$0.94 \pm 0.04$	$< 10^9$	$0.99 \pm 0.01$

probably observed by other authors in Ni/SiC diodes,<sup>32</sup> although they did not give such an interpretation. This carrier injection which decreases the resistivity is still efficient at lower current density, so that the hole concentration at interface is underestimated even at the bias voltage where ideality factors are measured, at least when complete ionization of acceptors is not achieved. Correlatively, the effective resistivity is overestimated when its equilibrium value is taken into account as done in the present calculation, increasing thoughtlessly the simulated voltage drop and ideality factor in Fig. 4(a') at the two lowest temperatures. This injection effect probably occurs because the lightly doped layer is only 1.4  $\mu\text{m}$  thick and would disappear for the larger thicknesses suited to higher voltage operation. In any cases, it must be noticed that all the previous models discussed and built in this work are applicable to a range of bias voltages and currents limited by the occurrence of flat bands in the junction but that high injection effects may be present near flat bands and beyond.

### F. Characteristics and origin of barrier height inhomogeneities in the three types of interface

The linear relationship between the effective barrier height as a function of the ideality factor function  $(n_b - 1)/n_b$  is actually checked for diodes prepared with the same procedure on three different substrates either without intentional post-annealing or annealed near 350 °C in Fig. 8. The correction of the constant term in Eq. (12) is done only in the case of indisputable relevance of the model of Subsection IV D and as it is not certain for interfaces of kind (a), extrapolated barrier heights  $\Phi_B^{app}$  and  $\Phi_B^{hom}$  will be considered as the same in Table III. It is noteworthy that the homogeneous barrier height  $\Phi_B^{hom}$  can be different in two families of diodes (IA and IB; IIA and IIB) on the same diamond stack, while it turns out to be very similar for the two families of diodes (IA and IIA) belonging to two distinct diamond samples, whose the initial surfaces are all oxygen-terminated. Such results confirm that oxygen terminations, which are responsible for the enhanced electron affinity of the oxygen-terminated diamond surfaces and highest barrier at interfaces build on such surfaces, are expected to be organized in domains displaying distinct electron affinities,<sup>21,34–36,38,39</sup> resulting in distinct barrier heights, and that the same kind of oxygen terminations can exist on different samples. This dispersion matches

TABLE III. Schottky barriers extrapolated at unity ideality factor at band bending  $U_b$  in different sets of diodes fabricated on three distinct diamond stacks numbered I, II, and III, according to best fits of Eq. (12) and  $\Phi_B^{hom}$  after the  $\gamma_0$  correction for the interface of kind (b).

Interface type, sample and diodes set identifiers	$\Phi_B^{app}$ (V)	$U_b$ (V)	$\Phi_B^{hom}$ (V) corrected for $\gamma_0$
(a) I A	$2.27 \pm 0.12$	$1.05 \pm 0.28$	
(a) I B	$2.54 \pm 0.14$	$1.30 \pm 0.24$	
(a) II A	$2.21 \pm 0.04$	$0.97 \pm 0.04$	
(a) II B	$1.61 \pm 0.06$		
(b) III	$1.94 \pm 0.04$	$0.73 \pm 0.08$	$2.04 \pm 0.04$

with that of the various molecules and bonds presented in Subsection IV A and probably also the lack of full coverage by oxygen related molecules. The linear relationship of Eq. (12) or (15) seems to apply irrespective of the scale of the barrier inhomogeneities in comparison to the Debye length provided ideality factor is measured at high enough band bending, typically two third of the barrier height, as justified in Subsection IV E. But because the interface annealed at 350 °C (Fig. 8(III)) is a matter of the lowered barrier pinched-off patch model detailed in Subsection IV D, the correction which gives the homogeneous barrier from the apparent one is only exerted in this case in Table III where the parameters are collected and displayed for all the diodes families. It must be noticed that the coherence of the various  $\Phi_B^{hom}$  values appearing in Tables II and III is reasonable and that an average value of  $2.04 \pm 0.04$  V can be inferred for the interface of kind (b), only about 0.2–0.5 V below the values at stake for the interfaces of kind (a). The relevance of the model relying for interfaces of kind (b) on lowered barrier patches with sizes comparable or smaller than the Debye length and depicted by a patch parameter distribution centered on a peculiar value  $\gamma_0 > 0$ , with a much higher patch density than for unannealed interfaces, demonstrates that the main barrier inhomogeneities take place now along this microscopic scale, in contrast to what happened in unannealed interfaces. One must remind that the patch parameters  $\gamma_p$ ,  $\sigma_p$  and  $\gamma_0$  depends on the one third power of the product of the square radius  $R_0$  and initial barrier lowering  $\Delta_p$  so that similar values of the two last quantities will not involve necessarily the same  $R_0$  and  $\Delta_p$ , which can move in opposite directions. From results given in Table II, such statements suggest that the 350 °C anneal resulted in the partial and random cancellation of the dipoles  $\text{O}^{-\nu'} - \text{C}^{+\nu'}$  whose stability is mainly governed by the enthalpy of the thermodynamical chemistry of these species and temperature, leaving the interface in an intermediate state and inducing new barrier lowering with a magnitude equal to the difference of the homogeneous potential barrier in interfaces of kinds (b) and (c), i.e.,  $\Delta_p \approx 1.1$  V at a microscopic scale, and increasing considerably the patch density. On the contrary, the initial inhomogeneities in unannealed interfaces of kind (a) likely resulted from the oxygen terminations dispersion over areas with larger size but smaller barrier lowering and much lighter density, with typical  $\Delta_p \approx 0.3$  V, similar to the difference in potential barriers reported for various interfaces of type (a) in Table III. To comply with the similarity of  $\sigma_p$  and  $\gamma_0$  for interfaces of kinds (a) and (b) in Table II, patches area has to be decreased by a factor of nearly four when going from case (a) to case (b), leading to a very good relevance of the model developed in Subsection IV D. In the case of interfaces of kind (c) annealed at 450 °C, these dipoles have completely disappeared, involving a barrier height as low as  $0.96 \pm 0.04$  V (average from Table II) and very low barrier fluctuations, as indicated by a central patch parameter  $\gamma_0$  one decade smaller than that of other cases, which induced an almost ideal behavior of the current-voltage characteristics. In this last case, residual barrier inhomogeneities could be due to the random influence of the ionized acceptors close enough to the interface, as it can be evidenced according to

the model sketched in Fig. 6(d) and invoked in Subsection IV C, but the calculation will not be developed further and the reader interested in this question is invited to refer to Ref. 20 and references therein. An other residual source of barrier inhomogeneities lies in the possible fluctuations of the oxide thickness, because of the link between these two quantities as discussed in Sec. V. Regardless, indications derived from modeling the electrical properties of the junctions match very well the conclusions of the HRTEM and EELS studies developed in Section II, which showed the sharpening of the interfacial oxide layer after annealing and led to the very probable hypothesis of a chemical mechanism involving bond strengthening between the first oxygen layer and the last carbon one. The main consequence of this bond transformation shows through the very large change occurring in the averaged barrier heights of interfaces (a) and (c), with a difference near 1.4 V, resulting from the partial or complete cancellation of the dipoles  $O^{-\nu'} - C^{+\nu'}$  and also other dipole changes as discussed in Section V. The case of the diodes set IIB in Fig. 8 does not comply with any previous models, a fact which suggests that the main part of the current in these diodes is not governed by an exponential law depending on the applied voltage, which was a common hypothesis of all the previous calculations. Therefore, leakage currents like those which might occur in threading dislocations or defects appearing as dark spots in cathodoluminescence images<sup>28</sup> could be responsible for a behavior characterized by rather higher ideality factors and constant apparent barrier height in Fig. 8(IIB). Finally, homogeneous barrier heights  $\Phi_{B,2}^{hom}$  appearing in Table II can be considered as the most representative of the physical situation of each interface, except that unannealed interfaces of type (a) may experience two or three different values like mentioned in Table III, the lowest being about 0.2 V below that indicated in Table II for a homogeneous set of diodes. This local barrier lowering may agree the quantity  $\Delta\Phi$  invoked in Subsection IV E over areas with lateral size larger than the Debye length to build the last electrical model relying on the nonpinched-off channels. It can be concluded that, despite some minor imperfect agreements between experimental data and models of inhomogeneous barriers detailed in this section and their limitations to the depletion regime of Schottky junctions, more information and deeper physical insight into the situation of these metal-diamond interfaces have been gained and can be reinvested in barrier height models discussed in Sec. V. The most important quantity which can be extracted from the analysis of electrical characteristics of Schottky diodes is obviously the true potential barrier height at an interface free of inhomogeneities and it has been defined at the beginning of this study as  $\Phi_B^{hom}$ . It is always underestimated if the barrier height is measured from the slope of a Richardson plot and a relevant value  $\Phi_B^{hom}$  needs to be deduced either from adjustment of the measured barrier height as a function of temperature, or from the direct adjustment of the current-voltage density with the appropriate model chosen among those described in this section, or from the statistics of barrier heights as a function of ideality factors in a set of diodes, or preferably from several methods.

## V. BARRIER HEIGHT MODELS AT METAL-OXYGENATED DIAMOND INTERFACES

The barrier heights issue at metal-diamond interfaces belongs to the long time debated topic of how the Fermi level position is determined at semiconductor surfaces and interfaces, discussed as early as in the 1930s by Sir Nevill Mott<sup>49</sup> concerning the rectification theory and by Walter Schottky.<sup>50</sup> Because this first model, which stated the linear dependence of the barrier height upon the metal work function with a unity slope, did not comply with the huge amount of data gathered since its publication, other explanations have been proposed to justify the weaker dependence experimentally observed, known as Fermi level pinning. New barrier height models have been progressively introduced within the framework of the “metal induced gap states” principle<sup>51</sup> or its generalization to “interface induced gap states”<sup>24</sup> in order to link band alignment and either the work function or electronegativity of the metal at the broadest possible panel of metal-semiconductor interfaces. All rely on the existence of an interface state density localized in the first elementary cells of the semiconductor which is neutral when the Fermi level coincides with an energy level  $\Phi_0$  characteristic of the semiconductor and referred as to the neutral level, defined here as the energy difference between such a level and the valence band edge at interface. Deviations from this position and from neutrality occur if a metal having an electronegativity different from that of the semiconductor is put in intimate contact with the semiconductor surface, assuming that the interface states inside the semiconductor remain invariant. This last hypothesis leads to a negative feedback effect due to the reaction of the charge inside interface states onto the voltage jump due to the double layer of the areal dipole astride the interface, which induces a linear relationship between the barrier height and the difference of the metal and semiconductor electronegativities  $X_m - X_s$ , with either a positive slope  $S_X$  on a n-type semiconductor, or a negative one,  $-S_X$ , on a p-type semiconductor as here

$$e_0 \Phi_{Bp}^{hom} = \Phi_0 - S_X (X_m - X_s), \quad (18a)$$

where

$$S_X = \frac{A_X}{1 + (e_0^2 / \epsilon_i \epsilon_0) D_{is} d_{di}} \quad (18b)$$

with  $D_{is}$  the interface state density and  $A_X$  a coefficient which depends on the electronegativity scale, equal to 0.86 if the Miedema scale is used.<sup>24</sup> This theory was rather successful for intimate metal-semiconductor contacts, which have been better and better controlled at an atomic scale for the 1970s, sometimes with an epitaxial metal layer. However, some dispersion still remained, which was not attributable to experimental uncertainties. This is especially true for diamond, which has not been the subject of extensive reports since the 1990s, excepted to evidence the wide range of barrier heights existing for the same metal<sup>8</sup> and with the notable exception of the hydrogenated surface.<sup>16</sup> Such a dispersion has been ascribed to the various structures, terminations, ad-atoms and natures of bond which can exist at the diamond surfaces

and interfaces, like already invoked in the case of oxygen termination. Recently, measurements of barrier heights have been published at carefully prepared oxygenated and eventually post-annealed diamond surfaces.<sup>9,18,52–56</sup> Together with the present results for Zr-diamond interfaces, ideal barrier heights are plotted in Fig. 9 with error bars added according to the rules discussed in Sec. IV: either only above the published value when the method underestimated the ideal homogeneous barrier  $\Phi_{Bp}^{hom}$  or symmetrical when  $\Phi_{Bp}^{hom}$  is directly indicated by authors or reassessed with the help of an appropriate method among those discussed in Sec. IV. Despite some dispersion, illustrated sometimes in Figs. 9 and 10 with different barrier heights reported for the same metal in literature, two groups of data appear well separated, one for the contacts annealed at typical temperatures less than 250 °C or as-deposited and another for contacts annealed at temperatures in the range of 400–650 °C, as a function of the Miedema electronegativity difference between metal and carbon, the last one being left constant at 5.7 eV. Electronegativity was originally used to describe the interaction between two (or more) atoms in a molecule and thereafter in solids. But it is impossible here to describe the two electronic situations regarding barrier heights in unannealed and annealed interfaces with only two electronegativity values, one for the metal and the other for oxygenated diamond, since changes after annealing occurred while oxygen still remains at the interface as demonstrated in Section II. Even if the diamond electronegativity were shifted by about  $-1.5$  eV to take the oxygen terminations into account in the unannealed interfaces, although this is not a very sensible operation, the whole set of data does not show clearly any indisputable trend, testifying a first shortcoming. A second one appears if the search for a linear relationship is restricted to the second group of data, which shows a reasonable alignment depicted by the dashed line in Fig. 9, but characterized by a positive slope, in contradiction with Eq. (18a) and what is experimentally found for all other cases including that of a

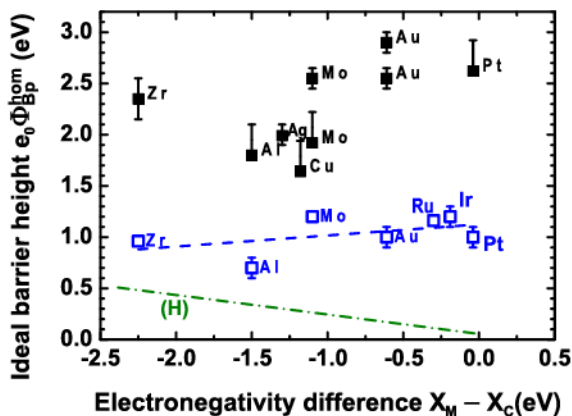


FIG. 9. Ideal barrier heights as a function of the Miedema electronegativity difference between metal and carbon (assumed to be 5.7 eV) for oxygenated interfaces annealed below 250 °C (full squares) and for those annealed in the range 400–650 °C (open squares), together with a linear fit in dashed line in the second case. The dashed-dotted line (H) is the best fit of barrier data on the hydrogenated surface by Tsugawa *et al.*<sup>16</sup> as a function of the same abscissa. Multiple data for the same metal (Au and Mo) come from different publications.

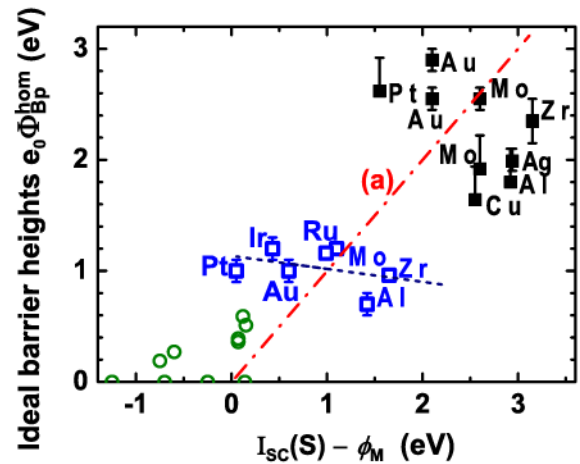


FIG. 10. Ideal barrier heights as a function of the difference between the ionization energy of diamond and the work function of metals (multiple data come from different publications) for (i) as-deposited interfaces (full squares) on an oxygenated (100)-oriented surface, (ii) for contacts annealed in the range 400–650 °C (open squares) on the same initial surface, together with a linear fit in dotted line, and (iii) for contacts on the hydrogenated (100)-oriented surface (open circles) from Ref. 16. Multiple data for the same metal (Au and Mo) come from different publications. The ionization energy includes the electron affinity shift due to surface terminations, yielding (i)  $\chi + \Delta\chi(S) = 1.7$  eV; (ii)  $\chi + \Delta\chi(S) = 0.3$  eV; and (iii)  $\chi + \Delta\chi(S) = -1.1$  eV, respectively, for the oxygenated, bare, and hydrogenated (100)-oriented surfaces from Ref. 33. The dashed-dotted line (a) displays Eq. (19a) where the last term is ignored, thus featuring the Mott-Schottky relationship.

hydrogenated diamond surface.<sup>16</sup> This is the second shortcoming. Incidentally, it is difficult to believe that the energy distribution of “interface induced interface states” may remain the same when going from the hydrogenated then air-exposed diamond surfaces to oxygenated ones, as it is well known that the former is provided with adsorbates and conducting whereas the latter is not.<sup>57</sup> Another approach, relying on physico-chemical quantities able to influence interface bonding, is necessary.

In the last twenty years, scientists performed modifications of the Schottky barrier heights by means of various adatoms and/or physical, chemical, and thermal treatments applied to the surface generally before metal deposition except for annealing. They realized that these changes are dependent on bonding between interface atoms, and that chemical interactions cannot be ignored between atoms in the neighborhood of the interface. A first improvement of the theory has been brought by Tung who showed that potential energies in the solids and through the interface were more appropriate to describe band alignment<sup>31</sup> in such a situation. This idea is applied to data addressed previously which are now plotted in Fig. 10. Second, the dipole strength of the various double layers occurring at interface is the relevant quantity to take the possible interlayer atoms, the different bonds<sup>58</sup> and even the possible new states due to transfer doping on the hydrogenated surface<sup>16</sup> into account. It is lumped into the last term in the following continuity equation which makes use of the metal work function  $\phi_M$  and electron affinity of the semiconductor as follows:

$$e_0 \Phi_{Bp}^{hom} = (I_{sc}(S) - \phi_M) - e_0 \Delta q d_{bd} N_{bd} / (\epsilon_i \epsilon_0), \quad (19a)$$

where the last term is the potential energy jump due to a surface dipole comprising a charge per bond  $\Delta q$  on the metal side and  $-\Delta q$  on the diamond side separated by the distance  $d_{bd}$ , with an areal density of dipoles  $N_{bd}$ , while the ionization energy given by

$$I_{SC}(S) = E_G + \chi + \Delta\chi(S) \quad (19b)$$

depends on the diamond band gap  $E_G$ , electron affinity  $\chi$  of the bare surface and possible change in electron affinity  $\Delta\chi(S)$  due to foreign atoms termination or particular reconstruction on each surface  $S$ , the  $\chi + \Delta\chi(S)$  values which are retained being indicated in the caption of Fig. 10.

When the last term is neglected in Eq. (19a), the Mott-Schottky relationship for contacts on p-type semiconductors is found, with a unity slope, sketched by a dashed-dotted line in Fig. 10. If the dispersion of data is forgotten in a first approach and the clouds of points related to the three categories of interface in this graph are replaced by their respective barycenters, one can guess that they align roughly on the Mott-Schottky line. This trend has been already evidenced in silicides on the n-type silicon interfaces.<sup>59</sup> The influence of the cloud related to the hydrogenated surfaces should be minored because Pt, Au, Cu, and Ag metal contacts are displayed with zero barrier heights, although they should be negative but cannot be actually measured and reported. More accurately, if one observes the barrier heights of each metal (Pt, Au, Mo, Al, Zr) whose contact on diamond has been measured in the two groups of oxygenated interfaces, respectively, before and after annealing, their difference lies in the range  $1.40 \pm 0.25$  eV for all of them, corresponding to the same change in electron affinity. This common shift indicates that the barrier height for a given metal is primarily controlled by the electron affinity of diamond, with a little influence of the dipole due to interface bonding, reflected in the last term of Eq. (19a), and testifies the disappearance of the oxygen terminations proper to initial oxygenated surfaces after annealing, or their transformation, irrespective of the presence of an oxide or not. As it was discussed in Subsection IV A, hydroxyl and carboxyl terminations likely exist before annealing and they can participate to bridged hydrogen bonds as suggested in Ref. 36, thus allowing adhesion of the atomic layers deposited on the surface by some kind of weak bonding. On the contrary, stronger, and therefore shorter bonds between carbon and atoms of the Zirconium oxide interlayer, that are mainly oxygen ones, would occur after annealing, in close correlation with the shrinkage of the oxide interlayer detected in Section II. But this statement does not mean that “interface induced gap states” have been suppressed or have never existed. They are just accommodating the electric charge which guarantees that the dipole layers, both necessary for setting the electron affinity and the bond dipole counterparts on the diamond side, can be present. Now, at a more subtle level, the general trend in each group of contacts made on the oxygenated surface has an inverted slope in comparison with the Mott-Schottky line, as already noticed in Fig. 9. The correlation coefficient is better in annealed interfaces, probably because the electron affinity dispersion due to various oxygen

terminations has been suppressed. The physical reason for the linear relationship depicted by a dotted line in Fig. 10 can be thus discussed with more confidence in the annealed interfaces than in the unannealed ones because the exact electron affinity is unknown in the second case for each metal and therefore replaced by the single value measured in vacuum as indicated in the caption of the figure. First, it is useful to notice that neither the first term in Eq. (19a), which also scales the abscissa in this diagram, nor the second term can account for the observed trend if this latter term is supposed to be proportional to the former one because the slope would be increased above one when the ionization energy is held constant. Therefore, one is forced to conclude that hidden physical parameters able to govern this second term might be involved. These are the nature of the bonds and interlayer, the charge transfer across them, their polarizability, and the interface structure with a special attention to the interlayer thickness and relative permittivity. In the case of metals like Pt, Ir, and Au, oxide formation is very unlikely since the enthalpy of formation is either positive or close to zero, whereas an oxide is present when Zr, as shown at the beginning of this study, and most probably Al, are used. If the interlayer is supposed to be a dielectric consisting of an ionic solid, its thickness  $t_{ox}$  is added to the bond length  $d_{bl}$  so that the total dipolar distance is roughly  $d_{bd} = t_{ox} + d_{bl}$ . Then this distance determines the strength of the last term in Eq. (19a) since the charge counterpart of the dipole on the metal side is now located at a slightly larger distance than  $t_{ox}$  from the last diamond atomic plane and if the charge inside the oxide layer is neglected at first approximation. Moreover, important effects are due to the charge transfer  $\Delta q$  which is governed by the nature of the bonds, electronegativity difference between the metal and semiconductor, the polarizability of bonds and interlayer thickness, as described in the bond polarization model proposed by Tung,<sup>31</sup> and also screening which can mainly accounted for by the relative permittivity occurring at the denominator of the last term in Eq. (19a). To get a deeper insight in the problem at least at a first order level of approximation, let us define the abscissa  $W_{SM} = (I_{SC}(S) - \phi_M)$  and take the derivative of the barrier height  $e_0 \Phi_{Bp}^{hom}$  when the electron affinity, and hence ionization energy are constant

$$\frac{d(e_0 \Phi_{Bp}^{hom})}{dW_{SM}} = 1 + \frac{d(e_0 \Delta q d_{bd} N_{bd} / (\epsilon_i \epsilon_0))}{d\phi_M}. \quad (20)$$

This slope would stay close to one whenever the second term is negligible but can become negative as observed in Fig. 10 if the second term is negative and its absolute value exceeds unity. Since the main trend occurring when the metal is changed to another one with an increased work function involves a decreased reactivity with oxygen and therefore a thickness reduction or disappearance of the oxide layer, one must wonder what are the resulting effects on the second term of Eq. (20), even if a continuous variation is more artificial than reality. The dipolar distance  $d_{bd}$  is obviously decreased while the interlayer permittivity  $\epsilon_i$  initially near that of high-k dielectric materials is going down closer to unity, resulting in a smaller screening effect. But because

theses two parameters are following the same direction of variation and influence the second term by their ratio, the resulting sign of the derivative turns out to be uncertain. Consequently, the fundamental issue relies mainly on the charge transfer  $\Delta q$  variation, which is dependent on the effective bonding at the metal-semiconductor interfaces,<sup>20,31</sup> including not only orbitals of the two original materials but also atoms or molecules belonging to the interlayer. In such a molecular orbital scheme, metals with the lowest work functions (and also more electropositive) would make more ionic bonds, with a polarizability likely augmented by the presence of additional oxygen bonds inside the interlayer, thus inducing a stronger positive charge transfer  $\Delta q$  in the orbitals of the last metal atomic layer. Conversely, noble metals (and also more electronegative ones) are expected to share the electrons of their d states in a more equalized way with carbon orbitals, while carbide forming metals would follow a medium behavior. Such a general trend of the charge transfer  $\Delta q$ , which would experience a decrease when the metal work function (and electronegativity) is increased, is able to justify the systematic negative sign of the derivative in the second member of Eq. (20). Consequently, the slope of barrier heights as a function of  $W_{SM} = (I_{SC}(S) - \phi_M)$  can take values smaller than one, as often observed in many semiconductors, and in the case of a magnitude of the absolute value of the last term in the same equation greater than unity, it can become negative as shown in Fig. 10, in contrast to what is known in all other semiconductors. Such a model can rely on the electronegativity difference between the semiconductor and metal, which mainly governs the dipole strength induced by interface bonding, but only for the last term in Eq. (19a), independent of the interface induced gap states at first order. At a second order level of approximation, the bonding nature of atoms inside the oxide and fixed charges in it will be also able to bring changes in  $\Delta q$  and these quantities probably contribute to the small deviations visible in Fig. 10 for annealed interfaces, together with the oxide interlayer thickness, permittivity, and changes in the atoms arrangement at interface and in the first diamond atomic layers. The same model also applies both to unannealed oxygenated interfaces and hydrogenated interfaces, however with larger fluctuations in comparison to a linear behavior, and a positive slope in the second case. It covers therefore all the situations, although it is difficult to afford quantitative parameters in the second term of Eq. (19a) for each metal in an accurate way.

## VI. CONCLUSION

In this work, interfaces of Zirconium with oxygenated diamond surfaces before and after two kinds of anneal has been characterized, on the one hand, by HRTEM imaging and EELS spectroscopy and, on the other hand, by thorough electrical measurements made on the Schottky junctions. HRTEM and EELS techniques evidenced an oxide interlayer comprising approximately one or two Zr oxide atomic layers, which sharpened after annealing. Electrical measurements were performed to collect and analyze current-voltage characteristics at several temperatures in many diodes in order to

investigate the detailed shape of the current density behavior with applied voltage, the Richardson constant, the apparent barrier height and ideality factor. Models taking the barrier height and current density inhomogeneities into account have been implemented and brought face to face with experimental results. From these comparisons, several physical parameters have been estimated. The Richardson constant turned out to be close to one tenth of the standard value, and even one thirteenth when the barrier height disorder reached its maximum value. The effect of different shapes of barrier fluctuations has been studied either numerically in the case of local barrier enhancements or from two analytical models adapted to local barrier lowering and current crowding in the active layer of the diode. In the former case, which happens when fixed repulsive charges are close to the interface like evidenced in metal-ZrO<sub>2</sub>-diamond structures, the image force effect is the only relevant one as far as current-voltage characteristics are concerned. In the case of random patches comprising a smaller barrier than the ideal homogeneous one, it has been shown that barrier inhomogeneities can be characterized by several parameters related to their amplitude, density, and to the presence or absence of both the pinch-off effect in these lowered barrier patches and current crowding in narrowed channels of the depletion zone. Mixing two of the last effects turns out to be necessary to quantitatively explain the curvature of current-voltage characteristics of unannealed interfaces in a semi-logarithmic plot. The ideal homogeneous barrier is the truly representative physical quantity of the interface because it is free from the local and random inhomogeneities which are responsible for the nonideality of the diodes. It has been inferred from matching previous models to electrical data. Rules and uncertainties have been derived for a confident evaluation of this fundamental quantity. All other parameters have been extracted in turn from the comparison of the non ideal behaviors with the quantitative predictions of the models. Main conclusions were the strong reduction of both the barrier inhomogeneities and homogeneous barrier of 1.4 eV after annealing interfaces at 450 °C. Because of the known inhomogeneity of the oxygen terminations and enhancement of the electron affinity by also 1.4 eV on the initial oxygenated diamond surface, these facts strongly suggested that original oxygen terminations vanished after such an annealing and are replaced by stronger bonds between carbon and atoms of the Zirconium oxide interlayer. Then, the more general issue of barrier height determination and Fermi level pinning has been addressed by means of an analysis of the experimental data collected in the present work and in recent literature, reassessed with the help of the methods presented before when necessary. The same evolution of barrier heights for four other metals after annealing confirms the disappearance of oxygen terminations, irrespective of the presence of an oxide interlayer, and the electron affinity of the diamond surfaces as a relevant quantity for barrier height description. For the whole set of metals in contact with either unannealed or annealed oxygenated surfaces, or hydrogenated surfaces, a rough but clear alignment of barrier heights along the Mott-Schottky straight line, with a unity slope, really emerged regarding the difference between the

ionization energy of diamond surfaces and metal work function. However, for each particular interface, the behavior at a smaller scale appeared different. In the case of annealed oxygenated interfaces, the slope turns out to be slightly negative, a result incompatible with the “interface induced gap states” model which assumes these states as invariant from one metal to another. On the contrary, the bond-polarization scheme, which relies on the interface dipole strength, itself dependent of the molecular orbitals involved in the bonds across the interface, may justify the slopes both at a global level and for a particular surface. All these concerns have been presented and discussed with the help of new experimental results, improved models and recent high quality experimental works in the purpose of fostering new advances in understanding the old problem of potential barrier at metal-covalent semiconductor interfaces.

## ACKNOWLEDGMENTS

Part of this work was made possible through grants from the Spanish Ministry of Economy and Competitiveness (ref: TEC2014-54357-C2-2-R, HiVolt-nano project) and from the European H2020 Program (ref: SEP-210184415, Green Diamond project). The authors also wish to thank “Ministerio de Ciencia e Innovación” for the grants BES-2010-039524 and EEBB-I-13-07696 of the project TEC2009-11399 and Bruno Fernandez for his technical assistance in the Nanofab facilities.

- <sup>1</sup>P.-N. Volpe, J. Pernot, P. Muret, and F. Omnès, *Appl. Phys. Lett.* **94**, 092102 (2009).
- <sup>2</sup>P.-N. Volpe, P. Muret, J. Pernot, F. Omnès, T. Teraji, Y. Koide, F. Jomard, D. Planson, P. Brosselard, N. Dheilily, B. Vergne, and S. Schamholz, *Appl. Phys. Lett.* **97**, 223501 (2010).
- <sup>3</sup>A. Vescan, I. Daumiller, P. Gluche, W. Ebert, and E. Kohn, *Diamond Relat. Mater.* **7**, 581 (1998).
- <sup>4</sup>P. Muret, F. Pruvost, C. Saby, E. Lucazeau, T. N. Tan, E. Gheeraert, and A. Deneuve, *Diamond Relat. Mater.* **8**, 961 (1999).
- <sup>5</sup>M. Liao, J. Alvarez, and Y. Koide, *Jpn. J. Appl. Phys., Part 1* **44**, 7832 (2005).
- <sup>6</sup>M. Craciun, C. Saby, P. Muret, and A. Deneuve, in *Carbon Materials for Active Electronics: Proceedings of Symposium L, E-MRS Spring Meeting, 2003* [Diamond Relat. Mater. **13**, 292 (2004)].
- <sup>7</sup>C. Saby, P. Muret, F. Pruvost, and G. Patrat, *Diamond Relat. Mater.* **11**, 1332 (2002).
- <sup>8</sup>D. A. Evans, O. R. Roberts, G. T. Williams, A. R. Vearey-Roberts, F. Bain, S. Evans, D. P. Langstaff, and D. J. Twitchen, *J. Phys.: Condens. Matter* **21**, 364223 (2009).
- <sup>9</sup>T. Teraji, Y. Garino, Y. Koide, and T. Ito, *J. Appl. Phys.* **105**, 126109 (2009).
- <sup>10</sup>P. K. Baumann and R. J. Nemanich, *J. Appl. Phys.* **83**, 2072 (1998).
- <sup>11</sup>H. Kawarada, *Surf. Sci. Rep.* **26**, 205 (1996).
- <sup>12</sup>M. Aoki and H. Kawarada, *Jpn. J. Appl. Phys., Part 2* **33**, L708 (1994).
- <sup>13</sup>J. Alvarez, F. Houzé, J. Kleider, M. Liao, and Y. Koide, in *proceedings of the E-MRS 2006 Symposium S: Material Science and Technology of Wide Bandgap Semiconductors 2006, Spring Meeting of the European Materials Research Society* [Superlattices Microstruct. **40**, 343 (2006)].
- <sup>14</sup>A. Daicho, T. Saito, S. Kurihara, A. Hiraiwa, and H. Kawarada, *J. Appl. Phys.* **115**, 223711 (2014).
- <sup>15</sup>H. Kawarada, H. Tsuboi, T. Naruo, T. Yamada, D. Xu, A. Daicho, T. Saito, and A. Hiraiwa, *Appl. Phys. Lett.* **105**, 013510 (2014).
- <sup>16</sup>K. Tsugawa, H. Noda, K. Hirose, and H. Kawarada, *Phys. Rev. B* **81**, 045303 (2010).

- <sup>17</sup>K. Ikeda, H. Umezawa, K. Ramanujam, and S. ichi Shikata, *Appl. Phys. Express* **2**, 011202 (2009).
- <sup>18</sup>T. Teraji, Y. Koide, and T. Ito, *Phys. Status Solidi (RRL)* **3**, 211 (2009).
- <sup>19</sup>A. Traoré, P. Muret, A. Fiori, D. Eon, E. Gheeraert, and J. Pernot, *Appl. Phys. Lett.* **104**, 052105 (2014).
- <sup>20</sup>R. T. Tung, *Appl. Phys. Rev.* **1**, 011304 (2014).
- <sup>21</sup>J.-C. Arnault (unpublished).
- <sup>22</sup>E. H. Rhoderick, *J. Phys. D: Appl. Phys.* **5**, 1920 (1972).
- <sup>23</sup>E. H. Rhoderick and R. H. Williams, *Metal-Semiconductor Contacts*, 2nd ed. (Clarendon Press, Oxford, 1988).
- <sup>24</sup>W. Mönch, *Electronic Properties of Semiconductor Interfaces*, Surface Sciences (Springer-Verlag, Berlin, Heidelberg, 2004).
- <sup>25</sup>C. R. Crowell and M. Beguwal, *Solid-State Electron.* **14**, 1149 (1971).
- <sup>26</sup>H. Card and E. Rhoderick, *J. Phys. D: Appl. Phys.* **4**, 1589 (1971).
- <sup>27</sup>J. Andrews and M. Lepselter, *Solid-State Electron.* **13**, 1011 (1970).
- <sup>28</sup>S. Ohmagari, T. Teraji, and Y. Koide, *J. Appl. Phys.* **110**, 056105 (2011).
- <sup>29</sup>J. H. Werner and H. H. Güttler, *J. Appl. Phys.* **69**, 1522 (1991).
- <sup>30</sup>R. T. Tung, *Phys. Rev. B* **45**, 13509 (1992).
- <sup>31</sup>R. T. Tung, *Mater. Sci. Eng. R* **35**, 1 (2001).
- <sup>32</sup>P. M. Gammon, A. Pérez-Tomás, V. A. Shah, O. Vavasour, E. Donchev, J. S. Pang, M. Myronov, C. A. Fisher, M. R. Jennings, D. R. Leadley, and P. A. Mawby, *J. Appl. Phys.* **114**, 223704 (2013).
- <sup>33</sup>J. Ristein, M. Riedel, and L. Ley, *J. Electrochem. Soc.* **151**, E315 (2004).
- <sup>34</sup>F. Klauser, S. Ghodbane, R. Boukherroub, S. Szunerits, D. Steinmüller-Nethl, E. Bertel, and N. Memmel, *Diamond Relat. Mater.* **19**, 474 (2010).
- <sup>35</sup>S. Ghodbane, D. Ballutaud, F. Omnès, and C. Agnès, *Diamond Relat. Mater.* **19**, 630 (2010).
- <sup>36</sup>S. J. Sque, R. Jones, and P. R. Briddon, *Phys. Rev. B* **73**, 085313 (2006).
- <sup>37</sup>H. Notsu, I. Yagi, T. Tatsuma, D. A. Tryk, and A. Fujishima, *J. Electroanal. Chem.* **492**, 31 (2000).
- <sup>38</sup>C. K. Fink and S. J. Jenkins, *J. Phys.: Condens. Matt.* **21**, 264010 (2009).
- <sup>39</sup>J. Robertson and M. Rutter, *Diamond Relat. Mater.* **7**, 620 (1998).
- <sup>40</sup>P. Muret and C. Saby, *Semicond. Sci. Technol.* **19**, 1 (2004); A typographic error in Table II of this reference must be corrected by changing the minus sign into plus sign in each of the three last columns at the last line which recapitulates the electron affinities, only that of the hydrogenated surface being really negative.
- <sup>41</sup>H. Siringhaus, T. Meyer, E. Y. Lee, and H. von Känel, *Phys. Rev. B* **53**, 15944 (1996).
- <sup>42</sup>P. R. Muret, *J. Vac. Sci. Technol. B* **32**, 03D114 (2014).
- <sup>43</sup>H. B. Michaelson, *J. Appl. Phys.* **48**, 4729 (1977).
- <sup>44</sup>S. Jain and W. E. Dahlke, *Solid-State Electron.* **29**, 597 (1986).
- <sup>45</sup>S. Collins, D. Lowe, and J. R. Barker, *J. Phys. C: Solid State Phys.* **20**, 6233 (1987).
- <sup>46</sup>R. H. Cox and H. Strack, *Solid-State Electron.* **10**, 1213 (1967).
- <sup>47</sup>D. Defives, O. Noblanc, C. Dua, C. Brylinski, M. Barthula, and F. Meyer, *Mater. Sci. Eng. B* **61–62**, 395 (1999).
- <sup>48</sup>P. Muret, D. Eon, A. Traoré, A. Maréchal, J. Pernot, and E. Gheeraert, *Physica Status Solidi A* **212**(11), 2501 (2015).
- <sup>49</sup>N. F. Mott, *Proc. R. Soc. London, Ser. A* **171**, 27 (1939).
- <sup>50</sup>W. Schottky, *Z. Phys.* **113**, 367 (1939).
- <sup>51</sup>J. Tersoff, *Phys. Rev. Lett.* **52**, 465 (1984).
- <sup>52</sup>S. Koné, G. Civrac, H. Schneider, K. Isoird, R. Issaoui, J. Achard, and A. Gicquel, in *Proceedings of Diamond 2009, The 20th European Conference on Diamond, Diamond-Like Materials, Carbon Nanotubes and Nitrides, Part 2* [Diamond Relat. Mater. **19**, 792 (2010)].
- <sup>53</sup>H. Umezawa, M. Nagase, Y. Kato, and S. I. Shikata, *Diamond Relat. Mater.* **24**, 201 (2012).
- <sup>54</sup>A. Nawawi, K. Tseng, Rusli, G. Amaratunga, H. Umezawa, and S. Shikata, *Diamond Relat. Mater.* **35**, 1 (2013).
- <sup>55</sup>K. Ueda, K. Kawamoto, T. Soumiya, and H. Asano, *Diamond Relat. Mater.* **38**, 41 (2013).
- <sup>56</sup>K. Ueda, K. Kawamoto, and H. Asano, *Jpn. J. Appl. Phys., Part 1* **53**, 04EP05 (2014).
- <sup>57</sup>J. Ristein, F. Maier, M. Riedel, J. Cui, and L. Ley, *Phys. Status Solidi A* **181**, 65 (2000).
- <sup>58</sup>R. T. Tung, *Phys. Rev. Lett.* **84**, 6078 (2000).
- <sup>59</sup>R. T. Tung, *J. Vac. Sci. Technol. B* **11**, 1546 (1993).

## Energy-band diagram configuration of Al<sub>2</sub>O<sub>3</sub>/oxygen-terminated p-diamond metal-oxide-semiconductor

A. Maréchal,<sup>1,2,3,a)</sup> M. Aoukar,<sup>1,4</sup> C. Vallée,<sup>1,4</sup> C. Rivière,<sup>1,2</sup> D. Eon,<sup>1,2</sup> J. Pernot,<sup>1,2,5</sup> and E. Gheeraert<sup>1,2</sup>

<sup>1</sup>Univ. Grenoble Alpes, F-38000 Grenoble, France

<sup>2</sup>CNRS, Inst. NEEL, F-38000 Grenoble, France

<sup>3</sup>CNRS, G2Elab, F-38000 Grenoble, France

<sup>4</sup>CNRS, LTM, F-38000 Grenoble, France

<sup>5</sup>Institut Universitaire de France, 103 Boulevard Saint Michel, 75005 Paris, France

(Received 12 May 2015; accepted 6 September 2015; published online 5 October 2015)

Diamond metal-oxide-semiconductor capacitors were prepared using atomic layer deposition at 250 °C of Al<sub>2</sub>O<sub>3</sub> on oxygen-terminated boron doped (001) diamond. Their electrical properties were investigated in terms of capacitance and current versus voltage measurements. Performing X-ray photoelectron spectroscopy based on the measured core level energies and valence band maxima, the interfacial energy band diagram configuration of the Al<sub>2</sub>O<sub>3</sub>/O-diamond is established. The band diagram alignment is concluded to be of type I with valence band offset  $\Delta E_v$  of  $1.34 \pm 0.2$  eV and conduction band offset  $\Delta E_c$  of  $0.56 \pm 0.2$  eV considering an Al<sub>2</sub>O<sub>3</sub> energy band gap of 7.4 eV. The agreement with electrical measurement and the ability to perform a MOS transistor are discussed. © 2015 AIP Publishing LLC. [<http://dx.doi.org/10.1063/1.4931123>]

Recent achievements in diamond device processing have made possible the development of bipolar junction transistor,<sup>1</sup> junction field effect transistor<sup>2</sup> using selectively grown n<sup>+</sup>-type diamond, p-i-n junction for power switch device applications,<sup>3</sup> and Schottky diodes showing power figure of merit of 244 MW cm<sup>-2</sup>.<sup>4</sup> In the view of developing high performance metal-oxide-diamond field effect transistor (diamond MOSFET), recent reports present the study of diamond based metal-oxide-semiconductor capacitors (MOSCAP) on hydrogen-terminated diamond (H-diamond) using various oxides and deposition techniques.<sup>5-7</sup> The electrical characterizations of these devices, i.e., current-voltage I(V) and capacitance-voltage C(V) measurements, showed low leakage current values and small interface states density. The good electrical properties, in terms of low leakage current densities, rely on the band configuration of the dielectric/H-diamond interface which shows large valence band offsets (2.9 eV for the Al<sub>2</sub>O<sub>3</sub>/H-diamond structure),<sup>8</sup> suitable for developing p-channels MOSFET as demonstrated by normally off operation of the H-diamond MOSFET of Liu *et al.*<sup>9</sup> For such transistors, the off-state will be ensured by the channel depletion. Another way to develop diamond MOSFET is the approach of an inversion n-channel (p-channel) into a p-type (n-type) diamond region separating two electrons (holes) reservoirs where the presence of p-n junctions ensures the off-state. In that case, among all the challenging developments required is the development of the MOS gate showing band offsets, high enough to prevent carriers injection from the channel to the gate metal. Thus, various oxides deposited on oxygen-terminated boron doped diamond (O-diamond) are under study. Recently, the authors of Ref. 10 demonstrated the operation of a diamond MOSCAP using a 118 nm thick Ta<sub>2</sub>O<sub>5</sub> dielectric layer deposited on (001) p-type O-diamond. The effect of oxide annealing on the

device electrical properties was studied. In particular, the authors qualitatively showed that the leakage current conduction was mainly governed by thermionic field emission at relatively low applied bias voltage and tunneling processes at high applied bias voltage. The observed leakage currents density could be attributed to the Ta<sub>2</sub>O<sub>5</sub> band gap of 4.4 eV (Ref. 11) which could result in low or inexistent barrier for holes at the Ta<sub>2</sub>O<sub>5</sub>/O-diamond interface. In the case of our previous work,<sup>12</sup> some of us studied low temperature atomic layer deposition (ALD)-Al<sub>2</sub>O<sub>3</sub> on boron doped O-diamond and observed high leakage currents densities. The leakage current characteristics showed the same tendencies than the ones reported in Ref. 10. We proposed theoretical band diagrams for the Al<sub>2</sub>O<sub>3</sub>/O-diamond capacitor and discussed about the effect of the low barrier height for holes. In the present work, we developed a MOS architecture and investigated its electrical properties. Leakage currents are still observed for negative bias voltage. Therefore, in order to demonstrate the presence of a barrier for holes at the Al<sub>2</sub>O<sub>3</sub>/O-diamond interface, we performed X-ray Photoelectron Spectroscopy (XPS). By performing XPS on three different samples, the Al<sub>2</sub>O<sub>3</sub>/O-diamond energy band diagram is established and discussed in terms of MOSFET fabrication.

The MOSCAP is a stack of a heavily (p<sup>++</sup>-type layer) and a lightly (p-type layer) boron-doped homoepitaxial diamond layer grown using a microwave plasma assisted chemical vapor deposition (MPCVD) NIRIM type reactor on a 3 × 3 mm<sup>2</sup> Ib high pressure high temperature (HPHT) (001) diamond substrate. The 470 nm thick heavily boron doped diamond layer was grown using a recipe described elsewhere.<sup>4</sup> On top of this layer, a lightly boron doped layer was grown using a gas mixture of methane ([CH<sub>4</sub>]/[H<sub>2</sub>] = 1%), diborane ([B]/[C] = 600 ppm), oxygen ([O<sub>2</sub>]/[H<sub>2</sub>] = 0.25%), and hydrogen at a pressure of 33 Torr and a temperature of 910 °C. Oxygen was used in the gas phase in order to increase the crystalline quality of the layer.<sup>13</sup> The p-type

<sup>a)</sup>Electronic mail: aurelien.marechal@neel.cnrs.fr

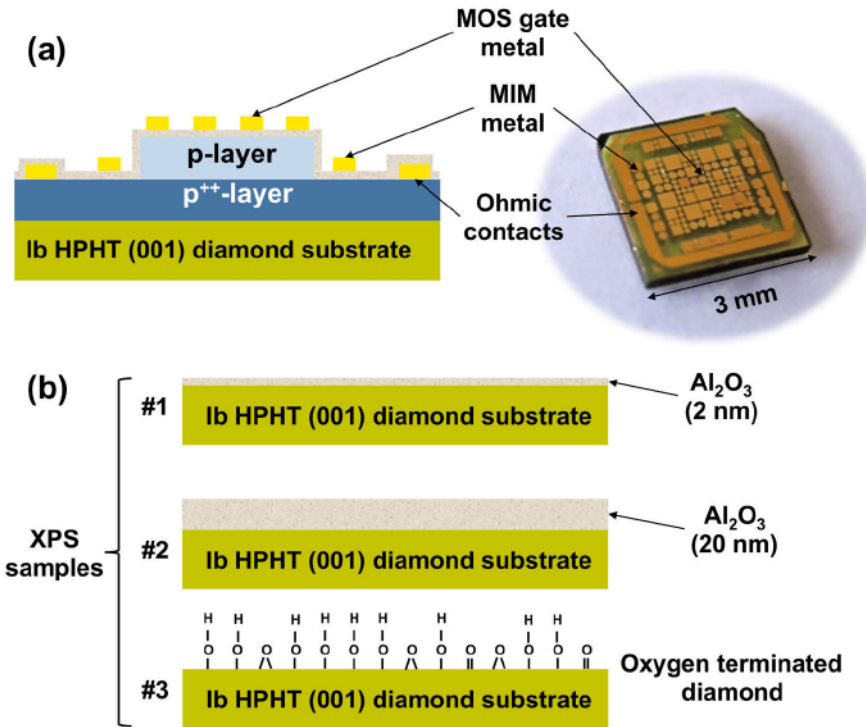


FIG. 1. (a) Schematic cross section (left) and picture of the  $\text{Al}_2\text{O}_3/\text{O}$ -diamond MOS device (right), showing the MIM, MOS and ohmic contacts, respectively. (b) Schematic cross section of the samples prepared for the XPS analysis.

layer thickness was measured by spectroscopic ellipsometry to be 590 nm. Previous to the deposition of the ohmic contacts, a mesa structure was defined using an  $\text{O}_2$  plasma inductively coupled plasma (ICP) etching process. The ohmic contacts were defined by laser lithography (Heidelberg DWL66FS) and electron beam (ebeam) evaporation of Ti/Pt/Au (30/50/40 nm) followed by standard liftoff technique. Vacuum Ultra Violet (VUV) light/ozone treatment<sup>14</sup> was performed achieving oxygen termination of the diamond surface (O-diamond) before oxide deposition. The oxide layer was deposited by ALD at 250 °C using a Savannah 100 deposition system from Cambridge NanoTech. The precursor was Trimethylaluminium (TMA), and water as oxidant. The pulse and exposure duration were 30 s and 15 ms, respectively, with typical base pressure of  $1.3 \times 10^{-1}$  Torr. TEM investigations recently revealed that the 100 °C ALD- $\text{Al}_2\text{O}_3$  layer was amorphous.<sup>15</sup> Here, the growth temperature was increased to increase the dielectric layer quality. However, the dielectric layer is supposedly amorphous. Moreover, further studies are needed to quantify the dielectric layer quality as a function of the growth temperature. The oxide thickness was measured by spectroscopic ellipsometry to be 20 nm. The MOSCAP and metal-insulator-metal capacitor (MIMCAP) contacts with various geometry were defined by laser lithography followed by ebeam evaporation of Ti/Pt/Au (30/50/40 nm) metal electrode. This structure offers the advantage of having both MIMCAPs and MOSCAPs on the same sample as shown in Fig. 1(a). As shown in the cross section, the oxide was also deposited on the peripheral ohmic contact. Even though, it did not influence the properties of the device, since the oxide below the tips transformed in a short circuit after the first voltage biasing. The electrical properties of the  $\text{Al}_2\text{O}_3/\text{O}$ -diamond MIM and MOSCAPS were investigated using a

Agilent E4980A Precision LCR Meter and a Keithley 6517B source-electrometer.

Fig. 2(a) represents the  $C(V)$  properties of a circular  $\text{Al}_2\text{O}_3/\text{O}$ -diamond MOSCAP with a 150  $\mu\text{m}$  diameter measured at room temperature. The frequency of the ac signal was varied from 1 kHz to 1 MHz with an amplitude of 50 mV biasing the structure from accumulation to deep depletion. No frequency dependence of the accumulation capacitance was observed in this frequency range. This results from the presence of the  $\text{p}^{++}$ -type layer which lowers the series resistance. In the case of high series resistance, the accumulation capacitance shows strong dependence with the ac signal frequency.<sup>12,16–18</sup> In Fig. 2(a), the 1 kHz curve (black squares) shows a plateau at  $-5$  V, which is probably

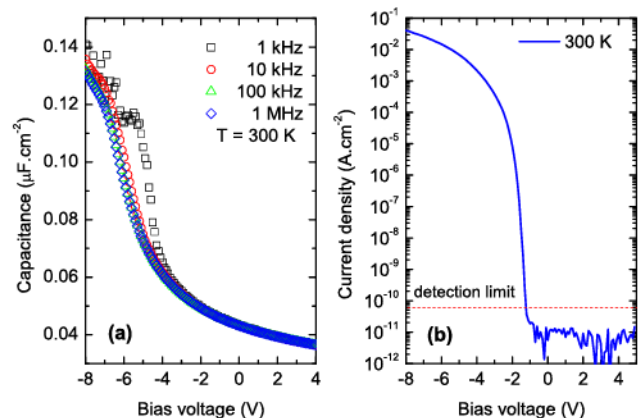


FIG. 2. (a)  $C(V)$  characteristic of the  $\text{Al}_2\text{O}_3/\text{O}$ -diamond capacitor measured from 1 kHz to 1 MHz. In this range, the frequency has no influence on the capacitance measured at  $-8$  V. (b)  $J(V)$  characteristic of the MOS device. In the depletion and deep depletion regimes, the current density is below the detection limit.

due to the interface states response to the ac signal. Moreover, hysteresis was observed (not shown here) when biasing the structure from accumulation to deep depletion and coming back to accumulation, signature of the presence of mobile charges in the dielectric layer. In addition, the analysis of the MIMCAP revealed that the oxide relative dielectric constant was close to 9. However, this value was found unreasonably low (of the order of 3) for the MOSCAP. Spectroscopic impedance<sup>16</sup> studies are undergoing to assess these issues. The doping level of the p-type diamond layer was extracted from the  $1/C^2(V)$  curve and measured to be  $4 \times 10^{17} \text{ cm}^{-3}$ .

Fig. 2(b) presents the current density vs voltage  $J(V)$  characteristics of the MOSCAP measured at room temperature. When a negative bias voltage is applied to the MOS contact, holes are accumulated in the diamond layer underneath the dielectric. Thus, if the dielectric is not perfect and the valence band offset at the  $\text{Al}_2\text{O}_3/\text{O-diamond}$  interface is not high enough, holes can leak from diamond to the metal electrode through the  $\text{Al}_2\text{O}_3$  layer. For the present MOSCAP, the leakage current density can be as high as  $7 \times 10^{-3} \text{ A cm}^{-2}$  at room temperature and  $-5 \text{ V}$ . As the bias voltage is increased towards the positive values, a space charge region (SCR) develops and the MOSCAP reaches the depletion and deep depletion working regime. This SCR prevents from leakage currents. As a result, the current density is below the detection limit. This behavior was not observed in recent works.<sup>12,18</sup> High leakage currents density observed in the deep depletion regime results in unreliable capacitance measurements (capacitance increase versus bias voltage) which could be misinterpreted and wrongly assigned to an inversion signature.<sup>18</sup> In the present work, the accumulation regime leakage currents have been identified to be mainly due to tunneling mechanisms of holes through the dielectric layer and will be the subject of our upcoming work. In order to determine if the measured leakage current is originating from a small or absent barrier for holes at the  $\text{Al}_2\text{O}_3/\text{O-diamond}$  interface, XPS measurements were performed on ALD- $\text{Al}_2\text{O}_3$  films deposited at  $250^\circ\text{C}$  on O-diamond (001) substrates using a Thermo Scientific Theta 300 spectrometer. Three samples were prepared as shown in Fig. 1(b), with  $\text{Al}_2\text{O}_3$  layer deposited using the experimental conditions and setup as described above. First, a 2 nm thin  $\text{Al}_2\text{O}_3$  film was deposited, allowing to identify the binding state between the O-diamond surface and the  $\text{Al}_2\text{O}_3$  layer. A second sample with a 20 nm thick  $\text{Al}_2\text{O}_3$  layer was deposited in the same conditions as the first one was prepared, as a calibration for the bulk binding state of the Al atoms. Finally, an O-diamond sample was prepared. This sample allowed to determine the binding energy of the C surface atoms. In Fig. 1(b), the surface terminations are also represented and mainly correspond to hydroxyl species as discussed in Ref. 19. The experiments were carried out using a high resolution monochromatic  $\text{Al K}\alpha$  ( $h\nu = 1486.68 \text{ eV}$ ) X-ray source. The core level spectra were recorded using a  $0.05 \text{ eV}$  step and a  $55 \text{ eV}$  pass energy as described in Ref. 5. The peak contributions were extracted by combining a Lorentzian and a Gaussian function. The background was subtracted using Shirley function.

On XPS spectra, the zero energy is usually at the Fermi level. Nevertheless, charge effect and surface contamination can compromise its position. The approach defended here is to use core level on three samples in order to determine the valence band offset between  $\text{Al}_2\text{O}_3$  and O-diamond. First, considering the mean free path of photoelectron in a material ( $\sim 2 \text{ nm}$ ), a 20 nm  $\text{Al}_2\text{O}_3$  layer serves as to determine the energy core level ( $E_{\text{CL}}$ ) for bulk  $\text{Al}_2\text{O}_3$ . The same approach is used for O-diamond. At last, with a 2 nm thick  $\text{Al}_2\text{O}_3$  layer, XPS measurement is sensitive to diamond and  $\text{Al}_2\text{O}_3$ . This sample allows to determine the valence band offset. On 2 nm thick  $\text{Al}_2\text{O}_3$ , C 1s spectrum shows clearly different peak contributions (see Fig. 3(e)). C-Al contribution is the one which is representative of the interface. The valence band discontinuity at the  $\text{Al}_2\text{O}_3/\text{O-diamond}$  interface is calculated using the following formula:<sup>20</sup>

$$\Delta E_v = (E_{\text{CL}} - E_{\text{VBM}})_{\text{O-diamond}} - (E_{\text{CL}} - E_{\text{VBM}})_{\text{Al}_2\text{O}_3} - \Delta E_{\text{CL}}, \quad (1)$$

where  $(E_{\text{CL}} - E_{\text{VBM}})_{\text{O-diamond}}$  is the difference in binding energy between the C 1s core level and the valence band maximum (VBM) of the O-diamond,  $(E_{\text{CL}} - E_{\text{VBM}})_{\text{Al}_2\text{O}_3}$  is the difference in binding energy between the Al  $2p_{3/2}$  and VBM of the 20 nm thick  $\text{Al}_2\text{O}_3$  film, and  $\Delta E_{\text{CL}}$  is the difference in binding energy between the Al  $2p_{3/2}$  and C 1s core level for the 2 nm thick  $\text{Al}_2\text{O}_3$  film. Fig. 3(a) shows the valence band spectrum of the 20 nm thick  $\text{Al}_2\text{O}_3$  layer. The VBM is extracted by extrapolating the linear fit to the abscissa axis. The inset represents the difference in energy between the Al  $2p_{3/2}$  and VBM  $(E_{\text{CL}} - E_{\text{VBM}})_{\text{Al}_2\text{O}_3}$ . The O-diamond valence band spectrum is shown in Fig. 3(c). The VBM are  $3.20 \pm 0.2 \text{ eV}$  and  $2.07 \pm 0.2 \text{ eV}$  for  $\text{Al}_2\text{O}_3$  and O-diamond, respectively. When the  $\text{Al}_2\text{O}_3$  is brought in contact with the O-diamond sample, a valence band discontinuity appears at the interface, as represented by  $\Delta E_p$  in Fig. 3(b). Fig. 3(d) shows the Al  $2p$  spectrum of the 20 nm thick  $\text{Al}_2\text{O}_3$ . The Al-O binding energy is extracted as being  $74.35 \pm 0.2 \text{ eV}$ . The 2 nm thin  $\text{Al}_2\text{O}_3$  C 1s spectrum allows to determine a C-Al binding energy of  $284.08 \pm 0.2 \text{ eV}$  as indicated by Fig. 3(e). Finally, the C 1s spectrum of the O-diamond sample allows to determine the core level binding energy of the C-C bonds, determined to be  $284.32 \pm 0.2 \text{ eV}$  (see Fig. 3(f)). In this figure, the  $\text{CH}_x$ , C-O-C, and C=O components can be identified with respective binding energies of  $284.93 \pm 0.2 \text{ eV}$ ,  $285.90 \pm 0.2 \text{ eV}$ , and  $287.20 \pm 0.2 \text{ eV}$  in good agreement with reported values.<sup>8,21</sup> Table I summarizes the C 1s, Al  $2p_{3/2}$ , and O 1s binding energies (eV) of the core level spectra for the O-terminated diamond, the 20 nm  $\text{Al}_2\text{O}_3$  and 2 nm  $\text{Al}_2\text{O}_3$  samples. Using Eq. (1) and the values reported in Table I, the valence band offset was calculated to be  $1.34 \text{ eV}$ . Taking into account the  $\text{Al}_2\text{O}_3$  band gap of  $7.4 \text{ eV}$ ,<sup>22</sup> the energy band diagram of the  $\text{Al}_2\text{O}_3/\text{O-diamond}$  interface can be established as shown in Fig. 4. This diagram clearly demonstrates a type I band alignment and the presence of a barrier for holes of  $1.34 \pm 0.2 \text{ eV}$ . The conduction band discontinuity is calculated to be  $0.56 \pm 0.2 \text{ eV}$  when considering an  $\text{Al}_2\text{O}_3$  energy band gap of  $7.4 \text{ eV}$ . Obviously, lower values could be found if the dielectric band gap would be smaller. The measured

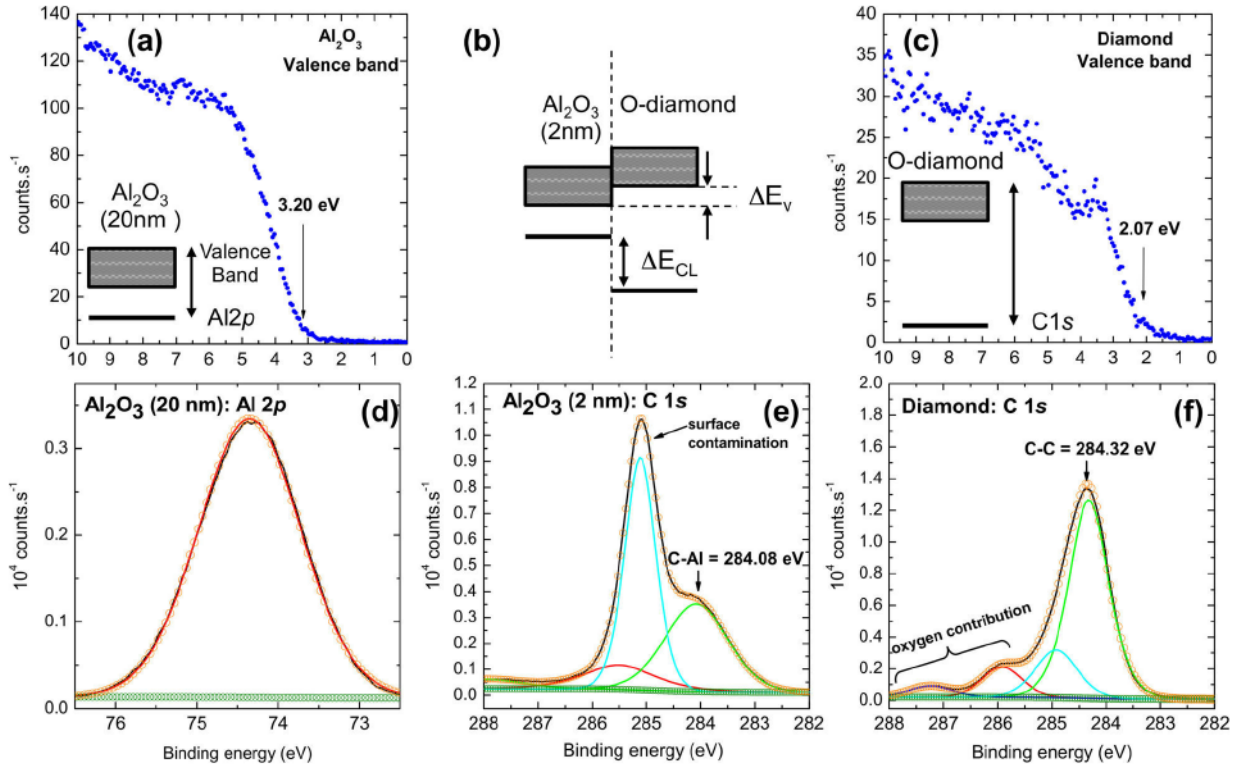


FIG. 3. (a) 20 nm thick  $\text{Al}_2\text{O}_3$  valence band spectra. The inset represents the Al 2p core level and the valence band of the dielectric layer. (b) When the 2 nm thin  $\text{Al}_2\text{O}_3$  is put in contact with the O-diamond surface, the valence band discontinuity  $\Delta E_v$  appears. The difference in energy between the two core levels is indicated. (c) O-diamond valence band spectra and the representation of the C 1s core level together with the valence band of O-diamond. (d) XPS spectrum of the 20 nm thick  $\text{Al}_2\text{O}_3$  layer corresponding to the Al 2p core level. (e) and (f) show the C 1s binding energies for the 2 nm  $\text{Al}_2\text{O}_3$  layer and O-diamond, respectively.

$\Delta E_v$  alone is not enough to explain the observed leakage currents. A model for the tunneling of holes between the semi-conducting diamond and the metal gate electrode, including the temperature dependence of the leakage current will be discussed in a future work. In conclusion,  $\text{Al}_2\text{O}_3/\text{O}$ -diamond MOS could be suitable for the development of normally off p-channel MOSFET, since confinement of holes at the interface could be realized by increasing the  $\text{Al}_2\text{O}_3$  layer thickness and quality. The lower  $\Delta E_v = 1.34 \pm 0.2$  eV in case of  $\text{Al}_2\text{O}_3/\text{O}$ -diamond than in case of  $\text{Al}_2\text{O}_3/\text{H}$ -diamond interface ( $\Delta E_v = 2.9 \pm 0.2$  eV)<sup>8</sup> was expected, even if a rigid application of the electron affinity  $\chi$  difference leads to a value of  $\Delta E_v = 0.8$  eV. At the opposite, n-type channel will

result in a too small barrier ( $\Delta E_c = 0.56 \pm 0.2$  eV) between the conduction bands of  $\text{Al}_2\text{O}_3$  and O-diamond, if assuming an energy band gap of  $E_g^{\text{Al}_2\text{O}_3} = 7.4$  eV.<sup>22</sup>

In summary, MOSCAP were fabricated on oxygen-terminated boron doped (001) diamond using 250 °C atomic

TABLE I. C 1s, Al 2p<sub>3/2</sub>, and O 1s binding energies (eV) of the core level spectra for the O-terminated diamond, the 20 nm  $\text{Al}_2\text{O}_3$  and 2 nm  $\text{Al}_2\text{O}_3$  samples. The valence band maxima (VBM) were recorded for the O-terminated diamond and the 20 nm thick  $\text{Al}_2\text{O}_3$  layer. The energy origin is taken at the Fermi level position.

		O-diamond	$\text{Al}_2\text{O}_3$ (2 nm)	$\text{Al}_2\text{O}_3$ (20 nm)
C 1s (eV)	C-C	284.32		284.2
	CH <sub>x</sub>	284.93		
	C-Al		284.08	
	C-O-C	285.90		
	C=O	287.20		
Al 2p <sub>3/2</sub> (eV)	Al-O		74.32	74.35
O 1s (eV)		530.60	530.46	530.69
VBM (eV)		2.07		3.20

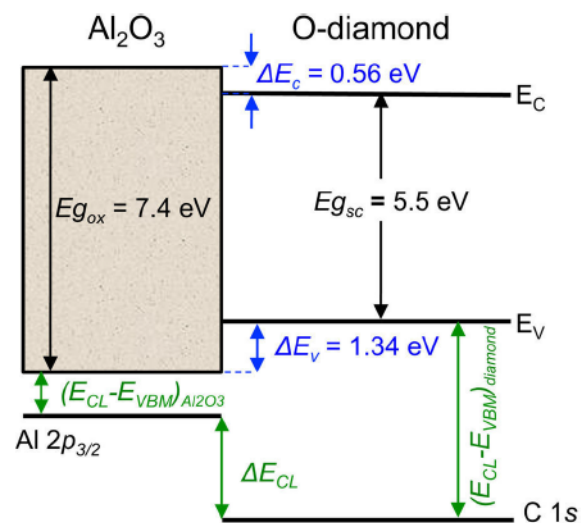


FIG. 4. Energy band diagram of the  $\text{Al}_2\text{O}_3/\text{O}$ -diamond heterostructure. The valence and conduction band offsets are represented. Also indicated are the differences in energy between core levels and valence band maxima for  $\text{Al}_2\text{O}_3$  and O-diamond as well as the difference in core level energy  $\Delta E_{CL}$ .  $E_v$  and  $E_c$  stand for valence band maximum and conduction band minimum, respectively.

layer deposition of Al<sub>2</sub>O<sub>3</sub>. Performing XPS measurements allowed to determine the valence band offset  $\Delta E_v$  between Al<sub>2</sub>O<sub>3</sub> and O-diamond of  $1.34 \pm 0.2$  eV, thus enabling to reconstruct the Al<sub>2</sub>O<sub>3</sub>/O-diamond energy band diagram. The band configuration is of type I as compared to the Al<sub>2</sub>O<sub>3</sub>/H-diamond which is of type II.<sup>8</sup> Thus, the Al<sub>2</sub>O<sub>3</sub>/O-diamond MOS could be suitable as a gate for the next generation inversion MOSFET.

This work was supported by French state funds ANR-10-LABX-51-01 (Labex LANEF du Programme d'Investissements d'Avenir). The authors thank L. Cagnon (Institut Néel, CNRS, Grenoble) for his expertise on the ALD system, the Nanofab technical staff (Nanofab, Institut Néel, CNRS, Grenoble), and P. Giroux (Institut Néel, CNRS, Grenoble) for the technical support on CVD growth systems.

- <sup>1</sup>H. Kato, T. Makino, M. Ogura, D. Takeuchi, and S. Yamasaki, *Diamond Relat. Mater.* **34**, 41 (2013).  
<sup>2</sup>T. Iwasaki, Y. Hoshino, K. Tsuzuki, H. Kato, T. Makino, M. Ogura, D. Takeuchi, T. Matsumoto, H. Okushi, S. Yamasaki, and M. Hatano, *Appl. Phys. Express* **5**, 091301 (2012).  
<sup>3</sup>D. Takeuchi, S. Koizumi, T. Makino, H. Kato, M. Ogura, H. Ohashi, H. Okushi, and S. Yamasaki, *Phys. Status Solidi A* **210**, 1961 (2013).  
<sup>4</sup>A. Traoré, P. Muret, A. Fiori, D. Eon, E. Gheeraert, and J. Pernot, *Appl. Phys. Lett.* **104**, 052105 (2014).  
<sup>5</sup>J. W. Liu, M. Y. Liao, M. Imura, H. Oosato, E. Watanabe, and Y. Koide, *Appl. Phys. Lett.* **102**, 112910 (2013).

- <sup>6</sup>J. W. Liu, M. Y. Liao, M. Imura, H. Oosato, E. Watanabe, A. Tanaka, H. Iwai, and Y. Koide, *J. Appl. Phys.* **114**, 084108 (2013).  
<sup>7</sup>J. Liu, M. Liao, M. Imura, A. Tanaka, H. Iwai, and Y. Koide, *Sci. Rep.* **4**, 6395 (2014).  
<sup>8</sup>J. W. Liu, M. Y. Liao, M. Imura, and Y. Koide, *Appl. Phys. Lett.* **101**, 252108 (2012).  
<sup>9</sup>J. W. Liu, M. Y. Liao, M. Imura, and Y. Koide, *Appl. Phys. Lett.* **103**, 092905 (2013).  
<sup>10</sup>S. Cheng, L. Sang, M. Liao, J. Liu, M. Imura, H. Li, and Y. Koide, *Appl. Phys. Lett.* **101**, 232907 (2012).  
<sup>11</sup>J. Robertson, *J. Vac. Sci. Technol A* **31**, 050821 (2013).  
<sup>12</sup>G. Chicot, A. Maréchal, R. Motte, P. Muret, E. Gheeraert, and J. Pernot, *Appl. Phys. Lett.* **102**, 242108 (2013).  
<sup>13</sup>F. Omnès, P. Muret, P.-N. Volpe, M. Wade, J. Pernot, and F. Jomard, *Diamond Relat. Mater.* **20**, 912 (2011).  
<sup>14</sup>T. Teraji, S. Koizumi, and Y. Koide, *J. Appl. Phys.* **104**, 016104 (2008).  
<sup>15</sup>J. C. Piñero, D. Araujo, A. Traoré, G. Chicot, A. Maréchal, P. Muret, M. P. Alegre, M. P. Villar, and J. Pernot, *Phys. Status Solidi A* **211**, 2367 (2014).  
<sup>16</sup>M. Liao, J. Liu, L. Sang, D. Coathup, J. Li, M. Imura, Y. Koide, and H. Ye, *Appl. Phys. Lett.* **106**, 083506 (2015).  
<sup>17</sup>K. K. Kovi, S. Majdi, M. Gabrysch, and J. Isberg, *Appl. Phys. Lett.* **105**, 202102 (2014).  
<sup>18</sup>K. K. Kovi, O. Vallin, S. Majdi, and J. Isberg, *IEEE Electron Device Lett.* **36**, 603 (2015).  
<sup>19</sup>R. Boukherroub, X. Wallart, S. Szunerits, B. Marcus, P. Bouvier, and M. Mermoux, *Electrochem. Commun.* **7**, 937 (2005).  
<sup>20</sup>E. A. Kraut, R. W. Grant, J. R. Waldrop, and S. P. Kowalczyk, *Phys. Rev. Lett.* **44**, 1620 (1980).  
<sup>21</sup>S. Ghodbane, D. Ballutaud, A. Deneuville, and C. Baron, *Phys. Status Solidi A* **203**, 3147 (2006).  
<sup>22</sup>H. J. Kim, S. Y. No, D. Eom, and C. S. Hwang, *J. Korean Phys. Soc.* **49**, 1271 (2006).

# Curriculum Vitae

Docteur Université Grenoble Alpes  
Semi-conducteurs à grand gap

# Aurélien MARECHAL

27 ans

## EXPERIENCES

### CNRS GRENOBLE

Institut Néel - G2Elab - UJF

2012 - 2015

#### ■ Chercheur : Transistors en diamant pour l'électronique de puissance

Modélisation des prototypes avec le logiciel Silvaco

- Implémentation des modèles propres au diamant
- Validation des modèles

Fabrication des prototypes

- Définition du cahier des charges des dispositifs visés
- Mise en pratique des procédés de fabrication en salle blanche : technique de croissance CVD, lithographie et gravure.

Tests et validations des prototypes

- Identification des paramètres clés liés aux composants
- Caractérisation électrique

Pilotage de projets

- Gestion du planning et des ressources
- Responsable d'équipements technologiques
- Responsable du suivi des échantillons dans le cadre de collaborations extérieures

Communication et veille technologique

- Recherche et identifications de solutions alternatives
- Valorisation des résultats : publications et conférences
- Rédaction de rapports et fiche techniques de protocoles expérimentaux

Encadrement et formation

- Expériences d'enseignement : école d'ingénieurs et IUT
- Formation et supervision de stagiaires

### CEA GRENOBLE

INAC - SPSMS

2012:6 mois

#### ■ Stage Master 2 : Contrôle cohérent de spin électronique unique dans des boîtes quantiques autoassemblées

Chargé de la caractérisation électrique de boîtes quantiques

- Maîtrise des outils de lithographie nanoélectronique
- Mesures électriques à très basse température

### CNRS GRENOBLE

Institut Néel - UJF

2011:3 mois

#### ■ Stage Master 1 : Développement de composants à effet de champ à base de diamant

Fabrication, tests et validations des prototypes



## FORMATION

**2015** : Doctorat Nanoélectronique et nanotechnologies, Grenoble.

**2012** : Master 2 Nanosciences, nanotechnologies, parcours recherche, spécialité Nanophysique, Nanostructures. Mention Bien. Université Joseph Fourier, Grenoble.

**2011** : Master 1 Sciences, Technologies, Santé, Majeure Physique. Mention Assez Bien. Université Joseph Fourier, Grenoble.

**2010** : Licence Sciences, Technologies, Santé, Mention Physique et sciences pour l'ingénieur. Université de Strasbourg.

**2008** : DUT Mesures Physiques, option Matériaux et contrôles physico-chimiques, Université de Savoie.

## COMPETENCES

Informatique : MS Office, OriginLab, Matlab, Nextnano, TCAD Silvaco, Latex.

Technologie salle blanche : CVD, lithographie, gravure plasma.

Anglais : courant

Italien : à réactiver

## LOISIRS

Escalade

Cyclisme

Moto

## CONTACT

6, rue Jean Moulin

38400 St Martin d'Hères

aur.marechal@gmail.com

06.82.71.23.20

## PUBLICATIONS

- 1- **A. Maréchal**, M. Aoukar, C. Vallée, C. Rivière, D. Eon, J. Pernot and E. Gheeraert, “*Energy-band diagram configuration of  $Al_2O_3$ /Oxygen-terminated p-diamond metal-oxide-semiconductor*”, Appl. Phys. Lett. (accepté).
- 2- P. Muret, A. Traoré, **A. Maréchal**, D. Eon, J. Pernot, J. Pinero, M. P. Villar, and D. Araujo, “*Potential barrier heights at metal on oxygen-terminated diamond interfaces*,” arXiv:1501.04790 [cond-mat], Jan. 2015.
- 3- J. C. Pinero, D. Araujo, A. Traore, G. Chicot, **A. Marechal**, P. Muret, M. P. Alegre, M. P. Villar, and J. Pernot, “*Metal-oxide-diamond interface investigation by TEM: Toward MOS and Schottky power device behavior*,” Phys. Status Solidi A-Apl. Mat., vol. 211, no. 10, pp. 2367–2371, Oct. 2014.
- 4- **A. Maréchal**, N. Rouger, J.-C. Crébier, J. Pernot, S. Koizumi, T. Teraji, and E. Gheeraert, “*Model implementation towards the prediction of  $J(V)$  characteristics in diamond bipolar device simulations*,” Diamond Relat. Mater., vol. 43, pp. 34–42, Mar. 2014.
- 5- **A. Maréchal**, N. Rouger, J.-C. Crébier, J. Pernot, S. Koizumi, T. Teraji, and E. Gheeraert, “*Diamond bipolar device simulation*,” 1st IEEE Workshop on Wide Bandgap Power Devices and Applications (WIPDA) 151 (2013).
- 6- G. Chicot, **A. Maréchal**, R. Motte, P. Muret, E. Gheeraert, and J. Pernot, “*Metal oxide semiconductor structure using oxygen-terminated diamond*,” Appl. Phys. Lett., vol. 102, no. 24, pp. 242108–242108–5, Jun. 2013.

## CONFERENCES

### ORAUX

- 1- **A. Maréchal**, C. Rivière, J. Pernot, N. Rouger, D. Eon, P. Muret, M. Aoukar, C. Vallée and E. Gheeraert, *Energy band diagram configuration of  $Al_2O_3$ /Oxygen-terminated boron doped diamond metal-oxide-semiconductor capacitor*, International Conference on Diamond and Carbon Materials 2015, Bad Homburg, Germany.
- 2- **A. Maréchal**, C. Rivière, J. Pernot, N. Rouger, D. Eon, P. Muret, M. Aoukar, C. Vallée and E. Gheeraert, *Properties of  $Al_2O_3$ /Oxygen-terminated boron doped diamond metal-oxide-semiconductor capacitor*, 3rd French-Japanese Workshop on Diamond Power Devices 2015, Nîmes, France.
- 3- **A. Maréchal**, G Chicot, N Rouger, P Muret, J Pernot, E Gheeraert, *Leakage current mechanisms in ALD  $HfO_2$ ,  $ZrO_2$  and  $Al_2O_3$  on O-terminated diamond*, 2nd French-Japanese Workshop on Diamond Power Devices 2014, Kyushu, Japan.
- 4- **A. Maréchal**, G Chicot, N Rouger, P Muret, J Pernot, E Gheeraert, *Leakage current conduction mechanisms in atomic layer deposited  $HfO_2$ ,  $ZrO_2$  and  $Al_2O_3$  on O-terminated diamond*, International Conference on Diamond and Carbon Materials 2014, Madrid, Spain.

### POSTERS

- 1- **A. Maréchal**, G. Chicot, N. Rouger, P. Muret, J. Pernot and E. Gheeraert, *Determination of band alignments of atomic layer deposited  $HfO_2$ ,  $ZrO_2$  and  $Al_2O_3$  on O-terminated diamond*, International Hasselt Diamond workshop 2015, SBDD XX, Hasselt, Belgium.
- 2- **A. Maréchal**, G Chicot, N Rouger, P Muret, J Pernot, E Gheeraert, *Leakage current conduction mechanisms in atomic layer deposited  $HfO_2$ ,  $ZrO_2$  and  $Al_2O_3$  on O-terminated diamond*, International Conference on Diamond and Carbon Materials 2014, Madrid, Spain.
- 3- **A. Maréchal**, G Chicot, N Rouger, P Muret, J Pernot, E Gheeraert, *Comparison of atomic layer deposited  $HfO_2$ ,  $ZrO_2$  and  $Al_2O_3$  on O-terminated boron doped diamond*, International Hasselt Diamond workshop 2014, SBDD XIX, Hasselt, Belgium.
- 4- **A. Marechal**, N. Rouger, J.-C. Crebier, J. Pernot, S. Koizumi, T. Teraji, E. Gheeraert, *Diamond bipolar device simulation*, Wide Bandgap Power Devices and Applications (WIPDA), 2013, Columbus, Ohio, USA.
- 5- **A. Maréchal**, N Rouger, J.-C Crébier, J Pernot, S Koizumi, T Teraji, E Gheeraert, *Parameter adjustment for diamond electronic devices simulation*, International Hasselt Diamond workshop 2013, SBDD XVIII, Hasselt, Belgium.

## PRIX

Elsevier DCM Young Scholar Award (Gold) at International Conference on Diamond and Carbon Materials 2014, Madrid, Spain

## BREVET

*Procédé de fabrication d'un empilement MOS sur un substrat en diamant*

G. Chicot, **A. Maréchal**, P. Muret, J. Pernot. FR11 62052 (2011). Etendu aux pays du PCT en déc. 2012



# Bibliography

- [3M ] *Smart Grid - 3M Smart Grid - 3M France.*
- [Antoniou 2010] M. Antoniou, F. Udrea and F. Bauer. *The Superjunction Insulated Gate Bipolar Transistor Optimization and Modeling.* IEEE Transactions on Electron Devices, vol. 57, no. 3, pages 594–600, March 2010.
- [Ariki 1994] Takuya Ariki, Shozo Shikama, Sei Suzuki, Yuzuru Otsuka, Tetsuro Maki and Takeshi Kobayashi. *Efficient Field Effect in Heavily Doped Thin-Film Diamond Metal-Insulator-Semiconductor Diode Employing BaTiO<sub>3</sub> Insulator Film.* Japanese Journal of Applied Physics, vol. 33, no. 6B, page L888, June 1994.
- [Baliga 1982] B. J. Baliga. *Semiconductors for high-voltage, vertical channel field-effect transistors.* Journal of Applied Physics, vol. 53, no. 3, page 1759, March 1982.
- [Baliga 1989] B. J. Baliga. *Power semiconductor device figure of merit for high-frequency applications.* Electron Device Letters, IEEE, vol. 10, no. 10, pages 455–457, October 1989.
- [Baliga 2012] B. Jayant Baliga. *Advanced High Voltage Power Device Concepts.* Springer New York, New York, NY, 2012.
- [Barjon 2014] J. Barjon, F. Jomard and S. Morata. *Arsenic-bound excitons in diamond.* Physical Review B, vol. 89, no. 4, page 045201, January 2014.
- [Borst 1995] T. H. Borst and O. Weis. *Electrical characterization of homoepitaxial diamond films doped with B, P, Li and Na during crystal growth.* Diamond and Related Materials, vol. 4, no. 7, pages 948–953, May 1995.

- [Boukherroub 2005] Rabah Boukherroub, Xavier Wallart, Sabine Szunerits, Bernadette Marcus, Pierre Bouvier and Michel Mermoux. *Photochemical oxidation of hydrogenated boron-doped diamond surfaces*. *Electrochemistry Communications*, vol. 7, no. 9, pages 937–940, September 2005.
- [Brezeanu 2008] M. Brezeanu, T. Butler, G.A.J. Amaratunga, F. Udrea, N. Rupesinghe and S. Rashid. *On-state behaviour of diamond Schottky diodes*. *Diamond and Related Materials*, vol. 17, no. 4–5, pages 736–740, April 2008.
- [Butler 2003] J. E. Butler, M. W. Geis, K. E. Krohn, J. Lawless Jr, S. Deneault, T. M. Lyszczarz, D. Flechtner and R. Wright. *Exceptionally high voltage Schottky diamond diodes and low boron doping*. *Semiconductor Science and Technology*, vol. 18, no. 3, page S67, March 2003.
- [Chelikowsky 1984] James R. Chelikowsky and Steven G. Louie. *First-principles linear combination of atomic orbitals method for the cohesive and structural properties of solids: Application to diamond*. *Physical Review B*, vol. 29, no. 6, pages 3470–3481, March 1984.
- [Cheng 2012] Shaoheng Cheng, Liwen Sang, Meiyong Liao, Jiangwei Liu, Masataka Imura, Hongdong Li and Yasuo Koide. *Integration of high-dielectric constant Ta<sub>2</sub>O<sub>5</sub> oxides on diamond for power devices*. *Applied Physics Letters*, vol. 101, no. 23, page 232907, December 2012.
- [Cheong 2007] Kuan Yew Cheong, Jeong Hyun Moon, Hyeong Joon Kim, Wook Bahng and Nam-Kyun Kim. *Analysis of current conduction mechanisms in atomic-layer-deposited Al<sub>2</sub>O<sub>3</sub> gate on 4H silicon carbide*. *Applied Physics Letters*, vol. 90, no. 16, page 162113, April 2007.
- [Chicot 2012] G. Chicot, T. N. Tran Thi, A. Fiori, F. Jomard, E. Gheeraert, E. Bustarret and J. Pernot. *Hole transport in boron delta-doped diamond structures*. *Applied Physics Letters*, vol. 101, no. 16, pages 162101–162101–4, October 2012.
- [Chicot 2013a] G. Chicot. *Field effect in boron doped diamond*. PhD Thesis, Université de Grenoble, 2013.
- [Chicot 2013b] G. Chicot, A. Marfchal, R. Motte, P. Muret, E. Gheeraert and J. Pernot. *Metal oxide semiconductor structure using oxygen-terminated diamond*. *Applied Physics Letters*, vol. 102, no. 24, pages 242108–242108–5, June 2013.

- [Chiu 2014] Fu-Chien Chiu. *A Review on Conduction Mechanisms in Dielectric Films*. Advances in Materials Science and Engineering, vol. 2014, page e578168, February 2014.
- [Clark 1964] C. D. Clark, P. J. Dean and P. V. Harris. *Intrinsic Edge Absorption in Diamond*. Proceedings of the Royal Society A: Mathematical, Physical and Engineering Sciences, vol. 277, no. 1370, pages 312–329, February 1964.
- [CREE ] CREE. *Z-FeTTM Silicon Carbide MOSFET*, [www.cree.com](http://www.cree.com).
- [Daicho 2014] Akira Daicho, Tatsuya Saito, Shinichiro Kurihara, Atsushi Hiraiwa and Hiroshi Kawarada. *High-reliability passivation of hydrogen-terminated diamond surface by atomic layer deposition of Al<sub>2</sub>O<sub>3</sub>*. Journal of Applied Physics, vol. 115, no. 22, page 223711, June 2014.
- [Deguchi 1996] Masahiro Deguchi, Makoto Kitabatake and Takashi Hirao. *Electrical properties of boron-doped diamond films prepared by microwave plasma chemical vapour deposition*. Thin Solid Films, vol. 281–282, pages 267–270, August 1996.
- [Department for Business 2011] Innovation & Skills Department for Business. *The UK Power electronics industry: a strategy for success - keeping the UK competitive.*, 2011.
- [Dimitrijević 2015] Sima Dimitrijević, Jisheng Han, Hamid Amini Moghadam and Amirhossein Aminbeidokhti. *Power-switching applications beyond silicon: Status and future prospects of SiC and GaN devices*. MRS Bulletin, vol. 40, no. 05, pages 399–405, May 2015.
- [Ding 2010] H. Ding, K. Isoird, H. Schneider, S. Kone and G. Civrac. *Basic parameters and models in simulation of CVD diamond devices*. Diamond and Related Materials, vol. 19, no. 5–6, pages 500–502, May 2010.
- [Dziewior 1977] J. Dziewior and W. Schmid. *Auger coefficients for highly doped and highly excited silicon*. Applied Physics Letters, vol. 31, no. 5, pages 346–348, September 1977.
- [Eeckhout 2015] Laetitia Van Eeckhout. *Avant 2022, les Indiens seront 1,4 milliard, plus nombreux que les Chinois*. Le Monde.fr, July 2015.

- [El-Hajj 2008] H. El-Hajj, A. Denisenko, A. Kaiser, R.S. Balmer and E. Kohn. *Diamond MISFET based on boron delta-doped channel*. *Diamond and Related Materials*, vol. 17, no. 7&Agrave;10, pages 1259–1263, July 2008.
- [Engel-Herbert 2010] Roman Engel-Herbert, Yoontae Hwang and Susanne Stemmer. *Comparison of methods to quantify interface trap densities at dielectric/III-V semiconductor interfaces*. *Journal of Applied Physics*, vol. 108, no. 12, page 124101, December 2010.
- [Engström 2014] Olof Engström. *The MOS System*. Cambridge University Press, September 2014.
- [Fiori 2012] A. Fiori. *Nouvelles générations de structures en diamant dopé au bore par technique de delta-dopage pour l'électronique de puissance: croissance par CVD et caractérisation*. PhD Thesis, Université de Grenoble, 2012.
- [Fiori 2014] A. Fiori, T. Teraji and Y. Koide. *Diamond Schottky diodes with ideality factors close to 1*. *Applied Physics Letters*, vol. 105, no. 13, page 133515, September 2014.
- [Fujimori 1990] Naoji Fujimori, Hideaki Nakahata and Takahiro Imai. *Properties of Boron-Doped Epitaxial Diamond Films*. *Japanese Journal of Applied Physics*, vol. 29, no. 5R, page 824, May 1990.
- [Fujiwara 2009] Hiroyuki Fujiwara. *Spectroscopic ellipsometry principles and applications*. Wiley, Chichester [u.a.], printed with corr édition, 2009.
- [Gajewski 2009] W. Gajewski, P. Achatz, O. A. Williams, K. Haenen, E. Bustarret, M. Stutzmann and J. A. Garrido. *Electronic and optical properties of boron-doped nanocrystalline diamond films*. *Physical Review B*, vol. 79, no. 4, page 045206, January 2009.
- [Garino 2012] Y. Garino, T. Teraji, A. Lazea and S. Koizumi. *Forward tunneling current in {111}-oriented homoepitaxial diamond p&Agrave;n junction*. *Diamond and Related Materials*, vol. 21, no. 0, pages 33–36, January 2012.

- [Geis 1991] M.W. Geis, J.A. Gregory and B.B. Pate. *Capacitance-voltage measurements on metal-SiO<sub>2</sub>-diamond structures fabricated with (100)- and (111)-oriented substrates*. IEEE Transactions on Electron Devices, vol. 38, no. 3, pages 619–626, March 1991.
- [Gheeraert 2000] E. Gheeraert, S. Koizumi, T. Teraji, H. Kanda and M. Nesladek. *Electronic states of phosphorus in diamond*. Diamond and Related Materials, vol. 9, no. 3–6, pages 948–951, April 2000.
- [Gheeraert 2001] E. Gheeraert, N. Casanova, S. Koizumi, T. Teraji and H. Kanda. *Low temperature excitation spectrum of phosphorus in diamond*. Diamond and Related Materials, vol. 10, no. 3–7, pages 444–448, March 2001.
- [Ghodbane 2006] S. Ghodbane, D. Ballutaud, A. Deneuve and C. Baron. *Influence of boron concentration on the XPS spectra of the (100) surface of homoepitaxial boron-doped diamond films*. physica status solidi (a), vol. 203, no. 12, pages 3147–3151, September 2006.
- [Hatano 2015] Mutsuko Hatano, Takayuki Iwasaki, Hiromitsu Kato, Toshiharu Makino, Masahiko Ogura, Daisuke Takeuchi and Satoshi Yamasaki. *Diamond junction FETs with the lateral p-n junctions*. In 3rd French-Japanese workshop on diamond power devices, Nîmes, 2015.
- [He 2002] Jin He, Xing Zhang, Yangyuan Wang and Xuemei Xi. *Optimum design of punch-through junction used in bipolar and unipolar high voltage power devices*. Solid-State Electronics, vol. 46, no. 6, pages 847–851, June 2002.
- [Hiraiwa 2012] Atsushi Hiraiwa, Akira Daicho, Shinichiro Kurihara, Yuki Yokoyama and Hiroshi Kawarada. *Refractory two-dimensional hole gas on hydrogenated diamond surface*. Journal of Applied Physics, vol. 112, no. 12, page 124504, December 2012.
- [Hiraiwa 2013] Atsushi Hiraiwa and Hiroshi Kawarada. *Figure of merit of diamond power devices based on accurately estimated impact ionization processes*. Journal of Applied Physics, vol. 114, no. 3, pages 034506–034506–9, July 2013.
- [Hiraiwa 2015] Atsushi Hiraiwa and Hiroshi Kawarada. *Blocking characteristics of diamond junctions with a punch-through design*. Journal of Applied Physics, vol. 117, no. 12, page 124503, March 2015.

- [Hoeb 2010] Marco Hoeb, Marianne Auernhammer, Sebastian J. Schoell, Martin S. Brandt, Jose A. Garrido, Martin Stutzmann and Ian D. Sharp. *Thermally Induced Alkylation of Diamond*. *Langmuir*, vol. 26, no. 24, pages 18862–18867, December 2010.
- [Hokazono 1999] A Hokazono, K Tsugawa, H Umezana, K Kitatani and H Kawarada. *Surface p-channel metal-oxide-semiconductor field effect transistors fabricated on hydrogen terminated (001) surfaces of diamond*. *Solid-State Electronics*, vol. 43, no. 8, pages 1465–1471, August 1999.
- [Hoshino 2012] Yuto Hoshino, Hiromitsu Kato, Toshiharu Makino, Masahiko Ogura, Takayuki Iwasaki, Mutsuko Hatano and Satoshi Yamasaki. *Electrical properties of lateral p-n junction diodes fabricated by selective growth of n<sup>+</sup> diamond*. *physica status solidi (a)*, vol. 209, no. 9, pages 1761–1764, September 2012.
- [Hosoda 2013] M. Hosoda, K. Kakushima, K. Natori, S. Yamasaki, H. Ohashi and H. Iwai. *On the electron conduction in n-diamond*. Ieee, New York, 2013. WOS:000319457000014.
- [Houssa 2000] M. Houssa, M. Tuominen, M. Naili, V. AfanasĀŽev, A. Stesmans, S. Haukka and M. M. Heyns. *Trap-assisted tunneling in high permittivity gate dielectric stacks*. *Journal of Applied Physics*, vol. 87, no. 12, pages 8615–8620, June 2000.
- [Howell 2008] Robert S. Howell, Steven Buchoff, Stephen Van Campen, Ty R. McNutt, Andris Ezis, Bettina Nechay, Christopher F. Kirby, Marc E. Sherwin, R. Chris Clarke and Ranbir Singh. *A 10-kV Large-Area 4H-SiC Power DMOSFET With Stable Subthreshold Behavior Independent of Temperature*. *IEEE Transactions on Electron Devices*, vol. 55, no. 8, pages 1807–1815, August 2008.
- [Iacopi 2015] Francesca Iacopi, Marleen Van Hove, Matthew Charles and Kazuhiro Endo. *Power electronics with wide bandgap materials: Toward greener, more efficient technologies*. *MRS Bulletin*, vol. 40, no. 05, pages 390–395, May 2015.
- [IEA 2015] IEA. *World Energy Outlook Special Report 2015: Energy and Climate Change*, 2015.
- [Iwasaki 2012] Takayuki Iwasaki, Yuto Hoshino, Kohei Tsuzuki, Hiromitsu Kato, Toshiharu Makino, Masahiko Ogura, Daisuke Takeuchi, Tsubasa Matsumoto, Hideyo

- Okushi, Satoshi Yamasaki and Mutsuko Hatano. *Diamond Junction Field-Effect Transistors with Selectively Grown  $n^+$ -Side Gates*. Applied Physics Express, vol. 5, no. 9, page 091301, 2012.
- [Iwasaki 2013] Takayuki Iwasaki, Yuto Hoshino, Kohei Tsuzuki, Hiromitsu Kato, Toshiharu Makino, Masahiko Ogura, Daisuke Takeuchi, Hideyo Okushi, Satoshi Yamasaki and Mutsuko Hatano. *High-Temperature Operation of Diamond Junction Field-Effect Transistors With Lateral  $p$ - $n$  Junctions*. IEEE Electron Device Letters, vol. 34, no. 9, pages 1175–1177, September 2013.
- [Iwasaki 2014] T. Iwasaki, J. Yaita, H. Kato, T. Makino, M. Ogura, D. Takeuchi, H. Okushi, S. Yamasaki and M. Hatano. *600 V Diamond Junction Field-Effect Transistors Operated at 200*. IEEE Electron Device Letters, vol. 35, no. 2, pages 241–243, February 2014.
- [Johnson 1965] E. Johnson. *Physical limitations on frequency and power parameters of transistors*. In IRE International Convention Record, volume 13, pages 27–34, 1965.
- [Kagata 2013] Yuma Kagata, Youhei Oda, Keita Hayashi, Nozomu Akagi, Takumi Shibata, Kouzi Eguchi, Tsuyoshi Yamamoto and Hitoshi Yamaguchi. *600 V-class Trench-Filling Super Junction Power MOSFETs for Low Loss and Low Leakage Current*. In 2013 25th International Symposium on Power Semiconductor Devices and Ics (ispd), pages 225–228. Ieee, New York, 2013. WOS:000331229500051.
- [Kahng 1976] D. Kahng. *A historical perspective on the development of MOS transistors and related devices*. IEEE Transactions on Electron Devices, vol. 23, no. 7, pages 655–657, July 1976.
- [Kamo 1983] M. Kamo, Y. Sato, S. Matsumoto and N. Setaka. *Diamond synthesis from gas phase in microwave plasma*. Journal of Crystal Growth, vol. 62, pages 642–644, 1983.
- [Kato 2005] Hiromitsu Kato, Satoshi Yamasaki and Hideyo Okushi.  *$n$ -type doping of (001)-oriented single-crystalline diamond by phosphorus*. Applied Physics Letters, vol. 86, no. 22, pages 222111–222111–3, May 2005.

- [Kato 2007] Hiromitsu Kato, Toshiharu Makino, Satoshi Yamasaki and Hideyo Okushi. *n-type diamond growth by phosphorus doping on (0 0 1)-oriented surface*. Journal of Physics D: Applied Physics, vol. 40, no. 20, page 6189, October 2007.
- [Kato 2008] Hiromitsu Kato, Hitoshi Umezawa, Norio Tokuda, Daisuke Takeuchi, Hideyo Okushi and Satoshi Yamasaki. *Low specific contact resistance of heavily phosphorus-doped diamond film*. Applied Physics Letters, vol. 93, no. 20, pages 202103–202103–3, November 2008.
- [Kato 2009] Hiromitsu Kato, Toshiharu Makino, Masahiko Ogura, Norio Tokuda, Hideyo Okushi and Satoshi Yamasaki. *Selective Growth of Buried  $n^{+}$  Diamond on (001) Phosphorus-Doped n-Type Diamond Film*. Applied Physics Express, vol. 2, no. 5, page 055502, 2009.
- [Kato 2012] Hiromitsu Kato, Kazuhiro Oyama, Toshiharu Makino, Masahiko Ogura, Daisuke Takeuchi and Satoshi Yamasaki. *Diamond bipolar junction transistor device with phosphorus-doped diamond base layer*. Diamond and Related Materials, vol. 27–28, no. 0, pages 19–22, July 2012.
- [Kato 2013] Hiromitsu Kato, Toshiharu Makino, Masahiko Ogura, Daisuke Takeuchi and Satoshi Yamasaki. *Fabrication of bipolar junction transistor on (001)-oriented diamond by utilizing phosphorus-doped n-type diamond base*. Diamond and Related Materials, vol. 34, pages 41–44, April 2013.
- [Kawakami 2005] Nobuyuki Kawakami, Yoshihiro Yokota, Takeshi Tachibana, Kazushi Hayashi and Koji Kobashi. *Atomic layer deposition of  $Al_2O_3$  thin films on diamond*. Diamond and Related Materials, vol. 14, no. 11–12, pages 2015–2018, November 2005.
- [Kawarada 1994] Hiroshi Kawarada, Makoto Aoki and Masahiro Ito. *Enhancement mode metal–semiconductor field effect transistors using homoepitaxial diamonds*. Applied Physics Letters, vol. 65, no. 12, pages 1563–1565, September 1994.
- [Kawarada 2012] Hiroshi Kawarada. *High-Current Metal Oxide Semiconductor Field-Effect Transistors on H-Terminated Diamond Surfaces and Their High-Frequency Operation*. Japanese Journal of Applied Physics, vol. 51, no. 9R, page 090111, September 2012.

- [Kawarada 2014] H. Kawarada, H. Tsuboi, T. Naruo, T. Yamada, D. Xu, A. Daicho, T. Saito and A. Hiraiwa. *C-H surface diamond field effect transistors for high temperature (400 ÅřC) and high voltage (500 V) operation*. Applied Physics Letters, vol. 105, no. 1, page 013510, July 2014.
- [Keyes 1972] R. W. Keyes. *Figure of merit for semiconductors for high-speed switches*. Proceedings of the IEEE, vol. 60, no. 2, pages 225–225, 1972.
- [KeysightTechnologies 2014] KeysightTechnologies. *Keysight E4980A/AL Precision LCR Meter, User’s Guide*, November 2014.
- [Kim 2006] Hyeong Joon Kim. *Property Improvement of Aluminum-Oxide Thin Films Deposited under Photon Radiation by Using Atomic Layer Deposition*. Journal of the Korean Physical Society, vol. 49, no. 3, pages 1271–1275, September 2006.
- [Klein 2007] T. Klein, P. Achatz, J. Kacmarcik, C. Marcenat, F. Gustafsson, J. Marcus, E. Bustarret, J. Pernot, F. Omnes, Bo E. Sernelius, C. Persson, A. Ferreira da Silva and C. Cytermann. *Metal-insulator transition and superconductivity in boron-doped diamond*. Physical Review B, vol. 75, no. 16, page 165313, April 2007.
- [Koide 2004] Yasuo Koide. *Depletion layer in pn-junction of diamond with phosphorus donor and boron acceptor*. Diamond and Related Materials, vol. 13, no. 11–12, pages 1963–1966, November 2004.
- [Koide 2015] Yasuo Koide. *H-Diamond MOSFETs with high-k oxide gate*. Nîmes, 2015.
- [Koizumi 1997] S. Koizumi, M. Kamo, Y. Sato, H. Ozaki and T. Inuzuka. *Growth and characterization of phosphorous doped {111} homoepitaxial diamond thin films*. Applied Physics Letters, vol. 71, no. 8, pages 1065–1067, August 1997.
- [Koizumi 2000] Satoshi Koizumi, Tokuyuki Teraji and Hisao Kanda. *Phosphorus-doped chemical vapor deposition of diamond*. Diamond and Related Materials, vol. 9, no. 3–6, pages 935–940, April 2000.
- [Koizumi 2002] Satoshi Koizumi, Kenji Watanabe, Masataka Hasegawa and Hisao Kanda. *Formation of diamond p–Sn junction and its optical emission characteristics*. Diamond and Related Materials, vol. 11, no. 3–6, pages 307–311, March 2002.

- [Koizumi 2013] Satoshi Koizumi and Toshiharu Makino. *n-Type Diamond Growth and Homoepitaxial Diamond Junction Devices*. In Rich P. Mildren and James R. Rabeau, editors, *Optical Engineering of Diamond*, pages 177–208. Wiley-VCH Verlag GmbH & Co. KGaA, Weinheim, Germany, March 2013.
- [Kolar 2012] J. W. Kolar, F. Krismer, Y. Lobsiger, J. Mühlethaler, T. Nussbaumer and J. Miniböck. *Extreme Efficiency Power Electronics*. Nuremberg, Germany, March 2012.
- [Kovi 2015] Kiran Kumar Kovi, Orjan Vallin, Saman Majdi and Jan Isberg. *Inversion in Metal-Oxide-Semiconductor Capacitors on Boron Doped Diamond*. *IEEE Electron Device Letters*, pages 1–1, 2015.
- [Kraut 1980] E. A. Kraut, R. W. Grant, J. R. Waldrop and S. P. Kowalczyk. *Precise Determination of the Valence-Band Edge in X-Ray Photoemission Spectra: Application to Measurement of Semiconductor Interface Potentials*. *Physical Review Letters*, vol. 44, no. 24, pages 1620–1623, June 1980.
- [Lagrange 1998] J.-P. Lagrange, A. Deneuville and E. Gheeraert. *Activation energy in low compensated homoepitaxial boron-doped diamond films*. *Diamond and Related Materials*, vol. 7, no. 9, pages 1390–1393, September 1998.
- [Lagrange 1999] J. P. Lagrange, A. Deneuville and E. Gheeraert. *A large range of boron doping with low compensation ratio for homoepitaxial diamond films*. *Carbon*, vol. 37, no. 5, pages 807–810, April 1999.
- [Lane 1980] W.A. Lane and C.A.T. Salama. *Epitaxial VVMOS power transistors*. *IEEE Transactions on Electron Devices*, vol. 27, no. 2, pages 349–355, February 1980.
- [Liao 2015] Meiyong Liao, Jiangwei Liu, Liwen Sang, David Coathup, Jiangling Li, Masataka Imura, Yasuo Koide and Haitao Ye. *Impedance analysis of Al<sub>2</sub>O<sub>3</sub>/H-terminated diamond metal-oxide-semiconductor structures*. *Applied Physics Letters*, vol. 106, no. 8, page 083506, February 2015.
- [Liu 2012] J. W. Liu, M. Y. Liao, M. Imura and Y. Koide. *Band offsets of Al<sub>2</sub>O<sub>3</sub> and HfO<sub>2</sub> oxides deposited by atomic layer deposition technique on hydrogenated diamond*. *Applied Physics Letters*, vol. 101, no. 25, page 252108, December 2012.

- [Liu 2013a] J. W. Liu, M. Y. Liao, M. Imura and Y. Koide. *Normally-off HfO<sub>2</sub>-gated diamond field effect transistors*. Applied Physics Letters, vol. 103, no. 9, page 092905, August 2013.
- [Liu 2013b] J. W. Liu, M. Y. Liao, M. Imura, H. Oosato, E. Watanabe, A. Tanaka, H. Iwai and Y. Koide. *Interfacial band configuration and electrical properties of LaAlO<sub>3</sub>/Al<sub>2</sub>O<sub>3</sub>/hydrogenated-diamond metal-oxide-semiconductor field effect transistors*. Journal of Applied Physics, vol. 114, no. 8, page 084108, August 2013.
- [Liu 2014a] J.-W. Liu, M.-Y. Liao, M. Imura, E. Watanabe, H. Oosato and Y. Koide. *Diamond field effect transistors with a high-dielectric constant Ta<sub>2</sub>O<sub>5</sub> as gate material*. Journal of Physics D: Applied Physics, vol. 47, no. 24, page 245102, June 2014.
- [Liu 2014b] Jiangwei Liu, Meiyong Liao, Masataka Imura, Akihiro Tanaka, Hideo Iwai and Yasuo Koide. *Low on-resistance diamond field effect transistor with high-k ZrO<sub>2</sub> as dielectric*. Scientific Reports, vol. 4, September 2014.
- [Liu 2014c] Jiangwei Liu, Meiyong Liao, Masataka Imura, Akihiro Tanaka, Hideo Iwai and Yasuo Koide. *Low on-resistance diamond field effect transistor with high-k ZrO<sub>2</sub> as dielectric*. Scientific Reports, vol. 4, September 2014.
- [Look 1989] D. C. Look. *Electrical characterization of GaAs materials and devices. Design and measurement in electronic engineering*. Wiley, Chichester ; New York, 1989.
- [Makino 2006] Toshiharu Makino, Hiromitsu Kato, Masahiko Ogura, Hideyuki Watanabe, Sung-Gi Ri, Y.G. Chen, Satoshi Yamasaki and Hideyo Okushi. *Electrical and optical characterizations of (001)-oriented homoepitaxial diamond p<sup>+</sup>n junction*. Diamond and Related Materials, vol. 15, no. 4, pages 513–516, April 2006.
- [Makino 2008] Toshiharu Makino, Hiromitsu Kato, Sung-Gi Ri, Satoshi Yamasaki and Hideyo Okushi. *Homoepitaxial diamond p<sup>+</sup>n<sup>+</sup> junction with low specific on-resistance and ideal built-in potential*. Diamond and Related Materials, vol. 17, no. 4, pages 782–785, April 2008.

- [Makino 2009] Toshiharu Makino, Satoshi Tanimoto, Yusuke Hayashi, Hiromitsu Kato, Norio Tokuda, Masahiko Ogura, Daisuke Takeuchi, Kazuhiro Oyama, Hiromichi Ohashi, Hideyo Okushi and Satoshi Yamasaki. *Diamond Schottky-pn diode with high forward current density and fast switching operation*. Applied Physics Letters, vol. 94, no. 26, page 262101, June 2009.
- [Makino 2012] Toshiharu Makino, Shokichi Kanno, Satoshi Yamasaki, Hiromitsu Kato and Hideyo Okushi. *Nonlinear behavior of current-dependent emission for diamond light-emitting diodes*. physica status solidi (a), vol. 209, no. 9, pages 1754–1760, September 2012.
- [Maréchal 2015] Aurélien Maréchal, Manuela Aoukar, C. Vallée, Chloé Rivière, David Eon, Julien Pernot and Etienne Gheeraert. *Energy-band diagram configuration of Al<sub>2</sub>O<sub>3</sub>/Oxygen-terminated p-diamond metal-oxide-semiconductor*. Applied Physics Letters, vol. Submitted, 2015.
- [Martens 2008] Koen Martens, Chi On Chui, Guy Brammertz, Brice De Jaeger, Duygu Kuzum, Marc Meuris, Marc Heyns, Tejas Krishnamohan, Krishna Saraswat, Herman E. Maes and Guido Groeseneken. *On the Correct Extraction of Interface Trap Density of MOS Devices With High-Mobility Semiconductor Substrates*. IEEE Transactions on Electron Devices, vol. 55, no. 2, pages 547–556, February 2008.
- [Masetti 1983] G. Masetti, Maurizio Severi and Sandro Solmi. *Modeling of carrier mobility against carrier concentration in arsenic-, phosphorus-, and boron-doped silicon*. IEEE Transactions on Electron Devices, vol. 30, no. 7, pages 764–769, 1983.
- [Massarani 1978] B. Massarani, J. C. Bourgoin and R. M. Chrenko. *Hopping conduction in semiconducting diamond*. Physical Review B, vol. 17, no. 4, pages 1758–1769, February 1978.
- [Mathieu 2004] Henry Mathieu. Physique des semiconducteurs et des composants Électroniques. Dunod, Paris, 2004.
- [Matsumoto 2014] Tsubasa Matsumoto, Hiromitsu Kato, Norio Tokuda, Toshiharu Makino, Masahiko Ogura, Daisuke Takeuchi, Hideyo Okushi and Satoshi Yamasaki. *Reduction of n-type diamond contact resistance by graphite electrode*.

- physica status solidi (RRL) – Rapid Research Letters, vol. 8, no. 2, pages 137–140, February 2014.
- [Monserrat 2014] Bartomeu Monserrat and R. J. Needs. *Comparing electron-phonon coupling strength in diamond, silicon, and silicon carbide: First-principles study*. Physical Review B, vol. 89, no. 21, page 214304, June 2014.
- [Mott 1987] N. F. Mott. *Conduction in non-crystalline materials*. Clarendon Press ; Oxford University Press, Oxford; New York, 1987.
- [Moulder 1992] John F. Moulder, Jill Chastain and Roger C. King. *Handbook of X-ray photoelectron spectroscopy: a reference book of standard spectra for identification and interpretation of XPS data*. Perkin-Elmer Eden Prairie, MN, 1992.
- [Muret 2014] Pierre R. Muret. *Comprehensive characterization of interface and oxide states in metal/oxide/semiconductor capacitors by pulsed mode capacitance and differential isothermal capacitance spectroscopy*. Journal of Vacuum Science & Technology B, vol. 32, no. 3, page 03D114, May 2014.
- [Muret 2015] P. Muret, D. Eon, A. Traoré, A. Maréchal, J. Pernot and E. Gheeraert. *Hole injection contribution to transport mechanisms in metal/p<sup>+</sup>/p<sup>++</sup> and metal/oxide/p<sup>+</sup>/p<sup>++</sup> diamond structures*. physica status solidi (a), pages n/a–n/a, August 2015.
- [Naka 2013] Nobuko Naka, Katsuyuki Fukai, Yushi Handa and Ikuko Akimoto. *Direct measurement via cyclotron resonance of the carrier effective masses in pristine diamond*. Physical Review B, vol. 88, no. 3, page 035205, July 2013.
- [Nakanishi 1994] Jiro Nakanishi, A. Otsuki, T. Oku, O. Ishiwata and Masanori Murakami. *Formation of ohmic contacts to p<sup>+</sup> type diamond using carbide forming metals*. Journal of Applied Physics, vol. 76, no. 4, pages 2293–2298, August 1994.
- [Nanjo 2013] T. Nanjo, A. Imai, Y. Suzuki, Y. Abe, T. Oishi, M. Suita, E. Yagyu and Y. Tokuda. *AlGa<sub>N</sub> Channel HEMT With Extremely High Breakdown Voltage*. IEEE Transactions on Electron Devices, vol. 60, no. 3, pages 1046–1053, March 2013.

- [Nawawi 2011] Arie Nawawi, King Jet Tseng, Rusli Rusli and Gehan A. J. Amaratunga. *Switching characteristics of diamond-based m-i-p+ diodes in power electronic applications*. pages 2676–2680. IEEE, September 2011.
- [Nicollian 1982] E. H Nicollian and J. R Brews. *MOS (metal oxide semiconductor) physics and technology*. Wiley-Interscience, Hoboken, N.J., 1982.
- [Noborio 2009] Masato Noborio, J. Suda and T. Kimoto. *1580-V #x2013;40- Double-RESURF MOSFETs on 4H-SiC*. IEEE Electron Device Letters, vol. 30, no. 8, pages 831–833, August 2009.
- [Ohashi 2012] Hiromichi Ohashi. *Power devices now and future, strategy of Japan*. pages 9–12. IEEE, June 2012.
- [Okano 1989] Ken Okano, Hidetoshi Naruki, Yukio Akiba, Tateki Kurosu, Masamori Iida, Yoichi Hirose and Terutaro Nakamura. *Characterization of Boron-Doped Diamond Film*. Japanese Journal of Applied Physics, vol. 28, no. 6R, page 1066, June 1989.
- [Okumura 2015] Hajime Okumura. *A roadmap for future wide bandgap semiconductor power electronics*. MRS Bulletin, vol. 40, no. 05, pages 439–444, May 2015.
- [Omnès 2011] Franck Omnès, Pierre Muret, Pierre-Nicolas Volpe, Mamadou Wade, Julien Pernot and François Jomard. *Study of boron doping in MPCVD grown homoepitaxial diamond layers based on cathodoluminescence spectroscopy, secondary ion mass spectroscopy and capacitance–voltage measurements*. Diamond and Related Materials, vol. 20, no. 7, pages 912–916, July 2011.
- [Ortiz-Conde 2002] A. Ortiz-Conde, F. J. Garc a S nchez, J. J. Liou, A. Cerdeira, M. Estrada and Y. Yue. *A review of recent MOSFET threshold voltage extraction methods*. Microelectronics Reliability, vol. 42, no. 4–5, pages 583–596, April 2002.
- [Otsuka 1995] Yuzuru Otsuka, Sei Suzuki, Shozo Shikama, Tetsuro Maki and Takeshi Kobayashi. *Fermi Level Pinning in Metal-Insulator-Diamond Structures*. Japanese Journal of Applied Physics, vol. 34, no. 5A, page L551, May 1995.

- [Oyama 2009] Kazuhiro Oyama, Sung-Gi Ri, Hiromitsu Kato, Masahiko Ogura, Toshiharu Makino, Daisuke Takeuchi, Norio Tokuda, Hideyo Okushi and Satoshi Yamasaki. *High performance of diamond p+-i-n+ junction diode fabricated using heavily doped p+ and n+ layers*. Applied Physics Letters, vol. 94, no. 15, pages 152109–152109–2, April 2009.
- [Pearson 1949] G. L. Pearson and J. Bardeen. *Electrical Properties of Pure Silicon and Silicon Alloys Containing Boron and Phosphorus*. Physical Review, vol. 75, no. 5, pages 865–883, March 1949.
- [Perevalov 2007] T. V. Perevalov, A. V. Shaposhnikov, V. A. Gritsenko, H. Wong, J. H. Han and C. W. Kim. *Electronic structure of  $\dot{I}\dot{s}$ -Al<sub>2</sub>O<sub>3</sub>: Ab initio simulations and comparison with experiment*. JETP Letters, vol. 85, no. 3, pages 165–168, April 2007.
- [Pernot 2008] J. Pernot and S. Koizumi. *Electron mobility in phosphorous doped {111} homoepitaxial diamond*. Applied Physics Letters, vol. 93, no. 5, pages 052105–052105–3, August 2008.
- [Pernot 2010] J. Pernot, P. N. Volpe, F. OmnÃ¡s, P. Muret, V. Mortet, K. Haenen and T. Teraji. *Hall hole mobility in boron-doped homoepitaxial diamond*. Physical Review B, vol. 81, no. 20, page 205203, May 2010.
- [Pinault-Thaury 2011] M. A. Pinault-Thaury, T. Tillocher, N. Habka, D. Kobor, F. Jomard, J. Chevallier and J. Barjon. *n-Type CVD diamond: Epitaxy and doping*. Materials Science and Engineering: B, vol. 176, no. 17, pages 1401–1408, October 2011.
- [Pinault 2007] M. A. Pinault, J. Barjon, T. Kociniewski, F. Jomard and J. Chevallier. *The n-type doping of diamond: Present status and pending questions*. Physica B: Condensed Matter, vol. 401–402, pages 51–56, December 2007.
- [Rashid 2006] S.J. Rashid, A. Tajani, L. Coulbeck, M. Brezeanu, A. Garraway, T. Butler, N.L. Rupesinghe, D.J. Twitchen, G.A.J. Amaratunga, F. Udrea, P. Taylor, M. Dixon and J. Isberg. *Modelling of single-crystal diamond Schottky diodes for high-voltage applications*. Diamond and Related Materials, vol. 15, no. 2–3, pages 317–323, February 2006.

- [Rashid 2008] S.J. Rashid, A. Tajani, D.J. Twitchen, L. Coulbeck, F. Udrea, T. Butler, N.L. Rupesinghe, M. Brezeanu, J. Isberg, A. Garraway, M. Dixon, R.S. Balmer, D. Chamund, P. Taylor and G. Amaratunga. *Numerical Parameterization of Chemical-Vapor-Deposited (CVD) Single-Crystal Diamond for Device Simulation and Analysis*. IEEE Transactions on Electron Devices, vol. 55, no. 10, pages 2744–2756, October 2008.
- [Raynaud 2010] Christophe Raynaud, Dominique Tournier, Hervé Morel and Dominique Planson. *Comparison of high voltage and high temperature performances of wide bandgap semiconductors for vertical power devices*. Diamond and Related Materials, vol. 19, no. 1, pages 1–6, January 2010.
- [Robertson 2000] John Robertson. *Band offsets of wide-band-gap oxides and implications for future electronic devices*. Journal of Vacuum Science & Technology B, vol. 18, no. 3, pages 1785–1791, May 2000.
- [Rouger 2015] N. Rouger. *Nouveau paradigme pour l'Œintégration des actifs en électronique de puissance*. HABILITATION A DIRIGER DES RECHERCHES, Université de Grenoble, Grenoble, 2015.
- [Russell 2012] S.A.O. Russell, S. Sharabi, A. Tallaire and D.A.J. Moran. *Hydrogen-Terminated Diamond Field-Effect Transistors With Cutoff Frequency of 53 GHz*. IEEE Electron Device Letters, vol. 33, no. 10, pages 1471–1473, October 2012.
- [Sah 1988] R.L-Y. Sah. *Evolution of the MOS transistor-from conception to VLSI*. Proceedings of the IEEE, vol. 76, no. 10, pages 1280–1326, October 1988.
- [Sato 2000] Toshimaro Sato, Kazutoshi Ohashi, Hiroyuki Sugai, Takashi Sumi, Katsuji Haruna, Hiroshi Maeta, Norimasa Matsumoto and Hideo Otsuka. *Transport of heavily boron-doped synthetic semiconductor diamond in the hopping regime*. Physical Review B, vol. 61, no. 19, pages 12970–12976, May 2000.
- [Schroder 2006] Dieter K Schroder. *Semiconductor material and device characterization*. IEEE Press ; Wiley, [Piscataway, NJ]; Hoboken, N.J., 2006.
- [Shklovskii 1984] B. I Shklovskii and A. L Efros. *Electronic properties of doped semiconductors*. Springer-Verlag, Berlin; New York, 1984.

- [Shockley 1948] W. Shockley and G. L. Pearson. *Modulation of Conductance of Thin Films of Semi-Conductors by Surface Charges*. Physical Review, vol. 74, no. 2, pages 232–233, July 1948.
- [Shockley 1952] W. Shockley and W. T. Read. *Statistics of the Recombinations of Holes and Electrons*. Physical Review, vol. 87, no. 5, pages 835–842, September 1952.
- [Shockley 1956] W. Shockley. *Transistor technology evokes new physics*. Nobel lecture, December 1956.
- [SILVACO 2010] Inc. SILVACO. ATLAS User's Manual. August 2010.
- [Simonot 2011] T. Simonot, H.X. Nguyen, N. Rouger, J.C. Crebier, A. Bourennane, L. Gerbaud and J.L. Sanchez. *Towards reduced threshold voltages for vertical power Mosfet transistors*. In 2011 IEEE International Symposium on Industrial Electronics (ISIE), pages 444–449, June 2011.
- [Stenger 2013] I. Stenger, M.-A. Pinault-Thaury, T. Kociniewski, A. Lusson, E. Chikoidze, F. Jomard, Y. Dumont, J. Chevallier and J. Barjon. *Impurity-to-band activation energy in phosphorus doped diamond*. Journal of Applied Physics, vol. 114, no. 7, page 073711, August 2013.
- [Svensson 1973] Christer Svensson and Ingemar Lundström. *Trap-assisted charge injection in MNOS structures*. Journal of Applied Physics, vol. 44, no. 10, pages 4657–4663, October 1973.
- [Sze 2007] S. M. Sze. Physics of semiconductor devices. Wiley-Interscience, Hoboken, N.J, 3rd ed édition, 2007.
- [Tanaka 1998] Hiroyuki Tanaka, Young Yun, Yusuke Shirakawa, Tetsuro Maki and Takeshi Kobayashi. *Improved Stability of Metal-Insulator-Diamond Semiconductor Interface by Employing BaF<sub>2</sub> Insulator Film*. Japanese Journal of Applied Physics, vol. 37, no. 12A, page L1444, December 1998.
- [Teraji 2008] T. Teraji, S. Koizumi and Y. Koide. *Ohmic contact for p-type diamond without postannealing*. Journal of Applied Physics, vol. 104, no. 1, pages 016104–016104–3, July 2008.

- [Teraji 2009] T. Teraji, Y. Garino, Y. Koide and T. Ito. *Low-leakage p-type diamond Schottky diodes prepared using vacuum ultraviolet light/ozon treatment*. Journal of Applied Physics, vol. 105, no. 12, page 126109, June 2009.
- [Terman 1962] L. M. Terman. *An investigation of surface states at a silicon/silicon oxide interface employing metal-oxide-silicon diodes*. Solid-State Electronics, vol. 5, no. 5, pages 285–299, September 1962.
- [Thion 2011] F. Thion, K. Isoird, D. Planson, M.-L. Locatelli and H. Ding. *Simulation and design of junction termination structures for diamond Schottky diodes*. Diamond and Related Materials, vol. 20, no. 5–6, pages 729–732, May 2011.
- [Tolbert 2005] L. M Tolbert, T. J. King, B. Ozpineci, G. Muralidharan, D. T. Rizy, A. S. Sabau, H. Zhang, W. Zhang, X. Yu, H. F. Huq and H. Liu. *Power electronics for distributed energy systems and transmission and distribution applications*. OAK RIDGE NATIONAL LABORATORY UT-BATTERELLE US DEPARTEMENT OF ENERGY, 2005.
- [Traoré 2014] A. Traoré, P. Muret, A. Fiori, D. Eon, E. Gheeraert and J. Pernot. *Zr/oxidized diamond interface for high power Schottky diodes*. Applied Physics Letters, vol. 104, no. 5, page 052105, February 2014.
- [Traoré 2015] Aboulaye Traoré. *High power diamond Schottky diode*. PhD thesis, Université de Grenoble, Grenoble, December 2015.
- [Udrea 2015] F. Udrea. *Wide bandgap devices for power electronics-their case versus silicon*. In 3rd French-Japanese workshop on diamond power devices, Nîmes, 2015.
- [Ueda 2006] K. Ueda, M. Kasu, Y. Yamauchi, T. Makimoto, M. Schwitters, D.J. Twitchen, G.A. Scarsbrook and S.E. Coe. *Diamond FET using high-quality polycrystalline diamond with  $f_T$  of 45 GHz and  $f_{max}$  of 120 GHz*. IEEE Electron Device Letters, vol. 27, no. 7, pages 570–572, July 2006.
- [Ueda 2010] Kenji Ueda and Makoto Kasu. *High Temperature Operation of Boron-Implanted Diamond Field-Effect Transistors*. Japanese Journal of Applied Physics, vol. 49, no. 4, page 04DF16, 2010.

- [Umezawa 2012] Hitoshi Umezawa, Masanori Nagase, Yukako Kato and Shin-ichi Shikata. *High temperature application of diamond power device*. Diamond and Related Materials, vol. 24, no. 0, pages 201–205, April 2012.
- [Umezawa 2013] Hitoshi Umezawa, Yukako Kato and Shin-ichi Shikata. *1  $\mu\text{m}$  On-Resistance Diamond Vertical-Schottky Barrier Diode Operated at 250  $^{\circ}\text{C}$* . Applied Physics Express, vol. 6, no. 1, page 011302, 2013.
- [Umezawa 2014] H. Umezawa, T. Matsumoto and S.-I. Shikata. *Diamond Metal-Semiconductor Field-Effect Transistor With Breakdown Voltage Over 1.5 kV*. IEEE Electron Device Letters, vol. 35, no. 11, pages 1112–1114, November 2014.
- [Varshni 1967] Y.P. Varshni. *Temperature dependence of the energy gap in semiconductors*. Physica, vol. 34, no. 1, pages 149–154, 1967.
- [Viljoen 1994] P. E. Viljoen, E. S. Lambers and P. H. Holloway. *Reaction between diamond and titanium for ohmic contact and metallization adhesion layers*. Journal of Vacuum Science & Technology B, vol. 12, no. 5, pages 2997–3005, September 1994.
- [Vincent 2008] Gilbert Vincent. *Metal oxide semiconductor structure and transistor behaviour using a single and simple graph ( $Q_{\text{eff}}$ ) which takes into account all the physical and electrical parameters*. Journal of Applied Physics, vol. 103, no. 7, page 074505, 2008.
- [Visser 1992] E P Visser, G J Bauhuis, G Janssen, W Vollenberg, J P van Enkevort and L J Giling. *Electrical conduction in homoepitaxial, boron-doped diamond films*. Journal of Physics: Condensed Matter, vol. 4, no. 36, pages 7365–7376, September 1992.
- [Vobecky 2014] J. Vobecky, T. Stiasny, V. Botan, K. Stiegler, U. Meier and M. Bellini. *New Thyristor Platform for UHVDC (>1 MV) Transmission*. In Renewable Energy and Energy Management; Proceedings of PCIM Europe 2014; International Exhibition and Conference for Power Electronics, Intelligent Motion, pages 1–6, May 2014.

- [Volpe 2009] Pierre-Nicolas Volpe, Julien Pernot, Pierre Muret and Franck Omnès. *High hole mobility in boron doped diamond for power device applications*. Applied Physics Letters, vol. 94, no. 9, pages 092102–092102–3, March 2009.
- [Volpe 2010] Pierre-Nicolas Volpe, Pierre Muret, Julien Pernot, Franck Omnès, Tokuyuki Teraji, Yasuo Koide, François Jomard, Dominique Planson, Pierre Brosselard, Nicolas Dheilily, Bertrand Vergne and Sigo Scharnholz. *Extreme dielectric strength in boron doped homoepitaxial diamond*. Applied Physics Letters, vol. 97, no. 22, pages 223501–223501–3, November 2010.
- [Werner 1997] M. Werner, R. Locher, W. Kohly, D.S. Holmes, S. Klose and H.J. Fecht. *The diamond Irvin curve*. Diamond and Related Materials, vol. 6, no. 2–4, pages 308–313, March 1997.
- [Werner 2003] Matthias Werner. *Diamond metallization for device applications*. Semiconductor Science and Technology, vol. 18, no. 3, page S41, March 2003.
- [Willatzen 1994] M. Willatzen, M. Cardona and N. E. Christensen. *Linear muffin-tin-orbital and  $k\text{-}\tilde{E}_p$  calculations of effective masses and band structure of semiconducting diamond*. Physical Review B, vol. 50, no. 24, pages 18054–18059, December 1994.
- [Windheim 1993] J. A. Von Windheim, V. Venkatesan, D. M. Malta and K. Das. *Electrical characterization of semiconducting diamond thin films and single crystals*. Journal of Electronic Materials, vol. 22, no. 4, pages 391–398, April 1993.
- [Yota 2013] Jiro Yota, Hong Shen and Ravi Ramanathan. *Characterization of atomic layer deposition  $\text{HfO}_2$ ,  $\text{Al}_2\text{O}_3$ , and plasma-enhanced chemical vapor deposition  $\text{Si}_3\text{N}_4$  as metal-insulator-metal capacitor dielectric for GaAs HBT technology*. Journal of Vacuum Science & Technology A: Vacuum, Surfaces, and Films, vol. 31, no. 1, page 01A134, 2013.